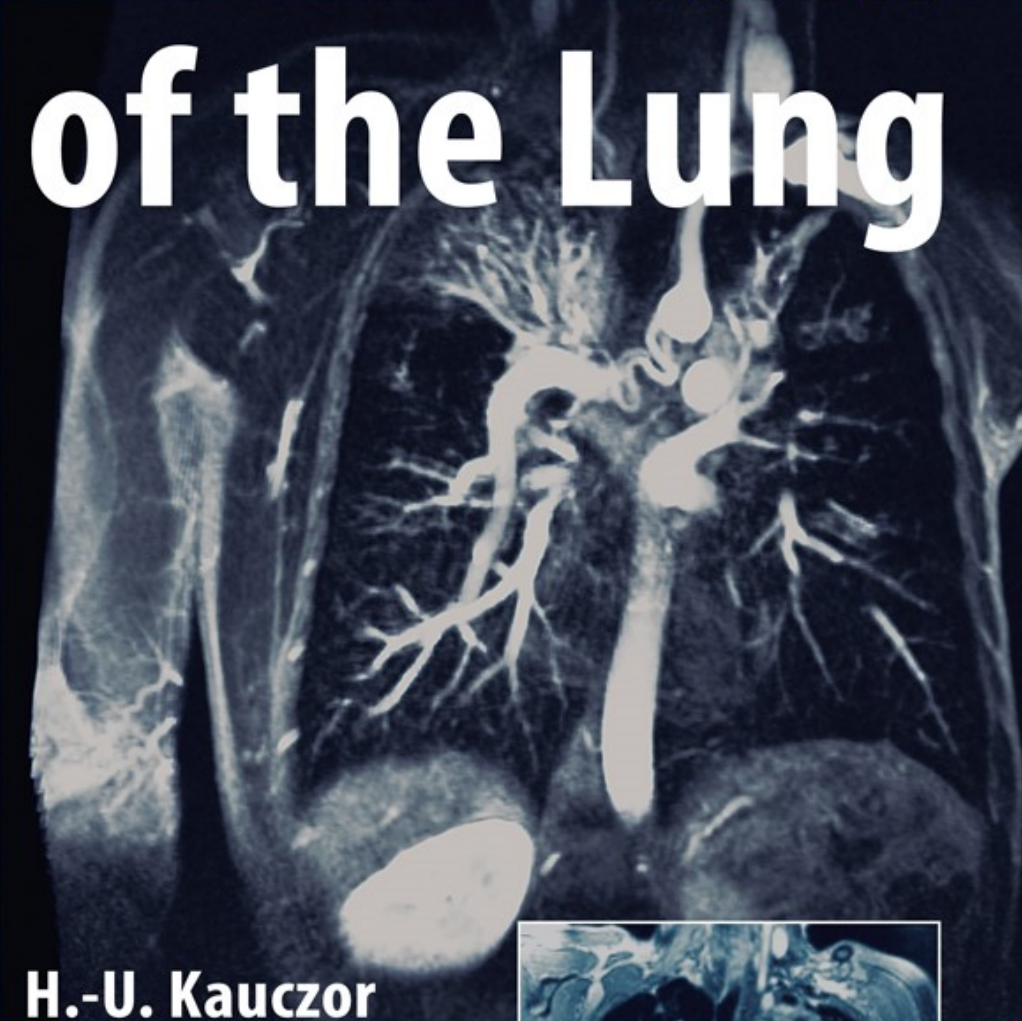


**MEDICAL
RADIOLOGY**

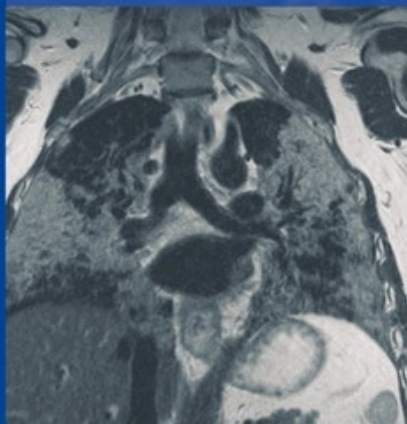
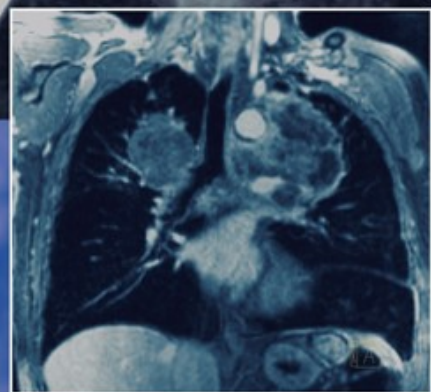
**Diagnostic
Imaging**

A.L. Baert
M. Knauth
K. Sartor

MRI of the Lung



H.-U. Kauczor
Editor



 Springer

MEDICAL RADIOLOGY

Diagnostic Imaging

Editors:

A.L. Baert, Leuven

M. Knauth, Göttingen

K. Sartor, Heidelberg

H.-U. Kauczor (Ed.)

MRI of the Lung

With Contributions by

T.A. Altes · J. Biederer · J.P. Butler · O. Dietrich · J. Dinkel · R. Eibel · M. Eichinger
S.B. Fain · C. Fink · A.F. Halaweish · H. Hatabu · C.P. Heussel · F.W. Hersman
C. Hintze · J.H. Holmes · M.I. Hrovat · H. Koyama · K.-F. Kreitner · S. Ley
J. Ley-Zaporozhan · K. Marten · F. Molinari · I. Muradian · Y. Ohno · S. Patz
C. Plathow · M. Puderbach · F. Risse · W.G. Schreiber · R.L. Sorkness · K. Takahashi
R. Tetzlaff · E.J.R. van Beek · J.M. Wild

Foreword by
A.L. Baert

HANS-ULRICH KAUCZOR, MD
Chairman, Medical Director
Diagnostic and Interventional Radiology
University Clinic Heidelberg
Im Neuenheimer Feld 110
69120 Heidelberg
Germany

MEDICAL RADIOLOGY · Diagnostic Imaging and Radiation Oncology

Series Editors:

A.L. Baert · L.W. Brady · H.-P. Heilmann · M. Knauth · M. Molls · C. Nieder · K. Sartor

Continuation of Handbuch der medizinischen Radiologie
Encyclopedia of Medical Radiology

ISBN 978-3-540-34618-0

e-ISBN 978-3-540-34619-7

DOI 10.1007/978-3-540-34619-7

Library of Congress Control Number: 2008925886

© 2009 Springer-Verlag Berlin Heidelberg

This work is subject to copyright. All rights are reserved, whether the whole or part of the material is concerned, specifically the rights of translation, reprinting, reuse of illustrations, recitation, broad-casting, reproduction on microfilm or any other way, and storage in data banks. Duplication of this publication or parts thereof is permitted only under the provisions of the German Copyright Law of September 9, 1965, in its current version, and permission for use must always be obtained from Springer. Violations are liable to prosecution under the German Copyright Law.

The use of general descriptive names, registered names, trademarks etc. in this publication does not imply, even in the absence of a specific statement, that such names are exempt from the relevant protective laws and regulations and therefore free for general use.

Product liability: the publishers cannot guarantee the accuracy of any information about dosage and application contained in this book. In every individual case the user must check such information by consulting the relevant literature.

Cover design: Verlagsservice Teichmann, Mauer, Germany

Production, reproduction and typesetting: le-tex publishing services oHG, Leipzig, Germany

Printed on acid-free paper

9 8 7 6 5 4 3 2 1

springer.com

Foreword

One of the aims of the book series “Medical Radiology – Diagnostic Imaging” is to publish novel work that explores new frontiers in the field of radiological imaging. The investigation of the potential application of MRI to the study of lung diseases is a challenging and exciting field of clinical research driven by the rapid development of new techniques and sequences for cardiac MRI as well as by the use of noble hyperpolarised gases as novel contrast agents. The specific ability of MRI to visualise simultaneously morphological changes and modifications in perfusion, ventilation and gas exchange has opened up totally new perspectives in lung imaging. MRI of the lung thus eminently illustrates the mutation of the discipline of radiology from pure morphology to combined morphological-functional imaging.

The editor, H-U. Kauczor, is known internationally for his original research in various fields, and particularly into new applications of CT and MRI in oncology and lung pathology. For many years he has been the inspiration and principal investigator of a leading and innovative radiological research group in Heidelberg. Their original ideas and dynamic work organisation have resulted in an impressive list of scientific publications on various applications of MR imaging of the lung.

I am very much indebted to the editor and the contributing authors, all outstanding experts in their fields, for preparing this fine volume on a highly active topic for our series. It is indeed one of the first handbooks to provide a comprehensive overview of our actual knowledge on the clinical role of MRI of the lung. In addition it outlines future perspectives for potential new applications of this imaging modality. I would like to congratulate them on this outstanding work at the cutting edge of radiology.

I highly recommend this volume to certified radiologists, particularly those with a special interest in chest imaging, and to radiologists in training. However, pneumologists, cardiologists and chest surgeons will also find it a very useful source of information for better diagnostic and therapeutic management of their patients.

I have no doubt that this volume will meet the appropriate interest and well deserved success with our readership.

Leuven

ALBERT L. BAERT

Preface

For a long time the lung has been regarded as the black hole in MRI. In the 1980s courageous physicists and radiologists have tried to investigate different lung diseases using MRI, but they could neither produce convincing image quality within a reasonable examination time nor generate a substantial clinical impact. MRI was accepted for some minor clinical indications, such as mediastinal tumors and chest wall invasion or Pancoast situation in lung cancer. With the advent of spiral and high resolution CT, structural imaging and characterization of lung disease based on patterns and compartments was of utmost interest. Also CT angiography of the pulmonary arteries and the diagnosis of pulmonary embolism were major developments with significantly superior results when compared to some half-hearted attempts to introduce MRA of the pulmonary arteries using 2D time-of-flight techniques. At this stage the scientific and clinical community as well as the scanner manufacturers lost interest in MRI of the lung. Over time, however, two different groups tackled MRI of the lung again. The first of these, radiologists working on cardiac MRI, realized that there are important cardiorespiratory interactions. They started to investigate MRI and contrast-enhanced MRA of pulmonary arteries and veins as well as analyze the function of the right ventricle. The second group, basic and laser physicists, came up with the idea that their hyperpolarized noble gases might be an attractive novel contrast mechanism for MRI of the lung. Thus, iatrogenic signal-enhancing compounds started to shed light into the black hole of MRI. Suddenly, more and more groups made basic research and development efforts to discover the unknown in MRI of the lung. It soon became very obvious that MRI will always be second to CT when it comes to the visualization of pulmonary structure, disease and patterns with high spatial resolution. Till now, the ability to provide different soft tissue contrasts (T1, T2, contrast-enhancement, fat suppression) has not really proven advantageous for MRI. However, the most appealing development was the introduction of functional imaging of the lung by MRI. More and more contrast mechanisms for functional studies were described. The MR hardware development – which was driven by cardiac MRI striving for higher and higher temporal resolution – allowed for a variety of techniques which cope with the challenges related to respiratory motion, as well as cardiac contraction and vascular pulsation. The diagnostic benefits stem from the ability of MRI to visualize changes in lung structure while simultaneously imaging different aspects of lung function, such as perfusion, respiratory motion, ventilation and gas exchange. On this basis, novel imaging findings, endpoints and quantitative surrogates for lung function can be obtained.

As all these techniques become more and more available they are being applied to a wide variety of different lung diseases. Most of these early clinical applications have been very successful and impressive, and important indications have emerged for MRI of the lung: pulmonary hypertension, congenital vascular anomalies, and cystic fibrosis. Other strongholds for MRI of the lung are staging lung cancer and malignant pleural mesothelioma as well as characterization of mediastinal and pleural tumors or even the diagnosis and follow-up of pulmonary embolism. This means that MRI can already substantially contribute to clinical diagnostic imaging in lung disease but at the same time it is heavily underused for two reasons: first the clinical indications and the potential advantages of MRI over CT or nuclear medicine are not widely known, and second the knowledge of how to carry out MRI of the lung and obtain high image quality providing a confident diagnosis is not widespread. However, standard protocols can now be implemented on up-to-date scanners, allowing MRI to be used as a first-line imaging modality for various lung diseases.

For me, as the editor of this book, it was an enormously invigorating experience bringing together renowned experts and the support from Professor Albert Baert and the publisher, Springer, to provide the first well illustrated and comprehensive textbook of “MRI of the Lung”. It provides an extensive overview of how to use MRI for imaging of different types of lung disease. Standard and easy-to-use protocols are presented and the MR strategies used in different clinical situations are explained. Special emphasis is placed on benign diseases requiring regular monitoring, given that it is patients with these diseases who derive the greatest benefit from the avoidance of ionizing radiation. I hope the book will be of great assistance to all who are establishing MRI of the lung in their daily clinical and research activities.

Heidelberg

HANS-ULRICH KAUCZOR

Contents

Technical

| | | |
|----------|--|-----------|
| 1 | General Requirements of MRI of the Lung and Suggested Standard Protocol | 3 |
| | JÜRGEN BIEDERER | |
| 2 | MR Angiography of the Pulmonary Vasculature | 17 |
| | CHRISTIAN FINK | |
| 3 | MR Perfusion in the Lung | 25 |
| | FRANK RISSE | |
| 4 | MRI of Pulmonary Ventilation | 35 |
| 4.1 | Hyperpolarised ³ He MRI: Physical Methods for Imaging Human Lung Function | 35 |
| | JIM M. WILD | |
| 4.2 | Hyperpolarized ¹²⁹ Xenon MRI of the Lung | 57 |
| | SAMUEL PATZ, IGA MURADIAN, MIRKO I. HROVAT, F. WILLIAM HERSMAN, HIROTO HATABU and JAMES P. BUTLER | |
| 4.3 | ¹⁹ Fluorine MRI | 69 |
| | WOLFGANG G. SCHREIBER | |
| 4.4 | Proton MRI: Oxygen-enhanced Lung MRI and Alternative Approaches | 75 |
| | OLAF DIETRICH | |
| 5 | Respiratory Mechanics and Pulmonary Motion | 91 |
| | RALF TETZLAFF | |

Clinical

| | | |
|----------|--|------------|
| 6 | Pulmonary Hypertension and Thromboembolic Disease | 107 |
| | SEBASTIAN LEY and KARL-FRIEDRICH KREITNER | |

| | | |
|-----------|---|-----|
| 7 | Vascular Anomalies and Diseases | 121 |
| | SEBASTIAN LEY and JULIA LEY-ZAPOROZHAN | |
| 8 | Asthma | 139 |
| | SEAN B. FAIN, JAMES H. HOLMES, and RONALD L. SORKNESS | |
| 9 | Chronic Obstructive Pulmonary Diseases | 155 |
| | JULIA LEY-ZAPOROZHAN, AHMED F. HALAWEISH and EDWIN J. R. VAN BEEK | |
| 10 | Cystic Fibrosis | 169 |
| | MICHAEL PUDERBACH, MONIKA EICHINGER and TALISSA A. ALTES | |
| 11 | Lung Cancer | 179 |
| | YOSHIHARU OHNO, HISANOBU KOYAMA, JULIEN DINKEL, and CHRISTIAN HINTZE | |
| 12 | Mediastinal Disease | 217 |
| | KOJI TAKAHASHI | |
| 13 | Pulmonary Infections – Pneumonia | 255 |
| | ROGER EIBEL | |
| 14 | Interstitial Lung Disease | 277 |
| | KATHARINA MARTEN and FRANCESCO MOLINARI | |
| 15 | Diseases of the Pleura and the Chest Wall | 291 |
| | CLAUS PETER HEUSSEL and CHRISTIAN PLATHOW | |
| | Subject Index | 307 |
| | List of Contributors | 311 |

Technical

General Requirements of MRI of the Lung and Suggested Standard Protocol

JÜRGEN BIEDERER

CONTENTS

- 1.1 Introduction 3
- 1.2 Proton-MRI of the Lung:
The Challenge 4
- 1.3 Strategies for Motion
Compensation 4
- 1.4 Strategies for Imaging
Lung Parenchyma Disease 5
- 1.5 Suggestions for a Lean
Standard Protocol 6
- 1.6 Specific Variations
of the Protocol 10
 - 1.6.1 Paramagnetic Contrast Agents 10
 - 1.6.2 Lung Perfusion and Angiography:
Temporal vs Spatial Resolution 10
 - 1.6.3 Mediastinum 12
 - 1.6.4 Chest Wall and Apex 13
 - 1.6.5 Paediatric Applications 13
- 1.7 Protocols for Ultra High
and Low Field Scanners 13
- References 14

KEY POINTS

MRI of the lung has been shown to be highly sensitive to infiltrative and solid pathology. It offers particular advantages beyond the scope of CT such as dynamic studies of respiratory mechanics and first pass perfusion imaging. However, challenges such as motion artifacts and low signal have delayed the introduction into clinical routine. This chapter discusses the strategies to overcome these obstacles and suggests a comprehensive protocol for a spectrum of indications. This comprises a basic selection of non-contrast enhanced sequences and can be extended by contrast enhanced series. Breath hold T1- and T2-weighted imaging are applied for the detection of small solid lesions and infiltrates. Inversion recovery series visualize enlarged lymph nodes and skeletal lesions. Steady-state gradient echo series in free breathing contribute to the detection of pulmonary embolism, cardiac dysfunction and impairment of respiratory mechanics. Tumors, suspicious pleural effusions and inflammatory diseases warrant additional contrast-enhanced sequences. Perfusion studies contribute to imaging of thromboembolic vascular and obstructive airway diseases.

1.1

Introduction

Evolving from a research tool, MRI of the lung is becoming increasingly important for specific clinical applications. The advantages over CT are not only limited to the lack of ionizing radiation, which is of particular interest for the assessment of lung disease in children (e.g. pneumonia, cystic fibrosis) or in patients who re-

quire frequent follow-up examinations (e.g. immunocompromised patients with fever of unknown origin). Chest wall invasion by a tumor and mediastinal masses are accepted indications benefiting from its superior soft tissue contrast. Dynamic examinations to study respiratory mechanics and contrast enhanced first pass perfusion imaging reach far beyond the scope of CT. High quality MRI can contribute significantly to clinical decision making in numerous pulmonary diseases from lung cancer over malignant pleural mesothelioma, acute pulmonary embolism, pulmonary arterial hypertension, airway disease such as cystic fibrosis to interstitial lung disease and pneumonia. Concepts for whole body MRI examinations for screening and staging require a comprehensive chest study to be complete. The extension of the examination towards the pulmonary circulation as well as diseases of the pulmonary circulation affecting the heart and great vessels widens the diagnostic scope of cardiovascular MRI. Nevertheless, the lung remains a difficult terrain for MRI. This chapter outlines the challenges for lung MRI such as motion artifacts and low signal and the strategies to overcome these obstacles. Finally, a standard protocol is suggested that can be performed with most state-of-the-art scanners and may be used as a “starter kit” by any interested reader of this book.

1.2

Proton-MRI of the Lung: The Challenge

One major problem in imaging thoracic organs is the continuous motion of all components induced by heart pulsation and respiration. Both are most prominent in the lower and anterior sections of the chest where classical T1- and T2-weighted spin-echo and fast spin-echo techniques yield very poor image quality. More specific problems are encountered if MRI is applied to imaging of lung parenchyma. MR signal is generated from protons within water molecules and organic material. The lungs contain only about 800 g of tissue and blood which is distributed over a volume of 4–6 L. Proton density and signal intensity are therefore extremely low compared to other parts of the body (ALBERTIN 1996). Further, local field inhomogeneities due to susceptibility artifacts at tissue-air or liquid-air interfaces of the alveoli result in rapid dephasing of the low signal with extremely short T2* (SU et al. 1995). Therefore, the lungs usual appear without any visible signal on conventional MR images. However, any pathology with higher proton density and therefore higher signal appears with a strong inherent contrast against the black background

of aerated lung tissue. Subtle changes of lung signal due to small lesions or fine reticulations can still be missed, in particular if motion artifacts are not sufficiently suppressed (BOTH et al. 2005).

1.3

Strategies for Motion Compensation

Principally, the problems encountered in motion compensation for lung imaging are well known from MRI of the heart. It appears to be the most straightforward approach to compensate for respiratory motion by triggering or gating correlated to the extension of a simple pneumatic belt or a compressible cushion placed at the upper abdomen or the chest of the patient. The pressure changes due to compression and decompression of the device are directly registered by the MR scanner. The ideal position of such a device depends on the individual respiratory pattern of the patient at rest. The trigger signal is usually set to expiration, because this is usually the longest and most reproducible phase of the respiratory cycle (BIEDERER et al. 2002a; BOTH et al. 2005). Imaging at end-expiration is principally favorable for imaging lung parenchyma, since proton density and lung signal intensity increase with deflation. However, appropriate instructions of the patient remain the key to high image quality without respiratory motion artifacts. In general, higher respiration frequencies are appreciated. This facilitates respiration-triggered imaging in pediatric patients.

Navigator sequences replace the respiration belt by continuous real time image acquisition from a small volume at the top of the diaphragm. The images are evaluated electronically for movements of the diaphragm and trigger settings can be applied interactively by the operator. As a disadvantage, respiratory motion is not tracked during the acquisition of the diagnostic images when the navigator has to be suppressed. We therefore still recommend additional application of a respiratory belt, if available, for uninterrupted control of the breathing maneuvers. The same navigator-technique can be used to adjust several slice blocks of a multi-breath-hold acquisition in case of variable respiratory levels. Control for cardiac pulsation artifacts is achieved with either ECG monitoring or peripheral pulse oximetry. Unfortunately, every triggering or gating prolongs the acquisition time while the compensation of motion artifacts usually remains incomplete (BIEDERER et al. 2002a). Simultaneous double-triggering or gating for respiration and cardiac pulsation is usually not favorable, although recommended by some authors (LEUTNER et al. 1999).

In conclusion, simply scaling up the sequence packages from cardiac MRI does not lead to a lean protocol. Full anatomic coverage for lung imaging requires larger volumes and more slices compared to cardiac MRI meanwhile examination time restrictions for clinical routine are the same (FINN et al. 2006; LIMA and DESAI 2004).

For practical use, the easiest way to overcome respiratory motion is therefore to use breath-hold techniques with full anatomic coverage (ideally the whole thorax) within a single 20-s breath-hold – and to ignore cardiac action. If acquisition time exceeds this limit or if a patient cannot hold his breath for 20 s, the examination can be split into blocks that are acquired within several breath-holds. However, splitting the acquisition introduces additional artifacts, if the level of the breath-holds is not reproducible (BIEDERER et al. 2001). Cardiac pulsation can be overcome with very fast single shot techniques such as fast spin-echo imaging using half Fourier acquisition (e.g. T2-HASTE) or very short echo times (e.g. ultra fast turbo-spin-echo UTSE) (LEUTNER et al. 1999). Fast low angle shot gradient echo and T1-weighted 3D gradient echo (e.g. Volume Interpolated Breath-hold Examination (VIBE)) also tend to be quite robust to cardiac motion, even without cardiac triggering or gating. Their image quality largely depends on the breath-hold capability and compliance of the patient more than the compensation for cardiac motion. Sometimes, readout-frequencies or their multiples appear to synchronize with heart action so that a “pseudo-gating” results in very sharp delineation of the heart. To our knowledge, this has not been further investigated so far, but it might be a useful approach to achieve more robustness of the gradient echo sequences against cardiac pulsation. The suggestions for a standard protocol in this chapter are based on breath hold sequences with acceptable robustness against cardiac pulsation to keep within an acceptable time frame for clinical routine.

Another approach is to acquire sets of single shot images without any instructions to the patient. This can be achieved with fast spin-echo imaging using half Fourier acquisition techniques (e.g. T2-HASTE, as mentioned above) or axial steady state gradient echo imaging (SS-GRE, TrueFISP) which are acquired with a slice overlap of, e.g., 50% during free breathing. The result is a series covering the whole chest with a pseudo-cine visualization of respiratory motion and cardiac action. The SS-GRE series is particularly interesting for this purpose, since its T1/T2-weighted contrast displays blood bright with good contrast against thrombotic material. It yields basic information on pulmonary motion during the respiratory cycle as well as on size, shape and patency of the central pulmonary vessels. Thus, it can be used

as a fast technique to exclude massive acute pulmonary embolism even in non-compliant patients during free breathing (KLUGE et al. 2005).

It can be anticipated for the near future that dedicated sequence designs will lead to more effective motion compensation. Parallel imaging contributes to further reduction of examination times and thus gives more room for triggering or gating (GRISWOLD et al. 2002; HEIDEMANN et al. 2003). Active breathing control based on online spirometry and a shutter valve to synchronize segmented k-space acquisition with selected phases of the respiratory cycle was presented recently (ARNOLD et al. 2007). Simple and robust techniques are sequence designs with rotating sets of phase encoding bars providing inherent motion compensation (PROPELLER or BLADE) (PIPE 1999; DENG et al. 2006). Self-navigated sequence design (BRAU and BRITAIN 2006) and retrospective gating of heavily oversampled K-space data (REMMERT et al. 2007) are promising candidates. Short echo time single shot imaging with radial K-space acquisition appears to be completely robust against motion artifacts (JERICIC et al. 2004). These are a few examples for a number of techniques under investigation and further aspects will be addressed in this book. For the time being, and to start off, the majority of users will have to rely on what is available on the clinical scanners. Therefore the protocol suggestions of this chapter are based on routine sequences.

1.4

Strategies for Imaging Lung Parenchyma Disease

In respect to MR imaging, diseases of the lung can be divided into two groups: Diseases which increase proton density (“plus pathology”) and diseases which reduce proton density of the lung (“minus pathology”). Any increase in lung proton density due to solid lesions or infiltration with liquids – fortunately the vast majority of cases – is easy to detect with MRI, in particular against the dark background of the healthy lung parenchyma. This implies that to visualize lung parenchyma signal itself is clinically not too important for morphologic imaging of lung disease – except for the few entities which produce “minus pathology”. These are mainly overinflation due to air trapping, emphysema or pneumothorax. These conditions can be only visualized, if intact lung structure and pathologic parts have a different signal. This can be achieved with contrast enhanced perfusion imaging or ventilation studies with hyperpolarized gases – while the first can be addressed within

a standard protocol suggestion, the latter remains to be reserved for specialized centres.

Compared to plain chest X-ray, MRI has been proven to yield a higher sensitivity for lung nodules but it does not yet match CT. Depending on the water content, nodules can be detected either on fast T1-weighted 3D-gradient echo images (VIBE), T2-weighted single shot partial-Fourier acquisition spin echo images (HASTE) or inversion recovery series (TIRM). SCHAEFER et al. 2005 have shown a similar detection rate of small pulmonary nodule of T1- and T2-weighted sequences, but the number of false positives was lower with fast T1-weighted gradient echo sequences. The sensitivity for lung nodules larger than 4 mm ranges between 80% and 90% and reaches 100% for lesions larger than 8 mm. Overall, it appears realistic to assume a threshold size of 3–4 mm for lung nodule detection with MRI, given that conditions are optimal (i.e. patient can keep a breath hold for 20 s or perfect gating/triggering) (BIEDERER et al. 2003a; BOTH et al. 2005; SCHROEDER et al. 2005; BRUEGEL et al. 2007; FINK et al. 2007). Exceptions are calcified nodules, which appear black. Thus, lung MRI cannot be recommended for staging chondrosarcoma or other entities with calcified metastases. Tools for lung nodule detection and computer aided lung nodule volumetry are under investigation, but so far not commercially available.

Unfortunately, T1-GRE images do not visualize infiltrative processes well. Experimental results show that the signal intensity of fluid inside lung tissue on T1-GRE is much too low to be of diagnostic use (BIEDERER et al. 2002b). Lung infiltration, e.g. due to pneumonia, can instead be readily detected on T2-weighted images as well as on TrueFISP and T2-TIRM (FINK et al. 2007). It is therefore commonly accepted to add T2-weighted sequences for the evaluation of pulmonary infiltrates. Fast T2-weighted single shot imaging techniques can be performed with partial-Fourier acquisition (e.g. HASTE) or ultra short TE (UTSE). A dark blood preparation pulse may be favorable for particular purposes such as imaging of the mediastinum. As an alternative to breath hold imaging, fast T2-weighted spin-echo sequences with respiratory triggering have produced reasonable results (LEUTNER and SCHILD 2001; BIEDERER et al. 2002a).

As discussed above, full anatomic coverage of the chest is highly appreciated to overcome respiratory motion artifacts or overlap-effects between multiple breath hold acquisition. Partial parallel imaging has contributed significantly to reduce examination times to breath hold periods of 20 s and less, each allowing to cover the complete chest with one acquisition. Modern

1.5-T scanners with parallel imaging technique allow acquisition 3D-data sets of the whole chest with voxel sizes of down to $1.6 \times 1.6 \times 4$ mm or isotropic voxels of $2 \times 2 \times 2$ mm within one breath-hold. Parallel imaging techniques use arrangements of multiple coils to acquire additional information along the phase encoding direction.

K-space data are partially reconstructed from spatial information, which originates from differences in the signal intensities depending on the distance of a location to the individual coils. The result is a substantial improvement in image acquisition speed, usually two- or threefold. For the lung, acceleration factors of 2–3 are reasonable; more than 3 can so far not be recommended. If available, GRAPPA-algorithms appear to produce a slightly better signal-to-noise ratio than T-SENSE.

1.5

Suggestions for a Lean Standard Protocol

The following suggestions for a lung imaging protocol are derived from MR sequence components of current standard installations. All protocol suggestions in this chapter are based on parallel acquisition techniques. The necessary hardware is nowadays available at most sites. Nevertheless, if parallel imaging techniques are not available, the protocol can be readily changed to multi-breath-hold acquisitions. The preparation for the examination includes instruction of the patient for the breathing maneuvers, the application of a respiratory belt and selection of a phased array body coil for thoracic imaging. ECG is not required on a routine basis but should be used if cardiac imaging sequences are planned, e.g. in case of tumor infiltration into the pericardium or large vessels of the mediastinum.

The imaging protocol starts with a gradient echo localizer in inspiration to plan the study (Table 1.1). The first sequences are acquired in breath-hold, usually starting with the coronal T2-HASTE (Fig. 1.1) followed by the transverse T1-3D-GRE (VIBE) (Fig. 1.2). As defined above, these sequences cover infiltrative disease and solid lung pathology, respectively. The T2-weighted single shot images provide high signal and good lesion-to-background contrast but due to partial Fourier acquisition and long echo trains the delineation of structures is slightly blurred. The overall signal of the T1-weighted 3D-GRE images is lower, but sharpness is improved due to a higher spatial resolution. Both se-

Table 1.1. Suggested standard protocol for MRI of the lung. The upper section of the table contains the components of the basic protocol, the lower section extensions to the protocol. Detailed sequence parameters are provided with the figures

| Sequence | Acquisition time | Respiratory level | Diagnostic yield |
|-------------------------|------------------|-------------------------|---|
| Basic protocol | | | |
| Localizer | 0:10 | Inspiratory breath hold | Study planning |
| T2-HASTE (Fig. 1.1) | 0:18 | Inspiratory breath hold | Infiltrative lung disease, cardiac morphology |
| T1-3D-GRE (Fig. 1.2) | 0:20 | Inspiratory breath hold | Solid pathology, mediastinum |
| T1/T2-SS-GRE (Fig. 1.3) | 0:56 | Free breathing | Pulmonary embolism, gross cardiac dysfunction |
| T2-STIR/TIRM (Fig. 1.4) | 1:28 | Multiple breath holds | Mediastinal lymph nodes |
| T1/T2-SS-GRE (Fig. 1.5) | 0:19 | In/expiration (“FEV1”) | Respiration mechanics |
| Protocol extensions | | | |
| T2-FSE (Fig. 1.6) | >5:0 | Respiration trigger | Mediastinal structures, infiltrative lung disease |
| 3D-perfusion (Fig. 1.7) | 0:29 | Inspiratory breath hold | Lung parenchymal perfusion |
| 3D-GRE angio (Fig. 1.8) | 0:21 | Inspiratory breath hold | Pulmonary angiogram |
| T1-3D-GRE post contrast | 0:20 | Inspiratory breath hold | Solid pathology, mediastinal and pleural disease |

Fig. 1.1. T2-weighted single shot half Fourier (T2 HASTE) in a healthy male 30-year-old volunteer

| | |
|------------------------------|-----------|
| resp. control | insp./bh. |
| slice orientation | Coronal |
| TA (min:s) | 0:18 |
| slices per acquisition | 30 |
| phase encoding | R>L |
| FOV (mm) | 450 |
| matrix | 256 |
| slice thickness | 8 |
| partial Fourier | 4/8 |
| pixel size (mm) | 1.8 × 1.8 |
| slice distance | 0% |
| TR (ms) | 600 |
| TE (ms) | 31 |
| flip-angle (°) | 180 |
| parallel acceleration factor | 2 |



Fig. 1.2. T1-weighted Volumetric interpolated 3D gradient echo sequence (VIBE) in a healthy male 30-year-old volunteer

| | |
|------------------------------|------------|
| resp. control | insp./bh |
| slice orientation | transverse |
| TA (min:s) | 0:20 |
| slices per acquisition | 72 |
| phase encoding | A>P |
| FOV (mm) | 400 |
| matrix | 256 |
| thickness | 4 |
| partial Fourier | off |
| pixel size (mm) | 1.6 × 1.6 |
| slice distance | 20% |
| TR (ms) | 3.15 |
| TE (ms) | 1.38 |
| flip-angle (°) | 8 |
| parallel acceleration factor | 2 |

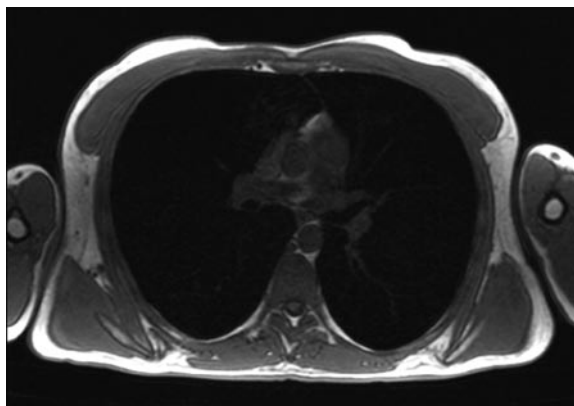


Fig. 1.3. T1/T2-weighted steady state gradient echo sequence (TrueFISP) in a healthy male 30-year-old volunteer; adjusted to free breathing semi-dynamic study of the chest

| | |
|------------------------------|-----------|
| resp. control | tidal |
| slice orientation | cor |
| TA (min:s) | 0:56 |
| slices per acquisition | ≤128 |
| phase encoding | R>L |
| FOV (mm) | 450 |
| matrix | 256 |
| slice thickness | 4 |
| partial Fourier | off |
| pixel size (mm) | 1.8 × 1.8 |
| slice distance | -50/0% |
| TR (ms) | 437.2 |
| TE (ms) | 1.16 |
| flip-angle (°) | 80 |
| parallel acceleration factor | 2 |



quences usually do not show a visible signal of healthy lung tissue, unless infiltrates, atelectasis or solid lesions are present.

A coronal T1/T2-weighted, free breathing SS-GRE sequence (TrueFISP) is acquired next (Fig. 1.3). This allows the patient to recover from the breath-hold maneuvers. Signal intensity of the SS-GRE images is intermediate, but basic information on pulmonary motion during the respiratory cycle and on cardiac action are generated within a very short time. This part of the pro-

col also allows for an exclusion of relevant pulmonary embolism due to a bright signal of the lung vessels with a good contrast against hypointense thrombotic material. The signal of health lung parenchyma on SS-GRE images is low, but still significantly higher than on the first sequences of the protocol.

Additionally, a STIR image series is acquired using a multiple breath-hold technique (Fig. 1.4). As already mentioned, inversion recovery sequences contribute significantly to the detection of mediastinal lymph

Fig. 1.4. Inversion recovery fast spin echo sequence (TIRM, STIR) in a healthy male 30-year-old volunteer

| | |
|------------------------------|-----------|
| resp. control | insp./bh |
| slice orientation | tra |
| TA (min:s) | 1:28 |
| slices per acquisition | 32 × 4 |
| phase encoding | A>P |
| FOV (mm) | 400 |
| matrix | 320 |
| slice thickness | 6 |
| partial Fourier | off |
| pixel size (mm) | 1.7 × 1.3 |
| slice distance | 10% |
| TR (ms) | 3500 |
| TE (ms) | 106 |
| flip-angle (°) | 150 |
| parallel acceleration factor | 2 |

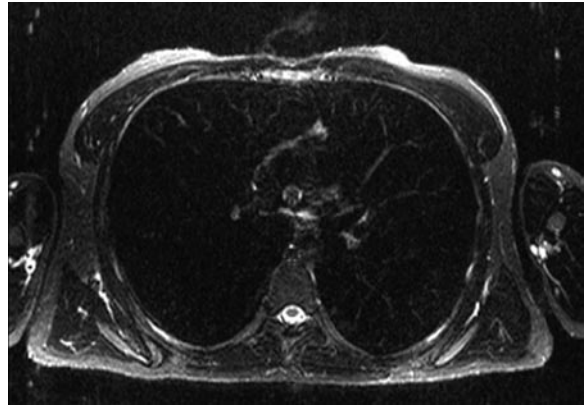


Fig. 1.5. T1/T2-weighted steady state gradient echo sequence (TrueFISP) in a healthy male 30-year-old volunteer; adjusted to study respiration dynamics. The FEV1-maneuver includes maximum in- and expiration manoeuvres and requires intensive interaction with the operator

| | |
|------------------------------|-----------|
| resp. control | FEV1 |
| slice orientation | cor |
| TA (min:s) | 0:19 |
| slices per acquisition | 1 × 60 |
| phase encoding | R>L |
| FOV (mm) | 400 |
| matrix | 256 |
| slice thickness | 10 |
| partial Fourier | off |
| pixel size (mm) | 2.4 × 1.6 |
| slice distance | -100% |
| TR (ms) | 317.1 |
| TE (ms) | 1.14 |
| flip-angle (°) | 67 |
| parallel acceleration factor | 2 |



nodes and edematous bone lesions while healthy lung parenchyma signal appears completely black.

The final acquisition is a single slice dynamic SS-GRE series for diaphragmatic function (Fig. 1.5). The series is focused on the highest elevation of the diaphragmatic dome to be acquired with a temporal resolution of 3–10 images per second, depending on the performance of the MR scanner (PLATHOW et al. 2006). Otherwise the parameters are identical to the third acquisition. The patient is instructed to breathe deeply just like during

a lung function test (so-called FEV1-maneuver). This short part of the protocol appreciates the potential of time-resolved MR image series to visualize functional aspects, i.e. on diaphragmatic function as a significant advantage compared to CT.

This basic protocol can be concluded after a total room time of approximately 15 min. Specific variations of the protocol and additional series as extensions to this protocol are added depending on the indication, i.e. post i.v. contrast scans.

1.6

Specific Variations of the Protocol

1.6.1

Paramagnetic Contrast Agents

Significant differences of the available paramagnetic contrast agents have not been shown so far. For simple post-contrast imaging, reasonable results are achieved with a simple manual i.v.-injection of 0.1–0.2 mmol gadolinium-DTPA (Magnevist®) per kg body weight (or equivalent). Lung perfusion imaging with time resolved contrast-enhanced magnetic resonance angiography warrants the use of a power injector.

Post-contrast scans improve the diagnostic yield of 3D-GRE sequences by clearer depiction of vessels, hilar structures and pleural enhancement. Parenchymal disease and solid pathologies are also enhanced. Thus, a study to exclude pulmonary malignancies, e.g. for staging purposes, should usually comprise contrast enhanced series, preferably with a fat-saturated 3D-GRE sequence. Contrast enhancement is also necessary in case of pleural processes (empyema, abscess, metastatic spread of carcinoma, mesothelioma) for the further evaluation of solid masses as well as functional imaging or angiography (BIEDERER et al. 2003b). Since the sequences so far listed only include a 3D-GRE sequence

without fat saturation, it might be favorable to acquire an additional fat-saturated scan before i.v. contrast administration to allow for a direct comparison of contrast uptake. The other sequence parameters are identical with the initial non-contrast enhanced acquisition.

Further options to extend the standard protocol are T1- and T2-weighted SE or FSE-sequences with respiratory triggering (or gating; Fig. 1.6). Traditionally, T1-weighted images are recommended for the detection of lymph nodes and tumor infiltration into the chest wall, but since T2-weighted sequences additionally contribute to the evaluation of lung parenchyma pathology and provide equal information about the chest wall and mediastinum, they are the method of choice to conclude the study, if desired.

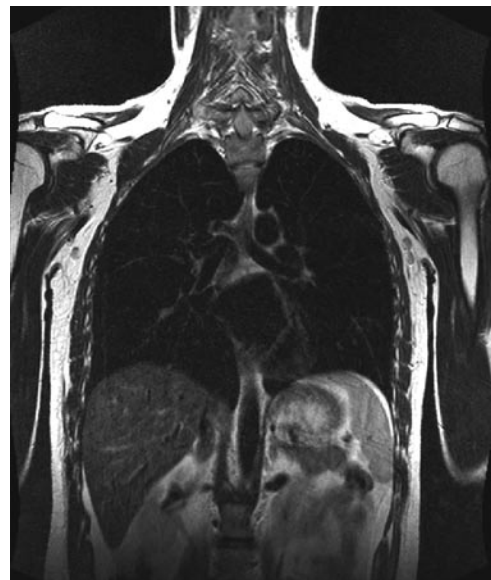
1.6.2

Lung Perfusion and Angiography: Temporal vs Spatial Resolution

One of the most common clinical problems to be addressed with MRI are diseases of the lung vessels and irregularities of pulmonary perfusion. Our suggestion for a standard protocol therefore comprises two optional variations of T1-weighted ultra-short TR and TE contrast-enhanced three-dimensional gradient echo sequences for breath hold magnetic resonance angio-

Fig. 1.6. Respiration-triggered T2-weighted fast spin echo sequence (T2-TSE) in a healthy male 30-year-old volunteer

| | |
|------------------------------|-----------|
| resp. control | tidal |
| slice orientation | coronal |
| TA (min:s) | 5:05+ |
| slices per acquisition | 45 |
| phase encoding | R>L |
| FOV (mm) | 500 |
| matrix | 512 |
| slice thickness | 4 |
| partial Fourier | 5/8 |
| pixel size (mm) | 1.3 × 1.0 |
| slice distance | 10% |
| TR (ms) | 1700 |
| TE (ms) | 100 |
| flip-angle (°) | 150 |
| parallel acceleration factor | 2 |



graphy (MRA) (PRINCE 2004): a dynamic series with high temporal resolution for first pass perfusion studies of the lung parenchyma (this can be only achieved on the cost of a lower spatial resolution) and an angiogram with high spatial resolution (resulting in lower temporal resolution).

At this point, a short overview is given to complete the suggestions for a standard protocol. Further technical aspects and recommendations for image post-processing of first pass contrast-enhanced lung parenchyma perfusion imaging and pulmonary MRA are addressed in dedicated chapters of this book.

For lung perfusion imaging, the scan time for each 3D data set should be reduced to less than 5 s (FINK et al. 2004; GOYEN et al. 2001; SCHOENBERG et al. 1999; HATABU et al. 1996). This can be achieved by most clinical MR scanners with parallel imaging capability. For lower performance systems, 2D perfusion MRI may still be favorable to provide optimum temporal resolution (LEVIN et al. 2001), but anatomic coverage and spatial resolution in the z-axis are usually not acceptable for clinical applications. The easiest approach to perfusion studies is to start contrast injection and the MR sequence simultaneously without bolus timing. Arterial-venous discrimination is improved by high temporal resolution and the study is robust to motion artifacts even in patients with severe respiratory disease and limited breath-hold capability. For documentation

and viewing, contrast-enhanced 3D perfusion MRI is usually processed by subtraction of mask image data acquired before contrast bolus arrival (Fig. 1.7). Since the acquisition time and diagnostic yield completely cover the information provided by a test bolus, the dynamic perfusion series may be used to calculate bolus timing for the following high spatial resolution angiogram (BIEDERER et al. 2006). Disadvantages compared to the test bolus method are the additional time needed for image post-processing and the slightly higher amount of contrast medium (0.07 mmol/kg patient weight). To synchronize bolus profiles with the angiogram, injection speed and the volume of the bolus plus sodium chloride chaser (at least 20 mL sodium chloride) should be the same. A highly efficient image reconstruction system and a power injector are prerequisites for this approach.

The pulmonary arteriogram is acquired with a minimum relaxation time (TR) of less than 5 ms and an echo time (TE) of less than 2 ms and with a high spatial resolution (e.g. a voxel size of $1.2 \times 1.0 \times 1.6$ mm requiring a breath-hold of 20–30 s). The short TR allows for short breath-hold acquisitions and the short TE minimizes background signal and susceptibility artifacts. The ability of the patient to hold the breath is crucial for image quality. Full anatomic coverage is achieved with image acquisition in coronal orientation and a single injection of contrast (0.1–0.2 mmol/kg flow rates between 2 and

Fig. 1.7. T1-weighted 4D contrast-enhanced first pass perfusion study in a healthy 24-year-old female subject (clinical study to exclude pulmonary embolism)

| | |
|------------------------------|-----------|
| resp. control | insp. |
| slice orientation | coronal |
| TA (min:s) | 0:29 |
| slices per acquisition | 32 × 20 |
| phase encoding | R>L |
| FOV (mm) | 500 |
| matrix | 256 |
| slice thickness | 54 |
| partial Fourier | 6/8 |
| pixel size (mm) | 3.6 × 2.0 |
| slice distance | 20% |
| TR (ms) | 1.64 |
| TE (ms) | 0.64 |
| flip-angle (°) | 40 |
| parallel acceleration factor | 2 |

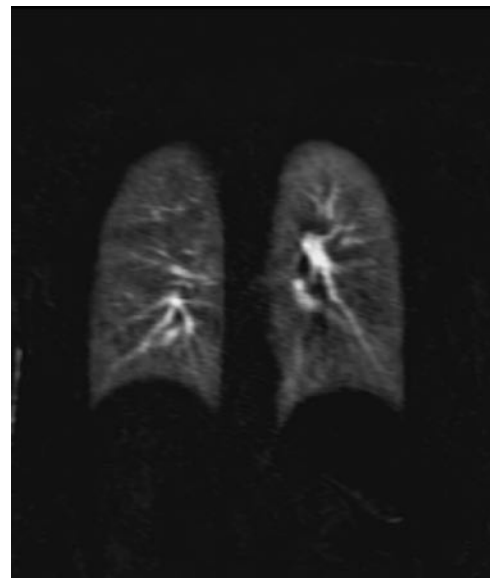


Fig. 1.8. T1-weighted 3D contrast-enhanced MRA in a healthy 24-year-old female subject (clinical study to exclude pulmonary embolism)

| | |
|------------------------------|-----------|
| resp. control | insp. |
| slice orientation | cor |
| TA (min:s) | 0:21 |
| slices per acquisition | 120 |
| phase encoding | R>L |
| FOV (mm) | 500 |
| matrix | 384 |
| slice thickness | 1.6 |
| partial Fourier | 6/8 |
| pixel size (mm) | 1.2 × 1.0 |
| slice distance | 20% |
| TR (ms) | 2.75 |
| TE (ms) | 1.12 |
| flip-angle (°) | 25 |
| parallel acceleration factor | 2 |



5 mL/s, minimum 20 mL saline flush administered by an automatic power injector) is sufficient. Vascular signal intensity is determined by the gadolinium (Gd) concentration at the time of central k-space acquisition, thus the scan delay should be individually adjusted using a care bolus procedure or a test bolus examination – ideally the first pass perfusion study as described above. One of the most frequent clinical problems to be addressed with MRA and perfusion imaging is the exclusion of pulmonary embolism in young women with potential pregnancy. For this particular purpose, it appears favorable to adjust the center of the k-space to maximum parenchymal perfusion (approximately 2 s later than central pulmonary artery peak contrast). The reconstructed MIP provides a very illustrative image of the lung parenchyma (see the example in Fig. 1.8). Image subtractions, multiplanar reformations (MPR) and maximum intensity projections (MIP) are the standard tools for viewing and documentation of the results.

1.6.3 Mediastinum

The mediastinum contains the heart and the large vessels, the trachea, the esophagus, neural structures as well as lymphatic tissues and the thoracic duct. Anatomically the mediastinum is traditionally divided into three compartments even though there is no physical barrier

between them. These are the anterior, middle and posterior mediastinum, mainly defined by the organs of the middle part like the heart and large vessels (STROLLO 1997a, b). The typical indications for cross sectional imaging of the mediastinum are masses originating from the present structures. While size and position of a tumor can be assessed with MRI as well as with CT, both modalities contribute to the characterization of tumors, e.g. with the detection of fat or calcifications inside a teratoma. In this case, CT has a higher sensitivity for small calcifications. Usually, CT is acquired with the administration of contrast media to obtain a sufficient contrast between vessels and soft tissues while most mediastinal masses can be readily identified on native MRI due to its inherent and excellent soft tissue contrast (LANDWEHR et al. 1999). However, for the assessment of unclear masses, the administration of paramagnetic contrast agent provides more insights into tumor composition and differentiation.

Basically, the mediastinum is fully covered with the suggestions for lung imaging within this chapter. Identification and classification of mediastinal processes is possible by using unsaturated and fat saturated native 3D gradient echo sequences and repeating the latter after contrast administration. With an in plane resolution of 1.6 mm, even very small lymph nodes can be detected. It is imperative however to apply fat saturation to contrast enhanced images, otherwise enhanced lymph nodes do not show within the surrounding fatty tissue.

The T2-weighted inversion recovery images (TIRM) of the protocol are well appreciated for the visualization of mediastinal lymph nodes (OHNO et al. 2004). Nevertheless, more specific protocols are warranted, if the clinical problem is directly related to the mediastinum and its structures. A quick method for scanning mediastinal masses is a black blood prepared Fourier fast spin echo sequence (HASTE) (HINTZE et al. 2006). Native MRI benefits from black blood techniques which reduce flow artifacts. It allows for identification of vessel walls and better differentiation to lymph nodes, but is used on the cost of signal intensity. The disadvantages of all available breath-hold-techniques are their limited spatial resolution and their only partially T1- or T2-weighted contrast. For the chest wall and the mediastinum, clear T1- and T2-contrast can be very helpful, in particular for the characterization of mediastinal masses. Conventional spin-echo and fast spin-echo imaging require acquisition times of a couple of minutes so that cardiac and respiratory motion have to be compensated for, i.e. with triggering or gating. Since respiratory motion usually plays a minor role, in particular while imaging the upper mediastinum, the benefits of respiration triggered sequences are limited and do not pay off for the significantly higher acquisition times. Conventional ECG-triggered T1-weighted spin echo and T2-weighted fast spin echo sequences provide excellent detail of structures close to the heart. Depiction of lymph nodes on both sequences is equal. Appropriate sequences are available on any standard installation. Thus, they were not specifically adapted for the purposes of our protocol suggestions. However, an excellent visualization of both, mediastinal lymph nodes and lung parenchyma, is achieved with the respiration-triggered T2-weighted fast spin echo sequence of the protocol (Fig. 1.6).

1.6.4 Chest Wall and Apex

Due to the above-mentioned technical difficulties, MRI of the chest was for a long time limited to the posterior chest wall and the upper thoracic outlet. Both locations are relatively static and can be examined with classical T1- and T2-weighted spin-echo and fast spin-echo techniques (SHIOTANI et al. 2000).

A typical indication for imaging the lung apices and the upper chest wall is infiltration of this region by a tumour, e.g. a Pancoast lesion. The structures of interest are the large vessels, the cervicobrachial plexus and the spine with the spinal cord. The preferred MR techniques

are conventional spinecho and fast (turbo-) spinecho sequences without specific motion compensation, since this part of the chest shows the least motion artefacts being distant from the heart and diaphragm. Towards the lower thoracic aperture, imaging the posterior chest wall remains easy while imaging the anterior chest wall becomes difficult due to respiratory motion. However, the conventional solution to this problem is easy and effective: The examination is performed in prone position. This has been used on a routine basis for breast MRI for many years and it is extremely helpful to remember this simple trick when a study is planned for imaging any other component of this location, e.g. an unclear mass or destruction of the sternum.

1.6.5 Paediatric Applications

The use of lung MRI is of particular interest for paediatric radiology. Except for ultrasound, which is particularly difficult in the lungs, lung MRI provides the only imaging modality for the chest without radiation exposure. The limitations of the suggested standard protocol in this chapter are twofold. The first is that breath-hold imaging requires a reasonable compliance of the patient. The authors have made good experience with children aged 10 years and more (EICHINGER et al. 2006). Acceptable results were achieved even in some younger subjects between 6 and 10 years if the interaction with the patient was good, even with breath-hold techniques. Single shot steady state imaging (TrueFISP) has been successfully implemented for children of less than 6 years (RUPPRECHT et al. 2002). In smaller children, the fast breathing frequency is in favor of respiration triggered sequences. The second limitation refers to the T1-weighted 3D-GRE (VIBE) acquisition, which suffers from low signal in small volumes and voxels, if the matrix is adapted to very small children.

1.7 Protocols for Ultra High and Low Field Scanners

The particular challenges of lung imaging with MR imply that imaging at 3 T might be unfavorable due to increasing susceptibility artifacts while a lower field strength, e.g. of 0.5 T, should achieve a relative increase the signal intensity for the lung parenchyma compared to 1.5 T.

Practice shows that 3-T images obtained with the protocol suggestions for 1.5 T are of similar quality (REGIER et al. 2007; LUTTERBEY et al. 2007, 2005). In a recently published observer preference study, the imaging characteristics of different pulse sequences used for lung MRI did not substantially differ between 1.5 T and 3 T (FINK et al. 2007). At both field strengths T 2-weighted half Fourier single shot sequences (HASTE) showed the highest signal-to-background ratio for infiltrates and were rated best for the delineation of infiltrates. 3D gradient echo sequences (VIBE) achieved the highest signal-to-background ratio for nodules and the best rating for the depiction of nodules at both field strengths. At 3 T, contrast and signal of gradient echo sequences improved slightly while steady state gradient echo sequences suffered from increasing off-resonance artifacts. To study respiratory dynamics at 3 T, gradient echo sequences should be preferred to steady state sequences. Image quality of inversion recovery sequences decreased minimally at 3 T. The respiration triggered fast spin echo sequence was the preferred sequence for the visualization of the mediastinum at both field strengths. Thus, at present, no advantage can be seen in using ultra-high-field MR for scanning lungs, but the above given protocol suggestions can be transferred to 3 T. Potential benefits of dedicated protocols specifically adapted to the requirements of ultra high field imaging have not been evaluated so far.

Principally, low-field scanners are economic and yield the advantages of open systems regarding patient compliance, in particular for children. Unfortunately, the protocol recommendations for 1.5-T systems cannot be transferred one by one. So far, T1-GRE and T2-FSE sequences have been successfully implemented on 0.5 T scanners (ABOLMAALI et al. 2004; SCHAEFER et al. 2002). Due to the lower gradient performance of the systems, 2D gradient echo sequences were preferred to 3D techniques. Steady state gradient echo sequences with strong T1/T2-contrast producing high signal of solid and liquid pathology have been found to be particularly useful as well. The lower prevalence of susceptibility artifacts at lower field strength is in favor of steady state imaging techniques. Also known as SS-FFE, TrueFISP or balanced steady-state acquisition with rewind gradient echo (BASG), they can be applied as 2D- or 3D-multislice-acquisitions or as single thick-slice technique (HEUSSEL et al. 2002). Clear protocol suggestions as defined for 1.5 T have not been published so far, but the general sequences parameters are available from the cited publications.

References

- Abolmaali ND, Schmitt J, Krauss S, Bretz F, Deimling M, Jacobi V, Vogl TJ (2004) MR imaging of lung parenchyma at 0.2 T: evaluation of imaging techniques, comparative study with chest radiography and interobserver analysis. *Eur Radiol* 14:703–708
- Albertin KH (1996) Structural organization and quantitative morphology of the lung. In: Cuttillo AG (ed) *Application of magnetic resonance to the study of lung*. Futura, Armonk, New York, USA, pp 73–114
- Arnold JF, Mörchel P, Glaser E, Pracht ED, Jakob PM (2007) Lung MRI using an MR-compatible active breathing control (MR-ABC). *Magn Reson Med* 58:1092–1098
- Biederer J, Graessner J, Heller M (2001) Magnetic resonance imaging of the lung with a volumetric interpolated 3D-gradient echo sequence. *Rofo* 173:883–887
- Biederer J, Reuter M, Both M, Muhle C, Grimm J, Graessner J et al. (2002a) Analysis of artefacts and detail resolution of lung MRI with breath-hold T1-weighted gradient-echo and T2-weighted fast spin-echo sequences with respiratory triggering. *Eur Radiol* 12:378–384
- Biederer J, Busse I, Grimm J, Reuter M, Muhle C, Freitag S et al. (2002b) [Sensitivity of MRI in detecting alveolar infiltrates: experimental studies]. *Rofo* 174:1033–1039
- Biederer J, Schoene A, Freitag S, Reuter M, Heller M (2003a) Simulated pulmonary nodules implanted in a dedicated porcine chest phantom: sensitivity of MR imaging for detection. *Radiology* 227:475–483
- Biederer J, Both M, Graessner J, Liess C, Jakob P, Reuter M et al. (2003b) Lung morphology: fast MR imaging assessment with a volumetric interpolated breath-hold technique: initial experience with patients. *Radiology* 226:242–249
- Biederer J, Puderbach M, Hintze C (2006) A practical approach to lung MRI at 1.5 T. *Magnetom Flash* 2/2006:38–43. Siemens MR Customer Magazine, Siemens AG, München
- Both M, Schultze J, Reuter M, Bewig B, Hubner R, Bobis I et al. (2005) Fast T1- and T2-weighted pulmonary MR-imaging in patients with bronchial carcinoma. *Eur J Radiol* 53:478–488
- Brau AC, Brittain JH (2006) Generalized self-navigated motion detection technique: Preliminary investigation in abdominal imaging. *Magn Reson Med* 55:263–270
- Bruegel M, Gaa J, Woertler K et al. (2007) MRI of the lung: value of different turbo spin-echo, single-shot turbo spin-echo, and 3D gradient-echo pulse sequences for the detection of pulmonary metastases. *J Magn Reson Imaging* 25:73–81
- Deng J, Miller FH, Salem R, Omary RA, Larson AC (2006) Multishot diffusion-weighted PROPELLER magnetic resonance imaging of the abdomen *Invest Radiol* 41:769–775
- Eichinger M, Puderbach M, Fink C, Gahr J, Ley S, Plathow C, Tuengerthal S, Zuna I, Muller FM, Kauczor HU (2006) Contrast-enhanced 3D MRI of lung perfusion in children with cystic fibrosis-initial results. *Eur Radiol* 16:2147–2152

- Fink C, Puderbach M, Bock M, Lodemann KP, Zuna I, Schmahl A et al. (2004) Regional lung perfusion: assessment with partially parallel three-dimensional MR imaging. *Radiology* 231:175–184
- Fink C, Puderbach M, Biederer J, Fabel M, Dietrich O, Kauczor HU, Reiser M, Schönberg S (2007) Lung MRI at 1.5 T and 3 T: observer preference study and lesion contrast using five different pulse sequences. *Invest Radiol* 42:377–383
- Finn JP, Nael K, Deshpande V, Ratib O, Laub G (2006) Cardiac MR imaging: state of the technology. *Radiology* 241:338–354
- Goyen M, Laub G, Ladd ME, Debatin JF, Barkhausen J, Truemmler KH et al. (2001) Dynamic 3D MR angiography of the pulmonary arteries in under four seconds. *J Magn Reson Imaging* 13:372–377
- Griswold MA, Jakob PM, Heidemann RM, Nittka M, Jellus V, Wang J, Kiefer B, Haase A (2002) Generalized autocalibrating partially parallel acquisitions (GRAPPA). *Magn Reson Med* 47:1202–1210
- Hatabu H, Gaa J, Kim D, Li W, Prasad PV, Edelman RR (1996) Pulmonary perfusion: qualitative assessment with dynamic contrast-enhanced MRI using ultra-short TE and inversion recovery turbo FLASH. *Magn Reson Med* 36:503–508
- Heidemann RM, Griswold MA, Kiefer B, Nittka M, Wang J, Jellus V, Jakob PM (2003) Resolution enhancement in lung 1H imaging using parallel imaging methods. *Magn Reson Med* 49:391–394
- Heussel CP, Sandner A, Voigtlander T, Heike M, Deimling M, Kuth R et al. (2002) [Prospective feasibility study of chest X-ray vs thoracic MRI in breath-hold technique at an open low-field scanner]. *Rofo* 174:854–861
- Hintze C, Biederer J, Wenz HW, Eberhardt R, Kauczor HU (2006) [MRI in staging of lung cancer]. *Radiologe* 46:251–259
- Jerecic R, Bock M, Nielles-Vallespin S, Wacker C, Bauer W, Schad LR (2004) ECG-gated ²³Na-MRI of the human heart using 3D-radial projection technique with ultra-short echo times. *MAGMA* 16:297–302
- Kluge A, Gerriets T, Müller C, Ekinci O, Neumann T, Dill T et al. (2005) [Thoracic real-time MRI: experience from 2200 examinations in acute and ill-defined thoracic diseases]. *Fortschr Roentgenstr* 177:1513–1521
- Landwehr P, Schulte O, Lackner K (1999) MR imaging of the chest: mediastinum and chest wall. *Eur Radiol* 9:1737–1744
- Leutner C, Schild H (2001) [MRI of the lung parenchyma]. *Rofo* 173:168–175
- Leutner C, Gieseke J, Lutterbey G, Kuhl CK, Flacke S, Glasmacher A et al. (1999) [MRT versus CT in the diagnosis of pneumonias: an evaluation of a T2-weighted ultrafast turbo-spin-echo sequence (UTSE)]. *Rofo* 170:449–456
- Levin DL, Chen Q, Zhang M, Edelman RR, Hatabu H (2001) Evaluation of regional pulmonary perfusion using ultrafast magnetic resonance imaging. *Magn Reson Med* 46:166–171
- Lima JA, Desai MY (2004) Cardiovascular magnetic resonance imaging: current and emerging applications. *J Am Coll Cardiol* 44:1164–1171
- Lutterbey G, Gieseke J, von FM, Morakkabati N, Schild H (2005) Lung MRI at 3.0 T: a comparison of helical CT and high-field MRI in the detection of diffuse lung disease. *Eur Radiol* 15:324–328
- Lutterbey G, Grohe C, Gieseke J et al. (2007) Initial experience with lung-MRI at 3.0 T: comparison with CT and clinical data in the evaluation of interstitial lung disease activity. *Eur J Radiol* 61:256–261
- Ohno Y, Hatabu H, Takenaka D, Higashino T, Watanabe H, Ohbayashi C, Yoshimura M, Satouchi M, Nishimura Y, Sugimura K (2004) Metastases in mediastinal and hilar lymph nodes in patients with non-small cell lung cancer: quantitative and qualitative assessment with STIR turbo spin-echo MR imaging. *Radiology* 231:872–879
- Pipe JG (1999) Motion correction with PROPELLER MRI: application to head motion and free-breathing cardiac imaging. *Magn Reson Med* 42:963–969
- Plathow C, Ley S, Zaporozhan J, Schobinger M, Gruenig E, Puderbach M et al. (2006) Assessment of reproducibility and stability of different breath-hold manoeuvres by dynamic MRI: comparison between healthy adults and patients with pulmonary hypertension. *Eur Radiol* 16:173–179
- Prince MR (2004) Gadolinium-enhanced MR aortography. *Radiology* 191:155–164
- Regier M, Kandel S, Kaul MG, Hoffmann B, Ittrich H, Bannmann PM, Kemper J, Nolte-Ernsting C, Heller M, Adam G, Biederer J (2007) Detection of small pulmonary nodules in high-field MR at 3 T: evaluation of different pulse sequences using porcine lung explants. *Eur Radiol* 17:1341–1351
- Remmert G, Biederer J, Lohberger F, Fabel M, Hartmann GH (2007) Four-dimensional magnetic resonance imaging for the determination of tumour movement and its evaluation using a dynamic porcine lung phantom. *Phys Med Biol* 52 N401–N415. doi:10.1088/0031-9155/52/18/N02
- Rupprecht T, Bowling B, Kuth R, Deimling M, Rascher W, Wagner M (2002) Steady-state free precession projection MRI as a potential alternative to the conventional chest X-ray in pediatric patients with suspected pneumonia. *Eur Radiol* 12:2752–2756
- Schaefer JF, Vollmar J, Schick F, Seemann MD, Mehnert F, Vonthein R, Aebert H, Claussen CD (2002) [Imaging diagnosis of solitary pulmonary nodules on an open low-field MRI system – comparison of two MR sequences with spiral CT] *Rofo* 174:1107–1114
- Schaefer JF, Vollmar J, Schick F, Seemann MD, Kamm P, Erdtmann B, Claussen CD (2005) [Detection of pulmonary nodules with breath-hold magnetic resonance imaging in comparison with computed tomography] *Rofo* 177:41–49
- Schoenberg SO, Bock M, Floemer F, Grau A, Williams DM, Laub G et al. (1999) High-resolution pulmonary arterio- and venography using multiple-bolus multiphase 3D-Gd-MRA. *J Magn Reson Imaging* 10:339–346

- Schroeder T, Ruehm SG, Debatin JF, Ladd ME, Barkhausen J, Goehde SC (2005) Detection of pulmonary nodules using a 2D HASTE MR sequence: comparison with MDCT. *Am J Roentgenol* 185:979–984
- Shiotani S, Sugimura K, Sugihara M, Kawamitsu H, Yamauchi M, Yoshida M et al. (2000) Diagnosis of chest wall invasion by lung cancer: useful criteria for exclusion of the possibility of chest wall invasion with MR imaging. *Radiat Med* 18:283–290
- Strollo DC, Rosado de Christenson ML, Jett JR (1997a) Primary mediastinal tumors. Part I. Tumors of the anterior mediastinum. *Chest* 112:511–522
- Strollo DC, Rosado-de-Christenson ML, Jett JR (1997b) Primary mediastinal tumors. Part II. Tumors of the middle and posterior mediastinum. *Chest* 112:1344–1357
- Su S, Saunders JK, Smith ICP (1995) Resolving anatomical details in lung parenchyma: theory and experiment for a structurally and magnetically inhomogeneous lung imaging model. *Magn Reson Med* 33:760–765
-

MR Angiography of the Pulmonary Vasculature

CHRISTIAN FINK

CONTENTS

- 2.1 Introduction 17
- 2.2 Imaging Technique 18
- 2.3 Postprocessing and Reporting 20
- 2.4 Clinical Applications:
Pulmonary Embolism 21
- References 22

KEY POINTS

Although still not considered as the first line imaging test for the assessment of pulmonary vascular disease, recent technical improvements such as parallel imaging have made pulmonary ce-MRA ready for clinical use as a radiation free alternative to pulmonary CT angiography. An interesting advantage over CT is the possibility to acquire time-resolved MRA data which can be used for an additional functional assessment of pulmonary blood flow. Especially in patients with low or moderate clinical probability for pulmonary embolism, pulmonary MRA might be considered as a radiation free alternative to CTA.

2.1

Introduction

Multi-detector Computed tomography angiography (CTA) of the lung is nowadays considered as the clinical standard of reference for the assessment of pulmonary vascular disease (REMY-JARDIN et al. 2007). In contrast, different to other vascular territories (e.g. the peripheral arteries of the lower legs), magnetic resonance angiography (MRA) is generally accepted only as a second-line imaging tool for the assessment of the pulmonary circulation. When compared to CT, the inferior spatial resolution and longer examination/breathhold times are looked upon as the major draw-

backs of pulmonary MRA. In potentially critically ill patients, as in patients with pulmonary embolism, the limited patient access in the magnet and the environment of the magnetic field are considered as a potential contraindication for MRI.

On the other hand there are also potential advantages of pulmonary MRA for the evaluation of lung disease. Above all this includes the lack of ionising radiation. Recently, several publications have raised concerns about the potential harmful effect of diagnostic CT studies, resulting in an increased life-time risk for the development of cancer (BRENNER and HALL 2007; EINSTEIN et al. 2007). Especially in young individuals with congenital or chronic disease requiring frequent follow-up examinations (e.g. congenital heart disease), radiation is a major clinical issue. Moreover, MRI has the unachieved potential to combine morphologic with functional imaging. In patients with lung diseases this could include the functional assessment of ventilation or perfusion, or the assessment of right heart function.

C. FINK, MD

Section Chief Cardiothoracic Imaging, Department of Clinical Radiology and Nuclear Medicine, University Medical Center Mannheim, Medical Faculty Mannheim–University of Heidelberg, Theodor-Kutzer-Ufer 1–3, 68167 Mannheim, Germany

2.2

Imaging Technique

Although several methods have been proposed for MRI of the pulmonary vasculature (including non-enhanced time of flight or black-blood angiography), gadolinium-enhanced 3D gradient echo MRA (ce-MRA) has been established as the standard method for pulmonary MRA. In general, short echo times, i.e. lower than 2–3 ms, should be used to eliminate susceptibility effects resulting from the very short T2* times of the lung (PRINCE et al. 2003).

There are two different approaches to contrast-enhanced pulmonary MRA. One approach is to acquire 3D volume data of the pulmonary vasculature with a high spatial resolution, ideally with isotropic spatial resolution in all directions. To improve the spatial resolution within an acquisition time suitable for breath-holding, the acquisition of two sagittal small field of view data sets with two separate contrast injections has been proposed (OUDKERK et al. 2002). Potential drawbacks of this approach are the requirement of a higher contrast agent dose and an unusual orientation of the source data, which might require further post-processing.

The vascular density of the chest is very high. Moreover, the lungs have a very short transit time, i.e. in the range of 3–5 s (FISHMAN 1963). As a consequence contrast-enhanced pulmonary MRA often has substantial venous contamination, potentially affecting the diagnostic accuracy. To reduce venous contamination, a very compact bolus profile should be aimed at by using a single dose (i.e. 0.1 mmol/kg b.w.) of gadolinium in combination with a high injection rate (e.g. 3–5 mL/s). Ideally, an automatic power injector and saline flush should be used. Another option to improve arteriovenous separation is the use of time-resolved imaging strategies which, depending on the acquisition time and injection protocol, will result in exclusive angiograms or venograms of the lungs (FINK et al. 2005; SCHOENBERG et al. 1999).

To ensure maximum vascular contrast of the pulmonary vessels in ce-MRA, the acquisition of the central k-space data has to be synchronized with the arrival of the contrast agent bolus in the pulmonary arteries, which can be achieved by a test bolus examination or bolus triggering. Another approach is to perform pulmonary MRA in a time-resolved fashion, as this technique is less sensitive for incorrect bolus timing. Depending on the breathhold capabilities of the patient and the temporal resolution of the sequence, the contrast injection is

synchronized with the start of the data acquisition. This enables one to acquire a non-enhanced data set, which can be used for subtraction. Then arterial, mixed arterial/venous and venous MRA data sets are acquired. In addition time-resolved MRA is less sensitive for motion artefacts (e.g. in dyspnoeic patients with PE) (GOYEN et al. 2001) (Fig. 2.1). Another and probably the most important advantage of time-resolved MRA is that it also allows functional information of the pulmonary circulation, such as the characterization of shunts or the assessment of capillary perfusion of the lung parenchyma to be obtained. Several studies have shown the feasibility of pulmonary perfusion MRI using a time-resolved MRA technique (FINK et al. 2004b; NIKOLAOU et al. 2005; OHNO et al. 2003).

The introduction of parallel imaging techniques has substantially improved the potential of pulmonary MRA. Compared to conventional MRI, with parallel imaging only a fraction of the phase encoding lines is acquired while the missing information is reconstructed to a full field-of-view image using the inherent spatial encoding of the different receiver coils (GRISWOLD et al. 2002). In practice, the temporal benefit of these partially parallel acquisition techniques is in the range of a factor of 2–3 (FINK et al. 2003). Using parallel imaging, the acquisition time can be reduced for high spatial resolution MRA without reducing the spatial resolution, or the spatial resolution can be increased to submillimeter isotropic resolution without prolonging the acquisition time. For time-resolved MRA, parallel imaging allows increase of the temporal resolution, allowing for functional MRA and perfusion imaging. In addition to parallel imaging, other k-space sampling techniques such as view-sharing can also be used for pulmonary MRA. In view-sharing some parts of k-space are updated more often than others, leading to an effective shortening of the total acquisition time. For 3D applications, KOROSIC et al. (1996) introduced the view sharing implementation TRICKS (time-resolved interpolated contrast kinetics) to visualize the transit of a contrast agent bolus. In TRICKS, the low frequency k-space data which contributes most significantly to the image content is sampled more frequently than the high frequency k-space data which is interpolated between consecutive time frames.

Further developments of alternative k-space sampling strategies such as a combination non-Cartesian k-space sampling (e.g. spiral k-space sampling) and view-sharing can further improve the spatial and temporal resolution of time-resolved pulmonary MRA data. In a recent publication by DU and BYDDER (2007), pulmonary MRA data was acquired with a spiral-TRICKS

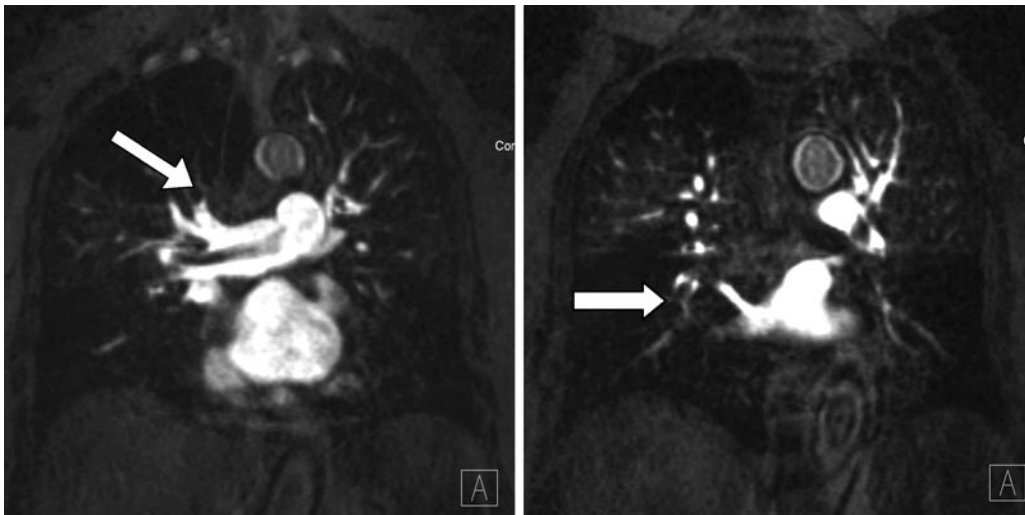


Fig. 2.1. Images of a time-resolved 3D MRA of a patient with acute central pulmonary embolism. Using parallel imaging the temporal resolution could be reduced to under 10 s per 3D data set without relevant trade-offs in the spatial resolution. The spatial resolution is sufficient to visualize peripheral emboli (*arrow*). Reproduced from FINK (2007) with permission)

MRA with a spatial resolution of $0.6 \times 0.6 \times 2 \text{ mm}^3$ and a temporal resolution of approximately 2 s.

With the introduction of clinical 3T MRI systems, high field imaging has also been evaluated for pulmonary MRA. In a feasibility study by NAEL et al. (2006a), 22 volunteers and 9 patients with mediastinal masses or pulmonary hypertension were examined with a high spatial resolution (reconstructed voxel size: $0.6 \times 0.9 \times 1.4\text{--}2.0 \text{ mm}^3$) and time-resolved (reconstructed voxel size: $1.6 \times 1.2 \times 12 \text{ mm}^3$, TA: 1.5 s) pulmonary MRA at 3 Tesla. Visualization up to fourth-order pulmonary arterial branches was observed in time-resolved MR angiograms and that up to fifth-order branches was observed in high spatial resolution MR angiograms with good image quality and high SNR. In a subsequent study by the same author, the feasibility of isotropic high spatial resolution MRA of the entire pulmonary circulation was evaluated using a 32-channel coil array. Using GRAPPA with an acceleration factor of six MRA data sets with a voxel size of $1 \times 1 \times 1 \text{ mm}^3$ were acquired in a breathhold time of 20 s and allowed the visualization of fifth-order arterial branches with high SNR and good image quality (NAEL et al. 2007). The same group also evaluated the feasibility

of pulmonary perfusion MRI at 3 Tesla using a time resolved MRA sequence. In comparison to 1.5 T, the results of pulmonary perfusion and flow indices were comparable at both magnetic fields, with no statistically significant difference. Significantly higher SNR values were found for vascular structures at 3.0 T, whereas the parenchymal enhancement was significantly lower at 3.0 T (NAEL et al. 2006b). Table 2.1 gives examples of time-resolved and high-resolution *ce*-MRA protocols.

Apart from advances in hardware and sequence techniques, new MR contrast agents can potentially improve pulmonary MRA. Recently, the first blood pool MR contrast agent (i.e. Gadofosveset Trisodium) has been approved for MRA. For pulmonary MRA, blood pool MR contrast agents are promising, as alternative imaging techniques, i.e. navigator gated MRA might be realized which cannot be used with conventional extracellular MR contrast agents (ABOLMAALI et al. 2002). Moreover, these chelates usually have a higher relaxivity which might be used to improve the spatial resolution (Fig. 2.2). Finally, time-resolved MRA (e.g. perfusion imaging) might be combined with high-spatial resolution MRA after a single injection (FINK et al. 2004a).

Table 2.1. Examples of high-resolution and time-resolved ce-MRA protocols

| | High-resolution MRA | | Time-resolved MRA | |
|-------------------------------|-------------------------|-------------------|-------------------|----------------|
| | 1.5 T | 3 T | 1.5 T | 3 T |
| Field strength | 1.5 T | 3 T | 1.5 T | 3 T |
| TR/TE [ms] | 2.9 × 1.2 | 2.98/1.13 | 1.98/0.81 | 2.06/0.81 |
| Sequence | 3D FLASH with GRAPPA ×2 | | | |
| Flip angle | 25 | 19–23 | 20 | 14–18 |
| Bandwidth [Hz] | 650 | 710 | 1120 | 1120 |
| Voxel size [mm ³] | 0.7 × 1 × 1.6 | 0.6 × 0.9 × 1.4–2 | 1.6 × 1.2 × 10 | 1.6 × 1.2 × 10 |
| FOV [mm ²] | 400 × 400 | 390 × 351 | 380 × 380 | 380 × 380 |
| Matrix | 512 × 410 | 640 × 374 | 320 × 240 | 320 × 240 |
| Acquisition time [s] | 22 | 20 | 1.5 | 1.5 |
| Reference | NIKOLAOU et al. 2005 | NAEL et al. 2006a | NAEL et al. 2006b | |

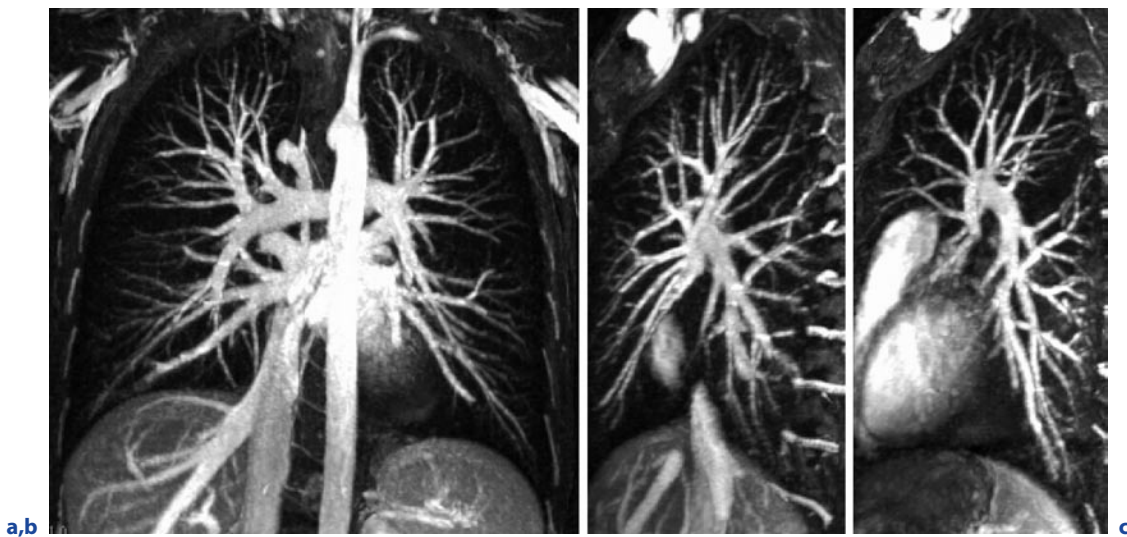


Fig. 2.2a–c. High-resolution contrast-enhanced MRA of the lung acquired with a blood pool MR contrast agent in a healthy volunteer. Using parallel imaging for ce-MRA isotropic spatial resolution can be achieved in a scan time of approximately 20 s. The isotropic spatial resolution allows a true 3D volumetric assessment of the pulmonary arterial tree. **a** Coronal maximum intensity projection (MIP). **b** Sagittal MIP of right lung. **c** Sagittal MIP of left lung. Reproduced from FINK et al. (2007) with permission

2.3

Postprocessing and Reporting

The use of spoiled gradient echo sequences with a high flip angle usually results in a good background suppression. To improve further the signal suppression of stationary tissue, e.g. for the preparation of MIP reconstructions, image subtraction can be used where

a non-enhanced mask data set is subtracted from the contrast-enhanced image data. In patients with lung disease, however, dyspnea may result in different diaphragm positions of the non-enhanced and contrast-enhanced data set resulting in misalignment artefacts. Similar to other vascular territories, 3D pulmonary ce-MRA data can be postprocessed using multiplanar reconstructions (MPR), maximum-intensity projections (MIP), and volume rendering techniques (VRT).

Whereas MPR and MIP are routinely used with the source images for reporting, VRT is often used for demonstration purposes.

2.4

Clinical Applications: Pulmonary Embolism

Several studies have evaluated the feasibility and diagnostic accuracy of pulmonary ce-MRA for the assessment of patients with suspected pulmonary embolism (PE) (Fig. 2.1).

In an early study by MEANEY et al. (1997) in 30 patients with suspected PE ce-MRA with a slice thickness ranging between 3 and 4 mm yielded a sensitivity and specificity for the detection of PE between 75%–100% and 95%–100% as compared to conventional pulmonary DSA. In addition, a good interobserver agreement (kappa values of 0.57–0.83) was demonstrated. A subsequent study by GUPTA et al. (1999) evaluated the accuracy of pulmonary ce-MRA in 36 patients with intermediate or low probability lung scintigraphy. Also in this study all patients underwent pulmonary DSA, which demonstrated PE in 13 patients. Pulmonary ce-MRA diagnosed 12 patients as having PE but missed 2 cases. This resulted in a sensitivity of 85% and specificity of 96%. Both missed pulmonary emboli were isolated and subsegmental in location. Similar to the study by MEANEY et al. (1997), the spatial resolution of MRA was low, using a slice thickness of 3.4 mm. In the largest study so far, OUDKERK et al. (2002) assessed the accuracy of pulmonary ce-MRA in 141 patients with an abnormal perfusion lung scintigraphy and compared the findings with pulmonary DSA. To improve the spatial resolution 2 separate slabs using a small field of view and 512 matrix were acquired with a reconstructed slice thickness of 1.25 mm. Ce-MRA detected 27 of 35 cases with confirmed PE, resulting in an overall sensitivity 77%. The sensitivity for isolated subsegmental, segmental and central/lobar PE was 40%, 84% and 100%, respectively. Ce-MRA demonstrated emboli in two patients with a normal angiogram, i.e. the specificity was 98%.

In a more recent study, BLUM et al. (2005) examined 89 patients with suspected PE using coronal, axial and sagittal orientated ce-MRA. The images were interpreted independently by two teams of radiologists. Different to the previous studies, a heterogeneous combination of clinical probability, D-dimer testing, spiral CT, compression venous ultrasound and pulmonary DSA served as the gold standard in this study. In addition the study cohort had a much higher prevalence of PE (i.e. 71%). Depending on the team of readers the

sensitivity and specificity of ce-MRA ranged between 31% and 71% and 85% and 92%, respectively. The lower accuracy in this study can partially be explained by the low spatial resolution of MRA, using a section thickness between 3.4 and 4.2 mm.

In another study performed on 48 patients with suspected PE, PLESZEWSKI et al. (2006) reported a sensitivity and specificity of 82% and 100%, respectively. Similarly to the study by BLUM et al. (2005), a combination of different imaging methods served as the gold standard in this study.

In the most recently published study by KLUGE et al. (2006), pulmonary ce-MRA was performed in 62 patients with suspected PE. Using parallel imaging their MRA technique achieved a substantially higher spatial resolution ($0.7 \times 1.2 \times 1.5$ mm) than the previous studies in a short acquisition time of 15 s. With this technique a sensitivity of 81% and specificity of 100% was achieved with pulmonary ce-MRA when compared to 16-slice CTA.

Time-resolved ce-MRA has also been evaluated for the assessment of patients with suspected PE. In a feasibility study, GOYEN et al. (2001) examined eight dyspneic patients with known or suspected PE using a time-resolved ce-MRA with a scan time of less than 4 s. Pulmonary ce-MRA allowed the assessment of the pulmonary arterial tree up to a subsegmental level, and identified PE in all four subsequently confirmed cases. All patients could hold their breath for at least 8 s, during which time a dataset with an angiogram of the pulmonary arteries could be obtained. In a study by OHNO et al. (2004), the diagnostic accuracy of time-resolved ce-MRA with parallel imaging (SENSE) was compared with CTA and ventilation-perfusion scintigraphy (VQ scan) in 48 patients with suspected PE. Conventional pulmonary DSA served as the gold standard. In this study time-resolved MRA had a higher sensitivity (92% vs 83% (CTA) and 67% (VQ scan)) and specificity (94% vs 94% (CTA) and 78% (VQ scan)) for the detection of PE than CTA and VQ scan.

In a more recent study by ERSOY et al. (2007), the efficiency of time-resolved ce-MRA was evaluated in 27 patients with clinically suspected pulmonary embolism and contraindication to iodinated contrast agents. Using ce-MRA as a screening test a confident exclusion or inclusion of pulmonary embolism was possible in 96% of patients.

Based on the promising results of those studies, the large multicenter trial PIOPED III trial was initiated in 2006 to assess the accuracy of ce-MRA in patients with suspected pulmonary embolism. Depending on the results of this study, MRA might be considered as a first-line imaging test for the exclusion of PE in the future.

References

- Abolmaali ND, Hietschold V, Appold S, Ebert W, Vogl TJ (2002) Gadomer-17-enhanced 3D navigator-echo MR angiography of the pulmonary arteries in pigs. *Eur Radiol* 12:692–697
- Blum A, Bellou A, Guillemin F, Douek P, Laprevote-Heully MC, Wahl D (2005) Performance of magnetic resonance angiography in suspected acute pulmonary embolism. *Thromb Haemost* 93:503–511
- Brenner DJ, Hall EJ (2007) Computed tomography – an increasing source of radiation exposure. *N Engl J Med* 357:2277–2284
- Du J, Bydder M (2007) High-resolution time-resolved contrast-enhanced MR abdominal and pulmonary angiography using a spiral-TRICKS sequence. *Magn Reson Med* 58:631–635
- Einstein AJ, Henzlova MJ, Rajagopalan S (2007) Estimating risk of cancer associated with radiation exposure from 64-slice computed tomography coronary angiography. *Jama* 298:317–323
- Ersoy H, Goldhaber SZ, Cai T et al. (2007) Time-resolved MR angiography: a primary screening examination of patients with suspected pulmonary embolism and contraindications to administration of iodinated contrast material. *AJR Am J Roentgenol* 188:1246–1254
- Fink C (2007) Pulmonary MRA. In: Reiser MF, Semmler W, Hricak H (eds) *Magnetic resonance tomography*. Springer, Berlin Heidelberg New York, pp 804–809
- Fink C, Bock M, Puderbach M, Schmahl A, Delorme S (2003) Partially parallel three-dimensional magnetic resonance imaging for the assessment of lung perfusion – initial results. *Invest Radiol* 38:482–488
- Fink C, Ley S, Puderbach M, Plathow C, Bock M, Kauczor HU (2004a) 3D pulmonary perfusion MRI and MR angiography of pulmonary embolism in pigs after a single injection of a blood pool MR contrast agent. *Eur Radiol* 14:1291–1296
- Fink C, Puderbach M, Bock M et al. (2004b) Regional lung perfusion: assessment with partially parallel three-dimensional MR imaging. *Radiology* 231:175–184
- Fink C, Puderbach M, Ley S et al. (2005) Intraindividual comparison of 1.0 M gadobutrol and 0.5 M gadopentetate dimeglumine for time-resolved contrast-enhanced three-dimensional magnetic resonance angiography of the upper torso. *J Magn Reson Imaging* 22:286–290
- Fink C, Ley S, Schoenberg SO, Reiser MF, Kauczor HU (2007) Magnetic resonance imaging of acute pulmonary embolism. *Eur Radiol* 17:2546–2553
- Fishman AP (1963) Dynamics of the pulmonary circulation. In: Hamilton WF (ed) *Handbook of physiology*. American Physiological Society, Washington D.C., pp 1667–1743
- Goyen M, Laub G, Ladd ME et al. (2001) Dynamic 3D MR angiography of the pulmonary arteries in under four seconds. *J Magn Reson Imaging* 13:372–377
- Griswold MA, Jakob PM, Heidemann RM et al. (2002) Generalized autocalibrating partially parallel acquisitions (GRAPPA). *Magn Reson Med* 47:1202–1210
- Gupta A, Frazer CK, Ferguson JM et al. (1999) Acute pulmonary embolism: diagnosis with MR angiography. *Radiology* 210:353–359
- Kluge A, Luboldt W, Bachmann G (2006) Acute pulmonary embolism to the subsegmental level: diagnostic accuracy of three MRI techniques compared with 16-MDCT. *AJR Am J Roentgenol* 187:W7–14
- Korosec FR, Frayne R, Grist TM, Mistretta CA (1996) Time-resolved contrast-enhanced 3D MR angiography. *Magn Reson Med* 36:345–351
- Meaney JF, Weg JG, Chenevert TL, Stafford-Johnson D, Hamilton BH, Prince MR (1997) Diagnosis of pulmonary embolism with magnetic resonance angiography. *N Engl J Med* 336:1422–1427
- Nael K, Michaely HJ, Kramer U et al. (2006a) Pulmonary circulation: contrast-enhanced 3.0-T MR angiography – initial results. *Radiology* 240:858–868
- Nael K, Michaely HJ, Lee M, Goldin J, Laub G, Finn JP (2006b) Dynamic pulmonary perfusion and flow quantification with MR imaging, 3.0 T vs 1.5 T: initial results. *J Magn Reson Imaging* 24:333–339
- Nael K, Fenchel M, Krishnam M, Finn JP, Laub G, Ruehm SG (2007) 3.0 Tesla high spatial resolution contrast-enhanced magnetic resonance angiography (CE-MRA) of the pulmonary circulation: initial experience with a 32-channel phased array coil using a high relaxivity contrast agent. *Invest Radiol* 42:392–398
- Nikolaou K, Schoenberg SO, Attenberger U et al. (2005) Pulmonary arterial hypertension: diagnosis with fast perfusion MR imaging and high-spatial-resolution MR angiography – preliminary experience. *Radiology* 236:694–703
- Ohno Y, Kawamitsu H, Higashino T et al. (2003) Time-resolved contrast-enhanced pulmonary MR angiography using sensitivity encoding (SENSE). *J Magn Reson Imaging* 17:330–336
- Ohno Y, Higashino T, Takenaka D et al. (2004) MR angiography with sensitivity encoding (SENSE) for suspected pulmonary embolism: comparison with MDCT and ventilation-perfusion scintigraphy. *AJR Am J Roentgenol* 183:91–98
- Oudkerk M, van Beek EJ, Wielopolski P et al. (2002) Comparison of contrast-enhanced magnetic resonance angiography and conventional pulmonary angiography for the diagnosis of pulmonary embolism: a prospective study. *Lancet* 359:1643–1647
- Pleszewski B, Chartrand-Lefebvre C, Qanadli SD et al. (2006) Gadolinium-enhanced pulmonary magnetic resonance angiography in the diagnosis of acute pulmonary embolism: a prospective study on 48 patients. *Clin Imaging* 30:166–172
- Prince MR, Grist TM, Debatin JF (2003) *3D contrast MR angiography*. Springer, Berlin Heidelberg New York

Remy-Jardin M, Pistoletti M, Goodman LR et al. (2007) Management of suspected acute pulmonary embolism in the era of CT angiography: a statement from the Fleischner Society. *Radiology* 245:315–329

Schoenberg SO, Bock M, Floemer F et al. (1999) High-resolution pulmonary arterio- and venography using multiple-bolus multiphase 3D-Gd-mRA. *J Magn Reson Imaging* 10:339–346

MR Perfusion in the Lung

FRANK RISSE

CONTENTS

| | | |
|-------|--|----|
| 3.1 | Introduction | 25 |
| 3.2 | Technical Challenges | 26 |
| 3.3 | Measurement Techniques | 26 |
| 3.3.1 | Contrast-enhanced Perfusion Imaging | 26 |
| 3.3.2 | Arterial Spin Labeling | 28 |
| 3.4 | Image Processing | 29 |
| 3.4.1 | Perfusion Quantification | 31 |
| | References | 33 |

3.1

Introduction

Perfusion is the blood flow of an organ at the capillary level, i.e. it is the amount of arterial blood delivered to a tissue in a certain time period. The unit of perfusion is $\text{mL min}^{-1} 100 \text{ g}^{-1}$ or, more commonly in lung perfusion imaging, $\text{mL min}^{-1} 100 \text{ mL}^{-1}$. Perfusion is closely related to the supply of organs and moreover to the function of the organ. It is altered in various diseases of the lung such as pulmonary hypertension or cystic fibrosis. Therefore, perfusion is an important functional parameter in diagnosis of pulmonary diseases.

The standard clinical tool for the assessment of perfusion is still $^{99\text{m}}\text{Tc}$ -Technetium labelled macroaggregated albumin scintigraphy despite the low spatial resolution and the lack of morphological information. However, MRI is a promising alternative providing morphologi-

KEY POINTS

Pulmonary perfusion is the blood flow of an organ at the capillary level. It is closely related to the blood supply of the lung and moreover to lung function. It is altered in various diseases of the lung such as pulmonary hypertension or cystic fibrosis, etc. Therefore, perfusion is an important functional parameter in the diagnosis of pulmonary diseases and quantitative values are urgently required to study physiology and pathophysiology of various lung diseases as well as monitor treatment response and identify differences under therapy. Pulmonary perfusion MRI is based on three-dimensional time-resolved contrast-enhanced T1-weighted sequences. The rapid acquisition of perfusion images facilitates the tracking of the first pass of a contrast agent through the lung parenchyma. Based on this information, it is possible to quantify perfusion in the entire lung using the indicator dilution theory. Quantification is challenging due to potential extravasation of the contrast agent during the first pass as well as the non-linear relationship between the concentration of the contrast agent and signal intensity. Some of these challenges can be addressed by a dual bolus technique.

cal and functional information. First experiments in rats using a spin echo sequence after the administration of contrast agent had already shown the potential of pulmonary perfusion MRI in an experimental set up (BERTHEZENE et al. 1992). As a result of the proceeding development of MR scanners, HATABU et al. (1996) were able to visualize the signal enhancement during the first pass of a contrast agent through the lungs in humans by utilizing a two-dimensional T1-weighted gradient echo sequence with short TE. Recently, investi-

F. RISSE, PhD

Dept. of Medical Physics in Radiology, German Cancer Research Center (DKFZ), Im Neuenheimer Feld 280, 69120 Heidelberg, Germany

gation of three-dimensional (3D) pulmonary perfusion by time-resolved contrast-enhanced MRI with acceptable temporal resolution and volume coverage has been proposed (FINK et al. 2004a, 2005a; NIKOLAOU et al. 2004; OHNO et al. 2004).

The rapid acquisition of perfusion images facilitates the tracking of the first pass of a contrast agent through the lung parenchyma. Based on this information, it is possible to quantify perfusion in 2D (HATABU et al. 1999; LEVIN et al. 2001) or, more recently, in 3D (FINK et al. 2004b; NIKOLAOU et al. 2004; OHNO et al. 2004). The latter allows for the investigation of perfusion changes in global lung diseases affecting the entire lung. Quantitative values may be particularly useful in studying physiology and pathophysiology as well as in follow-up studies to monitor treatment response and identify differences under therapy.

3.2

Technical Challenges

MRI of the lung is challenging in general, but to obtain functional information is even more complex than to perform mere morphological images. Reasons are on the one hand the large gas-filled space with only a small percentage of parenchyma and on the other hand respiratory and cardiac motion.

Conventional MRI is based on the measurement of the macroscopic magnetization of protons within the measurement volume. Air is virtually invisible to MRI but represents the majority of the lung volume. The percentage of parenchyma with a proton density sufficient to be detected by MRI is rather small (ca. 20%–30%). Additionally, the large area of air-tissue-interfaces – the lung surface has an area of approximately 140 m² (THEWS 1997) – leads to strong susceptibility gradients which make the use of fast imaging techniques like echo planar imaging virtually impossible. Furthermore, the T2* of the lung is very short, only in the range of 1.0–2.5 ms in lung parenchyma (PRACHT et al. 2005). The signal-to-noise ratio (SNR) is therefore low compared to other organs due to the low proton density and the rapid decay of the measured signal. Furthermore, the proton density varies due to respiratory motion leading to a variation of the MR signal. The most common solution for these problems is to acquire the perfusion images using pulse sequences with short echo times and within one breath hold. The perfusion measurement is then limited to a maximum 20–25 s depending on the constitution of the subject but is often lower in patients. Another consequence of the MR signal dependency of

the variable proton density is the perfusion dependence on the respiratory level. Perfusion is altered, particularly when quantified, with different breath hold levels. That is the tissue density and thus the proton density is higher in an expiratory breath hold than in an inspiratory breath hold (FINK et al. 2005). This has to be considered in the interpretation of lung perfusion images.

Beside these challenges, the high blood flow, leading to short transit times and possible inflow artefacts has to be taken into account. Thus, fast acquisition techniques are required in contrast-enhanced perfusion MRI to measure the contrast agent bolus properly when the blood flow is high. Furthermore, artefacts due to cardiac motion might alter perfusion information in the region of the heart since usually no ECG triggering is used for lung perfusion MRI to achieve the high temporal resolution.

3.3

Measurement Techniques

Basically two measurement techniques are used in pulmonary perfusion MRI: The first, and more common technique, uses contrast media to measure the regional blood flow at the capillary level. It is relatively easy to use and provides a good contrast-to-noise ratio but cannot be repeated arbitrarily. The second technique, arterial spin labelling (ASL), utilizes the water protons of the blood as an endogenous, freely diffusible tracer by labelling the spins with dedicated radio-frequency pulses. The evolution of the spin labelling is then measured in the lung parenchyma to assess information about perfusion (MAI and BERR 1999).

3.3.1

Contrast-enhanced Perfusion Imaging

Dynamic contrast-enhanced MRI (DCE-MRI) is based on the tracking of the signal change due to the first passage of a contrast media bolus through the lung capillaries (Fig. 3.1). It is therefore referred to as the “bolus tracking” or “first pass” technique. Originally the bolus tracking technique was introduced for perfusion imaging of the brain (ROSEN et al. 1990) and later adapted for the lungs by HATABU et al. (1996). In pulmonary perfusion MRI, the tracking is performed using dynamic T1-weighted pulse sequences after the intravenous injection of a contrast agent with a high flow rate between 3 and 5 mL/s to achieve a compact and high bolus profile. A high temporal resolution of usually ≤ 1.5 s is required

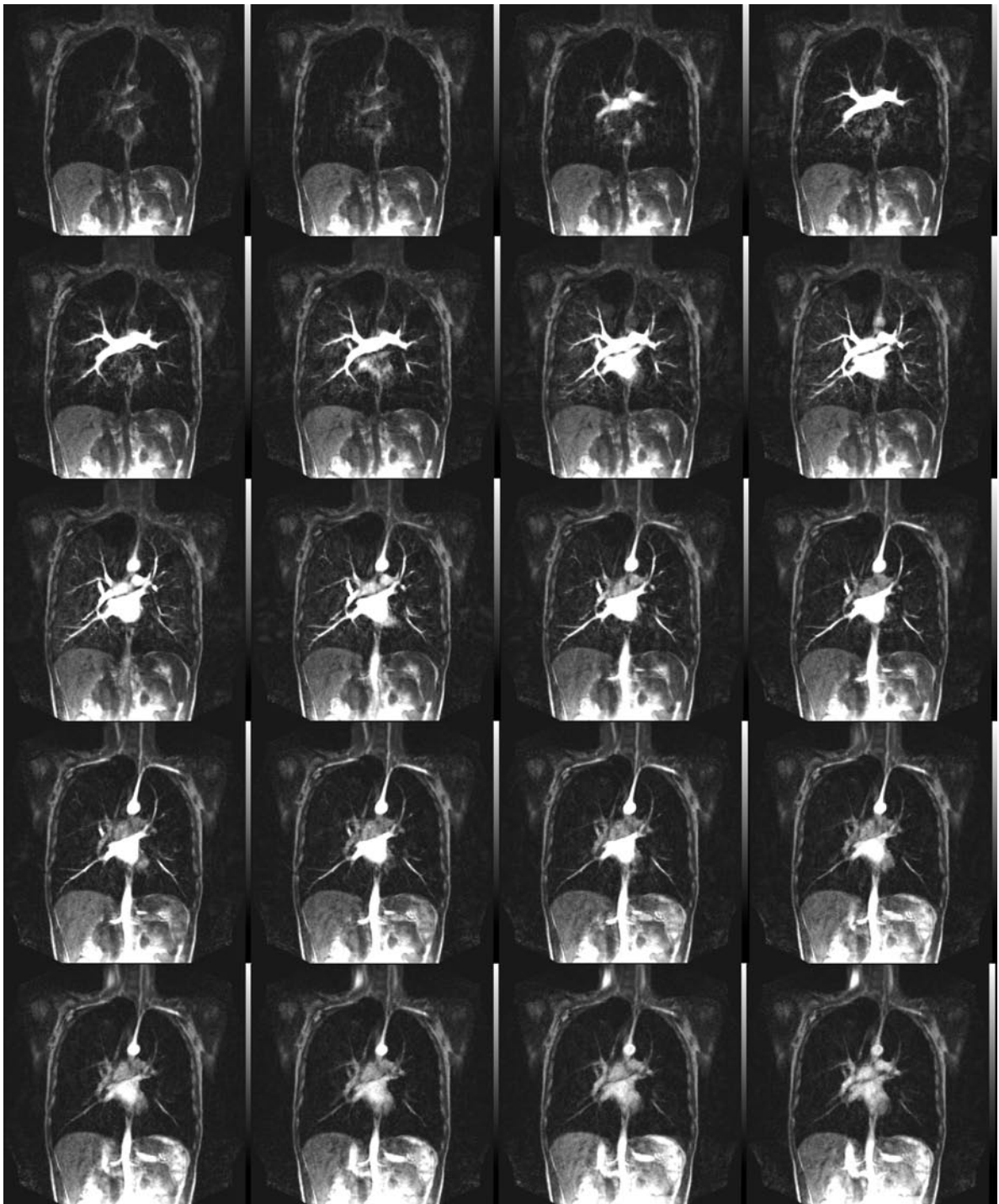


Fig. 3.1. First pass of a contrast agent through the central slice of a patient lung. The image acquisition was performed with a time-resolved 3D gradient echo pulse sequences with echo-sharing and parallel imaging. (Images courtesy of Dr. Christian Hintze, DKFZ, Heidelberg)

Table 3.1. Example for a clinical time-resolved 3D perfusion pulse sequence

| Name | Time-resolved echo-shared angiographic technique |
|--|--|
| Acronym | TREAT |
| Orientation | Coronal |
| No. of slices | 32 |
| No. of acquisitions | 20 |
| Flip angle/echo time/repetition time | 40°/0.64 ms/1.64 ms |
| Acquisition time | 1.5 s |
| Parallel imaging technique (acceleration factor) | GRAPPA (2) |
| Respiratory phase | Inspiration |

for an adequate acquisition of the bolus due to the high injection rates and the short contrast agent transit times through the lungs of approximately of 3–4 s (FISHMAN 1963).

Typical pulse sequences used for DCE-MRI in the lungs are fast gradient echo techniques like fast low angle shot (FLASH) or turbo FLASH. Both should be applied with short echo times below 1 ms due to the low $T2^*$ of 1.0–2.5 ms in lung parenchyma (PRACTH et al. 2005) to achieve a sufficient contrast-to-noise ratio. Nowadays, most lung DCE-MRI studies are performed using 3D techniques to acquire images of the entire thorax since the most pulmonary diseases are affecting the whole lung. Very short repetition times are therefore used to track the short signal change induced by the contrast agent. Present parallel imaging techniques like SENSE (PRUESSMANN et al. 1999) or GRAPPA (GRISWOLD et al. 2002) allow for a reduction of k-space lines and thus for shorter acquisition times per image. These techniques can also be used to improve the spatial resolution with the same acquisition time. Furthermore, the amount of k-space data can be reduced by acquiring only the central part of the k-space, i.e. the part that determines the image contrast, with high temporal resolution and updating the outer parts at a lower rate. This “view-sharing” technique was originally developed for contrast-enhanced MR angiography by KOROSIC et al. (1996). A combination of both, parallel imaging and view-sharing, showed recently superior spatial and image quality compared to only parallel imaging at the same temporal resolution (FINN et al. 2005b, c). An example for a clinical 3D perfusion sequence is given in Table 3.1. However, the use of 3D sequences is done on the cost of a lower temporal resolution compared to 2D techniques with acquisition times in the range of milli-

seconds. The temporal resolution is particularly important for perfusion quantification, where an exact tracking of the bolus is crucial.

3.3.2 Arterial Spin Labeling

Beside the contrast-enhanced perfusion MRI, ASL is the second method for the assessment of lung perfusion with MRI. In contrast to DCE-MRI, no contrast agent is necessary but the water protons of the blood are labeled with dedicated inversion pulses and used as an endogenous tracer. Usually, a control and a tag image are acquired and then subtracted to suppress the static background. The labeling can either be done in a continuous or pulsed mode, where the pulsed techniques allow for the quantification of perfusion mostly based on the general kinetic model of BUXTON et al. (1998). Several acquisitions are often required in ASL to achieve a sufficiently high SNR which makes it particularly difficult in lung perfusion imaging. Initial experiments were successfully performed by MAI and BERR (1999) and more recently, ASL techniques were used to determine the heterogeneity of lung perfusion (HOPKINS et al. 2005) and to quantify perfusion imaging (BOLAR et al. 2006).

However, ASL is usually not used in routine lung diagnostics for several reasons. A major drawback is the subtraction of two images which makes the technique particularly sensitive to respiratory and cardiac motion (MAI and BERR 1999), especially when several acquisitions are necessary. ECG and cardiac triggering can reduce these artefacts but without omitting them totally. New single-shot techniques do not require separate con-

trol images and might overcome these limitations also allowing for quantitative measurements within a single breath hold (BOLAR et al. 2006; PRACHT et al. 2005).

3.4

Image Processing

The investigation of contrast-enhanced perfusion data sets requires usually post-processing of the acquired images to achieve either a better visualisation of perfusion or obtain quantitative perfusion parameters.

The idea of most visualisation methods is to condense the information of the time-resolved 3D images. The reading of several hundred images is very time consuming and requires an experienced radiologist. Additionally, the visual presentation of the diagnostic findings to non-radiologists is difficult. Therefore, perfusion-weighted subtraction images can be generated on most MR scanners (Fig. 3.2). A pre-contrast image is subtracted from a dedicated contrast-enhanced image, typically with the one exhibiting maximum signal enhancement. The choice of the images is often done



Fig. 3.2. Perfusion-weighted subtraction image of a patient with chronic obstructive pulmonary disease. The image is generated by subtracting a pre-contrast image from the image with the signal maximum and shows multiple patchy perfusion image

by choosing the eligible image frames from signal-time-curves generated from a drawn region-of-interest (ROI) (FINK et al. 2004a). However, this approach has some drawbacks. Usually an additional investigation of a selection of original images has to be carried out. Furthermore, the choice of the images to be processed is observer-dependent and not always reproducible, particularly when a ROI analysis is performed. A suboptimal selection might mask regions of impaired perfusion in the subtraction images. Moreover, the temporal information is lost, although this is of utmost importance in diseases with inhomogeneous and delayed perfusion.

A possible solution is to compute qualitative and/or quantitative parameters. Common practise is to generate parameter images where qualitative parameters are displayed as colour-coded overlays (Fig. 3.3). These parameter images can be generated automatically on the MR scanners of most manufacturers. Usually the following parameters are calculated: the maximum signal enhancement or peak, the bolus arrival time and the time-to-peak. Some recent scanner software has also the option to compute quantitative parameters (cf. Sect. 3.4.1). The advantage compared to subtraction images is the consideration of the temporal information, e.g. delayed perfusion cannot be masked by the choice of a suboptimal ROI.

Nowadays, lung perfusion MRI is nearly exclusively done in 3D. Nevertheless, the reading of the generated colour-coded perfusion parameter maps is based on the 2D presentation hampering the visualization of perfusion defects in all three dimensions. But a 3D visualization would be desirable to fully exploit the volumetric information of perfusion MRI data sets. Recently, the implementation of an algorithm for a 3D visualization of functional perfusion parameters for better anatomic orientation and an improved representation of perfusion changes was presented (KUDER et al. 2007). The perfusion parameters calculated from 3D MR data sets were visualized in different cutting planes using a specially adapted interpolation algorithm as well as 3D volume rendering (Fig. 3.4). This might be helpful for the investigation of the exact localization and dimensions of abnormal perfusion by using the additional two cutting planes, e.g. for the planning of surgical therapy of lung emphysema or tumors. Furthermore, 3D parametric perfusion visualization might be used for radiation therapy planning to limit radiation dose to healthy perfused lung.

Beside the visual and qualitative analysis of the perfusion images, quantitative analysis is desirable for the estimation of regional lung function or in follow-up examination under therapy.

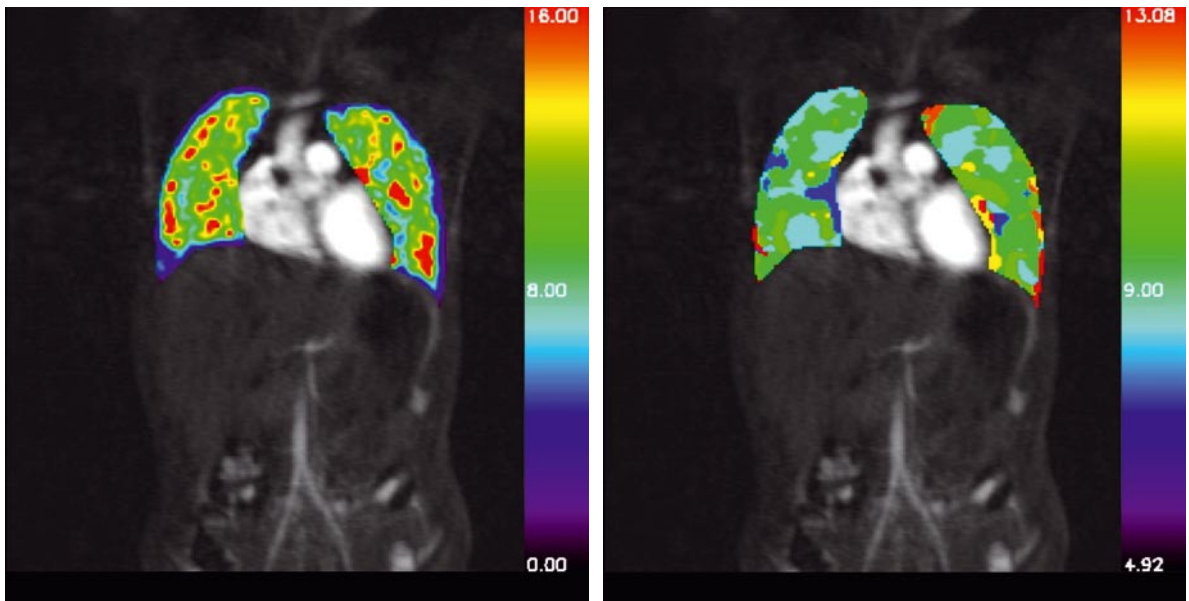


Fig. 3.3. Colour-coded parameter maps of a patient. Maximum signal enhancement or peak map on the *left*; Time-to-peak map on the *right*

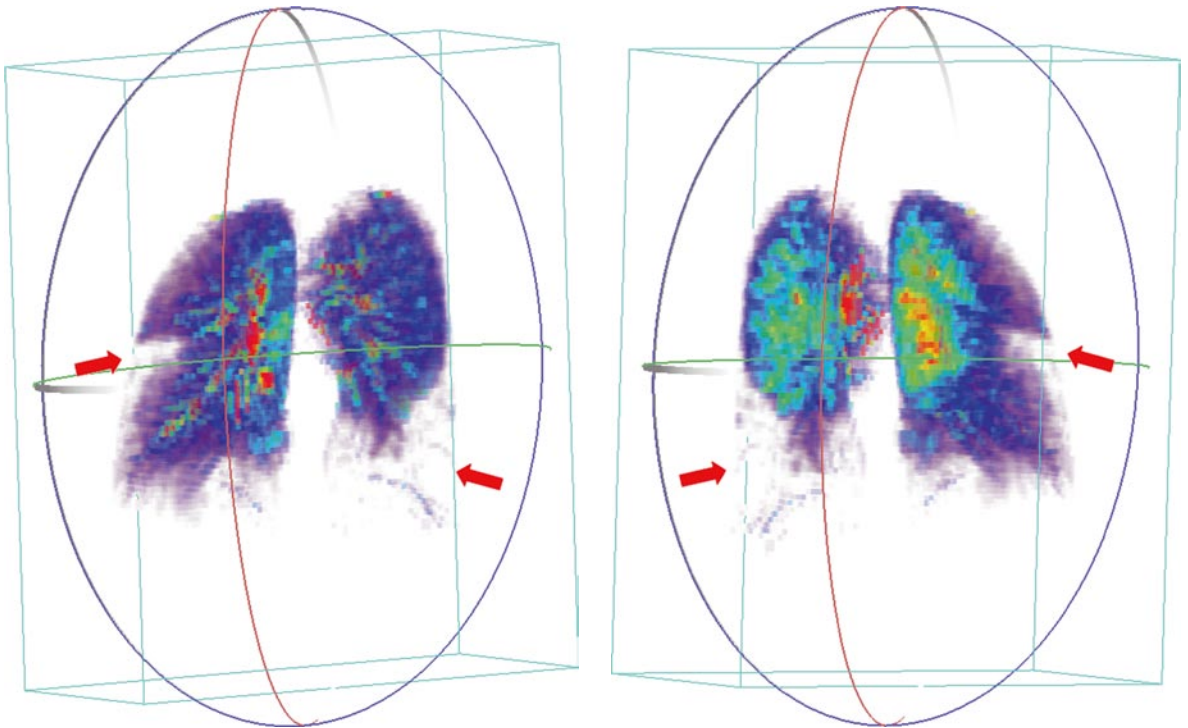


Fig. 3.4. 3D volume rendering of the regional pulmonary blood flow in a patient with acute pulmonary embolism (arrows) (From KUDER et al. 2007 with permission)

3.4.1 Perfusion Quantification

The pioneering work in the area of lung perfusion quantification was done by the group of Rob Edelman (CHEN et al. 1999; HATABU et al. 1999; STOCK et al. 1999). LEVIN et al. (2001) presented an approach to lung perfusion quantification using the so-called “gamma-variate” function on a pixel-by-pixel basis in healthy volunteers. In more recent studies, quantification of pulmonary perfusion is mostly done based on the indicator dilution theory (MEIER and ZIERLER 1954) modified for the use with MRI (FINN et al. 2004b, 2005; OHNO et al. 2004, 2007). Initially, an arterial input function (AIF) is defined in the feeding artery, i.e. the large pulmonary artery in case of the lung. The quantification is either done for the mean signal-time course of a defined region or for each pixel of the lung. Assuming a linear relationship between the measured MR signal and the contrast agent concentration, the signal can be converted to a relative concentration by

$$C(t) = k \frac{S(t) - S_0}{S_0}, \quad (3.1)$$

where $S(t)$ is the signal-time course, S_0 the mean signal before the arrival of contrast agent (the baseline) and k an unknown constant depending of the specific tissue characteristics, parameters of the pulse sequence, the contrast agent and the inspiration level. The inspiration level affects the density of the lung parenchyma and must therefore be constant during the measurement.

If the amount of contrast agent extravasating during the first pass through the lung is negligible, the measurement volume can be described by the convolution integral

$$C(t) = F[C_a(t) \otimes R(t)] = F \int_0^{\infty} C_a(t) \cdot R(t - \tau) d\tau, \quad (3.2)$$

where \otimes denotes the convolution. $C_a(t)$ is the concentration-time course of the AIF, F the regional blood flow and R the amount of contrast agent remaining in the measurement volume at time point t (Fig. 3.5). The pulmonary blood flow is therefore the initial height of $R(t_0)$, or the maximum of $R(t)$ in case of a delay between $C_a(t)$ and $C(t)$ and can be assessed by the deconvolution of the measured $C_a(t)$ and $C(t)$.

The regional blood volume may generally be calculated by

$$PBV = \frac{\int_0^{\infty} C(t) dt}{\int_0^{\infty} C_a(t) dt}. \quad (3.3)$$

However, the difference in the hematocrit of the large pulmonary artery and the lung parenchyma should be corrected by the additional factor $c_H = (1-h_G)/(1-h_C)$ (BRIX et al. 1997), where h_G is the hematocrit of the artery and h_C of the capillaries.

According to the central volume theorem (ZIERLER 1962), the mean transit time (MTT), the mean time a tracer particle needs to pass through the measurement volume, is

$$MTT = \frac{rBV}{F}. \quad (3.4)$$

It can also be calculated by the area height relation of the residual function

$$MTT = \frac{\int_0^{\infty} R(t) dt}{R(0)}. \quad (3.5)$$

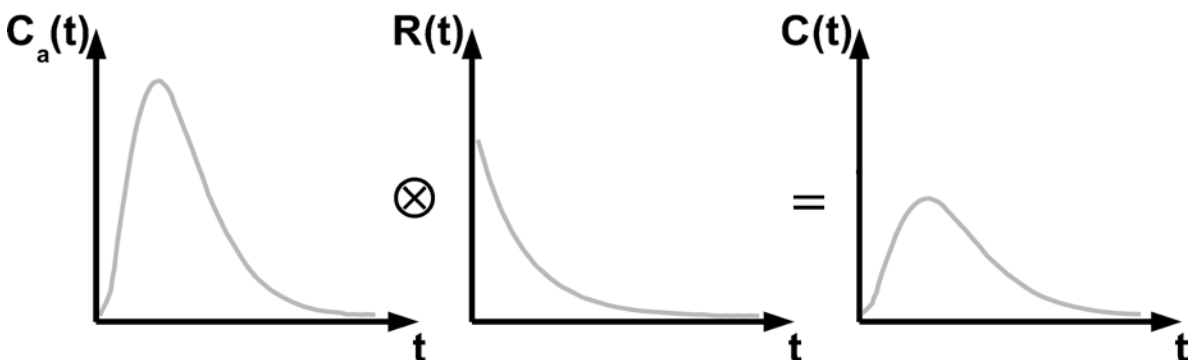


Fig. 3.5. Schematic representation of Eq. (3.2). The arterial input function $C_a(t)$ is measured in the large pulmonary artery, the tissue response $C(t)$ in a region-of-interest in the lung parenchyma or for each pixel in the lungs. The residual function $R(t)$ can be determined by the deconvolution of $C_a(t)$ and $C(t)$

A problem in quantification arises from Eq. (3.2) or actually from the discrete form of Eq. (3.2)

$$C(t) = F\Delta t \sum_{i=1}^j C_a(t_i) \cdot R(t_j - t_i) \quad (3.6)$$

as used in MRI. The solution starts to oscillate, i.e. generate meaningless results, when solved directly by, e.g., Fourier transformation in the presence of noise. Therefore, regularization tools are needed for the calculation of $R(t)$. A simple tool is the truncated singular value decomposition (tSVD), which provides stable solution in the presence of noise as shown in brain perfusion MRI (ØSTERGAARD et al. 1996). Equation (3.6) can be written in matrix notation:

$$Ax = b \quad (3.7)$$

with

$$A = \begin{pmatrix} C_a(t_1) & 0 & \dots & 0 \\ C_a(t_2) & C_a(t_1) & \dots & 0 \\ \vdots & \vdots & \ddots & \vdots \\ C_a(t_n) & C_a(t_{n-1}) & \dots & C_a(t_1) \end{pmatrix}, \quad (3.8)$$

$$x = F\Delta t \begin{pmatrix} R(t_1) \\ R(t_2) \\ \vdots \\ R(t_n) \end{pmatrix}, \quad b = \begin{pmatrix} C(t_1) \\ C(t_2) \\ \vdots \\ C(t_n) \end{pmatrix}.$$

Matrix A can be simplified as (HANSEN 1987)

$$A = USV^T = \sum_{i=1}^n u_i \sigma_i v_i^T \quad (3.9)$$

with $U = (u_1, \dots, u_n)$, $V = (v_1, \dots, v_n)$ and $S = \text{diag}(\sigma_1, \dots, \sigma_n)$. S has non-negative elements in decreasing order:

$$\sigma_1 \geq \sigma_2 \geq \dots \geq \sigma_n \geq 0. \quad (3.10)$$

Values of σ close to zero are probably caused by noise and generate the oscillations. The “noise problem” is now analyzed and can be resolved by setting an adequate threshold to truncate the “noisy” σ values. All σ below this threshold are simply set to zero and Eq. (3.6) can be solved. tSVD was successfully used in several lung perfusion studies (FINK et al. 2004, 2005; OHNO et al. 2004). However, the application of a fixed threshold with very variable noise levels and tissue characteristics as in lung perfusion MRI will lead to a suboptimal regularization of Eq. (3.6). LIU et al. (1999) therefore introduced an adaptive threshold for cerebral perfusion measurements to handle this problem but extensive simulations have to be done to compute the optimal threshold. Alternatives

like the Tikhonov regularization with the L-curve criterion are proposed for perfusion MRI (CALAMANTE et al. 2003; SOURBRON et al. 2004) where the optimal level of regularization is estimated automatically.

The administration of contrast agents is mostly done at doses up to 0.1 mmol/kg body weight to achieve a sufficient contrast-to-noise ratio (CNR) for diagnosis of perfusion defects. Similar to quantitative perfusion MRI in other body regions, e.g. cardiac perfusion MRI, linearity between local tissue contrast agent concentrations and the MR signal intensity, especially in the central pulmonary arteries, is a prerequisite. But the most commonly used pulse sequence FLASH has only a limited range of linearity for low contrast agent concentration, whereas signal saturation occurs for higher concentrations (Fig. 3.6).

The construction of the AIF is also described in Fig. 3.7. The new AIF can then be used to NIKOLAOU et al. (2004) found a dose of 0.05 mmol/kg body weight as appropriate for their lung perfusion protocol. In another study, OHNO et al. (2007) investigated bolus injection protocols with constant bolus volume of 5 mL but different contrast agent concentrations in dependence of the subject’s body weight and compared the perfusion parameters to perfusion single photon emission computed tomography (SPECT) measurements. Based on their results, a concentration of 0.3 mmol/mL Gd-DTPA was recommended for patients with a body weight <70 kg, and a concentration of 0.5 mmol/mL for patients with ≥ 70 kg body weight.

However, the total dose of contrast agent may not be reduced arbitrarily because of the resulting low CNR of the lung parenchyma, particularly in low perfused regions. As a consequence, the AIF signal is saturated

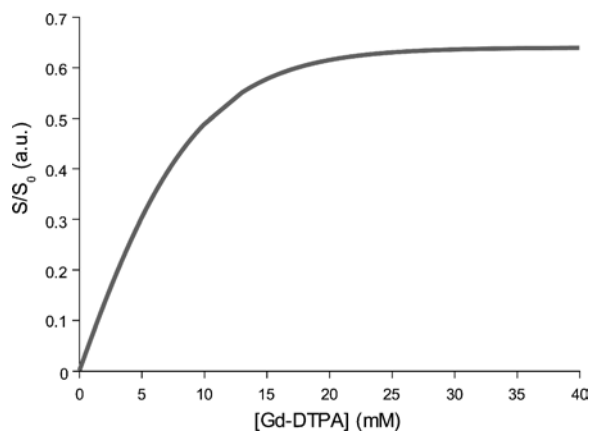


Fig. 3.6. Simulated normalized signal of a 3D FLASH sequence for different contrast agent concentrations. The non-linear behaviour for higher concentrations can be clearly seen

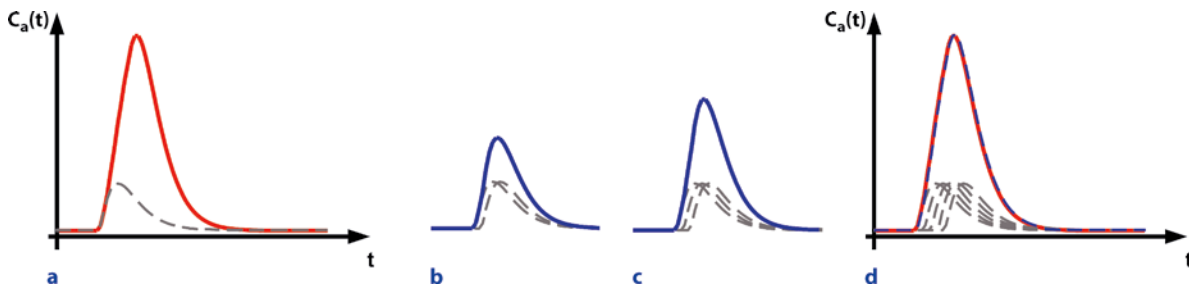


Fig. 3.7a–d. Calculation of the arterial input function for the dual bolus approach. **a** The theoretical input according to the second “clinical” bolus (*red*) and the measured low dose bolus. **b** In the first step, the prebolus volume is shifted according to its injection rate and added to the original prebolus. This re-

sults in the new input function (*blue*). **c** In the second step, the prebolus volume is again shifted and added to the intermediate result of step 1. **d** The procedure is repeated until the volume of the predicted volume of the second bolus (*red*) is reached (*blue*)

due to the high contrast agent concentration in pulmonary artery leading to an overestimation of perfusion parameters. Signal saturation might even occur in well-perfused healthy tissue (RISSE et al. 2006) for high doses. Therefore, a dual bolus approach to T1-weighted perfusion MRI was introduced, first to cardiac imaging (CHRISTIAN et al. 2004; KÖSTLER et al. 2004), and more recently, to lung perfusion MRI (RISSE et al. 2006). In addition to the “normal” contrast agent bolus, a prebolus with a low dose to achieve linearity is administered before the normal clinical dose. This prebolus is only used for the determination of the AIF in the large pulmonary artery, whereas the dataset acquired during the administration of the higher “clinical” dose yields the tissue signal. Admittedly, the prebolus cannot be used directly since according to Eq. (3.5) the dose differences would appear as an underestimation of the AIF signal, i.e. the calculation of perfusion parameters would yield too low values. Thus, assuming a linear and time-invariant system, the AIF bolus is calculated from the prebolus according to the dose of the second “high dose” bolus. In brief, the new AIF $C_a(t)$ is constructed by adding up the prebolus volume V_p until the volume of the corresponding second bolus V is reached. To take into account not only the volumes but also the kinetics, the prebolus is shifted by its injection duration τ during the construction process (KÖSTLER et al. 2004):

$$C_a(t) = \sum^{V/V_p} C_p(t + q\tau) \quad (3.11)$$

The construction of the AIF is also described in Fig. 3.7. The new AIF can then be used to calculate the regional perfusion parameters without the influence of saturation effects in the arterial input leading to more reliable perfusion quantification even when high clinical doses are needed. However, the application of a dual bolus technique is more complicated and a temporal gap be-

tween the first and second bolus is necessary to allow for a wash-out of the contrast agent before the second bolus administration. Furthermore, keeping to the linear relation between contrast agent concentration and MR signal for both measurements is still crucial.

References

- Berthezene Y, Vexler V, Clement O et al. (1992) Contrast-enhanced MR imaging of the lung: assessments of ventilation and perfusion. *Radiology* 183:667–672
- Bolar DS, Levin DL, Hopkins SR et al. (2006) Quantification of regional pulmonary blood flow using ASL-FAIRER. *Magn Reson Med* 55:1308–1317
- Buxton RB, Frank LR, Wong EC et al. (1998) A general kinetic model for quantitative perfusion imaging with arterial spin labeling. *Magn Reson Med* 40:383–396
- Calamante F, Gadian DG, Connelly A (2003) Quantification of bolus-tracking MRI: improved characterization of the tissue residue function using Tikhonov regularization. *Magn Reson Med* 50:1237–1247
- Chen Q, Levin DL, Kim D et al. (1999) Pulmonary disorders: ventilation-perfusion MR imaging with animal models. *Radiology* 213:871–879
- Christian TF, Rettmann DW, Aletras AH et al. (2004) Absolute myocardial perfusion in canines measured by using dual-bolus first-pass MR. *Radiology* 232:677–684
- Fink C, Puderbach M, Bock M et al. (2004a) Regional lung perfusion: assessment with partially parallel three-dimensional MR imaging. *Radiology* 231:175–184
- Fink C, Risse F, Buhmann R et al. (2004b) Quantitative analysis of pulmonary perfusion using time-resolved parallel 3D MRI – initial results. *Rofo* 176:170–174
- Fink C, Ley S, Risse F et al. (2005a) Effect of inspiratory and expiratory breathhold on pulmonary perfusion: assessment by pulmonary perfusion magnetic resonance imaging. *Invest Radiol* 40:72–79

- Fink C, Ley S, Kroeker R et al. (2005b) Time-resolved contrast-enhanced three-dimensional magnetic resonance angiography of the chest: combination of parallel imaging with view sharing (TREAT). *Invest Radiol* 40:40–48
- Fink C, Puderbach M, Ley S et al. (2005c) Time-resolved echo-shared parallel MRA of the lung: observer preference study of image quality in comparison with non-echo-shared sequences. *Eur Radiol* 156:2070–2074
- Fishman AP (1963) Dynamic of the pulmonary circulation. In: Hamilton WF (ed) *Handbook of physiology*. American Physiological Society, p 1708
- Griswold MA, Jakob PM, Heidemann RM et al. (2002) Generalized auto-calibrating partially parallel acquisitions (GRAPPA). *Magn Reson Med* 47:1202–1210
- Hansen PC (1987) The truncated SVD as a method for regularization. *BIT* 27:543–553
- Hatabu H, Gaa J, Kim D et al. (1996) Pulmonary perfusion: qualitative assessment with dynamic contrast-enhanced MRI using ultra-short TE and inversion recovery turbo FLASH. *Magn Reson Med* 36:503–508
- Hatabu H, Tadamura E, Levin DL et al. (1999) Quantitative assessment of pulmonary perfusion with dynamic contrast-enhanced MRI. *Magn Reson Med* 42:1033–1038
- Hopkins SR, Garg J, Bolar DS et al. (2005) Pulmonary blood flow heterogeneity during hypoxia and high-altitude pulmonary edema. *Am J Respir Crit Care Med* 171:83–87
- Korosec FR, Frayne R, Grist TM, Mistretta CA (1996) Time-resolved contrast-enhanced 3D MR angiography. *Magn Reson Med* 36:345–351
- Köstler H, Ritter C, Lipp M et al. (2004) Prebolus quantitative MR heart perfusion imaging. *Magn Reson Med* 52:296–299
- Kuder TA, Risse F, Eichinger M et al. (2007) New method for 3D parametric visualization of contrast-enhanced pulmonary perfusion MRI data. *Eur Radiol* (Epub ahead of print) DOI 10.1007/s00330-007-0742-7
- Levin DL, Chen O, Zhang M et al. (2001) Evaluation of regional pulmonary perfusion using ultrafast magnetic resonance imaging. *Magn Reson Med* 46:166–171
- Liu HL, Pu Y, Liu Y et al. (1999) Cerebral blood flow measurement by dynamic contrast MRI using singular value decomposition with an adaptive threshold. *Magn Reson Med* 42:167–172
- Mai VM, Berr SS (1999) MR perfusion imaging of pulmonary parenchyma using pulsed arterial spin labeling techniques: FAIRER and FAIR. *J Magn Reson Imaging* 9:483–487
- Meier P, Zierler KL (1954) On the theory of the indicator-dilution method for measurement of blood flow and volume. *J Appl Physiol* 6:731–744
- Nikolaou K, Schoenberg SO, Brix G et al. (2004) Quantification of pulmonary blood flow and volume in healthy volunteers by dynamic contrast-enhanced magnetic resonance imaging using a parallel imaging technique. *Invest Radiol* 39:537–545
- Ohno Y, Hatabu H, Murase K et al. (2004) Quantitative assessment of regional pulmonary perfusion in the entire lung using three-dimensional ultrafast dynamic contrast-enhanced magnetic resonance imaging: preliminary experience in 40 subjects. *J Magn Reson Imaging* 20:353–365
- Ohno Y, Murase K, Higashino T et al. (2007) Assessment of bolus injection protocol with appropriate concentration for quantitative assessment of pulmonary perfusion by dynamic contrast-enhanced MR imaging. *J Magn Reson Imaging* 25:55–65
- Pracht ED, Arnold JF, Wang T, Jakob PM (2005) Oxygen-enhanced proton imaging of the human lung using T2. *Magn Reson Med* 53:1193–1196
- Pruessmann KP, Weiger M, Scheidegger MB, Boesiger P (1999) SENSE: sensitivity encoding for fast MRI. *Magn Reson Med* 30:952–962
- Risse F, Semmler W, Kauczor HU, Fink C (2006) Dual bolus approach to quantitative measurement of pulmonary perfusion by contrast-enhanced MRI. *J Magn Reson Imaging* 24:1284–1290
- Rosen BR, Belliveau JW, Vevea JM et al. (1990) Perfusion imaging with NMR contrast agents. *Magn Reson Med* 14:249–265
- Sourbron S, Luytjens R, Van Schuerbeek P et al. (2004) Deconvolution of dynamic contrast-enhanced MRI data by linear inversion: choice of the regularization parameter. *Magn Reson Med* 52:209–213
- Stock KW, Chen Q, Levin DL et al. (1999) Demonstration of gravity-dependent lung perfusion with contrast-enhanced magnetic resonance imaging. *J Magn Reson Imaging* 9:557–561
- Thews G (1997) *Atmung*. In: Schmidt RF, Thews G (eds) *Physiologie des Menschen*, 27th edn. Springer, Berlin Heidelberg New York, pp 565–591
- Zierler KL (1962) Theoretical basis of indicator-dilution methods for measuring flow and volume. *Circ Res* 10:393–407

MRI of Pulmonary Ventilation

4.1 Hyperpolarised ^3He MRI: Physical Methods for Imaging Human Lung Function

JIM M. WILD

CONTENTS

| | | |
|---------|--|----|
| 4.1.1 | Introduction | 35 |
| 4.1.2 | Physical, Chemical and Medical Properties of ^3He and Gas Polarisation | 36 |
| 4.1.3 | Polarising the ^3He Nuclear Spin by Optical Pumping – Transfer of Angular Momentum from Photons | 36 |
| 4.1.4 | Storage, Transfer and NMR of HP Species | 38 |
| 4.1.5 | T1 Decay | 38 |
| 4.1.6 | In Vivo Administration of ^3He | 38 |
| 4.1.7 | MRI Hardware Considerations for HP ^3He | 39 |
| 4.1.7.1 | B_0 Field Strength | 39 |
| 4.1.7.2 | Radio-frequency (RF) Hardware | 39 |
| 4.1.8 | ^3He Imaging Pulse Sequence Considerations | 40 |
| 4.1.8.1 | Polarisation Usage | 40 |
| 4.1.9 | Physiological and Anatomical Sensitivity with HP ^3He | 43 |
| 4.1.9.1 | Ventilation Imaging | 43 |
| 4.1.9.2 | Dynamic Imaging | 44 |
| 4.1.9.3 | Measurement of Regional Oxygen Uptake with the Longitudinal Relaxation Time, T1 | 45 |
| 4.1.9.4 | Diffusion Measurement | 46 |
| 4.1.9.5 | Measuring Diffusion: Time-length Scale Dependence | 47 |
| 4.1.9.6 | Transverse Relaxation Time T2* | 53 |
| | References | 53 |

KEY POINTS

Gas imaging has opened the new field of direct imaging of pulmonary ventilation by MRI. The use of hyperpolarised ^3He gas for MRI of the lung has been pioneered by a number of groups worldwide. Due to the enormous progress in the fields of hyperpolarisation technology, administration of hyperpolarised ^3He , MR hardware, and MR pulse sequences significant progress has been made and the translation into the clinical arena has been accomplished. This chapter gives an overview of the technical methods for HP ^3He MRI for human lung imaging, focusing on gas polarisation methods, background physics, MRI hardware considerations, MRI pulse sequence considerations, safety considerations for imaging inhaled ^3He , and pulse sequence design for probing lung physiology and anatomy. Where possible the methods will be highlighted with reference to the literature and illustrated with clinical examples of images from the author's home group. For further discussion on the growing clinical applications the reader is referred to Chaps. 8, 9 and 10.

4.1.1 Introduction

It is now more than 12 years since the first images of hyperpolarised (HP) 3-helium (^3He) gas in human lungs were demonstrated (MIDDLETON et al. 1995; EBERT et al. 1996; MACFALL et al. 1996). In that time gas polarisation techniques and MRI methodology have developed such that HP gas MRI is now providing unsurpassed images of gas ventilation and simultaneous sensitivity to various functional aspects of lung physiology in a wide range of human lung diseases. Despite the

obvious potential for the images to shed new light on lung function, the technique has still to find general acceptance in the clinical mainstream for a variety of reasons. These include; advances in other techniques such as CT that are already well established and accepted in the chest radiology community, limited accessibility to the necessary technology for polarising and imaging ^3He and perhaps most importantly, the clear cut identification of clinical applications that will positively benefit from the technology.

Several comprehensive reviews have been written to date on both the physics of gas polarisation and non-clinical applications of HP gas NMR (GOODSON 2002; OROS and SHAH 2004) and the growing number of applications in biomedical science and clinical radiology (KAUCZOR and MAINZ HELIUM 2002; MOLLER et al. 2002; VAN BEEK et al. 2004; FAIN et al. 2007). It is fair to say that ^3He has made more impact to date than ^{129}Xe in human lung imaging, with numerous clinical research exams having been performed at over ten sites worldwide using whole body MRI scanners in a wide range of chest diseases including asthma (ALTES et al. 2001; SAMEE et al. 2003), cystic fibrosis (KOUPELLIS et al. 2005; DONNELLY et al. 1999), emphysema/COPD (SWIFT et al. 2005; KAUCZOR et al. 1996; SAAM et al. 2000; SALERNO et al. 2002; STAVNGAARD et al. 2005), lung transplant (GAST et al. 2003) and lung cancer (IRELAND et al. 2007). Recent developments in ^{129}Xe polarisation levels have however facilitated high quality human ^{129}Xe images in recent years (see Chap. 4.2).

4.1.2 Physical, Chemical and Medical Properties of ^3He and Gas Polarisation

^3He gas is a monatomic radio-stable isotope of the inert gas helium, it has a very low natural abundance on earth (0.000137% of natural abundant helium) with most of the ^3He being derived from beta decay of the tritium nucleus in the nuclear industry. From an MRI perspective, the spin 1/2 of the ^3He atom coupled with its relatively high gyromagnetic ratio ($\gamma_{^3\text{He}} = 32.3 \text{ MHz/T}$) make it very sensitive to NMR techniques. ^3He is a highly diffusive gas due to its low atomic weight, having a self diffusion coefficient of $2 \text{ cm}^2/\text{s}$, which is reduced to around $0.9 \text{ cm}^2/\text{s}$ in air. The diffusion coefficient can be measured with NMR, and the measured ^3He apparent diffusion coefficient (ADC) has a spatial dependence when introduced in to a porous medium whose walls inhibit free diffusion. This feature can be used to probe alveolar length scales in the lungs and is discussed later. As an inert gas, the NMR T1 relaxation time of ^3He is po-

tentially very long and can approach the dipole-dipole limit of days providing the gas is stored in a magnetically homogeneous environment. ^3He can be imaged in the gaseous state using conventional Boltzmann thermal polarisation of the Zeeman effect, however the low spin density of the gaseous state makes the signal too weak for in-vivo MRI. The polarisation can however be increased by using an alternative mechanism.

4.1.3 Polarising the ^3He Nuclear Spin by Optical Pumping – Transfer of Angular Momentum from Photons

Laser optical pumping (OP) with circularly polarised light at selective wavelengths can be used to drive the electronic spins of certain atoms in to non-Boltzmann distributions. The process of optical pumping of electronic spins was first discovered over 50 years ago (KASTLER 1950) and since then it has been used to transfer electronic spin polarisation to nuclear spin systems by the process of spin exchange (WALKER and HAPPER 1997). In optical pumping, the laser photons are wavelength matched to a chosen electronic orbital transition of the atomic system. For noble gas polarisation this system is generally the orbital energy levels of an alkali metal atom such as rubidium or the electron levels of meta-stable atoms of ^3He . The photons are circularly polarised with respect to the direction of an external B_0 field using a $\lambda/4$ optical polariser. The B_0 field produces a Zeeman splitting in these orbital energies, and subject to the angular momentum selection rules for transitions between the available orbital levels and their Zeeman sub-levels, a net exchange of angular momentum between the spin polarised photons and the electronic system can be made, resulting in a non-Boltzmann occupancy of selected electronic Zeeman states. Having established a hyper-populated electron Zeeman sub-level, spin polarisation is then transferred to the nuclear Zeeman system of the spin 1/2 noble gas atom of interest, e.g. ^3He or ^{129}Xe ; the process is thus called spin exchange optical pumping, (SEOP). The mechanism of spin polarisation exchange is the Fermi contact hyperfine interaction that relies on an overlap of the $^2S_{1/2}$ electron wave function with the noble gas nucleus. This interaction takes place in the case of ^3He SEOP during binary collisions between ^3He and alkali metal atoms in the vapour state. In the case of ^{129}Xe SEOP the spin polarisation exchange process may involve the temporary formation of an intermediate van der Waal's molecule with N_2 gas in the optical pumping cell. The rate of spin polarisation transfer is influenced by a number

of physical factors inside the optical pumping cell which include gas pressure, vapour pressure of the alkali metal, incident photon flux, gas temperature and propensity for formation of intermediate molecules. A fundamental limiting factor is the electron-nuclear cross section, i.e. the probability of finding the electron wave function at the nucleus of interest, α which is larger for ^{129}Xe -Rb than for ^3He -Rb explaining the generally longer SEOP spin-up times for ^3He . The process of SEOP was pioneered and refined by the Happer group at Princeton (WALKER and HAPPER 1997), and led to the design of a prototype commercial SEOP polariser with the formation of the MITI company. The patents for this design were subsequently bought by Nycomed-Amersham and then GE and despite phase II clinical trials, the device was never properly commercialised. At the time of writing there exists some ambiguity over future routes to commercialisation of SEOP for ^3He MRI. From a practical perspective this polariser uses a 60-W FAP laser at 795 nm and is capable of polarising approximately 1 L of ^3He to a polarisation of 25%–40% in a spin-up period of around 20 h. This provides sufficient HP ^3He gas to perform 3–4 in vivo imaging exams and hence large throughput clinical research studies really require a system that provides gas at a higher volume polarisation rate. Higher power lasers with narrowed optics (ZHU et al. 2005) provide more effective deposition of the polarised photon beam energy to the electron spin transition and are now routinely enabling polarisation levels of ^3He with SEOP – see Fig. 4.1.1a.

^3He can also be polarised by the alternative method of *meta-stable* spin exchange optical pumping (MEOP)

(COLEGROVE et al. 1963) whereby the paired electrons in the ground state 1^1S_0 need exciting in to the meta-stable 2^3S_1 state by means of a weak UV irradiation. Thereafter optical pumping of the 2^3S_1 2^3P_0 transition can take place with circularly polarised photons at $\lambda = 1083$ nm and nuclear spin polarisation is built up through collisions of the meta-stable ^3He atoms in the low pressure optical pumping cell. The process of meta-stable spin exchange is faster but because of the low pressure regime the volume of polarised ^3He gas needs to be compressed and extracted from the optical pumping cell for in vivo use. It is fair to say that the MEOP process is more demanding than SEOP in terms of reliable extraction of large volumes of polarised gas for in vivo MRI; however much of the physics and engineering involved has been refined by the Mainz Physics group who have been active in the area for many years (SCHMIEDESKAMP et al. 2003a). The Mainz metastable polariser and compressor (Fig. 4.1.1b) was originally built for production of HP ^3He for neutron spin filter work; however the group was already polarising gas for in vivo MRI more than 10 years ago (EBERT et al. 1996).

The potentially very long T1 of ^3He (days) facilitates the transport of HP ^3He . WILD et al. (2002b) and the Mainz Physics group have subsequently polarised and delivered gas to more than ten sites worldwide by road and air and have been extremely supportive of the development of clinical applications of ^3He . By comparison these T1s are much greater than the half-life of FDG used in PET (110 min), a technique that is performed routinely in hospitals without access to on-site cyclotrons.

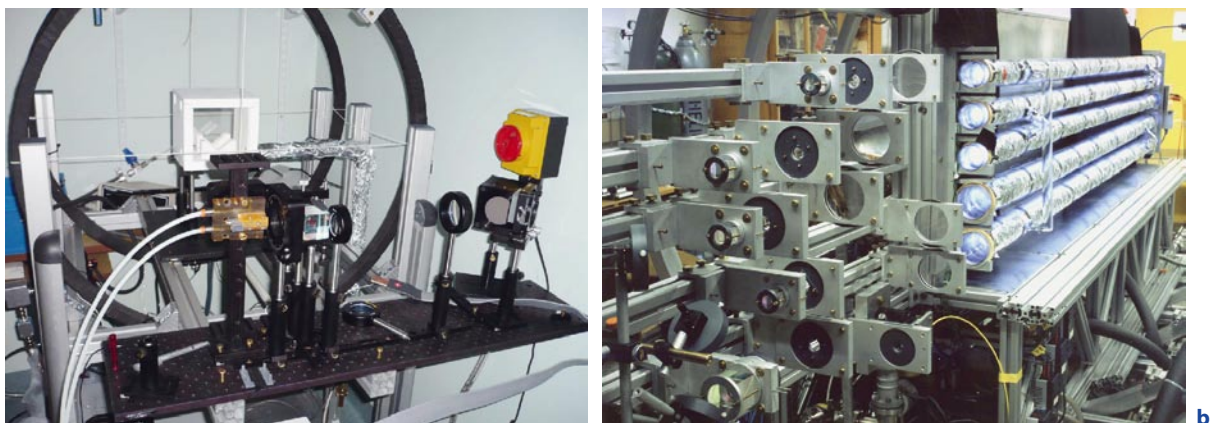


Fig. 4.1.1. **a** SEOP polariser in Sheffield with 100 W external cavity diode laser at 795 nm. **b** The Mainz Physics metastable ^3He polariser and compressor, image courtesy of Professor Werner Heil and Professor Ernst Otten

4.1.4 Storage, Transfer and NMR of HP Species

Having polarised the ^3He nucleus, it is vital that the polarisation is preserved in transit from the polariser to the NMR magnet. This journey may involve taking the polarised nuclear system from one B_0 to another through inhomogeneous field gradients. In noble gas OP, the polarising fields are typically very weak ($B_0 \sim 2\text{mT}$) whereas the NMR system may have a B_0 of several T. Therefore precautions need to be taken to prevent a non-adiabatic field change, as such the Zeeman polarisation needs to be preserved in a holding B_0 field (which can be weak; the earth's field may suffice for short journeys) to ensure the sample is not taken through a zero field condition (field direction change). In the context of a hyperpolarised nuclear Zeeman system ensemble, the *adiabatic* condition has the meaning that when an external factor such as the B_0 is changed the population of the Zeeman levels remains unchanged such that no transitions are induced.

4.1.5 T1 Decay

Having polarised a sample, the next challenge is storing it and delivering it to the NMR system. The T1 of the sample depends strongly upon the physical environment. For example pure ^3He gas has minimal spin-lattice interactions (T1 is virtually frequency independent) and in the limit has a T1 that represents the dipole-dipole interaction and is extremely long (>700 hours at 1 atm pressure). This opens up the possibility of transporting the polarised gas large distances from polarisation source to NMR site. Brownian diffusion of HP gases in the presence of macroscopic B_0 field gradients will reduce the T1 (SCHEARER and WALTERS 1965), as will microscopic field perturbations experienced during collisional contact of the gas with magnetic impurities in the walls of the storage cells (SCHMIEDESKAMP et al. 2003b). Furthermore, mixing with a paramagnetic gas such as oxygen will radically reduce the T1 (SAAM et al. 1995) (T1 ^3He in air ~ 20 s), an effect that will later be discussed as a means of probing lung oxygenation.

4.1.6 In Vivo Administration of ^3He

Having polarised the ^3He , it is typically mixed with a larger volume of nitrogen and delivered to the subject

for inhalation either by manual means from a sealed plastic bag or by an automated respirator device. The volume of ^3He used directly effects the signal to noise of the acquired images, with gas polarised to 30%, 300 ml of ^3He typically provides sufficient signal to noise for a complete imaging sequence at 1.5 T. To put the raw material costs into perspective, this volume of ^3He currently would cost approximately 40 Euros. There are concerns over the longevity of world supplies of ^3He , since it has a negligible natural abundance, being derived as a by product of the nuclear industry. One possibility is to scavenge the exhaled gas, since helium is insoluble in the blood, 90% of the gas gets exhaled within about ten breaths (Fig. 4.1.2) making recycling a cheap and viable option.

Another very important factor that should be considered is patient safety during breath-hold imaging exams. In Sheffield all subjects have been imaged with full vital signs monitoring. The blood oxygen saturation levels tend to take a dip towards the end of a long breath-hold (20 s) whilst this can be pre-empted by pre-washing the lungs with a high concentration of oxygen in patients without signs of emphysema. This measure can however degrade the SNR in the images by virtue of the T1 shortening effect of oxygen (DENINGER et al. 1999). In studies which compared the patients vital signs when gas was delivered as an anoxic 1-L dose from a bag or as a bolus via the respirator device chased with room air, it was observed that the latter mode of delivery prevented the blood O_2 saturation from falling (WOODHOUSE et al. 2006) – see Fig. 4.1.3.

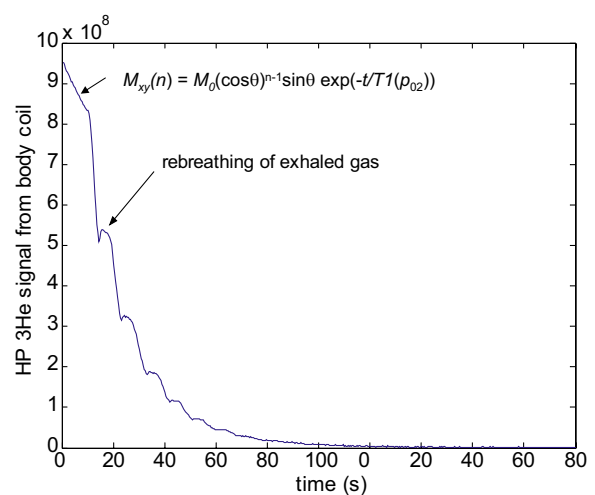


Fig. 4.1.2. Signal depolarisation and washout time course of HP ^3He signal in the lungs of a healthy volunteer

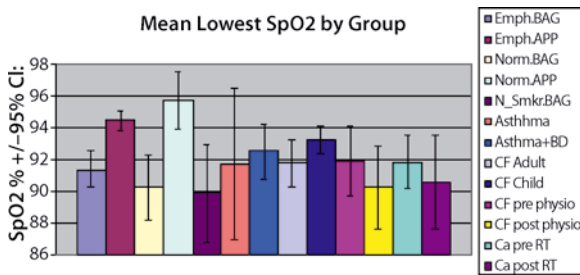


Fig. 4.1.3. Summary of blood oxygenation from vital signs monitoring in subject groups scanned with ^3He in Sheffield over the last 7 years (WOODHOUSE et al. 2006)

The pulse rate also starts to rise towards the end of the breath-hold exam, as might be expected, nevertheless these effects are rapidly reversible. No lasting adverse effects have been found in the experience at Sheffield (in excess of 100 patients and 100 volunteers) and in similar experience published by the University of Virginia only mild adverse events were reported in less than 10% of the subjects group (DE LANGE et al. 2003). This is also in agreement with recently published data from the University of Washington (LUTEY et al. 2008). From a regulatory perspective ^3He is now classed as an investigational medicinal product in Europe and the USA. In Europe a regulatory licence is needed and the Sheffield and Mainz groups have these granted from the UK and EU regulatory bodies for clinical research purposes.

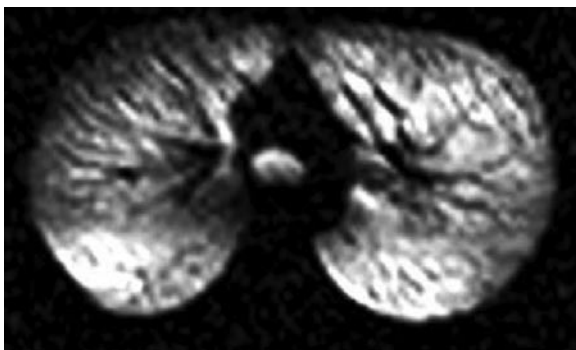


Fig. 4.1.4. Axial 2D SPGR image of HP ^3He in a healthy volunteer acquired at 3T in Sheffield

4.1.7

MRI Hardware Considerations for HP ^3He

4.1.7.1

B_0 Field Strength

The polarisation of ^3He is independent of the static magnetic field (B_0) of the MRI magnet and as such there is scope for high signal to noise ratio imaging at lower field strengths (DURAND et al. 2002; OWERS-BRADLEY et al. 2003; SALERNO et al. 2005; TSAI et al. 2008); indeed both ^3He proton MRI of lungs may benefit from lesser magnetic susceptibility artifacts than are found at clinical imaging field strengths of 1.5 T (MULLER et al. 2001). Some theoretical discussion has taken place as to the optimum theoretical field strength for HP gas imaging (PARRA-ROBLES et al. 2005); the answer is still very much dependent on the size of the object which dictates the electromagnetic field regime for RF coil coupling to the sample and the associated noise regime. Although interesting from a technical and theoretical point of view, this optimum B_0 has yet to be fully experimentally proven and from a practical point of view it is fair to say that high quality ^3He images are routinely acquired at 1.5 T. Low field imaging of HP gas represents a cheap solution and allows the possibility of probing the physiological effects of posture with magnets oriented in an upright position (TSAI et al. 2008); however the larger commercial MRI vendors are pushing their multi-nuclear imaging efforts on to higher field systems (1.5 T and above) and preliminary results at 3 T from Sheffield (see Fig. 4.1.4) and the Robarts Institute, Canada (PARRAGA et al. 2008) are encouraging.

4.1.7.2

Radio-frequency (RF) Hardware

Although non-proton imaging is possible on commercial MRI spectrometers, at the time of writing none of the major vendors offer an integrated complete hardware solution for ^3He MRI. Thus the interested party will either have to build their own transmit-receive switches and transmit-receive coils or purchase from a third party vendor. Transceiver coils for HP gas MRI need to be large enough to cover the FOV of the adult lungs and airways (approximately $30 \times 30 \times 18 \text{ cm}^3$) without subject discomfort. Furthermore, the coils must be able to function safely and efficiently, often within the confines of a clinical whole-body scanner which has limited bore access. Most whole-body systems are fitted with integrated proton body transmit coils and



Fig. 4.1.5. Custom birdcage quadrature body transmit-receive coil for ^3He at 1.5 T described in DE ZANCHE et al. (2008)

therefore resonant coupling between this volume resonator and the HP volume coil needs to be considered in the design process. Other design constraints include portability and minimisation of scanner down time due to hardware changes between ^1H and HP nuclear imaging exams. From an application perspective, HP gas MRI is very sensitive to flip angle by virtue of the non-renewable polarisation; thus the transmit coil must provide a uniform excitation angle across the whole of the lungs for a range of flip angles. A large volume resonator such as an insert birdcage provides a solution to many of these requirements (DE ZANCHE et al. 2008) – see Fig. 4.1.5 – although higher receive sensitivity may be attained with a closer fitting coil.

A close fitting transmit coil will invariably have a poorer B1 spatial homogeneity and may also pose problems with SAR and burning at the skin. A solution may be to use a volume coil as shown in Fig. 4.1.5 with a dedicated ^3He receiver array for increased sensitivity and also opens up the opportunity for parallel receiver imaging with ^3He (LEE et al. 2006).

4.1.8 ^3He Imaging Pulse Sequence Considerations

Having delivered the HP ^3He to the MRI system and administered to the subject, the T1 will rapidly decrease whenever exposed to oxygen in the air (SAAM et al. 1995). Thus the in-vivo acquisition window for an HP pulse sequence is generally short and is constrained

by the subject's breath-holding capability; for sick patients a breath-hold duration of less than 15 s is usually well tolerated (WOODHOUSE et al. 2006). The remaining challenge is effective use of the finite polarisation for high SNR MRI. Pulse sequence optimisation should also take in to account the fact that the lungs are a magnetically inhomogeneous medium with a 9 ppm difference in susceptibility between the parenchyma and air-spaces, and susceptibility artifacts may be misdiagnosed as impaired ventilation (WILD et al. 2003a). Moreover, the high diffusivity of ^3He poses a potential problem in that the imaging gradients act to dephase the transverse magnetisation.

4.1.8.1 Polarisation Usage

For a spoiled gradient echo (SPGR) sequence built up with a series of $n = 1$ to N , RF views of constant flip angle (CFA) α , the transverse magnetisation during a breath-hold HP gas acquisition decays as

$$M_{xy}(n) = M_0 \sin \alpha (\cos \alpha)^{n-1} \exp[-t/T1(pO_2)] \quad (1)$$

where $T1$ depends on the regional oxygen partial pressure, pO_2 , which itself changes during the breath-hold (DENINGER et al. 1999). The first section of the curve in Fig. 4.1.2 shows this behaviour as the subjects holds their breath and the signal depletes according to Eq. (1). This polarisation depletion from view to view using a spoiled gradient echo sequence (SPGR) imposes a k-space filter on the data in the RF encoding dimension (WILD et al. 2002a) which can cause blurring or signal attenuation. As such the choice of RF encoding trajectory is closely related to the flip angle used. For a Cartesian (spin-warp) SPGR sequence with fixed flip angle, a centric encoding order (centre out) will provide higher SNR at the expense of blurring in the image, whilst a sequential ordering will result in lower SNR in the images whilst preserving the fine structure (Fig. 4.1.6). A partial Fourier acquisition which exploits the phase conjugate symmetry in the higher spatial frequencies represents a compromise that relies on less RF pulses. As the number of RF views is reduced either by partial Fourier methods (WILD et al. 2003a), parallel imaging with receive coil arrays (LEE et al. 2006) or radial under-sampling (WILD et al. 2003b), the flip angle can be increased in order to use up the polarisation with less pulses. This provides the interesting possibility with HP gas MRI of SNR that is independent of the number of



Fig. 4.1.6. Coronal SPGR image acquired at 1.5 T with 128×128 matrix, 38-cm FOV, 10-mm slice

RF encoding steps (N) (MUGLER and BROOKEMANN 2005), a paradox with the familiar $\text{SNR} \propto \sqrt{N}$ relation which holds for conventional thermally polarised MRI.

A variable flip angle (VFA) approach can also be used in SPGR imaging with HP gases (ZHAO et al. 1996); here the flip angle is increased from view to view to maintain a constant transverse magnetisation thus minimising the k-space filtering effect. The flip angle for the n -th RF view is given by

$$\alpha(n) = \tan^{-1}[1/\sqrt{(N-n)}]. \quad (2)$$

The VFA approach is potentially the optimum strategy for SPGR imaging of ^3He ; however the idealised constant magnetisation profile can diverge if there is slight miscalibration in the RF transmit amplitude. Similarly, in 2D SPGR imaging the distribution of flip angles across the 2D slice profile (WILD et al. 2002a) can cause similar problems of divergence (TEH et al. 2007a). An alternative to spoiling the precious transverse magnetisation from view to view is to recycle it using steady state (WILD et al. 2006 – see Fig. 4.1.7), EPI (SAAM et al. 1999) or CPMG (DURAND et al. 2002) based refocusing strategies. All of these approaches allow potentially increased SNR by using a higher excitation flip angle and

subsequently refocusing residual transverse magnetisation with the finite longitudinal magnetisation.

However, any sequence that employs refocusing is constrained by the effect of diffusion attenuation of the transverse magnetisation which is considerable for ^3He in the lungs. The diffusion related signal loss is quantified by the signal attenuation at the centre of the read-out echo by the expression $\exp(-b(t)D)$, where

$$b(\tau) = \int_0^\tau |k(t)|^2 dt \quad (3)$$

b being the time dependent b -value derived from the gradient integral with time, where

$$k(t) = \gamma \int_0^t G(t') dt'$$

and G is the time varying imaging gradient waveform.

Figure 4.1.8 highlights the benefits of short echo time that can be achieved with radial and spiral imaging sequences which start to sample the centre of k-space at $\text{TE} \sim 0$. This is most beneficial when imaging with small FOVs (DRIEHUYS et al. 2007) or where diffusion is considerable such as in the upper airways (WILD et al. 2004). The same constraint of diffusion dephasing imposed by the imaging gradients applies to EPI sequences where the echo train length and spatial resolution is limited (SAAM et al. 1999). Nevertheless, single shot EPI provides an attractive means of rapidly tracking gas flow dynamics and has been used to estimate global lung ventilation volume with time during exhalation (TEH et al. 2007b). Diffusion dephasing also limits the minimum slice thickness in 2D imaging; when striving for high resolution images a 3D sequence is less prone to this source of attenuation in the slice direction and gives higher SNR for a given spatial resolution (WILD et al. 2004). A secondary effect in 2D imaging is the mixing of gas polarisation by diffusion between the slice being excited and the adjacent volume of gas; this is mitigated by keeping the sequence TR to a minimum and imaging slices in an interleaved fashion. This slice mixing effect is quantified by the expression below which describes the dissipation of the slice profile $f(z)$ with time due to diffusion with a Gaussian distribution:

$$f(z, t) = \frac{1}{2\sqrt{\pi Dt}} \int_{-\infty}^{\infty} f_0(z') \exp\left[-\frac{(z-z')^2}{4\pi Dt}\right] dz' \quad (4)$$

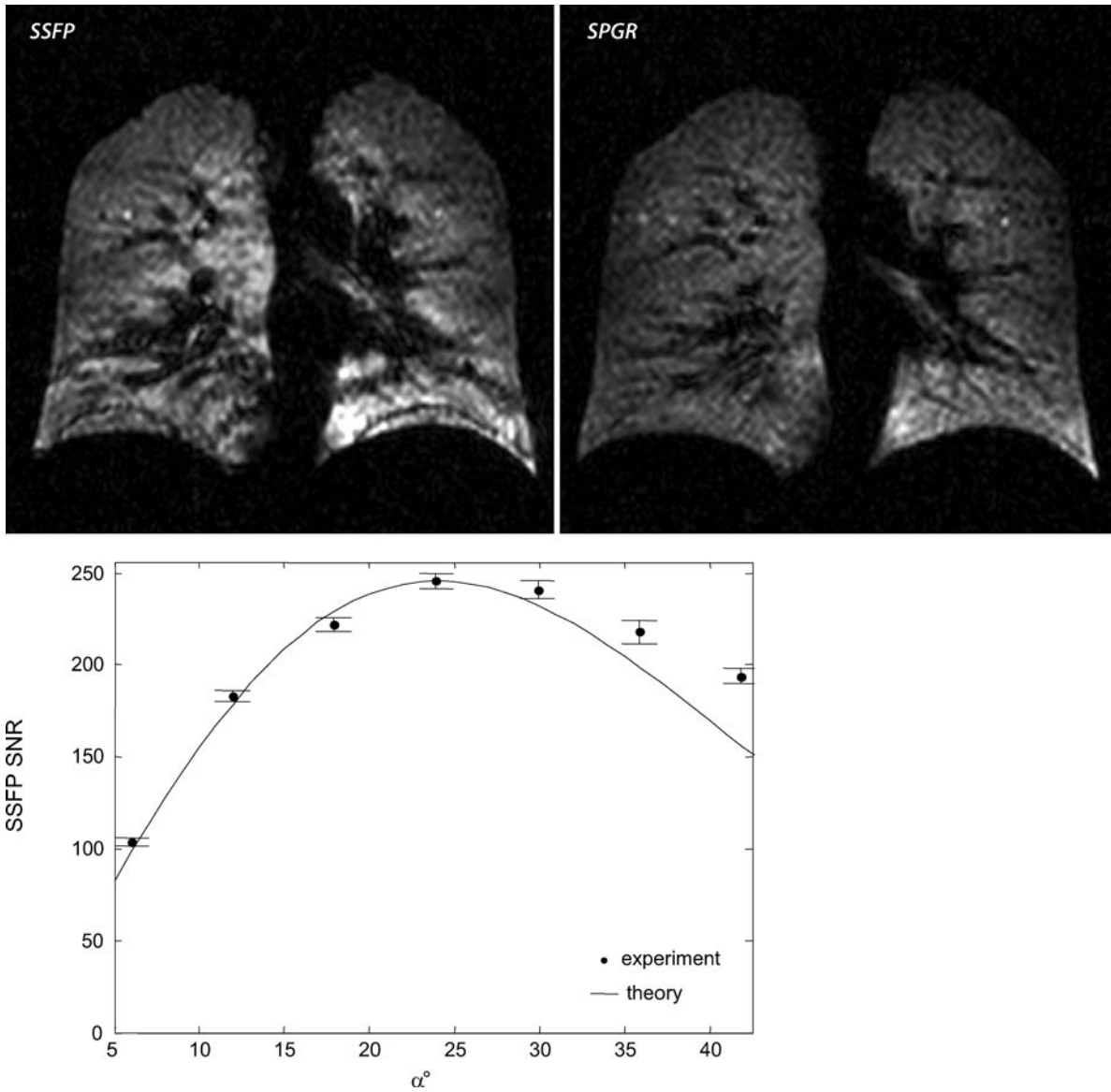


Fig. 4.1.7. Images from a healthy normal showing the performance of SPGR and SSFP sequences at 1.5 T. The images show that higher SNR can be achieved through use of a higher optimum flip angle and recycling the residual transverse magne-

tisation with SSFP (WILD et al. 2006), although the characteristic banding artifacts due to field inhomogeneity are evident near the diaphragm

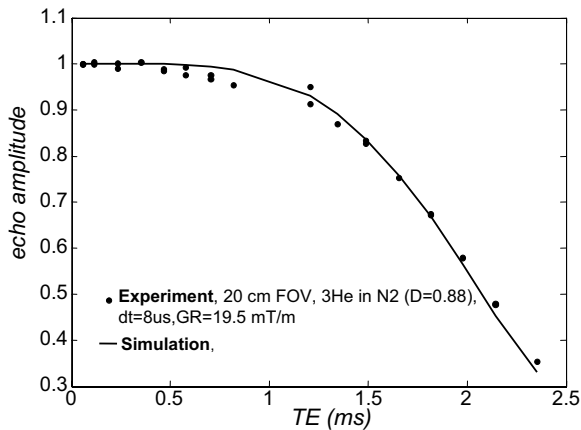


Fig. 4.1.8. How the signal is attenuated as a function of read gradient echo asymmetry for free ^3He in air

This process of slice mixing can in fact be used to measure long range diffusion coefficients (FICHELE et al. 2005) and is discussed later.

As well as mitigating the effect of diffusion dephasing, non-Cartesian sequences such as spiral (SALERNO et al. 2001) and radial (WILD et al. 2003b) offer the use of less RF pulses to sample k-space by angular under-sampling in either 2D or 3D (HOLMES et al. 2008). This is attractive not only from the point of polarisation usage but also in terms of allowing faster acquisition times for dynamic imaging of gas flow as discussed later.

4.1.9 Physiological and Anatomical Sensitivity with HP ^3He

The remainder of the chapter will focus on how ^3He images can be used to probe lung function. The emphasis is not on clinical examples but more on how to sensitise the MR pulse sequences to different aspects of lung physiology and micro-structure and how to quantify the results with image processing. For clinical examples the reader is referred to Chaps. 8 and 9.

4.1.9.1 Ventilation Imaging

The obvious use for HP ^3He images is to visualize ventilation distribution and homogeneity. For this purpose high resolution images at breath-hold are needed and

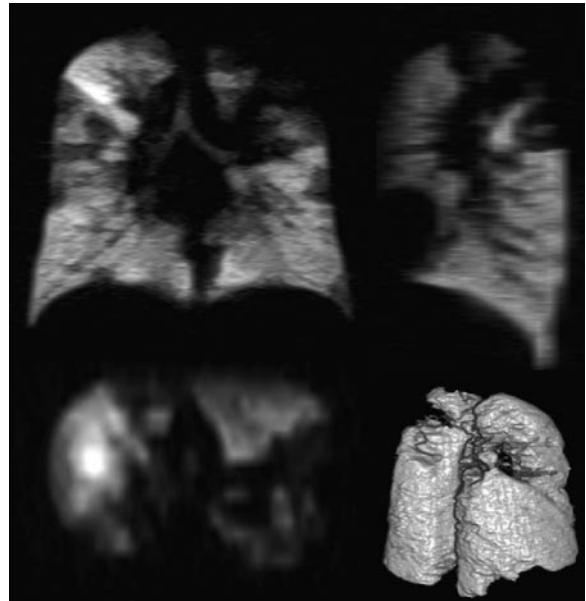


Fig. 4.1.9. Three-dimensional images and the ventilation volume from a 12-year-old child with cystic fibrosis

most groups still favour the robust 2D multi-slice SPGR sequence with Cartesian encoding. Ventilation homogeneity can be expressed qualitatively with radiological scoring procedures (KAUCZOR et al. 1996; DONNELLY et al. 1999; ALTES et al. 2001; GAST et al. 2002; STAVN-GAARD et al. 2005; VAN BEEK et al. 2007). The degree of ventilation heterogeneity can potentially be further quantified by texture analysis (AL-KADI and WATSON 2008) and lacunarity scoring that have been used in HRCT. A more quantitative approach is evaluation of regional ventilation volumes (WOODHOUSE et al. 2005). For the latter approach the dark space from ^1H lung MRI adds additional information on the potentially viable ventilated volume and can be used in tandem with the ^3He MRI ventilation images to calculate an index of percentage ventilated volume. A 3D imaging sequence (WILD et al. 2004) with its contiguous data reformat allows direct calculation of a measurement of regional lung volume as shown in Fig. 4.1.9 with the ability to reformat in any orientation.

One aspect worth considering, especially in studies designed to assess the effects of respiratory medication, is the baseline repeatability of the ventilation imaging which depends upon the respiratory manoeuvre and redistribution of ventilation defects which has been shown to change with time and posture in healthy normals (MATA et al. 2008). Figure 4.1.10 shows two sets

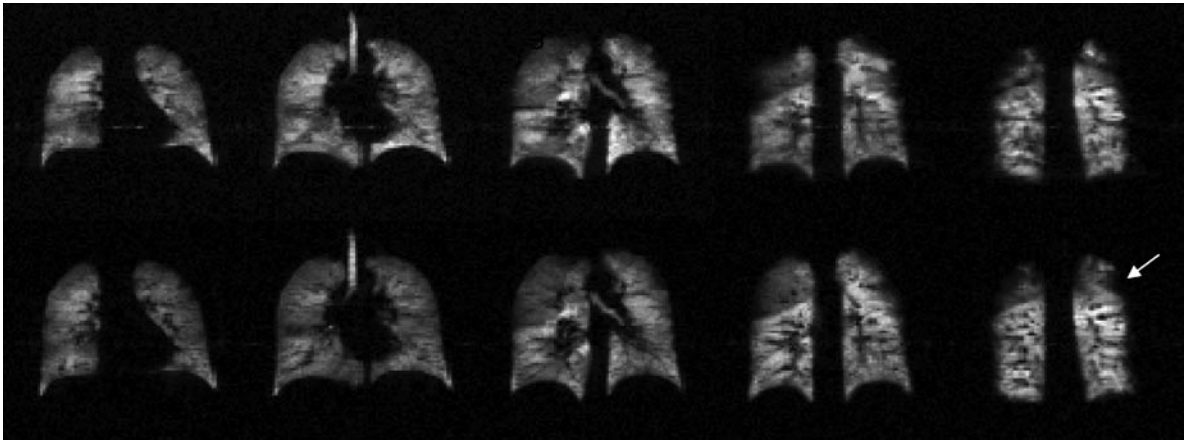


Fig 4.1.10. Repeatability of ventilation imaging in a patient with mild COPD. Note the slight redistribution of ventilation defects between scans (*arrow*)

of 2D ^3He scans acquired in the same session from a patient with mild COPD.

Lung ventilation volume from ^3He MRI has been shown to correlate both with spirometry in normals and in patients with disease (GAST et al. 2002; WOODHOUSE et al. 2005) and with lung volumes from plethysmography in normals (TEH et al. 2007b). Since the images supply spatially resolved data it is a shame to sacrifice the regional ventilation sensitivity by summing up all ventilated pixels in to a global index of lung ventilated volume. In Sheffield we have used a regional scheme by dividing each lung in to upper mid and lower lobes as a means of regionally quantifying changes in ventilation pre and post therapy; an alternative method may be to adopt core and peel methods used in HRCT (EVANS et al. 2008).

4.1.9.2 Dynamic Imaging

HP gas MRI is not constrained by saturation recovery of the signal and as such we can image with very short TR at high SNR. This opens up the possibility of imaging gas flow dynamics, wash in and washout and time resolved processes such as air trapping. Work to date in humans has largely focused on using very rapid time resolved 2D sequences such as partial Fourier Cartesian SPGR (SCHREIBER et al. 2000), spiral (SALERNO et al. 2001) and radial (WILD et al. 2003b – see Fig. 4.1.11) sequences. The non-Cartesian methods oversample the centre of k-space and can be readily adapted to sliding window reconstruction and thus seem to be particularly effective for 2D dynamic imaging. These sequences pro-

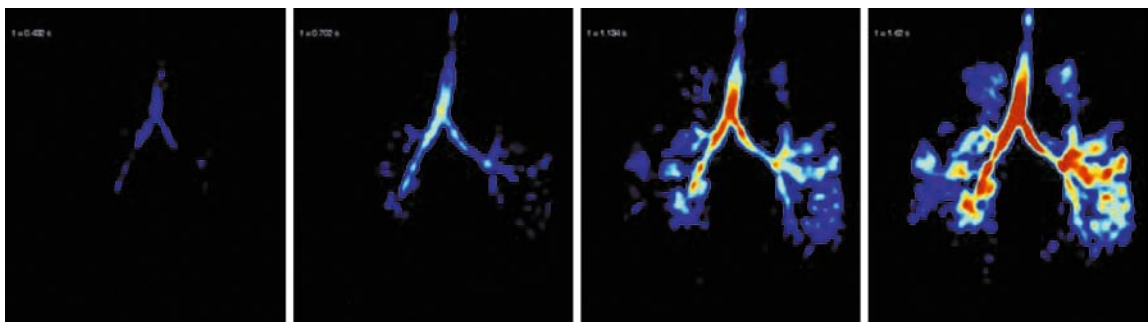


Fig. 4.1.11. Selected time frames from a dynamic time series acquired with a 2D radial sequence (WILD et al. 2003b) in a patient with severe COPD

vide a 2D planar view of the lungs with very fast temporal resolution and have been used to elucidate rates of gas flow in the major airways and periphery (KOUPELLIS et al. 2005; GAST et al. 2003). The time series of images obtained can be used to fit parametric maps of the signal kinetics such as the rise time, integrated total signal and gas flow rate on a pixel by pixel basis (KOUPELLIS et al. 2005; DUPUICH et al. 2003). By modulating the flip angle used with respect to the rate of inhalation, the images can be weighted according to gas flow rate in order to delineate the major airways where gas flux is highest (TOOKER et al. 2003).

Dynamic imaging sequences can potentially be run directly after a volumetric breath-hold exam in order to investigate the gas clearance rate (HOLMES et al. 2007). With the advent of faster volumetric imaging sequences that use state-of-the-art under-sampling and parallel imaging techniques, the possibility also exists for high temporal resolution 3D imaging of ventilation (TEH et al. 2007b; HOLMES et al. 2008) (see Fig. 4.1.12).

An alternative approach to imaging the rapid influx of signal is to monitor the slower wash-in of signal in a fashion similar to that used in nuclear medicine ventilation studies. In this approach the regional frac-

tional ventilation of gas exchanged per breath is derived (DENINGER et al. 2002b) as an index of regional gas ventilation. A final dynamic imaging approach is to exploit the phase contrast sensitivity to steady flow provided by MRI. Work in this field has used the methodology developed for phase contrast MR angiography and the preliminary results look useful for mapping of flow profiles and turbulence in the upper airways (DE ROCHEFORT et al. 2006).

4.1.9.3

Measurement of Regional Oxygen Uptake with the Longitudinal Relaxation Time, T1

As described in Eq. (1), the T1 decay of HP ^3He is strongly affected by the effect of mixing with oxygen in the air. When paramagnetic oxygen mixes with polarised ^3He in the lungs, a marked reduction in the ^3He T1 arises through the electron-nuclear spin dipolar coupling. SAAM et al. (1995) quantified the dependence of the ^3He T1 on oxygen concentration; the longitudinal relaxation rate ($1/T1$) is given by $\Gamma_{O_2}(t) = pO_2(t)/\xi$, where the coefficient ξ was determined empirically as

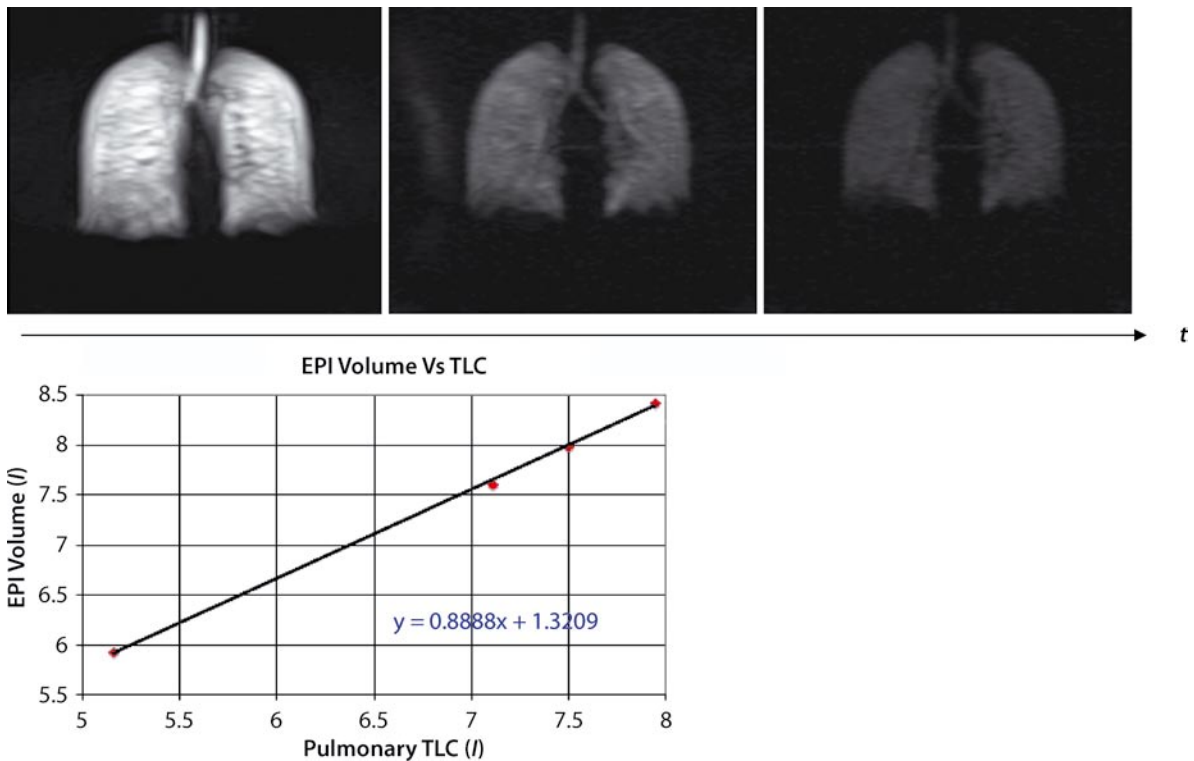


Fig. 4.1.12. Time resolved 3D imaging to mimic a spirometry manoeuvre and correlation with total lung capacity from plethysmography (adapted from TEH et al. 2007b)

2.61 bar \times s at 310 K temperature. This pO_2 dependence of the ^3He T1 was subsequently used by DENINGER et al. (1999) for in vivo quantification of pO_2 in a series of breath-hold experiments on pigs and humans. In breath-hold studies of HP ^3He , the image signal intensity, A_n , in a time series of n images acquired with N RF views per image, can be derived from Eq. (1) as

$$A_n = A_0 (\cos\alpha)^{nN} \exp\left(-\frac{1}{\xi} \int_0^{t_n} pO_2(t) dt\right) \quad (5)$$

Thus by acquiring time series of images with different inter image delay times, the RF depletion and T1 (pO_2) effects can be separated to give an estimate of the regional $pO_2(t)$. The method relies on the assumption that oxygen uptake in the human lung can be approximated by a linear rate constant, $pO_2(t) = p_0 - Rt$, which could represent a short time scale approximation to the exponential behaviour recently reported in rat lungs with ^3He T1 measurements (CIESLAR et al. 2007). Practically, these in vivo experiments used images acquired from whole lung projections (very thick 2D slices) with two sets of weightings – either different flip angles or different inter image delays. The dual scan

approach is ^3He intensive and prone to registration and breath-hold irreproducibility, as such single breath-hold versions of the method have recently been proposed (DENINGER et al. 2002a; FISCHER et al. 2004). For accurate fitting of the decay curve, SNR needs to be high so spatial resolution in the images is less paramount. Furthermore the effect of inter-slice diffusion of gas during the significant inter-image delay time (typically up to 7 s) can introduce erroneous decay rates which can be circumvented by using a 3D imaging sequence (WILD et al. 2005).

Whilst perhaps the most powerful tool with which to measure regional lung function, the pO_2 method still remains the least evaluated in a clinical setting and a robust solution that gives accurate data in a reasonable breath-hold duration remains to be fully evaluated.

4.1.9.4 Diffusion Measurement

One of the most powerful and proven aspects of HP ^3He MRI is its sensitivity to gas diffusion (random Brownian motion of the atoms). In air at STP the diffusion coefficient (D) for helium-3 is on the order $0.88 \text{ cm}^2 \text{ s}^{-1}$

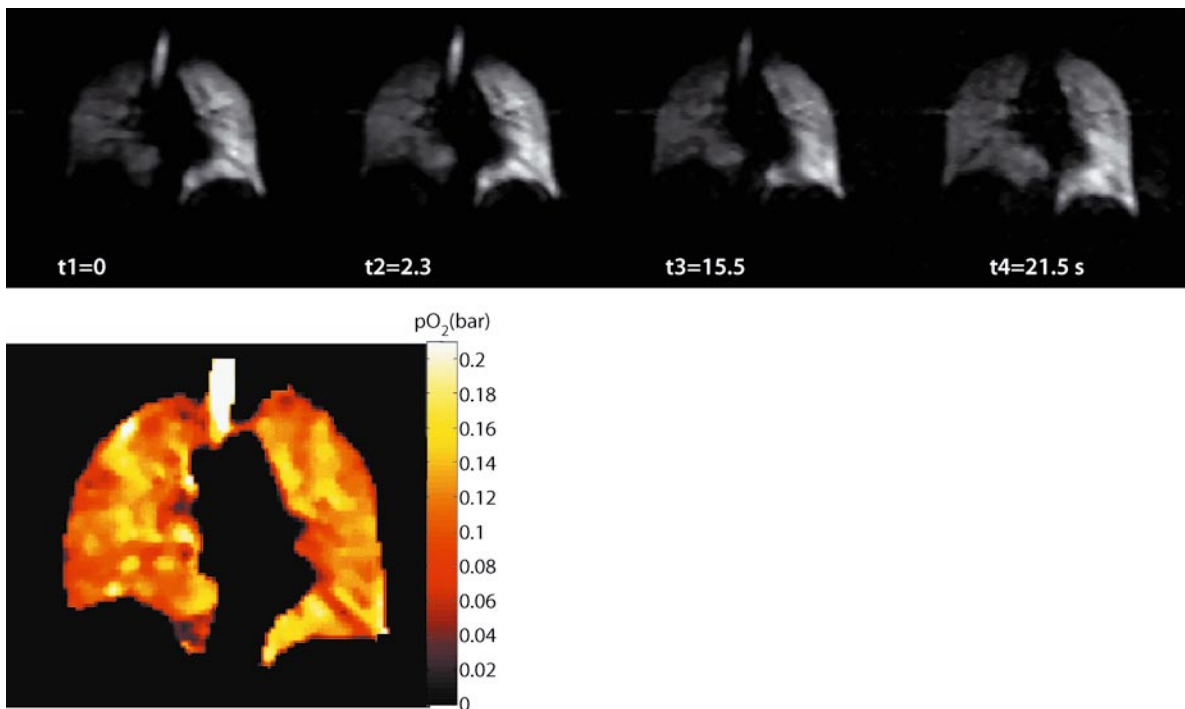


Fig. 4.1.13. Time course of images from one slice of a 3D (WILD et al. 2005) single scan pO_2 imaging sequence, with the calculated pO_2 map

(LINER and WEISSMAN 1972), and it can travel root mean square distances of millimeters within times of milliseconds as calculated from the solution to the 1D diffusion equation $\bar{x} = \sqrt{2Dt}$. For example, in an experimental time-frame of 5 ms the gas atoms can travel a root-mean-squared (RMS) distance of ≈ 1 mm. Considering the smallest confining structure in the lungs to be an alveolus, which is approximately 0.3 mm in diameter, the gas atoms can encounter the tissue walls multiple times during a typical MR sequence repetition time (TR), which is typically 5 ms. The confinement by the walls leads to a “restriction” in gas diffusion and hence the measured apparent diffusion coefficient (ADC) is much smaller in healthy lungs than for diffusion in free-space. Typical MRI measurements reveal that the helium-3 ADC is between $0.1 \text{ cm}^2 \text{ s}^{-1}$ and $0.2 \text{ cm}^2 \text{ s}^{-1}$ in healthy lungs (SWIFT et al. 2005; SAAM et al. 2000; SALERNO et al. 2002; FAIN et al. 2006), whereas in free-space it is $0.88 \text{ cm}^2 \text{ s}^{-1}$ when mixed with room air. The restricted diffusion process in the lungs is depicted in the schematic in Fig. 4.1.13.

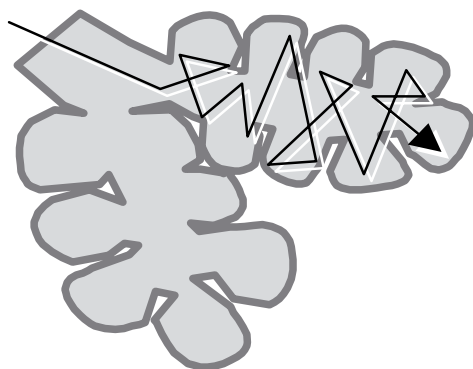
4.1.9.5

Measuring Diffusion: Time-length Scale Dependence

Diffusion acts to attenuate irreversibly the MR signal whenever a magnetic field gradient is present as discussed earlier. Hence, MRI sequences can be used to measure diffusion by using pulsed or static gradients after the application of the excitation RF pulse. These

methods stem from the seminal work of CARR and PURCELL (1954) and STEJSKAL and TANNER (1965). For HP ^3He , the most commonly employed method is the pulsed-gradient-spin-echo (PGSE) technique. It is easily implemented, robust, and, most importantly, it can be incorporated in to fast sequences that can be encompassed within a breath-hold. The standard PGSE method utilises two pulsed gradients separated by a time Δ , and a 180° refocusing pulse, all situated after the slice-selection gradient and (usually) before the phase encode step of the sequence. The same diffusion measurement can also be undertaken without the 180° refocusing; see Fig. 4.1.14. However, this essentially limits experimentation to shorter durations of Δ , since $T2^*$ causes signal attenuation. Furthermore, the refocusing pulse can mitigate some of the measurement errors due to superposition of background gradients. The simplified PSGE method is depicted in Fig. 4.1.15, which is incorporated within a standard gradient echo (SPGR) sequence block. The diffusion b -values are computed from Eq. (3) and the diffusion coefficient evaluated by an exponential fit to the expression $\exp(-bD)$. This sequence is best run in an interleaved mode where the acquisition of each line of k -space is repeated: the first interleave has no diffusion weighting (reference scan at matched TE), while the subsequent interleaves incorporate bipolar gradient waveform of different b . Interleaving in this fashion ensures a reduced sensitivity to motion artefacts and greatly reduces any flip-angle, and $T1$ relaxation bias in the measured ADC. However, it is crucial that each interleave has the same time-to-echo (TE) and repetition time (TR).

Healthy alveoli
LOW ADC $\sim 0.2 \times 10^{-4} \text{ m}^2 \text{ s}^{-1}$



Emphysema
HIGH ADC $\rightarrow 0.9 \times 10^{-4} \text{ m}^2 \text{ s}^{-1}$

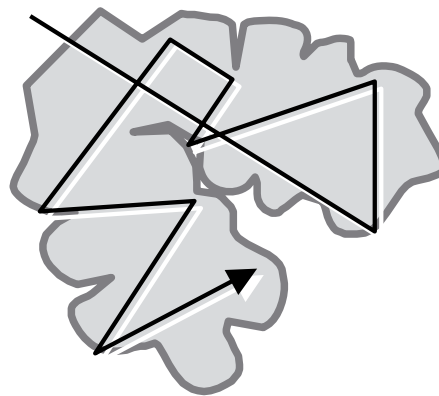


Fig. 4.1.14. Schematic of a healthy alveolar sac and an emphysematous alveolus

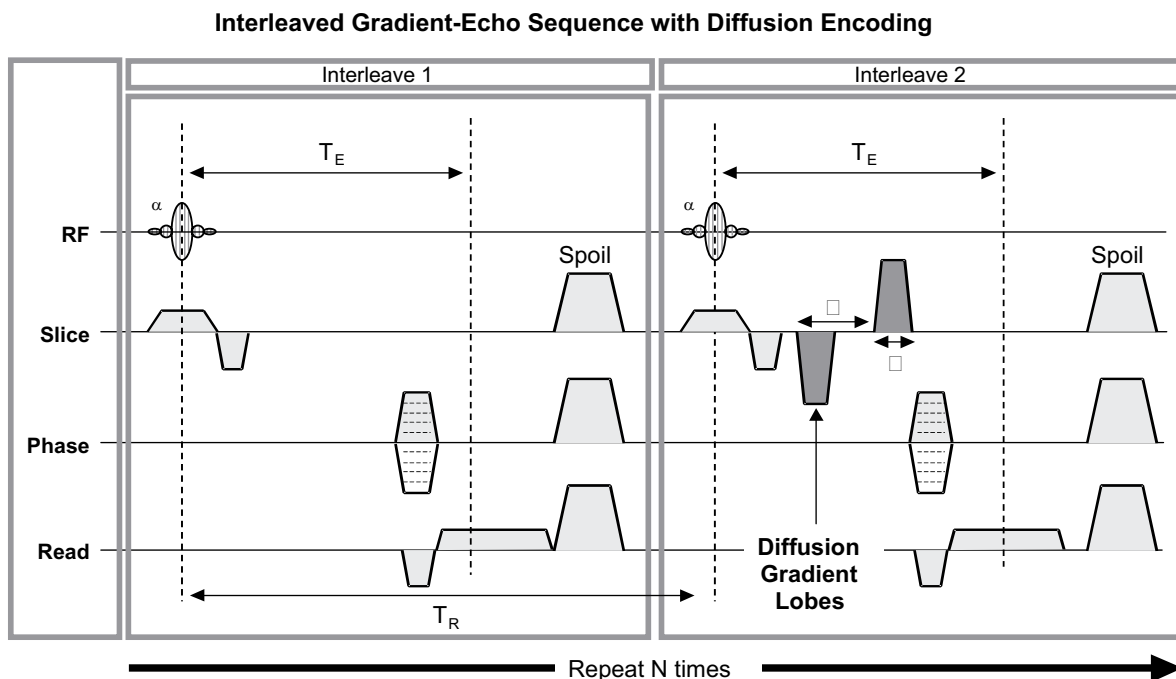


Fig. 4.1.15. PGSE sequence gradient echo (SPGR) sequence typically used for measuring ^3He ADC

Various diffusion investigations have been performed in human lungs using variations on the PGSE sequence as shown in Fig. 4.1.15. The first reported measurements of ^3He diffusion were by MUGLER et al. (1998) at a field strength of 1.5 T. Measurements were made using a bipolar gradient waveform (PGSE), with four b -values of 0.4, 0.8, 1.2 and 1.6 $\text{cm}^2 \text{s}^{-1}$. The ADC values were calculated on a pixel-by-pixel basis using a linear, least-squares fit to yield a single average ADC value for all four b -values. The overall mean ADC value over all healthy volunteers was found to be 0.25 $\text{cm}^2 \text{s}^{-1}$, almost a factor of four times smaller than unrestricted diffusion in free space.

A more comprehensive study, using 11 healthy volunteers and 5 patients with severe emphysema, was later reported by SAAM et al. (2000). Here, diffusion was encoded using only two b -values: for the healthy volunteers the values were $b = 0 \text{ cm}^2 \text{s}^{-1}$, and $b = 2.75 \text{ cm}^2 \text{s}^{-1}$; for the emphysema patients a lower b -value of 1.375 $\text{cm}^2 \text{s}^{-1}$ was selected. Diffusion in both experiments were encoded with a relatively long diffusion time of 7.5 ms. The results from the healthy volunteers yielded an average ADC value of 0.20 $\text{cm}^2 \text{s}^{-1}$, whereas the ADC values from the emphysema patients were greatly elevated, yielding an average of 0.50 $\text{cm}^2 \text{s}^{-1}$. The results clearly

demonstrated that destruction of the lung tissue lead to a higher ADC values, closer to the unrestricted diffusion coefficient. SALERNO et al. (2002) conducted a study in sixteen healthy volunteers, and eleven patients suffering from emphysema. The encoding methods were identical to those of MUGLER et al. (1998). Here, the ADC was on average 0.23 $\text{cm}^2 \text{s}^{-1}$ for healthy volunteers, and 0.45 $\text{cm}^2 \text{s}^{-1}$ for the patients with emphysema. In addition, the ADC values were compared to spirometry measurements taken before each scan. The ADC values were found to correlate strongly with the forced-expiratory-volume within 1 s (FEV_1). This was an important finding since spirometry is routinely used to assess disease severity. Various groups have since used PGSE sequences such as these to elucidate early emphysematous changes (SWIFT et al. 2005; FAIN et al. 2006) in smokers (see Fig. 4.1.16), growth of alveoli with age (FAIN et al. 2005), postural and anatomical gradients within the lung (FICHELE et al. 2004b), and subtle changes in asthma (WANG et al. 2008). PGSE ^3He ADC results have been shown to match well with the alveolar dimensions measured results from histological sections in experiments made in animal lungs (PECES-BARBA et al. 2003) and more recently in human lungs (WOODS et al. 2006).

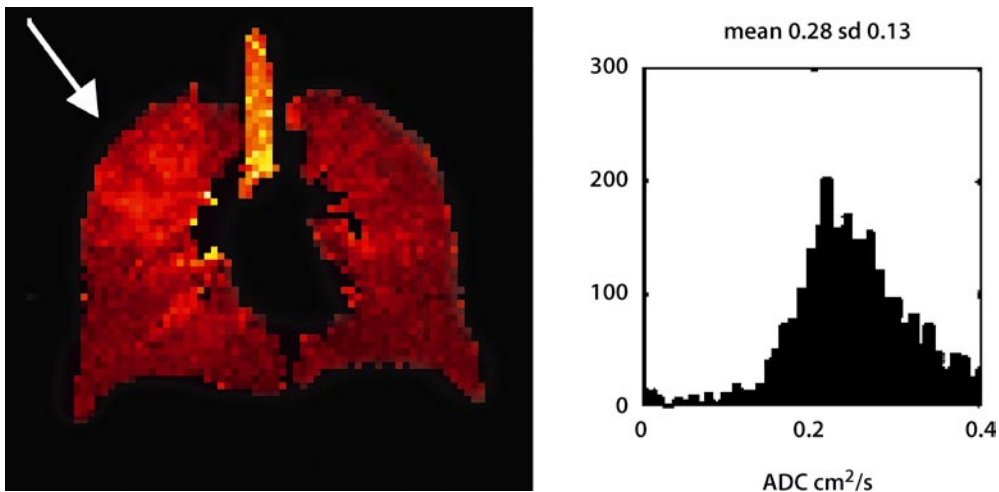


Fig. 4.1.16. ADC map and histogram from a patient with emphysema; a hot spot of elevated ADC is clearly seen in the upper right lobe. Images acquired with a PGSE SPGR sequence with b -values described in WILD et al. (2007)

The mean ADC value is clearly an indicator of alveolar size and hence disease severity in the case of emphysema; however, the inter-connected nature of the alveolar microstructure imposes a time-length scale dependence on the ADC that depends upon the diffusion weighting gradient strengths and timings (FICHELE et al. 2004a). In simple terms, if we give the gas a longer time to diffuse there is more chance of it hitting a wall and encountering a restriction thus giving a lower ADC. These effects are illustrated in Figs. 4.1.17 and 4.1.18.

This sequence timing dependence of the ADC means that care should be taken when making a direct comparison of ADC results measured at different sites with sequences with different diffusion weightings and international consensus on standardisation of b -value for ^3He ADC measurement would be worthwhile.

The time dependence of the PGSE sequence also indicates that with longer diffusion times we can potentially probe longer range diffusion in the lungs that represents inter-acinar connectivity and disease processes that lead to different gas mixing washout times. The problem with extending the diffusion time Δ to the tens of milliseconds needed to probe longer length scales is that T_2^* decay (approximately 25 ms for ^3He in the lungs at 1.5 T) can attenuate the signal before application of the second gradient pulse. To address this, the diffusion encoded magnetization can be stored in the longitudinal direction (with a flip back RF pulse of the opposite

phase, i.e. a stimulated echo sequence) where the longer T_1 s (~ 20 s) allow longer diffusion times, the magnetisation being read out with a third pulse with the same phase as the original excitation pulse; see Fig. 4.1.19.

Various manifestations of sequence for measurement of long time-scale diffusion have been proposed (OWERS-BRADLEY et al. 2003; WOODS et al. 2004; FICHELE et al. 2005; WANG et al. 2006); these authors all give ADC values approximately an order of magnitude less than those measured with PGSE, which indicates we are measuring gas mixing by convection/diffusion through collateral connectivity over a longer length scale (CONRADI et al. 2008). Whether this is more or less sensitive than the shorter time scale measurements to different aspects of lung micro-structure in healthy and diseased lungs remains to be fully investigated but preliminary comparison show differences in sensitivity (WANG et al. 2008).

Much work has been performed in modeling the affect of diffusion inside geometrical models that mimic the lung micro-structure; this is an area of theoretical study in its own right and the reader is referred to the papers from the various groups active in this field who have proposed analytical (YABLONSKIY et al. 2002; CONRADI et al. 2004; GREBENKOV et al. 2007; SUKSTANSKII and YABLONSKIY 2008) and numerical models (FICHELE et al. 2004a, 2005; VERBANCK and PAIVA 2007) of restricted diffusion.

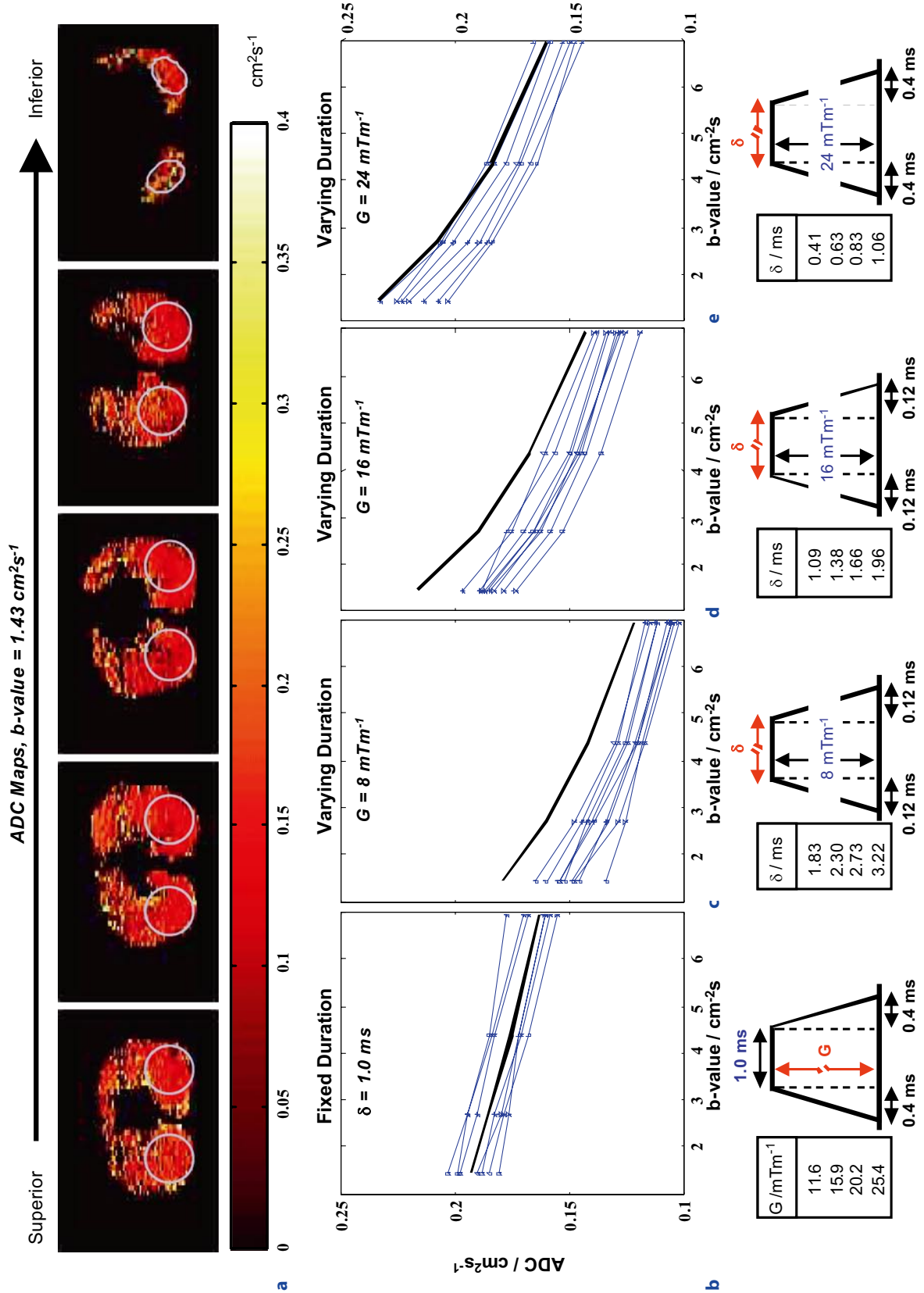


Fig. 4.1.17. a–e.

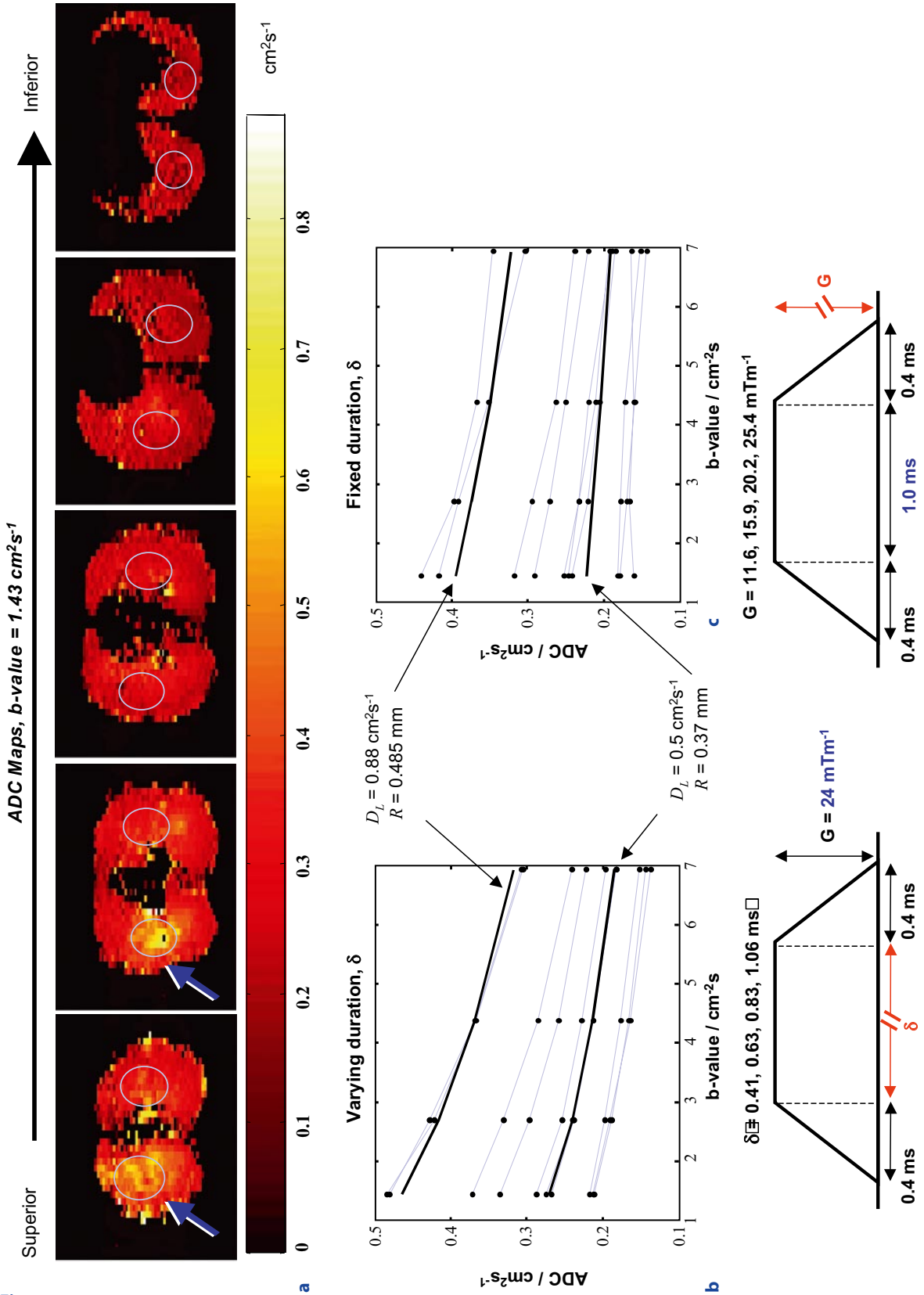


Fig. 4.1.18a-c.

Fig. 4.1.17a–e. Axial ADC maps of a healthy male (aged 34) were taken using a range of different b-values and gradient durations. Data from ten regions-of-interest (ROI) from a total of five slices are plotted, the gradient schemes are depicted below each data set. The overall ADCs are seen to decrease as gradient strength decreases. The difference in ADC seen between each ROI data is due to a superior-inferior variation in alveolar density. The *thick, black line* corresponds to the “cylinder model” (YABLONSKIY et al. 2002), plotted for $R = 0.33$ mm, $DL = 0.47$ cm² s⁻¹; see text

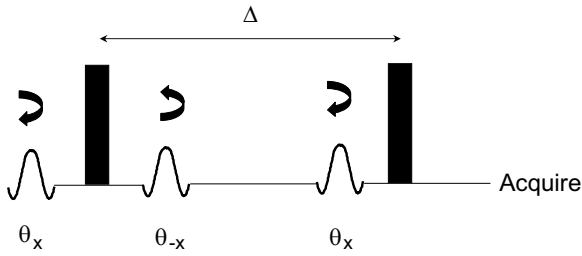


Fig. 4.1.18a–c. Axial ADC maps of a relatively healthy female smoker (aged 51) were taken using a range of different b-values and gradient durations. **a** ROIs plotted. **b** Gradient duration is varied. **c** Gradient strength is varied. The ADC is clearly a strong function of time and gradient strength, and is seen to decrease with increasing b-value. Theoretical curves (*in thick black*) are shown for comparison with the “cylinder model”; see text. *Blue arrows* indicate regions of large ADC values, and hence tissue destruction. Adapted from FICHELE et al. (2005)

Fig. 4.1.19. The stimulated echo sequence used for long diffusion time measurements. Magnetisation is tipped into the transverse plane by the first pulse, diffusion encoding is applied with the first gradient pulse, and the encoded magnetisation is then stored in the longitudinal direction by tipping back with a pulse of opposite phase. The encoded magnetization is then readout and rephased with a second diffusion gradient of the same shape and direction

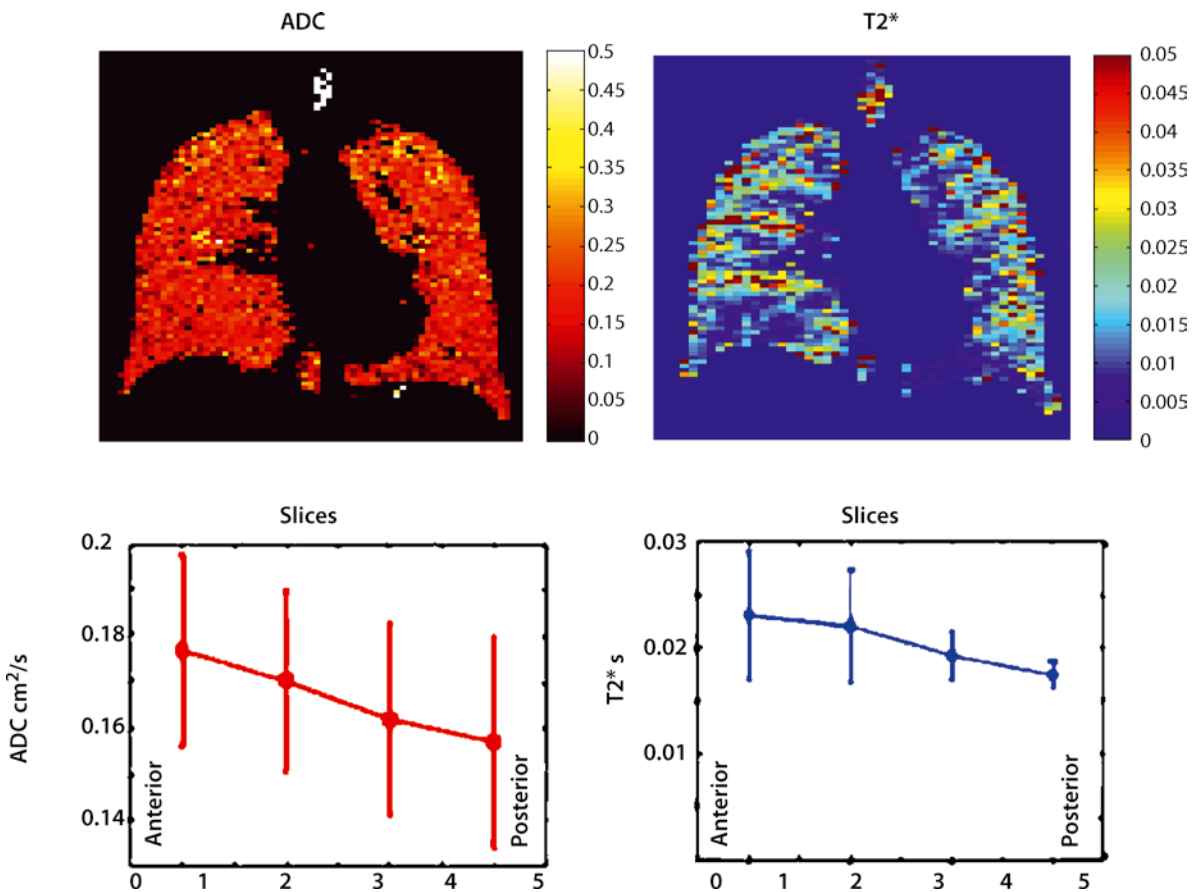


Fig. 4.1.20. Side by side comparison of ³He ADC and T2* maps from a healthy normal and pooled data analysed on a slice by slice basis indicating both parameters show an anatomical trend from anterior to posterior

4.1.9.6

Transverse Relaxation Time T_2^*

As mentioned earlier, the lungs are a magnetically inhomogeneous medium due to the magnetic susceptibility difference between air and parenchyma (9 ppm volume susceptibility difference) creating microscopic field gradients. The diffusion of ^3He in these gradients gives rise to a microscopic (sub-pixel) T_2^* which can be measured at breath-hold with interleaved SPGR sequence blocks of different TE. The T_2^* could thus provide an additional means of exploring the lung physiology with sensitization to both the susceptibility differences in the perfused micro-vasculature (VIGNAUD et al. 2005) and anatomical gradients in the T_2^* within the lung having been reported (AJRAOUI et al. 2008)(Fig. 4.1.20).

References

- Ajraoui S, Ireland R., Lee KJ, Woodhouse N, Wild JM (2008) Anatomical trends in coregistered ADC and T_2^* maps of ^3He gas in the lungs of healthy normals. *Proc Int Soc Magn Reson Med* 16
- Al-Kadi OS, Watson D (2008) Texture analysis of aggressive and nonaggressive lung tumor CE CT images. *IEEE Trans Biomed Eng* 55(7):1822–1830
- Altes TA, Powers PL, Knight-Scott J et al. (2001) Hyperpolarized ^3He MR lung ventilation imaging in asthmatics: preliminary findings. *J Magn Reson Imag* 13(3):378–384
- Carr H, Purcell EM (1954) Effects of diffusion on free precession in nuclear magnetic resonance experiments. *J Chem Phys* 94:630–638
- Cieslar K, Alsaid H, Stupar V et al. (2007) Measurement of nonlinear $p\text{O}_2$ decay in mouse lungs using ^3He -MRI. *NMR Biomed* 20(3):383–391
- Colegrove D, Schearer LD, Walters GK (1963) *Phys Rev* 132:2561–2572
- Conradi MS, Bruns MA, Sukstanskii AL et al. (2004) Feasibility of diffusion-NMR surface-to-volume measurements tested by calculations and computer simulations. *J Magn Reson* 169(2):196–202
- Conradi MS, Yablonskiy DA, Woods JC et al. (2008) The role of collateral paths in long-range diffusion of ^3He in lungs. *Acad Radiol* 15(6):675–682
- De Lange E, Altes T, Harding D et al. (2003) Hyperpolarized gas MR imaging of the lung: safety assessment of inhaled helium-3. *Proceedings RSNA K03–879*
- de Rochefort L, Maitre X, Fodil R et al. (2006) Phase-contrast velocimetry with hyperpolarized ^3He for in vitro and in vivo characterization of airflow. *Magn Reson Med* 55(6):1318–1325
- De Zanche N, Chhina N, Teh K et al. (2008) Asymmetric quadrature split birdcage coil for hyperpolarized ^3He lung MRI at 1.5 T. *Magn Reson Med* 60(2):431–438
- Deninger AJ, Eberle B, Bermuth J et al. (1999) Quantification of regional intrapulmonary oxygen partial pressure evolution during apnea by (^3He) MRI. *J Magn Reson* 141(2):207–216
- Deninger AJ, Eberle B, Bermuth J et al. (2002a) Assessment of a single-acquisition imaging sequence for oxygen-sensitive (^3He)-MRI. *Magn Reson Med* 47(1):105–114
- Deninger AJ, Mansson S, Petersson JS et al. (2002b) Quantitative measurement of regional lung ventilation using ^3He MRI. *Magn Reson Med* 48(2):223–232
- Donnelly LF, MacFall JR, McAdams HP et al. (1999) Cystic fibrosis: combined hyperpolarized ^3He -enhanced and conventional proton MR imaging in the lung – preliminary observations. *Radiology* 212(3):885–889
- Driehuys B, Walker J, Pollaro J et al. (2007) ^3He MRI in mouse models of asthma. *Magn Reson Med* 58(5):893–900
- Dupuich D, Berthezene Y, Clouet PL et al. (2003) Dynamic ^3He imaging for quantification of regional lung ventilation parameters. *Magn Reson Med* 50(4):777–783
- Durand E, Guillot G, Darrasse L et al. (2002) CPMG measurements and ultrafast imaging in human lungs with hyperpolarized helium-3 at low field (0.1 T). *Magn Reson Med* 47(1):75–81
- Ebert M, Grossmann T, Heil W et al. (1996) Nuclear magnetic resonance imaging with hyperpolarised helium-3. *Lancet* 347(9011):1297–1299
- Evans A, McCormack G, Santyr G et al. (2008) Mapping and quantifying hyperpolarized ^3He magnetic resonance imaging apparent diffusion coefficient gradients. *J Appl Physiol* 105(2):693–699
- Fain SB, Altes TA, Panth SR et al. (2005) Detection of age-dependent changes in healthy adult lungs with diffusion-weighted ^3He MRI. *Acad Radiol* 12(11):1385–1393
- Fain SB, Panth SR, Evans MD et al. (2006) Early emphysematous changes in asymptomatic smokers: detection with ^3He MR imaging. *Radiology* 239(3):875–883
- Fain SB, Korosec FR, Holmes JH et al. (2007) Functional lung imaging using hyperpolarized gas MRI. *J Magn Reson Imaging* 25(5):910–293
- Fichele S, Paley MN, Woodhouse N et al. (2004a) Investigating ^3He diffusion NMR in the lungs using finite difference simulations and in vivo PGSE experiments. *J Magn Reson* 167(1):1–11
- Fichele S, Woodhouse N, Swift AJ et al. (2004b) MRI of helium-3 gas in healthy lungs: posture related variations of alveolar size. *J Magn Reson Imaging* 20(2):331–335
- Fichele S, Paley MN, Woodhouse N et al. (2005) Measurements and modeling of long range ^3He diffusion in the lung using a “slice-washout” method. *J Magn Reson* 174(1):28–33
- Fischer MC, Spector ZZ, Ishii M et al. (2004) Single-acquisition sequence for the measurement of oxygen partial pressure by hyperpolarized gas MRI. *Magn Reson Med* 52(4):766–773
- Gast KK, Viallon M, Eberle B et al. (2002) MRI in lung transplant recipients using hyperpolarized ^3He : comparison with CT. *J Magn Reson Imaging* 15(3):268–274

- Gast KK, Puderbach MU, Rodriguez I et al. (2003) Distribution of ventilation in lung transplant recipients: evaluation by dynamic ^3He -MRI with lung motion correction. *Invest Radiol* 38(6):341–348
- Goodson BM (2002) Nuclear magnetic resonance of laser-polarized noble gases in molecules, materials, and organisms. *J Magn Reson* 155(2):157–216
- Grebenkov DS, Guillot G, Sapoval B (2007) Restricted diffusion in a model acinar labyrinth by NMR: theoretical and numerical results. *J Magn Reson* 184(1):143–156
- Holmes JH, Korosec FR, Du J et al. (2007) Imaging of lung ventilation and respiratory dynamics in a single ventilation cycle using hyperpolarized He-3 MRI. *J Magn Reson Imaging* 26(3):630–636
- Holmes JH, O'Halloran RL, Brodsky EK et al. (2008) 3D hyperpolarized He-3 MRI of ventilation using a multi-echo projection acquisition. *Magn Reson Med* 59(5):1062–1071
- Ireland RH, Bragg CM, Mc Jury M et al. (2007) Feasibility of image registration and intensity-modulated radiotherapy planning with hyperpolarized helium-3 magnetic resonance imaging for non-small-cell lung cancer. *Int J Radiat Oncol Biol Phys* 68:273–281
- Kastler A (1950) Quelques suggestions concernant la production optique et la detection optique d'une inégalité de population des niveaux de quantification spatiale des atomes. Application à l'expérience de Stern et Gerlach et à la resonance magnétique. *J Phys Radium* 11:255–265
- Kauczor HU, Mainz Helium P (2002) Hyperpolarized ^3He gas as a novel contrast agent for functional MRI of ventilation. *Acad Radiol* 9(suppl 2):S504–506
- Kauczor HU, Hofmann D, Kreitner KF et al. (1996) Normal and abnormal pulmonary ventilation: visualization at hyperpolarized He-3 MR imaging. *Radiology* 201(2):564–568
- Koumellis P, van Beek EJ, Woodhouse N et al. (2005) Quantitative analysis of regional airways obstruction using dynamic hyperpolarized ^3He MRI—preliminary results in children with cystic fibrosis. *J Magn Reson Imaging* 22(3):420–426
- Lee RF, Johnson G, Grossman RI et al. (2006) Advantages of parallel imaging in conjunction with hyperpolarized helium – a new approach to MRI of the lung. *Magn Reson Med* 55(5):1132–1141
- Liner J, Weissman S (1972) Determination of the temperature dependence of gaseous diffusion coefficients using gas chromatographic apparatus. *J Chem Phys* 56:2288–2290
- Lutey BA, Lefrak SS, Woods JC et al. (2008) Hyperpolarized ^3He MR imaging: physiologic monitoring observations and safety considerations in 100 consecutive subjects. *Radiology* 248(2):655–661
- MacFall JR, Charles HC, Black RD et al. (1996) Human lung air spaces: potential for MR imaging with hyperpolarized He-3. *Radiology* 200(2):553–558
- Mata J, Altes T, Knake J et al. (2008) Hyperpolarized ^3He MR imaging of the lung: effect of subject immobilization on the occurrence of ventilation defects. *Acad Radiol* 15(2):260–264
- Middleton H, Black RD, Saam B et al. (1995) MR imaging with hyperpolarized ^3He gas. *Magn Reson Med* 33(2):271–275
- Moller HE, Chen XJ, Saam B et al. (2002) MRI of the lungs using hyperpolarized noble gases. *Magn Reson Med* 47(6):1029–1051
- Mugler JP, Brookeman JR (2005) Signal-to-noise considerations for parallel imaging with hyperpolarized gases. *Proc Intl Soc Magn Reson Med* 13:485
- Mugler JP, Brookemann JR, Knight-Scott J, Maier T, De Lange EE, Bogorad PL (1998) Regional measurement of the ^3He diffusion coefficient in the human lung. *Proc Int Soc Magn Reson Med* (6)
- Muller CJ, Loffler R, Deimling M et al. (2001) MR lung imaging at 0.2 T with T1-weighted true FISP: native and oxygen-enhanced. *J Magn Reson Imaging* 14(2):164–168
- Oros AM, Shah NJ (2004) Hyperpolarized xenon in NMR and MRI. *Phys Med Biol* 49(20):21
- Owers-Bradley JR, FICHELE S, Bennattayalah A et al. (2003) MR tagging of human lungs using hyperpolarized ^3He gas. *J Magn Reson Imaging* 17(1):142–146
- Parra-Robles J, Cross AR, Santyr GE (2005) Theoretical signal-to-noise ratio and spatial resolution dependence on the magnetic field strength for hyperpolarized noble gas magnetic resonance imaging of human lungs. *Med Phys* 32(1):221–229
- Parraga G, Mathew L, Etemad-Rezai R et al. (2008) Hyperpolarized ^3He magnetic resonance imaging of ventilation defects in healthy elderly volunteers: initial findings at 3.0 Tesla. *Acad Radiol* 15(6):776–785
- Peces-Barba G, Ruiz-Cabello J, Cremillieux Y et al. (2003) Helium-3 MRI diffusion coefficient: correlation to morphometry in a model of mild emphysema. *Eur Respir J* 22(1):14–19
- Saam B, Happer W, Middleton H (1995) Nuclear relaxation of ^3He in the presence of O_2 . *Phys Rev A* 52(1):862–865
- Saam B, Yablonskiy DA, Gierada DS et al. (1999) Rapid imaging of hyperpolarized gas using EPI. *Magn Reson Med* 42(3):507–514
- Saam B, Yablonskiy DA, Kodibagkar VD et al. (2000) MR imaging of diffusion of (^3He) gas in healthy and diseased lungs. *Magn Reson Med* 44(2):174–179
- Salerno M, Altes TA, Brookeman JR et al. (2001) Dynamic spiral MRI of pulmonary gas flow using hyperpolarized (^3He): preliminary studies in healthy and diseased lungs. *Magn Reson Med* 46(4):667–677
- Salerno M, de Lange EE, Altes TA et al. (2002) Emphysema: hyperpolarized helium 3 diffusion MR imaging of the lungs compared with spirometric indexes – initial experience. *Radiology* 222(1):252–260
- Salerno M, Brookeman JR, de Lange EE et al. (2005) Hyperpolarized ^3He lung imaging at 0.5 and 1.5 Tesla: a study of susceptibility-induced effects. *Magn Reson Med* 53(1):212–216

- Samee S, Altes T, Powers P et al. (2003) Imaging the lungs in asthmatic patients by using hyperpolarized helium-3 magnetic resonance: assessment of response to methacholine and exercise challenge. *J Allergy Clin Immunol* 111(6):1205–1211
- Scheerer LD, Walters GK (1965) Nuclear spin-lattice relaxation in the presence of magnetic-field gradients. *Phys Rev A* 139:1398–1402
- Schmiedeskamp JD, Ebert M, Heil W, Hiebel S, Otten E, Surkau R, Rudersdorf D, Wolf M, Grossmann T (2003a) Large scale production and handling of spin polarized helium-3 for MRT of lungs. *Proc Int Soc Magn Reson Med*, p 1392
- Schmiedeskamp JH, Heil W, Otten E, et al. (2003b) Paramagnetic relaxation of spin polarized He-3 at bare glass surfaces Part I. *Eur Phys J D* 38(3):427–438
- Schreiber WG, Weiler N, Kauczor HU et al. (2000) [Ultrafast MRI of lung ventilation using hyperpolarized helium-3]. *Rofo* 172(2):129–133
- Stavngaard T, Sogaard LV, Mortensen J et al. (2005) Hyperpolarized 3He MRI and 81mKr SPECT in chronic obstructive pulmonary disease. *Eur J Nucl Med Mol Imaging* 32(4):448–457
- Stejskal EO, Tanner JE (1965) Spin diffusion measurements: spin echoes in the presence of a time-dependent field gradient. *J Chem Phys* 42:288–292
- Sukstanskii AL, Yablonskiy DA (2008) In vivo lung morphometry with hyperpolarized 3He diffusion MRI: theoretical background. *J Magn Reson* 190(2):200–210
- Swift AJ, Wild JM, Fичele S et al. (2005) Emphysematous changes and normal variation in smokers and COPD patients using diffusion 3He MRI. *Eur J Radiol* 54(3):352–358
- Teh K, Lee KJ, Wild JM (2007a) Slice profile effects in variable flip angle hyperpolarized 3He MRI. *Proc Int Soc Magn Reson Med* 15:1297
- Teh K, Parnell SR, Woodhouse N, Wild JM (2007b) Time resolved lung ventilation volume measurement with multislice EPI using hyperpolarized 3He. *Proc Int Soc Magn Reson Med* 15:944
- Tooker AC, Hong KS, McKinstry EL et al. (2003) Distal airways in humans: dynamic hyperpolarized 3He MR imaging – feasibility. *Radiology* 227(2):575–579
- Tsai LL, Mair RW, Rosen MS et al. (2008) An open-access, very-low-field MRI system for posture-dependent 3He human lung imaging. *J Magn Reson* 193(2):274–285
- van Beek EJ, Hill C, Woodhouse N et al. (2007) Assessment of lung disease in children with cystic fibrosis using hyperpolarized 3-helium MRI: comparison with Shwachman score, Crispin-Norman score and spirometry. *Eur Radiol* 17(4):1018–1024
- van Beek EJ, Wild JM, Kauczor HU et al. (2004) Functional MRI of the lung using hyperpolarized 3-helium gas. *J Magn Reson Imaging* 20(4):540–554
- Verbanck S, Paiva M (2007) Simulation of the apparent diffusion of helium-3 in the human acinus. *J Appl Physiol* 103(1):249–254
- Vignaud A, Maitre X, Guillot G et al. (2005) Magnetic susceptibility matching at the air-tissue interface in rat lung by using a superparamagnetic intravascular contrast agent: influence on transverse relaxation time of hyperpolarized helium-3. *Magn Reson Med* 54(1):28–33
- Walker TG, Happer W (1997) Spin exchange optical pumping of noble-gas nuclei. *Rev Mod Phys* (69):629–642
- Wang C, Miller GW, Altes TA et al. (2006) Time dependence of 3He diffusion in the human lung: measurement in the long-time regime using stimulated echoes. *Magn Reson Med* 56(2):296–309
- Wang C, Altes TA, Mugler JP III et al. (2008) Assessment of the lung microstructure in patients with asthma using hyperpolarized 3He diffusion MRI at two time scales: comparison with healthy subjects and patients with COPD. *J Magn Reson Imaging* 28(1):80–88
- Wild JM, Paley MNJ, Viallon M et al. (2002a) k-space filtering in 2D gradient-echo breath-hold hyperpolarized He-3 MRI: spatial resolution and signal-to-noise ratio considerations. *Magn Reson Med* 47(4):687–695
- Wild JM, Schmiedeskamp J, Paley MNJ et al. (2002b) MR imaging of the lungs with hyperpolarized helium-3 gas transported by air. *Phys Med Biol* 47(13):N185–N190
- Wild JM, Fичele S, Woodhouse N et al. (2003a) Assessment and compensation of susceptibility artifacts in gradient echo MRI of hyperpolarized 3He gas. *Magn Reson Med* 50(2):417–422
- Wild JM, Paley MN, Kasuboski L et al. (2003b) Dynamic radial projection MRI of inhaled hyperpolarized 3He gas. *Magn Reson Med* 49(6):991–997
- Wild JM, Woodhouse N, Paley MN et al. (2004) Comparison between 2D and 3D gradient-echo sequences for MRI of human lung ventilation with hyperpolarized 3He. *Magn Reson Med* 52(3):673–678
- Wild JM, Fичele S, Woodhouse N et al. (2005) 3D volume-localized pO₂ measurement in the human lung with 3He MRI. *Magn Reson Med* 53(5):1055–1064
- Wild JM, Teh K, Woodhouse N et al. (2006) Steady-state free precession with hyperpolarized 3He: experiments and theory. *J Magn Reson* 183(1):13–24
- Wild JM, Woodhouse N, Teh K (2007) Single-scan acquisition of registered hyperpolarized (3)He ventilation and ADC images using a hybrid 2D gradient-echo sequence. *Magn Reson Med* 57(6):1185–1189
- Woodhouse N, Wild JM, Paley MN et al. (2005) Combined helium-3/proton magnetic resonance imaging measurement of ventilated lung volumes in smokers compared to never-smokers. *J Magn Reson Imaging* 21(4):365–369
- Woodhouse N, Mills GH, Flemming S, Fичele S, van Beek EJ (2006) Comparison of hyperpolarized 3-He administration methods in healthy as diseased subjects. *Proc ISMRM* 2006, p 1288
- Woods JC, Yablonskiy DA, Chino K et al. (2004) Magnetization tagging decay to measure long-range (3)He diffusion in healthy and emphysematous canine lungs. *Magn Reson Med* 51(5):1002–1008

- Woods JC, Choong CK, Yablonskiy DA et al. (2006) Hyperpolarized ^3He diffusion MRI and histology in pulmonary emphysema. *Magn Reson Med* 56(6):1293–1300
- Yablonskiy DA, Sukstanskii AL, Leawoods JC et al. (2002) Quantitative in vivo assessment of lung microstructure at the alveolar level with hyperpolarized ^3He diffusion MRI. *Proc Natl Acad Sci U S A* 99(5):3111–3116
- Zhao L, Mulkern R, Tseng CH et al. (1996) Gradient-echo imaging considerations for hyperpolarized ^{129}Xe MR. *J Magn Reson B* 113:179–183
- Zhu H, Ruset IC, Hersman FW (2005) Spectrally narrowed external-cavity high-power stack of laser diode arrays. *Opt Lett* 30(11):1342–1344
-

MRI of Pulmonary Ventilation

4.2 Hyperpolarized ^{129}Xe MRI of the Lung

SAMUEL PATZ, IGA MURADIAN, MIRKO I. HROVAT, F. WILLIAM HERSMAN,
HIROTO HATABU and JAMES P. BUTLER

CONTENTS

| | | |
|---------|--|----|
| 4.2.1 | Introduction | 58 |
| 4.2.2 | ^{129}Xe Polarizer Technology | 58 |
| 4.2.2.1 | Method: Counter-current Polarization | 59 |
| 4.2.3 | Safety of ^{129}Xe : Breathing Protocol for ^{129}Xe and Safety Issues | 60 |
| 4.2.4 | ^{129}Xe Spectra in the Lung | 61 |
| 4.2.5 | Diffusion of Xenon from Alveolar Gas Spaces to Septal Tissue | 61 |
| 4.2.6 | Interphase Diffusion Using Xenon Transfer Contrast (XTC) | 64 |
| 4.2.7 | Clinical Potential | 66 |
| | References | 66 |

KEY POINTS

Hyperpolarized xenon-129 (^{129}Xe) has enormous potential to provide noninvasive functional information about the lung. In particular, because inhaled xenon follows the same pathway as oxygen, diffusing from alveolar gas spaces to septal tissue and blood, gas exchange parameters can be measured. For example, by measuring the time-dependent septal uptake of ^{129}Xe , information about alveolar surface area, septal thickness and vascular transit times can be obtained. A principal obstacle to the development and application of this technology to humans has been the lack of a polarizer that can provide sufficient quantities of highly polarized ^{129}Xe gas. This problem, however, has recently been solved. To obtain quantitative measures of pulmonary function with ^{129}Xe , two methods have been studied. One is a direct method that measures the magnetic resonance signal from the gas spaces and from the different septal tissue compartments. In principal this is straightforward since the signal from each compartment can be distinguished due to a unique chemical shift frequency. In practice, however, there are limitations because of the very small signal available to measure in the septal tissue. Thus, the direct measurement of ^{129}Xe interphase diffusion in humans has been principally confined to whole lung measurements. To obtain regional maps of ^{129}Xe interphase diffusion, the Xenon Transfer Contrast (XTC) method has been utilized. XTC is an indirect method that measures the attenuation in the gas phase magnetization due to interphase diffusion between the gas phase and septal tissue compartments. Using XTC, regional maps of interphase diffusion in humans has been demonstrated.

SAMUEL PATZ, PhD, IGA MURADIAN, PhD,
HIROTO HATABU, MD
Center for Pulmonary Functional Imaging, Department of Radiology, Brigham & Women's Hospital and Harvard Medical School, Boston, MA 02115, USA

MIRKO I. HROVAT, PhD
Mirtech, Inc., Brockton, MA 02301, USA

F. WILLIAM HERSMAN, PhD
Department of Physics, University of New Hampshire, Durham, NH 03824, Xemed LLC, Durham, NH 03824, USA

JAMES P. BUTLER, MD
Dept. Environmental Health, Harvard School of Public Health and Dept. of Medicine, Harvard Medical School, Boston, MA 02115, USA

4.2.1

Introduction

There has been considerable interest in hyperpolarized ^{129}Xe because of its unique properties. Not only can one obtain beautiful images of ventilation similar to what can be obtained with hyperpolarized ^3He , but unlike ^3He , which has negligible solubility in tissue, xenon follows a pathway similar to oxygen, i.e. diffusing from alveolar gas spaces to septal tissue (parenchyma and red blood cells). A further extremely advantageous property of xenon in septal tissue is that it has significantly different magnetic resonance precession frequencies from that of the gas phase. This makes it straightforward to independently measure the magnetic resonance signal in both the gas and tissue phases allowing measurement of the interphase diffusion kinetics. Properties such as the alveolar surface area, septal thickness, and blood kinetic exchange rates can be measured non-invasively. These physiological parameters are directly related to different diseases and are therefore potentially extremely important. For example, alveolar surface area is a direct measure of emphysematous disease, septal thickness is a direct measure of restrictive pulmonary diseases such as interstitial lung disease, and vascular kinetic parameters such as mean transit time are direct measures of pulmonary vascular disease.

In 1994, the very first images demonstrating pulmonary ventilation using a hyperpolarized noble gas were reported in an excised mouse lung using ^{129}Xe (ALBERT et al. 1994). However, despite this important first step, the vast majority of work in this field has been performed with hyperpolarized ^3He . There are several principal reasons for this disparity. First, the gyromagnetic ratio of ^{129}Xe is three times smaller than that of ^3He . This means that the inherent signal to noise ratio (SNR) will be smaller compared to ^3He by the same ratio. In addition, ^3He is supplied with an isotopic concentration of 100% as compared to the natural abundance of ^{129}Xe , which is only 26%. This creates an additional factor of four reduction in SNR, and when combined with the gyromagnetic ratio factor, represents a total factor of 12 in inherent loss of SNR for ^{129}Xe . The low natural abundance of ^{129}Xe can be partially mitigated by purchasing more expensive enriched ^{129}Xe , typically enriched to 86%. Note that the cost per liter of both enriched 86% ^{129}Xe and 100% ^3He is presently around \$250. Finally, a third problem for xenon has been the lack of polarizers that can produce liter quantities of gas with high polarization (PATZ et al. 2007). Thus, much of the early work in ^{129}Xe has been done in animal models where smaller quantities of gas are required. More recently, however,

a ^{129}Xe polarizer capable of producing 1–2 L/h at 50% polarization (RUSER et al. 2006) has become available enabling more routine investigation in humans.

4.2.2

^{129}Xe Polarizer Technology

The commercialization of hyperpolarized noble gases began in the United States with the formation of Magnetic Imaging Technologies Incorporated (MITI) in 1996 as a spin-off company from the research group of Will Happer at Princeton. Happer's group had performed much of the fundamental science of spin exchange optical pumping (SEOP) through the 1980s and early 1990s. Due to his reputation in this area, he was approached by xenon spectroscopists Balamore and Albert from Stony Brook seeking stronger signals for their studies of biochemical mechanisms of anesthesia. Their collaboration led to the recognition that hyperpolarized gases could be produced in large quantities, breathed, and imaged in vivo. MITI continued technical refinement, produced and sold a few polarizers, and began collaborating with academics to develop imaging strategies. In 1999 MITI was bought by Nycomed Amersham, who began the process to seek regulatory approval. While they applied for hyperpolarized noble gases to be classified by the US FDA as a device, instead these gases were classified as drugs. The projected expense required for human trials leading to regulatory approval mushroomed.

Two gases, ^3He and ^{129}Xe , can be hyperpolarized by SEOP. This process uses circularly polarized light tuned to an absorption line in rubidium to polarize rubidium vapor. Collisions between the rubidium atoms and the noble gas atoms transfer the polarization from the rubidium electron to the noble gas nucleus. The technology for achieving high polarizations with ^3He had been a focus of Happer's group due to its applications in fundamental high-energy physics. Consequently liter quantities of >35% polarized ^3He were routinely achievable. In contrast, liter-quantities of xenon could be produced with polarizations typically less than 5%–7%. This is largely because xenon poses an additional challenge: the electrons of xenon usually depolarize the rubidium electron before the rubidium electron can polarize the xenon nucleus. Xenon polarization has low intrinsic photon efficiency.

Nycomed Amersham decided to concentrate their resources on FDA approval of hyperpolarized helium imaging. ^3He offered a magnetic moment three times greater than ^{129}Xe and the polarization was 5 to 10 times higher, yielding a signal strength advantage of

up to 30. In spring of 2004, General Electric acquired Amersham Health and with it the license to the original Princeton US patent covering medical imaging of hyperpolarized gases. More recently, however, both in 2007 and 2008, GE Healthcare announced their intentions at the Hyperpolarized Noble Gas Study Section meetings held at the ISMRM in Berlin (2007) and Toronto (2008) that they were not vigorously pursuing ^3He but rather were much more interested in ^{129}Xe .

Development of an alternative ^{129}Xe polarizer was being pursued by F. W. Hersman at the University of New Hampshire where he had been building a technology development program to produce polarized helium cells to serve as particle beam targets for nuclear physics experiments. In 1997 after learning of the need for better methods to polarize xenon, he conceived of the counter-flow method and invented the counter-flow xenon polarizer (RUSET et al. 2006). His team finally achieved a technological breakthrough in 2004. Magnetization output, the product of polarization times production rate, exceeded the output of the commercial Amersham polarizer by a factor of fifty (RUSET et al. 2006).

4.2.2.1

Method: Counter-current Polarization

The counter-flow polarizer (Fig. 4.2.1) embodies a main operating principle and two auxiliary supporting ideas, enabling a new regime of operation. The main principle is to flow the mixed gases along a long reaction chamber towards a laser beam emanating from the opposite direction. The gases are initially illuminated with the attenuated beam achieving some degree of polarization, but near the end of the process when gases are highly polarized they are subjected to the most intense laser light to assure 100% rubidium polarization and raise the xenon polarization still further. This “counter-current” principle is also used in efficient heat exchangers.

The first auxiliary idea is to saturate the flowing gases with rubidium in a preparatory chamber outside the laser polarization region. This assures homogeneous saturation of the gases to a well-defined rubidium density (dependent on the thermal bath temperature) essentially independent of flow velocity and laser power. The design had the rubidium droplets in the polarization chamber. Higher flow rates resulted in incomplete saturation of the flowing gases with rubidium. Higher laser intensity resulted in a non-linear runaway condition, in which laser power absorption heated the gas vaporizing additional rubidium, which in turn increased laser absorption. Higher laser intensity in the system actually

reduces rubidium density (higher temperature at constant partial pressure) maintaining stability. The second auxiliary idea is to extract the rubidium in the presence of the polarizing light. By bringing the mixed flowing gases into contact with a cold surface in the presence of the laser light, the rubidium remains polarized, continuing to transfer polarization to the xenon, until it is extracted. The system exhausted mixed gases from the chamber still saturated with rubidium. That strategy can allow the rubidium to quickly lose its polarization and begin to depolarize the xenon.

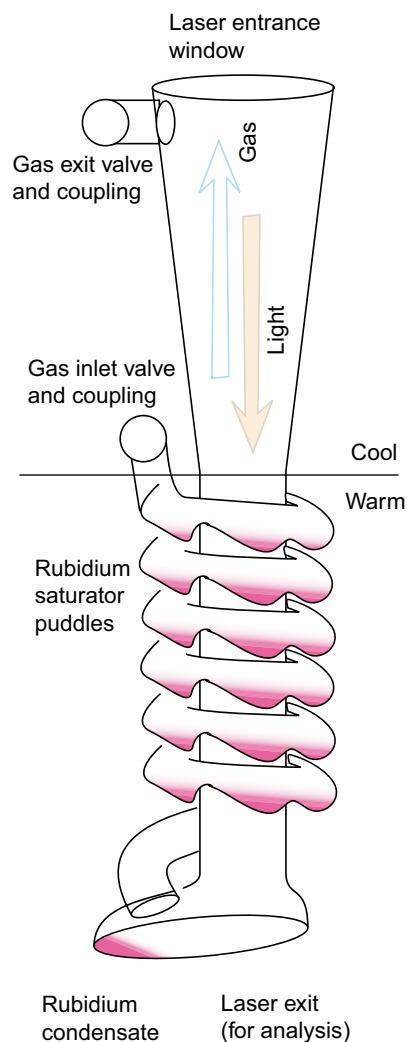


Fig. 4.2.1. Schematic of the Hersman polarizer; University of New Hampshire, USA. The laser light enters the polarization column along a *direction opposite the flow of gas*. Reprinted with permission from PATZ et al. (2007)

The new operating regime enabled by these advances is: high gas flow velocity, low gas pressure, and very low xenon partial pressure. The key benefit to low xenon partial pressure is the resulting ability to maintain high rubidium polarization with the laser. High xenon partial pressure leads to rapid rubidium depolarization. Of course low xenon partial pressure then requires higher flow rates to polarize the same quantity of xenon. The key benefit to low total gas pressure is the increase in polarization transfer from rubidium to xenon. Rubidium transfers polarization to xenon by two distinct processes: instantaneous binary collisions and formation of van der Waals molecules. Spin exchange by molecule formation has much higher probability if the molecule is not broken up by a subsequent collision, and therefore dominates at low pressures. Hersman and his colleagues are able to achieve almost an order of magnitude increase in spin exchange rate and flow at much higher velocities. Low pressure however can reduce the efficiency of extracting the laser light by the rubidium. Most polarizers require higher pressure to pressure broaden the rubidium absorption spectral line. The University of New Hampshire group achieved efficient laser absorption by increasing the length of the cell by a factor of ten, from a previous maximum length of 20 cm to almost 2 m. These combined improvements provide quantities of 10–20 L of ^{129}Xe polarized within 1 h and with polarization up to and exceeding 50%. This polarization technology has enabled high-quality human MR imaging protocols (PATZ et al. 2007).

4.2.3

Safety of ^{129}Xe : Breathing Protocol for ^{129}Xe and Safety Issues

To date, two groups have reported ^{129}Xe MRI studies in humans. MUGLER et al. (1997) performed initial studies on a few healthy subjects with an inhalation of a 500-cc bolus of xenon gas. This was followed by further preliminary results measuring ^{129}Xe apparent diffusion coefficient (ADC) (MUGLER et al. 2004). These studies represented important first steps in human ^{129}Xe MRI but were limited because of the polarizer performance. Most human studies to date have been performed at Brigham and Women's Hospital, Boston, USA with the polarizer described in the previous section (PATZ et al. 2007, 2008). The protocol used in Boston requires all inhaled gas mixtures to contain at least 21% oxygen and no more than 70% xenon. In addition, the estimated alveolar xenon concentration can be no more than 35%. It is important to stay well below an alveolar concentration of ~70%, because of well known anesthetic ef-

fects above that concentration (LATCHAW et al. 1987). Standard spirometry was performed on each subject to obtain their residual volume RV and total lung capacity TLC. These values were used to calculate the volume of additional air needed to be inhaled, if any, in order to satisfy the concentration requirements in the lung for a particular volume of xenon and oxygen that was being inhaled. Breath-hold times are limited to 40 s for healthy subjects and 20 s for those with mild to moderate lung disease. Baseline measurements of the saturation of peripheral blood oxygen (SpO_2), ECG, blood pressure, heart rate, and respiratory rate are required to be made for each subject before beginning a series of experiments and 10 min after each breath-hold experiment. SpO_2 and heart rate are also monitored while in the MRI scanner. Several practice sessions are performed outside the scanner, some with air and one with a volume of xenon equal to the maximum that would be used for any of the experiments planned for that particular subject. The practice breaths familiarize the subject with the protocol and allow them to experience what breathing ^{129}Xe will be like. We also checked to make sure the SpO_2 stays within allowed limits: no lower than an absolute value of 85% for healthy subjects. To date, 26 subjects have participated in various experiments involving at least 350 xenon breath-hold experiments. Three of the 26 subjects had mild interstitial lung disease and performed 32 breath-hold experiments. The remainder of the experiments was performed by healthy subjects. There have been no adverse events. Before breathing xenon, a subject is instructed to perform two cycles of a deep breath to TLC followed by exhalation to close to RV. This ensures there is an identical breathing history before the experiment for each subject.

The lack of adverse events as well as the fact that there was no significant effect on heart rate, respiratory rate, SpO_2 and blood pressure is perhaps not surprising, especially in light of the fact that a different isotope of xenon has been used safely for many years to measure cerebral blood flow with CT. For example, LATCHAW et al. (1987) reviewed adverse reactions for xenon CT in a multi-center study involving 1830 patients and concluded that the side effects of xenon gas are minimal when its percentage concentration in the gas inhaled is less than 32%. Note that xenon CT typically involves continuous breathing of xenon for 5 min whereas our MRI protocol calls for a single breath repeated at most every 10 min. In addition, in the early limited studies of MUGLER et al. (1997), they reported only occasional lightheadedness, dry mouth and mild throat irritation when subjects inhaled 500 cc of laser polarized ^{129}Xe . Occasional light-headedness was also observed by YONAS et al. (1981) in their xenon CT studies.

4.2.4 ¹²⁹Xe Spectra in the Lung

The gyromagnetic ratio for ¹²⁹Xe in the gaseous phase is 11.78 MHz/T, approximately one quarter that of protons. Xenon is soluble in tissue and after allowing equilibrium to be established between gas and tissue (i.e. xenon partial pressures in each media are identical), the concentration in tissue relative to gas is given by the Ostwald solubility coefficient (also known as the partition coefficient), $\lambda \sim 0.1$ (EGER and LARSON 1964). There are only a few published xenon spectra from the human lung. The first was from MUGLER et al. (1997) reporting initial results in two human volunteers. Referenced to the gas phase at 0 ppm, Mugler et al. reported three spectral peaks: human subject 1: 185–186, 195–196, and 216 ppm; human subject 2: 182–183, 195–196, and 216 ppm. Identification of the peaks was made by comparison with animal studies (SAKAI et al. 1996; WAGSHUL et al. 1996): the most shifted peak at 216 ppm was assigned to red blood cells, the peak at 195–196 ppm to lung parenchyma, and the least shifted peaks to plasma and/or well vascularized other tissues in the thorax such as the heart myocardium.

A typical spectrum from a human lung at 0.2 T field strength is shown in Fig. 4.2.2. This spectrum was obtained at a lung volume close to functional residual capacity (FRC). The ratio of the total dissolved to gas phase signals was measured to be 0.022 (PATZ et al. 2008). Notice that, at this low field strength, the chemical shift separation between dissolved phase compo-

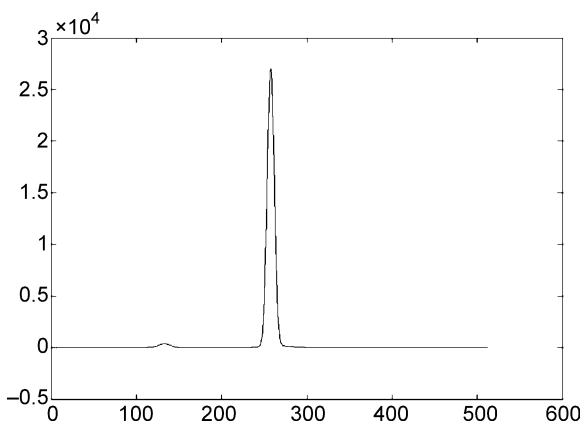


Fig. 4.2.2. ¹²⁹Xe human lung spectra at 0.2 T. The *large peak* is the gas peak and relative to it is the *dissolved phase peak* at +205ppm (+485Hz). The line widths (FWHM) of the gas/dissolved phase lines are $\sim 20/100$ Hz respectively. The ratio of the dissolved to gas spectral integrals of the signal is 0.022

nents is sufficiently small that all the dissolved phase spectral components appear as a single peak.

The dissolved/gas phase signal ratio directly reflects the relative quantity of hyperpolarized ¹²⁹Xe magnetization in the two phases. The fact that the dissolved phase xenon signal is ~ 50 times less than the xenon gas phase signal means that the SNR of the dissolved phase is quite low. Thus, human experiments that involve measurement of gas exchange kinetics and that require direct measurement of both gas and dissolved phase signals have principally been performed using whole lung spectroscopy. Direct imaging of the dissolved phase to provide regional maps of gas exchange is difficult because the signal strength from the dissolved phase is divided by a large number of voxels. Imaging experiments of gas exchange kinetics have therefore primarily relied on a measurement technique that does not directly measure the dissolved phase signal but rather observes a modulation of the gas phase signal due to interphase diffusion between gas and dissolved phases. This technique, known as xenon transfer contrast (XTC) (RUPPERT et al. 2000a, 2004), will be described in detail below.

It is important to appreciate the origin of the relatively small quantity of ¹²⁹Xe in the dissolved phase. In the absence of blood flow effects, the equilibrium magnetization ratio between the alveolar gas and dissolved phases is predicted to be

$$\frac{M_{diss}}{M_{gas}} = \frac{\lambda V_{diss}}{V_{gass}} \quad (1)$$

The volume of the dissolved and gas phases is given by V_{diss} and V_{gas} and their ratio can be expressed in terms of the porosity $\phi = V_{gas} / (V_{gas} + V_{diss})$. For a lung volume close to FRC, $\phi \sim 0.8$, which gives a predicted value for $M_{diss}/M_{gas} = 0.02$, which is in very close agreement with the experimentally determined value at 0.2 T.

4.2.5 Diffusion of Xenon from Alveolar Gas Spaces to Septal Tissue

A very simple pulse sequence, Chemical Shift Saturation Recovery (CSSR), can be used to obtain important information about the lung. By applying a selective 90° radio frequency pulse centered in the dissolved phase frequencies, one can destroy the dissolved phase ¹²⁹Xe magnetization. This creates an ideal step function initial condition (Fig. 4.2.3a) where the ¹²⁹Xe magnetization is initially zero in the dissolved phase and relatively uniform in the gaseous phase. The ¹²⁹Xe magnetization in the gaseous phase is relatively uniform because the

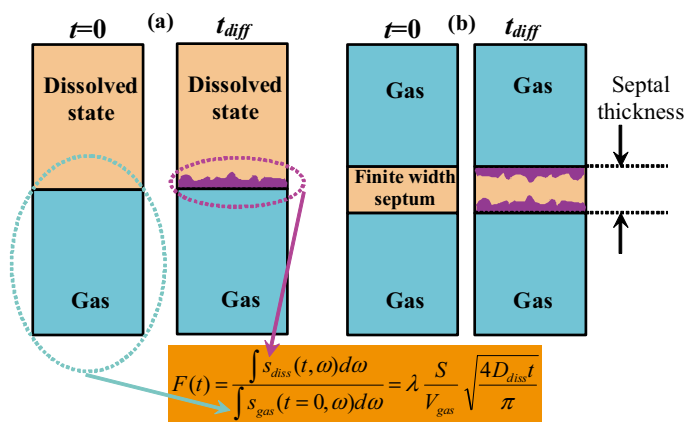


Fig. 4.2.3. Schematic of Chemical Shift Saturation Recovery (CSSR) method. (a) Idealized 1D semi-infinite phases. (b) A more realistic model with a finite width septum. Net diffusion from gas to dissolved phase after time t_{diff} is shown in purple. Reprinted with permission from PATZ et al. (2007)

gas phase is diffusively well mixed. Then, by observing the recovery of the dissolved state ^{129}Xe magnetization (Fig. 4.2.4), one can measure important functional components of the lung. For example, BUTLER et al. (2002) demonstrated the ability to measure quantitatively the surface area per unit volume of gas S/V_{gas} in porous polyethylene phantoms. Measurements of S/V_{gas} were obtained both with a ^{129}Xe magnetic resonance method and by confocal microscopy. Good agreement between the two methods provided strong evidence that S/V_{gas} can be measured non-invasively with ^{129}Xe .

BUTLER et al. (2002) showed that, for a semi-infinite medium (Fig. 4.2.3a), the fraction $F(t)$ of the ^{129}Xe magnetization that diffuses into the dissolved phase during a diffusion time t relative to the ^{129}Xe magnetization initially in the gas phase, is proportional to S_A/V_{gas} :

$$F(t) = \frac{\int s_{diss}(t, \omega) d\omega}{\int s_{gas}(t=0, \omega) d\omega} = \lambda \frac{S_A}{V_{gas}} \sqrt{\frac{4D_{diss}t}{\pi}} = K\sqrt{t},$$

$$K = \lambda \frac{S_A}{V_{gas}} \sqrt{\frac{4D_{diss}}{\pi}}. \tag{2}$$

Here, the integrals are over the spectral width of the dissolved s_{diss} and gas s_{gas} signals, and D_{diss} is the diffusivity of ^{129}Xe in the dissolved phase. V_{gas} is the gas volume and S_A is the surface area between the two phases. For lung parenchyma, S_A is the alveolar surface area. The analytical form of Eq. (2) is only valid for short times where the semi-infinite approximation is valid, i.e. the septa are far from being saturated. Since the septa are not semi-infinite (Fig. 4.2.3b), for a long time F saturates and does not increase as \sqrt{t} . Note also that, because F is the ratio of dissolved to gas phase magnetization, it is an intensive rather than extensive quantity. This is important experimentally because of the following. During a static breath-hold experiment, the gas phase magnetization decays. There are two mechanisms responsible for this decay. One is due to the presence of paramagnetic oxygen, which decreases T_1 to ~ 20 s and second, the small flip angle RF pulses that are used to interrogate the gas phase magnetization also deplete the nonrenewable magnetization reservoir. Because F is an intensive quantity, as long as the SNR remains adequate, measurements can be made throughout the decay of the gas phase magnetization. Thus, because F is an inten-

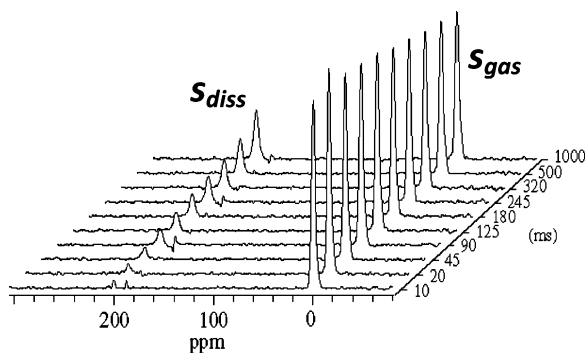


Fig. 4.2.4. Chemical Shift Saturation Recovery (CSSR) experiment on porous polyethylene. Here the gas phase is at 0 ppm and the dissolved phase is at ~ 200 ppm. At time $t=0$, the dissolved phase magnetization is set to zero using a selective 90° RF pulse. The rate at which the dissolved phase signal recovers is due to the diffusion of ^{129}Xe from the gas spaces into the dissolved phase and is proportional both to the surface area between the two phases and increases diffusively as \sqrt{t} . Reprinted with permission from BUTLER et al. (2002)

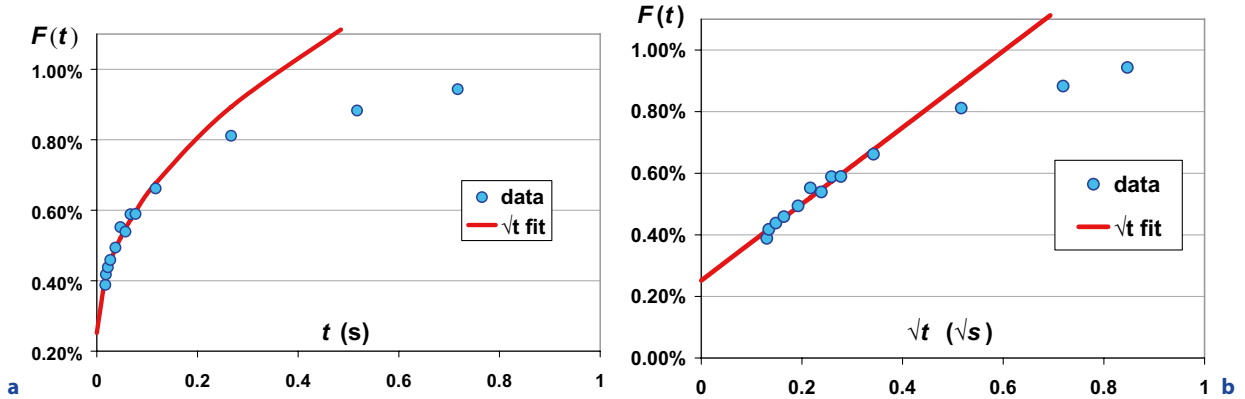


Fig. 4.2.5a,b. Experimentally measured $F(t)$ shown with blue dots as a function of diffusion time t (a) and \sqrt{t} for the early time data (b) where the semi-infinite approximation for the

gas and dissolved phases holds. Lung volume was fixed and in the example shown here, it is at total lung capacity (TLC). Reprinted with permission from PATZ et al. (2007, 2008)

sive quantity, one can continue to make measurements throughout the natural decay of the gas phase magnetization and this significantly increases the efficiency of data collection.

A typical example from recently reported CSSR results in healthy humans (PATZ et al. 2008) is shown in Fig. 4.2.5. For diffusion times less than ~ 100 ms, the behavior of $F(t)$ is described quite well by a diffusive \sqrt{t} dependence as demonstrated by the red line in Fig. 4.2.5. Initial measurements from four healthy subjects at multiple lung volumes (PATZ et al. 2008) were undertaken to measure S_A/V_{gas} as a function of lung volume. Figure 4.2.6 shows the data after converting the measured slope (see Eq. 2) to S_A/V_{gas} using literature values for $\lambda \sim 0.1$ and $D_{\text{diss}} \sim 3 \times 10^{-6} \text{ cm}^2/\text{s}$ (STA and ECKMANN 2003). Note that, as expected, as lung volume increases, S_A/V_{gas} decreases (GIL et al. 1979). Note also that the fits to the CSSR data include a DC offset term F_0 : $F(t) = F_0 + K\sqrt{t}$. This is necessary because the shortest diffusion time at 0.2 T was 17 ms, during which one estimates ^{129}Xe diffuses within the parenchyma by $\sim 3 \mu\text{m}$, thereby saturating the thinner, connective tissue portions of the septa. These thinner regions remain saturated at all longer diffusion times and therefore appear as a DC offset. Thus, the time-dependent diffusion that was observed most likely corresponds to the thicker portions of the septa occupied by capillaries. Consequently, these CSSR-determined values of S_A/V_{gas} should be smaller than those obtained from histology. A comparison with literature values (COXSON et al. 1999) shows this to be the case; these values are $\sim 40\%$ lower than those obtained morphometrically from humans post lobectomy.

S_A/V_{gas} is important because septal surface area is lost in emphysematous disease. In fact, the “gold standard” method in which emphysematous damage is determined in animal research is to sacrifice the animal, fix the lungs and then measure what is known as the mean linear intercept L_m by examining sections under the microscope. L_m is the mean distance between air and gas portions of the parenchyma on a microscope slide. Mathematically, $S_A/V_T = 2/L_m$ where V_T is the total volume = $V_{\text{gas}} + V_{\text{diss}}$. Thus apart from a small correction factor to convert V_T to V_{gas} , ^{129}Xe interphase diffu-

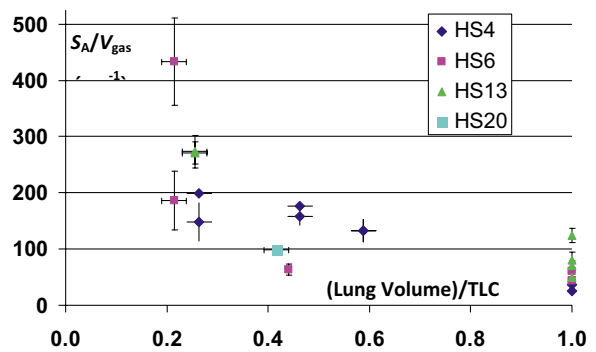


Fig. 4.2.6. Alveolar surface area per unit volume of gas as a function of lung volume normalized to total lung capacity (TLC). Data was obtained from four normal, healthy adults. Note that HS stands for “Human Subject”. Also note that to convert from S_A/V_{gas} to K , a value of $S_A/V_{\text{gas}} = 100 \text{ cm}^{-1}$ corresponds to $K = 0.0195 \text{ s}^{-1/2}$. Reprinted with permission from PATZ et al. (2008)

sion experiments can non-invasively measure the same quantity as the “gold standard” histology method.

Similar methods have been used by several other investigators in animals (RUPPERT et al. 2000a, b, 2004; MANSSON et al. 2003; DRIEHUYS et al. 2006; ABDEEN et al. 2006; CAI et al. 2006) with great success. RUPPERT et al. (2000b) performed CSSR in a canine model and measured the time dependence of the dissolved phase peaks. MANSSON et al. (2003) reported ^{129}Xe diffusion results in a rat model and fit their data to a 1D diffusion model that included a three compartment model: gas, parenchymal boundary layer, and red blood cells. They obtained estimates for alveolar wall thickness, pulmonary perfusion, capillary diffusion length and mean transit time of the blood in the gas exchange region. DRIEHUYS et al. (2006) reported ^{129}Xe diffusion studies in rats treated with bleomycin as a model of interstitial disease. A time lag in the red blood cell spectral peak of the diseased animals was observed and confirmed with histology. Then, by directly sampling the dissolved phase signal, but after a suitable time delay that allowed ^{129}Xe to diffuse from gas spaces into the red blood cells in the normal lung but was not long enough to allow it to diffuse into the red blood cells of the diseased lung with a thicker parenchymal boundary between alveolar gas and red blood cells, striking images were obtained demonstrating a gross difference between a treated and untreated lung in the same animal. Also, ABDEEN et al. (2006) utilized measurements of xenon diffusion into septal tissue and gas phase imaging to measure lung vol-

ume and gas transfer constants. Combining these with a measured end inspiratory pressure during a breath-hold experiment, they obtained a diffusing capacity of xenon for lung parenchyma and red blood cells. Finally, CAI et al. (2006), comparing healthy rabbits to those with a model of emphysema, demonstrated in a study of eight rabbits, a high degree of correlation between the slope of the XTC depolarization curve and S_A/V_T as determined by morphometry.

4.2.6 Interphase Diffusion Using Xenon Transfer Contrast (XTC)

Direct imaging of the dissolved phase signal in the lung, where the signal from the dissolved phase magnetization is split up into the number of imaging voxels, can be difficult (MURADIAN et al. 2006). This is because the dissolved phase magnetization is only ~2% of that in the gas phase. Animal experiments are much more feasible (RUPPERT et al. 2004; DRIEHUYS et al. 2006) because tidal volumes are much smaller and a single batch of polarized gas can be used for many signal averages. Therefore, for human images of interphase diffusion between alveolar gas spaces and septal tissue, the XTC method developed by RUPPERT et al. (2000a) was used. As originally implemented, XTC is a two breath protocol, which works well for an anesthetized animals. This is problematic, however, for alive, awake humans because

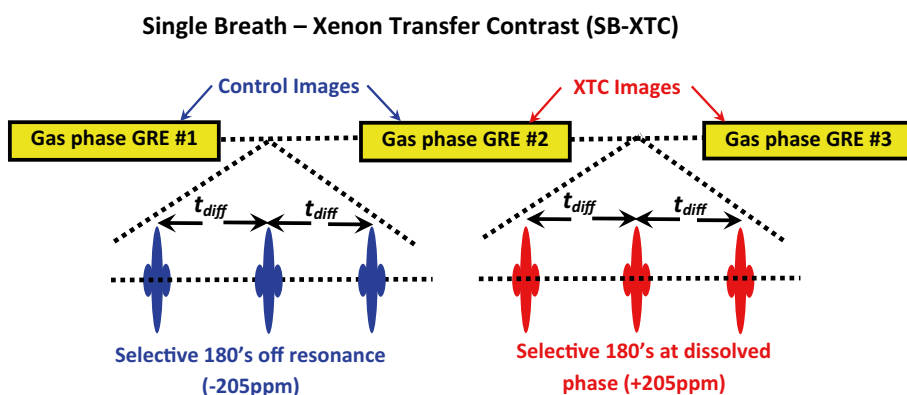


Fig. 4.2.7. Schematic of single breath XTC method. The attenuation between the control images is due to (1) depletion of ^{129}Xe magnetization due to the RF pulses used for the imaging and (2) T_1 decay due to the presence of oxygen. The attenuation between the XTC images is due to the above two mechanisms plus (3) interphase diffusion. Note that the selective 180s between the XTC images are located in the center of the dissolved phase resonances (+205 ppm) whereas the 180s between the control images are off resonance (–205 ppm). The gas phase is at 0 ppm. Reprinted with permission from PATZ et al. (2008)

of reproducibility issues between two static breath-hold experiments. For this reason, the technique was modified to a single breath (SB-XTC) method (PATZ et al. 2007, 2008) (Fig. 4.2.7).

XTC measures the diffusion into the dissolved phase indirectly by looking at the attenuation in the gas phase signal after multiple opportunities for interphase diffusion. If the gas phase magnetization decays by a fraction r , then after n opportunities for interphase diffusion, the gas phase magnetization will decay by r^n . Typically $r \sim 0.99$ and $n=44$, from which one would predict to see the gas phase magnetization attenuated by a factor of $(0.99)^{44} = 0.64$.

RUPPERT et al. (2000a) implemented XTC by two separate breath hold experiments. One experiment, the control experiment, measures the voxel by voxel attenuation due to two “unwanted” sources of attenuation, i.e. T_1 decay due to the presence of oxygen and depletion of the ^{129}Xe magnetization reservoir due to the RF pulses used for imaging. A second XTC experiment mea-

sures the attenuation from the two “unwanted” sources as well as that due to interphase diffusion. The interphase diffusion part can then be solved for by using the results from the control experiment to remove the “unwanted” sources of attenuation in the XTC experiment. A typical example of data obtained with SB-XTC from a healthy subject in the supine position is shown in Fig. 4.2.8. These images were acquired at a lung volume of 47% of TLC, which is close to FRC. Imaging parameters were (matrix 64 readout) \times 32 (phase encode), pixel size 4.69 mm \times 9.38 mm, TE/TR = 5.23/28.47 ms, FOV=300 mm, readout bandwidth = ± 2893.5 Hz). The interphase diffusion time was chosen to be 62 ms in order to lie well within the early time regime, i.e. F linear with \sqrt{t} , that was measured with CSSR. Fig. 4.2.8a–c shows the three acquired SB-XTC images, from which a map of F_{XTC} is calculated as shown in Fig. 4.2.8d. The histogram for Fig. 4.2.8d is shown in Fig. 4.2.8e and Fig. 4.2.8f shows $\langle F_{\text{XTC}} \rangle$ (averaged right/left) as a function of superior/inferior position. Note that there is a

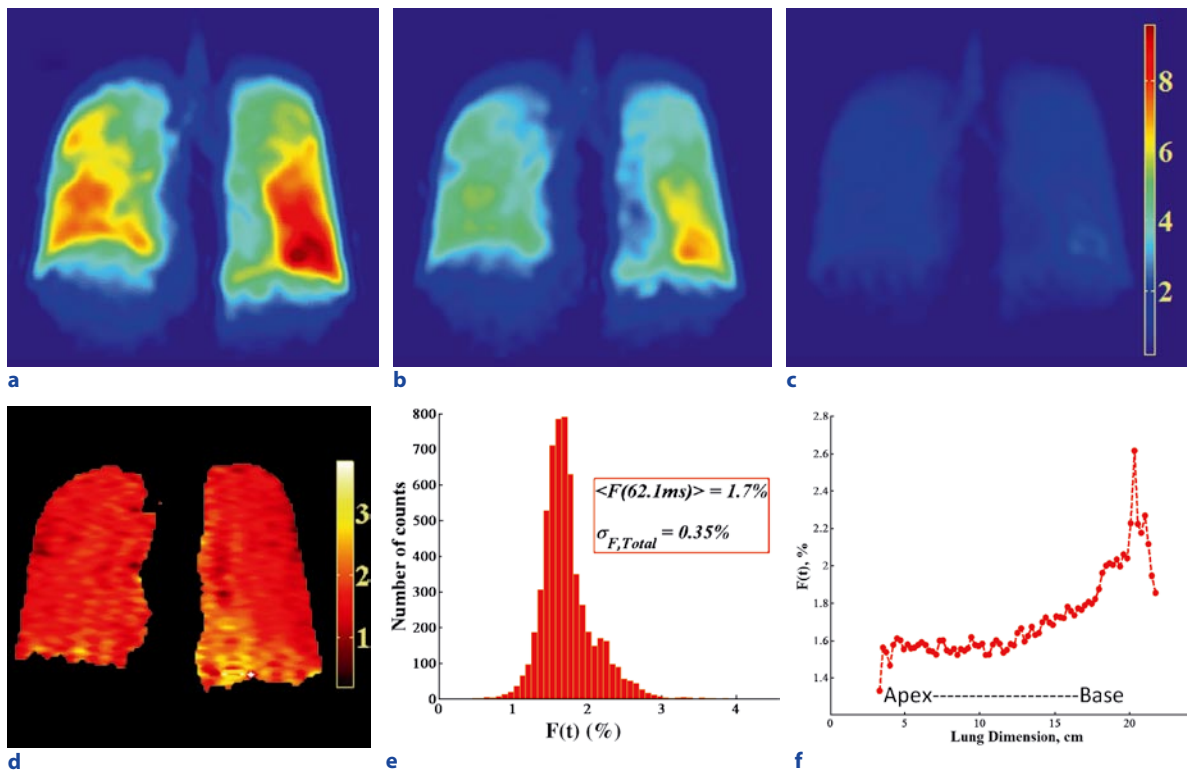


Fig. 4.2.8 a–f. Example of coronal projection images obtained with the SB-XTC method during a breath-hold at 47% of TLC. Image **c** has been scaled to remove the attenuation observed from **a** to **b** due to T_1 relaxation and RF pulses so that the observed attenuation from **b** to **c** is only due to ^{129}Xe diffusion

between gas and tissue phases. The subject is in the supine position. A volume of 1 L of 86% enriched ^{129}Xe was inhaled. Also shown are **d** the resulting F_{XTC} map, **e** its histogram and **f** a plot of the \bar{F}_{XTC} as a function of superior (apex)/inferior (base) position. Reprinted with permission from PATZ et al. (2008)

superior/inferior gradient in $\langle F_{\text{XTC}} \rangle$ despite the fact that the subject is supine. In identical experiments acquired at a higher lung volume (PATZ et al. 2007) this gradient disappears. This behavior is consistent for a number of subjects (MURADIAN et al. 2007) and believed to be due to a residual memory effect of being in the vertical position for a substantial portion of our lives. Closer to TLC, the lung is expected to be more homogeneous, which supports this observation that any residual gradient disappears at higher lung volumes.

An important question is whether or not F_{XTC} can be directly converted to S_A/V_{gas} in a similar manner as F_{CSSR} . This is still an open question. RUPPERT et al. (2004) argue that for very long interphase diffusion times t , $F_{\text{XTC}}(t) = 2F_{\text{CSSR}}(t)$. In a direct comparison, whole lung spectroscopic measurements of both F_{XTC} and F_{CSSR} vs t on the same subject were performed under identical conditions (PATZ et al. 2008). This very preliminary data showed $K_{\text{XTC}}/K_{\text{CSSR}} = 2.52 \pm 0.17$, where K is the slope of F vs \sqrt{t} . WANG et al. (2008) have also recently presented results demonstrating that the very early time dependence has multiple time constants, indicating that different dissolved state components have different kinetics.

Ultimately, one would like to have spatial maps of the $F(t)$ curve in order to obtain regionally specific functional information about the lung. This would potentially provide unique functional information about the lung from a noninvasive test. However, this will require a high throughput polarizer ($\sim 10\text{L/hr}$ @ 50% polarization). Using the images in Fig. 4.2.8 as an example, a separate breath-hold experiment, each using $\sim 1\text{L}$ of hyperpolarized ^{129}Xe , will be necessary to obtain regional data for a single diffusion time. And multiple diffusion times will need to be acquired to obtain data similar to Fig. 4.2.5 for each image voxel.

4.2.7

Clinical Potential

Current day pulmonary diagnostic methods are lacking in many ways. Spirometry and pulmonary function tests only provide global measures of lung function. And in addition, these tests measure the cooperative behavior of the lung and do not differentiate between specific sub-components of lung function. Computed tomography (CT) is often used to clinically diagnose and follow subjects with emphysema and interstitial lung disease. However, CT is a measure of lung density and cannot differentiate between alveolar surface area and septal thickness; rather it is sensitive to the product of these quantities, which determines tissue density.

Further, CT uses ionizing radiation, which is particularly unsuitable for repeat studies in pediatric patients. The fact that xenon follows a similar pathway as oxygen and that its kinetic behavior can be followed with MR offers an unprecedented opportunity to obtain functional information about the lung non-invasively. The scientific community now needs to perform studies to demonstrate definitively that hyperpolarized ^{129}Xe can positively influence clinical management and outcome.

References

- Abdeen N, Cross A, Cron G et al. (2006) Measurement of xenon diffusing capacity in the rat lung by hyperpolarized ^{129}Xe MRI and dynamic spectroscopy in a single breath-hold. *Magn Reson Med* 56:255–264
- Albert MS, Cates GD, Driehuis B et al. (1994) Biological magnetic resonance imaging using laser-polarized ^{129}Xe . *Nature* 370:199–201
- Butler JP, Mair RW, Hoffmann D et al. (2002) Measuring surface-area-to-volume ratios in soft porous materials using laser-polarized xenon interphase exchange NMR. *J Phys Condens Matter* 14:L297–L304
- Cai J, Mata JF, Ruppert K et al. (2006) Characterizing surface-to-volume ratio using hyperpolarized xenon-129 exchange dynamics in a rabbit model. *Proc 14th Intl Soc Magn Reson Med*, p 863
- Coxson HO, Rogers RM, Whittall KP et al. (1999) A quantification of the lung surface area in emphysema using computed tomography. *Am J Respir Crit Care Med* 159:851–856
- Driehuis B, Cofer GP, Pollaro J, Mackel JB, Hedlund LW, Johnson GA (2006) Imaging alveolar-capillary gas transfer using hyperpolarized ^{129}Xe MRI. *PNAS* 103:18278–18283
- Eger EL, Larson CP (1964) Anaesthetic solubility in blood and tissues. *Brit J Anaesth* 36:140–149
- Gil J, Bachofen H, Gehr P, Weibel WR (1979) Alveolar volume-surface area relation in air- and saline-filled lungs fixed by vascular perfusion. *J Appl Physiol Respirat Environ Exercise Physiol* 47:990–1001
- Latchaw RE, Yonas H, Pentheny SL, Gur D (1987) CT cerebral blood flow determination. *Radiology* 163:251–254
- Mansson S, Wolber J, Driehuis B, Wollmer P, Golman K (2003) Characterization of diffusing capacity and perfusion of the rat lung in a lipopolysaccharide disease model using hyperpolarized ^{129}Xe . *Magn Reson Med* 50:1170–1179
- Mugler JP, Driehuis B, Brookeman JR et al. (1997) MR imaging and spectroscopy using hyperpolarized ^{129}Xe gas: preliminary human results. *Magn Reson Med* 37:809–815
- Mugler JP, Mata JF, Wang H-TJ et al. (2004) The apparent diffusion coefficient of ^{129}Xe in the lung: preliminary results. *Proc 11th Intl Soc Magn Reson Med*, p 769
- Muradian I, Patz S, Butler JP et al. (2006) Hyperpolarized ^{129}Xe human pulmonary gas exchange with 3-point Dixon technique. *Proc 14th Intl Soc Magn Reson Med*, p 1297

- Muradian I, Butler J, Hrovat M et al. (2007) Human regional pulmonary gas exchange with xenon polarization transfer (XTC). Proc 15th Intl Soc Magn Reson Med, p 454
- Patz S, Hersman FW, Muradian I et al. (2007) Hyperpolarized ^{129}Xe MRI: a viable functional lung imaging modality? Eur J Radiol 64:334–344
- Patz S, Muradian I, Hrovat MI et al. (2008) Human pulmonary imaging and spectroscopy with hyperpolarized ^{129}Xe at 0.2 T. Acad Radiol 15:713–727
- Ruppert K, Brookeman JR, Hagspiel KD, Mugler JP (2000a) Probing lung physiology with xenon polarization transfer contrast (XTC). Magn Reson Med 44:349–357
- Ruppert K, Brookeman JR, Hagspiel KD, Driehuys B, Mugler JP (2000b) NMR of hyperpolarized ^{129}Xe in the canine chest: spectral dynamics during a breath-hold. NMR Biomed 13:220–228
- Ruppert K, Mata JF, Brookeman JR, Hagspiel KD, Mugler JP (2004) Exploring lung function with hyperpolarized ^{129}Xe nuclear magnetic resonance. Magn Reson Med 51:676–687
- Ruset IC, Ketel S, Hersman FW (2006) Optical pumping system design for large production of hyperpolarized ^{129}Xe . Phys Rev Lett 96:053002
- Sakai K, Bilek AM, Oteiza E et al. (1996) Temporal dynamics of hyperpolarized ^{129}Xe resonances in living rats. J Magn Reson Series B 111:300–302
- Sta MN, Eckmann DM (2003) Model predictions of gas embolism growth and reabsorption during xenon anesthesia. Anesthesiology 99:638–645
- Wagshul ME, Button TM, Li JF et al. (1996) In vivo MR imaging and spectroscopy using hyperpolarized ^{129}Xe . Magn Reson Med 36:183–191
- Wang Y, Mata JF, Cai J et al. (2008) Detection of a new pulmonary gas-exchange component for hyperpolarized xenon-129. Proc 16th Intl Soc Magn Reson Med, p 201
- Yonas H, Grundy B, Gur D, Shabason L, Wolfson SK, Cook EE (1981) Side Effects of xenon inhalation, J Comput Assist Tomogr 5:591–592

MRI of Pulmonary Ventilation

4.3 ¹⁹Fluorine MRI

WOLFGANG G. SCHREIBER

CONTENTS

| | | |
|---------|---|----|
| 4.3.1 | Introduction | 69 |
| 4.3.2 | Principles of F-19 MRI of Fluorinated Gases | 69 |
| 4.3.2.1 | Imaging Strategy | 69 |
| 4.3.2.2 | Gases | 70 |
| 4.3.3 | Application of Fluorinated Gas Imaging | 72 |
| 4.3.3.1 | Animal and Ex Vivo Studies | 72 |
| 4.3.3.2 | Human Application of ¹⁹ F-MRI | 73 |
| 4.3.4 | Conclusion | 73 |
| | References | 73 |

4.3.1 Introduction

The low proton spin density usually makes the lung appear black on conventional clinical H-1 MRI. Intrapulmonary gas can be visualized directly if special provisions are made to optimize the SNR, e.g., by significantly enhancing the level of nuclear polarization (i.e., hyperpolarized He-3 or Xe-129), or alternatively by using extensive spatial and temporal signal averaging. The latter approach is particularly useful if it is used in combination with short T1 gases, because in this case imaging times remain within acceptable limits for in vivo use. Such gases are fluorinated gases like sulphur hexafluoride (SF₆), hexafluoroethane (C₂F₆; Fig. 4.3.1), tetrafluoromethane (CF₄), and octafluorobutane (C₄F₈). These gases are chemically inert, demonstrate no toxic effects, and they contain multiple F-19 atoms, which –

KEY POINTS

Fluorine MRI of the lung is an interesting new approach that may have the potential for broader use than MRI based on hyperpolarized gases like He-3 or Xe-129. Although in general the image quality is worse in fluorine MRI than that obtained with hyperpolarized gases, the latter approach has the advantage of very simple requirements: only an MRI system with non-proton imaging capabilities and a dedicated fluorine-19 MRI coil are required. Fluorinated gases do not need complex treatment before use – this makes their application less demanding on the local infrastructure and, potentially, may also reduce costs. However, currently, the most significant drawback of these gases is that they have not yet been approved for human application.

for a particular type of gas – all resonate at the same Larmor frequency. Moreover, and of particular use for imaging, their T1 relaxation time at 1.5 T, atmospheric pressure, and room temperature ranges from a few milliseconds for SF₆ (1.7 ms) up to 42 ms for C₄F₈ (Kuethe et al. 1998).

4.3.2 Principles of F-19 MRI of Fluorinated Gases

4.3.2.1 Imaging Strategy

The signal-to-noise ratio (SNR) on an MRI image obtained from a fluorinated gas with a single chemical shift component is proportional to a variety of factors (Eq. 4.3.1):

W. G. SCHREIBER, PhD
Section of Medical Physics, Department of Radiology, Mainz University Hospital, Langenbeckstr. 1, 55131 Mainz, Germany

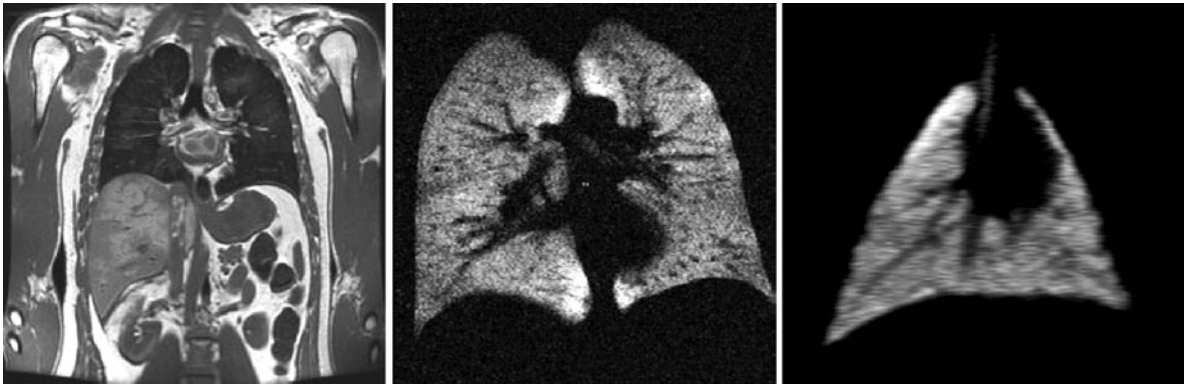


Fig. 4.3.1 Magnetic resonance imaging of the lung using different approaches. *Left:* conventional H-1 image of a human thorax and abdomen. The lung is largely dark. *Center:* hyperpolarized He-3 image of a healthy volunteer obtained within

a measurement time of 1 s. *Right:* F-19 MRI of a porcine lung obtained within 25 min during ventilation with a 70/30% mixture of C_2F_6 and oxygen. No hyperpolarization of the gas was performed in the F-19 image

$$SNR \propto k_{Seq, T_1, R} \rho P V_{voxel} \sqrt{NEX}$$

where $k_{Seq, T_1, R}$ denotes a proportionality factor depending on the pulse sequence type (e.g., spoiled gradient echo, fast low angle shot), imaging parameters (e.g., TR, flip angle, bandwidth), and gas parameters (e.g., T_1 , diffusion coefficient, number of atoms per molecule), ρ denotes the density of the gas, P nuclear polarization, V_{voxel} the volume of the voxel, and NEX the number of signal averages used for image reconstruction. Increasing V_{voxel} , i.e., spatial averaging, is particularly effective in improving the SNR: increasing typical voxel dimensions ($1 \times 1 \times 5 \text{ mm}^3$) to acceptable voxel dimensions for lung MRI ($5 \times 5 \times 20 \text{ mm}^3$) results in an SNR improvement of $5 \times 5 \times 20 = 500$ times if all other imaging parameters are kept fixed. Further improvement can be achieved if a gas with multiple atoms per molecule is used.

What is the influence of the pulse sequence? Assuming a spoiled gradient echo pulse sequence, the optimal SNR depends on TR/T_1 , where TR is the pulse sequence repetition time, and T_1 denotes the T_1 relaxation time of the gas. In consequence, if T_1 is short, TR may be short as well. Comparing the T_1 of F-19 atoms in SF_6 (1.6 ms) with the T_1 of protons in blood (1,400 ms) shows that TR may be reduced by a factor of $1,400 \text{ ms}/1.6 \text{ ms} = 875$ without losing signal intensity from saturation of the magnetization due to excessive radio frequency pulsing. Alternatively, imaging time may be kept fixed at longer times, but multiple signal averages can be used

(improvement of the SNR according to Eq. 4.3.1 by a factor of $\sqrt{875} \approx 30$).

The combination of these approaches is sufficient to obtain reasonable SNR from intrapulmonary fluorinated gases: the total SNR improvement at scan times similar to that required for H-1 MRI of blood can be more than a factor of $500 \times 30 = 15,000$. This is sufficient to compensate for the three orders of magnitude lower spin density of gases than that of solid tissue or fluids (Fig. 4.3.1).

4.3.2.2 Gases

Fluorinated gases are characterized by their physical characteristics as well as their MR parameters (Table 4.3.1). It is evident that these gases have significantly higher molecular weight than the respiratory gases that would be the gases of main interest, but have no usable magnetic properties. At this time it is unclear how differing molecular weights and viscosity influence the spatiotemporal distribution of the different fluorinated gases in the lung and, in consequence, their diagnostic value.

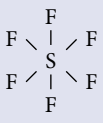
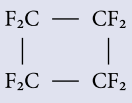
The T_1 relaxation time not only determines the optimal TR (see above), but also the required echo time and, hence, imaging bandwidth. Therefore, in our experience C_2F_6 and C_4F_8 produce better images than SF_6 and CF_4 because they do not require extremely short echo times and high receiver bandwidths. In general,

imaging bandwidths to the order of 100–200 Hz/pixel can be used successfully with these gases.

More detailed information on adequate imaging parameters can be obtained from the computer simulations shown in Fig. 4.3.2. For a given MR system and with a given field of view, the readout bandwidth per pixel defines the minimum pulse sequence repetition time (TR) and echo time (TE). Moreover, the bandwidth per pixel influences the noise of the images. It turns out that despite the very short T_1 relaxation time

of SF_6 (and CF_4) it is better to use medium bandwidth pulse sequences with 400–500 Hz/pixel rather than the shortest possible TE and TR, i.e., the highest possible bandwidth. For a gas with a T_1 relaxation time of several milliseconds (C_2F_6) and in particular for C_4F_8 , it is better to use a lower bandwidth and longer echo times, because the longer readout period significantly reduces the image noise without compromising the signal intensity by T_2 relaxation until the gradient echo appears.

Table 4.3.1 Properties of gases for MRI of the lung

| Gas | Chemical structure [†] | Molecular-weight [†] | Density (kg/m ³), @ 1.013 bar, 288 K ^a | Viscosity (μPa s) @ 273 K ^a | Solubility (mg/L water) ^a | Larmor frequency (MHz) @ 1.5 T | T_1 (ms) @ 1.5 T, 293 K |
|----------|---|-------------------------------|---|--|--------------------------------------|--------------------------------|---------------------------|
| SF_6 |  | 146.056 | 6.27 | 14.2 | 41 | 59.81026 | 1.81 ± 0.01 |
| C_2F_6 | $F_3C - CF_3$ | 138.02 | 5.84 | 13.64 | n.a. | 59.80167 | 7.83 ± 0.02 |
| CF_4 |  | 88.01 | 3.72 | 16.1 | 20 | 59.80313 | 1.88 ^b |
| C_4F_8 |  | 200.04 | 8.82 | 10.92 | 140 | 59.89879 | (47) |
| He-3 | | 3 | 0.13 | (20.0) | | (48.48) | n.a. |
| Xe-129 | | 129 | (5.90) | (23.2) | | (17.66) | n.a. |
| N_2 | | 28.03 | 1.185 | 16.58 | 20 | | |
| O_2 | | 31.9988 | 1.354 | 19.1 | 39 | | |
| CO_2 | | 44.01 | 1.87 | 13.73 | 2,000 | – | |

Larmor frequencies and T_1 relaxation times are given only for fluorinated gases (own unpublished data, if not stated otherwise). For comparison, physical parameters are also given for He-3 and Xe-129 as well as for physiologic respiratory gases

^aAir liquide

^bMOHANTY and BERNSTEIN (1970)

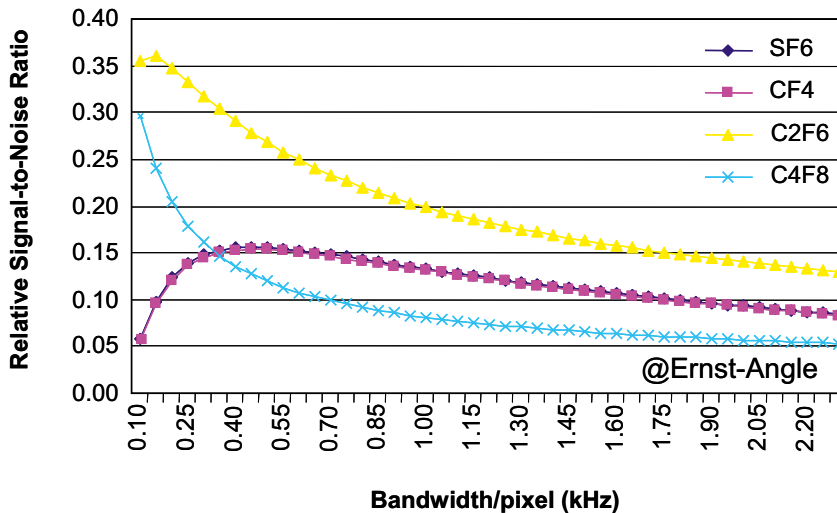


Fig. 4.3.2 Computer simulation of the relative signal intensity for a spoiled gradient echo pulse sequence on a clinical MRI system as a function of pulse sequence bandwidth per pixel, if imaging is performed at the Ernst angle for each gas and for the shortest pulse sequence repetition time possible at a specific bandwidth per pixel (full k-space acquisition, centric echo position). Because of the short T_1 relaxation time of SF_6 and CF_4 gas, both require a relatively high imaging bandwidth (i.e., short TR and TE). For the other two gases longer echo times can be used, i.e., a lower imaging bandwidth

4.3.3 Application of Fluorinated Gas Imaging

4.3.3.1 Animal and Ex Vivo Studies

It is interesting to note that F-19 MRI of CF_4 was performed in dogs as early as 1984 (RINCK et al. 1984). However, imaging times lasted 4 h at that time; this is impractical for human use and also for most preclinical studies.

This methodology was improved using SF_6 and state-of-the-art MR technology for the in vivo imaging of rats (KUETHE et al. 1998) and pigs (SCHREIBER et al. 2001). The pig study showed that even single breath-hold scan times can be achieved by using the spatial and temporal averaging techniques described above and using modern scanner hardware. Recently, subsecond scan times were obtained in pigs using C_2F_6 gas after optimizing the imaging bandwidth according to the simulations shown in Fig. 4.3.2 (WOLF et al. 2006). Moreover, the image quality achieved was sufficient to measure wash-in time constants of C_2F_6 gas during a multiple-breath wash-in maneuver.

An interesting physiologic application of F-19 MRI using SF_6 gas has been demonstrated by KUETHE et al. (2000). They performed imaging of SF_6 at two different

oxygen concentrations. In regions with a low ventilation-perfusion ratio intrapulmonary oxygen enhances rapidly if high oxygen concentrations are inspired. By comparison with an image obtained at a low inspiratory oxygen concentration they were able to identify obstructed rat lungs (KUETHE et al. 2000). In a subsequent study (CHANG AND CONRADI 2006), the dependence of the T_1 relaxation time of SF_6 was used for the mapping of the regional distribution of the ventilation-perfusion ratio in a rat lung obstruction model (ADOLPHI AND KUETHE 2008).

Diffusion of fluorinated gas can be measured to probe the lung's microstructure using similar methodology to that of hyperpolarized gas imaging, i.e., using short bipolar diffusion gradients between the radio-frequency pulse and the data readout of the pulse sequence. Two factors complicate the measurement of the apparent diffusion coefficient (ADC) of a fluorinated gas in the lung. First, because of the higher molecular weight of fluorinated gases with respect to He-3, diffusion is much slower, i.e., diffusion gradients need to be stronger and/or longer. The latter approach of obtaining sufficient diffusion weighting is limited by the second problem, i.e., the short T_1 and T_2 relaxation times. For most of the gases under consideration these short relaxation times limit the duration of the diffusion gradients and, thus, the achievable diffusion weighting. Despite

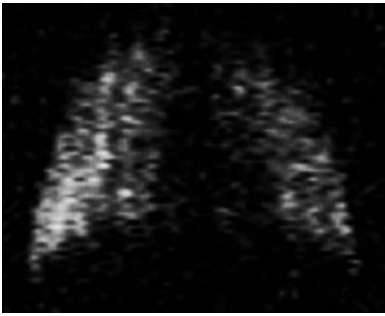


Fig. 4.3.3 Coronal fluorine MRI in a human volunteer obtained after inspiration of four breaths of a 78% SF₆/22% oxygen gas mixture (no slice selection). The image demonstrates the expected homogenous distribution of SF₆ gas in the lung

these complications, RUIZ-CABELLO et al. (2005) and JACOB et al. (2005) have been able to measure the ADC in rats *in vivo* and in excised human lungs respectively. In the latter study, a reduction of the free diffusivity of C₂F₆ gas (ADC₀=0.033 cm²/s) to 0.018 cm²/s was found in normal lung tissue, while in emphysematous lungs the diffusivity was almost equal to that of freely diffusing C₂F₆ gas (0.031 cm²/s).

4.3.3.2

Human Application of ¹⁹F-MRI

Currently, all published data on fluorine MRI of the lung have been obtained from animals or from excised human lungs because the gases are not approved for human use. Recently, we have obtained under conditions of a controlled clinical investigation and with approval of the local ethics committee the first images in a healthy human volunteer after inspiration of four breaths of a mixture of 78% SF₆ gas and 22% oxygen (Fig. 4.3.3; WOLF et al. submitted). The inspiration of this gas was well tolerated by the volunteer, and neither sPO₂ nor blood pressure levels were significantly altered during or after the experiment.

Although this is promising in terms of the future use of fluorinated gases, more data are required before a broader application of these gases in regular patient or volunteer studies becomes feasible.

4.3.4

Conclusion

Compared with hyperpolarized gases, the quality of images obtained using fluorinated gases is often significantly lower, or the measurement time is at least

one order of magnitude longer than that used for hyperpolarized gas imaging. It appears that most of the measurement techniques available with hyperpolarized gases may also become available with fluorinated gases, although differences in the imaging protocol may be required (i.e., multiple breath wash-in of the fluorinated gas rather than single-bolus He-3 measurements). However, the image quality appears to be sufficient to obtain functional and/or physiologic information from, for example, dynamic studies.

In conclusion, fluorine MRI is a promising new approach for MRI of the lung which is currently limited to animal studies. However, the low toxicity of the inert fluorinated gases in combination with low costs may make it an interesting new diagnostic tool in the future.

Acknowledgements

The help of Uschi Wolf, PhD, Alexander Scholz, MD, Ana Ros Garcia, MSc, and Maxim Terekhov, PhD, is appreciated. Financial support was granted by the German Research Council (DFG, Grant # FOR 474 and SCHR 687/2 and SCHR 687/5).

References

- Adolphi NL, Kuethe DO (2008) Quantitative mapping of ventilation-perfusion ratios in lungs by ¹⁹F MR imaging of T₁ of inert fluorinated gases. *Magn Reson Med* 59:739–746
- Chang YV, Conradi MS (2006) Relaxation and diffusion of perfluorocarbon gas mixtures with oxygen for lung MRI. *J Magn Reson* 181:191–198
- Jacob RE, Chang YV, Choong CK, Bierhals A, Hu DZ, Yablonskiy DA, Woods JC, Gierada DS, Conradi MS (2005) ¹⁹F MR imaging of ventilation and diffusion in excised lungs. *Magn Reson Med* 54:577–585
- Kuethe DO, Caprihan A, Fukushima E, Waggoner RA (1998) Imaging lungs using inert fluorinated gases. *Magn Reson Med* 39: 85–88
- Kuethe DO, Caprihan A, Gach HM, Lowe IL, Fukushima E (2000) Imaging of obstructed ventilation with NMR using inert fluorinated gases. *J Appl Physiol* 88:2279–2286
- Mohanty S, Bernstein HJ (1970) Fluorine relaxation by NMR absorption in gaseous CF₄, SiF₄, and SF₆. *J Chem Phys* 53:461–462
- Rinck PA, Petersen SB, Lauterbur PS (1984) NMR imaging of fluorine-containing substances. ¹⁹-fluorine ventilation and perfusion studies. *Fortschr Röntgenstr* 140:239–243
- Ruiz-Cabello J, Perez-Sanchez JM, Perez de Alejo R, Rodriguez I, Gonzalez-Mangado N, Peces-Barba G, Cortijo M (2005) Diffusion-weighted ¹⁹F-MRI of lung periphery: influence of pressure and air-SF₆ composition on apparent diffusion coefficients. *Resp Physiol Neurobiol* 148:43–56

- Schreiber WG, Eberle B, Laukemper-Ostendorf S, Markstaller K, Weiler N, Scholz A, Bürger K, Heussel CP, Thelen M, Kauczor HU (2001) Dynamic ^{19}F -MRI of pulmonary ventilation using sulfur hexafluoride (SF_6) gas. *Magn Reson Med* 45:605–613
- Wolf U, Scholz A, Heussel CP, Markstaller K, Schreiber WG (2006) Subsecond fluorine-19 MRI of the lung. *Magn Reson Med* 55:948–951
- Wolf U, Scholz A, Terekhov M, Münnemann K, Kreitner KF, Werner C, Düber C, Schreiber WG (2008) Fluorine-19 MRI of the lung. First human experiment (submitted)
-

MRI of Pulmonary Ventilation

4.4 Proton MRI: Oxygen-enhanced Lung MRI and Alternative Approaches

OLAF DIETRICH

CONTENTS

| | | |
|---------|---|----|
| 4.4.1 | Introduction | 76 |
| 4.4.2 | Oxygen-enhanced Lung MRI | 76 |
| 4.4.2.1 | Contrast Mechanism and Physiology | 76 |
| 4.4.2.2 | MRI Pulse Sequences | 77 |
| 4.4.2.3 | Acquisition Paradigms and Data Evaluation | 79 |
| 4.4.2.4 | Clinical Applications | 80 |
| 4.4.2.5 | Advanced Techniques: Multi-slice Imaging | 80 |
| 4.4.2.6 | Advanced Techniques: ECG and Respiratory Triggering | 81 |
| 4.4.2.7 | Advanced Techniques: Parallel Imaging | 82 |
| 4.4.3 | Alternative Approaches | 84 |
| 4.4.3.1 | Non-contrast-enhanced Dynamic Lung Imaging | 84 |
| 4.4.3.2 | Aerosolized Gadolinium-based Contrast Agents | 86 |
| 4.4.3.3 | Water-in-perfluorocarbon Emulsions | 86 |
| 4.4.4 | Conclusions | 87 |
| | References | 87 |

KEY POINTS

The direct visual assessment of the lung parenchyma and imaging of lung ventilation using proton MRI is considerably more difficult than MRI of most other organs due to the very low signal intensity of the lung parenchyma. The low signal intensity is caused by the low average proton density and the short T_2^* relaxation time of lung tissue.

Several methods for proton-MRI-based ventilation measurements have been proposed in order to overcome these difficulties. Currently the most established technique is oxygen-enhanced MRI of the lung, employing inhaled molecular oxygen as a T_1 -reducing contrast agent, which enhances the signal of the protons in the lung. The clinical application of oxygen-enhanced lung MRI has been assessed in several studies. Main advantages of oxygen-enhanced MRI are the general availability of oxygen and the relative safety of oxygen administration. Potential limitations of oxygen-enhanced lung MRI are the relatively low signal enhancement corresponding to a T_1 reduction of about 10 %, and the complex contrast mechanism with contributions due to ventilation, perfusion, and oxygen-diffusion properties of the lung.

Newer techniques based on non-enhanced dynamic MR acquisitions appear to be a promising tool for ventilation assessment that may be available in the near future. Other proposed techniques such as imaging after administration of aerosolized gadolinium contrast agents or after infusion of water-in-perfluorocarbon emulsions into the lung require still considerably more research before they might become applicable in clinical MR imaging.

O. DIETRICH, PhD

Josef Lissner Laboratory for Biomedical Imaging, Department of Clinical Radiology, University Hospitals – Grosshadern, Ludwig Maximilian University of Munich, Marchioninstr. 15, 81377 Munich, Germany

4.4.1 Introduction

Magnetic resonance proton imaging of the human lung is considerably more difficult than proton MRI of most other organs or tissues due to the very low signal intensity of the lung parenchyma in acquisitions with practically all available pulse sequences. The low signal intensity is caused by the low average proton density and the short T_2' relaxation time of lung tissue. Both properties are a consequence of the heterogeneous microstructure of the lung parenchyma which consists mainly of microscopic air-filled alveoli with a large interface between air spaces and tissue or blood. Hence, the physical density (and consequently the proton density) of the lung tissue is very low and, in addition, large local variations of susceptibility occur within small spatial scales. These susceptibility variations influence the homogeneity of the static magnetic field and, thus, the Larmor frequencies of the protons within a single image voxel, which leads to substantially reduced T_2' relaxation times. A direct visual assessment of the lung parenchyma is therefore generally difficult with conventional proton MRI.

Several techniques have been proposed to overcome these limitations of proton MRI of the lung and to improve the visualization either of the lung parenchyma or of inhaled gas in order to directly depict pulmonary ventilation. Direct visualization of the inhaled gas is possible with hyperpolarized noble gases such as helium-3 or xenon-129 and is described in detail in Chaps. 4.1 and 4.2, respectively. An alternative approach is based on fluorine-19 MRI of inert fluorinated gases and is discussed above in Chap. 4.3. All these techniques require a certain amount of additional hardware – at least specifically adapted radio-frequency (RF) equipment such as RF receive coils tuned to the Larmor frequency of helium, xenon, or fluorine, and, for MRI of hyperpolarized noble gases, also complex and expensive hardware devices to prepare the hyperpolarized state of the gases.

Alternative approaches are based on the visualization of the optimized or enhanced proton signal of the lung tissue, i.e. ventilation is measured indirectly in contrast to the direct visualization of the inhaled gases mentioned above. Several different methods have been proposed that will be described in detail below: non-enhanced ventilation measurements based on signal changes (ZAPKE et al. 2006; TOPF et al. 2006; MARCUS et al. 2007) or tissue-displacement tracking (VOORHEES et al. 2005) in dynamic MR acquisitions during respiration, contrast-enhanced lung MRI using inhaled aerosols of gadolinium-based contrast agents (BERTHEZENE

et al. 1992; SUGA et al. 2002a; HAAGE et al. 2005) or administering water-in-perfluorocarbon emulsions (HUANG et al. 2002, 2004), and oxygen-enhanced lung MRI (EDELMAN et al. 1996; CHEN et al. 1998; LOFFLER et al. 2000) exploiting the T_1 -shortening effect of inhaled molecular oxygen (O_2). An obvious advantage of these techniques is that standard RF equipment available for conventional proton MRI can be used. However, the contrast is generally lower than in direct visualization of ventilation and the interpretation of the measured signal is more difficult due to the indirect nature of these imaging approaches.

Of these proton-MRI approaches, oxygen-enhanced imaging of the lung is by far the most established technique with a large number of published technical and clinical studies. Consequently, the main focus of the following sections lies on oxygen-enhanced lung MRI including the introduction of its physiological and technical basis, details of implementation such as multi-slice-acquisition techniques as well as triggering schemes, and discussion of the specific advantages and applications of parallel-imaging techniques. The alternative proton-MRI approaches for pulmonary ventilation MRI are subsequently presented in Sect. 4.4.3.

4.4.2 Oxygen-enhanced Lung MRI

4.4.2.1 Contrast Mechanism and Physiology

Inhaled molecular oxygen (O_2) was first suggested in 1996 by EDELMAN et al. as paramagnetic contrast agent for proton MRI of the lung. The underlying contrast mechanism of molecular oxygen is similar to the one of gadolinium-based contrast agents (although of a substantially smaller extent): the longitudinal relaxation (T_1) of the protons of the blood is shortened depending on the O_2 concentration. The measured absolute T_1 values of lung tissue vary to a certain degree in different publications, and oxygen-induced relative T_1 reductions between 7 % and 14 % are observed after inhalation of pure oxygen (Table 4.4.1). This effective reduction results from differently changed T_1 values of all protons that contribute to the voxel signal, i.e. it is averaged over all kinds of tissue such as blood, blood vessels, alveolar cells, and connective tissue within each single voxel. The most important contribution, however, is caused by the increased concentration of solved oxygen in the capillary blood of the lung. Hence, oxygen-based lung imaging provides combined information about

three physiological parameters (EDELMAN et al. 1996; LOFFLER et al. 2000):

- The inhaled oxygen must reach the lung area under consideration; thus, sufficient *ventilation* of the area is a necessary precondition for oxygen-induced reduction of T_1 relaxation.
- In addition, fresh capillary blood must be supplied in which the oxygen can be solved; lung *perfusion* therefore is a second requirement for the observation of reduced T_1 values.
- Finally, the transition of the oxygen from the alveoli into the capillaries of the lung, i.e. molecular oxygen *diffusion*, is required for signal enhancement.

Thus, oxygen-enhanced lung MRI can be regarded as imaging of “lung function” understood as the combination of these three parameters. With respect to the contribution of perfusion in oxygen-enhanced lung MRI, a recently published study by LEY et al. (2007) is noteworthy. The authors demonstrate that lung perfusion is influenced by the inhaled oxygen concentration: a significantly increased perfusion was found during inhalation of oxygen compared to inhalation of room air. The consequences of this effect on oxygen-enhanced lung MRI have not yet been evaluated.

As an alternative to T_1 -based oxygen-enhanced proton MRI, the measurement of the oxygen-induced reduction of transversal T_2^* relaxation has been proposed by PRACHT et al. (2005). This technique is based on the T_2^* reduction by about 10 % from an original range

between 1.7 ms and 2.0 ms during inhalation of room air to values between 1.2 ms and 1.7 ms during inhalation of pure oxygen. The measurement of this effect is difficult and prone to systematic errors because of the extremely short T_2^* relaxation times. This approach, however, might be useful to determine ventilation properties with reduced contributions of perfusion and diffusion effects.

4.4.2.2 MRI Pulse Sequences

Several pulse sequences can be employed for oxygen-enhanced T_1 -weighted lung MRI provided the following prerequisites are fulfilled:

- The pulse sequences must provide sufficient T_1 weighting to be sensitive to the oxygen-induced T_1 shortening. This is usually achieved by a magnetization preparation with an inversion pulse (180° pulse, inversion-recovery technique). Typical inversion times between the 180° pulse and the readout are either about 700 ms (EDELMAN et al. 1996; STOCK et al. 1999; OHNO et al. 2001; VANINBROUKX et al. 2003; NAISH et al. 2005) or about 1300 ms (LOFFLER et al. 2000; MULLER et al. 2002; MAI et al. 2003; DIETRICH et al. 2005).
- Fast data acquisition is recommendable to reduce motion artifacts caused by cardiac motion, blood flow, and respiration. Single-shot sequences (with

Table 4.4.1. T_1 relaxation times of lung tissue

| | B_0 (T) | T_1 (ms) breathing room air | T_1 (ms) breathing pure oxygen | T_1 reduction |
|----------------------------------|-----------|-------------------------------|----------------------------------|-----------------|
| EDELMAN et al. (1996) | 1.5 | 913 | 837 | 9.3 % |
| CHEN et al. (1998) | 1.5 | 1352 | 1183 | 12.5 % |
| STOCK et al. (1999) | 1.5 | 904 | 790 | 12.6 % |
| | 0.2 | 632 | 586 | 7.3 % |
| LOFFLER et al. (2000) | 1.5 | 1219 | 1074 | 11.9 % |
| NAKAGAWA et al. (2001) | 1.5 | 1147 | 1070 | 6.7 % |
| JAKOB et al. (2001) | 1.5 | 1249 | 1141 | 8.6 % |
| MAI et al. (2002) | 1.5 | 1399 | 1207 | 13.7 % |
| JAKOB et al. (2004) ^a | 1.5 | 1298 | 1160 | 10.6 % |
| DIETRICH et al. (2006b) | 3.0 | 1281 | 1102 | 14.0 % |

^a T_1 relaxation times calculated from $T_1(0)$ and oxygen transfer function (OTF)

complete data acquisition after a single excitation) and very fast gradient-echo sequences have successfully been employed in order to avoid motion-related effects.

- The pulse sequences should be insensitive to variations of susceptibility and to short T_2^* relaxation times; this requirement excludes echo-planar techniques or gradient-echo sequences with non-ultra-short echo times.

A pulse sequence with the listed properties that has been frequently employed for oxygen-enhanced lung MRI is e.g. the single-shot turbo-spin-echo sequence with centrally reordered k-space sampling, which is also known as RARE (rapid acquisition with relaxation enhancement) sequence (CHEN et al. 1998; STOCK et al. 1999; LOFFLER et al. 2000; MULLER et al. 2002; VAN-INBROUKX et al. 2003). A similar sequence with even shorter acquisition time is the half-Fourier-acquired single-shot turbo-spin-echo (HASTE) sequence (EDEL-MAN et al. 1996; OHNO et al. 2001; NAKAGAWA et al.

2001; MAI et al. 2003; DIETRICH et al. 2005). OHNO et al. (2004) confirmed that the signal-to-noise ratio of HASTE sequences improve if the shortest possible inter-echo spacing, i.e. the shortest readout times, is used.

Oxygen MRI of the lung at low fields below 0.5 Tesla has been performed with fast steady-state-free-precession (SSFP) techniques such as the TrueFISP sequence (MULLER et al. 2001). Finally, snapshot-FLASH sequences with ultra-short echo times below 2 ms have been used for oxygen-enhanced lung MRI; these sequences are particularly suited for the measurement of quantitative T_1 maps (JAKOB et al. 2001; ARNOLD et al. 2007). All listed pulse sequences are typically combined with an inversion-recovery preparation to achieve sufficient T_1 weighting. PUDERBACH et al. (2007) demonstrated that the chosen inversion-pulse type may influence the assessment of oxygen enhancement.

T_1 -weighted saturation-recovery measurements instead of inversion-recovery measurements can be utilized for oxygen-enhanced lung MRI as well. The dynamic signal range of saturation-recovery experiments

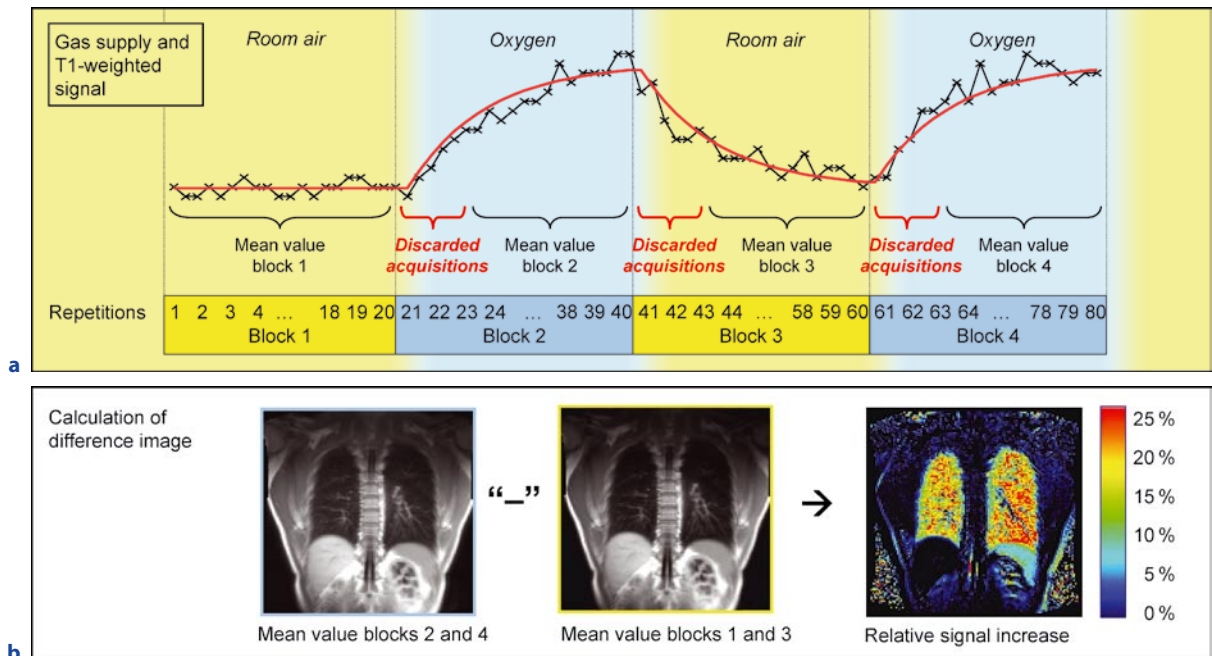


Fig. 4.4.1a,b. Block paradigm for oxygen-enhanced lung MRI. **a** Data acquisition: T_1 -weighted images are continuously acquired in four blocks with 4×20 repetitions; in blocks 1 and 3 room air is supplied, in blocks 2 and 4 pure oxygen. The T_1 -weighted signal varies relatively slowly after switching the gas supply and reaches exponentially its new steady state. Thus, several repetitions are discarded before calculating the

pixel-by-pixel mean value of each block. **b** The relative signal increase (or relative enhancement ratio) is calculated as the difference of the averaged images in blocks 2 and 4 on the one hand and 1 and 3 on the other hand, normalized to the averaged room air image. The lung parenchyma and the spleen appear hyperintense in the difference map. Figure reprinted with permission from: DIETRICH (2007b)

is only half as large as that of inversion-recovery experiments; consequently, the contrast-to-noise ratio of oxygen-induced signal changes is smaller as well. On the other hand, the saturation preparation is generally more robust than inversion preparation, particularly in the presence of B_1 inhomogeneities. Thus, especially at higher field strengths such as 3 Tesla, saturation-recovery measurements may be advantageous compared to inversion-recovery measurements (DIETRICH et al. 2006b). In addition, imaging time can be reduced, since no longitudinal relaxation is required between readout and the following preparation (NAISH et al. 2005).

4.4.2.3

Acquisition Paradigms and Data Evaluation

Several approaches for the acquisition and qualitative or quantitative data evaluation of oxygen-enhanced lung MRI have been proposed. A relative simple technique for the visualization of the ventilated lung tissue is based on difference images: Difference maps of T_1 -weighted images acquired during the inhalation of oxygen on the one hand and of room air on the other hand show the lung parenchyma hyperintense relative to the surrounding tissue due to the change of longitudinal relaxation after O_2 inhalation. Typically, a block paradigm is used for data acquisition consisting of alternating blocks with inhalation of room air and oxygen as illustrated in Fig. 4.4.1. The acquisition of several repetitions is required since both the expected signal difference and the signal-to-noise ratio of the lung tissue are relatively small. Thus, averaging of, e.g., 20–40 times repeated acquisitions breathing oxygen and of a similar number of acquisitions breathing room air is used to increase the signal-to-noise ratio of the resulting difference maps.

The signal difference, ΔS , can be either visualized directly (CHEN et al. 1998; STOCK et al. 1999; MAI et al. 2000; NAKAGAWA et al. 2001):

$$\Delta S = S_{O_2} - S_{\text{room air}}$$

or as relative difference, $\Delta S_{\text{relative}}$, (or relative enhancement ratio, RER) after pixelwise normalization to the room-air signal (EDELMAN et al. 1996; MULLER et al. 2002; OHNO et al. 2002; DIETRICH et al. 2005; ARNOLD et al. 2007):

$$\Delta S_{\text{relative}} = \text{RER} = \frac{S_{O_2} - S_{\text{room air}}}{S_{\text{room air}}}$$

Calculating absolute or relative difference maps is a relatively simple way to visualize lung function and

can be performed on most MRI systems without additional post-processing software. In order to calculate these difference maps, however, it must be taken into consideration that a certain time interval is required after switching the gas supply from air to oxygen (and vice versa) until T_1 (and, hence, the T_1 -weighted signal intensity) reaches a steady-state value as demonstrated in Fig. 4.4.1. This process is described by an exponential change with time constants between 23 s and 83 s in healthy volunteers (ARNOLD et al. 2004; NAISH et al. 2005).

The interval of intermediate signals between the steady states could be avoided by waiting a few minutes after switching the gas supply before the data acquisition is continued (MAI et al. 2003). However, MULLER et al. (2002) demonstrated that the slope of the signal increase correlates well with other clinical parameters. Hence, it appears useful to acquire data continuously in order to measure the intermediate signal dynamics as well and, thus, to be able to determine both the difference image and the time constants or slopes of the signal change. Thus, when calculating relative or absolute difference maps, a certain number of acquisitions within each block of the paradigm should be discarded after switching the gas supply to avoid systematically decreased differences. E.g., in a paradigm of 4×20 respiratory-triggered acquisitions an optimized ratio of signal difference and statistical error was found if about 5–8 acquisitions were discarded (DIETRICH et al. 2006a).

As an alternative to the evaluation of the absolute or relative difference of T_1 -weighted images, it has been proposed by MAI et al. (2003) to compute the cross-correlation between the time-response function of each pixel in a series of T_1 -weighted acquisitions and the input function representing the paradigm of alternating room air and oxygen administration. Based on this approach, MOLINARI et al. (2007) have introduced the fraction of oxygen-activated pixels (OAP %), i.e. the number of pixels with a correlation coefficient greater than 0.5 divided by the total number of pixels in the considered region of interest, in order to compare acquisitions of, e.g., healthy volunteers and patients.

Finally, instead of the alternating administration of room air and pure oxygen, measurements can also be performed at more than two different concentrations of oxygen of e.g. 21 % (room air), 40 %, 60 %, 80 %, and 100 %. Based on quantitative T_1 measurements at these different O_2 levels, the oxygen transfer function (OTF) can be determined as illustrated in Fig. 4.4.2 (JAKOB et al. 2004). The OTF describes the change of T_1 in lung tissue depending on the concentration of oxygen, C_{O_2} , in the administered gas, i.e. it is similarly defined as the

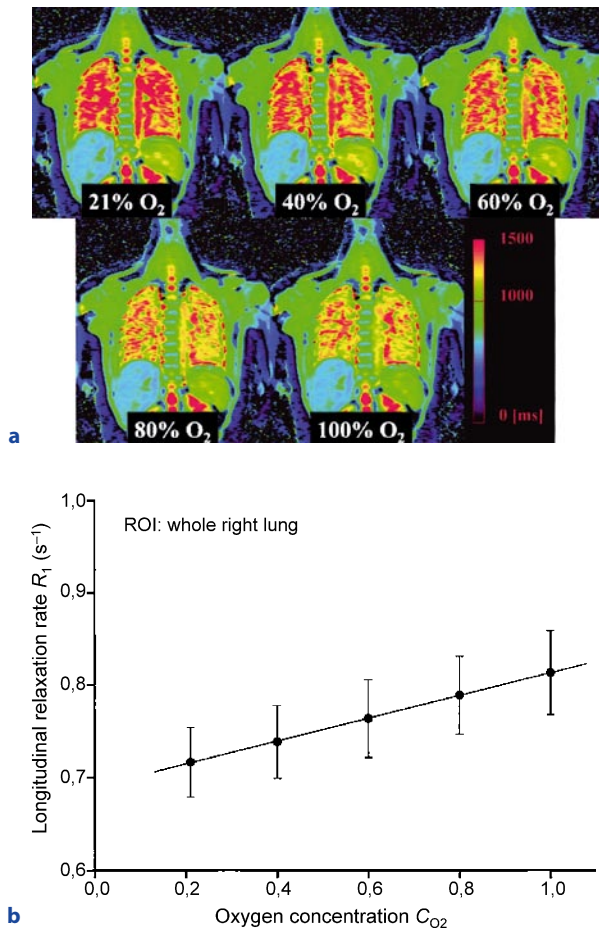


Fig. 4.4.2a,b. Measurement of the oxygen transfer function (OTF). **a** T_1 maps of a 30-year-old healthy female volunteer breathing different oxygen concentrations, C_{O_2} . **b** A linear relationship between the oxygen concentration, C_{O_2} , and the longitudinal relaxation rate, R_1 , in the whole right lung. The fitted OTF and extrapolated relaxation time without oxygen, $T_1(0)$, were $(0.12 \pm 0.00) \times 10^{-2} s^{-1} (\%O_2)^{-1}$ and 1449 ± 2 ms, respectively, with an excellent correlation coefficient (R) of one. Reprinted with permission from JAKOB et al. (2004)

relaxivity of oxygen but does not require the measurement of the actual tissue concentration (in units of in mmol/L) of oxygen. The OTF is expressed in units of $s^{-1} (\%O_2)^{-1}$ and the change of T_1 is described by

$$\frac{1}{T_1(C_{O_2})} = \frac{1}{T_1(0)} + \text{OTF} \times C_{O_2}.$$

To accelerate the acquisition of the required T_1 maps, a technique proposed by ARNOLD et al. (2007) can be used. T_1 can be estimated for different concentrations of oxygen based on a single T_1 map measured during inha-

lation of room air, and on T_1 -weighted images acquired for all other oxygen concentrations. In contrast to almost all other studies evaluating oxygen-enhanced lung MRI, ARNOLD et al. (2007) used carbogen (i.e. 95 % oxygen, 5 % carbon dioxide) instead of pure oxygen as T_1 -reducing contrast agent because carbogen is thought to be advantageous as a breathing gas during radiation therapy of patients with non-small-cell lung cancer.

4.4.2.4 Clinical Applications

Oxygen-enhanced lung imaging has been evaluated in several studies demonstrating a good correlation between MRI parameters and conventional methods of lung diagnostics such as evaluation of the diffusion capacity of carbon monoxide (DLCO), the forced expiratory volume in 1 s (FEV_1), or results of ventilation scintigraphy. OHNO et al. (2001, 2002) examined patients with lung cancer and with lung emphysema and demonstrated a good correlation of the maximum signal enhancement in oxygen-enhanced MRI on the one hand and FEV_1 and DLCO on the other hand. The same group described that oxygen-enhanced MRI could be used to successfully predict the postoperative FEV_1 in patients with bronchogenic carcinoma (OHNO et al. 2005). NAKAGAWA et al. (2001) demonstrated in patients with pulmonary embolism that oxygen-enhanced MRI did not show any ventilation defects in agreement with ventilation scintigraphy; in these patients ventilation contrast appears to dominate over the perfusion- and diffusion-based contributions. A study by MULLER et al. (2002) in patients with various pulmonary diseases showed a good correlation between the signal slope after switching the gas supply to pure oxygen and the DLCO. JAKOB et al. (2004) found in patients with cystic fibrosis that the oxygen transfer function correlates well with affected lung areas characterized by perfusion defects. In a study by MOLINARI et al. (2007), a significant smaller fraction of oxygen-activated pixels (OAP %) was found in patients with interstitial lung diseases than in healthy volunteers.

4.4.2.5 Advanced Techniques: Multi-slice Imaging

Oxygen-enhanced MRI of the lung is based on T_1 -weighting sequences such as single-shot turbo-spin-echo techniques or ultra-fast gradient-echo techniques. Both sequence types require an additional T_1 -sensitized-

ing magnetization preparation that is usually realized as an inversion pulse. This 180° RF pulse (as well as the refocusing RF pulses of the turbo-spin-echo sequence) can be implemented either as *slice-selective* pulses that influence only the spins in a two-dimensional section or as *non-selective* pulses that invert all spins within the RF coil. Multi-slice acquisitions with the same inversion time for all slices can be performed only with slice-selective inversion and refocusing pulses.

Most oxygen-enhanced imaging studies have been performed with non-selective inversion or refocusing pulses (JAKOB et al. 2001; NAKAGAWA et al. 2001; MAI et al. 2003; MOLINARI et al. 2007) such that an interleaved inversion and acquisition of multiple slices is not possible. Hence, either single-slice imaging was used or the total duration of acquisition was considerably prolonged in order to acquire up to four slices in successive imaging experiments.

The acquisition time of multiple slices can be decreased by employing slice-selective RF pulses and interleaving inversion preparation and image data readout, i.e. the inversion time, TI, between inversion and readout of a single slice is used to invert one or several more slices as demonstrated in Fig. 4.4.3. A potential disadvantage of using slice-selective inversion can be an increased sensitivity to perfusion effects: the signal within the slice will be influenced by inflowing non-inverted spins from outside the slice. To minimize this effect, the thickness of the inverted slice can be increased, e.g. by a factor of 2, with regard to the thickness of the image slice.

It has been demonstrated in a comparison of non-selective inversion and slice-selective inversion with doubled inversion slice thickness that similar results can be obtained with both techniques (DIETRICH et al. 2005). The T_1 -weighted images and calculated maps of relative signal increase showed some differences with respect to the signal within the pulmonary vessels. However, the signal increase in the large pulmonary vessels is less important for evaluation of the lung function than the signal distribution in the lung parenchyma which was similar for both techniques.

A fast multi-slice acquisition for oxygen-enhanced lung imaging is particularly valuable in clinical studies that require an assessment of the complete lung and, at the same time, are to be combined with several other MRI acquisitions of the lung such as pulmonary MR angiography or perfusion imaging. Single-slice techniques are often not acceptable in these studies because of their limited anatomic coverage or their long acquisition times.

4.4.2.6

Advanced Techniques: ECG and Respiratory Triggering

Reliable triggering is particularly important for MRI of the lung because of the high level of motion in the thorax due to pulsatile blood flow, cardiac motion, and respiration. VANINBROUKX et al. (2003) as well as MOLINARI et al. (2006) demonstrated that oxygen-

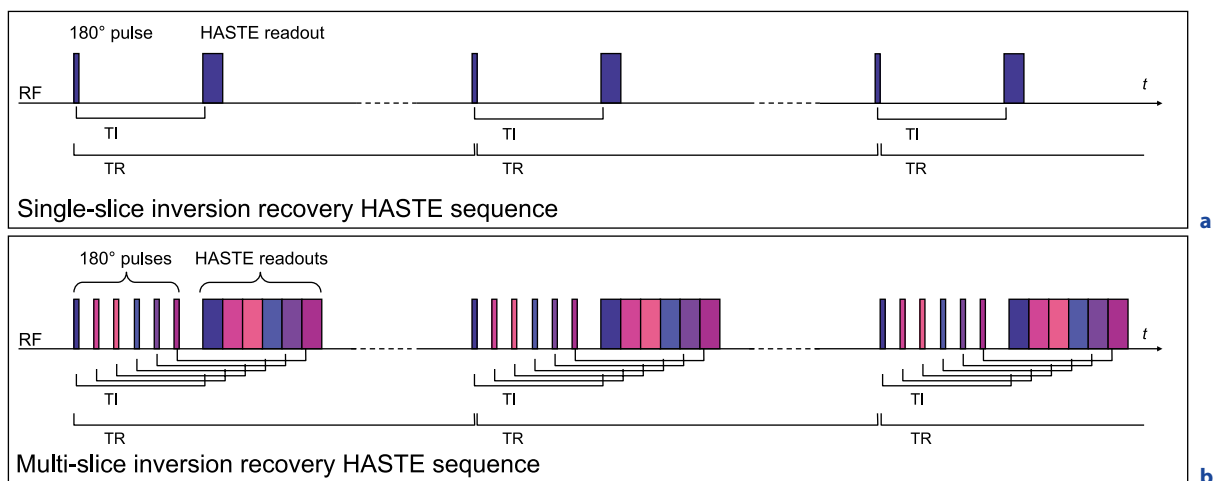


Fig. 4.4.3. **a** Three repetitions of a single-slice inversion-recovery HASTE sequence. Only a single slice is acquired; the inversion (180°) pulse as well as the refocusing pulses may be non-selective. **b** Three repetitions of a multi-slice inversion-

recovery HASTE sequence. Six slices (shown in different colors) are acquired; inversion (180°) pulses and readouts are interleaved. All 180° RF pulses must be slice-selective. Figure reprinted with permission from: DIETRICH (2007b)

enhanced MRI of the lung benefits from both ECG triggering and respiratory triggering in comparison to MRI without triggering. ECG triggering helps to acquire all repetitions in identical cardiac phases and to avoid motion artifacts due to acquisition during the systolic phase. Even more important is respiratory triggering to acquire all repetitions with identical positions of the diaphragm, since the signal intensity of the lung parenchyma depends substantially on the respiratory phase (MAI et al. 2000; BANKIER et al. 2004). The signal intensity typically varies by at least 50 % due to the change of proton density during respiration, and this signal variation is superimposed on the oxygen-induced signal increase. Different techniques for respiratory triggering have been applied including the frequently used pneumatic respiratory belts, pneumotachographic triggering (MOLINARI et al. 2006), or navigator techniques (MOLINARI et al. 2007). It appears advantageous to choose end-expiration for image acquisition to obtain the maximal lung signal and a more uniform diaphragm position than after repeated inspirations (LOSERT et al. 2002).

Thus, a combined application of ECG and respiratory triggering should be incorporated in a fast T_1 -weighting pulse sequence to facilitate robust oxygen-enhanced MRI of the lung in clinical routine. If combined with a multi-slice inversion-recovery single-shot turbo-spin-echo sequence, a complex trigger scheme is required to move the data readout into the diastolic phase. A possible trigger and sequence scheme, which has been evaluated by DIETRICH et al. (2005), is shown in Fig. 4.4.4; the acquisition is respiratory-triggered to start in end-expiration and an additional short delay, T_D , is calculated from the ECG signal such that the actual data readout takes place in the diastolic cardiac phase. Since the acquisition of all six slices cannot be fitted

into a single RR interval, the readout is divided into two parts with three HASTE readouts.

4.4.2.7 Advanced Techniques: Parallel Imaging

Parallel imaging has been one of the biggest innovations in magnetic resonance imaging in the last decade. Parallel-imaging techniques, which are also known as (partially) parallel acquisition techniques, have been developed since the mid-1990s with the aim to accelerate image acquisition (SODICKSON and MANNING 1997; PRUESSMANN et al. 1999; GRISWOLD et al. 2002; LARKMAN and NUNES 2007; SCHOENBERG et al. 2007). The basic idea of parallel imaging is to employ several independent receiver coil elements in parallel to reduce the number of required phase-encoding steps for a given image matrix size. Thus, a certain amount of the spatial encoding originally obtained by the (time-consuming) phase encoding steps is now substituted by evaluating data from several coil elements with spatially different coil sensitivity profiles. The reduction of phase-encoding steps is achieved by decreasing the sampling density in k-space, i.e. by k-space undersampling. Under-sampled data sets from each coil element are then used to reconstruct a single image corresponding to a fully sampled k-space.

Parallel imaging has been demonstrated to provide several advantages for single-shot MRI in general (GRISWOLD et al. 1999; DIETRICH 2007a) and, in particular, for single-shot MRI of the lung (HEIDEMANN et al. 2003; EIBEL 2007) due to shorter echo trains, reduced blurring, and shorter echo times. For oxygen-enhanced MRI of the lung with the ECG- and respiratory-triggered multi-slice sequence shown in Fig. 4.4.4,

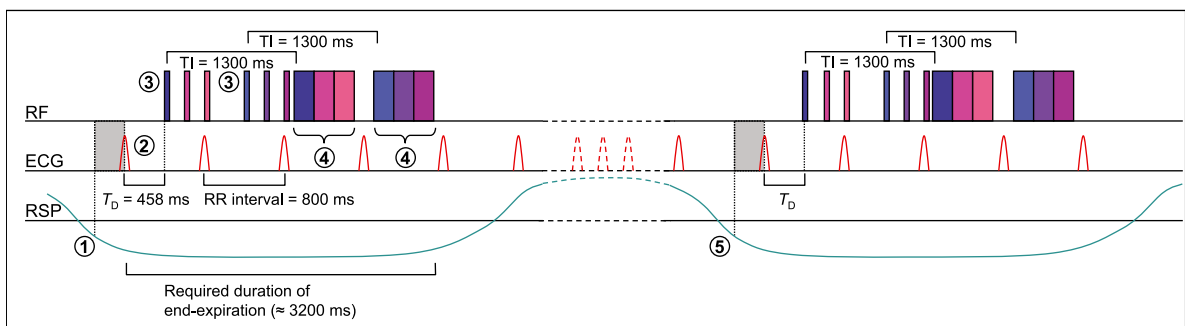


Fig. 4.4.4. Inversion-recovery HASTE sequence with respiratory (RSP) and ECG triggering. (1) Sequence starts in end-expiration. (2) After the next R wave, the delay T_D is inserted and (3) the slice-selective inversion pulses for 2×3 slices are applied.

(4) The delay T_D has been calculated from the current heart rate such that all six HASTE readouts lie in the diastole. (5) The sequence is repeated in the next respiratory cycle. Figure reprinted with permission from: DIETRICH (2007b)

parallel imaging exhibits specific advantages as a consequence of the reduced duration of the echo train, i.e. the shorter turbo-spin-echo readout. Using parallel imaging with an acceleration factor of 2, the number of echoes required for the acquisition of a 128×128 matrix with a HASTE sequence can be reduced from 72 to 36; thus, the total readout time can be decreased from 214 ms/slice to 115 ms/slice (for an echo spacing of 2.7 ms) including the time for signal excitation and spoiler gradients. In addition, a minimal echo time of 11 ms instead of 19 ms without parallel imaging can be achieved.

As a consequence of the shorter total readout time, the number of interleaved slices with inversion-recovery preparation acquired during end-expiration could be increased to six or more in contrast to only four slices without parallel imaging. The average required end-expiration time per repetition (cf. Fig. 4.4.4) to acquire six slices without motion artifacts could be significantly reduced from 4112 ms without to 2727 ms with parallel imaging (DIETRICH et al. 2005) resulting in considerably increased robustness of the sequence against respiratory motion artifacts. The synergistic effects of parallel imaging and oxygen-enhanced multi-slice MRI of the lung are discussed in much more detail in DIETRICH et al. (2005) and DIETRICH (2007b).

T_1 -weighted images acquired with the respiratory- and ECG-triggered inversion-recovery HASTE sequence described above with and without parallel imaging are shown in Fig. 4.4.5. The sequence was implemented on a 1.5-T whole-body MRI system (Magnetom Sonata, Siemens Medical Solutions, Erlangen, Germany) with a high-performance gradient system (maximum gradient strength: 40 mT m^{-1} , maximum gradient slope: 200 T/m/s) and a dedicated parallel-imaging eight-channel surface-coil system. T_1 weighting of the HASTE sequence was achieved with an inversion time of 1300 ms. The echo time was 19 ms without and 11 ms with parallel imaging and the repetition time was one respiratory cycle (thus ranging between about 5 s and 10 s). Up to six coronal slices were acquired with a field of view of $400 \times 400 \text{ mm}^2$, a 128×128 matrix, a slice thickness of 8 mm, and a gap between the slices of 16 mm. The GRAPPA algorithm (GRISWOLD et al. 2002) was used for parallel-imaging reconstruction based on the 24 central k-space lines for auto-calibration. The image acquisition was repeated 80 times in total, divided into 4 blocks with 20 repetitions each. The subjects were administered room air in the first and third block, and oxygen in the second and fourth block. Since the respiration frequency varied inter-individually between about 6/min and 10/min, the total acquisition time varied as well between 8 and 13 min.

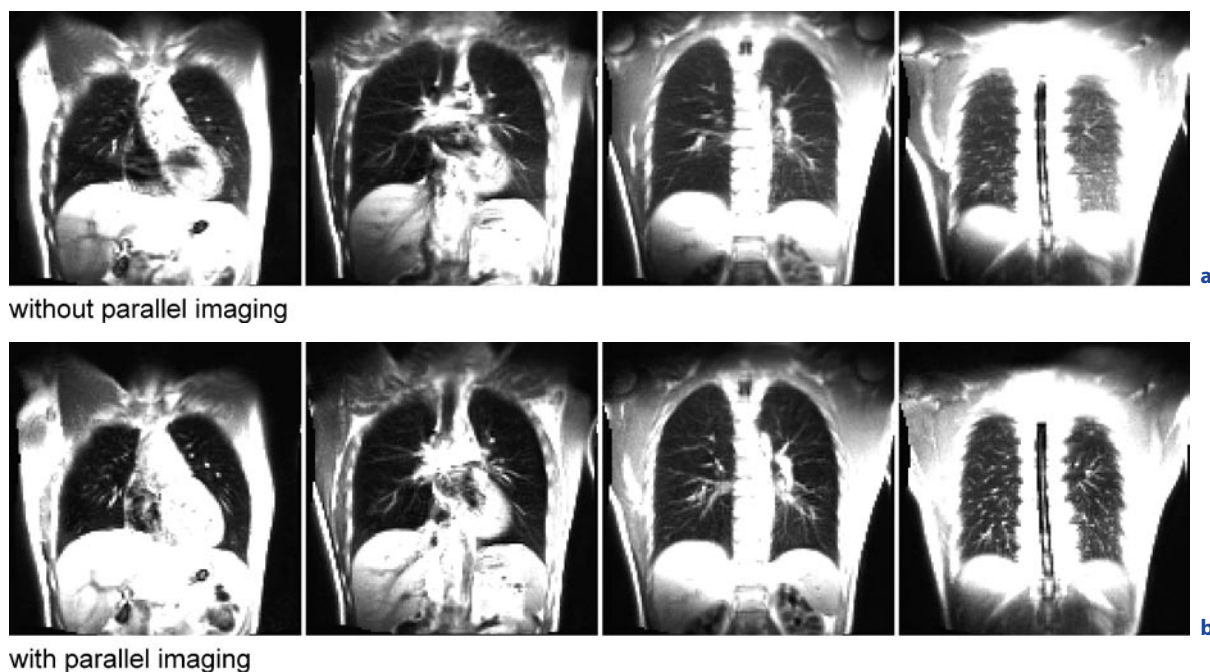


Fig. 4.4.5a,b. T_1 -weighted images acquired with a respiratory- and ECG-triggered inversion-recovery HASTE sequence (a) without and (b) with parallel imaging. Note the sharper

delineation of pulmonary vessels and the comparable signal-to-noise ratio with parallel imaging. Figure reprinted with permission from: DIETRICH (2007b)

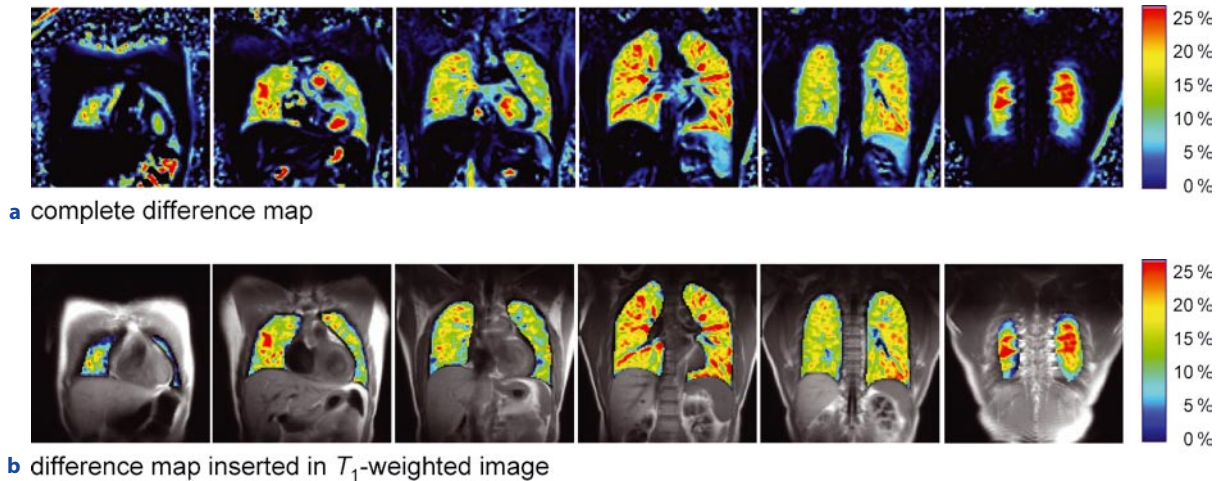


Fig. 4.4.6a,b. Parameter maps displaying the oxygen-induced relative signal increase in a healthy volunteer acquired with parallel imaging. The complete parameter maps (a) demonstrate that oxygen-induced signal enhancement is observed

predominantly in the lung, in the large cardiopulmonary vessels, in the spleen, and in the cardiac ventricles. The same data is shown inserted in the T_1 -weighted acquisition (b) after manual segmentation of the lungs

The T_1 -weighted images in Fig. 4.4.5 demonstrate the reduced blurring with parallel imaging. No degrading loss of signal-to-noise ratio is visible in the T_1 -weighted images acquired with parallel imaging in comparison to the non-accelerated acquisitions. Examples of oxygen-enhanced lung MRI in six coronal slices of a healthy volunteer are shown in Fig. 4.4.6.

4.4.3 Alternative Approaches

4.4.3.1 Non-contrast-enhanced Dynamic Lung Imaging

Although the signal of lung tissue in non-contrast-enhanced proton MRI is very low as described in Sect. 4.4.1, it is still possible to employ this signal directly to assess ventilation properties of the lung. One approach to deduce ventilation information from non-contrast-enhanced lung MRI is based on the evaluation of a series of dynamic lung images acquired during the respiratory cycle (RUPPRECHT et al. 2003; TOPF et al. 2004, 2005, 2006; ZAPKE et al. 2006; VOORHEES et al. 2005; MARCUS et al. 2007). These images are acquired with temporal resolutions between 119 ms (MARCUS et al. 2007) and 2 s (TOPF et al. 2005, 2006). Typically, only a single slice is acquired in order to optimize the temporal resolution.

Different MR imaging techniques have been proposed to obtain a sufficiently strong signal of the native lung tissue. For instance, it has been suggested to use

MRI systems with relatively low field strengths of, e.g., 0.2 Tesla (WAGNER et al. 2001; RUPPRECHT et al. 2002; ABOLMAALI et al. 2004). In spite of the generally lower signal-to-noise ratio (SNR) at low field strengths, the relative signal of the lung tissue is increased because of the substantially reduced susceptibility effects, which are proportional to the field strength. Balanced steady-state free-precession (SSFP) sequences such as the TrueFISP sequence are particularly suited for lung MRI at 0.2 Tesla because of their high SNR efficiency. At higher field strengths, single-shot fast-spin-echo techniques such as the HASTE sequence with relatively short echo times are generally preferred for visualization of the lung tissue.

RUPPRECHT et al. (2004) proposed that information about the pulmonary ventilation can be deduced directly from regional variations of the MR signal intensity during the respiratory cycle. In this study, the ratio of the volume of inhaled air (V_{air}) and the volume of lung parenchyma (V_{tissue}) in expiration is calculated from the signal during inspiration, S_{insp} , expiration, S_{exp} , as well as the noise signal, S_{noise} , as

$$\frac{V_{\text{air}}}{V_{\text{tissue}}} = \frac{S_{\text{exp}} - S_{\text{insp}}}{S_{\text{exp}} - S_{\text{noise}}}.$$

More generalized, this ratio can also be determined for every time, t , of the respiratory cycle based on the lung signal, $S(t)$, at time t :

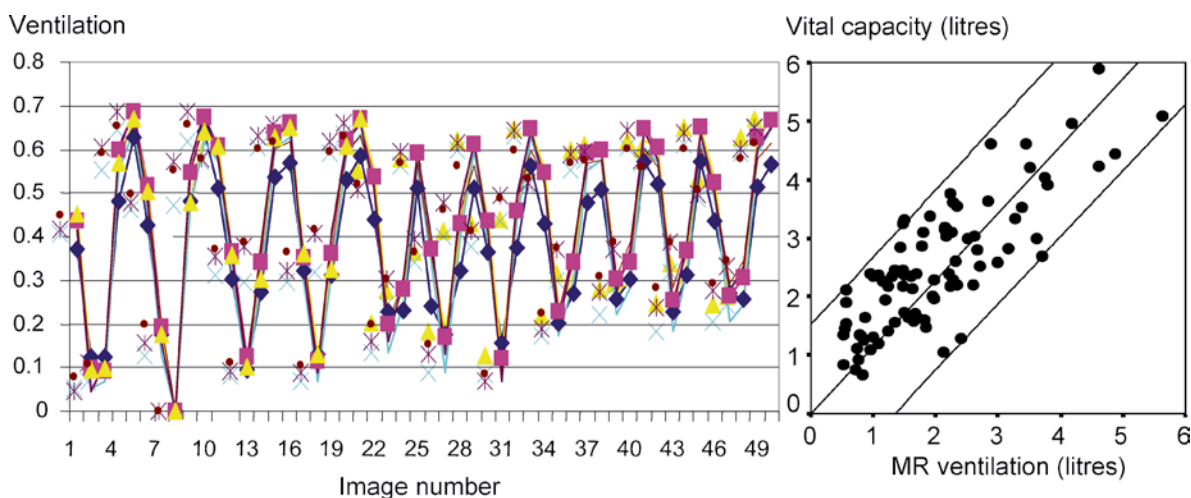
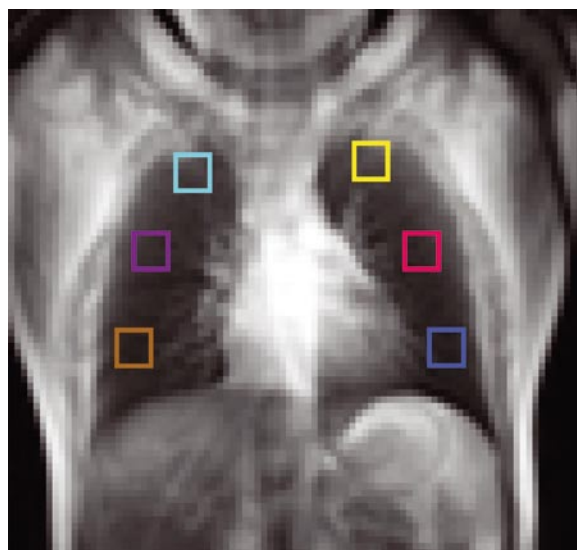
$$\frac{V_{\text{air}}(t)}{V_{\text{tissue}}} = \frac{S_{\text{exp}} - S(t)}{S_{\text{exp}} - S_{\text{noise}}}.$$

This approach has been evaluated in volunteers and patients using a TrueFISP sequence at 0.2 Tesla (RUPPRECHT et al. 2003; TOPF et al. 2004; ZAPKE et al. 2006) and with a HASTE sequence at 1.5 Tesla (TOPF et al. 2005, 2006). A good correlation was found between lung ventilation determined by MRI and the vital capacity derived from conventional pulmonary function test as shown in Fig. 4.4.7 (ZAPKE et al. 2006). This method, however, is complicated by the fact that lung tissue is moving significantly during the respiratory cycle. Hence, a substantial amount of post-processing is required in order to (non-rigidly) register all images acquired during the respiratory cycle to a reference image (ZAPKE et al. 2006) before evaluating the variation of MR signal intensity. A related approach, which correlates the signal intensity and the lung area during the respiratory cycle

(BANKIER et al. 2004) has been suggested by MARCUS et al. (2007).

Instead of evaluating the time dependence of the MR signal intensity during the respiratory cycle, ventilation information can also be deduced from direct monitoring of the displacement of lung tissue. Two different approaches for tissue displacement mapping have been suggested: motion tracking after a grid preparation using SPAMM tagging of the lung (CHEN et al. 2001; NAPADROW et al. 2001; VOORHEES et al. 2005) and direct tracking of the lung tissue analyzing the motion of vessels and other hyperintense structures (GEE et al. 2003; SUNDARAM and GEE 2005). Only a few results based on these techniques have been published; however, VOORHEES et al. (2005) demonstrated a good agreement of the regional lung volume change derived from the directly seg-

Fig. 4.4.7a-c. Non-contrast-enhanced dynamic lung MRI. **a** MR ventilation image of a patient with normal pulmonary function test. **b** Ventilation graphs that show the ventilation (i.e., the ratio of the volume of inhaled air, V_{air} , and the volume of lung parenchyma, V_{tissue}) in 50 images for each rectangular region shown in **a** during the respiratory cycles. The 50 measurements span a total of one minute. Ventilation measurements: Right: upper field (*turquoise*) 0.64 mL/cm³; middle field (*violet*) 0.68 mL/cm³; lower field (*brown*) 0.65 mL/cm³. Left: upper field (*yellow*) 0.67 mL/cm³; middle field (*pink*) 0.68 mL/cm³; lower field (*blue*) 0.62 mL/cm³. **c** Correlation of MR ventilation and vital capacity measured by conventional pulmonary function test ($r = 0.8$; $p \leq 0.001$, *black lines*: regression line and 95 % confidence interval). Reprinted with permission from ZAPKE et al. (2006)



mented volume and from the volume that was calculated using the regional tissue-displacement measurements.

More MRI studies have been performed that evaluate only global spirometric properties of the lung such as static or dynamic lung volumes (EICHINGER et al. 2007). These techniques for non-contrast-enhanced lung imaging and MR-spirometry-based ventilation measurements are discussed in Chap. 5.

4.4.3.2

Aerosolized Gadolinium-based Contrast Agents

MONTGOMERY et al. (1987) proposed to administer an aerosolized gadolinium-based contrast agent to decrease the T_1 relaxation time and to enhance the signal of extravascular water in the lungs; first MR experiments were performed in excised lung tissue of rats demonstrating a significant decrease of T_1 . BERTHEZÈNE et al. (1992) used a T_1 -weighting spin-echo sequence ($TR \approx 250$ ms, $TE = 6$ ms) and measured an MRI signal increase by more than 70 % in rats in vivo after inhalation of an aerosolized gadolinium contrast agent for 5 min. More animal studies were performed in the following years investigating safety aspects (BERTHEZÈNE et al. 1993), modified gadolinium formulations (MISSELWITZ et al. 1997), MRI in larger animals such as domestic pigs (HAAGE et al. 2000) and dogs (SUGA et al. 2002a), the signal enhancement behavior of various gadolinium-containing contrast agents (HAAGE et al. 2001b, 2002), and improved delivery devices for the administration of the gadolinium-DTPA aerosol (HAAGE et al. 2001a; SUGA et al. 2002b). The used aerosols had a mean particle size between 0.2 and 5.0 μm , and the original contrast-agent concentration before aerosolization ranged between 100 and 500 mmol/L. In these studies, HAAGE and co-workers applied a respiratory-gated T_1 -weighting two-dimensional multi-slice fast-spin-echo sequence with repetition times between 141 ms and 199 ms and an echo time of 8.5 ms for dynamic lung imaging. SUGA and co-workers acquired T_1 -weighted data with a fast three-dimensional spoiled-gradient-echo sequence with repetition time of 3.5 ms and an echo time of 0.9 ms. An alternative measurement approach is described by PRICE et al. (2004, 2005), who propose a single-point-imaging sequence for signal detection; this technique has the advantage to be very insensitive to susceptibility effects and short T_2' relaxation times in lung tissue.

The application of aerosolized gadolinium contrast agents in animals with functional impairments of the

lung was demonstrated by SUGA et al. (2002a,b, 2003) and by OGASAWARA et al. (2004); MRI was performed in dogs with acute airway obstruction with a balloon catheter and after pulmonary arterial embolization with enbucrilate. Areas of acute airway obstruction showed matched perfusion and aerosol deposit defects; while small areas affected by embolization showed only perfusion defects but normal aerosol images. The clearance of a gadolinium-based aerosol in bleomycin-injured dog lungs was investigated by SUGA et al. (2003). They found a heterogeneously reduced aerosol deposition in the affected lungs as well as a significantly decreased clearance half time.

The first applications of lung-ventilation MRI with aerosolized gadolinium chelates in human volunteers were described by HAAGE et al. (2003, 2005). An average signal enhancement of about 35 % was observed after 10 min inhalation of the gadolinium-DTPA aerosol; data was acquired with a T_1 -weighting fast-spin-echo sequence as described above. Examinations in 15 healthy volunteers were performed without any procedure-related complications or acute or delayed allergic reactions to the aerosolized contrast medium. The examination was followed by an 18-months observation period to exclude any delayed side effects such as pulmonary inflammations. No further studies are published up to now about the application of gadolinium aerosols in human volunteers or in patients.

4.4.3.3

Water-in-perfluorocarbon Emulsions

A further approach for proton-MRI ventilation measurements is based on the infusion of a water-in-perfluorocarbon emulsion into the lung (HUANG et al. 2002, 2004). Perfluorocarbon compounds have been used for liquid ventilation since the 1960s (LOWE 1987) exploiting the excellent solubility of O_2 and CO_2 in these substances. Fluorine-19-perfluorocarbon has been utilized in fluorine-19 MRI for lung visualization (cf. Chap. 4.3); however, no signal is emitted by these substances in proton MRI because of the lack of protons in perfluorocarbons. In order to employ perfluorocarbon-based liquid ventilation in proton MRI, HUANG et al. (2002) proposed to use water-in-perfluorocarbon emulsions that can provide both a fluorine-19 and a proton-MRI signal. After infusion of the water-in-perfluorocarbon emulsion into rat lungs, a substantial signal enhancement can be observed in proton MRI using, e.g., a spin-echo sequence with a repetition time of 900 ms and an echo time of 6 ms. HUANG et al. (2002) also performed diffusion-weighted proton MRI and found apparent

diffusion coefficients (ADC) of about 1×10^{-3} mm²/s in healthy lungs in contrast to substantially increased ADCs of about 3×10^{-3} mm²/s in injured lungs with induced pulmonary edema. The latter results are in parallel to diffusion measurements based on helium-3 lung MRI (cf. Chap. 4.1).

In a second study performed in mice, HUANG et al. (2004) measured the T_2^* relaxation time in lung tissue after infusion of a water-in-perfluorocarbon emulsion. Using a multi-echo spin-echo sequence with echo times between 5 and 120 ms, they found T_2^* values between 25 and 35 ms for a sufficiently high administered infusion dose. Thus, T_2^* is substantially increased compared to the relaxation times of typically less than 5 ms without infusion of the water-in-perfluorocarbon emulsion. This observation is explained by the considerably reduced susceptibility variation in lung tissue after filling of the air spaces with the liquid emulsion.

No further studies about applications of water-in-perfluorocarbon emulsions in animals or humans have been published yet.

4.4.4 Conclusions

Several methods for proton-MRI-based ventilation measurements are available. Currently the most established technique is oxygen-enhanced MRI of the lung, employing inhaled molecular oxygen as a T_1 -reducing contrast agent, which enhances the signal of the protons in the lung (cf. Sect. 4.4.2). The main advantages of oxygen-enhanced MRI are the general availability of oxygen in every clinical environment and the relative safety of oxygen administration in volunteers or patients. A large number of publications describe the application of oxygen-enhanced lung MRI in patients with several different lung pathologies. Technically, a certain amount of hardware is required to administer alternately room air and oxygen (pure or in several different concentrations) via a mask or a mouthpiece to the examined subject in the scanner. Disadvantages of oxygen-enhanced lung MRI are the relatively low signal enhancement corresponding to the T_1 reduction of about 10 %, and the complex contrast mechanism with contributions due to ventilation, perfusion, and oxygen-diffusion properties of the lung.

A second, newer approach for proton MRI of lung ventilation is based on the evaluation of a sequence of dynamic MR images acquired during the respiratory cycle without any additional exogenous contrast enhancement (cf. Sect. 4.4.3.1). The obvious advantage of this technique is that no additional hardware is required

which reduces costs and increases patient comfort during the examination. However, the proposed techniques are based on complex post-processing including non-rigid image registration, and the number of publications that evaluate this new promising approach is still rather small. More studies are required to establish this technique for use in clinical routine imaging.

Other available techniques for ventilation MRI are imaging after administration of aerosolized gadolinium contrast agents (cf. Sect. 4.4.3.2) or after infusion of water-in-perfluorocarbon emulsions into the lung (cf. Sect. 4.4.3.3). The former technique, however, involves complex and expensive hardware devices to prepare and administer the contrast-agent aerosol; a further disadvantage is that the inhalation of gadolinium-based contrast agents is still controversial and not yet thoroughly evaluated in humans. Up to now, no studies with aerosolized gadolinium contrast agents have been conducted in patients. Even less data are available on proton MRI during (partial) liquid ventilation employing water-in-perfluorocarbon emulsions, which has so far been tested only in small rodents.

In conclusion, proton-based ventilation MR imaging of the lungs is clinically feasible and well established with oxygen-enhanced MRI. Newer techniques based on non-enhanced dynamic MR acquisitions appear to be a promising tool for ventilation assessment that may be available in the near future. Other proposed techniques require still considerably more research before they might be applicable in clinical MR imaging.

References

- Abolmaali ND, Schmitt J, Krauss S, Bretz F, Deimling M, Jacobi V, Vogl TJ (2004) MR imaging of lung parenchyma at 0.2 T: evaluation of imaging techniques, comparative study with chest radiography and interobserver analysis. *Eur Radiol* 14:703–708
- Arnold JF, Fidler F, Wang T, Pracht ED, Schmidt M, Jakob PM (2004) Imaging lung function using rapid dynamic acquisition of T1-maps during oxygen enhancement. *MAGMA* 16:246–253
- Arnold JF, Kotas M, Fidler F, Pracht ED, Flentje M, Jakob PM (2007) Quantitative regional oxygen transfer imaging of the human lung. *J Magn Reson Imaging* 26:637–645
- Bankier AA, O'Donnell CR, Mai VM, Storey P, De Maertelaer V, Edelman RR, Chen Q (2004) Impact of lung volume on MR signal intensity changes of the lung parenchyma. *J Magn Reson Imaging* 20:961–966
- Berthezene Y, Vexler V, Clement O, Muhler A, Moseley ME, Brasch RC (1992) Contrast-enhanced MR imaging of the lung: assessments of ventilation and perfusion. *Radiology* 183:667–672

- Berthezène Y, Mühler A, Lang P, Shames DM, Clément O, Rosenau W, Kuwatsuru R, Brasch RC (1993) Safety aspects and pharmacokinetics of inhaled aerosolized gadolinium. *J Magn Reson Imaging* 3:125–130
- Chen Q, Jakob PM, Griswold MA, Levin DL, Hatabu H, Edelman RR (1998) Oxygen enhanced MR ventilation imaging of the lung. *MAGMA* 7:153–161
- Chen Q, Mai VM, Bankier AA, Napadow VJ, Gilbert RJ, Edelman RR (2001) Ultrafast MR grid-tagging sequence for assessment of local mechanical properties of the lungs. *Magn Reson Med* 45:24–28
- Dietrich O (2007a) Single-shot pulse sequences. In: Schoenberg SO, Dietrich O, Reiser MF (eds) *Parallel imaging in clinical MR applications*. Springer, Berlin Heidelberg New York, pp 119–126
- Dietrich O (2007b) Oxygen-enhanced imaging of the lung. In: Schoenberg SO, Dietrich O, Reiser MF (eds) *Parallel imaging in clinical MR applications*. Springer, Berlin Heidelberg New York, pp 429–440
- Dietrich O, Losert C, Attenberger U, Fasol U, Peller M, Nikolaou K, Reiser MF, Schoenberg SO (2005) Fast oxygen-enhanced multislice imaging of the lung using parallel acquisition techniques. *Magn Reson Med* 53:1317–1325
- Dietrich O, Losert C, Attenberger U, Reuter C, Fasol U, Peller M, Nikolaou K, Reiser MF, Schoenberg SO (2006a) Sauerstoff-MRT der Lunge: Optimierte Berechnung von Differenzbildern. *Radiologe* 46:300–308
- Dietrich O, Raya JG, Fasol U, Peller M, Reiser MF, Schoenberg SO (2006b) Oxygen-enhanced MRI of the lung at 3 Tesla: feasibility and T1 relaxation times. *Proc Intl Soc Magn Reson Med* 14:1307
- Edelman RR, Hatabu H, Tadamura E, Li W, Prasad PV (1996) Noninvasive assessment of regional ventilation in the human lung using oxygen-enhanced magnetic resonance imaging. *Nat Med* 2:1236–1239
- Eibel R (2007) Lung imaging. In: Schoenberg SO, Dietrich O, Reiser MF (eds) *Parallel imaging in clinical MR applications*. Springer, Berlin Heidelberg New York, pp 209–217
- Eichinger M, Tetzlaff R, Puderbach M, Woodhouse N, Kauczor HU (2007) Proton magnetic resonance imaging for assessment of lung function and respiratory dynamics. *Eur J Radiol* 64:329–334
- Gee J, Sundaram T, Hasegawa I, Uematsu H, Hatabu H (2003) Characterization of regional pulmonary mechanics from serial magnetic resonance imaging data. *Acad Radiol* 10:1147–1152
- Griswold MA, Jakob PM, Chen Q, Goldfarb JW, Manning WJ, Edelman RR, Sodickson DK (1999) Resolution enhancement in single-shot imaging using simultaneous acquisition of spatial harmonics (SMASH). *Magn Reson Med* 41:1236–1245
- Griswold MA, Jakob PM, Heidemann RM, Nittka M, Jellus V, Wang J, Kiefer B, Haase A (2002) Generalized autocalibrating partially parallel acquisitions (GRAPPA). *Magn Reson Med* 47:1202–1210
- Haage P, Adam G, Misselwitz B, Karaagac S, Pfeffer JG, Glowinski A, Döhmen S, Tacke J, Günther RW (2000) Aerosolisiertes Gadolinium-DTPA zur Darstellung der Lungenventilation in der Magnetresonanztomographie. *Rofo* 172:323–328
- Haage P, Adam G, Karaagac S, Pfeffer J, Glowinski A, Döhmen S, Günther RW (2001a) Mechanical delivery of aerosolized gadolinium-DTPA for pulmonary ventilation assessment in MR imaging. *Invest Radiol* 36:240–243
- Haage P, Karaagac S, Adam G, Glowinski A, Günther RW (2001b) Comparison of aerosolized gadoteridol and gadopentetate dimeglumine for magnetic resonance ventilation imaging of the lung. *Magn Reson Med* 46:803–806
- Haage P, Karaagac S, Adam G, Spüntrup E, Pfeffer J, Günther RW (2002) Gadolinium containing contrast agents for pulmonary ventilation magnetic resonance imaging: preliminary results. *Invest Radiol* 37:120–125
- Haage P, Karaagac S, Spüntrup E, Adam G, Günther RW (2003) MR-Bildgebung der Lungenventilation mittels aerosolierter Gadolinium-Chelate. *Fortschr Roentgenstr* 175:187–193
- Haage P, Karaagac S, Spüntrup E, Truong HT, Schmidt T, Günther RW (2005) Feasibility of pulmonary ventilation visualization with aerosolized magnetic resonance contrast media. *Invest Radiol* 40:85–88
- Heidemann RM, Griswold MA, Kiefer B, Nittka M, Wang J, Jellus V, Jakob PM (2003) Resolution enhancement in lung 1H imaging using parallel imaging methods. *Magn Reson Med* 49:391–394
- Huang MQ, Ye Q, Williams DS, Ho C (2002) MRI of lungs using partial liquid ventilation with water-in-perfluorocarbon emulsions. *Magn Reson Med* 48:487–492
- Huang MQ, Basse PH, Yang Q, Horner JA, Hitchens TK, Ho C (2004) MRI detection of tumor in mouse lung using partial liquid ventilation with a perfluorocarbon-in-water emulsion. *Magn Reson Imaging* 22:645–652
- Jakob PM, Hillenbrand CM, Wang T, Schultz G, Hahn D, Haase A (2001) Rapid quantitative lung 1H T1 mapping. *J Magn Reson Imaging* 14:795–799
- Jakob PM, Wang T, Schultz G, Hebestreit H, Hebestreit A, Hahn D (2004) Assessment of human pulmonary function using oxygen-enhanced T(1) imaging in patients with cystic fibrosis. *Magn Reson Med* 51:1009–1016
- Larkman DJ, Nunes RG (2007) Parallel magnetic resonance imaging. *Phys Med Biol* 52:R15–55
- Ley S, Puderbach M, Risse F, Ley-Zaporozhan J, Eichinger M, Takenaka D, Kauczor HU, Bock M (2007) Impact of oxygen inhalation on the pulmonary circulation: assessment by magnetic resonance (MR)-perfusion and MR-flow measurements. *Invest Radiol* 42:283–290
- Loffler R, Muller CJ, Peller M, Penzkofer H, Deimling M, Schwaiblmair M, Scheidler J, Reiser M (2000) Optimization and evaluation of the signal intensity change in multi-section oxygen-enhanced MR lung imaging. *Magn Reson Med* 43:860–866

- Losert C, Nikolaou K, Scheidler J, Mueller CJ, Schwaiblmair M, Reiser MF (2002) Optimized respiratory and ECG gating in oxygen-enhanced MR ventilation imaging of the lung. *Proc Intl Soc Mag Reson Med* 10:1971
- Lowe KC (1987) Perfluorocarbons as oxygen-transport fluids. *Comp Biochem Physiol A* 87:825–838
- Mai VM, Chen Q, Li W, Hatabu H, Edelman RR (2000) Effect of respiratory phases on MR lung signal intensity and lung conspicuity using segmented multiple inversion recovery turbo spin echo (MIR-TSE). *Magn Reson Med* 43:760–763
- Mai VM, Liu B, Li W, Polzin J, Kurucay S, Chen Q, Edelman RR (2002) Influence of oxygen flow rate on signal and T(1) changes in oxygen-enhanced ventilation imaging. *J Magn Reson Imaging* 16:37–41
- Mai VM, Tutton S, Prasad PV, Chen Q, Li W, Chen C, Liu B, Polzin J, Kurucay S, Edelman RR (2003) Computing oxygen-enhanced ventilation maps using correlation analysis. *Magn Reson Med* 49:591–594
- Marcus JT, Korporeaal JG, Rietema H, Boonstra A, Vonk Noordegraaf A (2007) MRI estimation of dynamic regional lung ventilation, derived from pulmonary density changes during respiration. *Proc Intl Soc Mag Reson Med* 15:2777
- Misselwitz B, Mühler A, Heinzelmann I, Böck JC, Weinmann HJ (1997) Magnetic resonance imaging of pulmonary ventilation. Initial experiences with a gadolinium-DTPA-based aerosol. *Invest Radiol* 32:797–801
- Molinari F, Gaudino S, Fink C, Corbo GM, Valente S, Pirroni T, Bonomo L (2006) Simultaneous cardiac and respiratory synchronization in oxygen-enhanced magnetic resonance imaging of the lung using a pneumotachograph for respiratory monitoring. *Invest Radiol* 41:476–485
- Molinari F, Eichinger M, Risse F, Plathow C, Puderbach M, Ley S, Herth F, Bonomo L, Kauczor HU, Fink C (2007) Navigator-triggered oxygen-enhanced MRI with simultaneous cardiac and respiratory synchronization for the assessment of interstitial lung disease. *J Magn Reson Imaging* 26:1523–1529
- Montgomery AB, Paaajanen H, Brasch RC, Murray JF (1987) Aerosolized gadolinium-DTPA enhances the magnetic resonance signal of extravascular lung water. *Invest Radiol* 22:377–381
- Muller CJ, Loffler R, Deimling M, Peller M, Reiser M (2001) MR lung imaging at 0.2 T with T1-weighted true FISP: native and oxygen-enhanced. *J Magn Reson Imaging* 14:164–168
- Muller CJ, Schwaiblmair M, Scheidler J, Deimling M, Weber J, Loffler RB, Reiser MF (2002) Pulmonary diffusing capacity: assessment with oxygen-enhanced lung MR imaging preliminary findings. *Radiology* 222:499–506
- Naish JH, Parker GJ, Beatty PC, Jackson A, Young SS, Waterton JC, Taylor CJ (2005) Improved quantitative dynamic regional oxygen-enhanced pulmonary imaging using image registration. *Magn Reson Med* 54:464–469
- Nakagawa T, Sakuma H, Murashima S, Ishida N, Matsumura K, Takeda K (2001) Pulmonary ventilation-perfusion MR imaging in clinical patients. *J Magn Reson Imaging* 14:419–424
- Napadow VJ, Mai V, Bankier A, Gilbert RJ, Edelman R, Chen Q (2001) Determination of regional pulmonary parenchymal strain during normal respiration using spin inversion tagged magnetization MRI. *J Magn Reson Imaging* 13:467–474
- Ogasawara N, Suga K, Kawakami Y, Yamashita T, Zaki M, Matsunaga N (2004) Assessment of regional lung function impairment in airway obstruction and pulmonary embolic dogs with combined noncontrast electrocardiogram-gated perfusion and gadolinium diethylenetriaminepentaacetic acid aerosol magnetic resonance images. *J Magn Reson Imaging* 20:46–55
- Ohno Y, Hatabu H, Takenaka D, Adachi S, Van Cauteren M, Sugimura K (2001) Oxygen-enhanced MR ventilation imaging of the lung: preliminary clinical experience in 25 subjects. *AJR Am J Roentgenol* 177:185–194
- Ohno Y, Hatabu H, Takenaka D, Van Cauteren M, Fujii M, Sugimura K (2002) Dynamic oxygen-enhanced MRI reflects diffusing capacity of the lung. *Magn Reson Med* 47:1139–1144
- Ohno Y, Oshio K, Uematsu H, Nakatsu M, Gefer WB, Hatabu H (2004) Single-shot half-Fourier RARE sequence with ultra-short inter-echo spacing for lung imaging. *J Magn Reson Imaging* 20:336–339
- Ohno Y, Hatabu H, Higashino T, Nogami M, Takenaka D, Watanabe H, Van Cauteren M, Yoshimura M, Satouchi M, Nishimura Y, Sugimura K (2005) Oxygen-enhanced MR imaging: correlation with postsurgical lung function in patients with lung cancer. *Radiology* 236:704–711
- Pracht ED, Arnold JF, Wang T, Jakob PM (2005) Oxygen-enhanced proton imaging of the human lung using T2*. *Magn Reson Med* 53:1193–1196
- Price A, Prior M, Busza A, Morris P (2004) Single point imaging (SPI) of lung tissue. *Proc Intl Soc Mag Reson Med* 12:858
- Price A, White A, Busza A, Morris P (2005) Gadolinium enhanced SPI to assess lung ventilation. *Proc Intl Soc Mag Reson Med* 13:45
- Pruessmann KP, Weiger M, Scheidegger MB, Boesiger P (1999) SENSE: sensitivity encoding for fast MRI. *Magn Reson Med* 42:952–962
- Puderbach M, Ohno Y, Kawamitsu H, Koyama H, Takenaka D, Nogami M, Obara M, Van Cauteren M, Kauczor HU, Sugimura K (2007) Influence of inversion pulse type in assessing lung-oxygen-enhancement by centrally-reordered non-slice-selective inversion-recovery half-Fourier single-shot turbo spin-echo (HASTE) sequence. *J Magn Reson Imaging* 26:1133–1138
- Rupperecht T, Böwing B, Kuth R, Deimling M, Rascher W, Wagner M (2002) Steady-state free precession projection MRI as a potential alternative to the conventional chest X-ray in pediatric patients with suspected pneumonia. *Eur Radiol* 12:2752–2756

- Rupprecht T, Kuth R, Deimling M, Wagner M (2003) Functional lung imaging by MRI – is there a simple solution for a complex problem? *Proc Intl Soc Mag Reson Med* 11:1371
- Schoenberg SO, Dietrich O, Reiser MF (eds) (2007) *Parallel imaging in clinical MR applications*. Springer, Berlin Heidelberg New York
- Sodickson DK, Manning WJ (1997) Simultaneous acquisition of spatial harmonics (SMASH): fast imaging with radiofrequency coil arrays. *Magn Reson Med* 38:591–603
- Stock KW, Chen Q, Morrin M, Hatabu H, Edelman RR (1999) Oxygen-enhanced magnetic resonance ventilation imaging of the human lung at 0.2 and 1.5 T. *J Magn Reson Imaging* 9:838–841
- Suga K, Ogasawara N, Okada M, Matsunaga N, Arai M (2002a) Regional lung functional impairment in acute airway obstruction and pulmonary embolic dog models assessed with gadolinium-based aerosol ventilation and perfusion magnetic resonance imaging. *Invest Radiol* 37:281–291
- Suga K, Ogasawara N, Tsukuda T, Matsunaga N (2002b) Assessment of regional lung ventilation in dog lungs with Gd-DTPA aerosol ventilation MR imaging. *Acta Radiol* 43:282–291
- Suga K, Yuan Y, Ogasawara N, Tsukuda T, Matsunaga N (2003) Altered clearance of gadolinium diethylenetriaminepentaacetic acid aerosol from bleomycin-injured dog lungs: initial observations. *Am J Respir Crit Care Med* 167:1704–1710
- Sundaram TA, Gee JC (2005) Towards a model of lung biomechanics: pulmonary kinematics via registration of serial lung images. *Med Image Anal* 9:524–537
- Topf HG, Wagner M, Kuth R, Kreisler P, Deimling M, Geiger B, Chefd'hotel C, Rupprecht T (2004) Measuring quantitative regional lung ventilation by alveolar ventilation imaging (AVI) – phantom data and results of a feasibility study in 50 patients. *Proc Intl Soc Mag Reson Med* 12:671
- Topf HG, Zapke M, Kuth R, Kreisler P, Deimling M, Geiger B, Chefd'hotel C, Rupprecht T (2005) 1.5 Tesla can do too – measuring quantitative regional lung ventilation by AVI (alveolar ventilation imaging) – phantom data and results of a feasibility study in 10 patients. *Proc Intl Soc Mag Reson Med* 13:46
- Topf HG, Biondetti P, Zapke M, Kuth R, Deimling M, Chefd'hotel C, Geiger B, Rupprecht T (2006) Quantitative regional lung ventilation – results in 15 single lung transplanted patients. *Proc Intl Soc Mag Reson Med* 14:1660
- Vaninbrouckx J, Bosmans H, Sunaert S, Demedts M, Delcroix M, Marchal G, Verschakelen J (2003) The use of ECG and respiratory triggering to improve the sensitivity of oxygen-enhanced proton MRI of lung ventilation. *Eur Radiol* 13:1260–1265
- Voorhees A, An J, Berger KI, Goldring RM, Chen Q (2005) Magnetic resonance imaging-based spirometry for regional assessment of pulmonary function. *Magn Reson Med* 54:1146–1154
- Wagner M, Böwing B, Kuth R, Deimling M, Rascher W, Rupprecht T (2001) Low field thoracic MRI – a fast and radiation free routine imaging modality in children. *Magn Reson Imaging* 19:975–983
- Zapke M, Topf HG, Zenker M, Kuth R, Deimling M, Kreisler P, Rauh M, Chefd'hotel C, Geiger B, Rupprecht T (2006) Magnetic resonance lung function – a breakthrough for lung imaging and functional assessment? A phantom study and clinical trial. *Respir Res* 7:106

Respiratory Mechanics and Pulmonary Motion

RALF TETZLAFF

CONTENTS

| | | |
|---------|--|-----|
| 5.1 | Introduction | 91 |
| 5.1.1 | Technical Issues | 93 |
| 5.1.2 | Magnetic Resonance- Compatible Spirometry | 94 |
| 5.2 | Respiratory Mechanics | 94 |
| 5.2.1 | Movement of the Diaphragm | 94 |
| 5.2.1.1 | Static Imaging | 95 |
| 5.2.1.2 | Dynamic Imaging | 97 |
| 5.2.1.3 | Chest Wall Movement | 97 |
| 5.2.1.4 | Volumetry | 98 |
| 5.2.2 | Applications in Lung Disease | 100 |
| 5.2.3 | Pulmonary Motion | 101 |
| | References | 102 |

5.1

Introduction

The active and passive components of the thorax that take part in respiratory motion form the respiratory pump. The passive components are the bones, ligaments, and articulations of the thoracic cage, and the active components are the several muscle groups carrying out the pumping work. Of these, the diaphragm affects most of the volume changes. Other muscles with minor contributions to lung volume are the external and internal intercostal muscles with in- and expiratory action, and the so-called accessory muscles (mainly the scaleni and sternocleidomastoid muscles), which can participate in respiratory action, but have other primary functions. The forces generated by the respiratory pump

KEY POINTS

Dynamic MRI of the lung allows for real-time imaging of normal respiratory motion in 2D and of slow respiratory motion in 3D. 3D reconstructions and quantitative analysis confirmed that the diaphragm essentially has a piston-like function, but also showed that respiratory motion has a complex distribution over the diaphragm and the thoracic wall, and is further changed with body position. MRI-derived volumetry is well correlated to spirometric measurements and can be obtained for single lungs, allowing for regional assessment of lung function. With computational image registration and grid-tagging MRI, lung motion can be measured even at a subsegmental level. First experimental applications in chronic obstructive pulmonary disease, scoliosis, and radiation therapy proved the potential for the diagnosis and quantitative assessment of altered respiratory motion. Thus, it seems only a question of time until dynamic MRI enhances our understanding and diagnostics of respiratory mechanics in pulmonary disease.

are transmitted to the lungs through the pleural space, which additionally reduces friction to allow the lung to deform freely. Pulmonary motion is the lung tissue's reaction to these forces and further depends on the elastic and resistive properties of the lung. Disease can affect any one of these components, e.g., in scoliosis, the rib cage can be deformed in a way that limits its response to muscular contraction, phrenic paresis immobilizes the affected hemidiaphragm, inflammation of the pleural space can lead to increased friction or immobilization through scarring, and various diseases of the lung can increase or reduce its compliance through alteration of

R. TETZLAFF, MD

German Cancer Research Center Heidelberg (DKFZ), Im Neuenheimer Feld 280, 69121 Heidelberg, Germany

the tissue's elasticity or increasing flow resistance in the airways (MEAD AND MACKLEM 1986).

To date, routine clinical assessment of the system has relied mainly on indirect lung function tests like spirometry and plethysmography. These do not directly measure the motion of the thoracic cage or the lung, but the resulting air movement at the level of the mouth (spirometry) or overall thoracic and abdominal volume changes (plethysmography). Consequently, the measurements cannot provide any regional functional indices. This has also a limiting effect on the sensitivity of the measurements because regional deficits are compensated for by healthy lung, and changes that are limited to a single lung can be undetectable (PLATHOW et al. 2006). Also, in cystic fibrosis, parenchymal defects may already be visible on computed tomography (CT) without corresponding findings in standard lung function tests (DE JONG et al. 2004, 2006).

With fluoroscopy or ultrasound it has been possible to directly measure the motion of the hemithorax or a

single lung for some time, but only CT and MRI make it possible to measure at defined locations in a reproducible manner without errors resulting from high inter-operator variability (e.g., ultrasound) or artifacts from magnification and parallax (e.g., fluoroscopy). As an impact of such motion measurements on patient care or outcome has not yet been demonstrated, radiation exposure from CT can hardly be justified. Radiation-free MRI is consequently the ideal tool for further research in this field, as well as for any clinical applications that eventually emerge. Furthermore, for real dynamic imaging during free breathing, MRI is unchallenged, as dynamic CT images are composed from several respiratory cycles, thus averaging out any intercycle variability and representing only a measurement of an averaged motion.

This chapter is intended to give an overview of the application of MRI for the analysis of respiratory mechanics, i.e., the movement of the walls of the thoracic cavity and the motion of the pulmonary tissue.

Table 5.1. Image parameters for sequences typically used for dynamic MRI. The abbreviations given are for Siemens scanners, abbreviations for other manufacturers can be found in the text

| Sequence type | FOV (mm) | Matrix | ST (mm) | TR (ms) | TE (ms) | FA | BW (Hz/pixel) | PAT-factor (u.c.) | Temporal resolution (images/s) |
|----------------------|----------|-----------|---------|---------|---------|-----|---------------|-------------------|--------------------------------|
| 2D-SS-GRE (TrueFISP) | 400 | 159 × 256 | 10 | 37.7 | 1.7 | 65° | 977 | 2 | 3 |
| 2D-GRE (FLASH) | 500 | 98 × 128 | 15 | 2.49 | 1.03 | 5° | 980 | 2 | 10 |
| 3D-GRE (FLASH) | 450 | 128 × 128 | 8 | 1.38 | 0.5 | 10° | 1,500 | 4 | 2 |

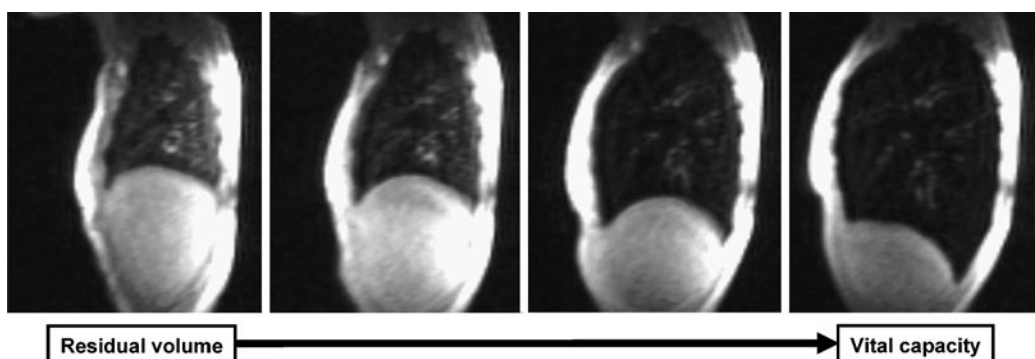


Fig. 5.1. Selected images from a sagittal 2D FLASH series of the right lung. The original series had a temporal resolution of 8.5 images per second and contained 13 images for inspiration from residual volume to vital capacity. The limited regional information inside the lung stems from the pulmonary blood vessels

5.1.1 Technical Issues

There are essentially two different approaches to the imaging of respiratory motion. The static approach uses standard imaging sequences, which are applied during repeated breath-holds to gather images in a minimum of two different respiratory positions (volumes). This approach relies on the same imaging techniques as those described for morphological imaging in the other chapters. It has the advantage of providing anatomical detail that is usable for further analysis like the application of registration algorithms. The drawback is that the lung is allowed to come to a state of uniform stress and pressure distribution during the breath hold. Differences in movement speed, caused by for example airway stenosis, cannot be detected.

The second approach uses fast imaging to capture images during free breathing. Unfortunately, in MRI, gains in speed always lead to reduction in detail. During quiet breathing, respiratory rates are around 12 cycles per minute (i.e., about 5 s per respiratory cycle) and normal respiratory excursion of the diaphragmatic

dome is about 1.5 cm. Thus, the maximum speed of the diaphragm is about 0.94 cm/s. Therefore, to avoid motion smear, imaging times should be well below 1 s for the imaging of quiet breathing. Even up-to-date MR scanners can only achieve such high temporal resolutions for dynamic 2D imaging, where acquisition times of down to 100 ms have been reported for pulmonary imaging (EICHINGER et al. 2007a). Sequences typically employed are spoiled gradient echo sequences (abbreviations: FLASH, Siemens; SPGR, General Electric; T1-FFE, Philips) and steady-state gradient echo sequences (abbreviations: trueFISP, Siemens; FIESTA, General Electric; balanced FFE, Philips; Table 5.1). The former has the advantage of higher temporal resolution (for an image example see Fig. 5.1), the latter the advantage of higher signal from the blood vessels that provide the main spatial information in dynamic lung MRI (PLATHOW et al. 2005b). For dynamic 3D imaging, acquisition times of down to 1 s are possible. With normal breathing this would still lead to considerable motion smear. Consequently, spatial information from inside the lungs in these images is very limited. Nevertheless, by using very slow controlled breathing, researchers

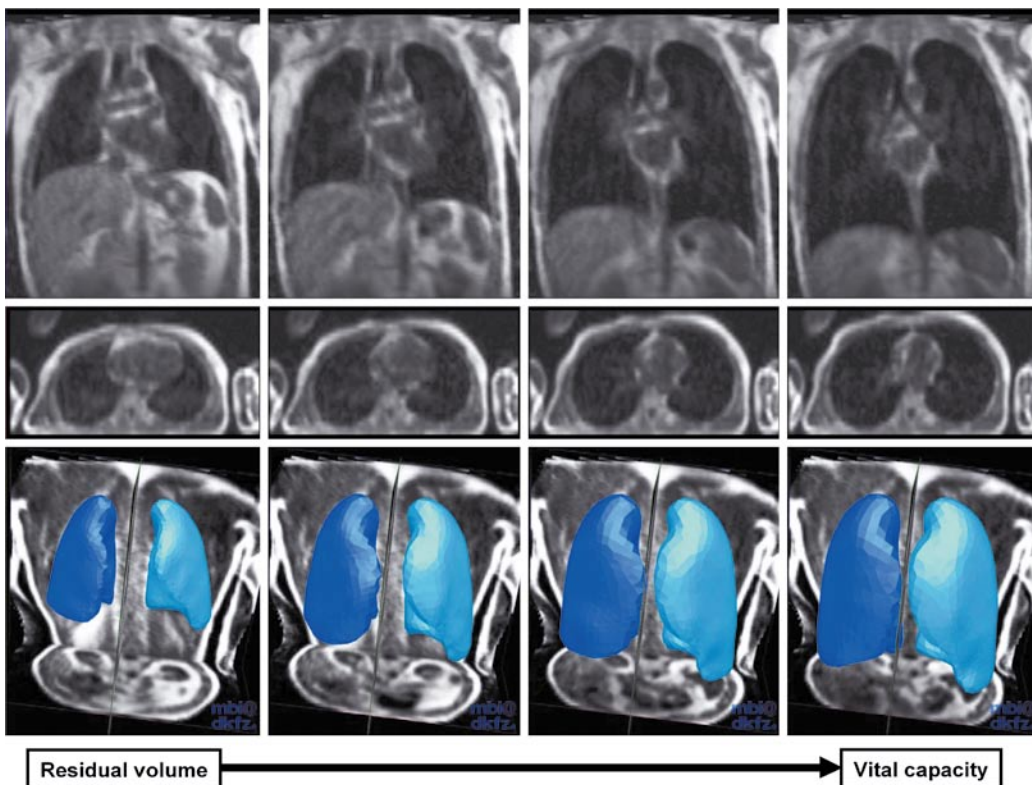


Fig. 5.2. Selected images from a sagittal 3D FLASH series with a temporal resolution of one image per second with 3D reconstruction of the lung by automatic segmentation. At this temporal resolution mostly noise is visible inside the lung. Nevertheless, the images are well suited to analysis of the thoracic configuration and lung volumetry, e.g., through automatic segmentation

obtained reasonably good results for dynamic 3D studies (PLATHOW et al. 2005a). If the interest lies mainly in volumetric or conformational information, even the low signal inside the lungs can be useful, since it facilitates automatic segmentation as the first step for further automatic analysis (Fig. 5.2).

5.1.2 Magnetic Resonance-Compatible Spirometry

Spirometry and plethysmography are the gold standard techniques for lung function testing. Diagnostic parameters derived from MRI measurements will have to be compared with these techniques. But both spirometry and plethysmography are characterized by high intrapersonal variability (MILLER et al. 2005). Therefore, for optimal comparability, the imaging and the lung function tests should be acquired simultaneously. Unfortunately, most spirometers are made with at least some metal parts, contain electronic components, and are therefore unsuitable for use inside the MRI scanner. However, commercially available spirometers can be adapted successfully for MR compatibility with some modifications. Two approaches have been reported so far (EICHINGER et al. 2007b; KONDO et al. 2000). Both worked with spirometers using pneumotachographs. These make subjects breathe through a metal sieve with low air flow resistance. The resistance causes a pressure drop that changes linearly with the air flow and is measured by an electronic component. To ensure MR compatibility, the metal parts were replaced with plastic substitutes and the pressure-sensitive electronics were put outside the scanner, connected by pressure-transducing plastic tubes. Such modifications can be made without affecting the measurement precision of the spirometer (EICHINGER et al. 2007b). Naturally, the spirometric measurements obtained during MRI differ from measurements obtained under standard conditions; the supine position as well as the use of surface coils reduces air flow during maximal respiratory maneuvers (EICHINGER et al. 2007b; MEYSMAN AND VINCKEN 1998). One problem for the comparative analysis of spirometry with MRI measurements is the missing temporal synchronization of the measurements that are acquired with two different computer systems. KONDO et al. (1995) solved this by recording the scanner noise on the spirometry system and using the increase in noise during imaging for temporal matching. Another solution would be to synchronize the system timers of the spirometer and the MRI scanner to the same network time server, so that the time information

in the image header and spirometry record can be used directly.

5.2 Respiratory Mechanics

Magnetic resonance imaging is an ideal tool for the analysis of the motion of the diaphragm and thoracic wall. The low signal of lung tissue leads to an excellent contrast to the surrounding high signal soft tissue structures. Thus, the combined action of the different components of the respiratory pump can be visualized and the functional principle analyzed.

Generally speaking, published research can be divided in two categories. The first analyzes the movement of individual components (lung, diaphragm, and rib cage) to obtain a better understanding of their individual action. The second approach attempts to calculate the lung volume changes by segmentation of the lungs or by measurement of surrogate markers on the acquired images.

Imaging techniques are basically the same for the two approaches, since for both, the whole thorax is imaged (in the case of 2D dynamic MRI one slice through the thorax).

The differences between the studies lie in the measurements and analysis of the images. The images can then be subjected to a qualitative analysis, and in many cases, meaningful information can be derived, e.g., a phrenic paresis is immediately evident from two images in inspiration and expiration. But for the differentiation of the severity of a disease, or for the detection of small abnormalities, quantitative measures are necessary.

As the field of research is still rather new and only a limited number of publications exist, no standards for the imaging procedures, the location of measurements, and the analysis of measurements have emerged. This limits the comparability of results from different studies. But the results published so far point in the same direction, making it only a matter of time before clinically meaningful measures and applicable measurement methods emerge.

5.2.1 Movement of the Diaphragm

The diaphragm is the biggest respiratory muscle and is alone responsible for most of the volume changes dur-

ing quiet, and to a somewhat lesser degree, during forced respiration. It is a flat muscle sheet with a central tendinous component. By its muscular insertions it can be divided in two components. The muscular fibers of the crural part arise from the first three lumbar vertebral bodies and the medial and lateral arcuate ligaments. The costal part inserts on the inner surfaces of the lower six ribs. During quiet breathing, a considerable proportion of the diaphragm is apposed to the inner rib cage and thus forms the cylindrical “area of apposition,” which is capped by the diaphragmatic dome (MEAD AND MACKLEM 1986). As it is normally hidden inside the body the exact area distribution between the apposition zone and diaphragmatic dome and the three-dimensional configuration are difficult to measure. Tomographic imaging has been a breakthrough in this respect.

5.2.1.1 Static Imaging

Several groups used static MRI at different respiratory volumes to gain further insight into the function of the diaphragm. Images were acquired during a breath hold with a relaxed diaphragm in sagittal and coronal orientation. On each of the resulting images, the diaphragmatic contour was traced. The combined tracings form a wireframe representation of the diaphragmatic contour (Fig. 5.3). From this, changes in diaphragmatic length (Table 5.2), area (Table 5.3), and curvature can be derived and correlated to the respective changes in lung volumes. According to these results, the Laplace law is applicable to at least the posterior part of the diaphragmatic dome. As the Laplace law links the pres-

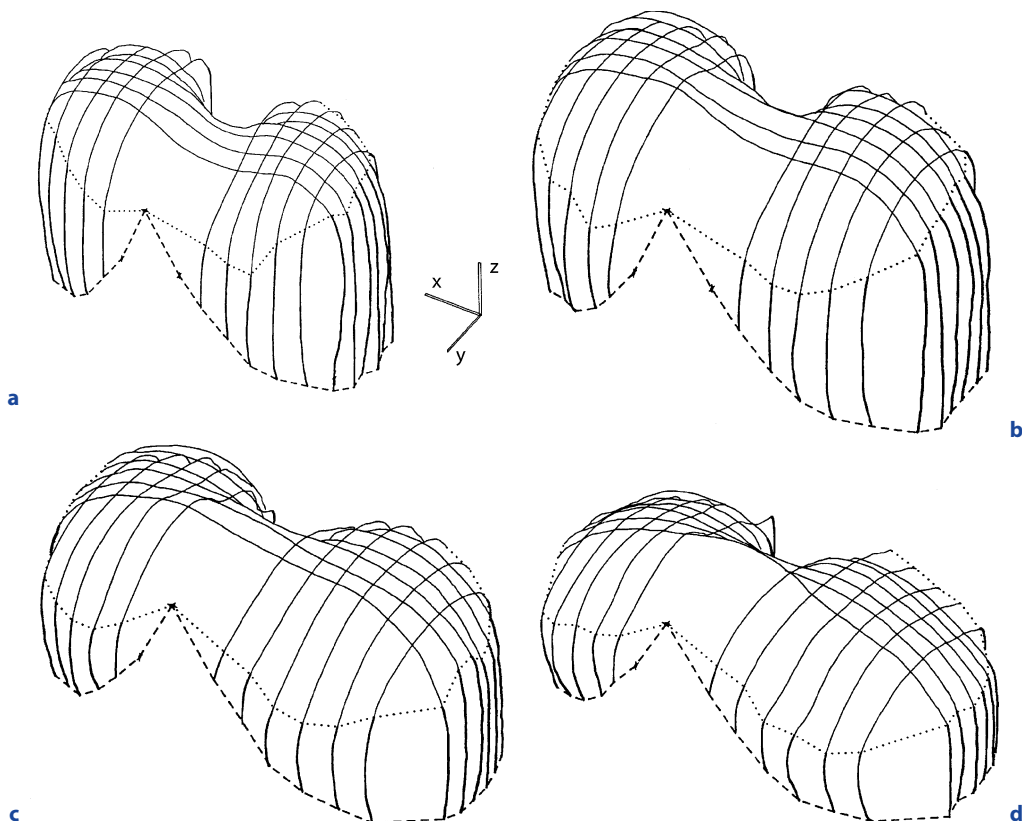


Fig. 5.3a–d. Wireframe reconstructions of the diaphragm at **a** residual volume, **b** functional residual capacity, **c** functional residual capacity plus one-half inspiratory capacity, and **d** vital capacity. *Dashed lines* show the lower costal margin, *dotted lines* the upper limit of the zone of apposition. The 3D axis indicates spatial orientation and scaling with a line length of 50 mm. (Reprinted with permission of the American Physiological Society (GAUTHIER 1994))

Table 5.2. Diaphragmatic lengths as a whole and separately for its appositional part (part that is directly apposed to the thoracic wall) and the diaphragmatic zone (apposed to the lung) at different lung volumes, as measured by CLUZEL et al. (2000). *RV* residual volume, *FRC* functional residual capacity, *TLC* total lung capacity

| | RV | FRC | TLC |
|--------------------|--------|--------|-----------------|
| Diaphragm | | | |
| Coronal | 507±72 | 485±77 | 365±79 |
| Sagittal left | 330±15 | 301±17 | 208±12 |
| Sagittal right | 368±20 | 354±22 | 228±23 |
| Appositional zone | | | |
| Coronal | 254±17 | 221±35 | 0 or close to 0 |
| Sagittal left | 163±16 | 127±21 | 0 or close to 0 |
| Sagittal right | 196±11 | 161±25 | 0 or close to 0 |
| Diaphragmatic zone | | | |
| Coronal | 253±69 | 264±64 | 365±79 |
| Sagittal left | 167±13 | 174±15 | 208±12 |
| Sagittal right | 173±17 | 194±8 | 228±23 |

Table 5.3. Areas of the whole diaphragm, the appositional part, the diaphragmatic dome, and the diaphragmatic muscle surface (the diaphragmatic area minus the central tendon area) as measured by CLUZEL et al. (2000)

| | RV | FRC | TLC |
|-----------------------------------|-----------|--------|-----------------|
| Total diaphragmatic area | 1,128±129 | 997±93 | 584±89 |
| Apposition area | 757±121 | 597±91 | 0 or close to 0 |
| Diaphragmatic dome area | 371±28 | 399±27 | 584±89 |
| Diaphragmatic muscle surface area | 985±129 | 854±93 | 441±98 |
| Percentage decrease | Reference | 13±8 | 55±11 |

sure across a surface with the surface's curvature and the pressure gradient across the surface, this allows the calculation of the diaphragmatic tension from its curvature and the transdiaphragmatic pressure (PAIVA et al. 1992). Further results confirm the remarkable ability of diaphragmatic fibers to shorten up to 55% during contraction (CLUZEL et al. 2000; GAUTHIER et al. 1994). This ability allows the diaphragm to effect the respiratory volume changes descending like a piston in a cylinder. While the diaphragmatic dome does change in form with anteroposterior widening, flattening, and dorsal rotation, the effect of these changes on transdiaphragmatic pressure are small. Consequently, the diaphragmatic action is described using the analogy of a widening piston in a widening cylinder, which means that volume changes through diaphragmatic ac-

tion are nearly linearly related to diaphragmatic muscle fiber length (GAUTHIER et al. 1994). These conclusions depend on the assumption that the apposition zone does not entirely disappear, even at total lung capacity. This is controversial as the location of the diaphragmatic costal attachment can only be derived indirectly and CLUZEL et al. (2000) found the apposition zone to disappear at total lung capacity (TLC). Thus, at least at volumes near TLC, the above results might not be entirely valid. As a further limitation, the results are based on imaging of the relaxed diaphragm. Thus, its form should be considerably influenced by the adjacent structures. The configuration during contraction, i.e., inspiration, might differ considerably. Also, the configuration will be different when not in the supine position, as described later on.

5.2.1.2 Dynamic Imaging

Most of the time during the respiratory cycle, the diaphragm is in motion, either actively contracting during inspiration or passively expanding during expiration. To truly understand its mode of function in contributing to lung volume changes, static analysis as described in the previous section is not ideal. But 3D MRI is not yet fast enough to allow comparable experimental designs. Dynamic 2D MRI offers the necessary speed. The sacrifice of spatial coverage can be compensated for by acquiring several sagittal image series at different lateral positions. Under the assumption that diaphragmatic motion is more or less constant during quiet respiration, these measurements show that the craniocaudal displacement of the diaphragm in a supine position is not evenly distributed. The diaphragmatic excursion increases from anterior to posterior and at each anteroposterior position from medial to lateral (Fig. 5.4). Using dynamic 2D MRI in coronal orientation it is possible to directly compare the movement of the left and right hemidiaphragm. Apparently, the two sides can move synchronously or one side can move slightly ahead of the other. The respective pattern can also change from inspiration to expiration. There is some discussion as to whether one hemidiaphragm moves more than the other one (see Table 5.4 for excursion data). The most recent study by KIRYU et al. (2006) found a larger excursion on the right and attributes the different findings of earlier studies to the averaging effect of the respective lower temporal resolution. (GIERADA et al. 1995; UNAL et al. 2000; TAKAZAKURA et al. 2004; KIRYU et al. 2006).

The results discussed so far are all based on imaging in the supine position. As postural changes have an effect on intra-abdominal pressure, diaphragmatic motion should differ in the upright position. In a study conducted in a vertical MRI, diaphragmatic excursion was 1–2 cm less than in the supine position. Differences were more pronounced in the posterior diaphragm. This reduces the difference of excursion between the anterior and posterior diaphragm from a maximum of 51 mm to 38 mm. This effect could be explained by the steeper anteroposterior abdominal pressure gradient in the supine position. The posterior diaphragm is consequently pushed more cranially. This has the side effect that through increased muscle fiber length the force–tension characteristic of the diaphragm is improved (TAKAZAKURA et al. 2004). The same effect can be observed when changing from supine to prone and either lateral decubitus position. The respective dependent diaphragm lies more cranially and starts to move later in inspiration and earlier in expiration (KIRYU et al. 2006).

5.2.1.3 Chest Wall Movement

Under physiologic conditions, the chest wall contributes much less to lung volume changes than the diaphragm. Nevertheless, the respiratory pump cannot be understood without examining all of its components. With the high contrast between the air-filled lung and the adjacent thoracic wall, MRI is an ideal instrument to quantitatively analyze chest wall movement. As in diaphragmatic imaging, dynamic analysis requires high temporal resolutions and consequently time-resolved 2D imaging is chosen in most of the studies.

The measurements show that under normal conditions, both sides of the thorax move synchronously and have the same maximal excursions (SUGA et al. 1999). However, differences are found between the upper and lower chest wall, which do not seem to move as a single functional unit. While the anteroposterior movement of the upper thorax is linearly related to lung volume

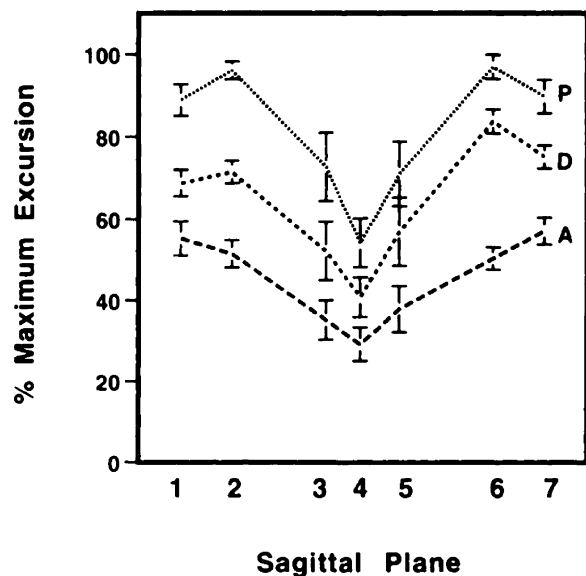


Fig. 5.4. Excursion of the diaphragm relative to its maximal excursion. The three lines represent the motion at three different anteroposterior positions, the middle line (D) was measured at the diaphragmatic dome, the top line (P) in the middle between D and the posterior costophrenic angle, the lower line (A) in the middle between D and the anterior costophrenic angle. Numbers on the horizontal axis indicate different lateral positions: midline (4), 2 cm to the right (3) and left (5) of midline, in the middle of the right (2) and left (6) hemithorax, positions 1 and 7 are in the middle between 3 and 5 and the lateral chest wall respectively. (Reprinted with permission of RSNA (GIERADA 1995))

Table 5.4. Excursion of left and right hemidiaphragm at different body positions

| | <i>n</i> | Body position | Right (cm) | Left (cm) |
|--------------------------|----------|---------------|------------|-----------|
| GIERADA et al. (1995) | 10 | Supine | 4.4 ± 1.3 | 4.2 ± 0.9 |
| UNAL et al. (2000) | 15 | Supine | 6.0 | 5.0 |
| TAKAZAKURA et al. (2004) | 10 | Sitting | 8 ± 2.3 | 8 ± 2.4 |
| | | Supine | 9.2 ± 2.1 | 10.3 ± 2 |
| KIRYU et al. (2006) | 8 | Supine | 8.9 ± 1 | 7.5 ± 1.1 |
| | | Prone | 9.3 ± 0.3 | 8.1 ± 0.6 |
| | | Right lateral | 9.1 ± 0.9 | 7.7 ± 1.1 |
| | | Left lateral | 8.4 ± 1.2 | 8.2 ± 1.2 |

changes, the lower thorax is poorly synchronized to lung volumes (KONDO et al. 2000). It is possible to deduct the respective contributions to lung volume changes. In comparison to diaphragmatic displacements, the anteroposterior thoracic expansion contributes only two-fifths to lung volume changes. The contribution of the transverse expansion of the thorax is only half of the latter (KONDO et al. 2000). These patterns have primarily been found in healthy young subjects, but a later study with elderly healthy subjects found no significant differences between age groups (KONDO et al. 2005).

5.2.1.4 Volumetry

While the previous sections described the contributions of dynamic MRI to the understanding of normal diaphragmatic and chest wall mechanics, the comparison of dynamic MRI measurements and standard lung function tests has received a lot of interest. As dynamic MRI makes it possible to image single lungs, and to some degree even distinguish lung lobes, good agreement of MRI measures with spirometry could pave the way to regional lung function testing on a split lung or even lobar basis.

Many studies used 3D imaging of the thorax to determine the volume of the low signal lung tissue. With this approach the temporal resolution is limited by the measurement time of the MRI. The fastest measurements of 3D images of the lung are reported to take about 1 s per volume (PLATHOW et al. 2005a). This is not sufficient to

measure lung volumes during tidal breathing at normal respiratory frequencies. In intentionally slow breathing, continuous volume measurements with 3D MRI correlate well with spirometric measurements (GIERADA et al. 1998; PLATHOW et al. 2005a). Alternatively, or to achieve higher temporal resolution, 2D imaging can be used. The area of the lung in sagittal and transversal sections is well correlated to spirometric lung volume ($r > 0.8$) (KONDO et al. 2000). From 2D imaging in different orientations, diameter measurements can be used to calculate lung volumes using a geometrical model of the lung. This has been reported to provide volume measurements with a high correlation to spirometric measurement (PLATHOW et al. 2004). The forced expiratory volume in the first second (FEV1) is a standard test for the assessment of obstructive lung disease. In this maneuver, the subject is asked to expire as fast as possible after maximal inspiration. The volume expired during the first second of this maneuver is measured. To derive this measure from dynamic MRI, only very fast imaging techniques are applicable. SWIFT et al. (2007) used 2D spoiled gradient echo sequences to image the thorax in the coronal and sagittal orientation with a temporal resolution of 5–10 images per second. From these images, volumes were calculated with an elliptical model, and the long and short axis measured on the sagittal and coronal image. They found a very high correlation to spirometry for FEV1 and FVC (correlation coefficients of 0.95 and 0.83 respectively).

These results indicate that static and dynamic volume measurements using MRI are feasible with adequate precision. Therefore, volume measurements of

Table 5.5. Volume distribution between the left and right lung. VC vital capacity

| Publication | Collective | Phase | Sample size | Left (%) | Right (%) |
|----------------------|-----------------------------|-------------|-------------|----------|-----------|
| CHAPMAN et al. 1990 | Infants 2–10 months | Mid-tidal | 9 | 47.2 | 52.8 |
| QANADLI et al. 1999 | Young adults 24–32 years | Inspiration | 15 | 48 | 52 |
| | | Expiration | 15 | 45 | 55 |
| | | VC | 15 | 49.7 | 50.3 |
| PLATHOW et al. 2005a | Young adults 19–35 years | VC | 20 | 45 | 55 |

single lungs should give meaningful results. Table 5.5 shows the MRI-derived volumes of single lungs found in different studies. All found a significant difference between the two lungs, with the right lung having a slightly higher volume. This agrees well with anatomical data and can easily be explained by the volume taken up by the heart on the left (MEAD AND MACKLEM 1986).

Measurements of thoracic diameters on dynamic MRI of single lungs also show good correlation (correlation coefficients above 0.85 for anteroposterior, craniocaudal, and lateral thoracic diameters) with spirometrically measured vital capacity (VC) and FEV1%. Even though the spirometric data available for comparison are global, the high correlation indicates the validity of measurements of single lungs. Further results, gained by inserting diameter measurements into a more complicated geometric model such as the one used by SWIFT et al. (2007), show that craniocaudal movement contributes most and lateral expansion least to lung volume changes, which is in good agreement with other physiological studies (PLATHOW et al. 2004).

The results described so far are based on the diameter differences between only two images out of the multitude of images acquired (e.g., the images with highest and lowest position of the diaphragm for VC or the image acquired 1 s after the highest diaphragm position for FEV1). With a simultaneous spirometric measurement using an MRI-compatible spirometer, the volume changes occurring between the acquisitions of two images (approximately 120 ms) can be compared with the corresponding dynamic MRI measurements. This is illustrated in Fig. 5.5a, where the volume changes

calculated from 2D MRI of the right lung are plotted together with simultaneously measured spirometric volume changes. From such 2D MRI measurements realistic flow volume curves of single lungs can be derived, as shown in Fig. 5.5b.

The normalized craniocaudal diameter changes for each hemithorax are highly correlated to normalized spirometric volumes (correlation coefficient of 0.93). The surrogate for FEV1% calculated from MRI measurements was also highly correlated to spirometric FEV1% for each hemithorax (correlation coefficient of 0.71) (TETZLAFF et al. in press).

When comparing lung volume measured with MRI with spirometrically measured volumes it is important to keep in mind that the former usually also contains volume occupied by the lung tissue and blood content. From MRI volumetry at maximal inspiration combined with plethysmographic measurement of TLC, this volume can be calculated to be around 840 ml (QANADLI et al. 1999), which is in good agreement with indicator dilution studies that found the blood volume in healthy subjects to be about 250 ml (DOCK et al. 1961) and the tissue volume about 600 ml (CANDER AND FORSTER 1959).

In all MRI measurements, post-processing is needed to extract the volumes or volume surrogates from the images. The post-processing techniques range from manual (CHAPMAN et al. 1990; O'CALLAGHAN et al. 1987, 1988; PLATHOW et al. 2004) to semiautomatic (TETZLAFF et al. submitted). Even though the post-processing method very likely influences the precision of the measurements, this error is rarely evaluated. Time

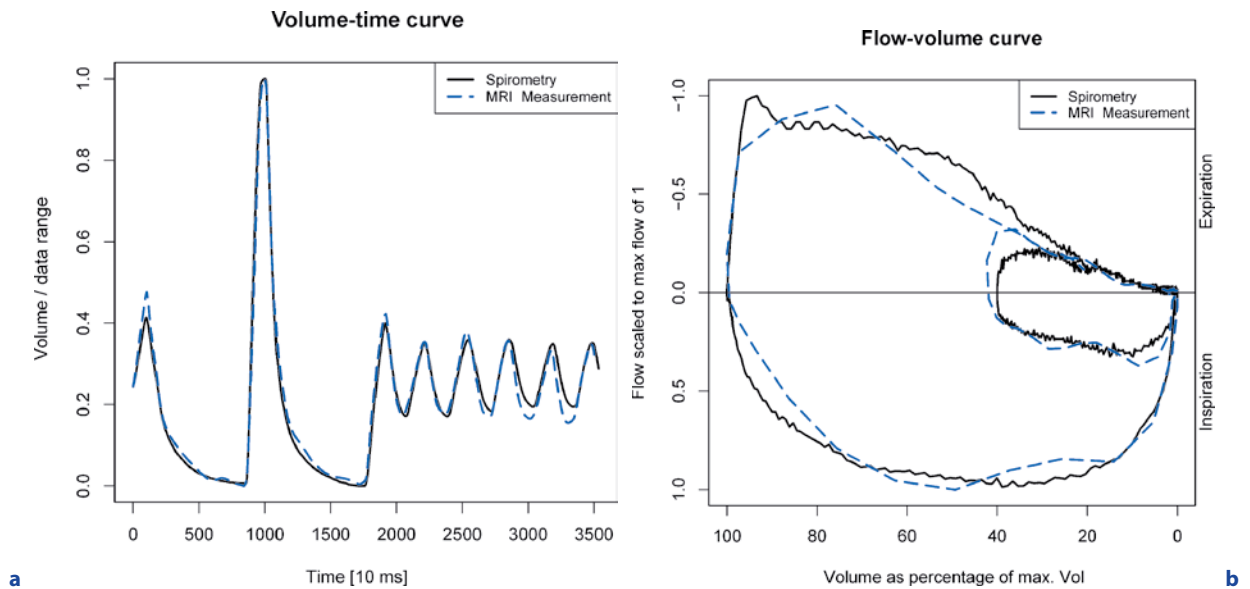


Fig. 5.5. **a** Normalized volume–time curves from spirometric measurements and calculated from 2D MRI (product of the anteroposterior and craniocaudal diameters). **b** Flow–volume curve calculated from the same data as those used in **a**. The

curve derived from 2D MRI closely follows the course of the spirometric curve and only fails to exactly reproduce the sharp downturn at the beginning of the measurement

savings from semiautomatic measurement come at a cost, as was recently shown for the measurement of thoracic diameters. This could be accelerated by a factor of four compared with manual measurements and the agreement with manual measurement was reduced to about 3 mm, the side length of a single voxel in the study (TETZLAFF et al. submitted).

5.2.2 Applications in Lung Disease

The previous paragraphs showed the potential of dynamic MRI of the lung in supplementing established methods for the evaluation of lung function. For first evaluations in patients, most groups have chosen emphysema as one of the most common chronic pulmonary diseases, with potential severe impairment of respiratory mechanics.

Dynamic MRI shows the diaphragm flattened and with less and irregular movement. Occasionally, an asynchronous movement was seen between the hemidiaphragms. The maximum craniocaudal dimension correlates well with TLC% and is not significantly changed. But the minimum craniocaudal dimensions are significantly greater than in normal subjects and correlate well with RV%. The effect of therapy, e.g., lung volume reduction therapy, is clearly visible, with

increased craniocaudal motion in the operated hemithorax. The effect can even be seen in the contralateral hemithorax. Improvements seen with dynamic MRI were also paralleled with better scores on the Fletcher dyspnea scale (SUGA et al. 1999). For the lateral and anteroposterior thoracic dimension, similar findings were reported (GIERADA et al. 1998; IWASAWA et al. 2002).

Adolescent idiopathic scoliosis is another condition in which patients suffer from insufficient respiratory function, which is most likely explained by malfunctioning of the respiratory pump. Compared with normal subjects, 2D dynamic MRI shows that the anteroposterior thoracic movement in these patients is limited (KOTANI et al. 2004). The diaphragm is elevated in inspiration just as in expiration, but the amplitude of its motion is unchanged compared with healthy subjects. Postoperatively, dynamic MRI shows an improvement in the amplitude of thoracic expansion and an increase in diaphragmatic movement (CHU et al. 2006, 2007).

One of the most interesting studies conducted compared lung motion before and after radiotherapy for lung tumors using 2D dynamic MRI. It could be shown that the craniocaudal lung motion of the tumor-bearing hemithorax was reduced after radiotherapy. As lung function testing was not significantly different after radiotherapy, this shows the potential of dynamic MRI to detect functional pulmonary changes with higher

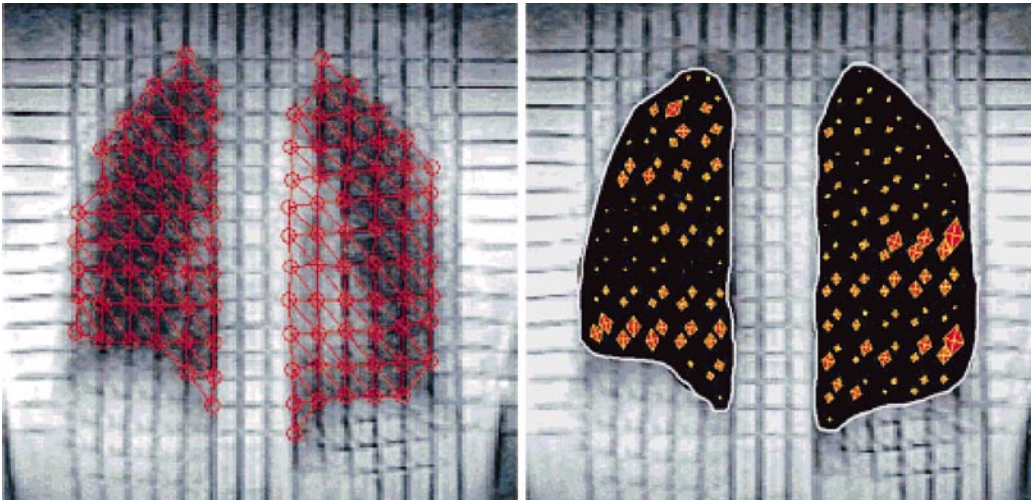


Fig. 5.6. Quantitative evaluation of the lung deformation in the coronal plane during forced inspiration by grid-tagging MRI. The *left* image shows a mesh of triangular elements fitted to the tagging grid for calculation of the strain tensor that is visualized in the *right* image (Reprinted with permission of John Wiley & Sons, Inc. (CHEN 2001))

sensitivity than spirometric measurements (PLATHOW et al. 2006).

5.2.3 Pulmonary Motion

The quantification of true parenchymal lung motion is the most challenging, but at the same time the most promising field of investigation in dynamic MRI of the lung. The specific detection of spatial variations of tissue motion would most likely allow the detection of regionally confined alterations of the lungs and mechanical properties through, for example, cellular infiltrates or connective tissue proliferation. While the low signal of well-aerated lung tissue facilitated the measurement of chest wall motion, registration of tissue motion requires the detection of recognizable landmarks throughout the pulmonary parenchyma. In currently available sequences for dynamic MRI, the central vessels mainly provide sufficient signal to provide such landmarks. As the vessels taper toward the periphery, their contrast to lung tissue rapidly decreases and no usable landmarks can be found in a major proportion of the lung volume.

Therefore, the most promising approach to the imaging of pulmonary motion lies in creating landmarks through MR grid-tagging. While MR tagging for mo-

tion analysis is an established technique in cardiac imaging (REICHEK 1999), the short $T2^*$ time of lung tissue complicates the technique in lung imaging, with rapid fading of the saturation stripes. Nevertheless, it has been shown that a rectangular grid of saturation stripes can still be identified 1,000 ms after its application. Using 2D MRI with a temporal resolution of up to eight images per second allowed imaging of pulmonary tissue motion over the short time span of at least 1 s (CHEN et al. 2001). From such tagged images, the 2D tissue strain tensor (represented by a 2×2 matrix) can be calculated (Fig. 5.6). From its elements, measures to quantitatively describe lung deformation can be derived. The trace of the vector (sum of the diagonal elements) can be considered to be a generalized direction-independent strain magnitude. In coronal images of healthy volunteers, this was maximal at the base and apex of the lung, with lower values at the hilum where the large bronchi and vessels reduce the lung elasticity. The directional dominance of shear could also be calculated and showed that craniocaudally oriented strain was predominant at the apex and base of the lung. In the middle lung field, strain was more laterally oriented. On sagittal images, the maximum tissue expansion occurred at the apex and was greater posteriorly than anteriorly (NAPADOW et al. 2001). The imaging sequence was further improved to allow for continuous measurement through repeated grid application. In extension to

the work described above the authors were able to calculate the regional air flow rate and volumetric strain, and the derived volume time and flow–volume curves for the upper, middle, and lower lung fields of each single lung (VOORHEES et al. 2005). Even though limited to 2D imaging, these results point in the right direction to considerably improve lung function diagnostics in the future. Unfortunately, to date, no application in lung disease has been reported.

Alternative methods of assessing regional lung tissue motion are deformable registration algorithms. These match a series of images by deforming them in order to achieve congruence of structural image information. Unfortunately, the limited signal of pulmonary tissue only implies the relative absence of such structural information. On the other hand, the registration approach is not dependent on a specific imaging sequence and could make a more general application of motion detection possible. Registration techniques have been evaluated on 2D dynamic MRI with only a small error of the registration process in comparison to landmarks defined by experts. Naturally, the landmarks were set according to the present structural information; namely, the central vessel structures. The performance in the peripheral lung tissue was not accessible to evaluation. While the algorithm conveniently and automatically quantifies visible lung motion, it simply cannot find structures invisible to human observers (GEE et al. 2003). In a follow-up study, SUNDARAM AND GEE (2005) examined healthy volunteers and mice. In the volunteers, motion detection worked well over the diaphragm and hilar vessels, but performance was worse more distant from these high-signal structures. For the mouse experiment, normal mice were compared with mice from a transgenic strain of sickle cell disease (SCD) that is highly susceptible to the clogging of small vessels under hypoxia. The registration was already able to detect differences in observed motion between normal and normoxic SCD mice, which further increased with hypoxia. This ability to detect motion changes over time appears promising for the assessment of disease progression with follow-up examinations. Thus, evaluations confirmed that registration is a valuable technique for motion detection, but requires further improvement of pulmonary MRI to extend the good results from high signal structures to the low-signal peripheral lung tissue.

References

Cander L, Forster RE (1959) Determination of pulmonary parenchymal tissue volume and pulmonary capillary blood flow in man. *J Appl Physiol* 14:541–551

- Chapman B, O'Callaghan C, Coxon R et al. (1990) Estimation of lung volume in infants by echo planar imaging and total body plethysmography. *Arch Dis Child* 65:168–170
- Chen Q, Mai VM, Bankier AA, Napadow VJ, Gilbert RJ, Edelman RR (2001) Ultrafast MR grid-tagging sequence for assessment of local mechanical properties of the lungs. *Magn Reson Med* 45:24–28
- Chu WC, Li AM, Ng BK et al. (2006) Dynamic magnetic resonance imaging in assessing lung volumes, chest wall, and diaphragm motions in adolescent idiopathic scoliosis versus normal controls. *Spine* 31:2243–2249
- Chu WC, Ng BK, Li AM, Lam TP, Lam WW, Cheng JC (2007) Dynamic magnetic resonance imaging in assessing lung function in adolescent idiopathic scoliosis: a pilot study of comparison before and after posterior spinal fusion. *J Orthop Surg* 2:20
- Cluzel P, Similowski T, Chartrand-Lefebvre C, Zelter M, Derenne JP, Grenier PA (2000) Diaphragm and chest wall: assessment of the inspiratory pump with MR imaging – preliminary observations. *Radiology* 215:574–583
- De Jong PA, Nakano Y, Lequin MH et al. (2004) Progressive damage on high resolution computed tomography despite stable lung function in cystic fibrosis. *Eur Respir J* 23:93–97
- De Jong PA, Lindblad A, Rubin L et al. (2006) Progression of lung disease on computed tomography and pulmonary function tests in children and adults with cystic fibrosis. *Thorax* 61:80–85
- Dock DS, Kraus WL, Mc GL, Hyland JW, Haynes FW, Dexter L (1961) The pulmonary blood volume in man. *J Clin Invest* 40:317–328
- Eichinger M, Tetzlaff R, Puderbach M, Woodhouse N, Kauczor HU (2007a) Proton magnetic resonance imaging for assessment of lung function and respiratory dynamics. *Eur J Radiol* 64:329–334
- Eichinger M, Puderbach M, Smith HJ et al. (2007b) Magnetic resonance-compatible-spirometry: principle, technical evaluation and application. *Eur Respir J* 30:972–979
- Gauthier AP, Verbanck S, Estenne M, Segebarth C, Macklem PT, Paiva M (1994) Three-dimensional reconstruction of the in vivo human diaphragm shape at different lung volumes. *J Appl Physiol* 76:495–506
- Gee J, Sundaram T, Hasegawa I, Uematsu H, Hatabu H (2003) Characterization of regional pulmonary mechanics from serial magnetic resonance imaging data. *Acad Radiol* 10:1147–1152
- Gierada DS, Curtin JJ, Erickson SJ, Prost RW, Strandt JA, Goodman LR (1995) Diaphragmatic motion: fast gradient-recalled-echo MR imaging in healthy subjects. *Radiology* 194:879–884
- Gierada S, Hakimian S, Slone RM, Yusef RD (1998) MR analysis of lung volume and thoracic dimensions in patients with emphysema before and after lung volume reduction surgery. *Am J Roentgenol* 170:707–714
- Iwasawa T, Kagei S, Gotoh T et al. (2002) Magnetic resonance analysis of abnormal diaphragmatic motion in patients with emphysema. *Eur Respir J* 19:225–231

- Kiryu S, Loring SH, Mori Y, Rofsky NM, Hatabu H, Takahashi M (2006) Quantitative analysis of the velocity and synchronicity of diaphragmatic motion: dynamic MRI in different postures. *Magn Reson Imag* 24:1325–1332
- Kondo T, Kobayashi I, Taguchi Y, Ohta Y, Yanagimachi N (2000) A dynamic analysis of chest wall motions with MRI in healthy young subjects. *Respirology* 5:19–25
- Kondo T, Kobayashi I, Taguchi Y, Hayama N, Tajiri S, Yanagimachi N (2005) An analysis of the chest wall motions using the dynamic MRI in healthy elder subjects. *Tokai J Exp Clin Med* 30:15–20
- Kotani T, Minami S, Takahashi K et al. (2004) An analysis of chest wall and diaphragm motions in patients with idiopathic scoliosis using dynamic breathing MRI. *Spine* 29:298–302
- Mead J, Macklem PT (1986) The respiratory system. American Physiological Society, Bethesda
- Meysman M, Vincken W (1998) Effect of body posture on spirometric values and upper airway obstruction indices derived from the flow-volume loop in young nonobese subjects. *Chest* 114:1042–1047
- Miller MR, Hankinson J, Brusasco V et al. (2005) Standardisation of spirometry. *Eur Respir J* 26:319–338
- Napadow VJ, Mai V, Bankier A, Gilbert RJ, Edelman R, Chen Q (2001) Determination of regional pulmonary parenchymal strain during normal respiration using spin inversion tagged magnetization MRI. *J Magn Reson Imaging* 13:467–474
- O’Callaghan C, Small P, Chapman B et al. (1987) Determination of individual and total lung volumes using nuclear magnetic resonance echo-planar imaging. *Ann Radiol* 30:470–472
- O’Callaghan C, Chapman B, Coxon R et al. (1988) Evaluation of infants by echo planar imaging after repair of diaphragmatic hernia. *Arch Dis Child* 63:186–189
- Paiva M, Verbanck S, Estenne M, Poncelet B, Segebarth C, Macklem PT (1992) Mechanical implications of in vivo human diaphragm shape. *J Appl Physiol* 72:1407–1412
- Plathow C, Ley S, Fink C et al. (2004) Evaluation of chest motion and volumetry during the breathing cycle by dynamic MRI in healthy subjects: comparison with pulmonary function tests. *Invest Radiol* 39:202–209
- Plathow C, Schoebinger M, Fink C et al. (2005a) Evaluation of lung volumetry using dynamic three-dimensional magnetic resonance imaging. *Invest Radiol* 40:173–179
- Plathow C, Klopp M, Fink C et al. (2005b) Quantitative analysis of lung and tumour mobility: comparison of two time-resolved MRI sequences. *Br J Radiol* 78:836–840
- Plathow C, Hof H, Kuhn S et al. (2006) Therapy monitoring using dynamic MRI: analysis of lung motion and intrathoracic tumor mobility before and after radiotherapy. *Eur Radiol* 16:1942–1950
- Qanadli SD, Orvoen-Frija E, Lacombe P, Paola RD, Bittoun J, Frija G (1999) Estimation of gas and tissue volumes by MRI: functional approach of lung imaging. *J Comput Assist Tomogr* 23:743–748
- Reichek N (1999) MRI myocardial tagging. *J Magn Reson Imaging* 10:609–616
- Suga K, Tsukuda T, Awaya H et al. (1999) Impaired respiratory mechanics in pulmonary emphysema: evaluation with dynamic breathing MRI. *J Magn Reson Imaging* 10:510–520
- Sundaram TA, Gee JC (2005) Towards a model of lung biomechanics: pulmonary kinematics via registration of serial lung images. *Med Image Anal* 9:524–537
- Swift AJ, Woodhouse N, FICHELE S et al. (2007) Rapid lung volumetry using ultrafast dynamic magnetic resonance imaging during forced vital capacity maneuver – correlation with spirometry. *Invest Radiol* 42:37–41
- Takazakura R, Takahashi M, Nitta N, Murata K (2004) Diaphragmatic motion in the sitting and supine positions: healthy subject study using a vertically open magnetic resonance system. *J Magn Reson Imaging* 19:605–609
- Tetzlaff R, Eichinger M, Schöbinger M, Puderbach M, Meinzner H-P, Kauczor H-U (2008) Semiautomatic assessment of respiratory motion in dynamic MRI – comparison with simultaneously acquired spirometry. *ROFO* (in press)
- Unal O, Arslan H, Uzun K, Ozbay B, Sakarya ME (2000) Evaluation of diaphragmatic movement with MR fluoroscopy in chronic obstructive pulmonary disease. *Clin Imaging* 24:347–350
- Voorhees A, An J, Berger KI, Goldring RM, Chen Q (2005) Magnetic resonance imaging-based spirometry for regional assessment of pulmonary function. *Magn Reson Med* 54:1146–1154

Clinical

Pulmonary Hypertension and Thromboembolic Disease

SEBASTIAN LEY and KARL-FRIEDRICH KREITNER

CONTENTS

- 6.1 **Introduction** 107
- 6.2 **Lung Parenchyma** 109
- 6.3 **Macro- and Microvasculature** 109
 - 6.3.1 Pulmonary Hypertension 109
 - 6.3.2 Chronic Thromboembolic Pulmonary Hypertension 110
 - 6.3.3 Systemic Blood Supply to the Lungs (Bronch systemic Shunt) 113
- 6.4 **Functional Assessment** 114
 - 6.4.1 Morphology 114
 - 6.4.2 Flow and Pulsatility of Pulmonary Arteries 114
 - 6.4.3 Evaluation of the Right Ventricle and the Interventricular Septum 115
- References** 116

KEY POINTS

Pulmonary hypertension (PH) is a disease group that includes a wide variety of reasons leading to an increased pulmonary arterial pressure. This chapter describes the basic mechanisms that lead to PH and the possibilities of MRI in diagnosing different aspects. A MR imaging protocol is provided making MRI a one-stop shop for classification of the underlying disease and assessment of hemodynamics.

6.1

Introduction

Pulmonary hypertension (PH) is characterized by an elevation of the arterial pressure and vascular resistance within the pulmonary circulation. Precapillary PH has to be differentiated from postcapillary PH (ROSENKRANZ 2007). In patients with postcapillary PH, diseases of the left heart (atrial, ventricular, valvular) cause pulmonary venous congestion, which in turn leads to an elevation of pulmonary capillary pressure (PCP) and pulmonary arterial pressure (PAP). In contrast, precapillary PH is characterized by an isolated elevation of PAP with normal PCP and accounts for the majority of patients referred to tertiary pulmonary hypertension centers (BLYTH et al. 2005). Since in this setting the pulmonary hypertensive state is limited to the arterial component of the pulmonary vasculature, pulmonary arterial hypertension (PAH) is distinguished from other forms of PH. The most important consequence of PAH is chronic overload of the right heart (cor pulmonale) which ultimately leads to right heart failure and is thus responsible for the poor prognosis of patients with severe PAH. Based on invasive measurements by right

S. LEY, MD
Department of Pediatric Radiology, University Hospital Heidelberg, Im Neuenheimer Feld 430, 69120 Heidelberg, Germany

K.-F. KREITNER, MD
Department of Diagnostic and Interventional Radiology, Johannes Gutenberg-University Mainz, Langenbeckstrasse 1, 55131 Mainz, Germany

heart catheterization, PAH is defined as an elevation of the mean pulmonary arterial pressure (PAPm) above 25 mmHg at rest and/or above 30 mmHg during exercise in the setting of normal or reduced cardiac output and normal PCP (BARST et al. 2004). Pulmonary vascular resistance (PVR) is elevated above 3 mmHg/l/min (Wood units).

In 1998, the WHO (Evian) classification system of PH was proposed, which sought to categorize different forms of pulmonary hypertension (PH) according to similarities in pathophysiological mechanisms, clinical presentation and therapeutic options. In 2003 in Venice, modifications were made to this system, with the aim of making it more comprehensive, easier to follow and more practical for clinicians (Table 6.1) (SIMONNEAU et al. 2004). In this system, the risk factors and associated conditions were updated and modifications were proposed, including replacing the term 'primary pulmonary hypertension' with 'idiopathic pulmonary arterial hypertension (IPAH)'.

Patients suffering from PH often present with non-specific symptoms, namely shortness of breath on minimal physical exertion, fatigue, chest pain and fainting. Therefore, diagnosis often occurs late in the course of the disease when prognosis is poor and treatment options are limited (TUDER et al. 2007).

The incidence of IPAH is approximately 2–3 persons per 1 million per year (f:m = 1.7–3:1) (CHATTERJEE

et al. 2002; TAICHMAN and MANDEL 2007). It is a genetic disorder with a familial accumulation. For acquired ("secondary") forms of PH which are a common complication of many different disease entities only some examples are given: 50% of patients with chronic hypoxemia, such as in chronic obstructive pulmonary disease (COPD), develop PH. COPD is the third most frequent cause of death worldwide, mostly related to late complications, such as PH. Of patients with scleroderma, 40% develop PH. There are more than 500,000 cases of acute pulmonary embolism per year in the United States with subsequent obstruction of the pulmonary arterial vascular bed. Approximately 3%–4% of these patients will develop a chronic and fatal late form called chronic thromboembolic pulmonary hypertension (PENGO et al. 2004).

Naturally, different types of PH require different treatment regimens making a precise categorization mandatory (PROVENCHER et al. 2005; PURI et al. 2007). The diagnostic workup of these patients needs to differentiate between the different causes of PH (MCCLAUGHLIN and MCGOON 2006). This includes, besides patient history and laboratory findings, the assessment of cardiac function, lung function, pulmonary blood pressures and pulmonary vasculature. Thus, the actual diagnostic pathway includes a broad spectrum of examinations, mainly echocardiography, invasive right heart catheterization and ventilation/perfusion scintigraphy.

Table 6.1. Classification of pulmonary hypertension according to the world conference on pulmonary hypertension (Venice 2003)

| |
|--|
| <p>1. Pulmonary arterial hypertension (PAH)</p> <p>1.1 Idiopathic (IPAH) – Cause unknown</p> <p>1.2 Familial (FPAH) – Genetic background</p> <p>1.3 Associated with (APAH) – Collagen vascular disease, congenital systemic-to-pulmonary shunts, portal hypertension, HIV infection, drugs and toxins, etc.</p> <p>1.4 Associated with significant venous or capillary involvement –Pulmonary veno-occlusive disease (PVOD), pulmonary capillary hemangiomatosis (PCH)</p> <p>1.5 Persistent pulmonary hypertension of the newborn (PPHN)</p> |
| <p>2. Pulmonary hypertension with left heart disease</p> <p>Left-sided ventricular or atrial heart disease, left-sided valvular heart disease</p> |
| <p>3. Pulmonary hypertension associated with lung disease and/or hypoxemia</p> <p>COPD, interstitial lung disease, sleep-disordered breathing, alveolar hypo-ventilation disorders, chronic exposure to high altitude, developmental abnormalities</p> |
| <p>4. Pulmonary hypertension due to chronic thrombotic and/or embolic disease (CTEPH)</p> <p>Thromboembolic obstruction of the proximal/distal pulmonary arteries;</p> <p>non-thrombotic pulmonary embolism (tumor, parasites, foreign material)</p> |
| <p>5. Miscellaneous</p> <p>Sarcoidosis, histiocytosis X, lymphangiomatosis, compression of pulmonary vessels (adenopathy, tumor, fibrosing mediastinitis, etc.)</p> |

Table 6.2. Proposed MR imaging protocol for imaging patients with suspected pulmonary hypertension

| Rationale | Sequences |
|----------------------|--|
| Morphology I | HASTE tra & cor, VIBE tra |
| Function (perfusion) | FLASH 3D (time resolved), 0.1 mmol/kg BW |
| Morphology II | VIBE tra & cor |
| Function (cardiac) | Cine of the right ventricle, flow |
| Vasculature | FLASH 3D (high spatial resolution), 0.1 mmol/kg BW |

Magnetic Resonance Imaging (MRI) has emerged as a versatile diagnostic tool allowing for morphological evaluation of the lung parenchyma, pulmonary arteries and cardiac function (LEY et al. 2005; NAGENDRAN and MICHELAKIS 2007). The diagnostic capabilities in the context of PH are described in detail in the following paragraphs. A basic MR imaging protocol is given in Table 6.2.

6.2

Lung Parenchyma

Pulmonary hypertension (PH) associated with respiratory systemic disorders is a distinct group in the categorization of PH. It is evolving as an important factor that can adversely affect prognosis and outcome in chronic lung disease (PRESBERG and DINCER 2003). Especially chronic obstructive pulmonary disease (COPD) and idiopathic pulmonary fibrosis (IPF) are associated with intimal thickening or medial smooth muscle cell hypertrophy leading to mild to moderate PH (TUDER et al. 2007; WRIGHT et al. 2005; RYU et al. 2007). The most common cause is COPD; PH occurs in approximately 5% of patients with severe emphysema (SCHARF et al. 2002). In a series with 215 patients with severe COPD, moderate (9.8%) or severe (3.7%) PH was found more frequently than observed before (THABUT et al. 2005). In advanced COPD, therapy directed at controlling the pulmonary artery pressure has been recommended (WEITZENBLUM and CHAOUAT 2005). Many patients with COPD and severe PH have an additional cause of pulmonary pressure elevation, such as left ventricular disease, pulmonary embolism, or sleep apnea syndrome; these conditions should be ruled out routinely, as they may be treatable (CHAOUAT et al. 2005).

Evaluation of the lung parenchyma using MRI is not yet common but possible even in severe COPD patients

with reduced parenchymal structure (LEY-ZAPOROZHAN et al. 2007, 2008). IWASAWA et al. 2007 reported that lung signal change measured by MRI correlates with airflow obstruction in COPD patients.

Idiopathic pulmonary fibrosis (IPF) is a disease of unknown etiology associated with progressive parenchymal fibrosis. Little is known about PH in IPF but several retrospective analyses indicate that PH in IPF may be frequent. In a large trial in patients awaiting lung transplantation due to IPF, it was found that PH affects approximately 45% of these patients; however, severe PH was relatively infrequent. Typical lung parenchymal changes due to fibrosis can be nicely visualized by MRI (PRIMACK et al. 1994; JUNG et al. 2000; ALTES et al. 2007). Detailed description of the possibilities of MRI in detection and characterization of lung parenchymal changes can be found in Chaps. 9 (COPD), 10 (cystic fibrosis) and 14 (interstitial lung disease).

6.3

Macro- and Microvasculature

6.3.1

Pulmonary Hypertension

The exact processes that initiate the pathological changes seen in PAH are still unknown even if we now understand more and more of the mechanisms involved. It is recognised that PAH has a multi-factorial pathobiology that involves various biochemical pathways and cell types (TUDER et al. 2007; GALIE et al. 2004). The imaging hallmark in PH is vasoconstriction predominantly on a subsegmental level. The increased vascular resistance leads to dilation of the central pulmonary arteries (PERLOFF et al. 2003). Thus, a vascular pruning towards the lung periphery can be seen and the subpleural space is often spared (CHATTERJEE et al. 2002). An additional

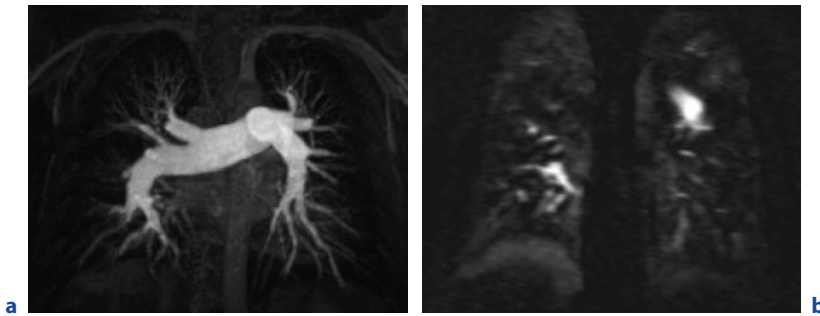


Fig. 6.1a,b. Patient suffering from PAH. Two years before this MRI examination an invasive pressure measurement revealed a mean pulmonary arterial pressure of 56 mmHg. **a** MR angiography (50 mm MIP) shows the dilated main and central pulmonary arteries and the tortuous course towards the periphery. However, all segmental arteries are visible. **b** MR perfusion (10 mm MIP) shows a massive reduction of pulmonary perfusion with a patchy pattern. No lobar perfusion defects can be found

finding of hypoxic pulmonary hypertension is an increase in vasomotor tone (SHIMODA et al. 2000). The peripheral vascular bed is the location, where modern pharmaceutical approaches are aiming at. First, the vasomotor tone should be decreased and second, vascular remodeling should be stopped or even reversed. Therefore, visualization and quantification of blood flow in the most peripheral zone is crucial for treatment monitoring or even human drug trials in patients suffering from PH. The overall possibilities for assessment of the pulmonary blood flow in different diseases leading to PH, including detailed technical description, are summarized elsewhere (LEY et al. 2004; COULDEN 2006).

In an early study analyzing the MRA features of PH, the most obvious finding was an abnormal proximal-to-distal tapering of all vessels being present (BERGIN et al. 1997). Collateral blood supply, via bronchial arteries to the lung parenchyma, was only observed in 1 out of 10 patients. Compared to healthy volunteers, the central pulmonary arteries were significantly enlarged. In a more recent study using parallel MR imaging techniques, the predominant MR angiographic findings were proximal-to-distal tapering and a tortuous course of the pulmonary arteries towards the periphery (Fig. 6.1) (LEY et al. 2005). In this series, no dilated bronchial arteries were found in PAH patients. Further technical developments will allow for more detailed evaluation of the pulmonary vasculature as demonstrated in a recent study where a spatial resolution of 1 mm isotropic datasets was achieved in a 20-s breath-hold (3-T MRI, dedicated 32 channel chest coil) (NAEL et al. 2007).

As PH predominantly affects the small vessels, detailed analysis of pulmonary perfusion is the most promising technique. 3D MRI pulmonary perfusion in

patients suffering from PH (except CTPEH) showed a predominantly peripheral, diffuse reduction of pulmonary perfusion (=patchy pattern) (80% of pulmonary lobes) and 20% of the lobes showed a normal perfusion (LEY et al. 2005). One advantage of MR perfusion measurements is the ability of absolute quantification, as demonstrated in an initial study with 40 PH patients (OHNO et al. 2004). In larger populations, quantitative perfusion analysis showed a marked reduction in pulmonary blood flow and an increase in mean transit time (OHNO et al. 2007; LEY et al. 2007b).

6.3.2 Chronic Thromboembolic Pulmonary Hypertension

The main contributor of chronic thromboembolic pulmonary hypertension (CTEPH) is obstruction of the large pulmonary arteries by acute and recurrent pulmonary emboli, and organization of these blood clots (DARTEVELLE et al. 2004). Up to now, the exact pathological pathways of the development of CTEPH are not yet fully understood (PEACOCK et al. 2006): in more than 50% of cases, patients with CTEPH lack a documented history of prior deep venous thrombosis (DVT) or PE. Thus, other conditions may be relevant for the onset of the disease (PEACOCK et al. 2006). It has been suggested that a primary arteriopathy and an endothelial dysfunction may lead to in situ (local) thrombosis in the lung, and that this could contribute to a subsequent failure of thrombotic resolution (EGERMAYER and PEACOCK 2000) – the thrombotic hypothesis. Furthermore, in some cases, a pulmonary arteriopathy could be the

initial pathology, and thromboembolic events may occur as clinical sequelae rather than as the initiating factor (MCNEIL and DUNNING 2007). Additionally, small-vessel hypertensive arteriopathy, similar to that seen in other forms of pulmonary hypertension (PH), develops in small unobstructed vessels (DARTEVELLE et al. 2004; FRAZIER et al. 2000).

In the THESEE study, in which perfusion lung scans were performed in 157 patients 8 days and 3 months after acute PE, a residual obstruction after 3 months was found in 66% of patients, and 10% of patients showed no resolution at all (WARTSKI and COLLIGNON 2000). In a CTA series including 62 patients, at follow-up 13% of patients presented with only partial or no thrombotic resolution despite adequate anticoagulation therapy (REMY-JARDIN et al. 1997). Based on these data, it can be understood that PENGO et al. 2004 found a cumulative incidence of symptomatic CTEPH of 3.8% after 2 years in patients with an acute episode of pulmonary embolism.

The combination of a high diagnostic sensitivity together with a radiation free technique makes perfusion MRI the optimal tool for monitoring of thrombus resolution during anticoagulation therapy (KLUGE et al. 2005). In a follow-up study, 33 patients with acute PE were examined with pulmonary perfusion MRI initially

and 1 week later. A subgroup of eight patients also underwent a second follow-up examination. Between both examinations, pulmonary perfusion changed noticeably, i.e. the time-to-peak enhancement decreased, and the peak enhancement of affected areas increased (KLUGE et al. 2005).

In CTEPH, the thromboembolic material follows an aberrant path of organization and recanalization – instead of thrombolysis – leading to characteristic abnormalities such as intraluminal webs and bands, pouch-like endings of arteries, irregularities of the arterial wall and stenotic lesions (Fig. 6.2) (DARTEVELLE et al. 2004; FRAZIER et al. 2000; AUGER et al. 2004). This aberrant path of obstruction and reopening occurs in repeated cycles over many years. Patients become symptomatic if approximately 60% of the total diameter of the pulmonary arterial bed is obstructed. This obstruction leads to an increase in pulmonary arterial pressure and vascular resistance with subsequent cor pulmonale ending in right heart failure with a corresponding 5-year-survival of only 30%.

The primary treatment of CTEPH is surgical pulmonary endarterectomy (PEA), which leads to a permanent improvement of the pulmonary hemodynamics (MADANI and JAMIESON 2006; PUIS et al. 2005). The technical feasibility and success of surgery mainly

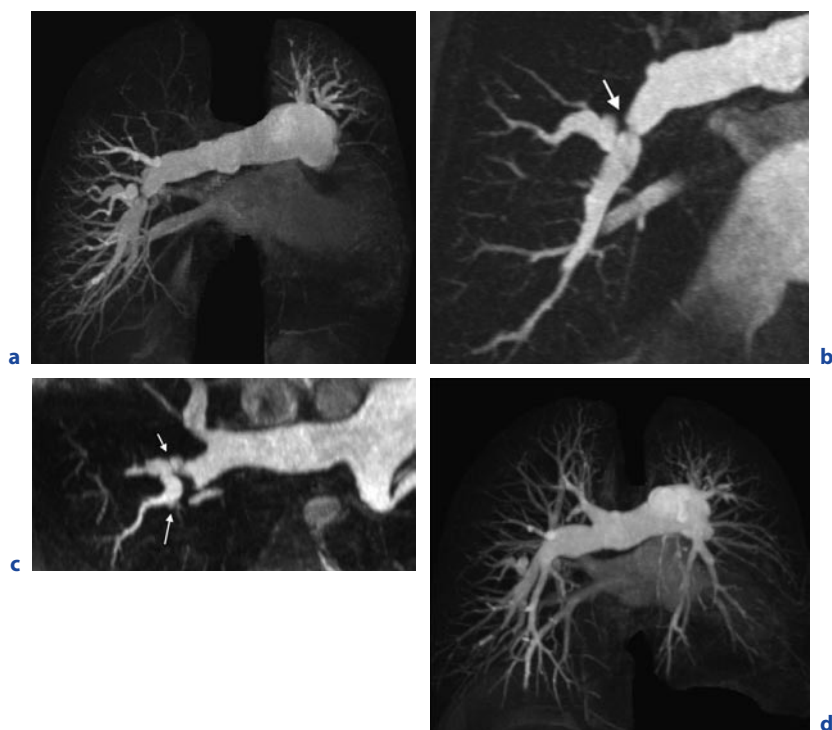


Fig. 6.2a–d. A 32-year-old female CTEPH patient with the characteristic angiographic findings: intraluminal webs and bands, abrupt vessels cut-offs, and abnormal proximal-to-distal tapering. **a** Maximum intensity projection (MIP) reconstruction of preoperative ce-MRA (TR/TE = 3.34/1.23 ms; flip angle = 25°, iPAT-factor = 2, GRAPPA algorithm). **b,c** Multiplanar reconstructions demonstrate intraluminal webs and bands in the pulmonary arteries (arrows). **d** Postoperatively, there is a nearly complete normalization of pulmonary arterial vasculature in the right lung and a reopening of many segmental pulmonary arteries in the left

depend on the localization of the thromboembolic material: surgical accessibility is given if the organized thrombi are not located distal to the lobar arteries or to the origin of the segmental vessels in order to develop a safe dissection plane for endarterectomy (JAMIESON and KAPELANSKI 2000). Between 10% and 50% of referred patients may not be considered eligible for this procedure either because of inaccessible distal thromboembolism or due to other serious comorbidities (PEACOCK et al. 2006). In these subjects, PAH-specific drug treatment can reduce the symptoms (HOEPER et al. 2005). In rare cases, balloon angioplasty may be considered. Lung (or heart-lung) transplantation can also be considered in selected cases where PEA is not indicated, or when significant pulmonary hypertension persists following PEA.

Especially for diagnosis and follow-up of CTEPH patients MRI is well suited (LEY et al. 2003a; PRINCE et al. 2004). However, there are only few studies available exploring the usefulness of contrast-enhanced-(CE-) MRA in the diagnostic work-up of CTEPH. In a study with 34 patients depiction of typical findings for CTEPH could be done using CE-MRA (KREITNER et al. 2004). This comprised the detection of wall-adherent thromboembolic material in the central parts of the pulmonary arteries down to the segmental level, intraluminal webs and bands, abnormal proximal-to-distal tapering and abrupt vessel cutoffs (Fig. 6.2). A thorough analysis of source images and the creation of multiplanar reformations were most important for the exact assessment of the morphological findings. Maximum intensity projections on the other hand provided an overview and an impression of the arterial vascular tree that was comparable to those provided by the DSA images. Compared with selective DSA, pulmonary CE-MRA depicted all patent vessel segments down to the level of segmental arteries (533/533 vessel segments).

For subsegmental arteries, DSA significantly detected more patent vessel segments than MRA (733 vs 681). MRA was superior to DSA in delineating the exact central beginning of the thromboembolic material. In all cases, the most proximal site as assessed by MRA corresponded to the beginning of the dissection procedure during PEA. However, as all patients suffered from CTEPH and were candidates for surgery, there was no statement regarding the ability of CE-MRA in the differentiation of other causes of pulmonary hypertension. Postoperatively, CE-MRA enabled the delineation of re-opened segmental arteries and a decrease in the diameter of the central pulmonary arteries. A complete normalization of pulmonary arterial vasculature was not documented in any of the cases.

CE-MRA of the PA in coronal orientation can be acquired in approximately 20 s which is tolerated by most of the CTEPH patients. However, the most dorsal and proximal vascular segments are often cut-off. In a series of 15 patients with CTEPH the diagnostic accuracy of coronal MRA was compared to a sagittal approach with two separate datasets. Sagittal CE-MRA provided a higher resolution and shorter acquisition time (Fig. 6.3). It proved to be superior in all assessed criteria like image quality, vessel coverage, depiction of patent peripheral arteries and pathological findings compared to coronal MRA, especially on a segmental level (OBERHOLZER et al. 2004).

In a study on 29 patients with either CTEPH or primary pulmonary hypertension (PPH), CE-MRA ($1.0 \times 0.7 \times 1.6 \text{ mm}^3$) was compared with DSA and/or CT-angiography (NIKOLAOU et al. 2005). CE-MRA had sensitivities between 83% and 86% for the detection of complete vessel obstructions and free-floating thrombi, and sensitivities between 50% and 71% for the depiction of older and/or organized thrombi, webs and bands. The specificities ranged between 73% and 95%

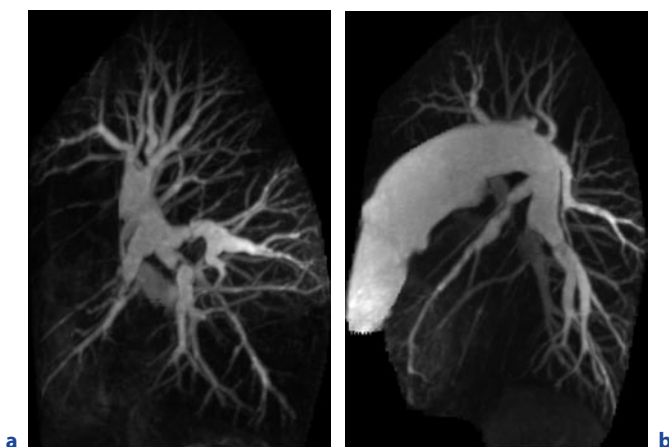


Fig. 6.3. Sagittal data sets of right (a) and left (b) pulmonary arteries. MIP reconstructions of preoperative ce-MRA ((TR/TE = 3.34/1.24 ms; flip angle = 25°, iPAT-factor = 2, GRAPPA algorithm), acquisition time = 13 s, 10 mL of gadobutrol). Complete coverage of the pulmonary arterial vasculature

for non-obstructing findings, and from 91% to 96% for occluding findings, respectively. CE-MRA enabled correct differentiation of PPH and CTEPH in 24 of 29 patients (83%). As in acute PE, pulmonary perfusion MRI should be performed for identification of the typical wedge-shaped perfusion defects (NIKOLAOU et al. 2005). Perfusion defects were classified either as patchy and/or diffuse (indicative of PPH) or segmental and/or circumscribed (indicative of CTEPH). Compared with perfusion scintigraphy as the standard of reference, MRI had an overall sensitivity of 77% in detecting perfusion defects on a per-patient basis. Compared with the final diagnosis, MR perfusion enabled a correct diagnosis of PPH or CTEPH in 20 (69%) of 29 patients. The combined interpretation of MR perfusion and CE-MRA led to a correct diagnosis of PPH or CTEPH in 26 (90%) of 29 patients when compared with the final reference diagnosis (combination of perfusion scintigraphy with DSA or CT angiography). In another study, MR perfusion was used to differentiate patients with idiopathic pulmonary arterial hypertension (IPAH), CTEPH and healthy volunteers (LEY et al. 2005). Based on a per-segment analysis, patients with PPH showed a patchy and/or diffuse reduction of perfusion in 71 (79%) of 90 segments, a normal finding in 18 (20%) of 90 segments, and one focal defect (1%). Patients with CTEPH showed focal perfusion defects in 47 (52%), an absent segmental perfusion in 23 (26%) and a normal perfusion in 20 (22%) of 90 segments. On a per-patient basis, there was no difficulty in differentiating the two pathologic entities and in depicting the healthy volunteers. Semiquantitative analysis showed that healthy volunteers demonstrated a significantly shorter transit time than patients with IPAH and CTEPH (14 ± 1 s vs 22 ± 4 s and 25 ± 11 s, respectively). No difference was found between both patient populations.

6.3.3 Systemic Blood Supply to the Lungs (Bronchosystemic Shunt)

Beside the pulmonary arteries, the lung parenchyma is maintained by bronchial arteries – the direct systemic arterial blood supply of the airways and lung parenchyma (CARVALHO et al. 2007). The bronchial arteries arise from the aorta, with a high level of variability, and drain into the pulmonary veins (BAILE et al. 1985; HARTMANN et al. 2007). In pathological conditions even arteries from the celiac trunk and intercostal arteries can supply to the lung parenchyma (REMY-JARDIN et al. 2004). Normally they only contribute to nutrition supply and do not take part in gas exchange. During

baseline condition, they have a maximum diameter of 1.5 mm and are rarely seen on helical CT (KAUCZOR et al. 1994). In special pathologic conditions (e.g., occlusion of one main pulmonary artery), they also participate in blood oxygenation – up to 25% of bronchial circulation can do so (ROBERTSON et al. 1984). In CTEPH, the flow through the bronchial arteries increases and they become visible on helical CT angiography due to dilatation of the vessels (Fig. 6.4). Another important finding is that dilated bronchial arteries are positively correlated with a lower mortality rate after pulmonary thromboendarterectomy (KAUCZOR et al. 1994). PERLOFF et al. 2003 evaluated patients with Eisenmenger syndrome and patients with PPH. There was no bronchosystemic shunt seen in patients with Eisenmenger syndrome, but in PPH. Dilated bronchial arteries are also found in patients with inflammatory bronchial arterial disease (like asthma and cystic fibrosis), being a major cause of hemoptysis (ANTONELLI et al. 2002; GREEN et al. 2006).

Up to now, direct visualization of the bronchial arteries was a domain of CT. Due to improved spatial resolution of MRA it is possible to visualize them also with MRI. Functional assessment of the shunt volume was performed by MRI in patients suffering from CTEPH (LEY et al. 2002). The shunt volume, calculated by phase-contrast flow measurements in the pulmonary arteries and ascending aorta, correlated well ($r = 0.86$) with the cross sectional area of the bronchial arteries, measured on CTA.



Fig. 6.4. A 67-year-old male patient with CTEPH. Coronary MPR shows a good delineation of dilated bronchial arteries (arrows) supplying the parenchyma of both lungs. Note wall-adherent thromboembolic material in the left pulmonary artery (asterisk)

6.4

Functional Assessment

6.4.1

Morphology

The enlargement of the central pulmonary arteries can be used as an indirect sign to estimate the severity of the pressure, although this is just a rough estimation as the individual pressure is heavily dependent on the cardiac condition. In a study of 32 patients with PH a diameter of the main pulmonary artery above 28.6 mm readily predicted the presence of pulmonary hypertension (KURIYAMA et al. 1984). A diameter of 29 mm or greater has a sensitivity of 87% and specificity of 89% for the diagnosis of PH. If this finding is associated with a segmental artery-to-bronchus ratio greater than one in three or more pulmonary lobes, the specificity for the diagnosis of PH rises to 100% (BUGNONE et al. 2002).

6.4.2

Flow and Pulsatility of Pulmonary Arteries

Phase-contrast measurements of flow and velocity can be regarded as a link between macro- and microcirculation. They enable the determination of cardiac output of the right and left ventricles with low inter- and intraobserver variability and can be performed selectively in the right and left pulmonary arteries (GATEHOUSE et al. 2005). Furthermore, they allow for a flow-profile analysis that could be the basis for an estimation of mean pulmonary arterial pressure (MPAP) and pulmonary vascular resistance (PVR). In an animal model of pulmonary hypertension (pigs with infusion of thromboxane A₂) the acceleration time showed the highest linear correlation with invasively measured mPAP ($r^2=0.75$) (ABOLMAALI et al. 2007). By multiple regression analysis, the estimate of mPAP was further increased by taking the maximum of mean velocities into account ($r=0.897$). In another animal study, systolic pressure measurements in the main pulmonary artery showed good linear correlation with average flow per minute ($r=0.66$), peak velocity ($r=0.66$) and average velocity ($r=0.62$) (LEY et al. 2008).

The pressure wave velocity, determined by phase-contrast flow measurements, correlated well with invasively determined mean pressure in the main pulmonary artery ($r=0.82$) in 15 PH patients (LAFFON et al.

2001). However, calculation of the pressure wave velocity is not yet an established parameter for pressure estimation. Flow measurements allow for discrimination of volunteers and patients with PH (LEY et al. 2007a). The patients showed a significantly reduced peak velocity (cm/sec) and pulmonary blood flow (L/min). In this group of PH patients, no relevant broncho-systemic shunting was found. In a large study on 59 patients of whom 42 patients had PAH, the average velocity showed the best correlation with mPAP ($r=-0.73$) and sPAP ($r=-0.76$). Average velocity (cutoff value=11.7 cm/s) revealed PAH with a sensitivity of 92.9% (39 of 42) and a specificity of 82.4% (14 of 17) (SANZ et al. 2007).

Before treatment of PH can be initiated, the individuals' response to the application of vasodilators has to be tested. This is usually performed during invasive right heart catheterization with direct pressure measurements (ROSENKRANZ 2007). The mean pulmonary artery distensibility was used as a noninvasive marker of acute vasodilator responsiveness in IPAH patients (JARDIM et al. 2007). The pulmonary artery distensibility was significantly higher in responders to treatment. A receiver operating characteristic curve analysis has shown that 10% distensibility was able to differentiate responders from non-responders with 100% sensitivity and 56% specificity.

In CTEPH patients, a good correlation between maximum peak velocity in the pulmonary arteries and MPAP was found; however, the maximum peak velocity did not enable a reliable estimation of MPAP (KREITNER et al. 2004). This was mainly due to the limited temporal resolution of 110 ms. In the meantime, phase-contrast sequences with a temporal resolution between 10 and 12 ms were implemented for better assessment of pulmonary arterial flow (ABOLMAALI et al. 2004). In CTEPH patients the net forward volume in the pulmonary artery was significantly lower than that in the aorta (KREITNER et al. 2004). This flow difference can be explained by the broncho-systemic shunt volume that is caused by dilatation of bronchial arteries that originate from the aorta and supply the lung parenchyma. In a former study performed on a subset of CTEPH patients, there was a significant correlation between the cross-sectional area of bronchial arteries as determined by helical CT and the shunt volume between the systemic arterial and pulmonary venous circulation as determined by MR phase-contrast flow measurements (LEY et al. 2002). After surgery, there was a complete resolution of this broncho-systemic shunt volume.

6.4.3 Evaluation of the Right Ventricle and the Interventricular Septum

With increasing severity of pulmonary hypertension, there is progressive right ventricular myocardial hypertrophy, dilatation of the right ventricle and atrium, and a reduction in right ventricular contractility. Moreover, changes in right ventricular relaxation time are observed (CASO et al. 2001). As the right ventricular systolic pressure approaches that of the left ventricle, a paradoxical systolic motion of the interventricular septum is observed (Fig. 6.5). However, the progress of right

ventricular dysfunction may vary considerably in time, probably dependent on the duration of the underlying disease and the ability of the right ventricle to adapt to the increased afterload.

Cine MR imaging is an accepted reference standard for the assessment of global and regional left and right ventricular function (ALFAKIH et al. 2003; KUNZ et al. 2005). Furthermore, MRI has shown to be more independent of the experience of the examining physician or technician (PATTYNAMA et al. 1995).

MRI datasets allow for a detailed geometric analysis of the interventricular septal curvature (MOSES and AXEL 2004). In 37 patients with pulmonary hyperten-

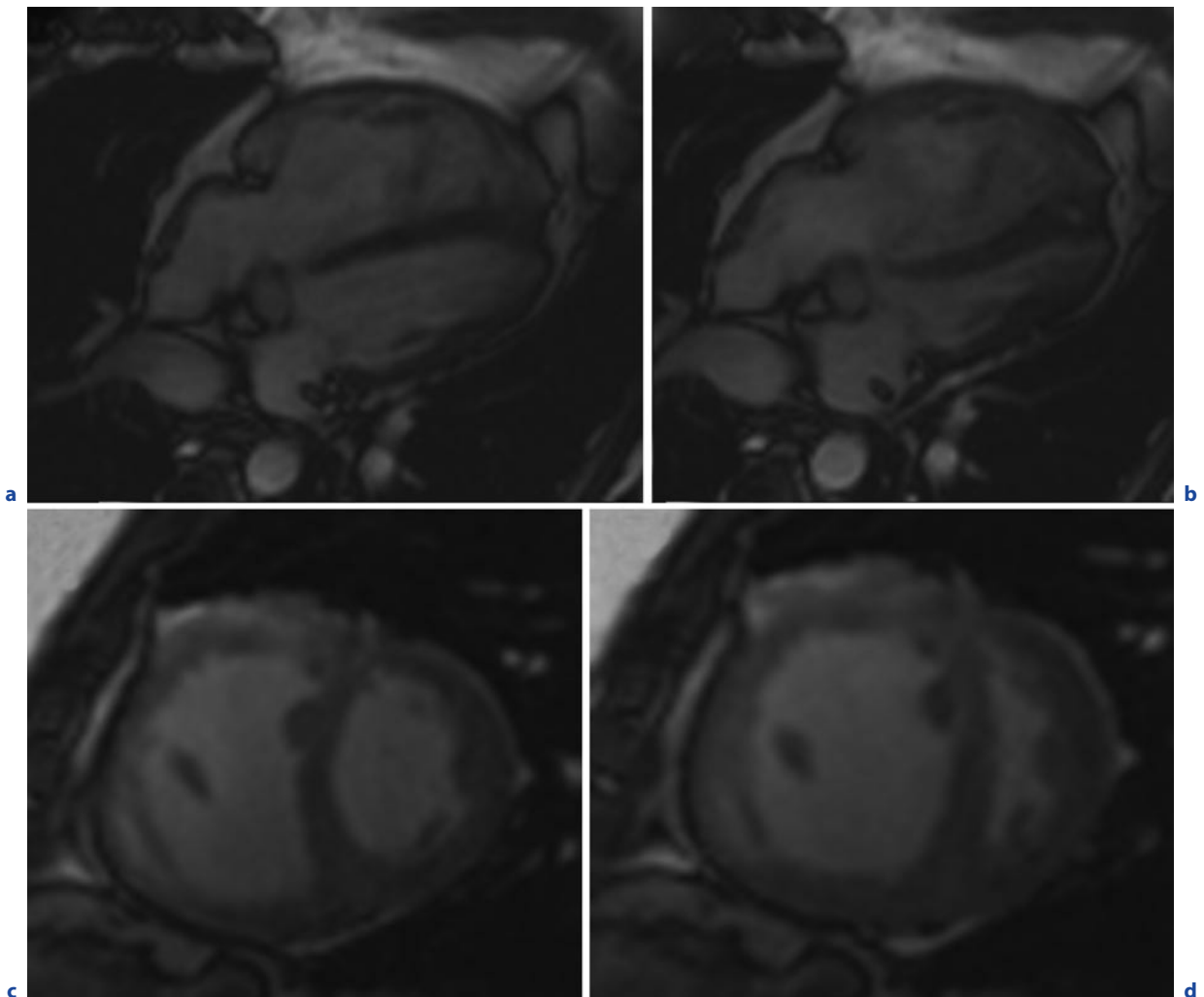


Fig. 6.5a–d. Patient suffering from PAH. Four chamber view of the patient shows a dilated right ventricle with myocardial hypertrophy in the diastolic phase (**a**) and bowing of the interventricular septum towards the left ventricle (paradoxical

septal movement) in the systole (**b**). Short axis view during diastole (**c**) and systole (**d**) even better illustrates the paradoxical septal movement

sion, systolic PAP higher than 67 mmHg may be expected when leftward curvature of the interventricular septum is observed (ROELEVELD et al. 2005a). The left ventricular cavity deformation (expressed as the septal-to-free wall curvature ratio) was assessed in 46 PH patients (systolic PAP > 46 mmHg). A direct linear correlation between the pressure rise in the right ventricle during systole and the curvature ratio was observed ($r = 0.85$, $P < 0.001$) (DELLEGROTtagLIE et al. 2007).

Cine imaging in CTEPH patients typically reveals a hypertrophy and dilatation of the right ventricle, a reduced right ventricular ejection fraction without substantial impairment of left ventricular interventricular septum (KREITNER et al. 2007). After successful PEA, there is a significant improvement or normalization of the right ventricular ejection fraction with the interventricular septum returning to a normal movement in most cases (KREITNER et al. 2004; LEY et al. 2003b). The increased vascular resistance in CTEPH patients goes along with a decreased ejection fraction: the right ventricular ejection fraction showed a good negative correlation with the MPAP. However, analogous to the maximum peak velocity in the same study, a precise estimation of MPAP was not possible. Interestingly, the differences between the pre- and postoperative results of the right ventricular ejection fraction and MPAP showed the best correlation ($r = 0.8$, slope = 0.98).

Another study examined 17 patients with CTEPH, before and at 4 months after PEA using Cine-MRI and invasive pressure measurements. After PEA pulmonary hemodynamics improved, and right and left ventricular volumes and leftward ventricular septal bowing normalized; right ventricular mass decreased significantly ($p < 0.0005$), but did not completely normalize. The change in total pulmonary resistance correlated with the change in right ventricular ejection fraction, right ventricular mass and leftward ventricular septal bowing (REESINK et al. 2007).

At present, cine and phase-contrast MR imaging enable a reliable assessment of the functional improvement of the CTEPH patient after technically successful (KREITNER et al. 2004; LEY et al. 2003b). The absolute estimation of PAP using MRI is actually still not possible (ROELEVELD et al. 2005b).

References

Abolmaali ND, Esmaili A, Feist P, Ackermann H, Requardt M, Schmidt H, Vogl TJ (2004) [Reference values of MRI flow measurements of the pulmonary outflow tract in healthy children]. *Rofo Fortschr Geb Rontgenstr Neuen Bildgeb Verfahr Fortschr Geb Rontgenstr Neuen Bildgeb Verfahr* 176:837–845

Abolmaali N, Seitz U, Esmaili A, Kock M, Radeloff D, Ackermann H, Vogl TJ (2007) Evaluation of a resistance-based model for the quantification of pulmonary arterial hypertension using MR flow measurements. *J Magn Reson Imaging* 26:646–653

Alfakih K, Plein S, Thiele H, Jones T, Ridgway JP, Sivananthan MU (2003) Normal human left and right ventricular dimensions for MRI as assessed by turbo gradient echo and steady-state free precession imaging sequences. *J Magn Reson Imaging* 17:323–329

Altes TA, Eichinger M, Puderbach M (2007) Magnetic resonance imaging of the lung in cystic fibrosis. *Proc Am Thorac Soc* 4:321–327

Antonelli M, Midulla F, Tancredi G, Salvatori FM, Bonci E, Cimino G, Flaishman I (2002) Bronchial artery embolization for the management of nonmassive hemoptysis in cystic fibrosis. *Chest* 121:796–801

Auger WR, Kerr KM, Kim NH, Ben-Yehuda O, Knowlton KU, Fedullo PF (2004) Chronic thromboembolic pulmonary hypertension. *Cardiol Clin* 22:453–466, vii

Baile EM, Ling H, Heyworth JR, Hogg JC, Pare PD (1985) Bronchopulmonary anastomotic and noncoronary collateral blood flow in humans during cardiopulmonary bypass. *Chest* 87:749–754

Barst RJ, McGoon M, Torbicki A, Sitbon O, Krowka MJ, Olschewski H, Gaine S (2004) Diagnosis and differential assessment of pulmonary arterial hypertension. *J Am Coll Cardiol* 43:40S–47S

Bergin CJ, Hauschildt J, Rios G, Belezzuoli EV, Huynh T, Chanick RN (1997) Accuracy of MR angiography compared with radionuclide scanning in identifying the cause of pulmonary arterial hypertension. *AJR Am J Roentgenol* 168:1549–1555

Blyth KG, Groenning BA, Martin TN, Foster JE, Mark PB, Dargie HJ, Peacock AJ (2005) Contrast enhanced-cardiovascular magnetic resonance imaging in patients with pulmonary hypertension. *Eur Heart J* 26:1993–1999

Bugnone AN, Viamonte M Jr, Garcia H (2002) Imaging findings in human immunodeficiency virus-related pulmonary hypertension: report of five cases and review of the literature. *Radiology* 223:820–827

Carvalho P, Anderson DK, Charan NB (2007) Bronchial arterial imaging using helical computed tomography. *Pulm Pharmacol Ther* 20:104–108

Caso P, Galderisi M, Cicala S, Cioppa C, D'Andrea A, Lagioia G, Liccardo B, Martiniello AR, Mininni N (2001) Association between myocardial right ventricular relaxation time and pulmonary arterial pressure in chronic obstructive lung disease: Analysis by pulsed Doppler tissue imaging. *J Am Soc Echocardiogr* 14:970–977

Chaouat A, Bugnet AS, Kadaoui N, Schott R, Enache I, Ducolone A, Ehrhart M, Kessler R, Weitzenblum E (2005) Severe pulmonary hypertension and chronic obstructive pulmonary disease. *Am J Respir Crit Care Med* 172:189–194

Chatterjee K, De Marco T, Alpert JS (2002) Pulmonary hypertension: hemodynamic diagnosis and management. *Arch Intern Med* 162:1925–1933

- Coulden R (2006) State-of-the-art imaging techniques in chronic thromboembolic pulmonary hypertension. *Proc Am Thorac Soc* 3:577–583
- Dartevelle P, Fadel E, Mussot S, Chapelier A, Herve P, de Perrot M, Cerrina J, Ladurie FL, Lehouerou D, Humbert M, Sitbon O, Simonneau G (2004) Chronic thromboembolic pulmonary hypertension. *Eur Respir J* 23:637–648
- Dellegrottaglie S, Sanz J, Poon M, Viles-Gonzalez JF, Sulica R, Goyenechea M, Macaluso F, Fuster V, Rajagopalan S (2007) Pulmonary hypertension: accuracy of detection with left ventricular septal-to-free wall curvature ratio measured at cardiac MR. *Radiology* 243:63–69
- Egermayer P, Peacock AJ (2000) Is pulmonary embolism a common cause of chronic pulmonary hypertension? Limitations of the embolic hypothesis. *Eur Respir J* 15:440–448
- Frazier AA, Galvin JR, Franks TJ, Rosado-de-Christenson ML (2000) From the archives of the AFIP: pulmonary vasculature: hypertension and infarction. *RadioGraphics* 20:491–524
- Galie N, Torbicki A, Barst R, Dartevelle P, Haworth S, Higenbottam T, Olschewski H, Peacock A, Pietra G, Rubin LJ, Simonneau G, Priori SG, Garcia MA, Blanc JJ, Budaj A, Cowie M, Dean V, Deckers J, Burgess EF, Lekakis J, Lindahl B, Mazzotta G, McGregor K, Morais J, Oto A, Smiseth OA, Barbera JA, Gibbs S, Hoeper M, Humbert M, Naeije R, Pepke-Zaba J (2004) Guidelines on diagnosis and treatment of pulmonary arterial hypertension. The Task Force on Diagnosis and Treatment of Pulmonary Arterial Hypertension of the European Society of Cardiology. *Eur Heart J* 25:2243–2278
- Gatehouse PD, Keegan J, Crowe LA, Masood S, Mohiaddin RH, Kreitner KF, Firmin DN (2005) Applications of phase-contrast flow and velocity imaging in cardiovascular MRI. *Eur Radiol* 15:2172–2184
- Green FH, Butt JC, James AL, Carroll NG (2006) Abnormalities of the bronchial arteries in asthma. *Chest* 130:1025–1033
- Hartmann IJ, Remy-Jardin M, Menchini L, Teisseire A, Khalil C, Remy J (2007) Ectopic origin of bronchial arteries: assessment with multidetector helical CT angiography. *Eur Radiol* 17:1943–1953
- Hoeper MM, Kramm T, Wilkens H, Schulze C, Schafers HJ, Welte T, Mayer E (2005) Bosentan therapy for inoperable chronic thromboembolic pulmonary hypertension. *Chest* 128:2363–2367
- Iwasawa T, Takahashi H, Ogura T, Asakura A, Gotoh T, Kagei S, Nishimura J, Obara M, Inoue T (2007) Correlation of lung parenchymal MR signal intensity with pulmonary function tests and quantitative computed tomography (CT) evaluation: a pilot study. *J Magn Reson Imaging* 26:1530–1536
- Jamieson SW, Kapelanski DP (2000) Pulmonary endarterectomy. *Curr Probl Surg* 37:165–252
- Jardim C, Rochitte CE, Humbert M, Rubinfeld G, Jasinowolinski D, Carvalho CR, Souza R (2007) Pulmonary artery distensibility in pulmonary arterial hypertension: an MRI pilot study. *Eur Respir J* 29:476–481
- Jung JI, Park SH, Lee JM, Hahn ST, Kim KA (2000) MR characteristics of progressive massive fibrosis. *J Thorac Imaging* 15:144–150
- Kauczor H-U, Schwickert HC, Mayer E, Schweden F, Schild HH, Thelen M (1994) Spiral CT of bronchial arteries in chronic thromboembolism. *J Comput Assist Tomogr* 18:855–861
- Kluge A, Gerriets T, Lange U, Bachmann G (2005) MRI for short-term follow-up of acute pulmonary embolism. Assessment of thrombus appearance and pulmonary perfusion: a feasibility study. *Eur Radiol* 15:1969–1977
- Kreitner KF, Ley S, Kauczor HU, Mayer E, Kramm T, Pitton MB, Krummenauer F, Thelen M (2004) Chronic thromboembolic pulmonary hypertension: pre- and postoperative assessment with breath-hold MR imaging techniques. *Radiology* 232:535–543
- Kreitner KF, Kunz RP, Ley S, Oberholzer K, Neeb D, Gast KK, Heussel CP, Eberle B, Mayer E, Kauczor HU, Duber C (2007) Chronic thromboembolic pulmonary hypertension – assessment by magnetic resonance imaging. *Eur Radiol* 17:11–21
- Kunz RP, Oellig F, Krummenauer F, Oberholzer K, Romanechen B, Vomweg TW, Horstick G, Hayes C, Thelen M, Kreitner KF (2005) Assessment of left ventricular function by breath-hold cine MR imaging: comparison of different steady-state free precession sequences. *J Magn Reson Imaging* 21:140–148
- Kuriyama K, Gamsu G, Stern RG, Cann CE, Herfkens RJ, Brundage BH (1984) CT-determined pulmonary artery diameters in predicting pulmonary hypertension. *Invest Radiol* 19:16–22
- Laffon E, Laurent F, Bernard V, De Boucaud L, Ducassou D, Marthan R (2001) Noninvasive assessment of pulmonary arterial hypertension by MR phase-mapping method. *J Appl Physiol* 90:2197–2202
- Ley S, Kreitner K-F, Morgenstern I, Thelen M, Kauczor H-U (2002) Bronchopulmonary shunts in patients with chronic thromboembolic pulmonary hypertension: evaluation by helical CT and MR imaging. *AJR Am J Roentgenol* 179:1209–1215
- Ley S, Kauczor HU, Heussel CP, Kramm T, Mayer E, Thelen M, Kreitner KF (2003a) Value of contrast-enhanced MR angiography and helical CT angiography in chronic thromboembolic pulmonary hypertension. *Eur Radiol* 13:2365–2371
- Ley S, Kramm T, Kauczor HU, Mayer E, Heussel CP, Thelen M, Kreitner KF (2003b) [Pre- and postoperative assessment of hemodynamics in patients with chronic thromboembolic pulmonary hypertension by MR techniques]. *Rofu Fortschr Geb Rontgenstr Neuen Bildgeb Verfahr* 175:1647–1654
- Ley S, Kreitner K-F, Fink C, Heussel CP, Borst MM, Kauczor H-U (2004) Assessment of pulmonary hypertension by CT and MR imaging. *Eur Radiol* 14:359–368

- Ley S, Fink C, Zaporozhan J, Borst MM, Meyer FJ, Puderbach M, Eichinger M, Plathow C, Grunig E, Kreitner KF, Kauczor HU (2005) Value of high spatial and high temporal resolution magnetic resonance angiography for differentiation between idiopathic and thromboembolic pulmonary hypertension: initial results. *Eur Radiol* 15:2256–2263
- Ley S, Mereles D, Puderbach M, Gruenig E, Schock H, Eichinger M, Ley-Zaporozhan J, Fink C, Kauczor HU (2007a) Value of MR phase-contrast flow measurements for functional assessment of pulmonary arterial hypertension. *Eur Radiol* 17:1892–1897
- Ley S, Mereles D, Risse F, Grunig E, Ley-Zaporozhan J, Tecer Z, Puderbach M, Fink C, Kauczor HU (2007b) Quantitative 3D pulmonary MR-perfusion in patients with pulmonary arterial hypertension: correlation with invasive pressure measurements. *Eur J Radiol* 61:251–255
- Ley S, Unterhinninghofen R, Ley-Zaporozhan J, Schenk JP, Kauczor HU, Szabo G (2008) Validation of MR phase-contrast flow measurements in the main pulmonary artery and aorta using perivascular ultrasound in a large animal model. *Invest Radiol* 43(6):421–426
- Ley-Zaporozhan J, Ley S, Kauczor HU (2007) Proton MRI in COPD. *COPD* 4:55–65
- Ley-Zaporozhan J, Ley S, Kauczor HU (2008) Morphological and functional imaging in COPD with CT and MRI: present and future. *Eur Radiol* 18:510–521
- Madani MM, Jamieson SW (2006) Technical advances of pulmonary endarterectomy for chronic thromboembolic pulmonary hypertension. *Semin Thorac Cardiovasc Surg* 18:243–249
- McLaughlin VV, McGoon MD (2006) Pulmonary arterial hypertension. *Circulation* 114:1417–1431
- McNeil K, Dunning J (2007) Chronic thromboembolic pulmonary hypertension (CTEPH). *Heart* 93:1152–1158
- Moses DA, Axel L (2004) Quantification of the curvature and shape of the interventricular septum. *Magn Reson Med* 52:154–163
- Nael K, Fenchel M, Krishnam M, Finn JP, Laub G, Ruehm SG (2007) 3.0 Tesla high spatial resolution contrast-enhanced magnetic resonance angiography (CE-MRA) of the pulmonary circulation: initial experience with a 32-channel phased array coil using a high relaxivity contrast agent. *Invest Radiol* 42:392–398
- Nagendran J, Michelakis E (2007) MRI: one-stop shop for the comprehensive assessment of pulmonary arterial hypertension? *Chest* 132:2–5
- Nikolaou K, Schoenberg SO, Attenberger U, Scheidler J, Dietrich O, Kuehn B, Rosa F, Huber A, Leuchte H, Baumgartner R, Behr J, Reiser MF (2005) Pulmonary arterial hypertension: diagnosis with fast perfusion MR imaging and high-spatial-resolution MR angiography—preliminary experience. *Radiology* 236:694–703
- Oberholzer K, Romaneehsen B, Kunz P, Kramm T, Thelen M, Kreitner KF (2004) [Contrast-enhanced 3D MR angiography of the pulmonary arteries with integrated parallel acquisition technique (iPAT) in patients with chronic-thromboembolic pulmonary hypertension CTEPH – sagittal or coronal acquisition?]. *Rofo Fortschr Geb Rontgenstr Neuen Bildgeb Verfahr Fortschr Geb Rontgenstr Neuen Bildgeb Verfahr* 176:605–609
- Ohno Y, Hatabu H, Murase K, Higashino T, Kawamitsu H, Watanabe H, Takenaka D, Fujii M, Sugimura K (2004) Quantitative assessment of regional pulmonary perfusion in the entire lung using three-dimensional ultrafast dynamic contrast-enhanced magnetic resonance imaging: Preliminary experience in 40 subjects. *J Magn Reson Imaging* 20:353–365
- Ohno Y, Hatabu H, Murase K, Higashino T, Nogami M, Yoshikawa T, Sugimura K (2007) Primary pulmonary hypertension: 3D dynamic perfusion MRI for quantitative analysis of regional pulmonary perfusion. *AJR Am J Roentgenol* 188:48–56
- Pattynama PMT, Lamb HJ, van der Velde EA, van der Geest RJ, van der Wall EE, de Roos A (1995) Reproducibility of MRI-derived measurements of right ventricular volumes and myocardial mass. *J Magn Reson Imaging* 13:53–63
- Peacock A, Simonneau G, Rubin L (2006) Controversies, uncertainties and future research on the treatment of chronic thromboembolic pulmonary hypertension. *Proc Am Thorac Soc* 3:608–614
- Pengo V, Lensing AW, Prins MH, Marchiori A, Davidson BL, Tiozzo F, Albanese P, Biasiolo A, Pegoraro C, Iliceto S, Prandoni P (2004) Incidence of chronic thromboembolic pulmonary hypertension after pulmonary embolism. *N Engl J Med* 350:2257–2264
- Perloff JK, Hart EM, Greaves SM, Miner PD, Child JS (2003) Proximal pulmonary arterial and intrapulmonary radiologic features of Eisenmenger syndrome and primary pulmonary hypertension. *Am J Cardiol* 92:182–187
- Presberg KW, Dincer HE (2003) Pathophysiology of pulmonary hypertension due to lung disease. *Curr Opin Pulm Med* 9:131–138
- Primack SL, Mayo JR, Hartman TE, Miller RR, Muller NL (1994) MRI of infiltrative lung disease: comparison with pathologic findings. *J Comput Assist Tomogr* 18:233–238
- Prince MR, Alderson PO, Sostman HD (2004) Chronic pulmonary embolism: combining MR angiography with functional assessment. *Radiology* 232:325–326
- Provencher S, Jais X, Yaici A, Sitbon O, Humbert M, Simonneau G (2005) Clinical challenges in pulmonary hypertension: Roger S. Mitchell lecture. *Chest* 128:622S–628S
- Puis L, Vandezande E, Vercaemst L, Janssens P, Taverniers Y, Foulon M, Demeyere R, Delcroix M, Daenen W (2005) Pulmonary thromboendarterectomy for chronic thromboembolic pulmonary hypertension. *Perfusion* 20:101–108
- Puri A, McGoon MD, Kushwaha SS (2007) Pulmonary arterial hypertension: current therapeutic strategies. *Nat Clin Pract Cardiovasc Med* 4:319–329

- Reesink HJ, Marcus JT, Tulevski II, Jamieson S, Kloek JJ, Vonk Noordegraaf A, Bresser P (2007) Reverse right ventricular remodeling after pulmonary endarterectomy in patients with chronic thromboembolic pulmonary hypertension: utility of magnetic resonance imaging to demonstrate restoration of the right ventricle. *J Thorac Cardiovasc Surg* 133:58–64
- Remy-Jardin M, Louveigny S, Remy J, Artaud D, Deschildre F, Bauchart JJ, Thery C, Duhamel A (1997) Acute central thromboembolic disease: posttherapeutic follow-up with spiral CT angiography. *Radiology* 203:173–180
- Remy-Jardin M, Bouaziz N, Dumont P, Brillet PY, Bruzzi J, Remy J (2004) Bronchial and nonbronchial systemic arteries at multi-detector row CT angiography: comparison with conventional angiography. *Radiology* 233:741–749
- Robertson HT, Jindal SK, Lakshminarayan S, Albert R, Kirk W, Hlastala MP, Butler J (1984) Gas exchange properties of the bronchial circulation in a dog lobe maintained in zone 1 conditions. *Am Rev Respir Dis* 129:A229
- Roeleveld RJ, Marcus JT, Faes TJ, Gan TJ, Boonstra A, Postmus PE, Vonk-Noordegraaf A (2005a) Interventricular septal configuration at mr imaging and pulmonary arterial pressure in pulmonary hypertension. *Radiology* 234:710–717
- Roeleveld RJ, Marcus JT, Boonstra A, Postmus PE, Marques KM, Bronzwaer JG, Vonk-Noordegraaf A (2005b) A comparison of noninvasive MRI-based methods of estimating pulmonary artery pressure in pulmonary hypertension. *J Magn Reson Imaging* 22:67–72
- Rosenkranz S (2007) Pulmonary hypertension: current diagnosis and treatment. *Clin Res Cardiol* 96:527–541
- Ryu JH, Krowka MJ, Pellikka PA, Swanson KL, McGoon MD (2007) Pulmonary hypertension in patients with interstitial lung diseases. *Mayo Clin Proc* 82:342–350
- Sanz J, Kuschnir P, Rius T, Salguero R, Sulica R, Einstein AJ, Dellegrottaglie S, Fuster V, Rajagopalan S, Poon M (2007) Pulmonary arterial hypertension: noninvasive detection with phase-contrast MR imaging. *Radiology* 243:70–79
- Scharf SM, Iqbal M, Keller C, Criner G, Lee S, Fessler HE (2002) Hemodynamic characterization of patients with severe emphysema. *Am J Respir Crit Care Med* 166:–314–322
- Shimoda LA, Sham JS, Sylvester JT (2000) Altered pulmonary vasoreactivity in the chronically hypoxic lung. *Physiol Res* 49:549–560
- Simonneau G, Galie N, Rubin LJ, Langleben D, Seeger W, Domenighetti G, Gibbs S, Lebec D, Speich R, Beghetti M, Rich S, Fishman A (2004) Clinical classification of pulmonary hypertension. *J Am Coll Cardiol* 43:5S–12S
- Taichman DB, Mandel J (2007) Epidemiology of pulmonary arterial hypertension. *Clin Chest Med* 28:1–22, vii
- Thabut G, Dauriat G, Stern JB, Logeart D, Levy A, Marrash-Chahla R, Mal H (2005) Pulmonary hemodynamics in advanced COPD candidates for lung volume reduction surgery or lung transplantation. *Chest* 127:1531–1536
- Tuder RM, Marecki JC, Richter A, Fijalkowska I, Flores S (2007) Pathology of pulmonary hypertension. *Clin Chest Med* 28:23–42, vii
- Wartski M, Collignon MA (2000) Incomplete recovery of lung perfusion after 3 months in patients with acute pulmonary embolism treated with antithrombotic agents. THESEE Study Group. Tinzaparin ou Heparin Standard: Evaluation dans l'Embolie Pulmonaire Study. *J Nucl Med* 41:1043–1048
- Weitzenblum E, Chaouat A (2005) Severe pulmonary hypertension in COPD: is it a distinct disease? *Chest* 127:1480–1482
- Wright JL, Levy RD, Churg A (2005) Pulmonary hypertension in chronic obstructive pulmonary disease: current theories of pathogenesis and their implications for treatment. *Thorax* 60:605–609

SEBASTIAN LEY and JULIA LEY-ZAPOROZHAN

CONTENTS

- 7.1 **Imaging of Congenital Heart Disease** 122
- 7.2 **Congenital Pulmonary Vascular Diseases** 124
 - 7.2.1 Congenital Pulmonary Arterial Disorders 124
 - 7.2.1.1 Stenosis of the Pulmonary Valve, the Pulmonary Artery, and its Branches 124
 - 7.2.1.2 Pulmonary Sling (Origin of the Left Pulmonary Artery from the Right Pulmonary Artery) 126
 - 7.2.1.3 Anomalous Origin of One Pulmonary Artery 127
 - 7.2.1.4 Tetralogy of Fallot or Pulmonary Atresia with VSD or Hypoplastic Pulmonary Artery 128
 - 7.2.1.5 Pulmonary Sequestration 128
 - 7.2.1.6 Single-Ventricle Morphology 129
 - 7.2.1.7 Transposition of the Great Arteries 130
 - 7.2.2 Congenital Pulmonary Venous Disorders 131
 - 7.2.3 Pulmonary Arteriovenous Malformations 132
- 7.3 **Acquired Pulmonary Venous Disorders** 133
- 7.4 **Tumors of the Pulmonary Vessels** 133
 - 7.4.1 Central Pulmonary Arteries: Leiomyosarcoma 133
 - 7.4.2 Peripheral Pulmonary Arteries: Pulmonary Capillary Hemangioma 134
- 7.5 **Extravascular Disorders** 134
- References** 135

KEY POINTS

Pulmonary arterial vascular diseases can be either congenital or acquired. The spectrum of the congenital pulmonary vascular malformations includes abnormalities of the pulmonary arterial system and partial or total abnormal pulmonary venous return. Diseases of the pulmonary vessels, other than thromboembolic diseases (refer to Chap. 6), are either primary tumors of the vessels or external compression. The following sections are organized accordingly, covering congenital pulmonary vascular malformations, arteriovenous malformations and other diseases of the pulmonary vasculature. With increasing experience and development of new surgical techniques, more and more complex forms of congenital cardiovascular diseases can be corrected. All surgical approaches significantly benefit from detailed three-dimensional (3D) presentation of the complex anatomy, which can be acquired using MRI.

S. LEY, MD

Department of Pediatric Radiology, University Hospital Heidelberg, Im Neuenheimer Feld 430, 69120 Heidelberg, Germany

J. LEY-ZAPOROZHAN, MD

Department of Pediatric Radiology, University Hospital Heidelberg, Im Neuenheimer Feld 430, 69120 Heidelberg, Germany

7.1

Imaging of Congenital Heart Disease

The heterogeneity of anatomy, age, surgical procedure, and institutional management protocols contradicts development of clear imaging guidelines (BHAT ET SAHN 2004).

Echocardiography is the primary examination in neonates, infants, and young children, and therefore the most frequently used noninvasive technique to examine cardiac morphology and function. In older patients, particularly those with complex or surgically corrected malformations, information acquired with transthoracic echocardiography may not be satisfactory. Scar, bone, or lung tissue and chest deformations interfere with small acoustic windows. Transesophageal echocardiography obviously provides a better field of view in adults, especially since biplanar probes have become available. Still, echocardiography is often not sufficient in imaging of the pulmonary arteries.

Conventional digital catheter angiography (DA) has long been the gold standard for the evaluation of cardiac anatomy and function. Additionally, it is the only method to determine pulmonary vascular pressure and oxygen saturation. However, DA is invasive and has a considerable complication rate, and requires the use of ionizing radiation and intra-arterial administration of iodinated contrast media (HOEPER et al. 2006).

Due to fast acquisition of high-spatial resolution images, allowing for 3D postprocessing, MDCT is actually a very common imaging modality. However, the lack of hemodynamic measurements, application of radiation, and iodinated contrast media makes it an unfavorable imaging technique for pediatric patients, as it is known that children are more sensitive to the effects of ionizing radiation than adults are.

With the technical development of MRI, this technique has increasingly been used for noninvasive assessment of the pulmonary vasculature (EICHHORN et al. 2004; SIMONETTI and COOK 2006). As the pulmonary arteries are rarely affected alone, it is important to examine the heart, the pulmonary, and the systemic vasculature in the first workup with a focus on the vascular diameters for surgical connectivity. If only the pulmonary arteries are affected, then contrast-enhanced techniques are well suited for sufficient imaging. If the placement of a conduit is considered, the most important task for imaging is to preoperatively provide accurate luminal diameters in order to determine the prospective size of the conduits. Postoperatively, conduit stenosis or insufficiency has to be ruled out frequently. In case of slow and/or turbulent flow, contrast-enhanced imaging may

be quite difficult, as the contrast material might not fill the vascular lumen homogeneously. The visualization of all the vascular pathologies in complex congenital heart disease (CHD) is still a challenge for the radiological techniques CT and MRI. In these cases, the contrast bolus is often diluted due to intracardial or extracardial shunts with mixing of non-contrast-enhanced blood. Severe imaging artifacts can occur in CT and MRI after surgical and interventional procedures due to metal artifacts, such as conduits with valves, coil material, stents, from former interventions (MAINTZ et al. 2003).

Today, cardiovascular MRI is most often performed using 1.5-T scanners, due to the optimized coil and sequence technology (NAGANAWA et al. 2004). The increased specific absorption rate at high field MRI (3 T) is still a challenge for imaging using the standard steady-state free-precession techniques (GILMORE et al. 2004).

MRI in children younger than of 5 years usually requires some form of sedation to tolerate the examination. Subsequently, free-breathing techniques are necessary with increasing examination times. To acquire sharp images of the pulmonary vasculature, single-shot techniques like half-Fourier single-shot turbo spin echo (HASTE) or steady-state free-precession (SSFP) sequences are utilized (Fig. 7.1) (WEISS et al. 2005). Combining those with a saturation pulse, the vessels are dark and can be well delineated. However, they can still be hazy, and the saturation is not perfect in case of turbulent flow. Turbo spin echo (TSE) sequences are also fast imaging techniques with sharp delineation of the vessels (WEISS et al. 2005). For reduction of blurriness, averaging of the sequences (e.g., three averages) may be preferable. Usual acquisition times for a three-times-averaged TSE sequence of the thorax are 3 min. Using spin echo sequences, the internal vascular diameter is underestimated compared to DA. In a phantom study, an underestimation of 10–20% of linear dimensions was found (HOLMQUIST et al. 2001).

Another possible solution for visualization of the vasculature is the use of time-resolved MR angiography techniques. The spatial resolution is reduced ($1.4 \times 1.4 \times 2.0 \text{ mm}^3$) to increase temporal resolution (6 s per 3D data set) (FINK et al. 2003). Thus, motion artifacts are minimized, and a separation of arteries and veins can be achieved. Also, due to the time resolved approach, contrast media timing is not necessary.

The low body weight (b.w.) of children makes it necessary to apply 0.2 mmol/kg/b.w. of a 0.5 M contrast media (MACGOWAN et al. 2005). However, for evaluation of subtle stenoses, time-resolved MR angiography may be not sufficient. In a study including children from 2 days to 5 years, the delineation of the vascular lumen was therefore further increased by injection of

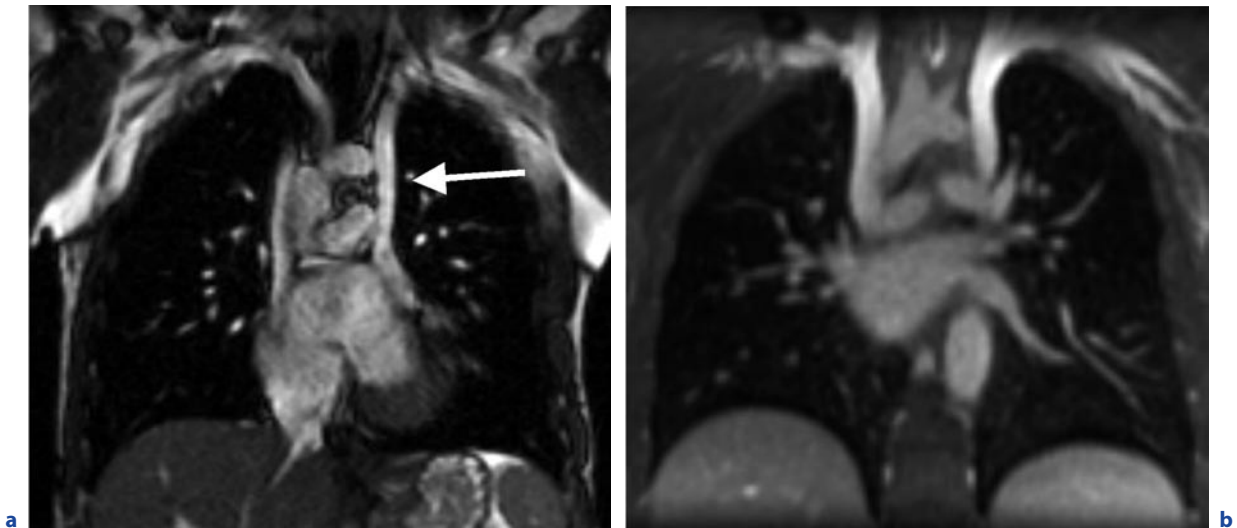


Fig. 7.1a,b. Steady state free-precession (SSFP) sequence (a) compared with a T1 GRE (VIBE) (b) acquired in coronal orientation. Images show a persistent left vena cava superior

(arrow). Note the good inherent vascular signal of the SSFP technique. These fast-acquisition techniques allow for a rapid evaluation of vascular pathologies

0.2 mmol/kg/b.w. of a 1 M contrast media (FRIES et al. 2005). However, the use of this contrast agent (e.g., gadobenate dimeglumine [Gd-BOPTA]) in children is off-label and requires special permission (GRIST and THORNTON 2005).

Especially in children with unknown CHD, time-resolved MR angiography also allows for characterization of the pulmonary perfusion, due to the time course of contrast enhancement in the lung parenchyma (i.e., pulmonary arterial or systemic) (BOLL et al. 2005).

In patients compliant in performing a breath-hold, acquisition of high-spatial-resolution angiography datasets ($1.2 \times 1.0 \times 1.6 \text{ mm}^3$) can be performed (LEY et al. 2005). Using this technique, even subtle variations in luminal diameters can be assessed.

A volume interpolated breath-hold technique (VIBE) (breath-hold preferred, averaging possible) allows for high-spatial-resolution T1-weighted imaging. After contrast media injection, it can be used to demonstrate the relationship between airways and the pulmonary vasculature (BIEDERER et al. 2003). This technique was already successfully combined with cardiac and respiratory gating and used in non-contrast-enhanced coronary arterial imaging in adults (JHOOTI et al. 2000). Due to double gating, this technique may be promising for pediatric imaging.

Another technique, also adapted from coronary imaging, is a free-breathing 3D double-slab fast imaging with steady-precession MR angiography (3D FISP MRA) (SORENSEN et al. 2004, 2005). The resolution with

a voxel size of $1.25 \times 1.25 \times 1.25 \text{ mm}^3$ enables excellent diagnosis, even in infants with vascular rings and slings (GREIL et al. 2005).

Major aortopulmonary collateral arteries (MAPCA) can also be visualized by MRA, but only if these arteries are markedly dilated (BOECHAT et al. 2005).

The creation of multiplanar reformats is necessary to accurately assess the vascular diameter after surgery (SORENSEN et al. 2005). After arterial switch operation (ASO) for complete transposition of the great arteries in some cases, narrowing of pulmonary arteries is associated with oval vessel diameters. In these patients, special attention should be focused on the central part of the pulmonary arteries, and MPRs have to be performed. Conventional angiography should only be performed when intervention is planned (WEISS et al. 2005).

Beside good visualization of the vasculature, MRI is capable of assessing the blood flow through arteries and veins by phase-contrast flow measurements (ROMAN et al. 2005; GATEHOUSE et al. 2005). This enables quantification of shunt volumes and can be used to identify stenosis by an increased peak velocity. The pressure gradient across a stenosis can be calculated with the modified Bernoulli equation (VARAPRASATHAN et al. 2002). However, quantitative pressure estimates of the pulmonary arterial system are still not possible using MRI. Therefore, invasive pressure measurements are still mandatory (NAKANISHI 2005).

A basic MRI examination protocol should include a contrast-enhanced angiography and techniques for

non-contrast-enhanced visualization of the pulmonary vasculature. The FOV should cover the entire thorax of the patient to include secondary anomalies not suspected before. Overall, MRI enables good visualization of the pulmonary vasculature with and without contrast media. It is capable of acquiring functional cardiac information or blood flow distribution to the pulmonary and systemic circulation. As the main drawback, rather long examination times and the use of sedatives are to be mentioned. A typical MR examination protocol is the following suggested MRI protocol for pediatric patients with proven or suggested congenital vascular disease (taken from LEY et al. 2007). (Note that these techniques are aimed for optimal visualization of the pulmonary arteries and include no functional cardiac information.):

- Localizer
- HASTE coronal dark blood (ECG and respiratory gated)
- HASTE transversal dark blood (ECG and respiratory gated)
- T1 TSE transversal dark blood (ECG gated, breath-hold or three averages)
- T1 TSE coronal dark blood (ECG gated, breath-hold or three averages)
- Time-resolved angiography (4 s per 3D dataset)
- Postcontrast T1 VIBE (breath-hold or three averages)
- 3D True fast imaging with steady-state precession (TrueFISP) coronal or transversal with ECG and respiratory gating ($1.0 \times 1.0 \times 1.0 \text{ mm}^3$)
- Phase-contrast flow measurements (pulmonary trunk, right and left pulmonary artery, and ascending aorta)

Recent advances in rapid MR imaging have enabled fully MR-guided intravascular interventions in closed-bore clinical whole-body MR scanners (SEQUEIROS et al. 2005). Dedicated active catheters and fast-imaging sequences with automatic slice positioning in combination with a dedicated user interface for intravascular procedures are a mandatory prerequisite for safe application of the technique (BOCK et al. 2006). First reports in animal models demonstrate the possibility of placing, i.e., Amplatzer® septal occluders under MRI guidance (RICKERS et al. 2003). MRI guidance of percutaneous transluminal balloon angioplasty (PCTA) of aortic coarctation was shown as a suitable alternative to conventional fluoroscopy for catheter-based treatment in a pilot study with patients (KRUEGER et al. 2006).

Coils, stents, occluders, and clips lead to enormous artifacts, making it sometimes impossible to perform MRI. After catheter interventional therapy for patent

ductus arteriosus, left pulmonary arterial stenosis may occur. Therefore, MDCT using a low-dose protocol should be performed to rule out pulmonary stenosis. Because of artifacts, echocardiography often does not provide enough information in this particular condition. DA should only be considered if a pressure measurement is necessary.

7.2

Congenital Pulmonary Vascular Diseases

CHD is the collective term for congenital malformations affecting the heart, pulmonary arteries, and aorta. Most cases of CHD are thought to be multifactorial and a result from a combination of genetic predisposition and environmental stimulus. Due to the complex nature of CHD, single numbers for uniform types of malformations affecting the pulmonary arteries are not known. In general, CHD occurs in 0.5–0.8% of live births, indicating that about 1.5 million children are born with a cardiac malformation worldwide each year (HOFFMAN 1996). The spectrum of anatomic malformations is reaching from relatively simple to very complex entities. About 2–3 out of 1,000 newborn infants will become symptomatic with heart disease in the first year of life. Nowadays, the diagnosis is most often established within the first month (BERNSTEIN 2004).

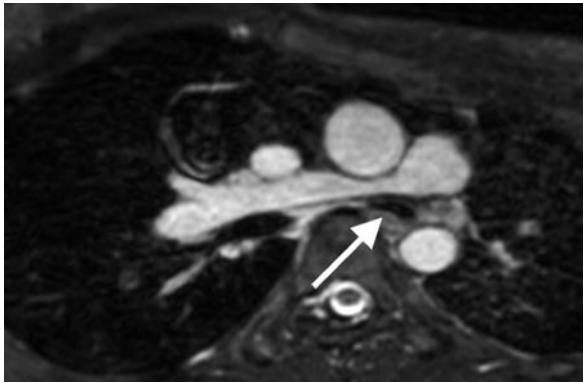
7.2.1

Congenital Pulmonary Arterial Disorders

7.2.1.1

Stenosis of the Pulmonary Valve, the Pulmonary Artery, and its Branches

The most common right ventricular outflow obstruction is isolated pulmonary stenosis, which accounts for 7–10% of all CHD. Stenosis may occur anywhere along the major branches of the pulmonary arteries, and ranges from mild to severe and from circumscribed to extensive forms (Fig. 7.2). Frequently, these anomalies are associated with other types of CHD, including tetralogy of Fallot (TOF), ventricular septal defect (VSD) and atrial septal defect (ASD). Moderate stenosis of the pulmonary arteries can be treated with repeated balloon angioplasty. In case of severe stenosis or hypoplasia of the pulmonary artery (Fig. 7.3), surgical interposition of patch material or a conduit becomes necessary. After this procedure, stenosis may occur at any structure within or in the neighborhood of the central pulmonary

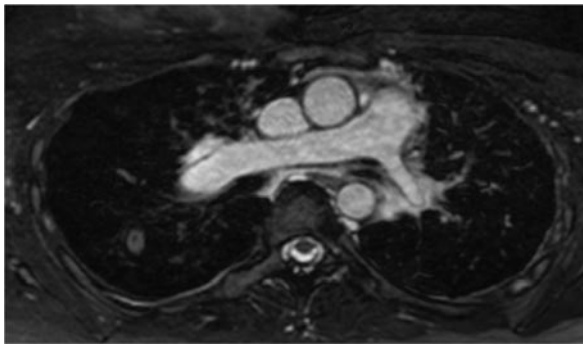


a

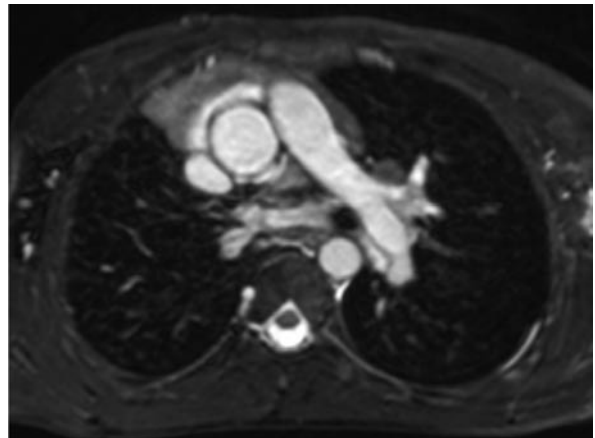


b

Fig. 7.2a,b. Stenosis of the right pulmonary artery in a 12-year-old girl. Images were acquired using an ECG-gated and respiratory-triggered 3D SSFP technique with isotropic 1 mm spatial resolution. Primary image acquisition was axial (**a**); however, the datasets allow for any reformation, like sagittal (**b**). The *arrow* points at the subsequent stenosis of the left main bronchi



a



c



b

Fig. 7.3a–e. Hypoplastic left pulmonary artery. (**a**) ECG-gated and respiratory-triggered 3D SSFP technique with isotropic 1-mm spatial resolution. Note the size difference between the right (normal) and hypoplastic left pulmonary artery. (**b**) High-spatial-resolution contrast-enhanced MRA showing the difference in blood distribution between both lungs. (**c–e**) Another patient with an aplasia of the right pulmonary artery. 3D SSFP technique (**c**) and contrast-enhanced time-resolved (**d, e**) (see next page)

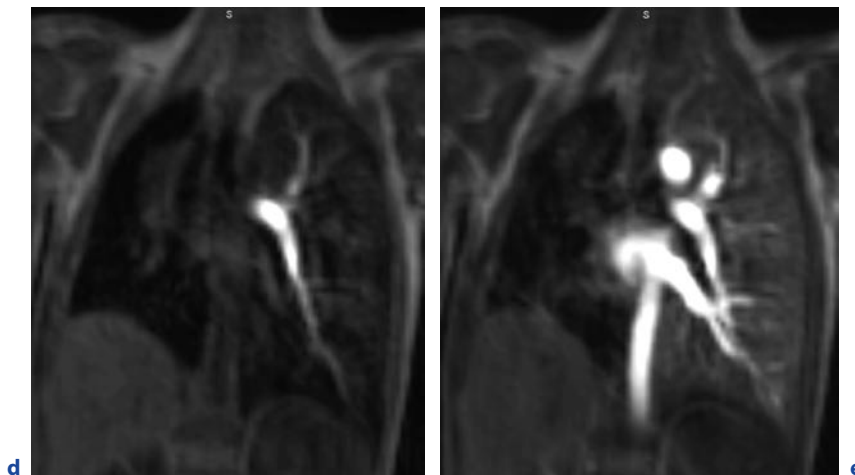


Fig. 7.3a–e. (continued) Hypoplastic left pulmonary artery. (c–e) Another patient with an aplasia of the right pulmonary artery. 3D SSFP technique (d, e) angiographic images nicely depict the lack of perfusion of the right lung as well as a smaller pulmonary volume on the right side

artery or the conduit. Therefore, visualization of the internal lumen of the conduit, its wall structure, and the anastomosis to the left and right pulmonary artery is important in the follow-up.

Circumscribed malformations of the pulmonary artery and its post interventional course can be visualized well using high-resolution MRA. Additional information about valve regurgitation can be obtained by MR phase-contrast imaging (GATEHOUSE et al. 2005). In a large study on 28 infants aged younger than 3 months with CHD mainly affecting the PA or RVOT, MRA proved to be in consensus with DA. However, in this study, a high dose of contrast media of 0.4–0.5 mmol/kg/b.w. was applied, and scanning was performed in suspended mechanical ventilation. However, no adverse

contrast media effects were found, and the pulmonary vessels were sharply delineated (PRAKASH et al. 2007).

7.2.1.2 Pulmonary Sling (Origin of the Left Pulmonary Artery from the Right Pulmonary Artery)

The left pulmonary artery arises aberrantly from the right pulmonary artery and runs behind the trachea and esophagus to the left side (Fig. 7.4) (BERDON 2000). This situation leads either to an acute and severe airway compression (infants) or to signs of chronic obstructive lung disease or asthma (childhood and young adults). In

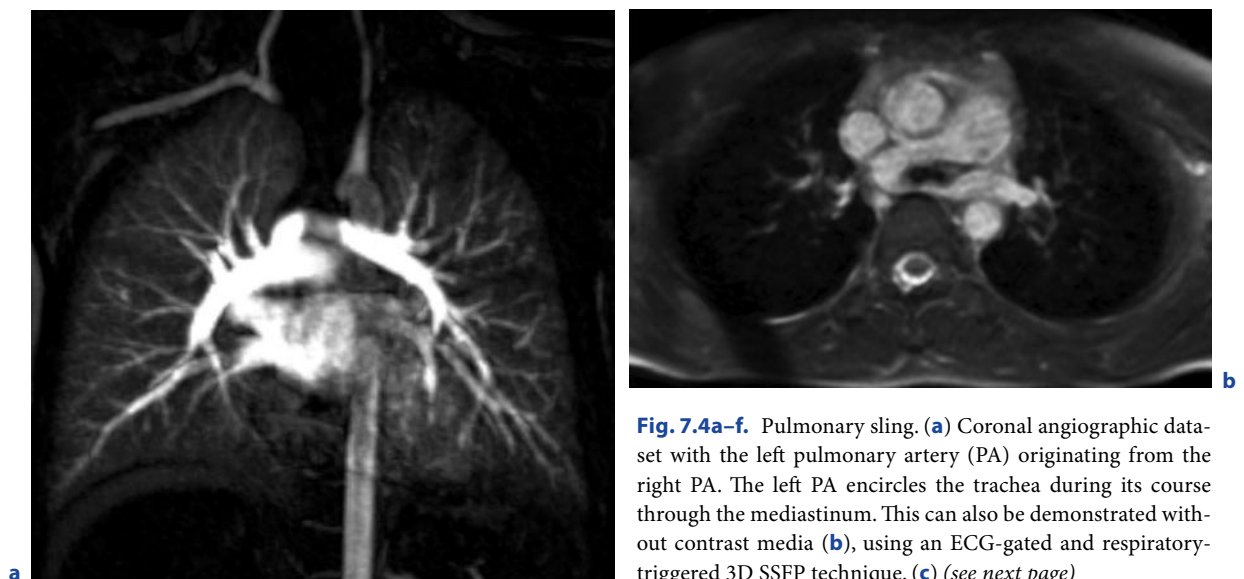


Fig. 7.4a–f. Pulmonary sling. (a) Coronal angiographic dataset with the left pulmonary artery (PA) originating from the right PA. The left PA encircles the trachea during its course through the mediastinum. This can also be demonstrated without contrast media (b), using an ECG-gated and respiratory-triggered 3D SSFP technique. (c) (see next page)

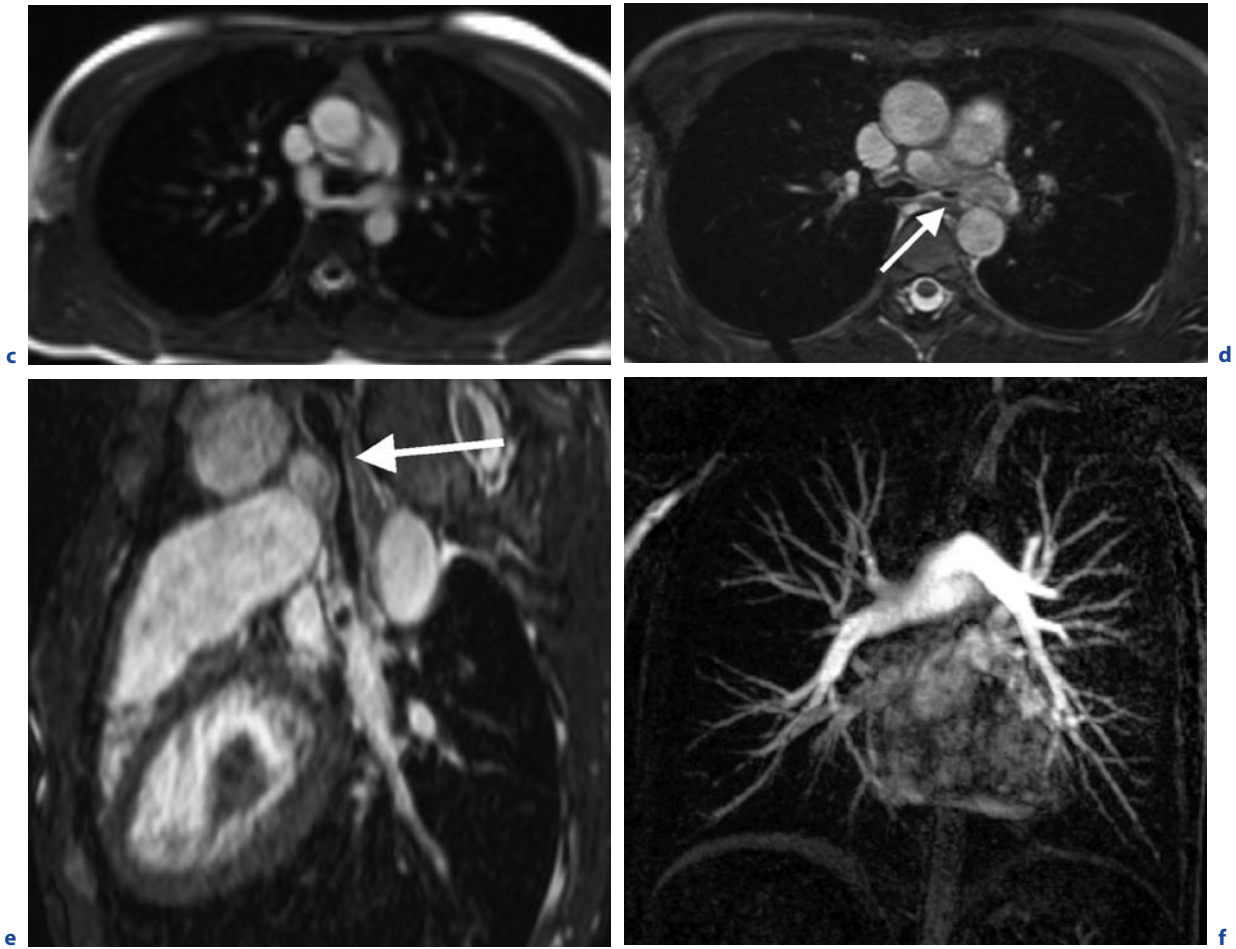


Fig. 7.4a–f. (continued) Pulmonary sling. (c) The SSFP cine sequence allows for functional assessment of the effect on the trachea showing no compression. (d) Patient after surgical correction of a pulmonary sling. The reinsertion of the left pulmonary artery is too far distally with subsequent compression of

the left main bronchus (arrow), which is even better illustrated in the sagittal reformat (e). (f) Contrast-enhanced MRA shows the anatomic course, which resembles a preoperative situation as in (a)

a large series, the prevalence of a pulmonary sling was 1 in 17,000 (186,213 school-aged children were examined) (Yu et al. 2008). Surgical correction is performed with attachment of the left pulmonary artery to the pulmonary trunk ventrally to the aorta. Imaging needs to display the pulmonary arterial anatomy as well as the relationship to the airways. MR imaging in 10 patients (aged 6 months to 11 years) with clinically suspected ring or sling malformation (3 of them with pulmonary sling) was able to demonstrate the topographic relation to the adjacent soft tissue structures (esophagus, trachea, or bronchi). MR findings were confirmed surgically (EICHORN et al. 2004).

7.2.1.3 Anomalous Origin of One Pulmonary Artery

In this rare malformation, one pulmonary artery originates abnormally from the aorta, leading to an unbalanced blood flow and unilateral pulmonary hypertension. Mainly, the right pulmonary artery shows an anomalous origin (82%). Surgical intervention includes resection of the abnormal pulmonary artery and anastomosis with the pulmonary trunk, using a small conduit. In order to achieve sufficient growth of the pulmonary vessels, conduits need to be replaced once or twice during childhood and adolescence. MRI is well suited for pre- and postoperative evaluation (KIM et al. 1995).

7.2.1.4 Tetralogy of Fallot or Pulmonary Atresia with VSD or Hypoplastic Pulmonary Artery

In these situations, blood flow through the pulmonary valve or artery is highly diminished or even absent, leading to severe cyanosis. TOF is the most common type of cyanotic CHD, with an incidence of 356 per million live births (DOREMAN and GEVA 2006). The degree of right ventricular outflow tract (RVOT) obstruction varies from mild to complete obstruction. Pulmonary blood flow is dependent on a patent ductus arteriosus (PDA) or collateral vessels (MAPCA) (Fig. 7.5). In order to obtain sufficient pulmonary blood flow and vessel growth of the pulmonary arteries, a stable aortopulmonary connection needs to be established. Later, further operations are usually necessary to palliate the malformation. The so-called Blalock-Taussig procedure was first successfully performed in 1944. The right or left subclavian artery and the ipsilateral pulmonary artery were connected in cyanotic patients with TOF (BLALOCK and TAUSSIG 1945). Nowadays, this operation is not performed often, as only one pulmonary artery will be sufficiently perfused. Central aortopulmonary shunts or a direct connection of the hypoplastic pulmonary trunk to the aorta are preferred, as they lead to a balanced growth of both pulmonary arteries (DUNCAN et al. 2003).

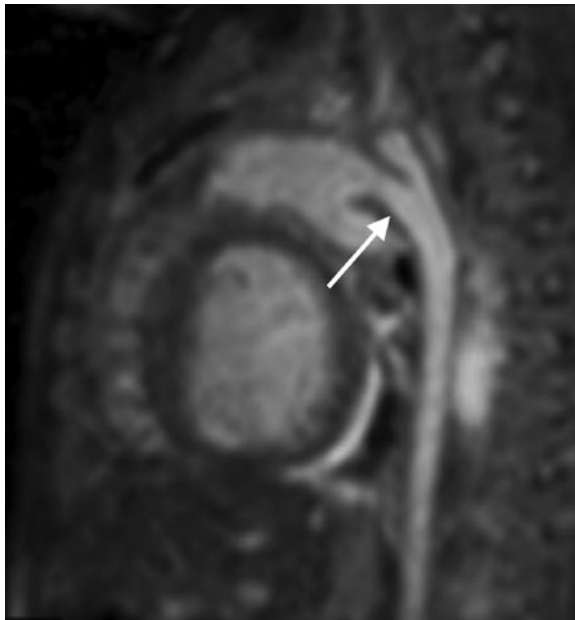


Fig. 7.5. Large open ductus arteriosus Botalli in newborn child with a TOF acquisition. Time-resolved contrast-enhanced angiography presents the vascular anatomy. The *arrow* points at the open ductus arteriosus Botalli

Preoperative assessment of the vascular structures (pulmonary arteries, aorta, and collaterals) is possible with MRI but requires relatively long scan times for complete anatomical coverage, and small vessels (<2 mm) may not be detected. Still, DA is preferred in most centers because of the potential risk of a cyanotic spell and the necessity of high-quality coronary imaging in very small infants. However, one study showed the excellent capabilities of MRI in 10 patients in whom the central pulmonary arteries had not been visualized at DA, and showed that angiography had failed to demonstrate the main pulmonary in seven cases the proximal left pulmonary artery in two cases, and the entire pulmonary arterial tree in one case (CHOE et al. 1998). At follow-up, growth of the pulmonary arteries can be evaluated excellently using MRI and should be preferred over MDCT. The time of re-intervention may be determined without serial DA or CTA.

Collateral vessels arising from the aortic arch (MAPCA) are mostly found in TOF or pulmonary atresia with VSD and with hypoplastic pulmonary artery. Lung perfusion is partly established by these systemic vessels. Surgeons are especially interested if these vessels are suitable for connection to the pulmonary arteries or if they provide an unbalanced, high-pressure blood flow situation, leading to pulmonary hypertension. Compared with DA, MRA has been shown to be highly accurate in depicting all sources of pulmonary blood supply in patients with complex pulmonary stenosis or atresia, including infants with multiple small aortopulmonary collaterals (GEVA et al. 2002).

7.2.1.5 Pulmonary Sequestration

Pulmonary sequestration is a multifocal malformation, which is defined as a segment of lung parenchyma that is separated from the tracheobronchial tree and is supplied with blood from a systemic rather than a pulmonary artery. The blood supply usually comes from the descending thoracic aorta, but in about 20% of cases, it comes from the upper abdominal aorta, celiac artery, or splenic artery (KONEN et al. 2003). Surgical procedures include ligation of the afferent vessels and/or resection of the pulmonary malformation.

In these malformations, MDCT is superior to most other techniques, providing excellent information of both the vessels supporting the malformation (arterial and venous) and especially the structure of the lung parenchyma inside the malformation. Visualization of the lung parenchyma is difficult using MRI or DA, however being an essential part of the diagnosis.

7.2.1.6 Single-Ventricle Morphology

In single-ventricle morphology of the heart (tricuspid atresia, double-inlet left ventricle), cavity volume increases as a consequence of the excessive volume load associated with parallel pulmonary and systemic circulations (GEWILLIG 2005). The Glenn procedure (hemi-Fontan) was conceived as a means of accomplishing early reduction of the volume load of the single ventricle, in anticipation of eventual completion with a Fontan-like operation. The Glenn procedure includes association of the superior vena(e) cava(e) (SVC) with the branch pulmonary arteries, augmentation of the central pulmonary arteries, occlusion of the inflow of the SVC into the right atrium, and elimination of other sources of pulmonary blood flow (like patent ductus arteriosus). Other cardiac malformations have to be corrected at the same time, or at least before a Fontan-like operation. This may include atrial septectomy, relief of aortic arch obstruction, repair, or revision of anomalous pulmonary venous connection, and other procedures (JACOBS and POURMOGHADAM 2003).

During total cavopulmonary connection (TCPC), the inferior vena cava (IVC) is connected to one pulmonary artery using an extra- or intracardiac conduit (Fig. 7.6)

(OHYE and BOVE 2001). Throughout the different surgical stages visualization and quantification of the caval connections to the pulmonary arteries is essential. Due to the complex and slow flow pattern, contrast-en-

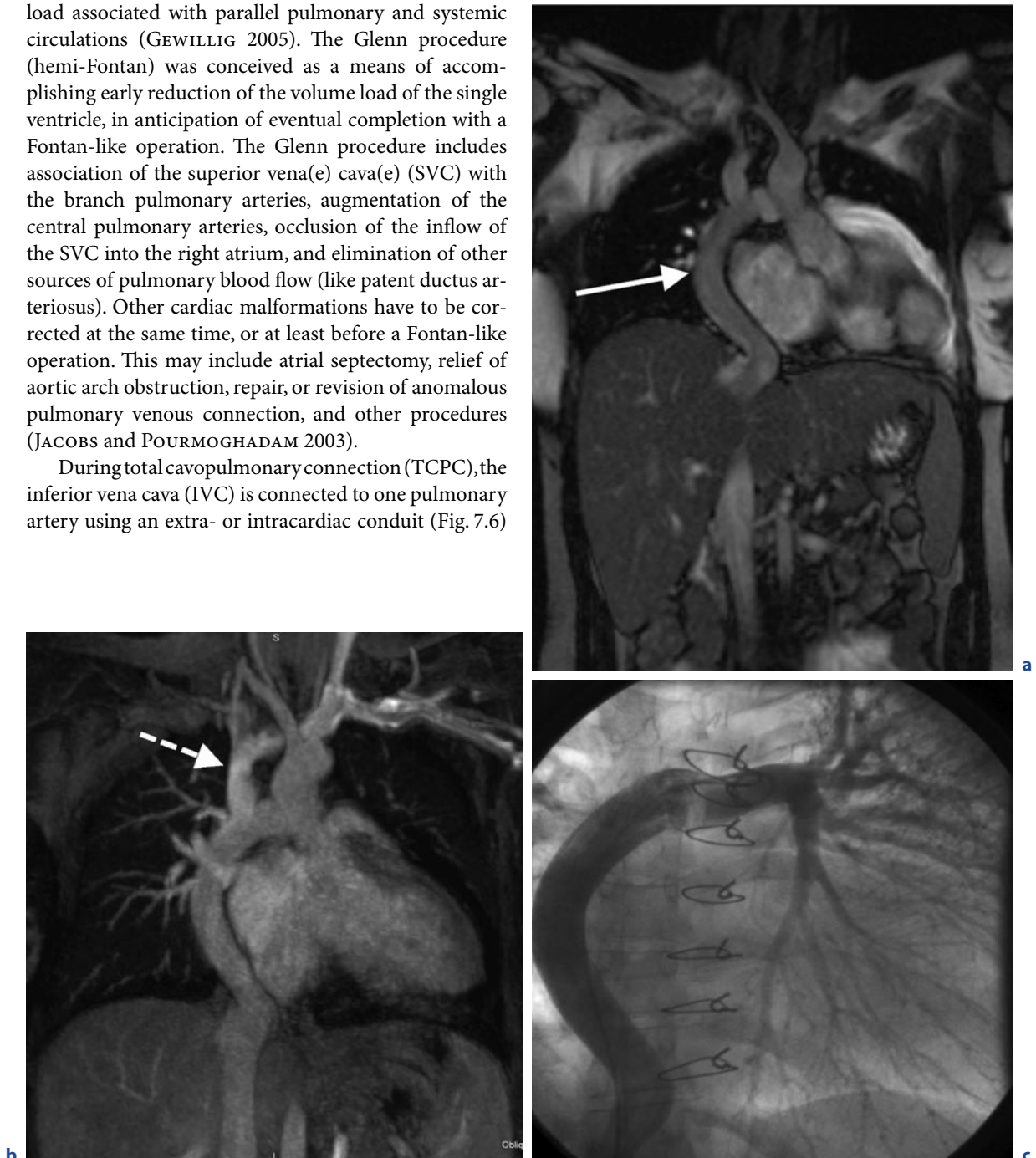


Fig. 7.6a–c. Female patient with a functional single ventricle after a total cavopulmonary connection. A large patch was formed running at the right lateral side of the heart (**a** arrow).

The superior vena cava was connected directly to the pulmonary arteries (**b** dotted arrow). (**c**) Conventional angiography of the inferior “vein” being connected to the pulmonary arteries

hanced imaging can be difficult in ruling out stenosis. Time-resolved MRA techniques describe the main blood flow direction and visualize pulmonary blood distribution. In addition, information of function of the single ventricle can be obtained. Still, DA is performed, mainly because exact estimation of pulmonary pressure is mandatory before Glenn procedure or TCPC.

7.2.1.7

Transposition of the Great Arteries

Transposition of the great arteries (TGA) accounts for approximately 5% of all CHD. In this anomaly, the aorta arises from the right ventricle and the pulmonary artery from the left ventricle, while the systemic and pulmonary veins return normally. In contrast to the normal situation, where the aorta is posterior to the pulmonary artery, the aorta is anterior and to the right of the pulmonary artery in D-transposition of the great arteries. Since the original report from JATENE and colleagues in 1976 the arterial switch operation (ASO) has become the procedure of choice for neonates with complete transposition of the great arteries. The operation involves dividing the aorta and pulmonary artery just above the sinuses and re-anastomosing them in their correct anatomic positions. The coronary arteries need to be removed from the former aortic root along

with a button of aortic wall and re-implanted into the so-called neo-aorta (former pulmonary root). Although anatomic correction is achieved, there is still concern about the mid- and long-term outcome of these patients. Postoperatively, there are three major problems requiring cardiac imaging (LOSAY et al. 2001). The first is the detection of coronary pathology, leading to myocardial dysfunction of both ventricles. The second is the aortic root dilation, leading to aortic regurgitation. The third and most frequent problem is the postoperative supravalvular pulmonary stenosis. In most cases, there is a stenosis of one or both pulmonary branches as they take their way around the ascending aorta. This region cannot be visualized sufficiently by echocardiography, and therefore, supplementary imaging is necessary. Assessment of the systemic right ventricular function is a key point in the follow-up of patients with TGA. Ejection fraction determined by cine MRI of the right ventricle correlates well with echocardiography in these patients (SALEHIAN et al. 2004). Furthermore, MRI allows excellent 3D visualization of the central and peripheral pulmonary vasculature after correction of TGA, and is therefore the modality of choice for follow-up (Fig. 7.7) (WEISS et al. 2005). In the case of severe pulmonary stenosis, additional DA is needed to measure pressure gradients across the stenosis (GUTBERLET et al. 2001).

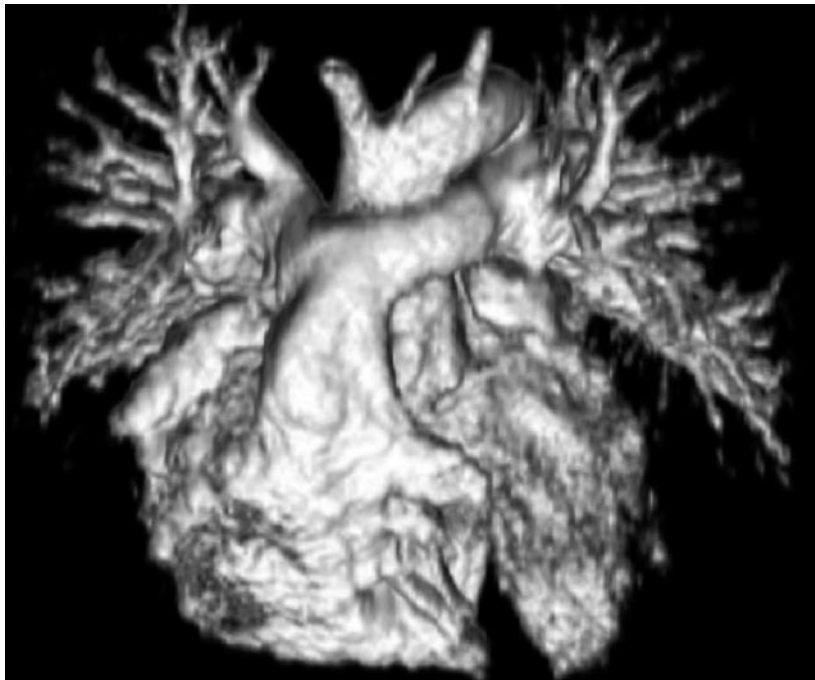


Fig. 7.7. Situation after surgical correction of transposition of the great arteries. This volume rendered image shows the anatomy, with the ventral position of the main pulmonary artery and the dorsal ascending aorta. The right and left pulmonary arteries run anterior of the aorta to the periphery

7.2.2 Congenital Pulmonary Venous Disorders

Generally, there are a total of four pulmonary veins (PVs), with one pair of veins opening into the left atrium on each side. Anomalous pulmonary venous drainage may be partial or complete, resulting in different levels of magnitude of left-to-right shunts. Young patients are usually asymptomatic; dyspnea on exertion becomes increasingly common in the third and fourth decades of life.

The complete form, known as total anomalous pulmonary venous connection (TAPVC), is compatible with life only in patients with a coexisting ASD or patent foramen ovale (STEIN 2007). Three main types are distinguished, in descending order of frequency:

1. Supracardiac type: the anomalous PVs unite posterior to the atria and drain into a left ascending vessel that opens into a persistent superior vena cava. The blood then enters the right atrium by way of the left innominate vein and right superior vena cava (Fig. 7.8).
2. Intracardiac type: the anomalous PVs unite to form a short vessel that opens into the coronary sinus.
3. Infracardiac type: the anomalous PVs drain into the portal vein, hepatic vein, left gastric vein, directly into the inferior vena cava, directly into the right atrium, or into the right atrium by way of a collecting vessel.

In partial anomalous pulmonary venous connection (PAPVC) some of the PVs are not connected to the right atrium (RA), and in few cases only a single vein communicates with that chamber. Evidence of right ventricular overload with no apparent intracardiac shunt should prompt a search for PAPVC. In the most common configuration, the right superior pulmonary vein opens into the superior vena cava or RA. A special form is the scimitar syndrome, with a hypoplastic right lung and partial or total anomalous drainage of the right pulmonary vein into the inferior vena cava (Fig. 7.9) (HOLT et al. 2004).

The relative frequency of PAPVC is approximately 0.6% of all congenital anomalies, while TAPVC ac-



Fig. 7.8. A 14-year-old boy with palpitations during exercise. During echocardiography, a turbulent flow profile in the SVC was detected. Gd-enhanced 3D MRA (oblique coronal subvolume maximal intensity projection) shows a partially anomalous pulmonary venous connection of the left upper pulmonary vein (*arrow*) to the left innominate vein

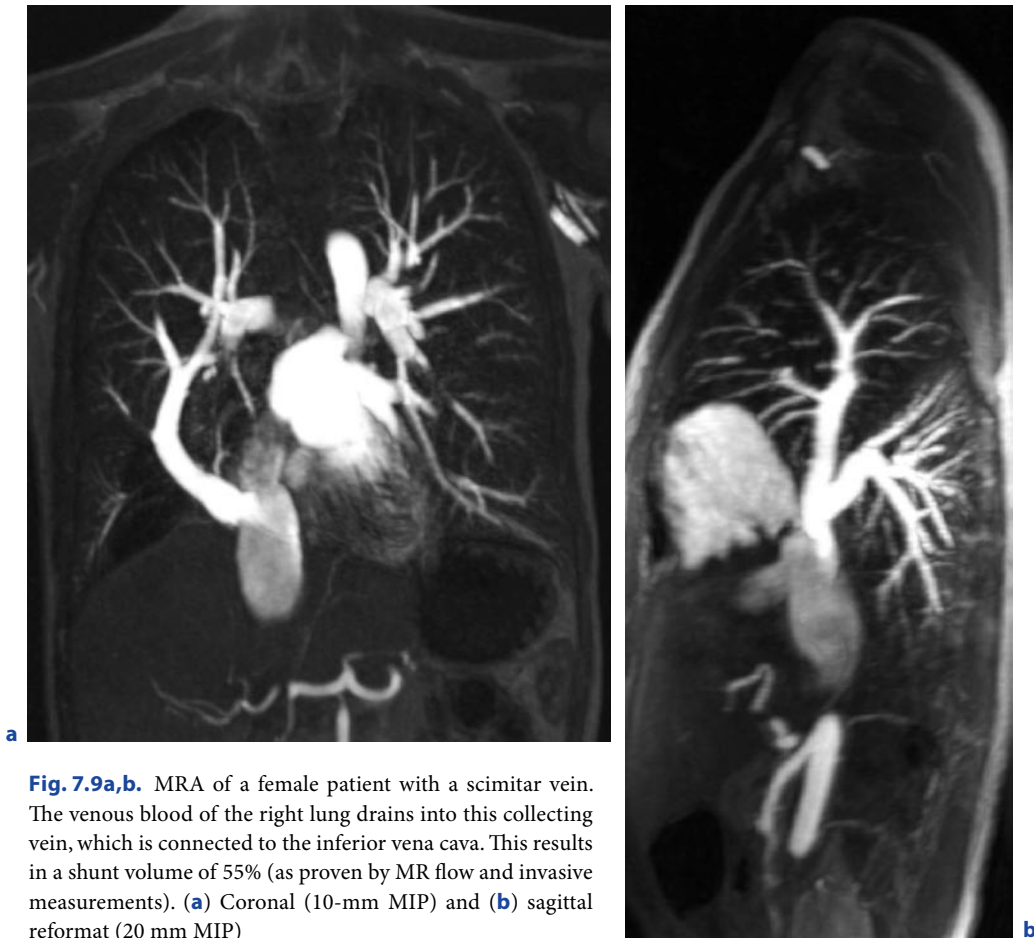


Fig. 7.9a,b. MRA of a female patient with a scimitar vein. The venous blood of the right lung drains into this collecting vein, which is connected to the inferior vena cava. This results in a shunt volume of 55% (as proven by MR flow and invasive measurements). (a) Coronal (10-mm MIP) and (b) sagittal reformat (20 mm MIP)

counts for 0.4% (Moos 2001). Anomalous pulmonary venous drainage imposes a volume overload on the pulmonary circulation, with subsequent volume loading and dilatation of the left ventricle. PAPVC is usually asymptomatic and is often detected incidentally.

If a clinical concern for PAPVC cannot be resolved by echocardiography with confidence, then MRI is the most appropriate additional test. PVs are generally adequately visualized in axial T1-weighted SE sequences. Adding thin-slice acquisitions or a dynamic GE sequence with bright-blood vascular imaging may also be productive in patients with more complex vascular anatomy.

Several studies assessing the accuracy and utility of contrast-enhanced 3D MRA have shown a high level of agreement between findings on MRA compared with surgical inspection and DA. For preoperative planning, 3D MIP reconstructions are valuable, as they clearly define the course of the PVs. MRA was uniformly more accurate than were transthoracic and transesophageal echocardiographies. MR studies often diagnosed previously unknown PAPVC or added new clinically important information regarding PAPVC anatomy (KIVELITZ

et al. 1999; GREIL et al. 2002; PRASAD et al. 2004; WALD and POWELL 2006). The shunt volume can be quantified by performing flow measurements in the ascending aorta and pulmonary trunk. It is worth noting that in patients with PAPVC, systemic blood flow/pulmonary blood flow (Q_p/Q_s) ratio measurements by oximetry in the catheterization laboratory are inherently inaccurate because of the difficulty in obtaining a reliable, representative mixed systemic venous saturation.

7.2.3 Pulmonary Arteriovenous Malformations

Pulmonary arteriovenous malformations (PAVMs) result from fistula formation between the pulmonary arteries and veins. Blood flow bypasses the pulmonary capillary bed, giving rise to a functional right-to-left shunt. The prevalence of PAVM is approximately 2–3 per 100,000 population. The great majority of PAVMs (80%) are congenital. Within this group, PAVMs are present in 47–80% of patients with autosomal dominant

Osler-Weber-Rendu syndrome (hereditary hemorrhagic telangiectasia) (KHURSHID and DOWNIE 2002). Other cases are not referable to a specific syndrome, although a genetic link to the 9q3 chromosome has been suggested.

Acquired AV shunts may have various causes like trauma, infection, metastatic carcinoma, mitral stenosis, and hepatic cirrhosis. AV shunts may develop due to metastatic involvement of the lung parenchyma. This possibility should be considered in patients who develop sudden hemoptysis after successful chemotherapy (CHOI et al. 2003).

A large, long-term follow-up study documented the superiority of sectional imaging modalities over conventional angiography. CTA (incremental and single-slice spiral CT) achieved a detection rate of 98% of all PAVMs, while angiography detected only 60% (REMY et al. 1992). In a study comparing DA and MRA, MRA could correctly define the location of the PAVMs in 16 of 16 cases. The parent vessel and the size of the feeding vessel could be accurately determined in 14 of 16 cases. In 2 cases, the feeding vessels were not contained in the slice package (MOHRS et al. 2002). This limitation no longer exists in the current generation of scanners, and both sectional modalities may be considered equivalent in the evaluation of PAVMs.

7.3

Acquired Pulmonary Venous Disorders

In the absence of congenital anomalies, there is rarely an indication for diagnostic imaging of the pulmonary veins. The most frequent indication at present is pre- and postinterventional imaging of the pulmonary veins before and after radiofrequency ablation. Atrial fibrillation is the most common cardiac arrhythmia, with a prevalence of approximately 5% in persons over 65 years of age (FALK 2001). Percutaneous catheter ablation using radiofrequency or cryoablation is a minimally invasive procedure for destroying arrhythmogenic foci. Because the origin of the pulmonary vein varies slightly due to the rotation of the left atrium during embryonic development, preinterventional imaging is recommended (also to exclude previously undetected normal variants or anomalous origin). 3D imaging is useful for planning the optimum size of the catheter balloon. The most frequent complication of catheter ablation (prevalence of 1.5–42%) is stenosis of the pulmonary veins. Other possible complications are thrombosis or dissection. Pulmonary vein stenosis develops during the first few days after the procedure, as initial tissue swelling is followed

by the development of fibrotic changes. Clinical manifestations are progressive dyspnea, orthopnea, nonproductive cough, infection, and hemoptysis (GHAYE et al. 2003). Time-resolved angiographic techniques with adequate in-plane resolution should be used to achieve optimum timing of the contrast bolus for pulmonary vein imaging (RAHMANI and WHITE 2008). Optimum bolus timing varies in different patients (and in different PV segments), especially in the presence of pulmonary vein stenosis. After contrast media application, MRI can be used for therapy control by using late-enhancement imaging techniques. This allows the precise localization of the scar tissue and the relationship to the orifice of the PV (PETERS et al. 2007).

7.4

Tumors of the Pulmonary Vessels

7.4.1

Central Pulmonary Arteries: Leiomyosarcoma

Leiomyosarcoma is the most frequent tumor of the pulmonary arteries and veins (pulmonary artery sarcomas [PAS] and pulmonary vein sarcomas [PVS]). It arises from the smooth muscle cells of the media (MAYER et al. 2007). Completely intravascular leiomyosarcomas are usually nodular, polypoid tumors that are fixed to the inner vessel wall. Intraluminal tumor growth expands the vessel diameter, and intracardiac tumor extension occasionally occurs. Besides leiomyosarcoma, the differential diagnosis of intrathoracic sarcomas should include angiosarcoma, rhabdomyosarcoma, and the sarcomatoid variant of mesothelioma.

Primary PAS affect both sexes equally and occur at a slightly earlier average age (50 years) than do the venous forms. The incidence ratio of PAS to PVS is approximately 20:1. Only 17 cases (mean age at radiologic diagnosis was 48 years) of PVS have been described in the literature.

PAS most commonly involve the main pulmonary artery trunk and may spread from there toward the peripheral arterial branches or may extend back into the right ventricle. Tumor growth may be completely extravascular (62%), completely intravascular (5%), or both extra- and intravascular (33%) (KREFT et al. 2004). Other studies indicate that approximately 50% of PAS are intravascular when diagnosed. The remaining half undergoes transmural spread into the lung parenchyma (FASSE et al. 1999). The clinical manifestations of PAS are nonspecific and may include dyspnea, chest pain, cough, hemoptysis, and signs of right heart failure. Be-

cause these tumors are often intraluminal, they may embolize and cause peripheral infarctions, producing clinical symptoms similar to those of acute or chronic recurrent pulmonary embolism. PVS are generally larger than PAS are. They remain asymptomatic until their growth interferes with pulmonary venous return. The most frequent clinical manifestations are dyspnea, hemoptysis, cough, chest pain, and weight loss. PVS have a tendency to spread into the left atrium (Yi 2004). PAS appears on CT and MR images as a convex intraluminal mass that usually begins in the pulmonary trunk and spreads in a peripheral or occasionally central fashion. Both primary and metastatic tumors of the pulmonary arteries may cause intraluminal-filling defects that are similar in appearance to chronic recurrent pulmonary emboli.

The tumors may be inhomogeneous as a result of hemorrhage, necrosis, or different tissue components. Thrombi may adhere to intraluminal tumor components and may in turn be infiltrated by tumor (KAUCZOR et al. 1994). Thus, delayed T1-weighted images after contrast administration are an essential part of the MRI protocol. Tumor enlargement over time may lead to vascular expansion with complete obliteration of the lumen. A convex shape of the filling defect does not support a diagnosis of chronic pulmonary embolism. Contrast enhancement on MRI is another indicator of intravascular tumor growth. Delayed imaging after contrast administration shows a highly variable degree of tumor enhancement, which is an important differentiating feature from chronic thromboembolic pulmonary hypertension (CTEPH) (KAMINAGA et al. 2003).

The treatment of choice is complete tumor resection based on an early preoperative diagnosis. Modern surgical techniques can be used to reconstruct the vascular defect with prosthetic material. Even if curative treatment is not an option, it appears that palliative surgery can significantly prolong patient survival.

7.4.2

Peripheral Pulmonary Arteries: Pulmonary Capillary Hemangioma

Most cases of pulmonary capillary hemangioma PCH involve bilateral disease with an unknown cause. Capillaries proliferate into the alveolar septa and other structures such as bronchial walls, pleura, and regional lymph nodes. Extrathoracic growth or metastasis has not previously been described. The disease is most prevalent in the third and fourth decades, with a range from 6 to 71 years, and affects males and females equally. Life expect-

tancy after symptom onset is 2–12 years in untreated cases.

Typical clinical manifestations are progressive shortness of breath, pleuritic chest pain, and frequent hemoptysis, often prompting a misdiagnosis of chronic thromboembolic pulmonary hypertension. With the progression of disease, patients develop clinical signs of cor pulmonale with elevated pulmonary artery pressures but normal pulmonary capillary wedge pressures on right heart catheterization.

To date, CT is the only sectional imaging modality that has been investigated in the literature. The principal CT findings are enlarged pulmonary arteries and numerous small, bilateral, ill-defined densities (ELTORKY et al. 1994). Compared with idiopathic pulmonary artery hypertension, perfusion scanning shows increased perfusion in the hemangiomatous tissue and decreased perfusion in occluded vessels, resulting in an inhomogeneous perfusion pattern.

The only curative treatment is bilateral lung transplantation, for which patients must be selected at a very early stage.

7.5

Extravascular Disorders

The most frequent extravascular disorder affecting the PA is mediastinal tumor spread with compression or infiltration of the PA and/or PV. Studies have documented the value of MRI in the detection and evaluation of mediastinal and arterial invasion by bronchial carcinoma. This information is critical in planning the resection of the carcinoma. When vascular invasion is present, the patient must be placed on a heart–lung machine during the operation, and a suitable vascular interposition graft should be ready for use. The long-term survival rate is significantly reduced in patients with pulmonary vascular invasion (CHUNWEI et al. 2003; OHNO et al. 2001). The lung parenchyma should also be evaluated during preoperative staging; thus, a CT is most often performed despite the high diagnostic quality of MRI.

The presence of aneurysms in the setting of Behçet's disease or Hughes-Stovin syndrome (KINDERMANN et al. 2003; OLIVER et al. 1997) and involvement by vasculitis are relatively rare indications for imaging of the pulmonary vessels. The primary sectional imaging study in these cases is still CT, whose capabilities have been greatly augmented by the advent of multidetector technology. MRA should be considered in cases where CT is contraindicated due to renal failure or thyroid dysfunction, and should be avoided in young patients.

References

- Berdon WE (2000) Rings, slings, and other things: vascular compression of the infant trachea updated from the midcentury to the millennium—the legacy of Robert E. Gross, MD, and Edward B. D. Neuhauser, MD. *Radiology* 216:624–632
- Bernstein D (2004) Congenital Heart Disease. In: Behrman RE, Kliegman R, Jenson HB (eds): *Nelson textbook of pediatrics*, 17 edn. Saunders, Philadelphia, pp 1499–1554
- Bhat AH, Sahn DJ (2004) Congenital heart disease never goes away, even when it has been “treated”: the adult with congenital heart disease. *Curr Opin Pediatr* 16:500–507
- Biederer J, Both M, Graessner J, Liess C, Jakob P, Reuter M, Heller M (2003) Lung morphology: fast MR imaging assessment with a volumetric interpolated breath-hold technique: initial experience with patients. *Radiology* 226:242–249
- Blalock A, Taussig HB (1945) The surgical treatment of malformations of the heart in which there is pulmonary stenosis or pulmonary atresia. *JAMA* 128:189–202
- Bock M, Umathum R, Zuehlsdorff S, Volz S, Fink C, Hallscheidt P, Zimmermann H, Nitz W, Semmler W (2006) Interventional magnetic resonance imaging: an alternative to image guidance with ionising radiation. *Radiat Prot Dosimetry* 117:74–78
- Boechat MI, Ratib O, Williams PL, Gomes AS, Child JS, Allada V (2005) Cardiac MR imaging and MR angiography for assessment of complex tetralogy of Fallot and pulmonary atresia. *Radiographics* 25:1535–1546
- Boll DT, Lewin JS, Young P, Siwik ES, Gilkeson RC (2005) Perfusion abnormalities in congenital and neoplastic pulmonary disease: comparison of MR perfusion and multislice CT imaging. *Eur Radiol* 15:1978–1986
- Choe YH, Ko JK, Lee HJ, Kang IS, Park PW, Lee YT (1998) MR imaging of non-visualized pulmonary arteries at angiography in patients with congenital heart disease. *J Korean Med Sci* 13:597–602
- Choi SH, Goo JM, Kim HC, Im JG (2003) Pulmonary arteriovenous fistulas developed after chemotherapy of metastatic choriocarcinoma. *AJR Am J Roentgenol* 181:1544–1546
- Chunwei F, Weiji W, Xinguan Z, Qingzen N, Xiangmin J, Qingzhen Z (2003) Evaluations of bronchoplasty and pulmonary artery reconstruction for bronchogenic carcinoma. *Eur J Cardiothorac Surg* 23:209–213
- Dorfman AL, Geva T (2006) Magnetic resonance imaging evaluation of congenital heart disease: conotruncal anomalies. *J Cardiovasc Magn Reson* 8:645–659
- Duncan BW, Mee RB, Prieto LR, Rosenthal GL, Mesia CI, Qureshi A, Tucker OP, Rhodes JF, Latson LA (2003) Staged repair of tetralogy of Fallot with pulmonary atresia and major aortopulmonary collateral arteries. *J Thorac Cardiovasc Surg* 126:694–702
- Eichhorn J, Fink C, Delorme S, Ulmer H (2004) Rings, slings and other vascular abnormalities. Ultrafast computed tomography and magnetic resonance angiography in pediatric cardiology. *Z Kardiol* 93:201–208
- Eltorky MA, Headley AS, Winer-Muram H, Garrett HE Jr, Griffin JP (1994) Pulmonary capillary hemangiomatosis: a clinicopathologic review. *Ann Thorac Surg* 57:772–776
- Falk RH (2001) Atrial fibrillation. *N Engl J Med* 344:1067–1078
- Fasse A, Kauczor HU, Mayer E, Kreitner KF, Heussel CP, Thelen M (1999) [Sarcoma of the pulmonary artery—pre- and postoperative radiologic findings in initial tumor manifestation and recurrence.] (In German) *Rofo* 170:112–118
- Fink C, Eichhorn J, Kiessling F, Bock M, Delorme S (2003) [Time-resolved multiphase 3D MR angiography in the diagnosis of the pulmonary vascular system in children.] (In German) *Rofo* 175:929–935
- Fries P, Altmeyer K, Seidel R, Massmann A, Kirchin MA, Schneider G (2005) Dynamic contrast enhanced MRA in pediatric patients after application of Gd-BOPTA. *Eur Radiol* 15:E8
- Gatehouse PD, Keegan J, Crowe LA, Masood S, Mohiaddin RH, Kreitner KF, Firmin DN (2005) Applications of phase-contrast flow and velocity imaging in cardiovascular MRI. *Eur Radiol* 15:2172–2184
- Geva T, Greil GF, Marshall AC, Landzberg M, Powell AJ (2002) Gadolinium-enhanced 3-dimensional magnetic resonance angiography of pulmonary blood supply in patients with complex pulmonary stenosis or atresia: comparison with x-ray angiography. *Circulation* 106:473–478
- Gewillig M (2005) The Fontan circulation. *Heart* 91:839–846
- Ghaye B, Szapiro D, Dacher JN, Rodriguez LM, Timmermans C, Devillers D, Dondelinger RF (2003) Percutaneous ablation for atrial fibrillation: the role of cross-sectional imaging. *Radiographics* 23:S19–S33; discussion S48–S50
- Gilmore JH, Zhai G, Wilber K, Smith JK, Lin W, Gerig G (2004) 3 Tesla magnetic resonance imaging of the brain in newborns. *Psychiatry Res* 132:81–85
- Greil GF, Kramer U, Dammann F, Schick F, Miller S, Claussen CD, Sieverding L (2005) Diagnosis of vascular rings and slings using an interleaved 3D double-slab FISP MR angiography technique. *Pediatr Radiol* 35:396–401
- Greil GF, Powell AJ, Gildein HP, Geva T (2002) Gadolinium-enhanced three-dimensional magnetic resonance angiography of pulmonary and systemic venous anomalies. *J Am Coll Cardiol* 39:335–341
- Grist TM, Thornton FJ (2005) Magnetic resonance angiography in children: technique, indications, and imaging findings. *Pediatr Radiol* 35:26–39
- Gutberlet M, Boeckel T, Hosten N, Vogel M, Kuhne T, Oellinger H, Ehrenstein T, Venz S, Hetzer R, Bein G, Felix R (2000) Arterial switch procedure for D-transposition of the great arteries: quantitative midterm evaluation of hemodynamic changes with cine MR imaging and phase-shift velocity mapping—initial experience. *Radiology* 214:467–475
- Hoeper MM, Lee SH, Voswinckel R, Palazzini M, Jais X, Marinelli A, Barst RJ, Ghofrani HA, Jing ZC, Opitz C, Seyfarth HJ, Halank M, McLaughlin V, Oudiz RJ, Ewert R, Wilkens H, Kluge S, Bremer HC, Baroke E, Rubin LJ (2006) Complications of right heart catheterization procedures in patients with pulmonary hypertension in experienced centers. *J Am Coll Cardiol* 48:2546–2552

- Hoffman JI (1995) Incidence of congenital heart disease: II. Prenatal incidence. *Pediatr Cardiol* 16:155–165
- Holmquist C, Hochbergs P, Bjorkhem G, Brockstedt S, Laurin S (2001) Pre-operative evaluation with MR in tetralogy of Fallot and pulmonary atresia with ventricular septal defect. *Acta Radiol* 42:63–69
- Holt PD, Berdon WE, Marans Z, Griffiths S, Hsu D (2004) Scimitar vein draining to the left atrium and a historical review of the scimitar syndrome. *Pediatr Radiol* 34:409–413
- Jacobs ML, Pourmoghadam KK (2003) The hemi-Fontan operation. *Semin Thorac Cardiovasc Surg Pediatr Card Surg Annu* 6:90–97
- Jatene AD, Fontes VF, Paulista PP, Souza LC, Neger F, Galantier M, Sousa JE (1976) Anatomic correction of transposition of the great vessels. *J Thorac Cardiovasc Surg* 72:364–370
- Jhooti P, Gatehouse PD, Keegan J, Bunce NH, Taylor AM, Firmin DN (2000) Phase ordering with automatic window selection (PAWS): a novel motion-resistant technique for 3D coronary imaging. *Magn Reson Med* 43:470–480
- Kaminaga T, Takeshita T, Kimura I (2003) Role of magnetic resonance imaging for evaluation of tumors in the cardiac region. *Eur Radiol* 13(Suppl):L1–L10
- Kauczor HU, Schwickert HC, Mayer E, Kersjes W, Moll R, Schweden F (1994) Pulmonary artery sarcoma mimicking chronic thromboembolic disease: computed tomography and magnetic resonance imaging findings. *Cardiovasc Intervent Radiol* 17:185–189
- Khurshid I, Downie GH (2002) Pulmonary arteriovenous malformation. *Postgrad Med J* 78:191–197
- Kim TK, Choe YH, Kim HS, Ko JK, Lee YT, Lee HJ, Park JH (1995) Anomalous origin of the right pulmonary artery from the ascending aorta: diagnosis by magnetic resonance imaging. *Cardiovasc Intervent Radiol* 18:118–121
- Kindermann M, Wilkens H, Hartmann W, Schafers HJ, Bohm M (2003) Images in cardiovascular medicine. Hughes-Stovin syndrome. *Circulation* 108:e156
- Kivelitz DE, Scheer I, Taupitz M (1999) Scimitar Syndrome: diagnosis with MR angiography. *AJR Am J Roentgenol* 172:1700
- Konen E, Raviv-Zilka L, Cohen RA, Epelman M, Boger-Megiddo I, Bar-Ziv J, Hegesh J, Ofer A, Konen O, Katz M, Gayer G, Rozenman J (2003) Congenital pulmonary venolobar syndrome: spectrum of helical CT findings with emphasis on computerized reformatting. *Radiographics* 23:1175–1184
- Kreft B, Flacke S, Zhou H, Textor J, Remig J, Schild HH (2004) [Diagnostic imaging of vascular leiomyosarcomas]. (In German) *Rofo* 176:183–190
- Krueger JJ, Ewert P, Yilmaz S, Gelernter D, Peters B, Pietzner K, Bornstedt A, Schnackenburg B, Abdul-Khaliq H, Fleck E, Nagel E, Berger F, Kuehne T (2006) Magnetic resonance imaging-guided balloon angioplasty of coarctation of the aorta: a pilot study. *Circulation* 113:1093–1100
- Ley S, Fink C, Zaporozhan J, Borst MM, Meyer FJ, Puderbach M, Eichinger M, Plathow C, Grunig E, Kreitner KF, Kauczor HU (2005) Value of high spatial and high temporal resolution magnetic resonance angiography for differentiation between idiopathic and thromboembolic pulmonary hypertension: initial results. *Eur Radiol* 15:2256–2263
- Ley S, Zaporozhan J, Arnold R, Eichhorn J, Schenk JB, Ulmer H, Kreitner KF, Kauczor HU (2007) Preoperative assessment and follow-up of congenital abnormalities of the pulmonary arteries using CT and MRI. *Eur Radiol* 17:151–162
- Losay J, Touchot A, Serraf A, Litvinova A, Lambert V, Piot JD, Lacour-Gayet F, Capderou A, Planche C (2001) Late outcome after arterial switch operation for transposition of the great arteries. *Circulation* 104:1121–1126
- MacGowan CK, Al-Kwif O, Varodayan F, Yoo SJ, Wright GA, Kellenberger CJ (2005) Optimization of 3D contrast-enhanced pulmonary magnetic resonance angiography in pediatric patients with congenital heart disease. *Magn Reson Med* 54:207–212
- Maintz D, Juergens KU, Wichter T, Grude M, Heindel W, Fischbach R (2003) Imaging of coronary artery stents using multislice computed tomography: in vitro evaluation. *Eur Radiol* 13:830–835
- Mayer F, Aebert H, Rudert M, Konigsrainer A, Horger M, Kanz L, Bamberg M, Ziemer G, Hartmann JT (2007) Primary malignant sarcomas of the heart and great vessels in adult patients—a single-center experience. *Oncologist* 12:1134–1142
- Mohrs OK, Voigtlander T, Heussel CP, Bardeleben S, Duber C, Kreitner KF (2002) [Morphologic and functional assessment of vascular abnormalities of the pulmonary vasculature by breath-hold MR techniques.] (In German) *Rofo* 174:467–473
- Moos A (2001) Heart disease in infants, children and adolescents. including the fetus and young adult. Lippincott Williams & Wilkins, Philadelphia
- Naganawa S, Kawai H, Fukatsu H, Ishigaki T, Komada T, Maruyama K, Takizawa O (2004) High-speed imaging at 3 Tesla: a technical and clinical review with an emphasis on whole-brain 3D imaging. *Magn Reson Med Sci* 3:177–187
- Nakanishi T (2005) Cardiac catheterization is necessary before bidirectional Glenn and Fontan procedures in single ventricle physiology. *Pediatr Cardiol* 26:159–161
- Ohno Y, Adachi S, Motoyama A, Kusumoto M, Hatabu H, Sugimura K, Kono M (2001) Multiphase ECG-triggered 3D contrast-enhanced MR angiography: utility for evaluation of hilar and mediastinal invasion of bronchogenic carcinoma. *J Magn Reson Imaging* 13:215–224
- Ohye RG, Bove EL (2001) Advances in congenital heart surgery. *Curr Opin Pediatr* 13:473–481
- Oliver TB, Stevenson AJ, Gillespie IN (1997) Pulmonary artery pseudoaneurysm due to bronchial carcinoma. *Br J Radiol* 70:950–951

- Peters DC, Wylie JV, Hauser TH, Kissinger KV, Botnar RM, Essebag V, Josephson ME, Manning WJ (2007) Detection of pulmonary vein and left atrial scar after catheter ablation with three-dimensional navigator-gated delayed enhancement MR imaging: initial experience. *Radiology* 243:690–695
- Prakash A, Torres AJ, Printz BF, Prince MR, Nielsen JC (2007) Usefulness of magnetic resonance angiography in the evaluation of complex congenital heart disease in newborns and infants. *Am J Cardiol* 100:715–721
- Prasad SK, Soukias N, Hornung T, Khan M, Pennell DJ, Gatzoulis MA, Mohiaddin RH (2004) Role of magnetic resonance angiography in the diagnosis of major aortopulmonary collateral arteries and partial anomalous pulmonary venous drainage. *Circulation* 109:207–214
- Rahmani N, White CS (2008) MR Imaging of Thoracic Veins. *Magn Reson Imaging Clin N Am* 16:249–262
- Remy J, Remy-Jardin M, Wattinne L, Deffontaines C (1992) Pulmonary arteriovenous malformations: evaluation with CT of the chest before and after treatment. *Radiology* 182:809–816
- Rickers C, Seethamraju RT, Jerosch-Herold M, Wilke NM (2003) Magnetic resonance imaging guided cardiovascular interventions in congenital heart diseases. *J Interv Cardiol* 16:143–147
- Roman KS, Kellenberger CJ, Farooq S, MacGowan CK, Gilday DL, Yoo SJ (2005) Comparative imaging of differential pulmonary blood flow in patients with congenital heart disease: magnetic resonance imaging versus lung perfusion scintigraphy. *Pediatr Radiol* 35:295–301
- Salehian O, Schwerzmann M, Merchant N, Webb GD, Siu SC, Therrien J (2004) Assessment of systemic right ventricular function in patients with transposition of the great arteries using the myocardial performance index: comparison with cardiac magnetic resonance imaging. *Circulation* 110:3229–3233
- Sequeiros RB, Ojala R, Kariniemi J, Perala J, Niinimäki J, Reinikainen H, Tervonen O (2005) MR-guided interventional procedures: a review. *Acta Radiol* 46:576–586
- Simonetti OP, Cook S (2006) Technical aspects of pediatric CMR. *J Cardiovasc Magn Reson* 8:581–593
- Sorensen TS, Korperich H, Greil GF, Eichhorn J, Barth P, Meyer H, Pedersen EM, Beerbaum P (2004) Operator-independent isotropic three-dimensional magnetic resonance imaging for morphology in congenital heart disease: a validation study. *Circulation* 110:163–169
- Sorensen TS, Beerbaum P, Korperich H, Pedersen EM (2005) Three-dimensional, isotropic MRI: a unified approach to quantification and visualization in congenital heart disease. *Int J Cardiovasc Imaging* 21:283–292
- Stein P (2007) Total anomalous pulmonary venous connection. *AORN J* 85:509–520; quiz 521–504
- Varaprasathan GA, Araoz PA, Higgins CB, Reddy GP (2002) Quantification of flow dynamics in congenital heart disease: applications of velocity-encoded cine MR imaging. *Radiographics* 22:895–905; discussion 905–896
- Wald RM, Powell AJ (2006) Simple congenital heart lesions. *J Cardiovasc Magn Reson* 8:619–631
- Weiss F, Habermann CR, Lilje C, Nimz M, Rasek V, Dallmeyer J, Stork A, Graessner J, Weil J, Adam G (2005) [MRI of pulmonary arteries in follow-up after arterial-switch-operation (ASO) for transposition of great arteries (D-TGA).] (In German) *Rofo* 177:849–855
- Yi ES (2004) Tumors of the pulmonary vasculature. *Cardiol Clin* 22:431–440, vi–vii
- Yu JM, Liao CP, Ge S, Weng ZC, Hsiung MC, Chang JK, Chen FL (2008) The prevalence and clinical impact of pulmonary artery sling on school-aged children: a large-scale screening study. *Pediatr Pulmonol*

Asthma

SEAN B. FAIN, JAMES H. HOLMES, and RONALD L. SORKNESS

CONTENTS

- 8.1 **Introduction** 140
- 8.2 **Background** 140
- 8.2.1 Clinical Applications of Imaging to Asthma 141
- 8.3 **Characterization of Ventilation Patterns in the Asthmatic Lung** 142
- 8.3.1 Basic MR Imaging Methods and Protocols 142
- 8.3.2 Dynamic Imaging of Respiratory Maneuvers 143
- 8.3.3 Diffusion Weighted HP He-3 MRI 143
- 8.3.4 Analysis Methods 144
- 8.4 **Initial Clinical Results** 146
- 8.4.1 Single Time-Point Studies 146
- 8.4.2 Longitudinal and Interventional Studies 147
- 8.5 **Emerging Techniques** 149
- 8.5.1 Four-Dimensional Imaging 149
- 8.5.2 Diffusion-weighted Imaging of Lung Micro-structure 150
- 8.5.3 Quantitative Ventilation and Perfusion 151
- 8.5.4 Multi-modality Airway Assessment 151
- 8.6 **Summary/Conclusions** 151
- References** 152

KEY POINTS

Asthma is a disease with significant clinical impact and growing incidence, particularly in children. The disease is characterized by a complex interplay of environmental and genetic factors that affect airway structure and function leading to persistent and spatially heterogeneous airway obstruction. Conventional methods for evaluating lung function using spirometry and plethysmography are not capable of assessing regional obstruction nor the regional dynamics of airway obstruction. Imaging methods have emerged as an attractive approach to evaluate heterogeneity and mechanisms of airway obstruction in the asthmatic lung. Specifically, hyperpolarized (HP) helium-3 (He-3) MRI has enabled visualization of the airspaces of the lungs, including the large airways and lung parenchyma, during breath-held and dynamic respiratory maneuvers. This method has been applied to study asthma phenotypes, disease progression, and response to interventions with methacholine and therapy. The number and size of ventilation defects correlate with disease severity and with spirometric measures, principally FEV1 percent predicted. More importantly, regional patterns of obstruction observed on HP He-3 MRI identify regions of persistent ventilation defects that may reflect underlying structural changes in the airways such as remodeling or chronic inflammation. Multi-modality comparisons between multi-detector computed tomography (MDCT) and emerging quantitative measures using proton and HP He-3 MRI will help evaluate regional structure-function relationships to assess causal mechanisms of disease and response to therapy.

SEAN B. FAIN, PhD

Associate Professor, Departments of Medical Physics and Radiology, University of Wisconsin – Madison, USA

JAMES H. HOLMES, PhD

Research Associate, Department of Medical Physics, University of Wisconsin – Madison, USA

RONALD L. SORKNESS, PhD

Professor, School of Pharmacy and Morris Institute for Respiratory Research, University of Wisconsin – Madison, USA

8.1

Introduction

This chapter explores the application of MRI to the study of asthma. Asthma affects millions of people worldwide and trends indicate increasing incidence particularly among children (NIH-NHLBI 2002). In the first third of the chapter, the clinical presentation of asthma is briefly introduced followed by a short review of the predominant imaging methods applied to the study of asthma, including hyperpolarized (HP) He-3 MRI. Next the basic HP He-3 MRI sequences for breath-held and dynamic imaging and their application to characterizing ventilation patterns in asthma are described as well as respiratory maneuvers that have been incorporated into clinical imaging protocols. Different approaches to the analysis and quantification of the observed ventilation defects in asthma are also briefly addressed.

The last two sections of the chapter address specific applications of HP He-3 MRI of ventilation to visualize obstructive patterns and emerging techniques respectively. Images of ventilation are being used to define asthma phenotypes, to explore mechanisms of airway closure, and to evaluate response to therapy. Several emerging techniques are presented with application to the study of airway remodeling and lung microstructure. Finally, there is a brief discussion of what has been learned about asthma and what remains to be studied and the role of functional lung imaging in this important area.

8.2

Background

Asthma is an obstructive airways disease characterized by episodic, reversible airway obstruction, and symptoms of wheezing, chest tightness, cough and difficulty breathing. Acute episodes of obstruction may be triggered by stimuli such as respiratory viral infections, exposure to allergens, or exercise, which are superimposed on an underlying chronic inflammatory process that renders the airways hyperresponsive to perturbations that in normal airways would evoke a negligible response. The etiology of the disease is recognized to be a complex combination of genetic and environmental risk factors. There are differing patterns of asthma (e.g. inception, lability, responsiveness to treatment, severity) that likely represent differences in the underlying airway pathophysiology, but the definitions of distinct asthma

phenotypes are at an early stage. Structural remodeling likely has a role in driving the obstructive physiology. Airway remodeling includes wall thickening stemming from a combination of subepithelial and smooth muscle thickening, and an increase in the mucus-producing structures (goblet cells and submucosal glands). Moreover, there is a wide spectrum of severity in patients with asthma and considerable debate as to the relative roles of the environmental and remodeling factors as a function of severity.

The uncertainty is in part due to the indirect nature of the information used to study asthma thus far. Much of what is known about asthma, and obstructive lung diseases in general, was gleaned from careful studies using whole lung measurements of air flow (i.e. spirometry), lung volume (i.e. plethysmography) (LEVITZKY 2003; EVANS and SCANLON 2003), and direct bronchoscopic assessment (BENAYOUN *et al.* 2003). Spirometry shows that obstructive lung diseases including asthma and chronic obstructive pulmonary disease (COPD) are characterized by a reduction in forced expiratory volume at 1 s (FEV_1), forced vital capacity (FVC; an indicator of the air trapping component of obstruction), and the FEV_1/FVC ratio (an indicator of the air-flow limitation component of obstruction) (EVANS and SCANLON 2003; WINN *et al.* 2003). However, spirometry is relatively nonspecific for distinguishing asthma from COPD and substantial overlap is common. Generally, COPD refers to a spectrum of obstructive lung diseases including chronic bronchitis, emphysema and asthmatic bronchitis (PETTY 2003), as opposed to typical asthma, which is largely characterized by more reversible obstruction. However, airway remodeling may lead to a non-reversible component in asthma as well as chronic reduction in FEV_1/FVC ratio and persistent air-flow limitation (SORKNESS *et al.* 2008). Bronchoscopic assessment and post-mortem histology support the existence of airway remodeling as a significant component of more severe asthma (BENAYOUN *et al.* 2003; JAMES *et al.* 2002). In several studies, more severe asthma is associated with decreased FVC and increased residual lung volume (RV) that suggest increased air trapping at low lung volumes (SORKNESS *et al.* 2008; BROWN *et al.* 2006).

Spirometric studies cannot explore the regional mechanics of airway obstruction and bronchoscopic assessment can only sample very limited regional structure. Therefore, imaging methods are well-positioned to study *in vivo* regional heterogeneity and dynamics of airway obstruction in asthma. This has led to the increasing role of multiple detector computed tomography (MDCT), MRI, and nuclear imaging using single

photon emission computed tomography (SPECT) and positron emission tomography (PET) in the study of asthma mechanisms and severity.

8.2.1 Clinical Applications of Imaging to Asthma

The application of MDCT provides direct measurement of structures in the large airways such as wall thickening, airway lumen narrowing and mucus plugging associated with increased asthma severity (BROWN et al. 2006; LITTLE et al. 2002) and in conjunction with various respiratory maneuvers such as deep inspiration (BROWN et al. 2000). However, MDCT cannot, at present, assess regional ventilatory and perfusion patterns of lung function although dual energy X-ray using inhaled xenon has been used to evaluate ventilation and perfusion in pre-clinical studies (HOFFMAN and CHON 2005; VAN BEEK and HOFFMAN 2008). The most important limitation of MDCT is the high ionizing radiation dose required for repeated images in longitudinal and interventional studies (HURWITZ et al. 2007).

SPECT or nuclear scintigraphy with inhaled technegas, i.e. technetium(Tc)-99m labeled aerosol, or Xe-133 (HOWARTH et al. 1999; NEWMAN et al. 2003) have been the primary clinical approaches to evaluating ventilatory patterns in the lungs (Fig. 8.1a). Conventional nuclear imaging methods remain limited in resolution, coverage and signal to noise. Nuclear imaging methods are challenged to depict the heterogeneity and dynamics of airway obstruction in asthma due to reduced spatial and temporal resolution. Nonetheless, recent work using N₂-13 gas PET has been applied successfully to

the study of asthma (VIDAL MELO et al. 2003) but with limited spatial coverage and extended breath-hold times. A niche exists for MRI applications to lung imaging that can exploit this modality's three-dimensional (3D) and time-resolved imaging capabilities while providing sufficient contrast resolution in the airways and lung parenchyma.

Various methods have been used to produce contrast using MRI of the lungs. For example, oxygen-enhanced T1 mapping techniques (CHEN et al. 1998; HATABU et al. 2001) have been used to assess ventilation patterns in chronic obstructive pulmonary disease (COPD) (OHNO et al. 2008), but the relatively low signal to noise ratio of this technique, and the confounding effects of motion near the diaphragm have challenged the extension of this approach to the study of asthma. The inhalation of HP He-3 gas followed by MRI has been shown to produce high contrast to noise images of the lung airspaces (MIDDLETON et al. 1995). This technique has played an increasing role in the assessment of asthma in pre-clinical (HOLMES et al. 2005b; DRIEHUYS et al. 2007) and clinical studies (ALTES et al. 2001). The hyperpolarized He-3 gas provides on the order of 10,000 times increase in polarization, which can readily overcome the lower density and lower nuclear gyromagnetic ratio of the helium gas compared to conventional proton MRI. Visualization of the airspaces of the large airways and parenchyma in asthma (Fig. 8.1c) is similar in concept to nuclear imaging with inhaled Xe-133 gas, but with superior signal to noise ratio, 3D coverage, and without the use of ionizing radiation.

While these capabilities have raised significant interest in the pulmonary research community (ALTES et al. 2001; SAMEE et al. 2003), less expensive whole

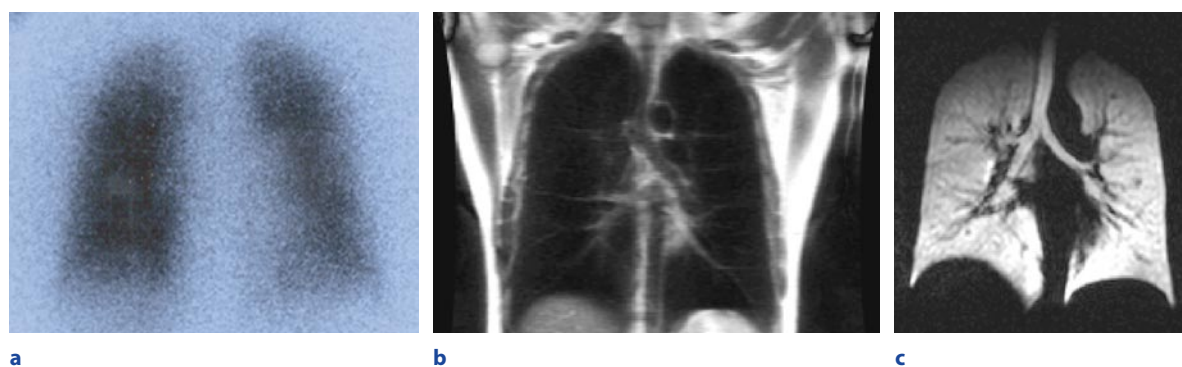


Fig. 8.1a–c. Xenon₁₃₃ scintigraphy of the lung airspace (c) juxtaposed with a conventional water proton MRI (b), and hyperpolarized He-3 MRI of the lungs in the same subject (a). Normal ventilation is depicted in all cases

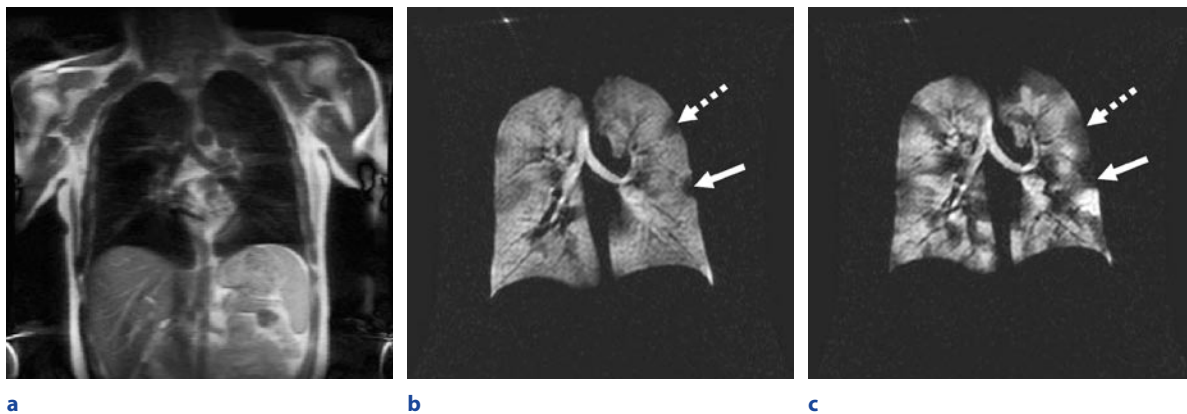


Fig. 8.2. **a** Proton image showing lung volume for a coronal slice through the trachea and primary bronchi. **b** Image of ventilation at the same slice location as in **a** in a subject with moderate asthma on Day 1 of a longitudinal study with small

peripheral defects indicated by arrows. **c** Day 2 after exposure to second hand smoke with more pronounced defects throughout including enlargement of the defect regions shown by the arrows in **b**

lung measures such as spirometry and plethysmography remain the primary tools for the diagnosis of asthma. The emerging clinical role of HP He-3 MRI is therefore principally in the characterization of asthma phenotypes, the visualization and testing of mechanisms underlying regional heterogeneity, and the evaluation of response to asthma therapies. These applications all exploit the ability of He-3 MRI to obtain safely repeated image sets for longitudinal studies without accumulating ionizing radiation dose. Interventions with methacholine (DE LANGE et al. 2007; SANI et al. 2008) and exercise challenge (SAMEE et al. 2003) have been safely performed and can provide a unique window into the dynamics of airway obstruction in asthma compared to normal subjects.

8.3

Characterization of Ventilation Patterns in the Asthmatic Lung

8.3.1 Basic MR Imaging Methods and Protocols

The basics of hyperpolarization of the He-3 preparation have already been described elsewhere and either metastability (GENTILE et al. 2000) or spin exchange optical pumping (WALKER and HAPPER 1997) methods can be used. The HP He-3 is typically mixed with nitrogen to a concentration range of 3.0–4.5 mM of polarized nuclei. The gas is typically delivered in a Tedlar® (DuPont™,

Wilmington DE) gas sampling bag through an attached tube.

To enable multi-nuclear MRI, clinical MRI scanners require specialized hardware for broad band transmit/receive (T/R), including radio frequency (RF) amplifiers, a T/R switch with pass band filters centered at the resonant frequency of the nucleus of interest (48.6 MHz for He-3 at 1.5 T). Most studies to date have been performed at 1.5 T although several research sites are conducting studies at lower field strength (DARRASSE et al. 1997; MAIR et al. 2005) and a few are using 3.0-T systems (PARRAGA et al. 2008). The patient or research subject is generally in the supine position. Consequently, gradients in ventilation and alveolar size are expected from anterior to posterior due to gravity dependence. Minimizing the duration of the study mitigates the development of posterior atelectasis and is not a common problem for typical exam times of 30 min or less.

Spin density images of ventilation have been most commonly used for the study of asthma to date. In a typical exam a scout image is first acquired for localization followed by acquisition of soft tissue anatomy with a breath-held conventional image at proton frequency. The anatomical scan uses a fast spin echo (FSE) or comparable gradient echo (GRE) acquisition at identical slice locations to those acquired for the He-3 MRI acquisition with lung volume matched (Figs. 8.1b and 8.2a) by having the subject inhale a bag of either helium-4 or air at equivalent volume to the He-3 dose.

The primary pulse sequence used for breath-held images of ventilation in HP He-3 MRI is a 2D multi-slice spoiled gradient recalled echo (2D SPGR) se-

Table 8.1. Typical imaging parameters used in applications described in the literature^a

| Method | TR/TE (ms) | Flip (deg) | Matrix | FOV (cm) | Slice (mm) | Polarized Gas Dose | Temporal resolution | Technique-Specific parameters |
|---------------------------------|------------|------------|--------------------------|----------|------------|---------------------------------|------------------------------|--|
| Ventilation (SAMEE et al. 2003) | 9/3.7 | 10 | 256×100 | 50×38 | 10 | 300 ml He-3 in 1 L | 10–13 s breath-hold from FRC | 14–16 coronal slices or 20–25 axial slices |
| Dynamic (KOUPELLIS et al. 2005) | 5.4/2 | 7 | 128 × 100 (proj. angles) | 41×41 | 10 | 5 ml He-3/kg body wgt. in 0.5 L | 0.54 s | 128 projection angles/frame |
| Diffusion (FAIN et al. 2006) | 8.4/4.5 | 7 | 128 × 80 | 38×30 | 15 | 4.5 mM polarized He-3 in 1 L | 14 s breath-hold from FRC | 10 coronal slices or 14–16 axial slices; b-value = 1.6 s/cm ² |

^aAll pulse sequences are SPGR performed using a 1.5-T clinical scanner in human subjects

quence. The flip angle is kept low (~7–10°) so as to preserve the HP magnetization throughout a 10–15 s breath-hold. The principal tradeoff for these studies is keeping the breath-hold duration sufficiently short to minimize stress on the patient while still allowing full coverage of the lungs within the field of view (FOV) of an axial or coronal slice orientation. A volume typically ranging from 0.5 to 1.0 L of HP He-3 is typically delivered by releasing a small plastic clamp that allows the subject to inhale the HP gas through the tube. In some studies the volume of the inhaled HP He-3 is adjusted for the subject's total lung capacity (TLC) to control for signal changes and inflation volume across subjects. The specifics for a standard protocol are summarized in Table 8.1.

8.3.2 Dynamic Imaging of Respiratory Maneuvers

Breath-held images of ventilation show patterns of airway obstruction at a fixed lung volume ~1 L above FRC, but this is measuring just one aspect of airway obstruction in asthma. A more complete study of the obstruction in asthma should include the dynamic components of the disease that have been shown to depend on airway size and lung volume (MEAD et al. 1967, 1970). Elements of airway dynamics and heterogeneity can be achieved using multiple breath-held maneuvers at different lung volumes or before and after intervention with bronchoconstrictors, bronchodilators, or exercise challenge. For example, He-3 MRI can be performed

under breath-hold before and after methacholine challenge (DE LANGE et al. 2007) or deep breathing maneuvers (SANI et al. 2008; BLACK et al. 2004) to assess airway response.

Dynamic MRI acquisition in combination with inspiratory or forced expiratory maneuvers can capture regional obstruction within a single respiratory cycle. Spiral (SALERNO et al. 2001) and PR acquisition (WILD et al. 2003) trajectories have been used to accelerate temporal and spatial resolution for assessing inspiratory obstruction in CF patients (KOUPELLIS et al. 2005) and COPD patients. In asthma, forced exhalation with dynamic HP He-3 MRI has shown retained signal intensity that correlates well with air trapping on MDCT and residual volume measurements with plethysmography (Fig. 8.3) (PANTH et al. 2004; HOLMES et al. 2005a). Standard imaging protocols for dynamic MRI using projection acquisition are listed in Table 8.1.

8.3.3 Diffusion Weighted HP He-3 MRI

Emerging acquisition methods using diffusion-weighted HP He-3 MRI of the gas within the airspaces of the lungs can measure microstructural changes in the emphysematous lung (SAAM et al. 2000; SALERNO et al. 2002; FAIN et al. 2005, 2006). These diffusion-weighted methods have recently shown promise for the measurement of microstructures linked to remodeling in asthma. For typical parameters using short time constant diffusion pulses (e.g. $\Delta = \delta = 1.5$ ms) (Table 8.1), the principal in-

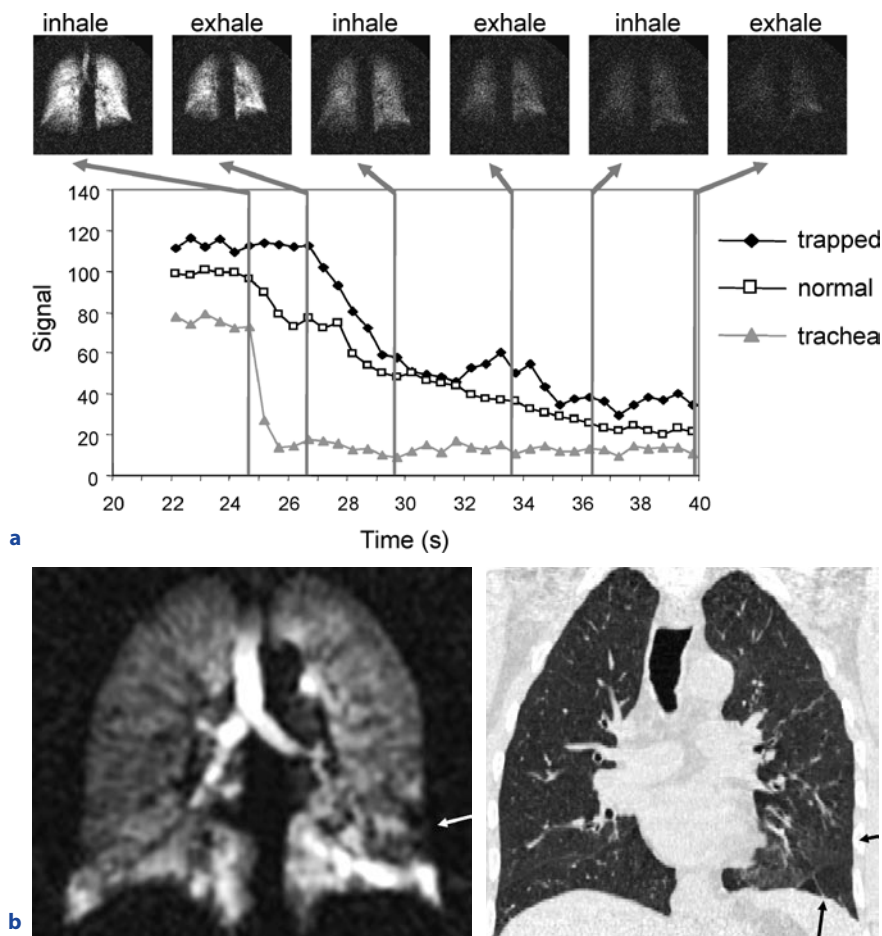


Fig. 8.3. **a** Respiratory dynamics for a subject with severe asthma showing gas trapping in the left lung base (*top, arrow*) and in signal-time curves. **b** Breath-held image of ventilation within the same respiratory cycle shows a defect region and hyperintense signal also in the left lung base. **c** Correspondence with hyperlucency and air trapping on CT (*black arrows*). FEV₁% predicted was 102%. (Reprinted from Holmes JH et al. (2007) *J Magn Reson Imaging* 26(3):630–636 with permission)

fluence on the apparent diffusion coefficient (ADC) is air trapping and hyperinflation in the small airways and alveolar spaces (Fig. 8.4). However, diffusion-weighted MRI in the asthmatic lung is an emerging technique and significant work and potential remains to be exploited using more optimized protocols for assessing lung microstructure in asthma (see Sect. 8.5).

8.3.4 Analysis Methods

The development of more objective quantitative measures of the severity and extent of ventilation defects

is critical to the advance of this technology. The most common metric used thus far in the literature is the mean number of volume defects per slice (VDS). Most commonly these scores have used consensus reading by a chest radiologist (HOLMES et al. 2007) although several blinded studies have been published recently (DE LANGE et al. 2006). This measure condenses the defect pattern into a single, whole lung metric, that has been used as an image marker for validating HP He-3 MRI images compared to spirometric measures, principally FEV₁% predicted (%p). Depending on the population studied, this measure correlates to FEV₁%p with correlation coefficients between 0.4 and 0.8 (DE LANGE et al. 2006; FAIN et al. 2008). However, the VDS measures de-

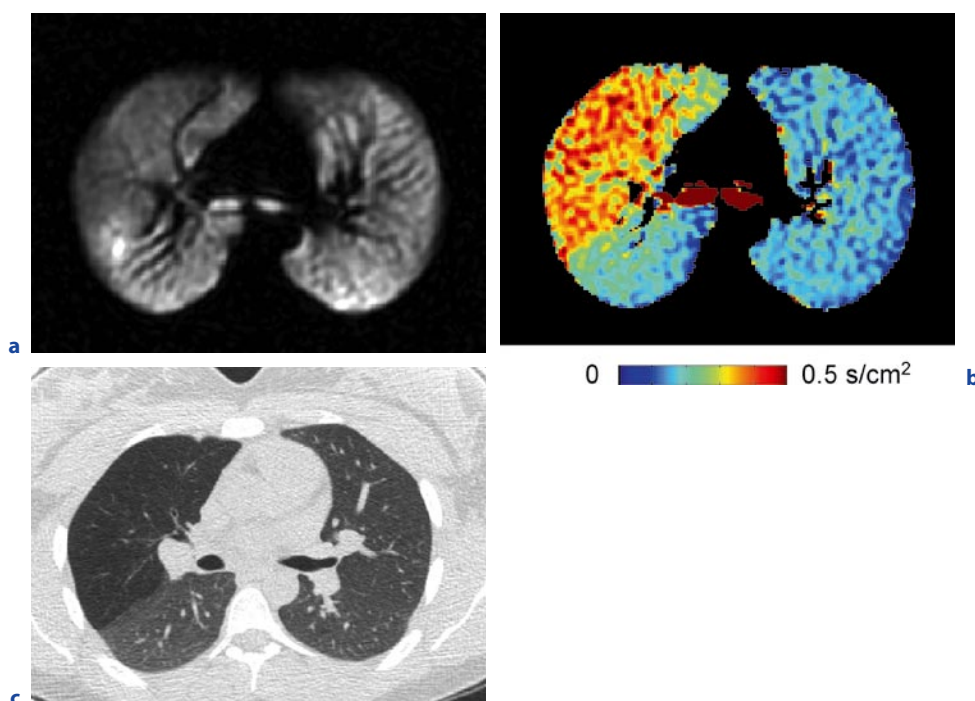


Fig. 8.4. **a** He-3 MR image of ventilation in a subject enrolled as a normal control in an asthma research study presenting with airway obstruction in the right upper bronchus (RB1) feeding the right upper lobe (RUL) due to pulmonary aneurysm. **b** Map of the apparent diffusion coefficient (ADC) derived from diffusion-weighted HP He-3 MRI ($\Delta\delta=1.25$ ms, $b = 1.6$ s/cm²). **c** Corresponding MDCT slice of through the RUL showing hyperlucency due to air trapping

fect size indirectly and ignores regional distribution of defects that are uniquely provided by imaging methods. Other subjective scores in the literature (PANTH et al. 2004) have similar limitations.

Attempts at providing more information about regional patterns and size of defects have recently been introduced. Defect volume by lung lobe as well as ventilated volume measurements have been introduced to account better for defect size and distribution (FAIN et al. 2008; WOODHOUSE et al. 2005). Proton MRI of the lungs is often used in conjunction with these methods to segment the total lung volume. The lung volume is then compared with the ventilated volume by setting a specific threshold value or by user-supervised segmentation of defect regions (Fig. 8.5). Regional assessment of defect volume allows cross-modality comparisons to abnormalities on MDCT and with local measures from bronchoscopy.

Other regional measures exploit the heterogeneity of the ventilation defect patterns by calculating the standard deviation over a finite region, typically 10% of the FOV, resulting in an image that can be characterized as a

heterogeneity map. However, these metrics need further validation. An important area for improvement is to consider methods for normalizing signal intensities in the images to capture gradations that likely correspond to different levels of airway obstruction. Examples of complete and partially obstructed regions are indicated by the solid and dotted arrows respectively in Fig. 8.2. At present the evaluation of severity of a defect based on signal intensity is largely subjective. These analysis methods must advance to more quantitative measures of ventilation in future studies.

There are emerging methods using hyperpolarized gas that are intrinsically more quantitative measures. The ADC derived from diffusion-weighted HP He-3 MRI acquisition, and the partial pressure of oxygen (PO_2) derived from T1 weighted acquisition, including both proton (CHEN et al. 1998) and HP He-3-enhanced MRI (DENINGER et al. 2002) are specific examples. However, these more quantitative metrics measure changes in lung microstructure and gas exchange respectively, and will likely be used to complement rather than replace images of ventilation in asthma.

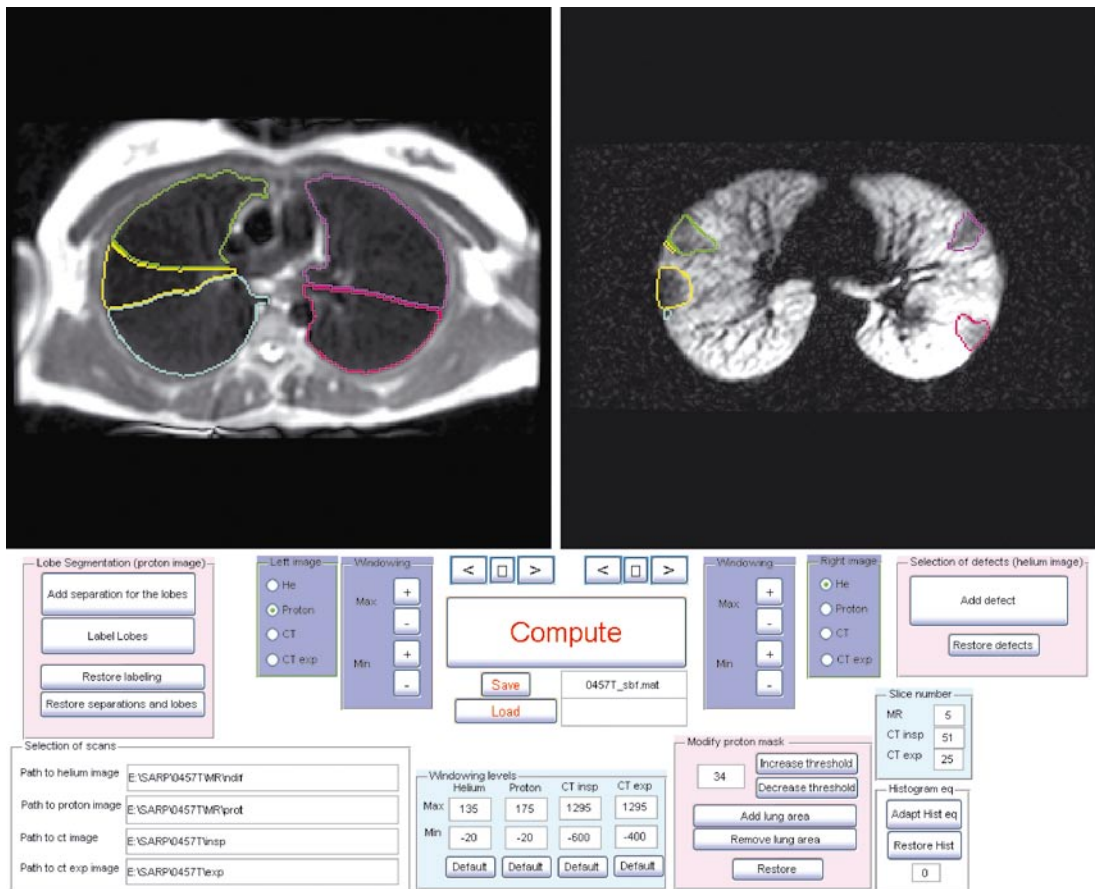


Fig. 8.5. Example of one graphic user interface (GUI) display showing equivalent axial proton MRI and HP MRI slices with segmented lung lobes defined based on thresholding and supervised segmentation. The HP MR image of ventilation in the right panel depicts ventilation defects segmented with lobe location indicated for each lobe by color code

8.4

Initial Clinical Results

8.4.1

Single Time-Point Studies

Single time-point studies have both validated image measures of ventilation defect relative to spirometry (DE LANGE et al. 2006) as well as tested the potential for detecting differences in asthma phenotype. In 58 patients with asthma and 18 control subjects, the VDS measure was shown to be higher in moderate to severe disease compared to mild asthma (mean 1.37 ± 0.24 vs 0.53 ± 0.12 , $p < 0.001$) and to correlate significantly with $FEV_1\%p$ ($r = -0.40$, $p = 0.002$), and FEV_1/FVC ($r = -0.51$, $p = 0.002$). Similar studies in 21 patients

with moderate to severe asthma found both defect score ($r = -0.76$, $p = 0.0002$) and percent defect volume ($r = -0.57$, $p = 0.007$) to correlate with $FEV_1\%p$, but in contrast to previous studies, there was not a significant correlation to FEV_1/FVC for either measure ($r = -0.24$, $p = 0.31$ and $r = -0.23$, $p = 0.31$) (FAIN et al. 2008). Since FEV_1/FVC is considered to be principally a measure of airflow limitation, the much stronger correlation of ventilation defect measures with $FEV_1\%p$ suggests a more prominent role of air trapping and small airways disease in this study population.

Another ongoing study seeks to detect differences in severe vs. non-severe (i.e. mild to moderate asthma patients) asthma using HP He-3 MRI of ventilation with respect to defect burden and correspondence of ventilation defects to air trapping on CT. In this study, subjects were grouped into severe and non-severe asthma based

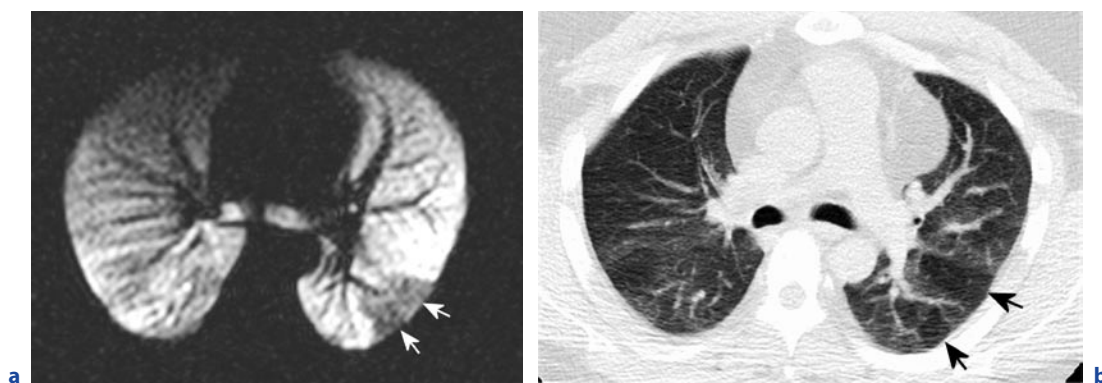


Fig. 8.6a,b. Example of spatial correspondence (**a**) between ventilation defects on HP MRI (*white arrows*) and (**b**) hyperlucency on MDCT (*black arrows*). These defects in the left lower lobe reflect obstructive physiology at different lung volumes: 15% of TLC for HP MRI in **a** and FRC for expiratory MDCT in **b**. (Reprinted from Fain SB et al. (2008) *Acad Radiol* 15(6):753–762 with permission)

on clinical symptoms and a threshold of >880 mcg/day of inhaled corticosteroids required to control symptoms (MOORE et al. 2007). The severe asthma phenotype has variously been estimated to have a prevalence of between 5% and 31% (MOORE et al. 1996), with the uncertainty largely determined by disagreement among experts about the key clinical features of more severe disease. A recent analysis of the National Medical Expenditure Survey found that 20% of asthmatics (“high cost patients”) accounted for 80% of the cost of asthma (total cost \$5.8 billion) (SMITH et al. 1997). Preliminary results suggest that patients with severe asthma are not necessarily distinguished by level of defect burden, but instead by greater regional air trapping on MDCT and on dynamic MRI. Ventilation defects on MRI overlap spatially with regions of air trapping on MDCT suggesting a common and more persistent source for these abnormalities (Fig. 8.6).

8.4.2 Longitudinal and Interventional Studies

The location and extent of defects through time, either during quiescent baseline periods of disease or during asthma exacerbation, have begun to identify the relative contributions of more persistent vs more dynamic components of obstructive disease. The level of primary airway involvement in asthma remains a topic of debate. Several studies using MDCT have pointed to a significant large airway component of obstruction (BROWN et al. 2006), while other studies have pointed to the dominance of the small airways (NEWMAN et al.

1994). The relative roles of airway hyperresponsiveness, and reversible vs non-reversible components of asthma is another area of contention. Computational modeling, for example, has suggested that heterogeneity could emerge from smooth muscle hypersensitivity combined with airway asymmetry (VENEGAS et al. 2005) rather than due to underlying structural changes in the airways.

Hyperpolarized He-3 MRI has informed this debate by evaluating the persistence and reversibility of defects in longitudinal and interventional studies. Longitudinal studies have begun to reveal important information about patterns of heterogeneity of ventilation over time. Interventional studies of bronchodilation or bronchoconstriction induced by albuterol or methacholine have made it possible to address issues of airway reversibility more directly. Rapid transfer and positioning of the patient followed by the application of fast MRI acquisitions make it possible to administer the challenge outside the magnet bore and acquire post-challenge images within 5 min. Similarly, regional assessment of previously inaccessible diseases such as exercise-induced bronchoconstriction (EIB) can now be evaluated by imaging before and after exercise challenge (SAMEE et al. 2003) or after withdrawal of therapy. In one study inhaled corticosteroid therapy was gradually withdrawn over a 4-week period in mild/moderate asthmatics (PANTH et al. 2004). Both dynamic and breath-held imaging of ventilation showed increased number and extent of ventilation defects and gas trapping in response to withdrawal of inhaled corticosteroid therapy. A significant drop in FEV₁p (from 115% to 94% predicted) corresponded with the increase in defects and a significant increase

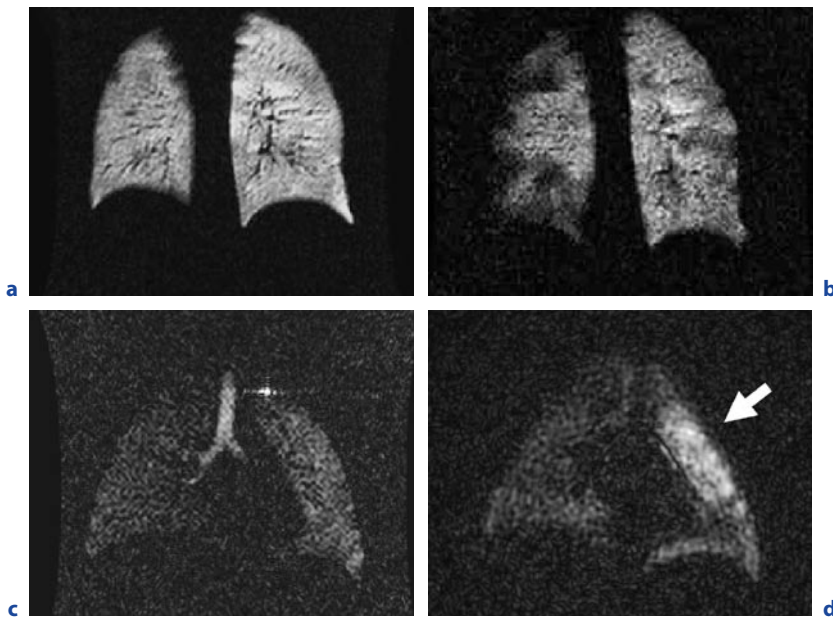


Fig. 8.7a-d. He-3 MRI ventilation images in a subject with mild asthma during inhaled corticosteroid (ICS) treatment (a,c) and after withdrawal of ICS treatment (b,d). The arrow in d indicates a region of gas trapping at forced expiration after withdrawal of therapy

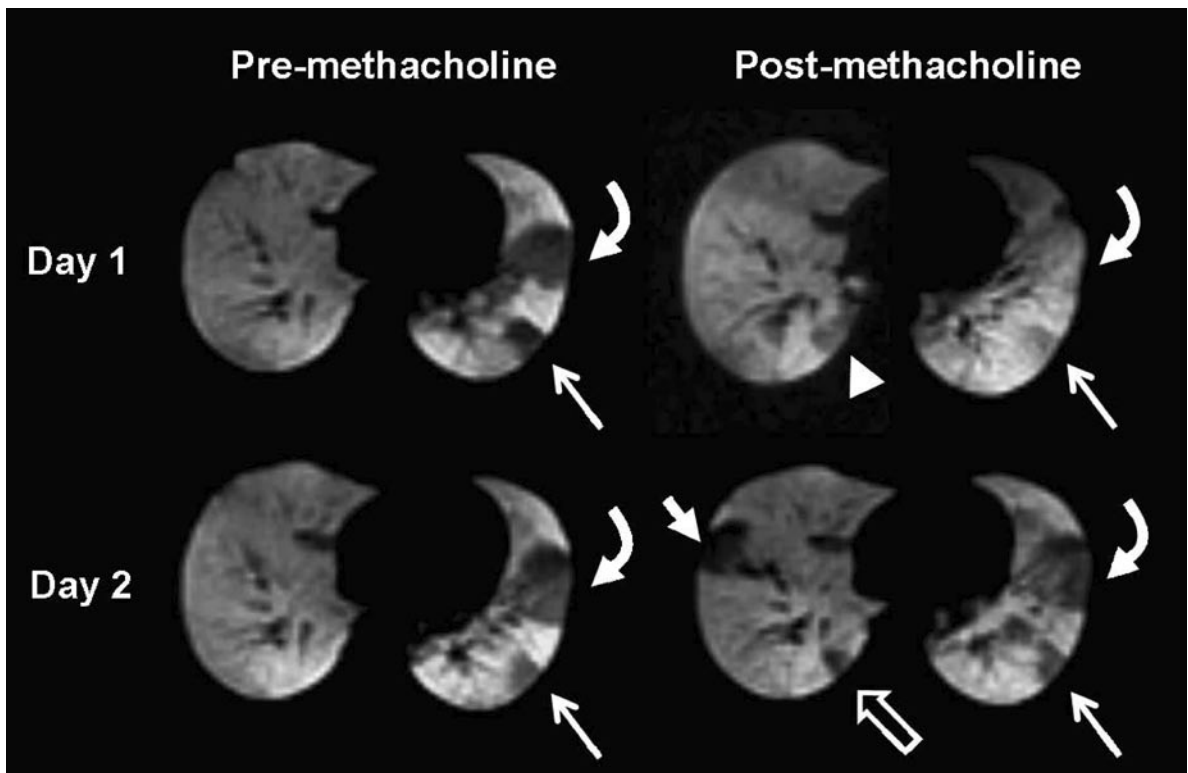


Fig. 8.8. Longitudinal study showing HP He-3 MRI on Day 1 (top row) and Day 2 (bottom row) before (left) and after (right) methacholine intervention. Note the persistent defects in the Day 1 and Day 2 baseline studies indicated by the curved and straight arrows. Note that post-methacholine several new defects emerge while other baseline defects resolve. (Reprinted from de Lange EE, Altes TA, Patrie J et al. (2007) J Allergy Clin Immunol 119:1072–1078 with permission)

in peripheral blood eosinophils was also observed (Fig. 8.7).

A longitudinal and interventional study by DE LANGE et al. (2007) found that up to 40% of the ventilation defects persisted in the same location over repeated acquisitions over varying time periods of several days to over a year. Up to 70% of defects overlapped when comparing time-points acquired post-methacholine challenge. Results of these longitudinal and interventional studies support regional heterogeneity of ventilation in asthma and a mixture of persistent (see arrows in left column, Fig. 8.8) and reversible regions of ventilation defect (see right column, Fig. 8.8). But challenging the airways with bronchoconstriction does not necessarily amplify the size of the defect and in some cases resolves baseline defects (Fig. 8.8).

The regional patterns of ventilation in asthma are central to understanding the mechanisms driving airway obstruction, and the results point to at least some persistent regions of abnormality. These regions may be proximal to airways that have undergone structural remodeling or are undergoing chronic inflammation,

while airways with a more reversible pattern may be proximal to regions of mucus plugging or more dominant smooth muscle tone. The apparent observation of both processes simultaneously is entirely consistent with the known complexity of this disease, but more work is necessary to provide a means to test mechanisms of airway obstruction and response to therapy more specifically.

8.5

Emerging Techniques

8.5.1

Four-Dimensional Imaging

Structure-function relationships in asthma are poorly understood at present in part due to the dearth of knowledge about the level of the airway tree that is principally involved in the obstructive physiology. Imaging can better address structure-function associations if spatial

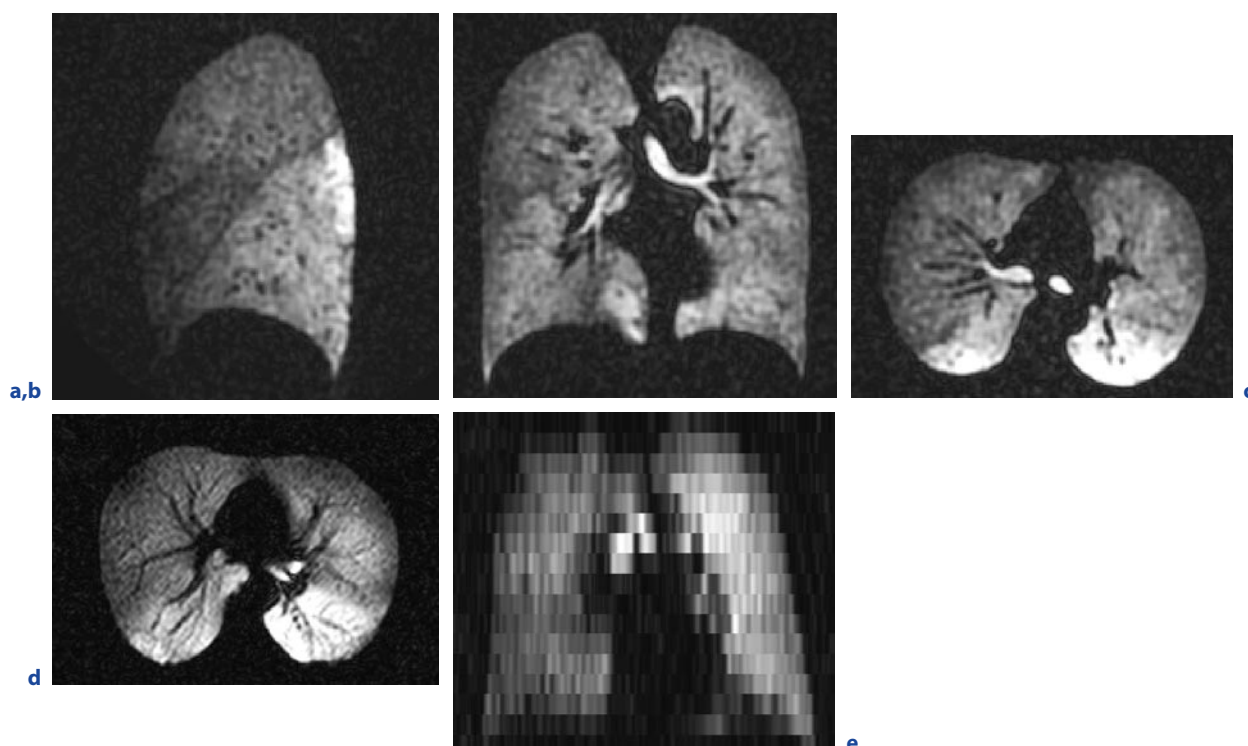


Fig. 8.9. Sagittal (a), coronal (b) and axial (c) views of ventilation images acquired using the multi-echo undersampled 3D Radial acquisition (VIPR) method at an isotropic spatial resolution of 3.3 mm. The 3D results are compared to (d,e) a conventional 2D multi-slice acquisition (see Table 8.1) to

emphasize the benefits of isotropic resolution for depicting images of ventilation of the lung anatomy. Note the fissures of the right lung lobes visible in a. (Reprinted from Holmes JH, O'Halloran RL, Brodsky EK et al. (2008) *Magn Reson Med* 59(5):1062–1071 with permission)

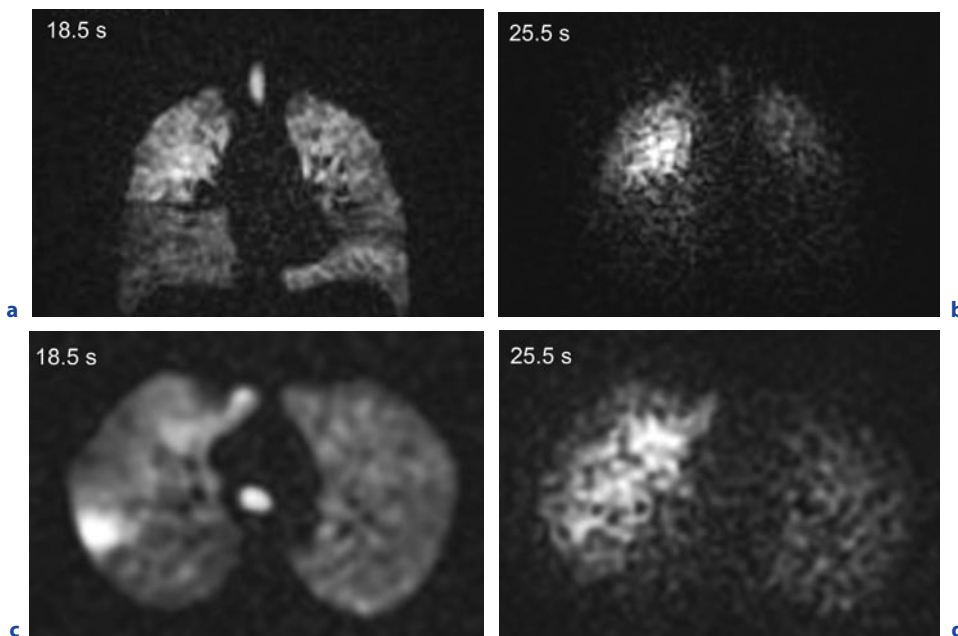


Fig. 8.10. **a,b** Coronal slices from peak inspiration and forced expiration of a 4D radial acquisition during single respiratory cycle of HP He-3 inhalation/exhalation. **c,d** Corresponding axial slices from the same time frames showing gas trapping in the right upper lobe

resolution can be improved sufficiently to identify functional ventilation defects in the context of the structural changes of the airway tree. While the spatial resolution of HP He-3 techniques is superior to nuclear imaging methods at present, it is insufficient to routinely identify the lobe boundaries or adequately measure large airway structures. For conventional acquisitions, the 1–1.5 cm slice thickness required to cover the lungs leads to significant partial volume artifact. Yet a better understanding of the interplay of ventilation defects and airway obstruction would benefit from the ability to identify the lung lobes and level of the airway tree where ventilation defects occur.

As shown by prior studies (WILD et al. 2004), important benefits of 3D acquisition include improved spatial resolution, improved signal to noise ratio and reduced sensitivity to slice profile compared to 2D multiple slice acquisitions. The 3D radial acquisition methods recently introduced (HOLMES et al. 2008) provide isotropic resolution that allows images to be reformatted in multiple planes with full lung coverage, and improved temporal resolution and spatial resolution in MRI allowing depiction of the lobar boundaries and 3D depiction of the large airways (Fig. 8.9).

Dynamic methods for imaging the airways in 2D have been demonstrated and compared to MDCT in phantom studies (LEWIS et al. 2005; TZENG et al. 2007). Using accelerated imaging methods and recon-

struction methods, such as parallel imaging (LEE et al. 2006) or HYPR methods (MISTRETTA et al. 2006; O'HALLORAN et al. 2008), 4D (3D + time) imaging of respiratory dynamics can be achieved and compared directly to CT (Fig. 8.10). It is expected that such 3D methods will be less affected by partial volume artifacts and thus more sensitive to small regions of gas trapping than 2D techniques allowing better correspondence with airway anatomy.

8.5.2 Diffusion-weighted Imaging of Lung Micro-structure

It has been shown in numerous studies that the HP He-3 gas can be used in conjunction with diffusion-weighted acquisition techniques to assess alveolar microstructure in COPD and emphysema (SAAM et al. 2000; SALERNO et al. 2002; FAIN et al. 2005, 2006). Diffusion-weighted imaging methods, while promising, are early in their application to asthma. Recent work suggests that diffusion weighted imaging can depict gas trapping (Fig. 8.4) and perhaps larger scale structural changes using long time constant diffusion weighting ($\Delta \approx 1.5$ s) based on a stimulated echo approach (WANG et al. 2006). Specific models of lung structure (YABLONSKIY et al. 2002) may also help to quantify the dimensions of the lung

microstructures allowing changes in airway structure to be tracked longitudinally for evaluating response to therapy.

8.5.3 Quantitative Ventilation and Perfusion

A more specific but difficult measure, particularly for image-based methods, is the alveolar ventilation (VA) to perfusion (Q) ratio (VA/Q). The VA/Q is the standard for measuring anomalies in lung function stemming from hypoxemia. Hypoxemic vasoconstriction is a normal process that reduces blood flow to areas with low ventilation in order to match ventilation to perfusion. VA/Q is regional by nature and may be important in asthma in order to provide an assessment of a given individual's ability to adapt to persistent obstruction and/or exacerbation due to heterogeneity in the ventilation (MUSCH et Venegas 2005).

However, the subjective nature of the typical images of ventilation provided using HP He-3 MRI is a significant limitation in moving towards quantitative VA/Q. Dynamic methods using HP He-3 show some promise to quantify ventilation by evaluating time constants of wash-in and wash-out of the gas (KOUPELLIS et al. 2005; HOLMES et al. 2007). However, issues of B1-uniformity and flip angle correction (MILLER et al. 2004) make true quantification of ventilation using these approaches difficult. Nonetheless, qualitative VA/Q may be obtained by combining HP He-3 ventilation with intravenous injection of gadolinium contrast-enhanced measures of perfusion (LEVIN and HATABU 2004) or possibly arterial spin labeling (ASL) perfusion methods (PRISK et al. 2007).

Using T1-weighted imaging techniques, VA/Q can be derived indirectly from depolarization of HP He-3 MRI due to the paramagnetic effects of regional alveolar oxygen concentration (RIZI et al. 2004). However, these methods are sensitive to low signal-to-noise, particularly in partially obstructed regions. The accuracy of modeling T1-decay with the reduced number of time points available within a limited breath-hold is an additional challenge for this technique (FISCHER et al. 2004). Accelerated acquisition methods may help make these techniques more robust for asthma applications (O'HALLORAN et al. 2008).

While there has been little application of HP Xe-129 MRI methods to clinical lung disease, the solubility of Xe-129 in the blood stream raises interesting applications. HP Xe-129 MRI has lagged behind HP He-3 methods largely because Xe-129 is more challenging to polarize, has a lower gyromagnetic ratio than He-3

(11.8 MHz/T vs 32.4 MHz/T) and protocols for its application are not as fully developed. Nonetheless, the ~200 ppm chemical shift between gas and dissolved phase may make HP Xe-129 a more attractive approach for quantifying VA/Q directly in a variety of lung diseases if the technical challenges can be overcome.

8.5.4 Multi-modality Airway Assessment

Combining functional images of ventilation from HP He-3 MRI with other modes of assessing lung disease is a potentially powerful approach to validating different airway mechanisms in asthma. Several cross-modality studies are in progress to combine functional images of ventilation from MRI to guide more localized quantitative measures of airway remodeling using bronchoscopic assessment, MDCT, and modeling. For example, bronchoalveolar lavage at ventilation defect sites on HP He-3 MRI show that neutrophil cell counts increase with extent of ventilation defect (FAIN et al. 2008). In addition, quantitative MDCT has been used to measure airway thickening associated with increased asthma severity (AYSOLA et al. 2008). Studies that combine HP He-3 MRI with MDCT can therefore provide a means of assessing airway remodeling specific to ventilation defect location in the same subject. A particularly novel approach is to combine imaging of ventilation to provide boundary conditions on modes of airway stiffness based on mechanical resistivity measures (TGAVALEKOS et al. 2005). Preliminary results from these cross-modality studies point to a more prominent involvement of the distal large (4th–6th generation) and small airways in asthma.

8.6 Summary/Conclusions

Ongoing clinical studies using MRI are leading to a better understanding of different asthma phenotypes and the underlying mechanism(s) driving airway obstruction in this disease. There have been important advances in understanding of regional heterogeneity in images of ventilation using HP He-3 MRI, including the recognition of regions of persistent ventilation defect based on longitudinal and interventional clinical studies.

Emerging techniques include 4D imaging of regional respiratory dynamics and diffusion-weighted HP He-3 MRI, T1-weighted PO₂ mapping, and more quantitative VA/Q approaches. These methods alone and in

concert with other modes of assessing lung disease such as MDCT imaging of airway structures show potential for evaluating the diffuse and complex features of asthma.

References

- Altes T, Powers P, Knight-Scott J, Rakes G, Platts-Mills T, de Lange EE, Alford B, Mugler J, Brookeman J (2001) Hyperpolarized ^3He MR lung ventilation imaging in asthmatics: preliminary findings. *J Magn Reson Imaging* 13:378–384
- Aysola RS, Hoffman EA, Gierada D, Wenzel S, Cook-Granroth J, Tarsi J, Zheng J, Schechtman KB, Ramkumar TP, Cochran R, Xueping E, Christie C, Newell J, Fain SB, Altes TA, Castro M, (SARP) and the SARP Network (2008) Airway remodeling measured by MDCT is increased in severe asthma and correlates with pathology. *Chest* epub
- Benayoun L, Druilhe A, Dombret M, Aubier M, Pretolani M (2003) Airway structural alterations selectively associated with severe asthma. *Am J Respir Crit Care Med* 167:1360–1368
- Black LD, Henderson AC, Atileh H, Israel E, Ingenito EP, Lutchen KR (2004) Relating maximum airway dilation and subsequent reconstriction to reactivity in human lungs. *J Appl Physiol* 96:1808–1814
- Brown RH, Croisille P, Mudge B, Diemer FB, Permutt S, Toggias A (2000) Airway narrowing in healthy humans inhaling methacholine without deep inspirations demonstrated by HRCT. *Am J Respir Crit Care Med* 161:1256–1263
- Brown RH, Pearse DB, Pyrgos G, Liu MC, Toggias A, Permutt S (2006) The structural basis of airways hyperresponsiveness in asthma. *J Appl Physiol* 101:30–39
- Chen Q, Jakob PM, Griswold MA, Levin DL, Hatabu H, Edelman RR (1998) Oxygen enhanced MR ventilation imaging of the lung. *Magma* 7:153–161
- Darrasse L, Guillot G, Nacher PJ, Tastevin G (1997) Low-field ^3He nuclear magnetic resonance in human lungs. *C R Acad Sci Ser II Fasc B Mec Phys Chim Astron* 324:691–700
- de Lange EE, Altes TA, Patrie JT, Gaare JD, Knake JJ, Mugler JP, Platts-Mills TA (2006) Evaluation of asthma with hyperpolarized helium-3 MRI: correlation with clinical severity and spirometry. *Chest* 130:1055–1062
- de Lange EE, Altes TA, Patrie JT, Parmar J, Brookeman JR, Mugler JP, Platts-Mills TA (2007) The variability of regional airflow obstruction within the lungs of patients with asthma: assessment with hyperpolarized helium-3 magnetic resonance imaging. *J Allergy Clin Immunol* 119:1072–1078
- Deninger AJ, Eberle B, Bermuth J, Escat B, Markstaller K, Schmiedeskamp J, Schreiber WG, Surkau R, Otten E, Kauczor HU (2002) Assessment of a single-acquisition imaging sequence for oxygen-sensitive (^3He)-MRI. *Magn Reson Med* 47:105–114
- Driehuys B, Walker J, Pollaro J, Cofer GP, Mistry N, Schwartz D, Johnson GA (2007) ^3He MRI in mouse models of asthma. *Magn Reson Med* 58:893–900
- Evans SE, Scanlon PD (2003) Current practice in pulmonary function testing. *Mayo Clin Proc* 78:758–763
- Fain SB, Altes TA, Panth SR, Evans MD, Waters B, Mugler JP, Korosec FR, Grist TM, Silverman M, Salerno M, Owers-Bradley J (2005) Detection of age-dependent changes in healthy adult lungs with diffusion-weighted ^3He MRI. *Acad Radiol* 12:1385–1393
- Fain SB, Panth SR, Evans MD, Wentland AL, Holmes JH, Korosec FR, O'Brien MJ, Fountaine H, Grist TM (2006) Early emphysematous changes in asymptomatic smokers: detection with ^3He MR imaging. *Radiology* 239:875–883
- Fain SB, Gonzalez-Fernandez G, Peterson ET, Evans MD, Sorkness RL, Jarjour NN, Busse WW, Kuhlman JE (2008) Evaluation of structure-function relationships in asthma using multidetector CT and hyperpolarized He-3 MRI. *Acad Radiol* 15:753–762
- Fischer M, Spector Z, Ishii M, Yu J, Emami K, Itkin M, Rizi R (2004) Single-acquisition sequence for the measurement of oxygen partial pressure by hyperpolarized gas MRI. *Magn Reson Med* 52:766–773
- Gentile TR, Jones GL, Thompson AK, Rizi RR, Roberts DA, Dimitrov IE, Reddy R, Lipson DA, Gefter W, Schnall MD, Leigh JS (2000) Demonstration of a compact compressor for application of metastability-exchange optical pumping of ^3He to human lung imaging. *Magn Reson Med* 43:290–294
- Hatabu H, Tadamura E, Chen Q, Stock KW, Li W, Prasad PV, Edelman RR (2001) Pulmonary ventilation: dynamic MRI with inhalation of molecular oxygen. *Eur J Radiol* 37:172–178
- Hoffman EA, Chon D (2005) Computed tomography studies of lung ventilation and perfusion. *Proc Am Thorac Soc* 2:492–498, 506
- Holmes J, Korosec F, Du J, Panth S, Grist T, Fain S (2005a) 3D/2D Hybrid PR for single acquisition dynamic and breath-held hyperpolarized He-3 MRI. In: Proceedings of the 13th Annual Meeting of ISMRM, Miami Beach, FL, USA, p 1808
- Holmes JH, Sorkness RL, Meibom SK, Sundaram SK, Perlman SB, Converse AK, Pyzalski RW, Hahn AD, Korosec FR, Grist TM, Fain SB (2005b) Noninvasive mapping of regional response to segmental allergen challenge using magnetic resonance imaging and [^3H]fluorodeoxyglucose positron emission tomography. *Magn Reson Med* 53:1243–1250
- Holmes JH, Korosec FR, Du J, O'Halloran RL, Sorkness RL, Grist TM, Kuhlman JE, Fain SB (2007) Imaging of lung ventilation and respiratory dynamics in a single ventilation cycle using hyperpolarized He-3 MRI. *J Magn Reson Imaging* 26:630–636
- Holmes JH, O'Halloran RL, Brodsky EK, Jung Y, Block WF, Fain SB (2008) 3D hyperpolarized He-3 MRI of ventilation using a multi-echo projection acquisition. *Magn Reson Med* 59:1062–1071
- Howarth DM, Lan L, Thomas PA, Allen LW (1999) $^{99\text{m}}\text{Tc}$ technegas ventilation and perfusion lung scintigraphy for the diagnosis of pulmonary embolus. *J Nucl Med* 40:579–584

- Hurwitz LM, Reiman RE, Yoshizumi TT, Goodman PC, Toncheva G, Nguyen G, Lowry C (2007) Radiation dose from contemporary cardiothoracic multidetector CT protocols with an anthropomorphic female phantom: implications for cancer induction. *Radiology* 245:742–750
- James AL, Maxwell PS, Pearce-Pinto G, Elliot JG, Carroll NG (2002) The relationship of reticular basement membrane thickness to airway wall remodeling in asthma. *Am J Respir Crit Care Med* 166:1590–1595
- Koumellis P, van Beek EJ, Woodhouse N, Fischele S, Swift AJ, Paley MN, Hill C, Taylor CJ, Wild JM (2005) Quantitative analysis of regional airways obstruction using dynamic hyperpolarized ^3He MRI-preliminary results in children with cystic fibrosis. *J Magn Reson Imaging* 22:420–426
- Lee RF, Johnson G, Grossman RI, Stoeckel B, Trampel R, McGuinness G (2006) Advantages of parallel imaging in conjunction with hyperpolarized helium – a new approach to MRI of the lung. *Magn Reson Med* 55:1132–1141
- Levin DL, Hatabu H (2004) MR evaluation of pulmonary blood flow. *J Thorac Imaging* 19:241–249
- Levitzky M (2003) *Pulmonary physiology*. McGraw-Hill, New York
- Lewis TA, Tzeng YS, McKinstry EL, Tooker AC, Hong K, Sun Y, Mansour J, Handler Z, Albert MS (2005) Quantification of airway diameters and 3D airway tree rendering from dynamic hyperpolarized ^3He magnetic resonance imaging. *Magn Reson Med* 53:474–478
- Little SA, Sproule MW, Cowan MD, Macleod KJ, Robertson M, Love JG, Chalmers GW, McSharry CP, Thomson NC (2002) High resolution computed tomographic assessment of airway wall thickness in chronic asthma: reproducibility and relationship with lung function and severity. *Thorax* 57:247–253
- Mair RW, Hrovat MI, Patz S, Rosen MS, Ruset IC, Topulos GP, Tsai LL, Butler JP, Hersman FW, Walsworth RL (2005) ^3He lung imaging in an open access, very-low-field human magnetic resonance imaging system. *Magn Reson Med* 53:745–749
- Mead J, Turner JM, Macklem PT, Little JB (1967) Significance of the relationship between lung recoil and maximum expiratory flow. *J Appl Physiol* 22:95–108
- Mead J, Takishima T, Leith D (1970) Stress distribution in lungs: a model of pulmonary elasticity. *J Appl Physiol* 28:596–608
- Middleton H, Black RD, Saam B, Cates GD, Cofer GP, Guenther R, Happer W, Hedlund LW, Johnson GA, Juvan K (1995) MR imaging with hyperpolarized ^3He gas. *Magn Reson Imaging* 33:271–275
- Miller GW, Altes TA, Brookeman JR, de Lange EE, Mugler JP (2004) Hyperpolarized ^3He lung ventilation imaging with B1-inhomogeneity correction in a single breath-hold scan. *Magma* 16:218–226
- Mistretta CA, Wieben O, Velikina J, Block W, Perry J, Wu Y, Johnson K, Wu Y (2006) Highly constrained backprojection for time-resolved MRI. *Magn Reson Med* 55:30–40
- Moore B, Weiss K, Sullivan S (1996) Epidemiology and socioeconomic impact of severe asthma. In: Szefer SJ, Lung DYM (eds) *Severe asthma: pathogenesis and clinical management, lung biology in health and disease*. Marcel Dekker, New York, pp 1–28
- Moore WC, Bleecker ER, Curran-Everett D, Erzurum SC, Ameredes BT, Bacharier L, Calhoun WJ, Castro M, Chung KF, Clark MP, Dweik RA, Fitzpatrick AM, Gaston B, Hew M, Hussain I, Jarjour NN, Israel E, Levy BD, Murphy JR, Peters SP, Teague WG, Meyers DA, Busse WW, Wenzel SE (2007) Characterization of the severe asthma phenotype by the National Heart, Lung, and Blood Institute's Severe Asthma Research Program. *J Allergy Clin Immunol* 119:405–413
- Musch G, Venegas JG (2005) Positron emission tomography imaging of regional pulmonary perfusion and ventilation. *Proc Am Thorac Soc* 2:522–527, 508–529
- Newman KB, Lynch DA, Newman LS, Ellegood D, Newell JD Jr (1994) Quantitative computed tomography detects air trapping due to asthma. *Chest* 106:105–109
- Newman S, Pitcairn G, Hirst P, Rankin L (2003) Radionuclide imaging technologies and their use in evaluating asthma drug deposition in the lungs. *Adv Drug Deliv Rev* 55:851–867
- NIH-NHLBI (2002) Expert Panel Report. Guidelines for the diagnosis and management of asthma. EPR-Update 2002 of NIH Publication 97-4051
- O'Halloran RL, Wen Z, Holmes JH, Fain SB (2008) Iterative projection reconstruction of time-resolved images using highly-constrained back-projection (HYPR). *Magn Reson Med* 59:132–139
- Ohno Y, Iwasawa T, Seo JB, Koyama H, Takahashi H, Oh YM, Nishimura Y, Sugimura K (2008) Oxygen-enhanced magnetic resonance imaging versus computed tomography: multicenter study for clinical stage classification of smoking-related chronic obstructive pulmonary disease. *Am J Respir Crit Care Med* 177:1095–1102
- Panth S, Fain S, Holmes J, Fuller S, Korosec F, Grist T (2004) Assessment of lung ventilation, gas trapping and pulmonary perfusion in patients with asthma during inhaled corticosteroid withdrawal. Proceedings of the 12th Annual Meeting of ISMRM, Kyoto, Japan, p 764
- Parraga G, Mathew L, Etemad-Rezai R, McCormack DG, Santyr GE (2008) Hyperpolarized (^3He) magnetic resonance imaging of ventilation defects in healthy elderly volunteers initial findings at 3.0 Tesla. *Acad Radiol* 15:776–785
- Petty T (2003) Chronic obstructive pulmonary disease. In: *Current diagnosis and treatment in pulmonary medicine*. McGraw-Hill, San Francisco, pp 82–90
- Prisk GK, Yamada K, Henderson AC, Arai TJ, Levin DL, Buxton RB, Hopkins SR (2007) Pulmonary perfusion in the prone and supine postures in the normal human lung. *J Appl Physiol* 103:883–894
- Rizi RR, Baumgardner JE, Ishii M, Spector ZZ, Edvinsson JM, Jalali A, Yu J, Itkin M, Lipson DA, Gefter W (2004) Determination of regional VA/Q by hyperpolarized ^3He MRI. *Magn Reson Med* 52:65–72

- Saam B, Yablonskiy D, Kodibagkar V, Leawoods J, Gierada D, Cooper J, Lefrak S, Conradi M (2000) MR imaging of diffusion of ^3He gas in healthy and diseased lungs. *Magn Reson Med* 44:174–179
- Salerno M, Altes T, Brookeman J, de Lange EE, Mugler J (2001) Dynamic spiral MRI of pulmonary gas flow using hyperpolarized ^3He : preliminary studies in healthy and diseased lungs. *Magn Reson Med* 46:667–677
- Salerno M, de Lange EE, Altes T, Truweit J, Brookeman J, Mugler J (2002) Emphysema: hyperpolarized helium 3 diffusion MR imaging of the lungs compared with spirometric indexes – initial experience. *Radiology* 222:252–260
- Samee S, Altes T, Powers P, de Lange EE, Knight-Scott J, Rakes G, Mugler J, Ciambotti J, Alford B, Brookeman J, Platts-Mills T (2003) Imaging the lungs in asthmatic patients by using hyperpolarized helium-3 magnetic resonance: assessment of response to methacholine and exercise challenge. *J Allergy Clin Immunol* 111:1205–1211
- Sani SZ, Tzeng YS, Cho MH, Y. Sun, Israel E, Albert MS, Lutchen KR (2008) Linking mechanical and ventilation heterogeneity in asthma via deep inspirations. *Proceedings of the International Conference of the ATS, Toronto, Canada*, p A563
- Smith D, Malone D, Lawson K, Okamoto L, Battista C, Saunders W (1997) A national estimate of the economic cost of asthma. *Am J Resp Crit Care Med* 156:787–793
- Sorkness RL, Blecker ER, Busse WW, Calhoun WJ, Castro M, Chung KF, Curran-Everett D, Erzurum SC, Gaston BM, Israel E, Jarjour NN, Moore WC, Peters SP, Teague WG, Wenzel SE (2008) Lung function in adults with stable but severe asthma: air trapping and incomplete reversal of obstruction with bronchodilation. *J Appl Physiol* 104:394–403
- Tgavalekos NT, Tawhai M, Harris RS, Musch G, Vidal-Melo M, Venegas JG, Lutchen KR (2005) Identifying airways responsible for heterogeneous ventilation and mechanical dysfunction in asthma: an image functional modeling approach. *J Appl Physiol* 99:2388–2397
- Tzeng YS, Hoffman E, Cook-Granroth J, Maurer R, Shah N, Mansour J, Tschirren J, Albert M (2007) Comparison of airway diameter measurements from an anthropomorphic airway tree phantom using hyperpolarized ^3He MRI and high-resolution computed tomography. *Magn Reson Med* 58:636–642
- van Beek EJ, Hoffman EA (2008) Functional imaging: CT and MRI. *Clin Chest Med* 29:195–216
- Venegas JG, Winkler T, Musch G, Vidal Melo MF, Layfield D, Tgavalekos N, Fischman AJ, Callahan RJ, Bellani G, Harris RS (2005) Self-organized patchiness in asthma as a prelude to catastrophic shifts. *Nature* 434:777–782
- Vidal Melo MF, Layfield D, Harris RS, O'Neill K, Musch G, Richter T, Winkler T, Fischman AJ, Venegas JG (2003) Quantification of regional ventilation-perfusion ratios with PET. *J Nucl Med* 44:1982–1991
- Walker TG, Happer W (1997) Spin-exchange optical pumping of noble-gas nuclei. *Rev Mod Phys* 69:629–642
- Wang C, Miller GW, Altes TA, de Lange EE, Cates GD Jr, Mugler JP (2006) Time dependence of ^3He diffusion in the human lung: measurement in the long-time regime using stimulated echoes. *Magn Reson Med* 56:296–309
- Wild J, Paley M, Kasuboski L, Swift A, Fичеle S, Woodhouse N, Griffiths P, van Beek EJ (2003) Dynamic radial projection MRI of inhaled hyperpolarized ^3He gas. *Magn Reson Med* 49:991–997
- Wild J, Woodhouse N, Paley M, Fичеle S, Said Z, Kasuboski L, van Beek EJ (2004) Comparison between 2D and 3D gradient-echo sequences for MRI of human lung ventilation with hyperpolarized ^3He . *Magn Reson Med* 52:673–678
- Winn R, Chan E, McKinley S, Geraci M (2003) Laboratory evaluation: pulmonary function testing. In: Hanley ME, Welsh CH (eds) *Current diagnosis and treatment in pulmonary medicine*. McGraw-Hill, San Francisco, pp 39–56
- Woodhouse N, Wild JM, Paley MN, Fичеle S, Said Z, Swift AJ, van Beek EJ (2005) Combined helium-3/proton magnetic resonance imaging measurement of ventilated lung volumes in smokers compared to never-smokers. *J Magn Reson Imaging* 21:365–369
- Yablonskiy D, Sukstanskii A, Leawoods J, Gierada D, Bretthorst G, Lefrak S, Cooper J, Conradi M (2002) Quantitative in vivo assessment of lung microstructure at the alveolar level with hyperpolarized ^3He diffusion MRI. *Proc Natl Acad Sci USA* 99:3111–3116

Chronic Obstructive Pulmonary Diseases

JULIA LEY-ZAPOROZHAN, AHMED F. HALAWEISH and EDWIN J. R. VAN BEEK

CONTENTS

| | | |
|---------|--|-----|
| 9.1 | Introduction | 155 |
| 9.2 | Parenchyma | 156 |
| 9.3 | Airways | 158 |
| 9.4 | Respiratory Dynamics | 158 |
| 9.5 | Ventilation | 160 |
| 9.5.1 | Oxygen-Enhanced Imaging | 160 |
| 9.5.2 | Hyperpolarized Noble Gas Imaging | 160 |
| 9.5.2.1 | Static Ventilation | 160 |
| 9.5.2.2 | Dynamic Assessment | 161 |
| 9.5.2.3 | ³ Helium Apparent Diffusion Coefficient (ADC) | 163 |
| 9.6 | Pulmonary Perfusion | 163 |
| 9.7 | Hemodynamics | 165 |
| | References | 166 |

KEY POINTS

MRI is becoming increasingly useful for imaging of lung structure and function, both in terms of airways imaging, assessment of ventilation and evaluation of lung perfusion and right heart function. This modality is highly versatile and capable of generating a range of inherent and exogenously introduced contrast mechanisms, while maintaining high resolution as well as incredible speed of data acquisition.

It is quite likely that MRI techniques will allow further evaluation of physiological and pathophysiological aspects of COPD, and this should ultimately lead to improved understanding and treatment of this heterogeneous diseases complex.

9.1

Introduction

Chronic obstructive pulmonary disease (COPD) is the fourth most common cause of death among adults (RABE et al. 2007). COPD is characterized by incompletely reversible (usually progressive) airflow limitation, which is associated with an abnormal inflammatory response of the lung to noxious particles or gases. It is caused by a mixture of airway obstruction (obstructive bronchiolitis) and parenchymal destruction (emphysema), the relative contributions of which are variable (RABE et al. 2007). Chronic bronchitis, or the presence of cough and sputum production for at least 3 months in each of 2 consecutive years, remains a clinically and epidemiologically useful diagnostic clas-

J. LEY-ZAPOROZHAN, MD
Department of Pediatric Radiology, University Hospital Heidelberg, Im Neuenheimer Feld 430, 69120 Heidelberg, Germany

A. F. HALAWEISH
Department of Biomedical Engineering\Radiology, University of Iowa Hospitals and Clinics, 200 Hawkins Drive, Iowa City, IA 52242-1077, USA

E. J. R. VAN BEEK, MD PhD
Department of Radiology, University of Iowa Hospitals and Clinics, 200 Hawkins Drive, Iowa City, IA 52242-1077, USA

sifying term. Pulmonary emphysema is a pathological term and is defined by the American Thoracic Society as an abnormal permanent enlargement of the air spaces distal to the terminal bronchioles, accompanied by the destruction of their walls. In a simplified way, obstructive airflow limitation leads to air-trapping with subsequent hyperinflation of the airspaces, which combined with inflammatory lung injury leads to destruction of the lung parenchyma. For severity assessment of COPD lung function tests, such as forced expiration volume in 1 s (FEV_1), FEV_1/FVC (forced vital capacity) and diffusing capacity for carbon monoxide (DLco) are used. However, pulmonary function tests only provide a global measure without any regional information and are not suitable for determination of structural abnormalities. Although extremely useful in clinical practice and for global management of patients, pulmonary function tests are known to be relatively insensitive to both early stages and small changes of manifest disease. Furthermore, pulmonary function tests are dependent upon the effort and compliance of the patient, and are difficult to reliably perform in young children. Chronic hyperinflation impacts on diaphragmatic geometry with subsequent dysfunction due to dissociation of the breathing mechanics. The disease also affects the pulmonary arteries: intimal thickening, smooth muscle hypertrophy and inflammation were described, which ultimately give rise to vascular remodeling (SZILASI et al. 2006). The direct vascular changes and hyperinflation lead to the precapillary type of pulmonary hypertension and pulmonary vascular flow disturbance (ROSENKRANZ 2007).

In contrast to pulmonary function tests, radiological imaging techniques may be able to differentiate the different components of obstructive lung disease on a regional basis, with the possibility of detecting early disease stages prior to the onset of severe symptoms. Computed tomography (CT) is the mainstay diagnostic modality in this field with emphasis on structural imaging of lung parenchyma and airways. Magnetic resonance imaging (MRI) has the potential to provide regional information about the lung without the use of ionizing radiation, but is hampered by several challenges: the low amount of tissue relates to a small number of protons leading to low signal, countless air-tissue interfaces cause substantial susceptibility artifacts and last but not least, respiratory and cardiac motion. In several lung diseases, such as tumors, the amount of protons or the blood volume is actually increased and motion is reduced, which provides better pre-conditions for MRI. In obstructive pulmonary disease, however, there are no facilitating disease-related effects as

there is loss of tissue and reduced blood volume due to hypoxic vasoconstriction and the degree of hyperinflation has a negative correlation with the MR signal (LEY-ZAPOROZHAN et al. 2008). The depiction of the airways by MRI is certainly limited to the central bronchi. Fortunately, MRI has shown significant potential beyond the mere visualization of structure by providing comprehensive information about "function", such as perfusion, hemodynamics, ventilation and respiratory mechanics.

9.2

Parenchyma

The most frequently utilized sequences in MRI of COPD are acquired in a single breath-hold. For fast T2-weighted imaging, single shot techniques with partial-Fourier acquisition (HASTE) or ultrashort TE (UTSE) are recommended (Figs. 9.1 and 9.2). The T2-weighted HASTE sequence in coronal and/or axial orientation allows for the depiction of pulmonary infiltrates, inflammatory bronchial wall thickening and mucus collections. T1-weighted 3D gradient echo sequences, such as VIBE, are suitable for the assessment of the mediastinum and common nodular lesions. The intravenous application of contrast material markedly improves the diagnostic yield of T1 weighted sequences by a clearer depiction of vessels, hilar structures and solid pathologies. A major goal in inflammatory obstructive airway disease is to differentiate inflammation within the wall from muscular hypertrophy, edema and mucus collection which cannot be achieved by CT, but can be addressed by the use of T1- and T2-weighted images as well as contrast enhancement (LEY-ZAPOROZHAN et al. 2008).

The extent of hyperinflation and hypoxic vasoconstriction is directly associated with the loss of signal (BANKIER et al. 2004). Thus, until now, MRI of the pulmonary parenchyma has only been successfully applied to diseases with an increase of tissue and resultant signal. While emphysematous destruction can hardly be diagnosed by a loss of signal, it is much easier to detect hyperinflation just by the size or volume of the thorax. In a recent study, it was shown that the change of parenchymal signal intensity measured by MRI at inspiration and expiration correlates with FEV_1 ($r=0.508$) and might warrant further studies as a predictor of airflow obstruction (IWASAWA et al. 2007).

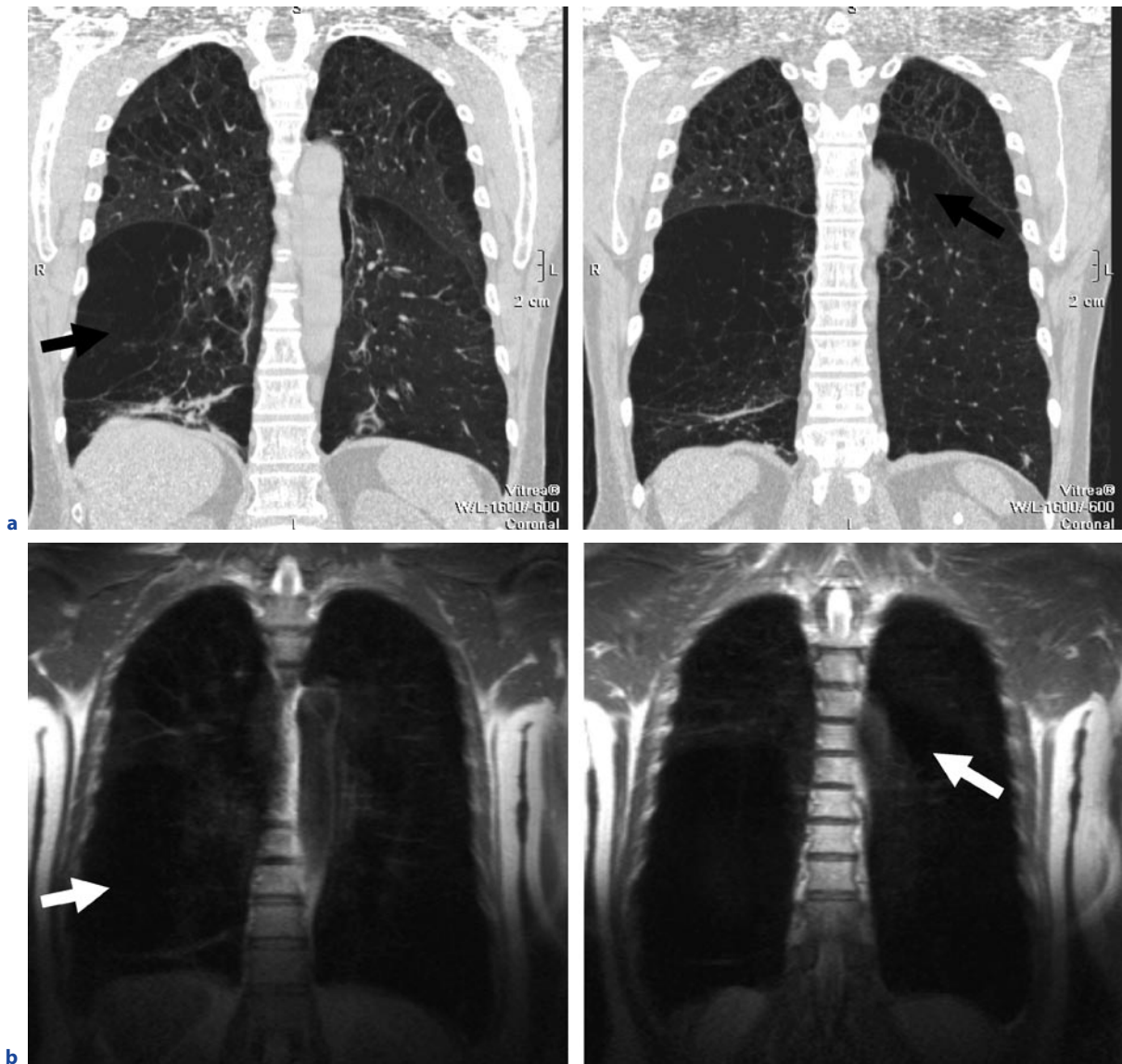


Fig. 9.1a,b. Coronal CT reformats (**a**) and corresponding coronal T2 weighted (HASTE) images (**b**): severe emphysema with predominance of the right lower lobe on CT corresponds

to a loss of MR signal (*arrows*) reflecting destruction of the parenchyma and paucity of pulmonary vasculature of the pulmonary vasculature



Fig. 9.2. Coronal T2 weighted (HASTE) image shows the typical flattening of the diaphragm in emphysema

9.3

Airways

Several pathological studies have shown that a major site of airway obstruction in patients with COPD is in airways smaller than 2 mm internal diameter (HOGG et al. 2004). The 2-mm airways are located between the 4th and the 14th generation of the tracheobronchial tree. Airflow limitation is closely associated with the severity of luminal occlusion by inflammatory exudates and thickening of the airway walls due to remodeling. Severe peripheral airflow obstruction can also affect the proximal airways from subsegmental bronchi to the trachea.

For assessment of tracheal instability MR cine acquisitions during continuous respiration or forced expiration are recommended (HEUSSEL et al. 2004). The depiction of airway dimensions and thickness of the airway walls by MRI under physiological conditions is limited to the central bronchi. For depiction of the bronchiectasis high spatial resolution is essential. By using a 3D volume interpolated gradient echo sequence (VIBE) with a voxel size of approximately $0.9 \times 0.88 \times 2.5$ mm a sensitivity of 79% and a specificity of 98% regarding the

visual depiction of bronchiectasis was shown compared to CT (BIEDERER et al. 2003).

9.4

Respiratory Dynamics

Respiration is the result of the complex interaction between chest wall and diaphragm motion, and it can be visualized by 2D or 3D dynamic MR techniques (CLUZEL et al. 2000; PLATHOW et al. 2004, 2005). For data acquisition time resolved techniques are used which can be based on FLASH or trueFISP sequences. This allows for a high temporal resolution down to 100 ms per frame.

Hyperinflation of the lung severely affects diaphragmatic geometry with subsequent reduction of the mechanical properties, while the effects on the mechanical advantage of the neck and rib cage muscles are less pronounced (DECRAMER 1997). The common clinical measurements of COPD do not provide insights into how structural alterations in the lung lead to dysfunction in the breathing mechanics, although treatments such as lung volume reduction surgery (LVRS) are thought to improve lung function by facilitating breathing mechanics and increasing elastic recoil (HENDERSON et al. 2007).

In contrast to normal subjects with regular, synchronous diaphragm and chest wall motion, dynamic MRI in patients with emphysema frequently showed reduced, irregular or asynchronous motion, with a significant decrease in the maximum amplitude and the length of apposition of the diaphragm (SUGA et al. 1999). In some patients the ventral portion of the hemidiaphragm moved downward at MRI while the dorsal part moved upward like a seesaw (IWASAWA et al. 2000). The paradoxical diaphragmatic motion correlated with hyperinflation, although severe hyperinflation tended to restrict both normal and paradoxical diaphragmatic motion (IWASAWA et al. 2002). After LVRS, patients showed improvements in diaphragm and chest wall configuration and mobility at MRI (SUGA et al. 1999). Ultrafast dynamic proton MRI was shown to be able to demonstrate the rapid volume changes observed during forced vital capacity maneuver (Fig. 9.3) and correlated closely with pulmonary function tests, but with the added advantage of providing regional information on changes in lung volumes during this procedure (EICHINGER et al. 2007; SWIFT et al. 2007).

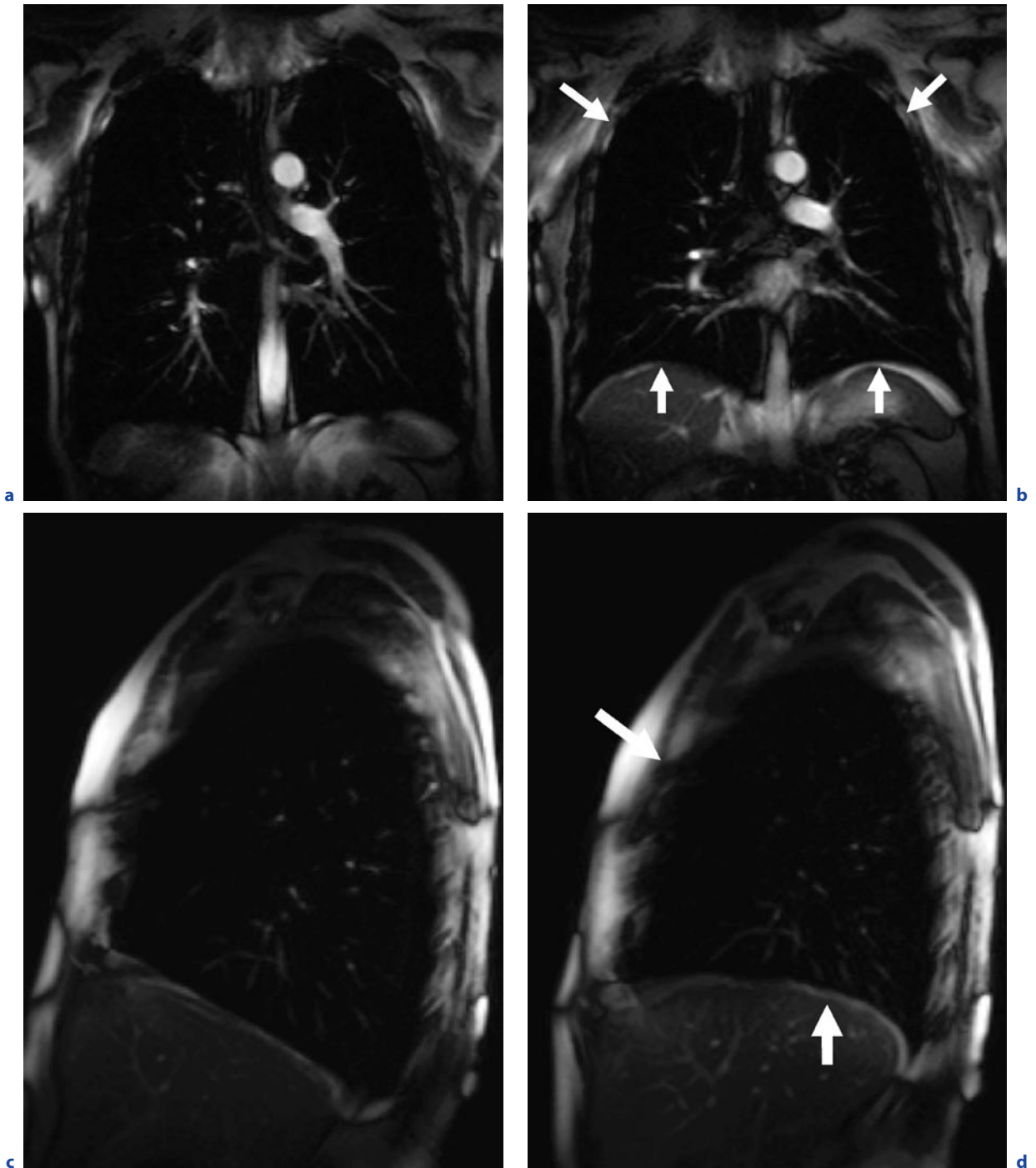


Fig. 9.3a–d. Coronal and sagittal MR images taken from a dynamic series acquired in a COPD patient during forced expiration reflecting maximum inspiration (**a,c**) and maximum expiration (**b,d**) shows motion of the diaphragm and thoracic wall (*arrows*)

9.5

Ventilation

As sufficient gas exchange depends on matched perfusion and ventilation, assessment of regional ventilation is important for the diagnosis and evaluation of pulmonary emphysema. Currently, the most established method for imaging regional lung ventilation are nuclear medicine studies using krypton-81m (Kr-81m), xenon-133 (Xe-133), radiolabeled aerosol (Technegas) and technetium-99m (Tc-99m)-labeled diethylentriaminepentaacetic acid (DTPA). The utility of nuclear medicine in pulmonary diseases has been well documented. However, these techniques are hampered by low spatial resolution and the necessity of inhalation of radioactive tracers, while 3D (SPECT) imaging will require approximately 20 min of imaging time, thus limiting the diagnostic power of the technique.

Although PFTs and nuclear medicine imaging have been established as the most common and reliable pulmonary function techniques, others such as contrast enhanced proton studies and hyperpolarized noble gas MRI are strong contenders in the functional imaging race, as they provide a rapid, high resolution regional quantification of disease progress and onset without the need for ionizing radiation tracers.

9.5.1

Oxygen-Enhanced Imaging

Oxygen-enhanced MRI requires no special scanner hardware, is easy to use and the overall material costs are low in comparison with noble gas imaging. The main idea behind this technique is to utilize the paramagnetic properties of inhaled oxygen (O_2) to obtain information regarding the pulmonary blood flow volume and integrity of the lung parenchyma (see Sect. 4.4). Several investigators reported that oxygen enhanced MRI could demonstrate regional ventilation (EDELMAN et al. 1996; LOFFLER et al. 2000; OHNO et al. 2001). The technique of oxygen-enhanced MRI has been successfully applied in volunteers; the translation into clinical examination however is difficult. Only few studies have successfully applied oxygen-enhanced MRI to patients with pulmonary diseases in a clinical setting. One of the reasons might be that the use of high oxygen concentrations (15 L/min) may not be without risk in patients with severe COPD.

In some basic measurements it was shown, that the T1 of the lung parenchyma is significantly shorter in patients with emphysema than in volunteers (STADLER

et al. 2008). In a preliminary study an inhomogeneous and weak signal intensity increase after application of oxygen was observed, compared to healthy volunteers (MULLER et al. 2002). OHNO et al (2003) demonstrated that regional changes in ventilation as observed in oxygen-enhanced MR reflected regional lung function. The maximum mean relative enhancement ratio correlated with the diffusion capacity for carbon monoxide ($r^2=0.83$), while the mean slope of relative enhancement was strongly correlated with the FEV₁ ($r^2=0.74$) and the maximum mean relative enhancement with the high-resolution CT emphysema score ($r^2=0.38$). Recent work also suggests that the simple administration of pure oxygen induces the pulmonary arteries to dilate resulting in an increase of pulmonary blood volume and a consecutive increase in signal intensity (LEY et al. 2007).

9.5.2

Hyperpolarized Noble Gas Imaging

Over the past decade hyperpolarized noble gas MRI using $^3\text{Helium}$ and $^{129}\text{Xenon}$ was developed to improve imaging of pulmonary structure, ventilation, dynamics and oxygen uptake. $^3\text{Helium}$ has become the most widely used gas for these studies as it provides higher signal-to-noise ratios than $^{129}\text{Xenon}$, due to its intrinsic gyromagnetic ratio, and its confinement to the airways and airspaces without dissolving into the surrounding tissue and bloodstream (VAN BEEK et al. 2004). Areas with ventilation defects caused by airway obstruction and emphysema represent the only limitation because they cannot be assessed due to lack of the tracer gas entering these areas. Thus, there is almost no information about these affected lung regions. Overall, the intrinsic high cost of these noble gases, the need for laser-induced hyperpolarization hardware, and the need for non-proton imaging hardware and software remain the major drawbacks of this technology on its way to broader clinical applications.

9.5.2.1

Static Ventilation

Airflow obstruction leads to a reduced level of $^3\text{Helium}$ in the distal lung regions allowing for sensitive detection of ventilation abnormalities (Figs. 9.4 and 9.5) (KAUCZOR et al. 1996). In healthy smokers with normal lung function even subtle ventilation defects were visualized demonstrating the high sensitivity of the technique (GUENTHER et al. 2000). The volume of ventilated

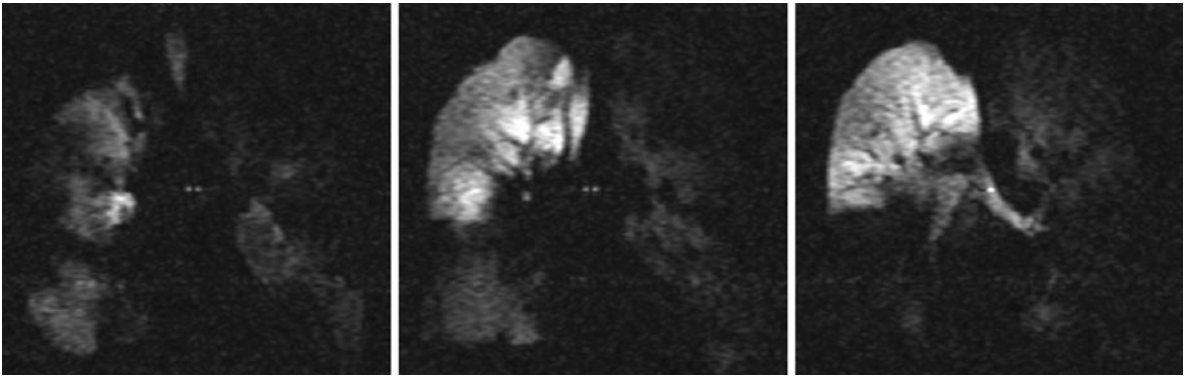


Fig. 9.4. MR ventilation images using hyperpolarized ^3He gas of a patient suffering from alpha1-antitrypsin-deficiency: good ventilation of the right upper lobe and large wedge-shaped ventilation defects in all remaining lung areas



Fig. 9.5. MR ventilation images using hyperpolarized ^3He gas of a patient suffering from COPD: focal and wedge-shaped ventilation defects in all parts of the lung

lung areas on ^3He -MRI correlated well with vital capacity ($r=0.9$) and the amount of non-emphysematous volume on CT ($r=0.7$) in patients with severe emphysema following single lung transplantation (ZAPOROZHAN et al. 2004). Ventilation defects correlated well with the parenchymal destruction assessed by HRCT in patients with severe emphysema following single lung transplantation (GAST et al. 2002). Quantification of ventilatory impairment can be achieved by automatic segmentation of the lung allowing for precise pre- and post-therapeutic comparison of ventilation (RAY et al. 2003). In addition, a proton- ^3He subtraction method has been shown to be reproducible and easily implementable, allowing for sensitive quantification of ventilated lung volumes (WOODHOUSE et al. 2005).

9.5.2.2 Dynamic Assessment

^3He MR imaging with high temporal resolution via ultra-fast Echo-planar (EPI), Gradient-echo and inter-

leaved spiral sequences allows for the visualization and assessment of the various inspiratory and expiratory phases of respiration. The instantaneous visualization of the bolus movement leads to a direct evaluation of the regional distribution of ventilation throughout the lungs, which may be quantified using a regional assessment (LEHMANN et al. 2004). Evaluation of the overall usefulness of the technique has shown considerable airflow abnormalities in diseased lung states and normal respiration stages in normal lungs (SALERNO et al. 2001; WILD et al. 2003). Normal respiration can be described by a rapid and homogenous distribution of the gas throughout the lung, whereas in diseased lungs, the airflow is inhomogeneous due to factors such as airway blockages and reduced lung compliance, leading to interspersed ventilation defects (Fig. 9.6). The observed ventilation defects vary from reduced inflow to air trapping as observed in the later phases of the respiratory cycle, which are more markedly visualized in subjects with CT proven centrilobular emphysema (GAST et al. 2003; GIERADA et al. 2000; WILD et al. 2003).

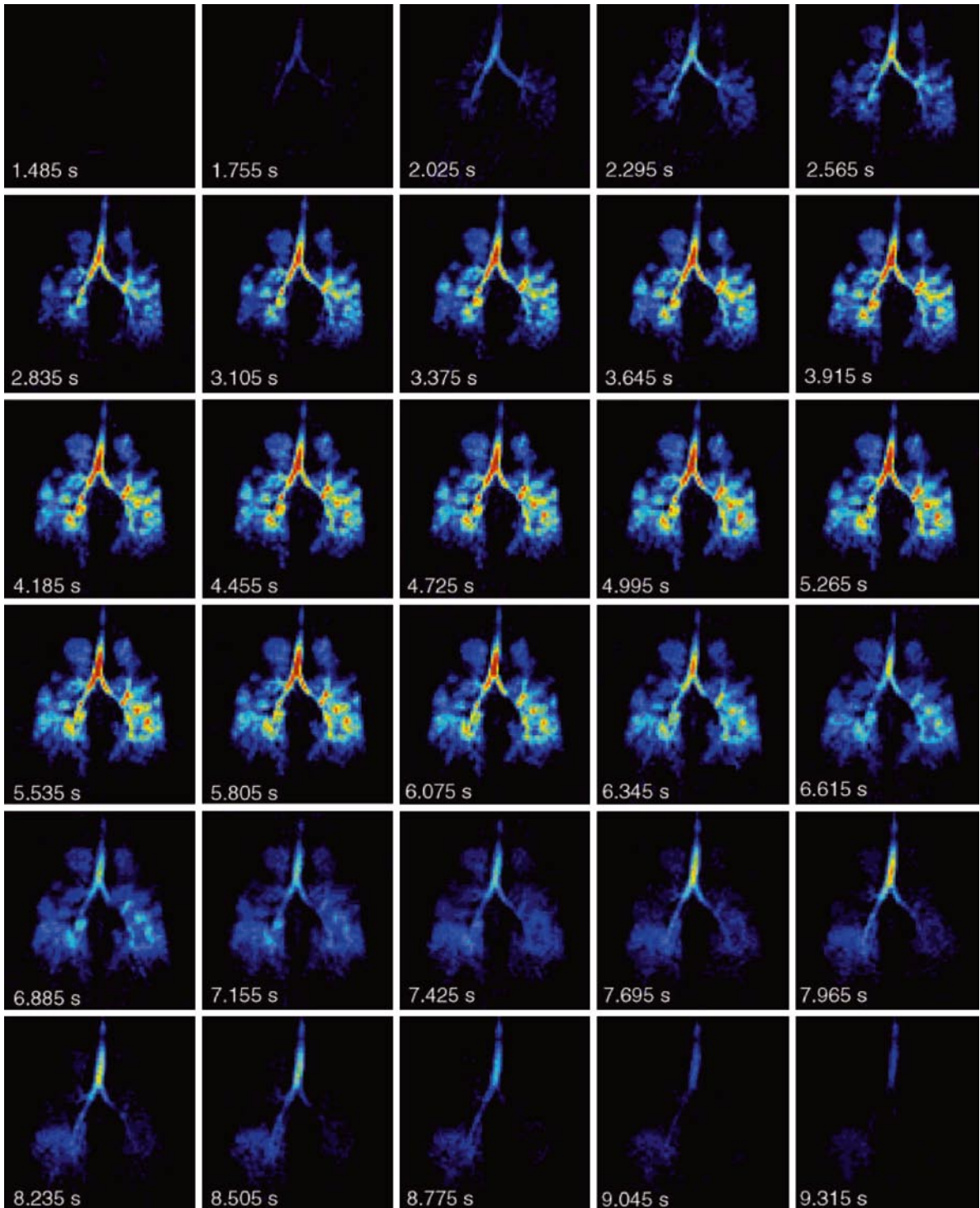


Fig. 9.6. Dynamic MR ventilation images using hyperpolarized ^3He gas from a COPD patient showing regions of ventilation obstruction in both lungs, particularly in the upper lobes and a delayed emptying/depolarization of gas in the lower left lobe, which could be indicative of air trapping (reprinted with permission from van Beek et al 2004)

9.5.2.3

³Helium Apparent Diffusion Coefficient (ADC)

The high diffusion coefficient of ³Helium gas makes it very suitable for the evaluation of the lung microstructure, connecting pores and pathways, leading to an overall assessment of the integrity and size of such structures. The ADC is a reflection of the restricted diffusion of ³Helium gas in a normal airway system due to the relatively small size of airways in relation to the diffusivity of the gas.

Similar to all other ³Helium techniques, the ADC is accomplished throughout one single breath hold, where a series of images is acquired and evaluated on a pixel-by-pixel basis. The introduction of the additional gradients into the sequences allows the monitoring of diffusion through signal decay incurred by motion of the helium molecules, thus creating a map of diffusion values representing the regional and global integrity of the lungs.

ADC maps of normal healthy volunteers have shown to be homogenous and uniform. On the other hand, in emphysematous subjects ADC maps were non-uniform and contained larger diffusion values. This non-uniformity of the ADC values correlates well with the nature of the disease, where the degree and location of destruction varies throughout the lung (CONRADI et al. 2005; LEY et al. 2004b; SALERNO et al. 2002). The ability to distinguish between normal and emphysematous lungs reflects the overall power of determining and quantifying airway enlargement along with tissue destruction. The mean ADC for emphysema patients (0.452 cm²/s) was found to be significantly larger ($p < 0.002$) than for normal volunteers (0.225 cm²/s) (SALERNO et al. 2002). In other studies, mean ADC values of emphysema patients were as low as 0.24 cm²/s and as high as 0.55 cm²/s (CONRADI et al. 2005; SWIFT et al. 2005). These values and their standard deviations correlated good ($r = -0.6$) with predicted percentages of FEV1 (SWIFT et al. 2005). This wide distribution of ADC values for the emphysema population can be attributed to the variability in airspace size and morphological alterations of the distal airspaces caused by the disease. The reproducibility of these ADC measures has been demonstrated to be very high, within 5% for consecutive scans (MORBACH et al. 2005).

9.6

Pulmonary Perfusion

Perfusion and ventilation are normally in balance, with hypoxic vasoconstrictive response providing a method to optimize lung function. In patients with COPD, ventilation is impaired due to airway obstruction and parenchymal destruction, leading to perfusion being moved to better ventilated lung regions or shunting of blood (moving through the lungs without reaching a capillary bed for gas exchange) (MOONEN et al. 2005). The reduction of the pulmonary vascular bed is related to the severity of parenchymal destruction (THABUT et al. 2005); however the distribution of perfusion does not necessarily match parenchymal destruction (LEY-ZAPOROZHAN et al. 2007; SANDEK et al. 2002). Conventional radionuclide perfusion scintigraphy has been used to assess these abnormalities, but it has substantial limitations with respect to spatial and temporal resolution. A superior technique is SPECT, which is rarely used as it is rather time consuming and not routinely applied. Inflammation appears to play a critical role in the maintenance of the hypoxic vasoconstrictive response, and PET studies with endotoxin challenge have shown that this response is shut off when inflammation and lung injury occur (GUST et al. 1998; SCHUSTER and MARKLIN 1986).

The basic principle of contrast-enhanced perfusion MRI is a dynamic acquisition during and after an intravenous bolus injection of a paramagnetic contrast agent. With the introduction of parallel imaging techniques, 3D perfusion imaging with a high spatial and temporal resolution, as well as an improved anatomical coverage and z-axis resolution can be acquired (FINK et al. 2004, 2005; LEY et al. 2004a). These data sets are also well suited for high quality multiplanar reformats. Due to high spatial resolution, detailed analysis of pulmonary perfusion and precise anatomical localization of the perfusion defects on a lobar and even segmental level can be performed (Fig. 9.7). Quantitative values for pulmonary perfusion can be obtained by applying the principles of indicator dilution techniques. The quantitative indices, such as mean transit time (MTT), pulmonary blood volume (PBV), and blood flow (PBF), are derived from the time intensity curve, defined by the dynamic series of perfusion MR images (also see Chap. 3).

MR perfusion allows for a high diagnostic accuracy in detecting perfusion abnormalities (FINK et al. 2004; SERGIACOMI et al. 2003). Furthermore, MR perfusion ratios correlate well with radionuclide perfusion scintigraphy ratios (MOLINARI et al. 2006; OHNO et al. 2004a).

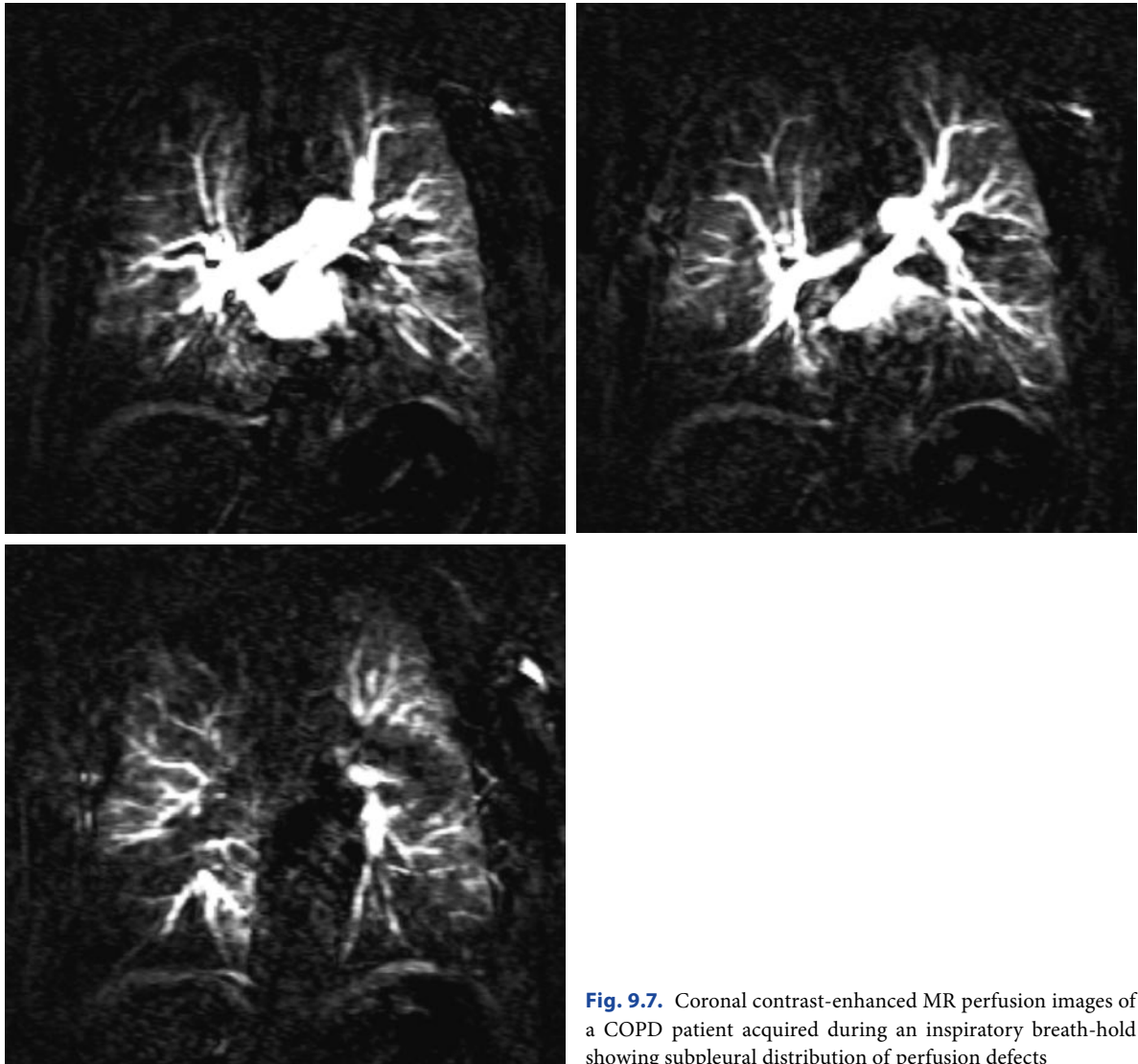


Fig. 9.7. Coronal contrast-enhanced MR perfusion images of a COPD patient acquired during an inspiratory breath-hold showing subpleural distribution of perfusion defects

Lobar and segmental analysis of the perfusion defects can be achieved (LEY-ZAPOROZHAN et al. 2007).

The perfusion abnormalities in COPD clearly differ from those caused by vascular obstruction. While wedge shaped perfusion defects occur in embolic vascular obstruction, a low degree of contrast enhancement is generally found in patients with COPD/emphysema (AMUNDSEN et al. 2002; MORINO et al. 2006). Furthermore, the peak signal intensity is usually reduced. These features allow for easy visual differentiation. In patients with COPD, the quantitative evaluation of 3D perfusion showed that the mean PBF, PBV and MTT were significantly decreased, and these changes showed a very heterogeneous distribution (OHNO et al. 2004b). It was discussed that patients with emphysema have hypoxia

as well as destruction of lung parenchyma and fewer alveolar capillaries. This causes increased pulmonary arterial resistance and, secondarily to adaptive processes, pulmonary hypertension and right ventricular dysfunction. Ultimately, this results in decreased pulmonary blood flow in addition to heterogeneous perfusion and decreased PBV. MTT is determined by the ratio between PBV and PBF. The results suggested that MTT is significantly decreased, reflecting a larger degree of decrease in PBV compared with PBF, with concomitant increased heterogeneity of regional PBV. Obviously, accurate quantitative measurements of such regional changes are important for improved understanding of lung pathophysiology in COPD.

9.7

Hemodynamics

Assessment of right ventricular function is important, as this is where the strain of perfusion obstruction and pulmonary hypertension eventually leads to the demise of the patient. MRI is able to assess right ventricular function through either phase contrast flow measurements in the pulmonary trunk (Fig. 9.8) or by short axis cine-acquisition of the right ventricle (GATEHOUSE et al. 2005; VONK-NOORDEGRAAF et al. 2005). Thus, early changes of the complex geometry of the right ventricular wall and chamber volume can be accurately measured.

Although pulmonary hypertension and cor pulmonale are rather common sequelae of COPD, the direct

mechanism remains unclear (SZILASI et al. 2006). In COPD patients the pulmonary vessels show a reduced capacity for vessel dilatation due to a defect in synthesis and/or release of nitric oxide. Prior to the onset of clinical symptoms patients exhibit signs of vascular bed obstruction and elevated pulmonary artery pressure including main pulmonary artery dilatation. Pulmonary hypertension is most often mild to moderate (mean pulmonary artery pressure in the range 20–35 mmHg), but it may worsen markedly during acute exacerbations, sleep and exercise. Assessment of the pulmonary arterial pressure is necessary in COPD patients for at least two reasons: such patients have a poor prognosis; and they need adequate treatment that might include pulmonary vasodilators.

It has been demonstrated by several studies that the level of pulmonary hypertension has a prognostic

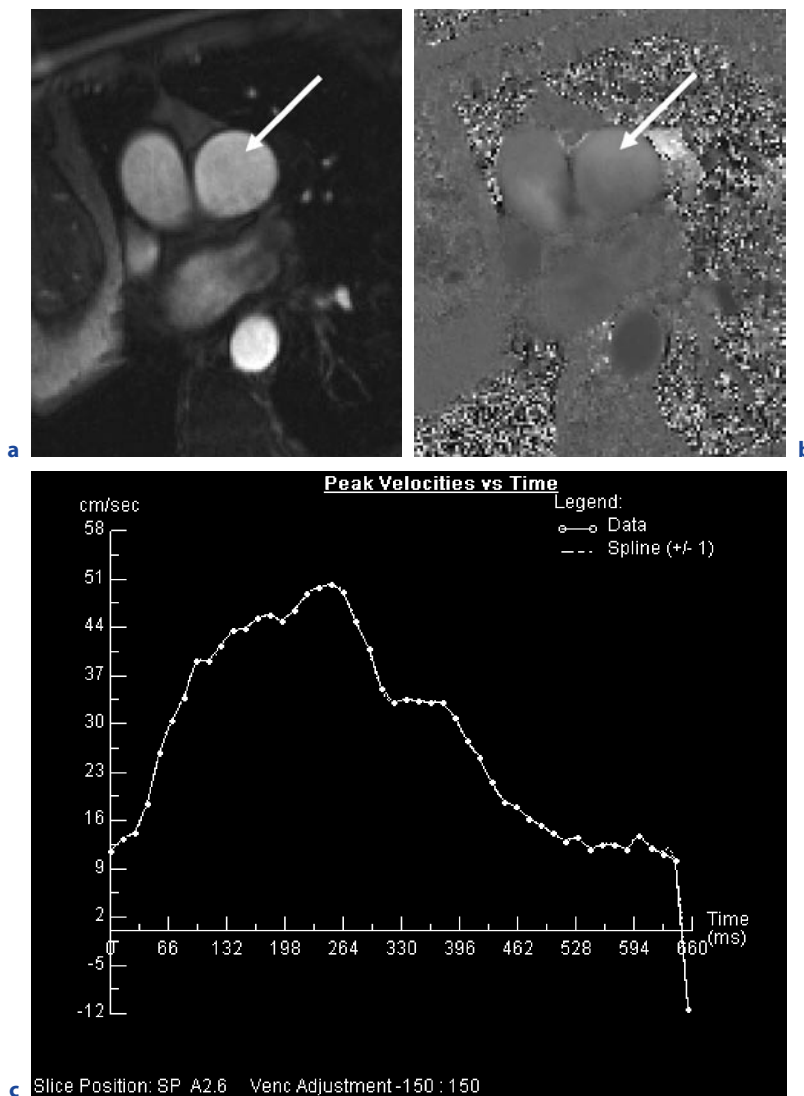


Fig. 9.8a–c. Quantitative flow measurement of pulmonary blood flow. Magnitude (a) and velocity encoded (b) image of the pulmonary trunk (arrow). Results of peak velocity over time (c) show the prolonged increase of velocity at the beginning of the systolic phase followed by an abnormal plateau during diastole

impact in COPD patients. In one of these studies, the 5-year survival rates were 50% in patients with mild (20–30 mmHg), 30% in those with moderate-to-severe (30–50 mmHg), and 0% in the small group (n=15) of patients with very severe pulmonary hypertension (>50 mmHg). Thus, severe pulmonary hypertension carries a poor prognosis, and this has also been observed in COPD patients receiving long-term oxygen therapy (WEITZENBLUM and CHAOUAT 2005).

Initially, a rise in pulmonary blood pressure leads to pulmonary artery dilatation while right ventricular performance is usually maintained. Evaluation of the right ventricle and pulmonary blood flow by echocardiography is difficult in patients with emphysema as the acoustic window is limited. Therefore, MRI has been used for imaging the right ventricle, and a loose correlation between increased right ventricular mass and the severity of emphysema was demonstrated (BOXT 1996).

In COPD patients with hypoxemia, increased right ventricular volumes, decreased right ventricular function, and impaired left ventricular diastolic function were shown (BUDEV et al. 2003). In a study by VONK-NORDEGRAAF et al. (1997) the right ventricular mass and ejection fraction in 25 clinically stable, normoxic COPD patients with emphysema were analyzed. The position of the heart appeared rotated and shifted to a more vertical position in the thoracic cavity due to hyperinflation of the lungs with an increase of the retrosternal space. The right ventricular wall mass was significantly higher (68 g) in the patient group compared to healthy volunteers (59 g). The right ventricular ejection fraction was unchanged (53%). In another study from the same group, structural and functional cardiac changes in COPD patients with normal P_aO_2 and without signs of right ventricular failure were evaluated. Compared to healthy volunteers, there were no indications of pulmonary hypertension. However the end-systolic and end-diastolic volumes of the right ventricle were significantly reduced (with normal ejection fraction), the right ventricular mass was significantly elevated while the left ventricular mass was within normal limits. The authors conclude that concentric right ventricular hypertrophy is the earliest sign of right ventricular pressure increase in patients with COPD. This structural adaptation of the heart initially does not alter right and left ventricular systolic function (VONK-NORDEGRAAF et al. 2005). As this is the only study so far in patients with mild emphysema, no strong conclusions can be drawn from this first description of the early adaptation mechanisms of the right ventricle in patients with normoxemia or mild hypoxemia and the consequences of any structural changes on right and left ventricular function.

References

- Amundsen T, Torheim G, Kvistad KA et al. (2002) Perfusion abnormalities in pulmonary embolism studied with perfusion MRI and ventilation-perfusion scintigraphy: an intra-modality and inter-modality agreement study. *J Magn Reson Imaging* 15:386–394
- Bankier AA, O'Donnell CR, Mai VM et al. (2004) Impact of lung volume on MR signal intensity changes of the lung parenchyma. *J Magn Reson Imaging* 20:961–966
- Biederer J, Both M, Graessner J et al. (2003) Lung morphology: fast MR imaging assessment with a volumetric interpolated breath-hold technique: initial experience with patients. *Radiology* 226:242–249
- Boxt LM (1996) MR imaging of pulmonary hypertension and right ventricular dysfunction. *Magn Reson Imaging Clin N Am* 4:307–325
- Budev MM, Arroliga AC, Wiedemann HP et al. (2003) Cor pulmonale: an overview. *Semin Respir Crit Care Med* 24:233–244
- Cluzel P, Similowski T, Chartrand-Lefebvre C et al. (2000) Diaphragm and chest wall: assessment of the inspiratory pump with MR imaging—preliminary observations. *Radiology* 215:574–583
- Conradi MS, Yablonskiy DA, Woods JC et al. (2005) ^3He diffusion MRI of the lung. *Acad Radiol* 12:1406–1413
- Decramer M (1997) Hyperinflation and respiratory muscle interaction. *Eur Respir J* 10:934–941
- Edelman RR, Hatabu H, Tadamura E et al. (1996) Noninvasive assessment of regional ventilation in the human lung using oxygen-enhanced magnetic resonance imaging. *Nat Med* 2:1236–1239
- Eichinger M, Tetzlaff R, Puderbach M et al. (2007) Proton magnetic resonance imaging for assessment of lung function and respiratory dynamics. *Eur J Radiol* 64:329–334
- Fink C, Puderbach M, Bock M et al. (2004) Regional lung perfusion: assessment with partially parallel three-dimensional MR imaging. *Radiology* 231:175–184
- Fink C, Ley S, Kroecker R et al. (2005) Time-resolved contrast-enhanced three-dimensional magnetic resonance angiography of the chest: combination of parallel imaging with view sharing (TREAT). *Invest Radiol* 40:40–48
- Gast KK, Viallon M, Eberle B et al. (2002) MRI in lung transplant recipients using hyperpolarized (^3He): Comparison with CT. *J Magn Reson Imaging* 15:268–274
- Gast KK, Puderbach MU, Rodriguez I et al. (2003) Distribution of ventilation in lung transplant recipients: evaluation by dynamic ^3He -MRI with lung motion correction. *Invest Radiol* 38:341–348
- Gatehouse PD, Keegan J, Crowe LA et al. (2005) Applications of phase-contrast flow and velocity imaging in cardiovascular MRI. *Eur Radiol* 15:2172–2184
- Gierada DS, Saam B, Yablonskiy D et al. (2000) Dynamic echo planar MR imaging of lung ventilation with hyperpolarized (^3He) in normal subjects and patients with severe emphysema. *NMR Biomed* 13:176–181

- Guenther D, Eberle B, Hast J et al. (2000) (3)He MRI in healthy volunteers: preliminary correlation with smoking history and lung volumes. *NMR Biomed* 13:182–189
- Gust R, Kozlowski J, Stephenson AH et al. (1998) Synergistic hemodynamic effects of low-dose endotoxin and acute lung injury. *Am J Respir Crit Care Med* 157:1919–1926
- Henderson AC, Ingenito EP, Salcedo ES et al. (2007) Dynamic lung mechanics in late-stage emphysema before and after lung volume reduction surgery. *Respir Physiol Neurobiol* 155:234–242
- Heussel CP, Ley S, Biedermann A et al. (2004) Respiratory luminal change of the pharynx and trachea in normal subjects and COPD patients: assessment by cine-MRI. *Eur Radiol* 14:2188–2197
- Hogg JC, Chu F, Utokaparch S et al. (2004) The nature of small-airway obstruction in chronic obstructive pulmonary disease. *N Engl J Med* 350:2645–2653
- Iwasawa T, Yoshiike Y, Saito K et al. (2000) Paradoxical motion of the hemidiaphragm in patients with emphysema. *J Thorac Imaging* 15:191–195
- Iwasawa T, Kagei S, Gotoh T et al. (2002) Magnetic resonance analysis of abnormal diaphragmatic motion in patients with emphysema. *Eur Respir J* 19:225–231
- Iwasawa T, Takahashi H, Ogura T et al. (2007) Correlation of lung parenchymal MR signal intensity with pulmonary function tests and quantitative computed tomography (CT) evaluation: a pilot study. *J Magn Reson Imaging* 26:1530–1536
- Kauczor HU, Hofmann D, Kreitner KF et al. (1996) Normal and abnormal pulmonary ventilation: visualization at hyperpolarized He-3 MR imaging. *Radiology* 201:564–568
- Lehmann F, Knitz F, Weiler N et al. (2004) A software tool for analysis and quantification of regional pulmonary ventilation using dynamic hyperpolarised-(3)He-MRI. *Rofo* 176:1399–1408
- Ley S, Fink C, Puderbach M et al. (2004a) Contrast-enhanced 3D MR perfusion of the lung: application of parallel imaging technique in healthy subjects. *Rofo* 176:330–334
- Ley S, Zaporozhan J, Morbach A et al. (2004b) Functional evaluation of emphysema using diffusion-weighted 3He-helium-magnetic resonance imaging, high-resolution computed tomography, and lung function tests. *Invest Radiol* 39:427–434
- Ley S, Puderbach M, Risse F et al. (2007) Impact of oxygen inhalation on the pulmonary circulation: assessment by magnetic resonance (MR)-perfusion and MR-flow measurements. *Invest Radiol* 42:283–290
- Ley-Zaporozhan J, Ley S, Eberhardt R et al. (2007) Assessment of the relationship between lung parenchymal destruction and impaired pulmonary perfusion on a lobar level in patients with emphysema. *Eur J Radiol* 63:76–83
- Ley-Zaporozhan J, Ley S, Kauczor HU (2008) Morphological and functional imaging in COPD with CT and MRI: present and future. *Eur Radiol* 18:510–21
- Ley-Zaporozhan J, Puderbach M, Kauczor HU (2008) MR for the evaluation of obstructive pulmonary disease. *Magn Reson Imaging Clin N Am* 16:291–308
- Loffler R, Muller CJ, Peller M et al. (2000) Optimization and evaluation of the signal intensity change in multisection oxygen-enhanced MR lung imaging. *Magn Reson Med* 43:860–866
- Molinari F, Fink C, Risse F et al. (2006) Assessment of differential pulmonary blood flow using perfusion magnetic resonance imaging: comparison with radionuclide perfusion scintigraphy. *Invest Radiol* 41:624–630
- Moonen M, Xu J, Johansson A et al. (2005) Effects of lung volume reduction surgery on distribution of ventilation and perfusion. *Clin Physiol Funct Imaging* 25:152–157
- Morbach AE, Gast KK, Schmiedeskamp J et al. (2005) Diffusion-weighted MRI of the lung with hyperpolarized helium-3: a study of reproducibility. *J Magn Reson Imaging* 21:765–774
- Morino S, Toba T, Araki M et al. (2006) Noninvasive assessment of pulmonary emphysema using dynamic contrast-enhanced magnetic resonance imaging. *Exp Lung Res* 32:55–67
- Muller CJ, Schwaiblmair M, Scheidler J et al. (2002) Pulmonary diffusing capacity: assessment with oxygen-enhanced lung MR imaging preliminary findings. *Radiology* 222:499–506
- Ohno Y, Chen Q, Hatabu H (2001) Oxygen-enhanced magnetic resonance ventilation imaging of lung. *Eur J Radiol* 37:164–171
- Ohno Y, Sugimura K, Hatabu H (2003) Clinical oxygen-enhanced magnetic resonance imaging of the lung. *Top Magn Reson Imaging* 14:237–243
- Ohno Y, Hatabu H, Higashino T et al. (2004a) Dynamic perfusion MRI versus perfusion scintigraphy: prediction of postoperative lung function in patients with lung cancer. *AJR Am J Roentgenol* 182:73–78
- Ohno Y, Hatabu H, Murase K et al. (2004b) Quantitative assessment of regional pulmonary perfusion in the entire lung using three-dimensional ultrafast dynamic contrast-enhanced magnetic resonance imaging: preliminary experience in 40 subjects. *J Magn Reson Imaging* 20:353–365
- Plathow C, Fink C, Ley S et al. (2004) Measurement of diaphragmatic length during the breathing cycle by dynamic MRI: comparison between healthy adults and patients with an intrathoracic tumor. *Eur Radiol* 14:1392–1399
- Plathow C, Schoebinger M, Fink C et al. (2005) Evaluation of lung volumetry using dynamic three-dimensional magnetic resonance imaging. *Invest Radiol* 40:173–179
- Rabe KF, Hurd S, Anzueto A et al. (2007) Global strategy for the diagnosis, management, and prevention of chronic obstructive pulmonary disease: GOLD executive summary. *Am J Respir Crit Care Med* 176:532–555
- Ray N, Acton ST, Altes T et al. (2003) Merging parametric active contours within homogeneous image regions for MRI-based lung segmentation. *IEEE Trans Med Imaging* 22:189–199
- Rosenkranz S (2007) Pulmonary hypertension: current diagnosis and treatment. *Clin Res Cardiol* 96(8):527–541

- Salerno M, Altes TA, Brookeman JR et al. (2001) Dynamic spiral MRI of pulmonary gas flow using hyperpolarized (3)He: preliminary studies in healthy and diseased lungs. *Magn Reson Med* 46:667–677
- Salerno M, de Lange EE, Altes TA et al. (2002) Emphysema: hyperpolarized helium 3 diffusion MR imaging of the lungs compared with spirometric indexes – initial experience. *Radiology* 222:252–260
- Sandek K, Bratel T, Lagerstrand L et al. (2002) Relationship between lung function, ventilation-perfusion inequality and extent of emphysema as assessed by high-resolution computed tomography. *Respir Med* 96:934–943
- Schuster DP, Marklin GF (1986) Effect of changes in inflation and blood volume on regional lung density – a PET study: 2. *J Comput Assist Tomogr* 10:730–735
- Sergiacomi G, Sodani G, Fabiano S et al. (2003) MRI lung perfusion 2D dynamic breath-hold technique in patients with severe emphysema. *In Vivo* 17:319–324
- Stadler A, Jakob PM, Griswold M et al. (2008) T(1) mapping of the entire lung parenchyma: Influence of respiratory phase and correlation to lung function test results in patients with diffuse lung disease. *Magn Reson Med* 59:96–101
- Suga K, Tsukuda T, Awaya H et al. (1999) Impaired respiratory mechanics in pulmonary emphysema: evaluation with dynamic breathing MRI. *J Magn Reson Imaging* 10:510–520
- Swift AJ, Wild JM, FICHELE S et al. (2005) Emphysematous changes and normal variation in smokers and COPD patients using diffusion 3He MRI. *Eur J Radiol* 54:352–358
- Swift AJ, Woodhouse N, FICHELE S et al. (2007) Rapid lung volumetry using ultrafast dynamic magnetic resonance imaging during forced vital capacity maneuver: correlation with spirometry. *Invest Radiol* 42:37–41
- Szilasi M, Dolinay T, Nemes Z et al. (2006) Pathology of chronic obstructive pulmonary disease. *Pathol Oncol Res* 12:52–60
- Thabut G, Dauriat G, Stern JB et al. (2005) Pulmonary hemodynamics in advanced COPD candidates for lung volume reduction surgery or lung transplantation. *Chest* 127:1531–1536
- van Beek EJ, Wild JM, Kauczor HU et al. (2004) Functional MRI of the lung using hyperpolarized 3-helium gas. *J Magn Reson Imaging* 20:540–554
- Vonk Noordegraaf A, Marcus JT, Roseboom B et al. (1997) The effect of right ventricular hypertrophy on left ventricular ejection fraction in pulmonary emphysema. *Chest* 112:640–645
- Vonk-Noordegraaf A, Marcus JT, Holverda S et al. (2005) Early changes of cardiac structure and function in COPD patients with mild hypoxemia. *Chest* 127:1898–1903
- Weitzenblum E, Chaouat A (2005) Severe pulmonary hypertension in COPD: is it a distinct disease? *Chest* 127:1480–1482
- Wild JM, Paley MN, Kasuboski L et al. (2003) Dynamic radial projection MRI of inhaled hyperpolarized 3He gas. *Magn Reson Med* 49:991–997
- Woodhouse N, Wild JM, Paley MN et al. (2005) Combined helium-3/proton magnetic resonance imaging measurement of ventilated lung volumes in smokers compared to never-smokers. *J Magn Reson Imaging* 21:365–369
- Zaporozhan J, Ley S, Gast KK et al. (2004) Functional analysis in single-lung transplant recipients: a comparative study of high-resolution CT, (3)He-MRI, and pulmonary function tests. *Chest* 125:173–181

MICHAEL PUDERBACH, MONIKA EICHINGER and TALISSA A. ALTES

CONTENTS

- 10.1 **Introduction** 170
- 10.2 **Structural Changes of CF Lung Disease on Proton-MRI** 170
 - 10.2.1 Bronchial Wall Thickening 171
 - 10.2.2 Mucus Plugging 171
 - 10.2.3 Bronchiectasis 171
 - 10.2.4 Air Fluid Levels 171
 - 10.2.5 Consolidation 171
 - 10.2.6 Mosaic Pattern 172
- 10.3 **Functional Lung MR Imaging** 173
 - 10.3.1 Pulmonary Perfusion 173
 - 10.3.2 Pulmonary Flow Measurements 173
 - 10.3.3 Oxygen-enhanced MRI 174
 - 10.3.4 Hyperpolarized Gas MRI 174
- 10.4 **Future Directions for MRI in CF** 175
- References** 175

KEY POINTS

Proton MRI is able to visualize the major changes in CF lung disease in a similar way to CT albeit there will be shortcomings in the detection of more subtle or smaller abnormalities. Further studies are warranted to determine whether the additional structural detail provided by CT is necessary for the evaluation of the severity and progression of CF lung disease. At the same time, proton and hyperpolarized gas MRI provide a broad spectrum of additional functional information in CF lung diseases which was previously not available to patients and clinicians. It is currently unknown whether the benefits derived from functional information about perfusion and/or ventilation by MRI will finally prevail over the mere structural information provided by CT in the clinical assessment of CF. It is conceivable that MRI and CT will be complementary as they have different advantages and disadvantages in elucidating the structure/function relationships. The MRI techniques to be applied in CF lung disease are novel and further development and studies are required to fully implement and assess their potential impact in CF.

M. PUDERBACH, MD
Department of Radiology, German Cancer Research Center (DKFZ), Im Neuenheimer Feld 280, 69120 Heidelberg, Germany

M. EICHINGER, MD
Department of Radiology, German Cancer Research Center (DKFZ), Im Neuenheimer Feld 280, 69120 Heidelberg, Germany

T. A. ALTES, MD
Department of Radiology, University of Virginia Medical Center, Charlottesville, VA 22908, Department of Radiology, Children's Hospital of Philadelphia, 34th St and Civic Center Blvd, Philadelphia, PA 19104, USA

10.1**Introduction**

Cystic fibrosis (CF) is an autosomal recessive disorder caused by gene mutations of the long arm of chromosome 7. This gene codes for the Cystic Fibrosis Transmembrane Regulator-Protein (CFTR), which functions as an anion channel. The impaired CFTR function causes aberrations of volume and ion composition of airway surface fluid, leading to viscous secretions with the consequence of bacterial colonization, chronic lung infection, air way obstruction and consecutive destruction of the lung parenchyma (GIBSON et al. 2003). Despite improved understanding of the underlying pathophysiology and the introduction of new therapies, CF remains one of the most life-shortening inherited diseases in the Caucasian population. The median survival of CF-patients is up to 37.4 years in Germany (STERN et al. 2008) and 36.8 years in the USA in 2005 (BEALL et al. 2005). Although CF affects most body systems, the majority of morbidity and mortality in CF-patients is due to chronic progressive lung disease.

The standard clinical tool for monitoring CF lung disease is pulmonary function testing. Pulmonary function tests provide a global measure of airflow obstruction and/or restriction, but provide no regional information about the lung function or information about lung structure. Although extremely useful, pulmonary function tests are known to be relatively insensitive to early lung disease and to small changes in the course of the disease. Furthermore, pulmonary function tests are dependent upon the effort and compliance of the patient, and are difficult for young children to perform. Yet pulmonary function tests remain one of the primary outcome measures in cystic fibrosis (CF) lung disease. A decrease of Forced Expiratory Volume in one second (FEV_1) was shown to be the most important prognostic factor for the course of the disease and the most significant predictor of mortality in a study of 673 patients with CF (KEREM et al. 1992). However, a more sensitive test that is not effort dependent and can be done by young children would be highly desirable for the assessment of cystic fibrosis lung disease.

The standard radiological tools for monitoring of lung disease in CF-patients are chest X-ray and thin-section computed tomography, evaluated using different scoring systems, e.g. the Crispin-Norman Score (CHRISPIN and NORMAN 1974) for chest X-ray and the Bhalla or in a modified form the Helbich-Score (BHALLA et al. 1991; HELBICH et al. 1999) for thin-section CT.

Chest CT provides submillimeter resolution images of lung structure and has been proposed as a possible

outcome measure for CF lung disease (BRODY et al. 1999, 2005; ROBINSON 2004). CT has been shown to be more sensitive to early CF lung disease than pulmonary function testing, likely due to the regional nature of the information obtained (BRODY et al. 2005). Despite the promising early studies related to the use of CT scanning in CF, a major drawback remains the radiation exposure associated with CT (BRENNER 2002, 2004; FRUSH et al. 2003; HUDA and VANCE 2007). Radiation safety concerns may ultimately limit the utility of CT in CF lung disease for applications in which multiple CT scans are required.

MRI of the chest has already been proposed as a potential imaging alternative in CF-patients in the late 1980s (FIEL et al. 1987). However, at this time, MRI technology was not able to produce comparable results to CT (CARR et al. 1995) or an adequate clinical input. Recently, new strategies have been implemented, ready to overcome the inherent difficulties of MRI of the lung, making this technique (morphological and functional MRI of the lung) especially attractive for imaging CF-patients. Recent studies compared low field MRI and chest X-ray or CT (ABOLMAALI et al. 2002; HEBESTREIT et al. 2004). Other studies compared CT, chest X-ray and proton MRI at 1.5 T (PUDERBACH et al. 2007 a, b). Further studies used functional MRI techniques like oxygen enhanced MRI (JAKOB et al. 2004), hyperpolarized helium (^3He)-MRI (DONNELLY et al. 1999; KOUMELLIS et al. 2005; MENTORE et al. 2005) or contrast enhanced MR perfusion (EICHINGER et al. 2006) to judge the functional impairment of the lung.

Currently, research with MRI in CF lung disease lags behind that with CT. In the following, we review the common findings of CF lung disease on conventional proton MRI and discuss some of the newer MRI techniques that provide functional information about CF lung disease.

10.2**Structural Changes of CF Lung Disease on Proton-MRI**

Using common proton-MRI sequences, it is possible to visualize the structural changes of CF lung disease including bronchial wall thickening, mucus plugging, bronchiectasis, air fluid levels, consolidation and segmental/lobar destruction, albeit with lower spatial and temporal resolution than with CT (PUDERBACH et al. 2007a). Although not yet proven, it seems likely that the lower spatial and temporal resolution of MRI will mean

that MRI is less sensitive than CT to specific imaging features such as distal bronchiectasis. However, this does not necessarily mean that MRI will provide less useful information about CF since sensitivity to these imaging features may not be critical for the assessment of the overall burden of disease (PUDERBACH et al. 2007b).

10.2.1 Bronchial Wall Thickening

The visualization of bronchial wall thickening is dependent on bronchial size, bronchial wall thickness and bronchial wall signal. In MRI studies of normal lung, only the central airways to the level of lobar bronchi are routinely visualized, and some segmental bronchi can be identified. This is in contrast to CT in which the sixth to eighth generation bronchi can be identified. However in CF patients, bronchial wall thickening of small airways enhances their detectability by MRI so that small airways with thick walls can be visualized in the lung periphery (Fig. 10.1) (PUDERBACH et al. 2007a). Interestingly, the T2 weighted signal of the thickened bronchial walls in CF varies from high intensity to low intensity. Since water and edema produce a high T2 weighted signal, it would not be surprising if the high bronchial wall signal is due to edema possibly caused by active inflammation. This is a phenomena not observed in CT. A T1 weighted sequence allows for evaluation of the contrast enhancement of the bronchial wall. In CF, different patterns of bronchial wall contrast enhancement have been observed. In some lung regions, bronchi demonstrate striking enhancement while in other regions weak contrast enhancement is observed. This phenomenon may also be related to inflammatory activity within the bronchial wall, but further studies are required to improve our understanding of these phenomena (Fig. 10.2).

10.2.2 Mucus Plugging

Mucus plugging is well visualized by MRI due to the high T2 weighted signal of its fluid content (Fig. 10.1). Mucus plugging in central large bronchi and peripheral small bronchi can be visualized on MRI. In central mucus plugging, there is high T2 weighted signal filling the bronchus within its course. Peripheral mucus plugging shows a grape like appearance of small T2 weighted high intensity areas, similar to the “tree in bud” phenomena in small airway inflammation on CT. Mucus plugging does not show contrast enhancement, thus mucus and

bronchial wall thickening can be differentiated by the combination of T2 weighted and contrast enhanced sequences. In CT, these two pathologic entities can not be reliably distinguished because the CT attenuation of mucus and soft tissue are similar.

Depending on the stage of disease, CF patients have an increased risk of hemoptysis. The localization of the origin of bleeding can be crucial for the outcome of the patient. With CT, mucus and blood are similar in attenuation and cannot be distinguished. On MRI, using the combination of T1 and T2 weighted and contrast enhanced sequences, mucus and fresh blood can be distinguished. Mucus has a high T2 weighted and low T1 weighted signal, while fresh blood has a low T2 weighted and T1 weighted signal.

10.2.3 Bronchiectasis

The MRI appearance of bronchiectasis is dependent on: bronchial level, bronchial diameter, wall thickness, wall signal and the signal within the bronchial lumen. Central bronchiectasis is well visualized on MRI independent of wall thickening or wall signal because of the anatomically thicker wall of the central bronchi. Peripheral bronchi starting at the third to fourth generation are poorly visualized by MRI except when they are pathological with bronchial wall thickening and/or mucus plugging.

10.2.4 Air Fluid Levels

Air fluid levels are indicative of active infection and occur in saccular or varicose bronchiectasis. Bronchial air fluid levels can be visualized by MRI because of the high T2 weighted signal from the fluid. However, discriminating between a bronchus with an air fluid level and one with a partial mucus plug or a severely thickened wall can be difficult. However, by evaluating the signal characteristics on T1 and T2 weighted, and contrast enhanced sequences, air fluid levels can frequently be differentiated (Fig. 10.2).

10.2.5 Consolidation

Consolidation in CF is mainly caused by alveolar filling with inflammatory fluid. The visualization of consolidation in MRI is based on the high T2 weighted signal

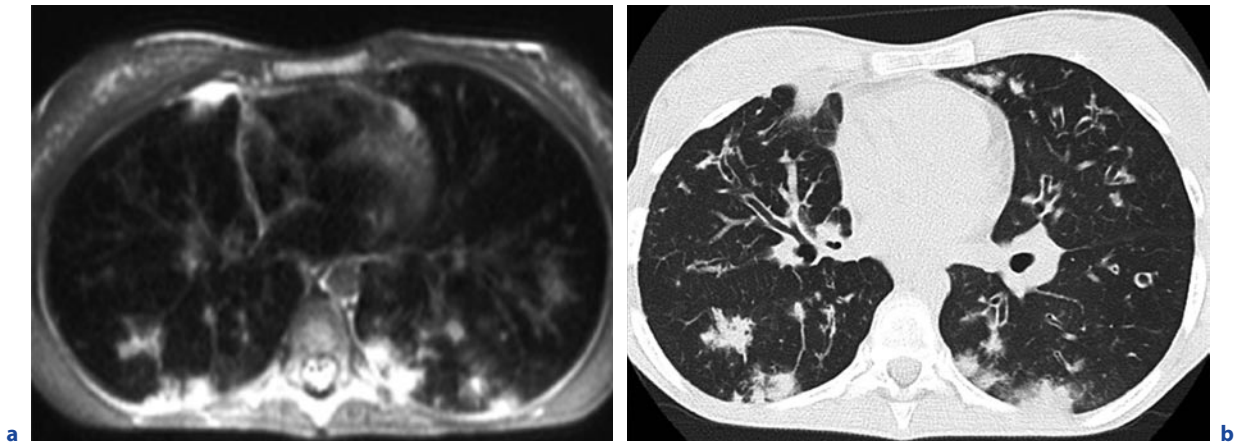


Fig. 10.1a,b. Transverse MR T2 weighted (HASTE) image (a) and corresponding CT image (b) of a 14 years old female with CF. In both images bronchial wall thickening, bronchiectasis, peripheral mucus plugging and dorsal consolidations are

demonstrated. (Reprint with permission. Altes TA, Eichinger M, Puderbach M (2007) Magnetic Resonance Imaging of the Lung in Cystic Fibrosis. *Proceedings of the American Thoracic Society* 4:322–325)

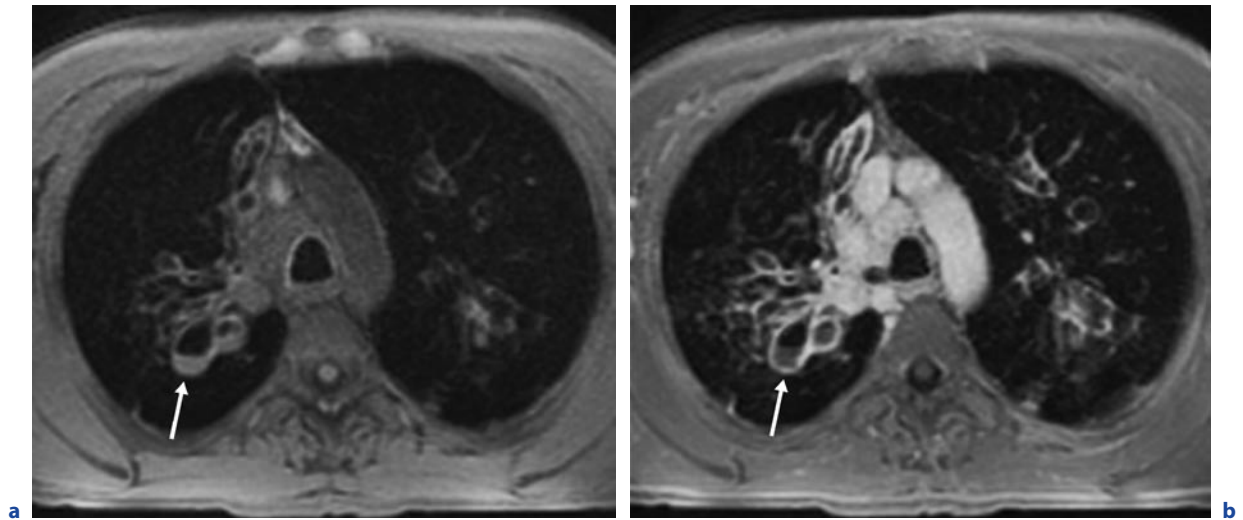


Fig. 10.2. T1 weighted MR images of a 43-year-old CF-patient (a) pre- and (b) post contrast media: contrast enhancement. The post contrast images demonstrate extensive bronchial wall enhancement and permit differentiation of a thickened wall from intrabronchial secretions, with intrabronchial fluid hav-

ing an air fluid level (arrow). (Reprint with permission. Altes TA, Eichinger M, Puderbach M (2007) Magnetic Resonance Imaging of the Lung in Cystic Fibrosis. *Proceedings of the American Thoracic Society* 4:322–325)

from the inflammatory fluid. Comparable to CT, MRI is able to visualize air bronchograms as low signal areas following the course of the bronchi within the consolidation (EIBEL et al. 2006; RUPPRECHT et al. 2002). With disease progression, complete destruction of lung segments or of a complete lung lobe can occur and these destructed lung areas have a similar appearance on MRI as CT (Fig. 10.3).

10.2.6 Mosaic Pattern

On CT, a mosaic pattern of lung attenuation is a common finding in CF patients. This pattern can be observed on inspiratory scans as areas of relative hyperlucency, which can be due to air trapping or regional hypoperfusion (mosaic perfusion). These two entities can be distinguished on expiratory CT images since regions of air trapping will not change significantly in vol-

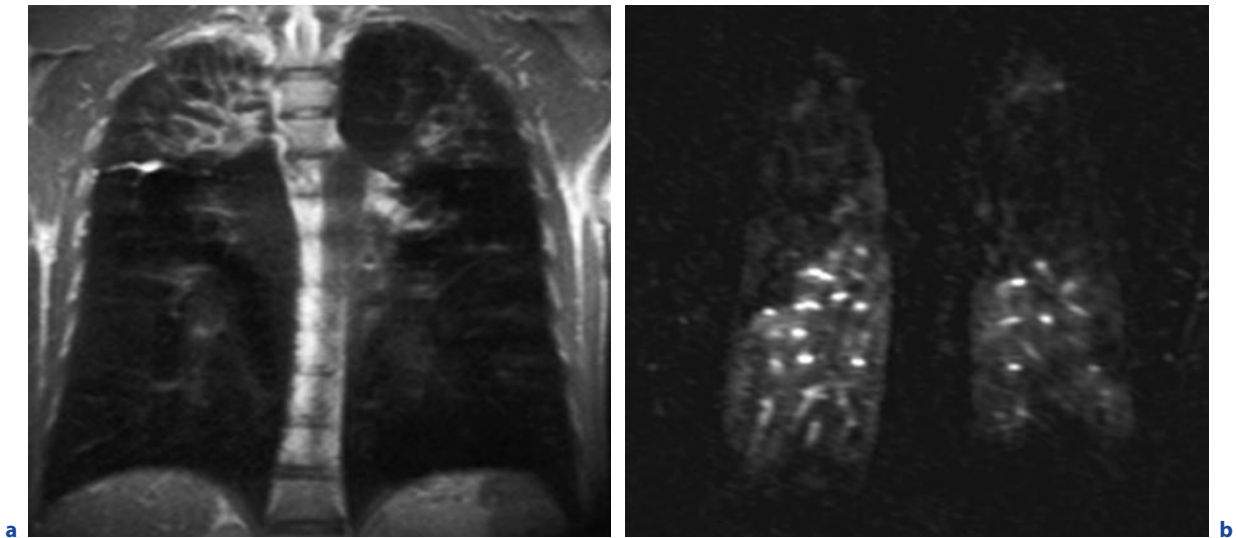


Fig. 10.3. **a** T2 weighted MR image of the patient shown in Fig 10.2 showing lobar destruction of the right upper lobe and severe bronchiectasis and wall thickening of the left lobe. **b** MR-Perfusion map of the corresponding lung region showing large perfusion defects in both upper lobes and an inhomogeneous

perfusion in the peripheral lower lobe zones. (Reprint with permission. Altes TA, Eichinger M, Puderbach M (2007) Magnetic Resonance Imaging of the Lung in Cystic Fibrosis. *Proceedings of the American Thoracic Society* 4:322–325)

ume and thus change little in measured CT attenuation. Conversely, in areas of hypoperfusion without air trapping, the lung attenuation will increase with expiration.

On MRI, the phenomena of air trapping is not typically apparent because even normal lung parenchyma has a very low signal, and an increase of the air content does not cause a detectable decrease in lung parenchymal signal. However, an approach to overcome this limitation might be the measurement of T1 relaxation times (STADLER et al. 2005). Mosaic perfusion also is not typically apparent on routine MR images, but MR-perfusion imaging has the potential to overcome this limitation (EICHINGER et al. 2006).

10.3

Functional Lung MR Imaging

In addition to visualization of structural changes within the lung, MRI can provide functional assessment of pulmonary hemodynamics and ventilation. Pulmonary perfusion imaging typically requires the administration of gadolinium based intravenous contrast. An inhaled contrast agent, either oxygen or a hyperpolarized noble gas, is required for MR lung ventilation imaging.

10.3.1

Pulmonary Perfusion

In CF, regional ventilatory defects cause changes in regional lung perfusion due to the reflex of hypoxic vasoconstriction or tissue destruction. A variety of MRI methods have been employed to assess lung perfusion, including methods that rely on the endogenous signal from blood (MAI and BERR 1999) and others that require the administration of intravenous contrast (HATABU et al. 1996; LEVIN and HATABU 2004). Using a contrast-enhanced 3D MRI acquisition in 11 children with CF, it was found that MRI-perfusion defects correlated with the degree of tissue destruction (Fig. 10.3) (EICHINGER et al. 2006). It is plausible that reversibility of perfusion defects after a therapeutic intervention might serve as an indicator for response to therapy and might differentiate between regions with reversible and irreversible disease.

10.3.2

Pulmonary Flow Measurements

Parenchymal destruction can lead to dilatation and flow augmentation of bronchial arteries. As bronchial

arteries are part of the systemic circulation, they do not contribute to blood oxygenation. Thus, a higher flow in the bronchial arteries leads to a shunt-volume, which can be assessed by MRI-based flow measurements. Decreased peak blood flow velocities in the right and left pulmonary arteries were found in 10 CF-patients as compared with 15 healthy volunteers, and this may represent early development of pulmonary hypertension in this patient group (LEY et al. 2005). However, the clinical significance of the systemic arterial shunt volume is not yet known.

10.3.3

Oxygen-enhanced MRI

Gaseous molecular oxygen is weakly paramagnetic and serves, if inhaled in high concentrations, as a contrast medium inducing a dose-dependent T1-signal increase which can be used to assess lung ventilation (EDELMAN et al. 1996). In a recent study of five CF patients and five healthy volunteers, the lungs of the CF patients had an inhomogeneous appearance following the inhalation of high oxygen concentrations suggesting inhomogeneous lung ventilation, presumably due to inhomogeneous lung ventilation (JAKOB et al. 2004). Since oxygen is soluble in blood, the oxygen-enhanced MR images depict a combination of ventilation and perfusion (KEILHOLZ et al. 2008). One of the difficulties with this method is that there is a relatively low difference in signal from the lung parenchyma with 21% vs 100% inspired oxygen concentration. This results in a relatively low signal to noise level in the resulting MR oxygen-enhanced images.

10.3.4

Hyperpolarized Gas MRI

Hyperpolarized helium-3 is a gaseous MRI contrast agent that, when inhaled, provides a very high MR signal from the airspaces of the lung. Hyperpolarized helium-3 MRI can be used to obtain information about lung function using static spin density imaging (DE LANGE et al. 1999; KAUCZOR et al. 1996; WOODHOUSE et al. 2005), dynamic spin density imaging (GAST et al. 2002; SALERNO et al. 2001) or oxygen-sensitive imaging (EBERLE et al. 1999; LEHMANN et al. 2004). In addition, lung structure at the alveolar and distal airway level can be assessed using diffusion-weighted imaging (MORBACH et al. 2005; SALERNO et al. 2002). The majority of studies investigating the use of hyperpolarized helium-3 MRI in CF have used static spin density im-

aging. Static spin density imaging, often referred to as ventilation imaging, is performed during a breath hold following the inhalation of the hyperpolarized helium-3 gas (ALTES et al. 2004). Well ventilated areas of the lung receive more helium gas and thus appear brighter than poorly ventilated areas of the lung on the MR images. Typically, the entire lung volume can be imaged in a 4–20-s breath hold, but the in plane spatial resolution is typically in the order of 3 mm and thus lower than with CT. Since children have smaller lungs than adults, the breath hold duration is shorter for children, and hyperpolarized helium MRI has been successfully performed in children as young as 4 years old without sedation (ALTES et al. 2008).

The first report of hyperpolarized helium-3 MRI in CF found extensive abnormalities of ventilation on static spin density images in four subjects with moderate to severe pulmonary CF and abnormal FEV1 % predicted (DONNELLY et al. 1999).

Also, using static spin density imaging, a study of 31 subjects (16 healthy volunteers and 15 patients with CF) found the CF patients had a significantly higher number of ventilation defects on helium MRI than the normal subjects (MENTORE et al. 2005). Even the four CF subjects with a normal FEV1 % predicted had significantly higher ventilation defect score than the normal subjects, suggesting hyperpolarized gas MRI may be more sensitive to ventilation abnormalities than spirometry. Moderate correlations between the ventilation defect score and spirometry were found (Fig. 10.4). In this study, eight of the CF patients underwent a therapeutic intervention first with nebulized albuterol followed by DNase and chest physical therapy. Repeated helium-3 MRI after therapy showed changes in the ventilation defect score. Thus, this study demonstrated the feasibility of using hyperpolarized helium-3 MRI as an outcome measure in the evaluation of airway clearance techniques.

A recent study of 18 children with CF (age 5 to 17 years) confirmed that hyperpolarized helium-3 MRI can be performed by children with CF and found moderate to weak correlations between static spin density hyperpolarized helium-3 MRI and spirometry or chest X-ray (VAN BEEK et al. 2007). It was the opinion of the authors that the weak correlations were the result of a greater sensitivity of hyperpolarized helium-3 MRI to ventilatory abnormalities than spirometry or chest X-ray. Another recent study compared static spin density helium-3 MRI with CT in eight adults with CF and found a strong correlation between the MRI percent ventilation and the Bhalla score (BHALLA et al. 1991) from CT (MCMAHON et al. 2006). Further, the correlations between hyperpolarized helium-3 MRI and

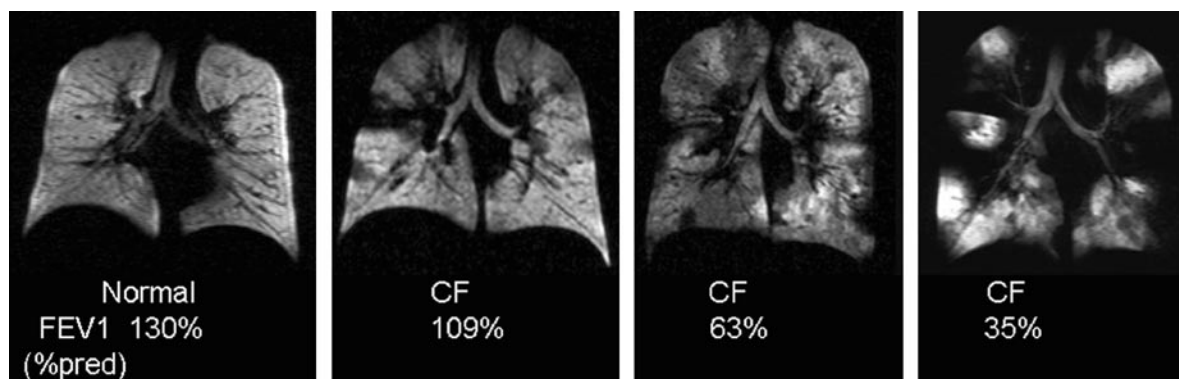


Fig. 10.4. Coronal hyperpolarized helium MR ventilation images from a normal subject and three different patients with CF. The CF patients have more ventilation defects than the normal subject, and the number of defects increases with worsening

FEV1 (% predicted). (Reprint with permission. Altes TA, Eichinger M, Puderbach M (2007) *Magnetic Resonance Imaging of the Lung in Cystic Fibrosis*. *Proceedings of the American Thoracic Society* 4:322–325)

spirometry were stronger than those between CT and spirometry. Thus, this study suggests that hyperpolarized helium-3 MRI may represent a safe alternative to CT for the evaluation of CF lung disease.

To date, little work has been done in CF evaluating the other mechanisms of contrast possible with hyperpolarized helium-3 MRI including dynamic ventilation (Koumellis et al. 2005), diffusion weighted, or oxygen sensitive imaging. Further, the special equipment required to perform hyperpolarized helium-3 MRI is both expensive and not yet widely available, and hyperpolarized helium-3 as a MRI contrast agent has not yet been approved by the Food and Drug Administration, so use of this technique is currently limited to a few academic medical centers.

10.4

Future Directions for MRI in CF

MRI of the lung is a promising but relatively new field. Thus, the majority of studies exploring lung MRI in CF have involved small numbers of subjects and have been observational, simply describing the imaging findings of CF. One of the issues related to using imaging as an endpoint is that the images themselves are not an endpoint. Typically information about the disease in question has to be extracted from the images. For example, nodal size is an imaging-based endpoint used in assessing metastatic disease. With chest CT, a variety of scoring systems for CF have been proposed to do just this, reduce a large set of images to a single number or small set of

numbers that characterize the disease severity/activity. The development of imaging-based endpoints or scores for lung MRI in CF is in its infancy. First the salient imaging features must be determined and a method, based on either human scoring or computer based image analysis, devised for quantifying these features. For proton MRI, methods based on the CT scoring schemes could be developed. For the functional lung MRI techniques, new analysis methods will need to be developed and specifically validated in CF. It has been proposed that to validate an endpoint or outcome surrogate, it must be shown to be accurate, reproducible, feasible over time, biologically plausible, reflect the severity of disease, improve rapidly with effective treatment, and correlated with true clinical outcomes (Brody 2004; Smith et al. 2003). Of these characteristics, lung MRI is biologically plausible and likely feasible over time. Clinical trials are required to determine whether endpoints derived from any of the lung MRI methods discussed above possess the remainder of these characteristics.

References

- Abolmaali N, Schmidt H, Anjorin A, Posselt H-G, Vogl TJ (2002) Chrispin-Norman-score and Bhalla-score of patients with cystic fibrosis: Comparative study of chest radiographs and MR-Imaging. Presented at European Congress of Radiology 2002
- Altes TA, Rehm PK, Harrell F, Salerno M, Daniel TM, de Lange EE (2004) Ventilation imaging of the lung: comparison of hyperpolarized helium-3 MR imaging with Xe-133 scintigraphy. *Acad Radiol* 11:729–734

- Altes T, Mata J, Froh D, Paget-Brown AO, de Lange EE, Mugler JP (2008) Abnormalities of lung structure in children with bronchopulmonary dysplasia as assessed by diffusion hyperpolarized helium-3 MRI. Presented at International Society of Magnetic Resonance in Medicine 2008
- Beall R J (2005) Executive Vice President for Medical Affairs of the Cystic Fibrosis Foundation (2005) Statement at NACFC 2005
- Bhalla M, Turcios N, Aponte V, Jenkins M, Leitman BS, McCauley DI, Naidich DP (1991) Cystic fibrosis: scoring system with thin-section CT. *Radiology* 179:783–788
- Brenner DJ (2002) Estimating cancer risks from pediatric CT: going from the qualitative to the quantitative. *Pediatr Radiol* 32:228–231
- Brenner DJ (2004) Radiation risks potentially associated with low-dose CT screening of adult smokers for lung cancer. *Radiology* 231:440–445
- Brody AS (2004) Scoring systems for CT in cystic fibrosis: who cares? *Radiology* 231:296–298
- Brody AS, Molina PL, Klein JS, Rothman BS, Ramagopal M, Swartz DR (1999) High-resolution computed tomography of the chest in children with cystic fibrosis: support for use as an outcome surrogate. *Pediatr Radiol* 29:731–735
- Brody AS, Tiddens HA, Castile RG, Coxson HO, de Jong PA, Goldin J, Huda W, Long FR, McNitt-Gray M, Rock M, Robinson TE, Sagel SD (2005) Computed tomography in the evaluation of cystic fibrosis lung disease. *Am J Respir Crit Care Med* 172:1246–1252
- Carr DH, Oades P, Trotman-Dickenson B, Mohiaddin R, Wells AU, Bush A (1995) Magnetic resonance scanning in cystic fibrosis: comparison with computed tomography. *Clin Radiol* 50:84–89
- Chrispin AR, Norman AP (1974) The systematic evaluation of the chest radiograph in cystic fibrosis. *Pediatr Radiol* 2:101–106
- de Lange EE, Mugler JP III, Brookeman JR, Knight-Scott J, Truwit JD, Teates CD, Daniel TM, Bogorad PL, Cates GD (1999) Lung air spaces: MR imaging evaluation with hyperpolarized ^3He gas. *Radiology* 210:851–857
- Donnelly LF, MacFall JR, McAdams HP, Majure JM, Smith J, Frush DP, Bogorad P, Charles HC, Ravin CE (1999) Cystic fibrosis: combined hyperpolarized ^3He -enhanced and conventional proton MR imaging in the lung--preliminary observations. *Radiology* 212:885–889
- Eberle B, Weiler N, Markstaller K, Kauczor HU, Deninger A, Ebert M, Grossmann T, Heil W, Lauer LO, Roberts TPL, Schreiber WG, Surkau R, Dick WF, Otten EW, Thelen M (1999) Analysis of intrapulmonary O_2 concentration by NIR imaging of inhaled hyperpolarized helium-3. *J Appl Physiol* 87:2043–2052
- Edelman RR, Hatabu H, Tadamura E, Li W, Prasad PV (1996) Noninvasive assessment of regional ventilation in the human lung using oxygen-enhanced magnetic resonance imaging. *Nat Med* 2:1236–1239
- Eibel R, Herzog P, Dietrich O, Rieger CT, Ostermann H, Reiser MF, Schoenberg SO (2006) Pulmonary abnormalities in immunocompromised patients: comparative detection with parallel acquisition MR imaging and thin-section helical CT. *Radiology* 241:880–891
- Eichinger M, Puderbach M, Fink C, Gahr J, Ley S, Plathow C, Tuengerthal S, Zuna I, Muller FM, Kauczor HU (2006) Contrast-enhanced 3D MRI of lung perfusion in children with cystic fibrosis-initial results. *Eur Radiol* 16:2147–2152
- Fiel SB, Friedman AC, Caroline DE, Radecki PD, Faerber E, Grumbach K (1987) Magnetic resonance imaging in young adults with cystic fibrosis. *Chest* 91:181–184
- Frush DP, Donnelly LF, Rosen NS (2003) Computed tomography and radiation risks: what pediatric health care providers should know. *Pediatrics* 112:951–957
- Gast KK, Puderbach MU, Rodriguez I, Eberle B, Markstaller K, Hanke AT, Schmiedeskamp J, Weiler N, Lill J, Schreiber WG, Thelen M, Kauczor HU (2002) Dynamic ventilation (^3He -magnetic resonance imaging with lung motion correction: gas flow distribution analysis. *Invest Radiol* 37:126–134
- Gibson RL, Burns JL, Ramsey BW (2003) Pathophysiology and management of pulmonary infections in cystic fibrosis. *Am J Respir Crit Care Med* 168:918–951
- Hatabu H, Gaa J, Kim D, Li W, Prasad PV, Edelman RR (1996) Pulmonary perfusion: qualitative assessment with dynamic contrast-enhanced MRI using ultra-short TE and inversion recovery turbo FLASH. *Magn Reson Med* 36:503–508
- Hebestreit A, Schultz G, Trusen A, Hebestreit H (2004) Follow-up of acute pulmonary complications in cystic fibrosis by magnetic resonance imaging: a pilot study. *Acta Paediatr* 93:414–416
- Helbich TH, Heinz-Peer G, Eichler I, Wunderbaldinger P, Gotz M, Wojnarowski C, Brasch RC, Herold CJ (1999) Cystic fibrosis: CT assessment of lung involvement in children and adults. *Radiology* 213:537–544
- Huda W, Vance A (2007) Patient radiation doses from adult and pediatric CT. *AJR Am J Roentgenol* 188:540–546
- Jakob PM, Wang T, Schultz G, Hebestreit H, Hebestreit A, Hahn D (2004) Assessment of human pulmonary function using oxygen-enhanced T1 imaging in patients with cystic fibrosis. *Magn Reson Med* 51:1009–1016
- Kauczor HU, Hofmann D, Kreitner KF, Nilgens H, Surkau R, Heil W, Potthast A, Knopp MV, Otten EW, Thelen M (1996) Normal and abnormal pulmonary ventilation: visualization at hyperpolarized He-3 MR imaging. *Radiology* 201:564–568
- Keilholz S, Knight-Scott J, Mata J, Fujiwara N, Altes T, Berr S, Hagspiel K (2008) The contributions of ventilation and perfusion in O_2 -enhanced MRI. Presented at International Society of Magnetic Resonance in Medicine 2008
- Kerem E, Reisman J, Corey M, Canny GJ, Levison H (1992) Prediction of mortality in patients with cystic fibrosis. *N Engl J Med* 326:1187–1191

- Koumellis P, van Beek EJ, Woodhouse N, Fичele S, Swift AJ, Paley MN, Hill C, Taylor CJ, Wild JM (2005) Quantitative analysis of regional airways obstruction using dynamic hyperpolarized ^3He MRI—preliminary results in children with cystic fibrosis. *J Magn Reson Imaging* 22:420–426
- Lehmann F, Eberle B, Markstaller K, Gast KK, Schmiedeskamp J, Blumler P, Kauczor HU, Schreiber WG (2004) A software program for quantitative analysis of alveolar oxygen partial pressure ($p(\text{A})\text{O}_2$) with oxygen-sensitive (^3He) MRI. *Rofo* 176:1390–1398
- Levin DL, Hatabu H (2004) MR evaluation of pulmonary blood flow. *J Thorac Imaging* 19:241–249
- Ley S, Puderbach M, Fink C, Eichinger M, Plathow C, Teiner S, Wiebel M, Muller FM, Kauczor HU (2005) Assessment of hemodynamic changes in the systemic and pulmonary arterial circulation in patients with cystic fibrosis using phase-contrast MRI. *Eur Radiol* 15:1575–1580
- Mai VM, Berr SS (1999) MR perfusion imaging of pulmonary parenchyma using pulsed arterial spin labeling techniques: FAIRER and FAIR. *J Magn Reson Imaging* 9:483–487
- McMahon CJ, Dodd JD, Hill C, Woodhouse N, Wild JM, Fичele S, Gallagher CG, Skehan SJ, van Beek EJR, Masterson JB (2006) Hyperpolarized (^3He) magnetic resonance ventilation imaging of the lung in cystic fibrosis: comparison with high resolution CT and spirometry. *Eur Radiol* 16:2483–2490
- Mentore K, Froh DK, de Lange EE, Brookeman JR, Paget-Brown AO, Altes TA (2005) Hyperpolarized $\text{HHe } 3$ MRI of the lung in cystic fibrosis: assessment at baseline and after bronchodilator and airway clearance treatment. *Acad Radiol* 12:1423–1429
- Morbach AE, Gast KK, Schmiedeskamp J, Dahmen A, Herweling A, Heussel CP, Kauczor HU, Schreiber WG (2005) Diffusion-weighted BM of the lung with hyperpolarized helium-3: a study of reproducibility. *J Magn Reson Imaging* 21:765–774
- Puderbach M, Eichinger M, Gahr J, Ley S, Tuengerthal S, Schmahl A, Fink C, Plathow C, Wiebel M, Muller FM, Kauczor HU (2007a) Proton MRI appearance of cystic fibrosis: comparison to CT. *Eur Radiol* 17:716–724
- Puderbach M, Eichinger M, Haeselbarth J, Ley S, Kopp-Schneider A, Tuengerthal S, Schmaehl A, Fink C, Plathow C, Wiebel M, Demirakca S, Muller FM, Kauczor HU (2007b) Assessment of morphological MRI for pulmonary changes in cystic fibrosis (CF) patients – comparison to thin-section CT and chest X-ray. *Invest Radiol* 42:715–725
- Robinson TE (2004) High-resolution CT scanning: potential outcome measure. *Curr Opin Pulm Med* 10:537–541
- Rupprecht T, Bowling B, Kuth R, Deimling M, Rascher W, Wagner M (2002) Steady-state free precession projection MRI as a potential alternative to the conventional chest X-ray in pediatric patients with suspected pneumonia. *Eur Radiol* 12:2752–2756
- Salerno M, Altes TA, Brookeman JR, de Lange EE, Mugler JP (2001) Dynamic spiral MRI of pulmonary gas flow using hyperpolarized He-3 : Preliminary studies in healthy and diseased lungs. *Magn Reson Med* 46:667–677
- Salerno M, de Lange EE, Altes TA, Truwit JD, Brookeman JR, Mugler JP (2002) Emphysema: hyperpolarized helium 3 diffusion MR imaging of the lungs compared with spirometric indexes – initial experience. *Radiology* 222:252–260
- Smith JJ, Sorensen AG, Thrall JH (2003) Biomarkers in imaging: realizing radiology's future. *Radiology* 227:633–638
- Stadler A, Jakob PM, Griswold M, Barth M, Bankier AA (2005) T1 mapping of the entire lung parenchyma: influence of the respiratory phase in healthy individuals. *J Magn Reson Imaging* 21:759–764
- Stern M, Wiedemann B, Wenzlaff P (2008) From registry to quality management: the German Cystic Fibrosis Quality Assessment project 1995–2006. *Eur Respir J* 31:29–35
- Van Beek EJR, Hill C, Woodhouse N, Fичele S, Fleming S, Howe B, Bott S, Wild JM, Taylor CJ (2007) Assessment of lung disease in children with cystic fibrosis using hyperpolarized $^3\text{-Helium}$ MRI: comparison with Shwachman score, Crispin-Norman score and spirometry. *Eur Radiol* 17:1018–1024
- Woodhouse N, Wild JM, Paley MNJ, Fичele S, Said Z, Swift AJ, van Beek EJR (2005) Combined helium-3/proton magnetic resonance imaging measurement of ventilated lung volumes in smokers compared to never-smokers. *J Magn Reson Imaging* 21:365–369

Lung Cancer

YOSHIHARU OHNO, HISANOBU KOYAMA, JULIEN DINKEL, and CHRISTIAN HINTZE

CONTENTS

| | | |
|----------|---|-----|
| 11.1 | Introduction | 180 |
| 11.2 | Detection of Pulmonary Nodules | 180 |
| 11.3 | Characterization and Management of Pulmonary Nodules or Masses on MR Imaging | 184 |
| 11.3.1 | Conventional T1-Weighted and T2-Weighted MRI Without and With Contrast Media | 184 |
| 11.3.1.1 | Bronchial Atresia and Bronchocele | 185 |
| 11.3.1.2 | Tuberculoma | 185 |
| 11.3.1.3 | Mucinous Bronchioalveolar Carcinoma | 188 |
| 11.3.1.4 | Hamartoma | 188 |
| 11.3.1.5 | Aspergilloma | 189 |
| 11.3.2 | Dynamic Contrast-enhanced MR Imaging of Pulmonary Nodules | 192 |
| 11.4 | Assessment of TNM Stages | 195 |
| 11.4.1 | MR Assessment of T Classification | 195 |
| 11.4.1.1 | Mediastinal Invasion | 196 |
| 11.4.1.2 | Distinguishing Lung Cancer from Secondary Change | 199 |
| 11.4.1.3 | Chest Wall Invasion | 200 |
| 11.4.1.4 | MR Assessment of Respiratory Tumor Motion | 202 |
| 11.4.2 | MR Assessment of N Classification | 203 |
| 11.4.3 | MR Assessment of M Classification | 205 |
| 11.4.3.1 | Adrenal Gland Metastasis | 206 |
| 11.4.3.2 | Bone Metastasis | 206 |
| 11.4.3.3 | Brain Metastasis | 207 |
| 11.4.3.4 | Whole-body MR Imaging for Assessment of M Classification in Lung Cancer Patients | 207 |
| | References | 210 |

Y. OHNO, MD, PhD

Director of Diagnostic and Functional Imaging Research, Director of Thoracic Radiology, Associate Professor of Radiology, Department of Radiology, Kobe University Graduate School of Medicine, 7-5-2 Kusunoki-cho, Chuo-ku, Kobe, 650-0017, Japan

KEY POINTS

Since the publication of the Radiologic Diagnostic Oncology Group Report (RDOG) in 1991, the clinical application of pulmonary magnetic resonance (MR) imaging to patients with lung cancer has been limited. MDCT is much more widely available for staging of lung cancer in clinical situations. Currently, FDG-PET or PET/CT is the only modality that reveals biological glucose metabolism of lung cancer, and ventilation and/ or perfusion scintigraphy is the only modality that demonstrates pulmonary function. However, recent advances of MR systems and utilization of contrast media make it possible to overcome the limitation of pulmonary MR imaging. Therefore, in the last several years, several investigators have demonstrated the significant comprehensive potential of MR imaging to substitute for MDCT and nuclear medicine examinations in lung cancer patients. Currently, MR imaging in lung cancer patients can be applied for (1) detection of pulmonary nodules; (2) characterization of solitary pulmonary nodules; and (3) assessment of TNM classification in routine clinical practice. We believe that further basic studies, as well as clinical applications of newer MR techniques, will play an important role in the future management of patients with lung cancer including MRI.

H. KOYAMA, MD, PhD

Department of Radiology, Kobe University Graduate School of Medicine, 7-5-2 Kusunoki-cho, Chuo-ku, Kobe, 650-0017, Japan

C. HINTZE, MD

German Cancer Research Center (DKFZ), Im Neuenheimer Feld 280, 69120 Heidelberg, Germany

J. DINKEL, MD, MSc

German Cancer Research Center (DKFZ), Im Neuenheimer Feld 280, 69120 Heidelberg, Germany

11.1

Introduction

Lung cancers are the most common cause of cancer-related death in the Western world, Japan, and South Korea. Non-small cell lung carcinoma (NSCLC) accounts for approximately 80% of all lung cancers, with small cell lung carcinoma (SCLC) accounting for the remainder. Despite major efforts aimed at improving survival during recent years, survival remains dismal at 14% for all stages. Imaging techniques currently are essential for the diagnosis, staging and follow-up of patients with lung cancer. The diagnosis of lung cancer has relied on findings on chest radiographs (CXR) and detection of cells in sputum or biopsy specimens. Perhaps even more important, however, are specific findings on chest computed tomography (CT) and metabolic information on positron emission tomography with 2-[fluorine-18]-fluoro-2-deoxy-D-glucose (FDG-PET) or FDG-PET co-registered or integrated with CT (co-registered or integrated FDG-PET/CT). Moreover, the staging and follow-up of lung cancer have relied more on CT, FDG-PET and/or FDG-PET/CT than on chest radiography. The goal of diagnosis and management of pulmonary nodules is to bring promptly to surgery all patients with operable malignant nodules while avoiding unnecessary thoracotomy for patients with benign lesions. It is therefore of the utmost importance to differentiate malignant from benign nodules in the least invasive manner and to make as specific and accurate diagnosis as possible. In addition, the preliminary goal of pre-therapeutic assessment of lung cancers is to avoid unnecessary surgery for patients with locally unresectable tumors and/or nodal or metastatic disease because the strongest prognostic indicator for survival in lung cancer is whether or not the tumor is resectable.

Currently, CT is considered to be the most widely applicable modality for evaluation of lung cancer, and a major breakthrough in CT technology has been the introduction of multidetector-row CT (MDCT), in which detector rows are exposed simultaneously. The performance of MDCT compared with single-detector CT is enhanced by a factor approximately equal to the number of rows. In addition, FDG-PET or PET/CT qualifies as another important innovation in lung cancer imaging. Standard imaging techniques are based on differences in the structure of tissues, whereas FDG-PET or PET/CT can show the enhanced glucose metabolism of lung cancer cells. For these reasons, MR imaging has been utilized for only a few cases, such as superior sulcus (Pancoast's) tumor, mediastinal invasion and chest wall invasion since 1991, when the Radiologic Diagnostic

Oncology Group (RDOG) reported no significant difference in the diagnostic capability of CT and conventional T1-weighted imaging for the staging of lung cancer except for mediastinal invasion (WEBB et al. 1991). However, recent advances in MR imaging techniques and utilization of contrast media have resulted in further improvement of the image quality and diagnostic capability of MR imaging for lung cancer patients.

In this chapter we describe the utility and capability of MR imaging for (1) detection of pulmonary nodules, (2) characterization and management of pulmonary nodules, and (3) assessment of tumor-node-metastasis (TNM) stages in lung cancer patients.

11.2

Detection of Pulmonary Nodules

A pulmonary nodule is radiologically defined as an intraparenchymal lung lesion that is less than 30 mm in diameter and is not associated with atelectasis or adenopathy (TUDDENHAM 1984). While one in 500 CXRs shows a lung nodule, 90% of these nodules are incidental radiological findings, detected accidentally on CXRs obtained for unrelated diagnostic workups. More than 150,000 patients per year in the United States present their physicians with the diagnostic dilemma of a pulmonary nodule. This number has increased even further due to incidental findings of lung nodules on chest CT (TUDDENHAM 1984). The devastating effect of lung cancer is directly associated with its delayed presentation. Patients with the best prognosis are those with stage IA disease, although approximately one half of all lung cancers unfortunately show extrathoracic spread at the time of diagnosis. Timely and accurate detection and diagnosis of the etiology of pulmonary nodules are therefore essential for making it possible for patients with malignancy to be cured.

Spiral CT or MDCT can be considered the current gold standard for the detection of lung nodules (DAVIS 1991; COSTELLO 1994; HENSCHKE et al. 2001; SCHAEFER-PROKOP and PROKOP 2002; SWENSEN et al. 2005; BACH et al. 2007). However, repeated follow-up CT examinations for detection of pulmonary metastases may be undesirable, especially for young patients, because of radiation exposure. Although radiation exposure is usually no major issue for cancer patients and low-dose CT techniques have been proved feasible to reduce the radiation dose, MR imaging does not require any ionizing radiation at all. It would therefore be helpful if MR imaging could be used for the detection of pulmonary nodules without administration of contrast media.

Several investigators have addressed this issue by using various sequences with 1.5 T and 3.0 T scanners since 1997. However, patient-related motion artifacts, susceptibility artifacts from the lungs and inferior spatial and temporal resolution as compared with those of CT reduce the quality of MR images of the lungs (KERSJES et al. 1997; VOGT et al. 2004; SCHROEDER et al. 2005; LUBOLDT et al. 2006; BRUEGEL et al. 2007; REGIER et al. 2007; Yi et al. 2007). All these studies assessed the detection rate (sensitivity) for pulmonary nodules, mainly pulmonary metastases, which was verified by single-helical CT or MDCT. The sensitivities for nodules equal to or less than 5 mm in diameter were reportedly less than 45%, although various sequences such as electrocardiograph (ECG)-triggered proton density weighted (PDW) or T2-weighted turbo spin-echo (SE), ECG-triggered PDW black-blood-prepared half-Fourier single-shot turbo SE (HASTE), respiratory-triggered T2-weighted short-inversion-time inversion recovery (STIR) turbo SE, pre- and post-contrast enhanced volumetric interpolated 3D gradient-echo (VIBE), T2-weighted triple inver-

sion black blood turbo spin-echo, etc. were tested with nodules equal to or more than 5 mm section thickness on 1.5 T or 3.0 T scanners (KERSJES et al. 1997; VOGT et al. 2004; SCHROEDER et al. 2005; LUBOLDT et al. 2006; BRUEGEL et al. 2007; REGIER et al. 2007; Yi et al. 2007). On the other hand, sensitivities for nodules equal to or more than 5 mm and less than 11 mm in diameter were reportedly between approximately 85% and 95%, and those for nodules with a diameter of more than 10 mm were more than 95% in these studies (KERSJES et al. 1997; VOGT et al. 2004; SCHROEDER et al. 2005; LUBOLDT et al. 2006; BRUEGEL et al. 2007; REGIER et al. 2007; Yi et al. 2007). Therefore, when considering the various guidelines for management of pulmonary nodules (KERSJES et al. 1997; VOGT et al. 2004; SCHROEDER et al. 2005; LUBOLDT et al. 2006; BRUEGEL et al. 2007; REGIER et al. 2007; Yi et al. 2007), MR imaging on 1.5 T and 3.0 T may have potential for the detection of or screening, without ionizing radiation exposure, for pulmonary nodules which are considered to need further intervention and treatment (Figs. 11.1–11.3), (Table 11.1). In addition,

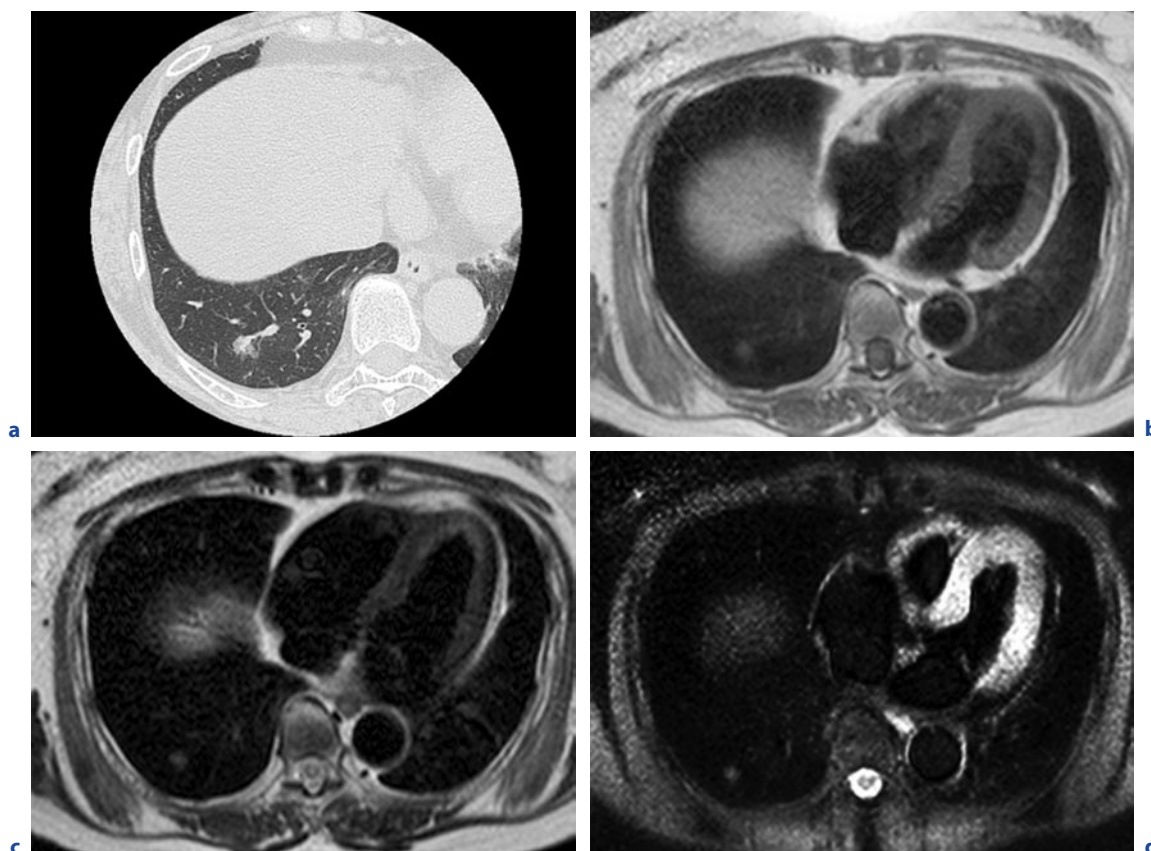


Fig. 11.1a–d. A 71-year-old female with adenomatous hyperplasia in the right lower lobe. Thin-section CT indicates ground-glass attenuation in the right lower lobe (a). Black-blood T1-weighted turbo SE (b), T2-weighted turbo SE (c) and STIR turbo SE (d) images show a nodule as, respectively, low, intermediate and high signal intensity in the right lower lobe

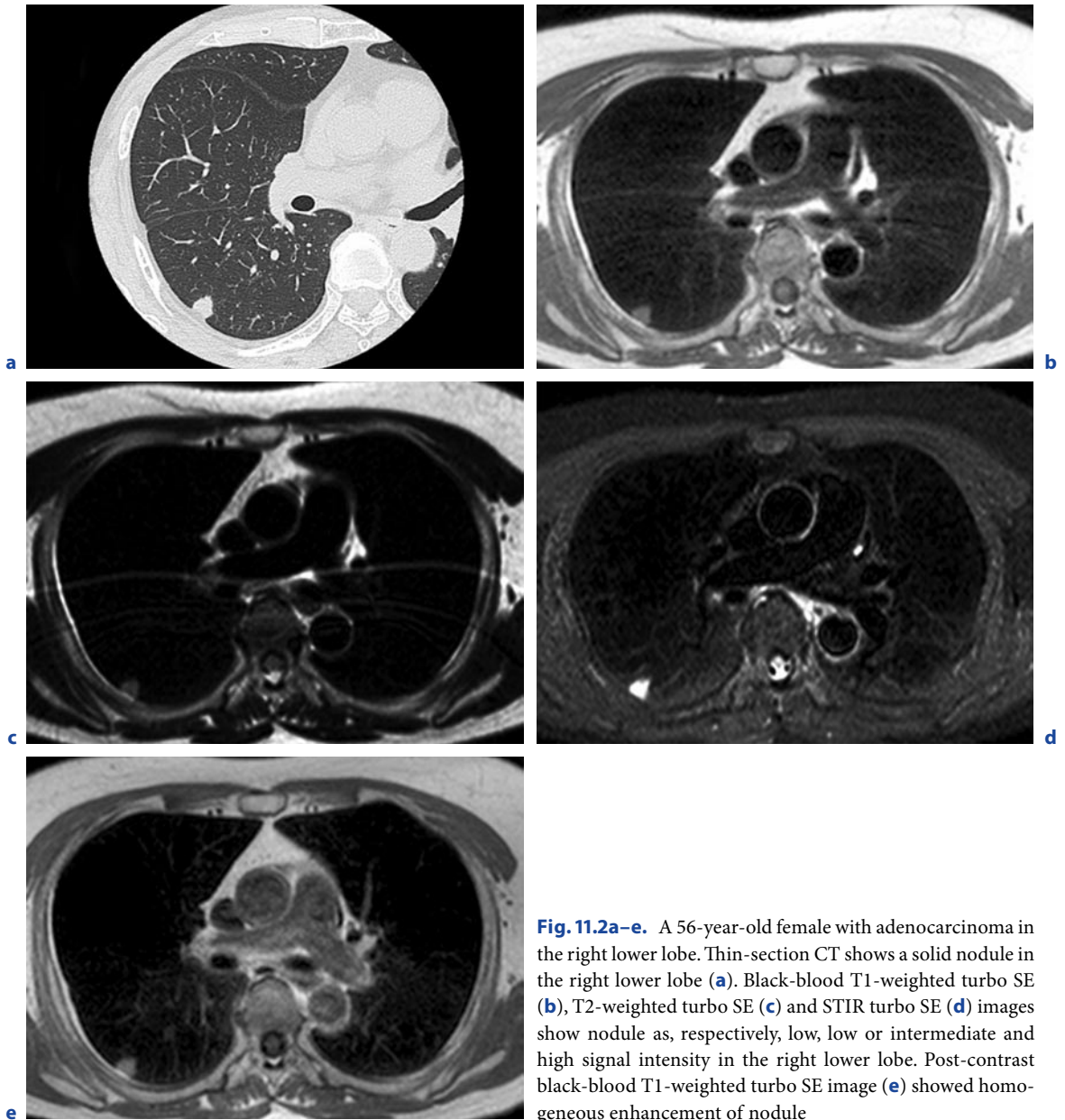


Fig. 11.2a–e. A 56-year-old female with adenocarcinoma in the right lower lobe. Thin-section CT shows a solid nodule in the right lower lobe (a). Black-blood T1-weighted turbo SE (b), T2-weighted turbo SE (c) and STIR turbo SE (d) images show nodule as, respectively, low, low or intermediate and high signal intensity in the right lower lobe. Post-contrast black-blood T1-weighted turbo SE image (e) showed homogeneous enhancement of nodule

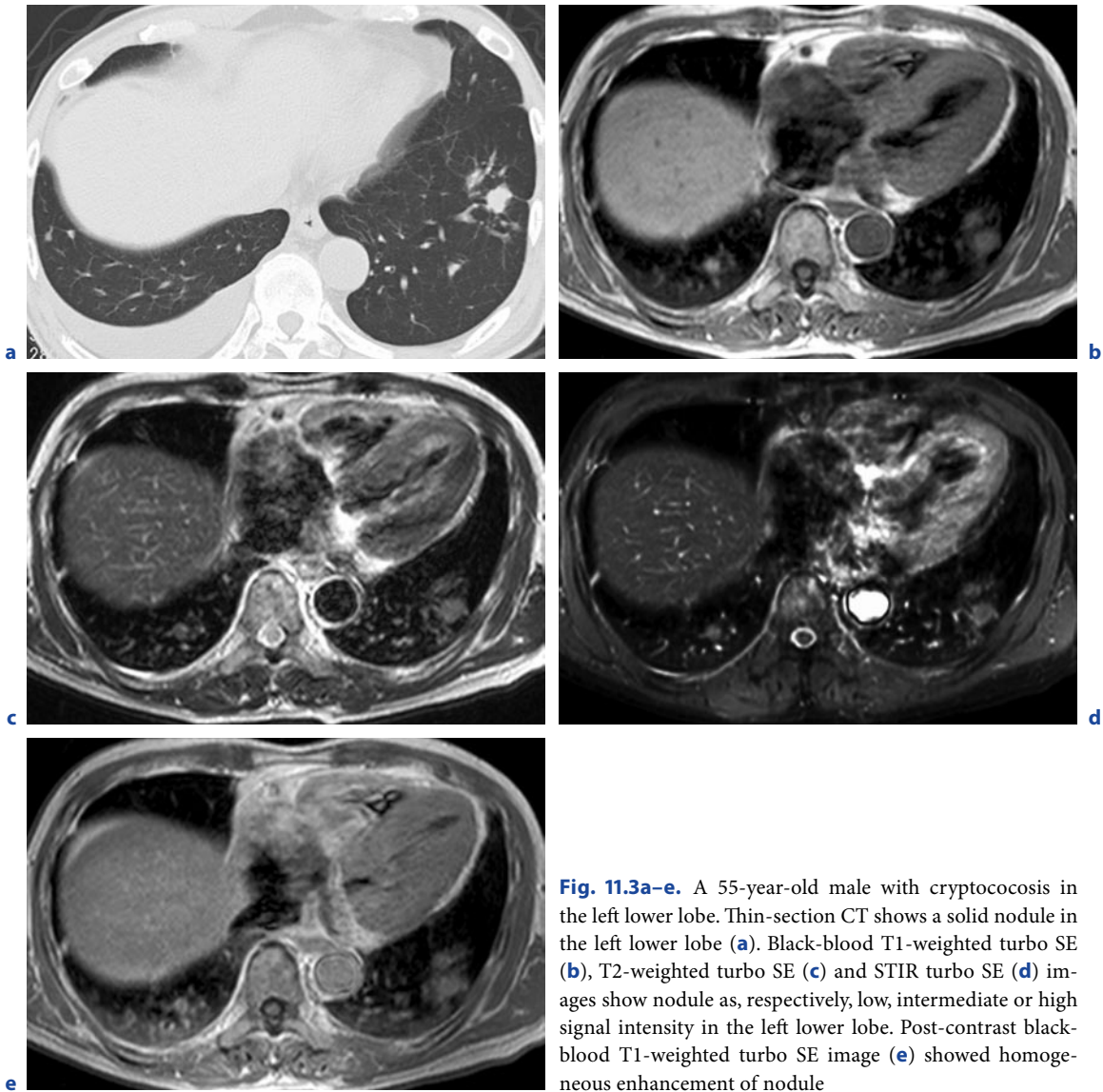


Fig. 11.3a–e. A 55-year-old male with cryptococosis in the left lower lobe. Thin-section CT shows a solid nodule in the left lower lobe (a). Black-blood T1-weighted turbo SE (b), T2-weighted turbo SE (c) and STIR turbo SE (d) images show nodule as, respectively, low, intermediate or high signal intensity in the left lower lobe. Post-contrast black-blood T1-weighted turbo SE image (e) showed homogeneous enhancement of nodule

Table 11.1. Recommended MR protocol for nodule detection and characterization

| No. | Recommended sequence | TR (ms) | TE (ms) | FA (°) | Matrix | Respiration | Suggestion |
|-----|--|-------------------------|---------|--------|---------------------|-------------|--|
| 1 | Pre-contrast-enhanced ECG-gated T1W-SE or TSE | 1 <R-R> | 15–25 | N/A | 256 × 256 | RT or RG | |
| 2 | ECG- and respiratory-gated T2W-TSE | 2 or 3 <R-R> | 90–100 | N/A | 256 × 256 | RT or RG | ETL should be less than 15 |
| 3 | Respiratory-gated STIR TSE | Up to respiratory cycle | 15 | N/A | 256 × 256 | RG | ETL should be less than 5, if sequentially-reordered phase encoding scheme is used |
| 4 | Dynamic MRI by using 3D ultra-fast T1-GRE | 2.4–2.7 | 0.6–0.7 | 20–40 | 128 × 128 | BH | Dynamic MR images should be obtained every 1.1 s after contrast media injection |
| | Dynamic MRI by using ECG-gated T1W-SE | 150-1 <R-R> | 10–15 | N/A | 128 × 128–256 × 256 | BH | Dynamic MR images should be obtained at 0, 1, 2, 3, 4, 5, 6 and 8 min after contrast media injection |
| 5 | Post contrast-enhanced ECG-gated T1W-SE or TSE | 1 <R-R> | 15–25 | N/A | 256 × 256 | RT or RG | |

SE: spin-echo, TSE: turbo spin-echo, GRE: gradient echo, TR: repetition time, TE: echo time, FA: flip angle, RT: respiratory-trigger, RG: respiratory-gated, ETL: echo train length

further improvements of MR systems and sequences can be expected to enable pulmonary metastasis surveillance and/or lung cancer screening as well as whole-body MR screening or staging in the near future.

11.3

Characterization and Management of Pulmonary Nodules or Masses on MR Imaging

Since the pulmonary nodule is one of the most common findings on chest radiographs and CT, it is important to differentiate malignant from benign nodules in the least invasive way and to make as specific and accurate diagnosis as possible. Investigators have used CT, MR imaging and FDG-PET or PET/CT to evaluate the radiological features, relaxation time, blood supply and metabolism of pulmonary nodules to differentiate malignant from benign nodules with promising results. (Table 11.1).

11.3.1

Conventional T1-Weighted and T2-Weighted MRI Without and With Contrast Media

Characterization of the primary tumor on CT and MR imaging is based on the imaging features of the nodule or mass itself and its relationship to the pleura, chest wall, airways, and mediastinum, as well as its relative enhancement by contrast media. Historically, non-contrast-enhanced MR imaging has shown limited potential for characterizing peripheral lung nodules and masses and identifying benign nature of nodules due to the low intrinsic signal intensity of the lung parenchyma, the relatively poor spatial resolution and patient-related motion artifacts (CASKEY et al. 1990; FEUERSTEIN et al. 1992; KONO et al. 1993; KERSJES et al. 1997; MCLLOUD and SWENSON 1999). In general, many pulmonary nodules, including lung cancers, pulmonary metastases and low-grade malignancies such as carcinoids and lymphomas are demonstrated as low or intermediate signal intensities on T1-weighted images and

as slightly high intensity on T2-weighted images when SE or turbo SE sequences are used (CASKEY et al. 1990; FEUERSTEIN et al. 1992; KONO et al. 1993; KERSJES et al. 1997; McLOUD and SWENSEN 1999) (Fig. 11.2). If the pulmonary nodule is less than 30 mm in diameter, malignant pulmonary nodules within the tumor usually show no macroscopic necrosis (CASKEY et al. 1990; FEUERSTEIN et al. 1992; KONO et al. 1993; KERSJES et al. 1997; McLOUD and SWENSEN 1999). Although enhancement levels vary due to underlying microscopically determined pathologic conditions such as tumor angiogenesis, tumor interstitial spaces, the presence or absence of fibrosis, and scarring and necrosis within the tumor, malignant pulmonary nodules show homogeneous enhancement but at a variety of levels on T1-weighted images after administration of contrast media (CASKEY et al. 1990; FEUERSTEIN et al. 1992; KONO et al. 1993; KERSJES et al. 1997; McLOUD and SWENSEN 1999). Consequently, when using pre- and post-contrast enhanced conventional T1-weighted images and T2-weighted images, clinicians in routine clinical practice often face a diagnostic dilemma in distinguishing malignant from benign pulmonary nodules such as organizing pneumonia, benign tumors and inflammatory nodules (CASKEY et al. 1990; FEUERSTEIN et al. 1992; KONO et al. 1993; KERSJES et al. 1997; McLOUD and SWENSEN 1999) (Figs. 11.2 and 11.3). It has therefore been suggested that enhancement patterns or blood supply evaluated with dynamic contrast-enhanced MR imaging may be helpful for diagnosis and management of pulmonary nodules (KONO et al. 1993; KUSUMOTO et al. 1994; HITTMAIR et al. 1995; GÜCKEL et al. 1996; FUJIMOTO et al. 2003; OHNO et al. 2002, 2004a; SCHAEFER et al. 2004, 2006; KONO et al. 2007; DONMEZ et al. 2007). However, it may be possible to diagnose several histological types of pulmonary nodules, such as bronchocele, tuberculoma, mucinous bronchioalveolar carcinoma (BAC), hamartoma and aspergilloma, on pre- or post-contrast enhanced T1-weighted images and T2-weighted image according to their specific MR findings.

11.3.1.1

Bronchial Atresia and Bronchocele

Bronchial atresia is a common focal pulmonary lesion, which can be diagnosed by using non-contrast enhanced T1- and T2-weighted images. Bronchial atresia is an uncommon anomaly characterized by focal obliteration of the bronchial lumen and the absence of communication between lobar, segmental or subsegmental bronchi and

the central airway (MENG et al. 1978; JEDERLINIC et al. 1987; FINCK and MILNE 1988; NAIDICH et al. 1988; BAILEY et al. 1990; KO et al. 1998; MATSUSHIMA et al. 2002). Mucus secreted within the patent airways distal to the point of atresia accumulates in the form of a plug or bronchocele which appears as a pulmonary nodule or mass (FINCK and MILNE 1988; NAIDICH et al. 1988; BAILEY et al. 1990; KO et al. 1998; MATSUSHIMA et al. 2002). The MR image of bronchoceles reportedly appears as a branching lesion with high signal intensity on T1- and T2-weighted images due to the dilated mucus-filled bronchi and mucocele formation distal to the atelectatic segment (FINCK and MILNE 1988; NAIDICH et al. 1988; BAILEY et al. 1990; KO et al. 1998; MATSUSHIMA et al. 2002) (Fig. 11.4).

11.3.1.2

Tuberculoma

Tuberculomas, observed as well-defined nodules located mainly in the upper lobes, may appear after primary or reactivated tuberculosis. Calcification occurs in about 20%–30% of cases (SOCHOCKY 1958). CT yields superior visualization of the calcifications and characteristics of the nodules. In rare cases, areas of diminished attenuation are seen, which represent caseous necrosis. The latter may be identified as tuberculoma, a nodule with a relatively low signal intensity in comparison with that of other pulmonary nodules on T2-weighted SE or turbo SE images (SAKAI et al. 1992; KONO et al. 1993; KUSUMOTO et al. 1994; PARMAR et al. 2000; CHUNG et al. 2000; SCHAEFER et al. 2006). In addition, several investigators have reported on typical MR findings of tuberculoma on post-contrast enhanced T1-weighted images known as “thin-rim enhancement” sign (SAKAI et al. 1992) (Fig. 11.5). Signal intensity at the center of tuberculomas is low or slightly enhanced, but the signal intensity of the fibrotic rim is markedly enhanced. These MR findings correspond well to those of pathological specimens (SAKAI et al. 1992; KONO et al. 1993; KUSUMOTO et al. 1994; PARMAR et al. 2000; CHUNG et al. 2000; SCHAEFER et al. 2006). Therefore, when tuberculoma is suspected or attempts are made to distinguish it non-invasively from malignant nodules, pre- and post-contrast enhanced conventional MR imaging may be the most suitable procedure because tuberculoma is one of the most well-known diseases that show intense FDG uptake and is difficult to distinguish from malignant nodules by when FDG-PET or PET/CT is used (CHANG et al. 2006).

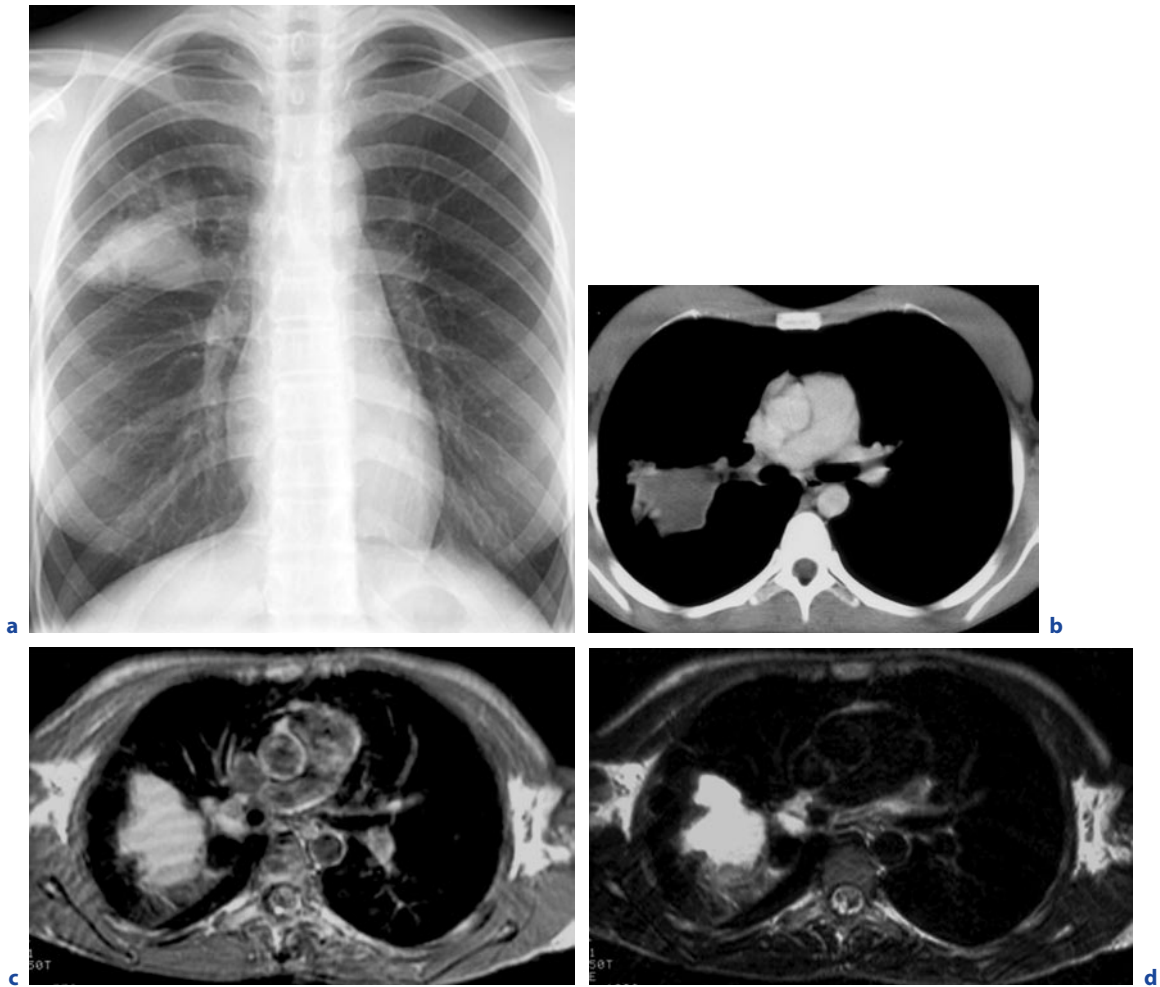


Fig. 11.4a-d. A 15-year-old female with bronchocele in the right upper lobe. Chest radiograph shows a mass in the right upper lung field (a). Contrast enhanced CT shows a mass with water density in the right upper lobe (b). Conventional T1-weighted SE (c) and T2-weighted turbo SE (d) images show the mass as high intensity due to mucus-filled bronchi and formation of a mucocele distal to the atelectatic segment, which was diagnosed as a bronchocele

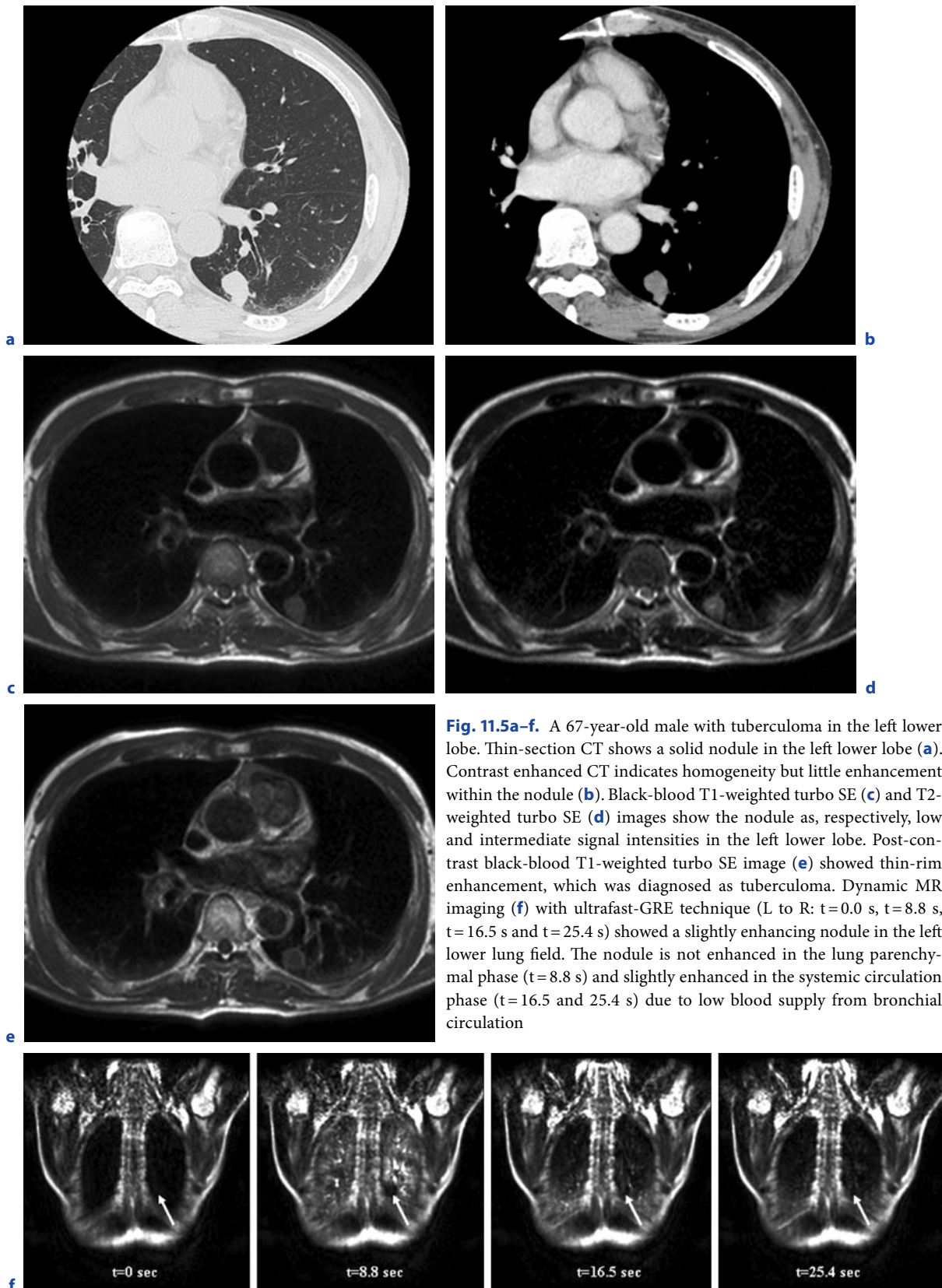


Fig. 11.5a-f. A 67-year-old male with tuberculoma in the left lower lobe. Thin-section CT shows a solid nodule in the left lower lobe (**a**). Contrast enhanced CT indicates homogeneity but little enhancement within the nodule (**b**). Black-blood T1-weighted turbo SE (**c**) and T2-weighted turbo SE (**d**) images show the nodule as, respectively, low and intermediate signal intensities in the left lower lobe. Post-contrast black-blood T1-weighted turbo SE image (**e**) showed thin-rim enhancement, which was diagnosed as tuberculoma. Dynamic MR imaging (**f**) with ultrafast-GRE technique (L to R: $t=0.0$ s, $t=8.8$ s, $t=16.5$ s and $t=25.4$ s) showed a slightly enhancing nodule in the left lower lung field. The nodule is not enhanced in the lung parenchymal phase ($t=8.8$ s) and slightly enhanced in the systemic circulation phase ($t=16.5$ and 25.4 s) due to low blood supply from bronchial circulation

11.3.1.3 Mucinous Bronchioalveolar Carcinoma

Adenocarcinoma of the lung constitutes a histologically and biologically heterogeneous group of tumors. Except for mucinous BAC, mucin production is seldom a truly prominent characteristic of this adenocarcinoma, so that there are no significant differences in the MR findings for adenocarcinoma of the lung and other subtypes of lung cancer. Mucinous BAC occasionally presents as a solitary pulmonary nodule with low or no uptake of contrast media on conventional post-contrast enhanced T1-weighted image, and thus may be difficult to differentiate from other benign nodules such as tuberculoma. However, many mucinous BACs demonstrate one of two radiological patterns, consolidation or diffuse disease. The consolidation may be segmental or may involve an entire lobe, and, with the exception of pulmonary vasculature, shows as high signal intensity on T2-weighted turbo SE images, which is known as “white lung sign” (Fig. 11.6). In addition, intratumoral vessels may be detected on contrast-enhanced T1-weighted images (GAETA et al. 2000, 2001, 2002).

11.3.1.4 Hamartoma

Pulmonary hamartomas, the third most common cause of solitary pulmonary nodules, are considered benign neoplasms that originate in fibrous connective tissue beneath the mucus membrane of the bronchial wall (BATESON 1973; SIEGELMAN et al. 1986). A few investigators have reported on MR imaging of hamartomas. SAKAI et al. (1994) found that all hamartomas appeared as a signal of intermediate intensity on T1-weighted SE images and as one of high intensity on T2-weighted SE images and four out of six hamartomas had a lobulated appearance separated by septa on T1- or T2-weighted SE images. In addition, pulmonary hamartomas pathologically diagnosed as lipomatous hamartoma sometimes show with high signal intensity on T1-weighted SE and T2-weighted turbo SE images (YILMAZ et al. 2004). Therefore, when these radiological findings are associated with a pulmonary nodule the nodule can be suspected of being a hamartoma, and the enhancement pattern within the nodule should be evaluated on post-contrast enhanced T1-weighted SE images, where the regions with less enhancement correspond to core

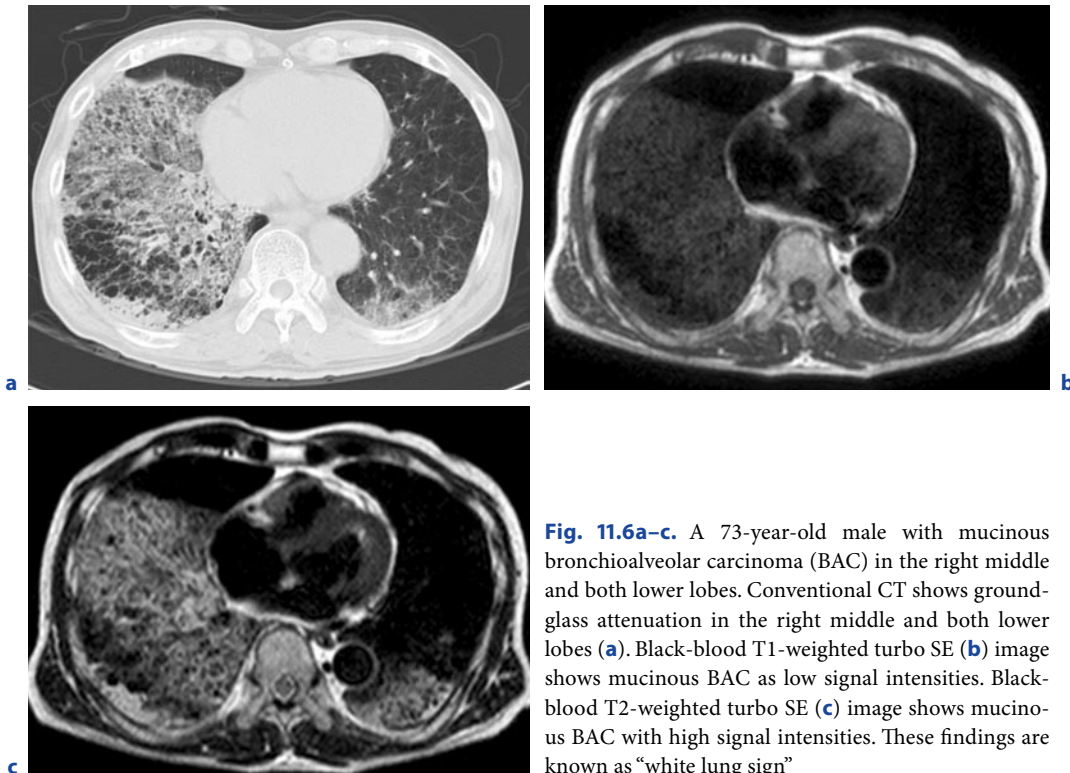


Fig. 11.6a–c. A 73-year-old male with mucinous bronchioalveolar carcinoma (BAC) in the right middle and both lower lobes. Conventional CT shows ground-glass attenuation in the right middle and both lower lobes (a). Black-blood T1-weighted turbo SE (b) image shows mucinous BAC as low signal intensities. Black-blood T2-weighted turbo SE (c) image shows mucinous BAC with high signal intensities. These findings are known as “white lung sign”

cartilaginous tissue and septa, and areas of marked contrast enhancement correspond to branching cleft-like mesenchymal connective tissue that dip into the cartilaginous core (SAKAI et al. 1994) (Fig. 11.7).

11.3.1.5 Aspergilloma

Saprophytic aspergillosis (aspergilloma) is characterized by *Aspergillus* infection without tissue invasion. It typically leads to conglomeration of intertwined fungal hyphae admixed with mucus and cellular debris within a pre-existing pulmonary cavity or ectatic bronchus (GEFTER 1992; AQUINO et al. 1994). A typical radiological finding of aspergilloma is a solid, round or oval mass with soft-tissue opacity within a lung cavity. The

mass is typically separated from the cavity wall by an airspace manifesting the so-called “air crescent” sign, and is often associated with thickening of the wall and adjacent pleura (GEFTER 1992; PARK et al. 2007). The most common underlying causes are healed tuberculosis, bronchiectasis, bronchial cyst and sarcoidosis. Other conditions that occasionally may be associated with aspergilloma include bronchogenic cyst, pulmonary sequestration, and pneumatoceles secondary to *Pneumocystis carinii* pneumonia in patients with acquired immunodeficiency syndrome.

The presence of a cavity within lung cancer is common and has been reported in 2%–16% of cases (FELSON and WIOT 1977). In general, lung cancer with a cavity typically shows a cavity wall with a thickness of more than 4 mm, spiculate or irregular inner and outer margins, enlarged lymph nodes, and a soft-tissue

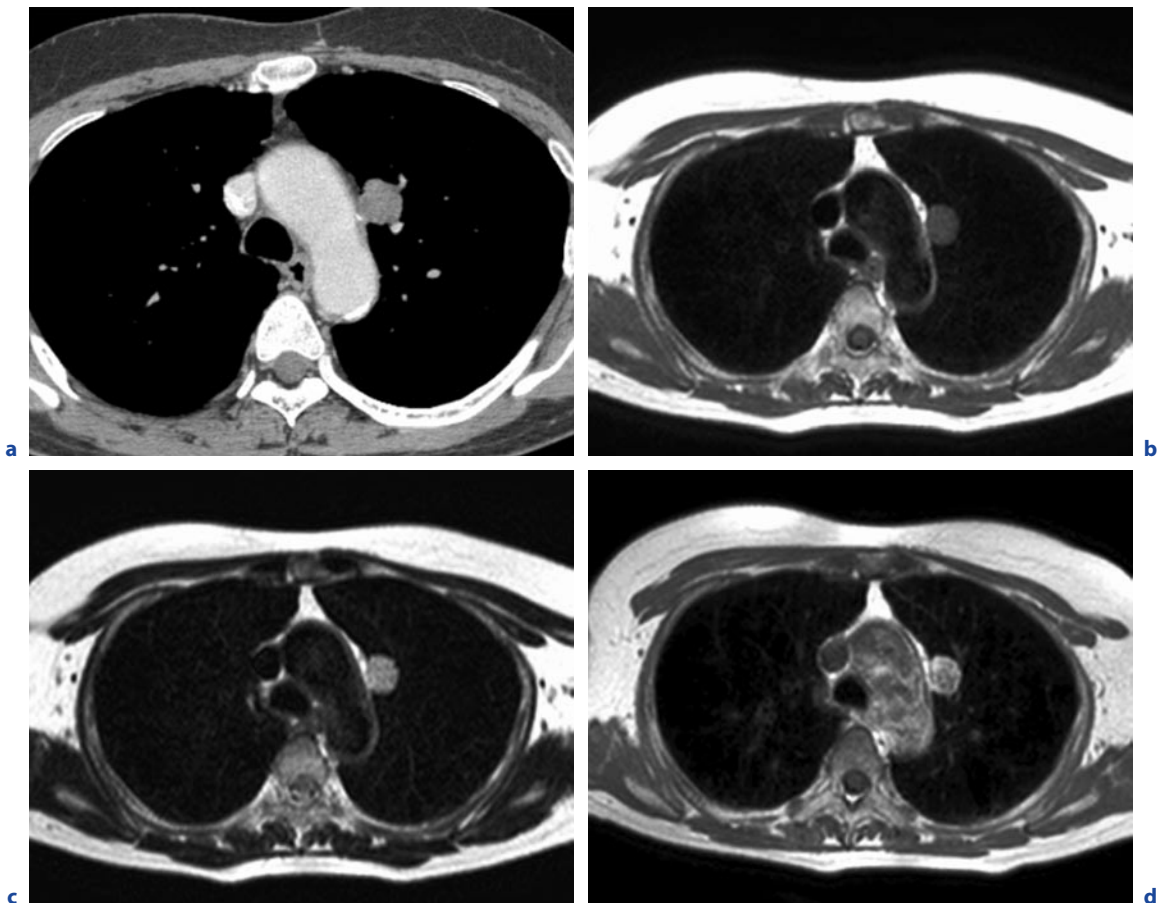


Fig. 11.7a–d. A 54-year-old male with hamartoma in the left upper lobe. Conventional contrast enhanced CT shows lobulated nodule in the left upper lobe (a). Black-blood T1-weighted turbo SE (b) and T2-weighted (c) images show a lobulated nodule as, respectively, low and high signal intensities in the left upper lobe. Post-contrast black-blood T1-weighted turbo SE (d) image shows less enhancement corresponding to core cartilaginous tissue, while areas of marked contrast enhancement correspond to cleft-like branching mesenchymal connective tissue

nodule or mass due to intracavitary tumorous mural regions associated with infiltration of the adjacent thoracic wall. In some cases, however, a lung cancer with a cavity may show a thin wall or “air crescent” sign on CXR or CT. It is therefore important to distinguish fungus ball from intracavitary tumorous mural regions by the “air crescent” sign in lung cancers with cavities, and pre- and post-contrast enhanced conventional T1- and T2-weighted SE or turbo SE images are helpful for this purpose.

Although a cavity may be present within lung cancer evidenced as a cavity and/or intracavitary mass shows a typical signal intensity pattern on pre- and post-contrast enhanced conventional T1- and T2-weighted SE or turbo SE images with as its characteristics a signal of low or intermediate intensity on pre-contrast enhanced T1-weighted images, one of intermediate or high intensity on T2-weighted images, and one of high intensity due to intensive and homogeneous enhancement on post-contrast enhanced

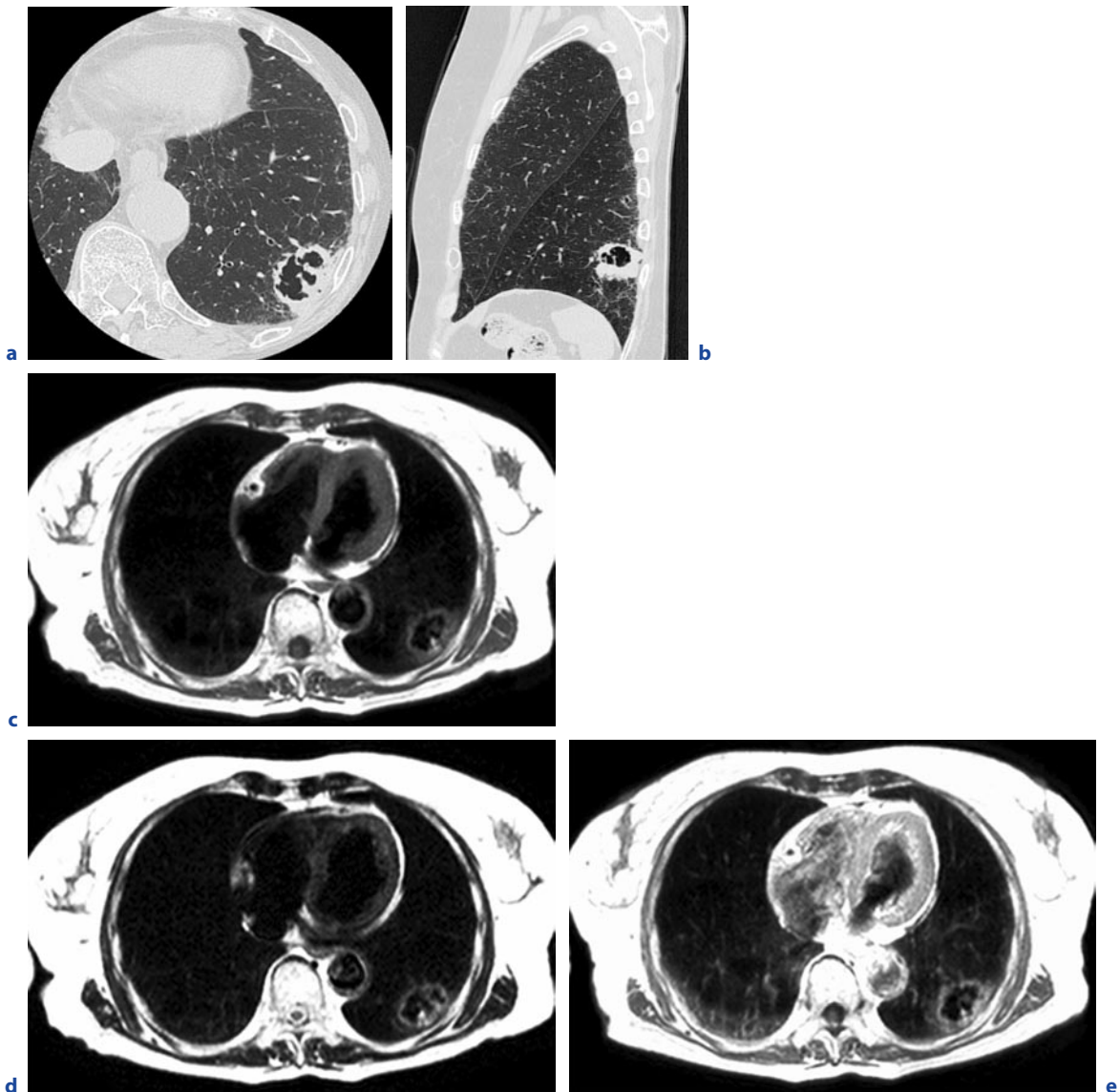


Fig. 11.8a–e. A 74-year-old male with squamous cell carcinoma in the left lower lobe. Thin-section CT (a) and sagittal reformat (b) show mass with irregularly thickened cavity wall in the left lower lobe. Black-blood T1-weighted turbo SE (c) and T2-weighted (d) images show mass with irregularly thickened cavity wall as, respectively, low and high signal intensities in the left lower lobe. Post-contrast black-blood T1-weighted turbo SE (e) image shows well-enhanced cavity wall corresponding to lung cancer

T1-weighted images (MA et al. 1985; VAN DER HEIDE et al. 1985; ZINREICH et al. 1988; HEROLD et al. 1989; FUJIMOTO et al. 1994; BLUM et al. 1994) (Fig. 11.8). In aspergilloma cases, on the other hand, the signal intensity of the intracavitary lesion is especially reduced on the T2-weighted SE or turbo SE image because of the presence of calcium, air, or ferromagnetic elements resulting from *Aspergillus* infection (HEROLD et al. 1989; FUJIMOTO et al. 1994; BLUM et al. 1994) (Fig. 11.9). Because of the presence of the ferromagnetic elements of

iron, magnesium, and manganese are essential to the metabolism of amino acids by fungi, FUJIMOTO et al. (1994) have suggested that the reduction in signal intensity on T1-weighted images and the marked reduction on T2-weighted images are characteristics of aspergilloma as well as mycetomas, and may be useful for differentiation of aspergilloma from intracavitary tumorous mural nodules.

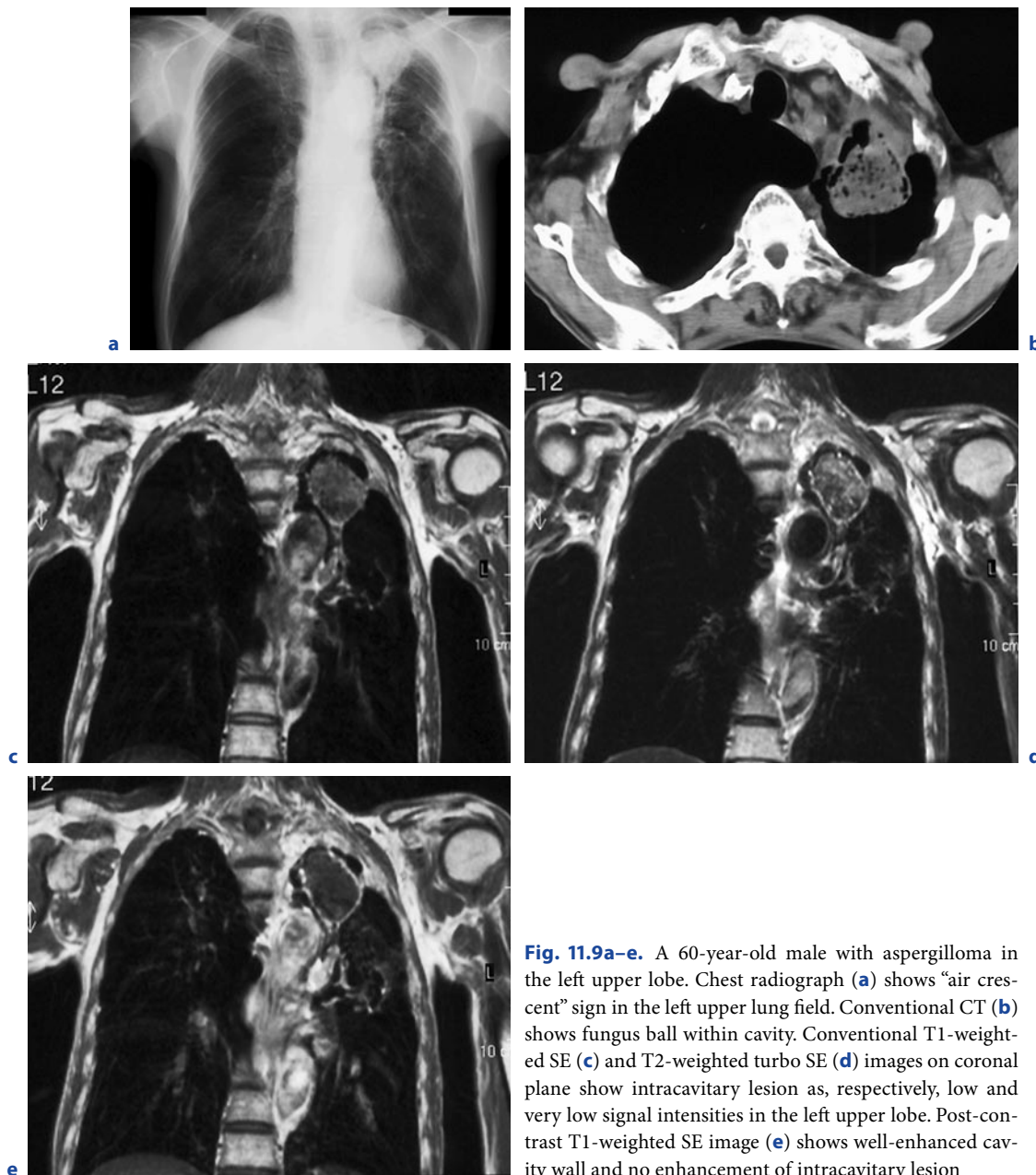


Fig. 11.9a–e. A 60-year-old male with aspergilloma in the left upper lobe. Chest radiograph (a) shows “air crescent” sign in the left upper lung field. Conventional CT (b) shows fungus ball within cavity. Conventional T1-weighted SE (c) and T2-weighted turbo SE (d) images on coronal plane show intracavitary lesion as, respectively, low and very low signal intensities in the left upper lobe. Post-contrast T1-weighted SE image (e) shows well-enhanced cavity wall and no enhancement of intracavitary lesion

11.3.2 Dynamic Contrast-enhanced MR Imaging of Pulmonary Nodules

Although in some cases benign or malignant focal lesions can be differentiated from others by using pre- and post-contrast enhanced conventional T1- or T2-weighted SE or turbo SE imaging, significant overlaps have been observed between benign and malignant lesions in routine clinical practice (KONO et al. 1993; KUSUMOTO et al. 1994). To overcome this problem, dynamic contrast-enhanced MR imaging has been proposed as an alternative technique for diagnosis and/or management of pulmonary nodules (Table 11.1). As a result of advances in MR systems and pulse sequences, there are now three major methods for dynamic MR imaging of the lung. Many investigators have proposed dynamic MR imaging be used for two-dimensional (2D) SE or turbo SE sequences or for various types of 2D or three-dimensional (3D) gradient-echo (GRE) sequences and that enhancement patterns within nodules and/or parameters determined from signal intensity-time course curves be assessed visually. These curves represent first transit and/or recirculation and wash-out of contrast media in 5 min or more with repeated breath holding (KONO et al. 1993; KUSUMOTO et al. 1994; HITTMAIR et al. 1995; GÜCKEL et al. 1996; OHNO et al. 2002, 2004a; FUJIMOTO et al. 2003; SCHAEFER et al. 2004, 2006; KONO et al. 2007; DONMEZ et al. 2007). Taking into account the inherent inhomogeneous composition of many intraindividual lung cancers and even within benign lesions such as central necrosis, only a dynamic contrast-enhanced 3D approach has the chance of depicting all underlying histologies. This is important for the primary diagnosis as well as during follow up examinations to assure evaluation of the same region of interest again. Recently, dynamic contrast enhanced MR perfusion imaging has been proposed for quantitative and qualitative assessment of regional pulmonary perfusion abnormalities by using 2D or 3D ultra-fast GRE sequences with sharp bolus profiles (HATABU et al. 1996, 1999; AMUNDSEN et al. 1997, 2000; LEVIN et al. 2001; MATSUOKA et al. 2001; OHNO et al. 2002, 2004c, 2005, 2007a, b; FINK et al. 2004). This technique allows for directly assessing the first passage of contrast media within nodules in less than 35 s within a single breath hold and to evaluate blood supply to nodules from pulmonary and/or bronchial circulation (OHNO et al. 2002, 2004c). It should be noted though that the ideal acquisition of contrast enhanced dynamic studies of tumor perfusion should not be limited to the first pulmonary passage of the contrast agent. Tumors will be supplied by systemic, bronchial arteries instead of

pulmonary arteries. In this case or due to inherent slow blood flow within a tumor an examination in a single breath hold might not be sufficient in detecting the full perfusion cycle of wash-in and wash-out. Examination of prolonged wash-out always reveals an underlying reperfusion of pulmonary tissue by both pulmonary and bronchial arteries. This circumstance has not been accounted for in the usual models for quantification of tissue perfusion so far.

Although there are various dynamic MR techniques, reported sensitivities range from 94% to 100%, specificities from 70% to 96%, and accuracies of more than 94% (KONO et al. 1993, 2007; KUSUMOTO et al. 1994; HITTMAIR et al. 1995; GÜCKEL et al. 1996; OHNO et al. 2002, 2004a; FUJIMOTO et al. 2003; SCHAEFER et al. 2004, 2006; DONMEZ et al. 2007). These specificities and accuracies for dynamic MR imaging are superior to those reported for dynamic CT, and almost equal to or superior to those for FDG-PET or PET/CT (SWENSEN et al. 1992, 1996, 2000; DEWAN et al. 1993; KONO et al. 1993; PATZ et al. 1993; KUSUMOTO et al. 1994; HITTMAIR et al. 1995; YAMASHITA et al. 1995; BURY et al. 1996; GÜCKEL et al. 1996; ZHANG and KONO 1997; OHNO et al. 2002, 2004a; FUJIMOTO et al. 2003; HERDER et al. 2004; SCHAEFER et al. 2004, 2006; YI et al. 2004, 2006; JEONG et al. 2005; JOSHI et al. 2005; MORI et al. 2005; BRYANT and CERFOLIO 2006; CHRISTENSEN et al. 2006; DONMEZ et al. 2007; KIM et al. 2007; KONO et al. 2007; LEE et al. 2007). Therefore, dynamic contrast-enhanced MR imaging may perform a complementary role in the diagnosis of pulmonary nodules assessed with FDG-PET or PET/CT. Although these results are highly promising further research in this field may be necessary in the light of recently published data regarding the MR signal dependency in perfusion studies on the contrast agent concentration. As quantification of perfusion parameters is dependent on an almost linear relationship of signal to concentration great care has to be taken regarding the dosage and application of contrast agents (PUDERBACH et al. 2008).

Although differentiation of malignant from benign pulmonary nodules by means of dynamic MDCT, dynamic MRI and PET or PET/CT with FDG has been tried in several studies, accurate separation of active infectious nodules from malignant neoplasms on the basis of dynamic CT and MR parameters and uptakes of FDG can be extremely difficult in view of the underlying pharmacokinetical, pathological and biological properties of malignant neoplasms and active infectious nodules. In addition, when considering the management of pulmonary nodules in clinical practice, it may be helpful to differentiate pulmonary nodules requiring further intervention and treatment (low or high grade

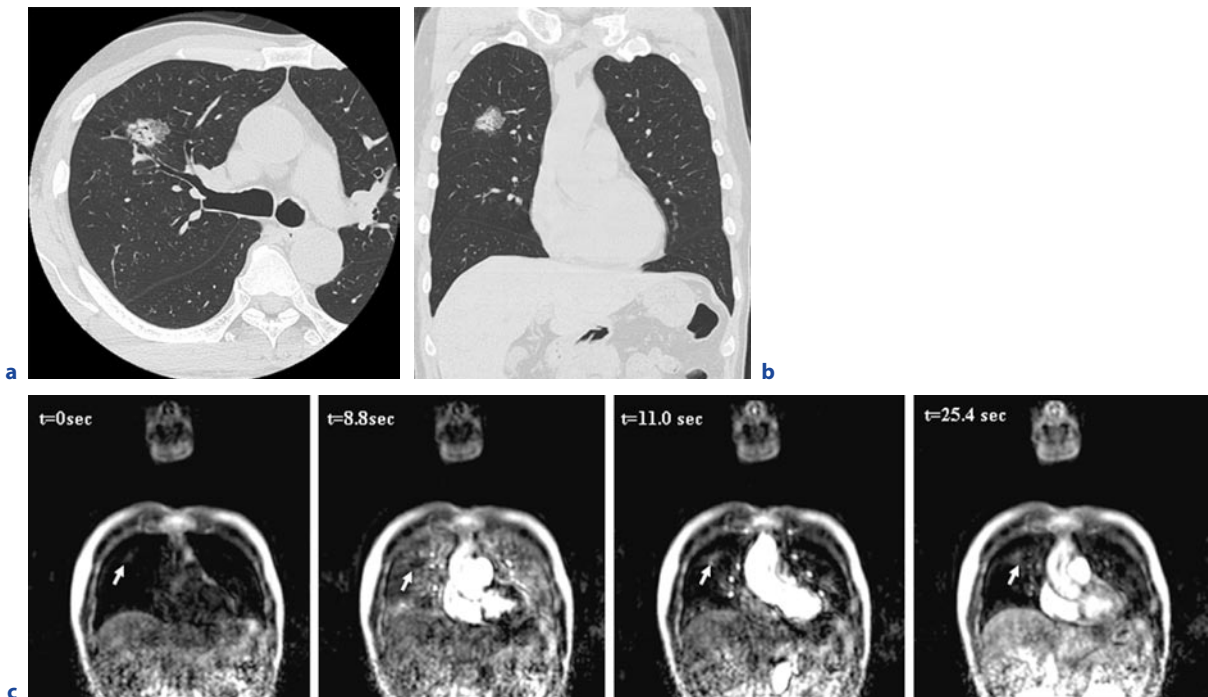


Fig. 11.10a–c. A 57-year-old female with adenocarcinoma with mixed subtype. Thin-section CT (**a**) and coronal reformat (**b**) show partly solid nodule in the right upper lobe. Dynamic MR imaging (**c**) with ultra-fast GRE technique (L to R: $t = 0.0$ s, $t = 8.8$ s, $t = 11.0$ s and $t = 25.4$ s) shows well-enhanced nodule

(*arrow*) in the right upper lung field. The nodule was not enhanced in the lung parenchymal phase ($t = 8.8$ s) and well enhanced in the systemic circulation phase ($t = 11.0$ and 25.4 s) due to enhanced blood supply from bronchial circulation

malignant tumors and active infectious nodules) from pulmonary nodules requiring no further evaluation (benign tumors and chronic infectious nodules) rather than to differentiate between malignant nodules and other nodules. For this latter differentiation, ultra-fast dynamic MR imaging can divide all nodules into the two categories (Figs. 11.5 and 11.10) (OHNO et al. 2002). This means that it may be better to use dynamic MR imaging in a complementary role to CT and FDG-PET or PET/CT to determine whether further intervention and treatment are indicated rather than to differentiate pulmonary nodules into malignant nodules and other nodules in routine clinical practice.

On the other hand, the results of several comparative studies of findings obtained with dynamic MR parameters and with immuno-histopathological examination of small peripheral lung cancers, the former showed good correlation with tumor angiogenesis (FUJIMOTO et al. 2003; SCHAEFER et al. 2006), and the potential for more accurate differentiation of subtypes of small peripheral adenocarcinomas than is possible with thin-section CT, or for prognosis both before and

after treatment (FUJIMOTO et al. 2003; OHNO et al. 2005; SCHAEFER et al. 2006).

Moreover, ultra-fast 3D dynamic MR data can also be used for the prediction of postoperative lung function for non-small cell lung cancer patients (OHNO et al. 2004b, 2007b). The semi-quantitative regional perfusion obtained from ultra-fast dynamic MR imaging shows good correlation with that assessed by perfusion scintigraphy, with a reported limit of agreement of $\pm 6\%$, which is insignificant enough to make ultra-fast dynamic MR imaging suitable for clinical purposes (OHNO et al. 2004b). Moreover, the prediction of postoperative lung function derived from dynamic MR imaging was more accurate than that derived from perfusion scintigraphy, single photon emission tomography (SPECT) or qualitatively assessed MDCT, which is predicted postoperative lung function from preoperative lung function and the number of lung segments in the total and resected lung evaluated by pulmonary surgeons, and the predictive accuracy is almost equal to that obtained with quantitatively assessed MDCT based on density-masked CT technique (OHNO et al.

Table 11.2. Stage grouping of lung cancer

| Overall stage | T stage | N stage | M stage |
|------------------|---------------|----------|---------|
| Occult carcinoma | Tx | N0 | M0 |
| Stage 0 | Tis (in situ) | N0 | M0 |
| Stage IA | T1 | N0 | M0 |
| Stage IB | T2 | N0 | M0 |
| Stage IIA | T1 | N1 | M0 |
| Stage IIB | T2 | N1 | M0 |
| | T3 | N0 | M0 |
| Stage IIIA | T1 or T2 | N2 | M0 |
| | T3 | N1 or N2 | M0 |
| Stage IIIB | Any T | N3 | M0 |
| | T4 | Any N | M0 |
| Stage IV | Any T | Any N | M1 |

Table 11.3. T classification – primary tumor

| | |
|------------|---|
| TX | Primary tumor cannot be assessed, or tumor proven by the presence of malignant cells in sputum or bronchial washings but not visualized by imaging or bronchoscopy |
| T0 | No evidence of primary tumor |
| Tis | Carcinoma in situ |
| T1 | Tumor 3 cm or less in greatest dimension, surrounded by lung or visceral pleura, without bronchoscopic evidence of invasion more proximal than the lobar bronchus (i.e., not in the main bronchus) ^a |
| T2 | Tumor with any of the following features of size or extent |
| | × More than 3 cm in greatest dimension |
| | × Involves main bronchus, 2 cm or more distal to the carina |
| | × Invades visceral pleura |
| | × Associated with atelectasis or obstructive pneumonitis that extends to the hilar region but does not involve the entire lung |
| T3 | Tumor of any size that directly invades any of the following: chest wall (including superior sulcus tumors), diaphragm, mediastinal pleura, parietal pericardium; or tumor in the main bronchus less than 2 cm distal to the carina but with involvement of the carina; or associated atelectasis or obstructive pneumonitis of the entire lung |
| T4 | Tumor of any size that invades any of the following: mediastinum, heart, great vessels, trachea, esophagus, vertebra body, carina; separate tumor nodule(s) in the same lobe; tumor with malignant pleural effusion ^b |

^aThe uncommon superficially spreading tumor of any size with its invasive component limited to the bronchial wall, which may extend proximal to the main bronchus, is classified as T1

^bMost pleural effusions associated with lung cancer are due to tumor. In a few patients, however, multiple cytopathological examinations of pleural fluid are negative for tumor, and the fluid is non-bloody and is not an exudate. Where these elements and clinical judgment dictate that the effusion is not related to the tumor, the effusion should be excluded as a staging element and the patient should be classified as T1, T2 or T3

Table 11.4. N classification – regional lymph nodes

| | |
|-----------|--|
| NX | Regional lymph nodes cannot be assessed |
| N0 | No regional lymph node metastasis |
| N1 | Metastasis in ipsilateral peribronchial and/or ipsilateral hilar lymph nodes and intrapulmonary lymph nodes, including involvement by direct extension |
| N2 | Metastasis in ipsilateral mediastinal, and/or subcarinal lymph node(s) |
| N3 | Metastasis in contralateral mediastinal, contralateral hilar, ipsilateral or contralateral scalene, or supraclavicular lymph node(s) |

Table 11.5. M classification – distant metastasis

| | |
|-----------|---|
| MX | Distant metastasis cannot be assessed |
| M0 | No distant metastasis |
| M1 | Distant metastasis includes separate tumor nodule(s) in a different lobe (ipsilateral or contralateral) |

2007b). Dynamic MR imaging may therefore be useful not only for the characterization of pulmonary nodules, but prediction of postoperative lung function may also assist the management of pulmonary nodules, including determination of whether further intervention and treatment and/or operability are indicated for lung cancer patients.

11.4

Assessment of TNM Stages

The international TNM classification proposed by the International Union against Cancer (UICC) has been widely used in the investigation and treatment of lung cancer (Tables 11.2–11.5), and shows that survival rates have improved with more accurate staging and more accurate differentiation between those patients who are candidates for surgical resection and those who are judged to be inoperable but would benefit from chemotherapy, radiotherapy, or both (SOBIN and WITTEKIND 2002). Therefore, accurate radiological staging may affect the management as well as the prognosis of patients. However, only approximately one-half of the TNM stages determined with CT systems in the past have agreed with operative staging, with patients being both under- and over-staged (LEWIS et al. 1990; GDEEDO et al. 1997).

Currently, newly developed MDCT systems, FDG-PET or PET/CT, are considered useful for precise assessment of tumor extent because of their multiplanar capability and for accurate diagnosis of metastatic lymph nodes by analyzing the glucose metabolism of

cancer cells in lung cancer patients. However, since 1991 it has been suggested that MR imaging, with its multiplanar capability and better contrast resolution of tumor and mediastinum or of tumor and chest wall or both than that of CT, may also be useful, but only for the assessment of mediastinal and chest wall invasions and determination of the short axis diameter of certain mediastinal lymph nodes (WEBB et al. 1991). However, recent advancements in MR systems, improved or newly developed pulse sequences and/or utilization of contrast media has resulted in improved diagnosis of TNM staging for lung cancer patients (Table 11.6).

11.4.1

MR Assessment of T Classification

T classification is the descriptor given to the primary tumor and its local extent (SOBIN and WITTEKIND 2002). The definitions are given in Table 11.3. While the T factor is subdivided into four groups, the distinction between T3 and T4 tumors is critical because it represents the dividing line between conventional surgical and non-surgical management for NSCLC patients (ARMSTRONG 2000). It is therefore more important to distinguish T3 from T4 tumors than to differentiate T1 and T2 tumors and determine nodal staging. For this reason, MR imaging may be helpful for assessment of mediastinal invasion, chest wall invasion and distinguishing primary tumors from secondary changes such as atelectasis or obstructive pneumonia, although it may be difficult to distinguish simple extension of the tumor into the mediastinal pleura or pericardium (T3) from actual invasion (T4).

Table 11.6. Recommended MR protocol for lung cancer staging

| No. | Recommended sequence | TR (ms) | TE (ms) | FA (°) | Matrix | Respiration | Suggestion |
|-----|--|-------------------------|---------|--------|-------------|-------------|--|
| 1 | Pre-contrast-enhanced ECG-gated T1W-SE or TSE | 1 <R-R> | 15–25 | N/A | 256×256 | RT or RG | |
| 2 | ECG- and respiratory-gated T2W-TSE | 2 or 3 <R-R> | 90–100 | N/A | 256×256 | RT or RG | ETL should be less than 15 |
| 3 | Respiratory-gated STIR TSE | Up to respiratory cycle | 15 | N/A | 256×256 | RG | ETL should be less than 5, if sequentially-reordered phase encoding scheme is used |
| 4 | ECG-gated contrast-enhanced MR angiography | 5.7 | 1.9 | 20 | 256×128–256 | BH | k-space segmentation should be adapted |
| | Time-resolved contrast-enhanced MR angiography | 4.0 | 1.2 | 20–30 | 512×333 | BH | Temporal resolution should be less than 4 s |
| 5 | Post contrast-enhanced ECG-gated T1W-SE or TSE | 1 <R-R> | 15–25 | N/A | 256×256 | RT or RG | |

SE: spin-echo, TSE: turbo spin-echo, GRE: gradient echo, TR: repetition time, TE: echo time, FA: flip angle, RT: respiratory-trigger, RG: respiratory-gated, ETL: echo train length

11.4.1.1 Mediastinal Invasion

Many surgeons consider minimal invasion of mediastinal fat as resectable (QUINT and FRANCIS 1999), so that clinicians want to know whether minimal mediastinal invasion (T3 disease) or actual invasion (T4 disease) has occurred before considering surgical resection. The accuracy of CT for evaluating hilar and mediastinal invasion of lung cancer has been investigated extensively over the last two decades. Sensitivity for assessment of mediastinal invasion by single detector computed tomography with or without the use of helical scanning ranged from 40% to 84% and specificity from 57% to 94% (BARON et al. 1982; MARTINI et al. 1985; QUINT et al. 1987, 1995; RENDINA et al. 1987; GLAZER et al. 1989; HERMAN et al. 1994; WHITE et al. 1994; TAKAHASHI et al. 1997).

The RDOG study compared CT with MR imaging for 170 patients with non-small cell lung cancer, although only T1-weighted images obtained without the use of cardiac or respiratory gating techniques were assessed in this study (WEBB et al. 1991). Although there was no significant difference between the sensitivity (63% and 56% for CT and MR imaging, respectively) and the specificity (84% and 80%) for distinguishing be-

tween T3-T4 tumors and T1-T2 tumors in this study, the RDOG reported that 11 patients showed mediastinal invasion and that the superior contrast resolution of MR imaging conferred a slight but statistically significant advantage over CT for accurate diagnosis of mediastinal invasion. In addition, delineation of tumor invasion of pericardium (T3) or heart (T4) was superior on MR imaging compared with CT scan when the cardiac-gated T1-weighted sequence was used for improved avoidance of cardiac motion artifacts (WHITE 1996). The normal pericardium has low signal intensity. Direct invasion of the cardiac chambers is readily demonstrated on T1-weighted images, because blood flowing through the cardiac chambers is signal void, so that the tumor is conspicuous because of its higher signal intensity. However, the accuracy of minimal mediastinal invasion assessment by both CT scanning and MR imaging is limited because it depends on visualization of the tumor within the mediastinal fat (WONG et al. 1999). In contrast to the assessment of mediastinal invasion, MAYR et al. (1987) found CT scanning to be more accurate than MR imaging in visualizing and assessing both normal and abnormal airways. They evaluated 319 normal and 79 abnormal bronchoscopically visualized bronchi. Their study found that CT scanning was accu-

rate in all cases, whereas MR imaging correctly identified only 45% of normal bronchi and 72% of abnormal bronchi (MAGDELEINAT et al. 2001). This discrepancy can be attributed both to the higher spatial resolution of CT scanning and to the low intrinsic MR imaging signal of air. Therefore, the relationship of lung cancer to central endobronchial extension is more accurately demonstrated on CT scans.

Recent advancement in MR systems, improved pulse sequences and utilization of contrast media have resulted in the introduction of new MR imaging techniques for assessment of mediastinal invasion of lung cancer. Contrast-enhanced MR angiography has been used for assessment of cardiovascular or mediastinal invasions (TAKAHASHI K et al. 2000; OHNO et al. 2001). OHNO et al. (2001) described a series of 50 NSCLC patients with suspected mediastinal and hilar invasion of lung cancer visualized with contrast-enhanced CT

scans, cardiac-gated MR imaging, and non-cardiac- and cardiac-gated contrast-enhanced MR angiographies (Fig. 11.11). In this study, sensitivities, specificities and accuracies of both contrast-enhanced MR angiography ranged from 78% to 90%, 73% to 87%, and 75% to 88%, respectively. These values were higher than those of contrast-enhanced single helical CT and conventional T1-weighted imaging (OHNO et al. 2001). Thus, contrast-enhanced MR angiography is thought to improve the diagnostic capability of MR imaging for mediastinal and hilar invasion.

In 2005, another new technique, cine MR imaging obtained with a steady-state free precession (SSFP) sequence was introduced as useful for evaluation of cardiovascular invasion in patients with thoracic mass (SEO et al. 2005). In this study, as well as previous electron beam CT or traditional cine MR studies (MURATA et al. 1994; SAKAI et al. 1997), the assessment of sliding

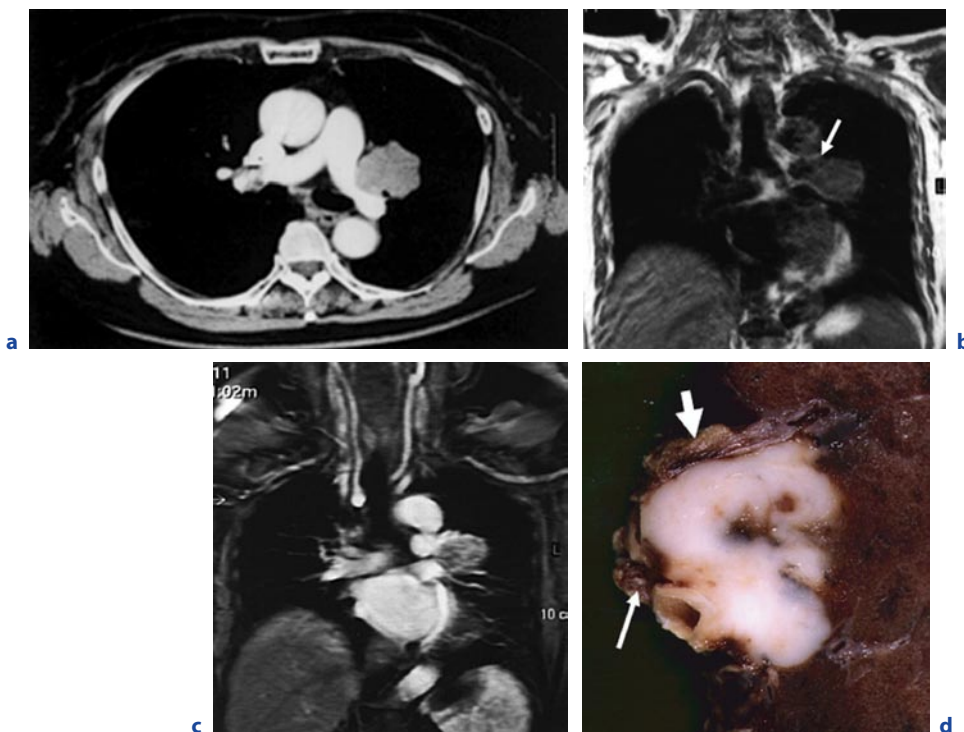


Fig. 11.11a–d. A 68-year-old female with squamous cell carcinoma in the left upper lobe. Contrast enhanced thin-section CT (a) suggests invasion to pulmonary vein and mediastinum, while conventional T1-weighted image (b) on coronal plane suggests invasion to pulmonary artery and mediastinum (arrow). Contrast-enhanced MR angiography (c) clearly shows invasion to pulmonary artery and vein, but not mediastinal invasion due to visualization of mediastinal fat between pulmonary artery and pulmonary vein as a *black area*. Macroscopical finding of the resected left upper lobe (d) shows invasion to left pulmonary artery (arrow) and left superior pulmonary vein (*large arrow*), but not mediastinal invasion

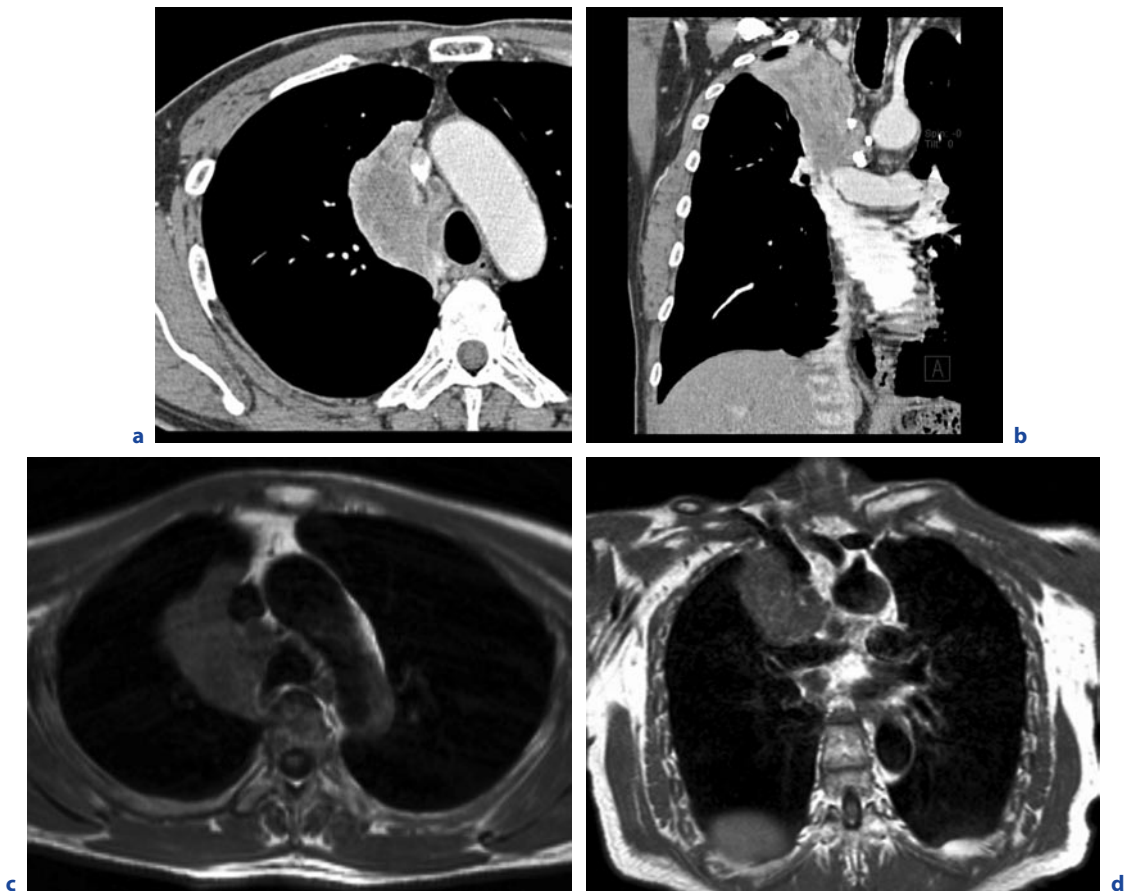


Fig. 11.12a–d. A 61-year-old male with squamous cell carcinoma in the right upper lobe. Contrast enhanced CT (**a**) suggests mediastinal invasion, while contrast enhanced coronal reformat (**b**) clearly demonstrates mediastinal invasion. Black-blood T1-weighted images on axial (**c**) and coronal (**d**) planes also clearly demonstrate invasion to superior venous cava and mediastinum

motions between thoracic masses and adjacent mediastinal structure demonstrated a very high diagnostic capability (sensitivity: 100%, specificity: 92.9%, accuracy: 94.4%) (SEO et al. 2005). However, only 9 of 26 lung cancer patients were included in this study since the others had mediastinal tumors. Further investigation thus seems to be warranted to determine the actual diagnostic capability of cine MR imaging for mediastinal invasion in NSCLC patients.

In addition, MDCT has been widely utilized during the past five years or so for routine clinical practice, and it was found that thin-section multiplanar reformatted (MPR) imaging from thin-section volumetric MDCT data was useful for the evaluation of *T* classification due to its multiplanar capability (HIGASHINO et al. 2005). HIGASHINO et al. (2005) suggested that mediastinal invasion that can be assessed from thin-section coronal

MPR images with 1 mm section thickness with greater sensitivity, specificity and accuracy than can be achieved with routine MDCT with 5 mm section thickness, and with slightly better specificity and accuracy than with thin-section axial MDCT with 1 mm section thickness. Although MR imaging is considered to show superior tissue contrast to that of MDCT, the similar multiplanar capability, faster scan time and better spatial resolution of thin-section MDCT may result in better assessment of mediastinal invasion in NSCLC patients than by previously described MR techniques (Fig. 11.12). Further investigations as well as comparative studies of thin-section MDCT and previously described or newly developed MR imaging techniques thus seem to be warranted to determine the actual significance of MR imaging for assessment of mediastinal invasion in routine clinical practice.

11.4.1.2 Distinguishing Lung Cancer from Secondary Change

Distinguishing primary lung cancer from secondary change is important for assessment of tumor extent and the therapeutic effect of chemotherapy and/or radiotherapy. While the therapeutic effect of conservative therapy has been assessed by using World Health Organization (WHO) criteria or response evaluation criteria in solid tumors (RECIST) (WORLD HEALTH ORGANIZATION 1979; THERASSE et al. 2000), it would be difficult to use CXR or plain or contrast-enhanced CT to evaluate tumor extent or therapeutic effect for cases with atelectasis or obstructive pneumonia.

MR imaging, on the other hand, has potential for distinguishing lung cancer from secondary change due to atelectasis or pneumonitis (KONO et al. 1993). In some cases, it can be difficult to distinguish lung cancer from post-obstructive atelectasis or pneumonitis because these secondary changes tend to be enhanced to a similar degree as the central tumor on contrast-enhanced CT scan. On T2-weighted MR imaging, however, post-obstructive atelectasis and pneumonitis often show higher signal intensity than does the central tumor. BOURGOUNIN et al. (1991) evaluated the histological findings of obstructive pneumonitis or atelectasis in

patients who had undergone surgical resection of lung cancer and had been evaluated preoperatively with MR imaging. They found that cholesterol pneumonitis and mucus plugs displayed higher signal intensity than the tumor on T2-weighted images, while atelectasis and organizing pneumonitis were isointense to the tumor. KONO et al. (1993) described a series of 27 patients with central lung cancer associated with atelectasis or obstructive pneumonitis (Fig. 11.13). These patients were examined with post-contrast enhanced T1-weighted MR imaging and the central tumor could be differentiated from adjacent lung parenchymal disease in 23 out of 27 patients (85%). The tumor was of lower signal intensity than the adjacent lung disease in 18 cases (67%) and of higher signal intensity in 5 (18%). These differences in signal intensity between primary tumor and secondary change were considered to be due to the presence of invasion of pulmonary vasculatures. Therefore, the use of T2-weighted or post-contrast enhanced T1-weighted images for assessment of tumor size and secondary change may be helpful for precise evaluation of tumor extent at the initial staging and for accurate prognosis for patients and assessment of therapeutic effect after conservative therapy and/or for comparative studies of standard and new chemo- and/or radiotherapy regimens (OHNO et al. 2000).

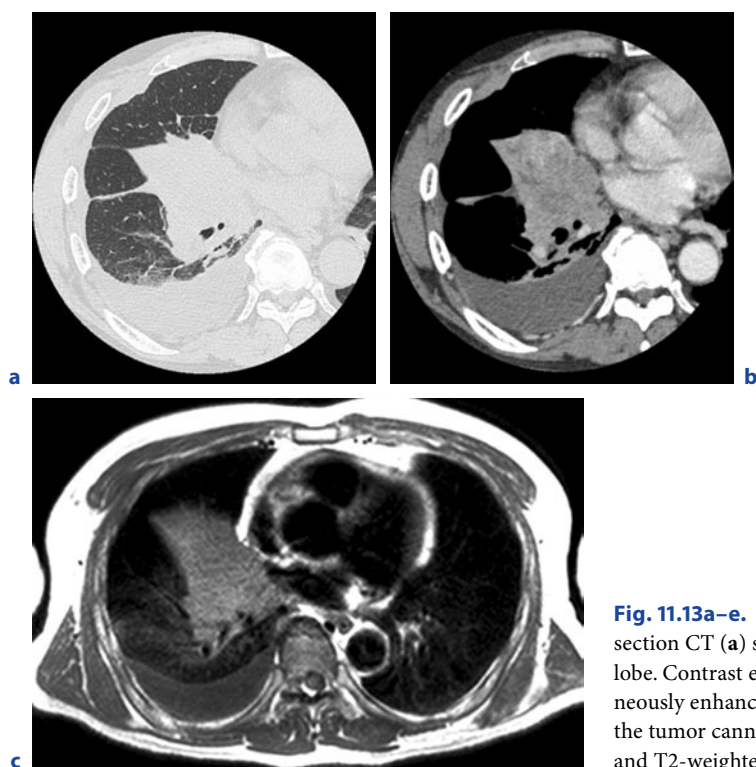


Fig. 11.13a–e. A 59-year-old male with adenocarcinoma. Thin-section CT (a) shows atelectasis in the right middle and lower lobe. Contrast enhanced thin-section CT (b) shows homogeneously enhanced atelectasis and pleural effusion, but the extent of the tumor cannot be determined. Black-blood T1-weighted (c) and T2-weighted (d) see next page

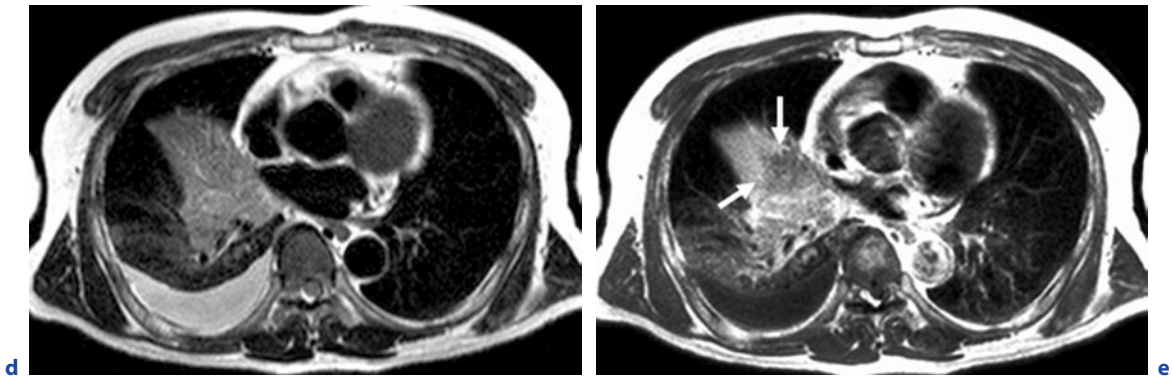


Fig. 11.13a–e. (continued) images show atelectasis and the tumor as, respectively, low and intermediate signal intensity. Mediastinal invasion is suspected, while pleural effusion is clearly seen. Post-contrast black-blood T1-weighted image (e) clearly shows the extent of lung cancer and secondary change (arrow)

11.4.1.3 Chest Wall Invasion

Chest wall invasion used to be considered a contraindication for surgical excision of lung cancer, but recent surgical advances have made chest wall excision feasible for the treatment of locally aggressive lung cancer and giving patients a better chance of survival (MAGDELEINAT et al. 2001). Preoperative visualization of chest wall invasion may therefore be helpful for surgical planning. On conventional CT scan, rib destruction is the only reliable sign of chest wall invasion since soft tissue masses in the chest wall correlate statistically with chest wall invasion. However, they are not reliable indicators for an individual patient, so that focal chest pain may still be the most reliable indicator of chest wall invasion. In fact, the reliability of conventional CT assessment of chest wall invasion in lung cancer patients varies widely with reported sensitivities ranging from 38% to 87% and specificities from 40% to 90% (QUINT and FRANCIS 1999). In addition to the technique of inducing artificial pneumothorax described elsewhere (WATANABE et al. 1991; YOKOI et al. 1991), MURATA et al. (1994) reported that dynamic expiratory multi-section CT reviewed as a cine loop was 100% accurate for identification of both chest wall and mediastinal invasion.

Another study has suggested that ultrasound (US) is an effective technique for diagnosis of chest wall invasion (SUZUKI et al. 1993). In this study, 120 lung cancer patients were examined, in 19 of whom invasion was pathologically proved. Sensitivity, specificity and accuracy of US were 100%, 98%, and 98%, respectively, while the corresponding values for conventional CT used in the same study were only 68%, 66%, and 67% (SUZUKI

et al. 1993). Therefore, US is also considered useful for assessment of chest wall invasion by some chest physicians, although the diagnostic capability of US depends on the experience and technical capability of the clinician.

Because of its multiplanar capability and better tissue contrast resolution compared to CT, MR imaging has also been advocated as effective for assessment of chest wall invasion (RAPOPORT et al. 1988; HEELAN et al. 1989; WEBB et al. 1991; PADOVANI et al. 1993; BONOMO et al. 1996). Sagittal and coronal plane images are better than axial CT images for displaying the anatomical relationship between tumor and chest wall structures (BONOMO et al. 1996; FREUNDLICH et al. 1996). MR imaging shows infiltration or disruption of the normal extra pleural fat plane on T1-weighted images or parietal pleural signal hyper intensity on T2-weighted images (Fig. 11.14). In addition, when STIR turbo SE imaging is used for this purpose, it can demonstrate lung cancer as high signal intensity within the suppressed signal intensities of chest wall structures, enabling clinicians to easily determine the tumor extent within chest wall (Fig. 11.14c). Moreover, PADOVANI et al. (1993) have suggested that the diagnostic yield can be further improved by intravenous administration of contrast media. In addition, superior sulcus or Pancoast tumors are good candidates for the demonstration of chest wall invasion on MR imaging. Since superior sulcus tumors occur in close proximity to the lung apex, their imaging has to include an evaluation of the relationship between the tumor and the brachial plexus, subclavian artery and vein, and adjacent chest wall. The axial scan plane of a CT scan is suboptimal for examining the lung apex where superior sulcus tumors are located, while direct

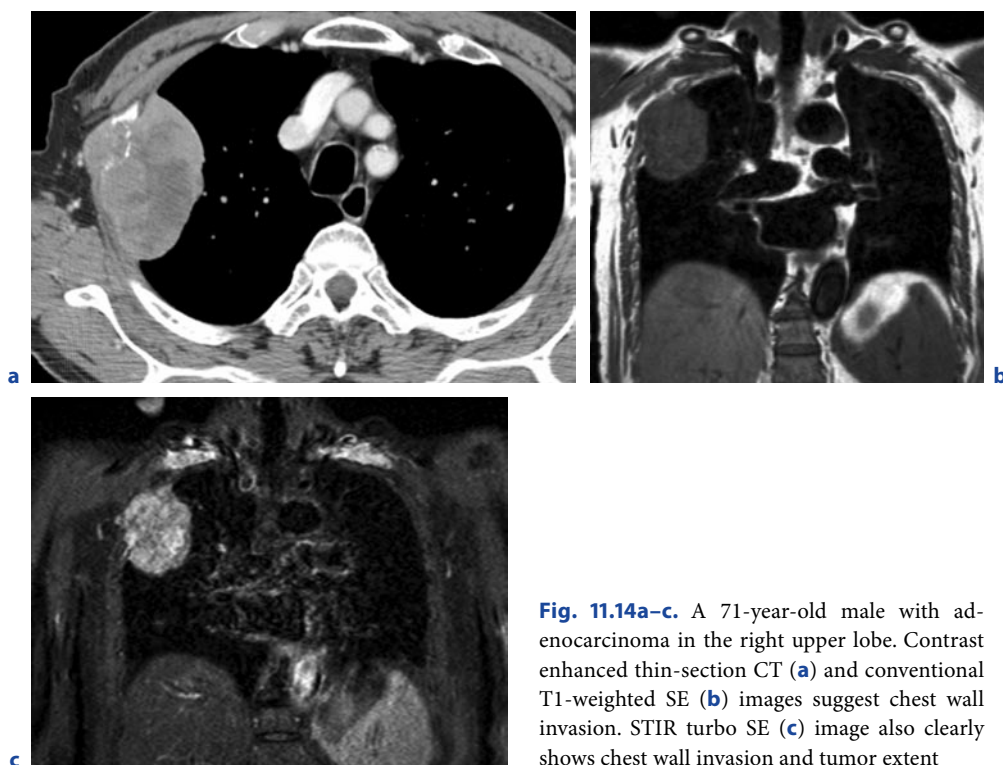


Fig. 11.14a-c. A 71-year-old male with adenocarcinoma in the right upper lobe. Contrast enhanced thin-section CT (**a**) and conventional T1-weighted SE (**b**) images suggest chest wall invasion. STIR turbo SE (**c**) image also clearly shows chest wall invasion and tumor extent

sagittal and coronal MR images are superior to CT for evaluating the local extent of disease in patients with superior sulcus tumors (RAPOPORT et al. 1988; HEELAN et al. 1989; WEBB et al. 1991; PADOVANI et al. 1993; BONOMO et al. 1996; FREUNDLICH et al. 1996). HEELAN et al. (1989) examined a series of 31 patients with superior sulcus tumors imaged with both CT and MR, and found that MR imaging showed 94% correlation with surgical and clinical findings, whereas the CT scans had an accuracy of only 63% for evaluating tumor invasion through the superior sulcus.

SAKAI et al. (1997) used dynamic cine MR imaging during breathing rather than static MR imaging for evaluating chest wall invasion in lung cancer patients. This study evaluated the movement of the tumor along the parietal pleura during the respiratory cycle displayed with a cine loop in a manner similar to dynamic expiratory multi-section CT (MURATA et al. 1994). Where the tumor had invaded the chest wall, it was fixed to the chest wall, while without invasion, the tumor was seen to move freely along the parietal pleura. In this study, the sensitivity, specificity, and accuracy of dynamic cine MR imaging for the detection of chest wall invasion were 100%, 70%, and 76%, respectively, and those of conventional CT and MR imaging were 80%, 65%, and 68% (SAKAI et al. 1997). Of special significance is

that the negative predictive value of dynamic cine MR imaging in this study was 100% without any need for ionizing radiation exposure. Dynamic cine MR imaging, when used in conjunction with static MR imaging, is therefore considered useful for further improvements of the assessment of chest wall invasion in lung cancer patients.

Currently, multiplanar capability, faster scan time and better spatial resolution of thin-section MDCT images may improve the diagnostic capability of CT for evaluation of chest wall invasion in NSCLC patients similar to that of mediastinal invasion. MR imaging is still considered to have superior tissue contrast compared with MDCT. HIGASHINO et al. (2005) also reported that thin-section sagittal MPR imaging with 1 mm section thickness could significantly improve diagnostic accuracy for chest wall invasion in comparison with routine MDCT with 5 mm section thickness, and showed slightly better diagnostic capability than thin-section MDCT with 1 mm section thickness. Therefore, further investigations as well as comparative studies of thin-section MDCT imaging and MR imaging used as described here, or of newly developed techniques will be needed to determine the actual significance of MR imaging for assessment of chest wall invasion in routine clinical practice.

11.4.1.4 MR Assessment of Respiratory Tumor Motion

The general objective of radiotherapy is to achieve tumor control by depositing a lethal dose in the target volume including potential microscopic spread of cancer cells, while sparing surrounding organs and tissue as best as possible. Therefore, precise localization of the target volume is needed. Actually, the recent advances in radiotherapy, including intensity modulated radiotherapy, adaptive radiotherapy as well as image guided radiotherapy allows for strong improvement of the accuracy of irradiation treatment. However, patient motion and especially respiratory motion has become a major obstacle for achieving high precision radiotherapy. Currently, in classic radiotherapy for lung tumors, such motion is accounted for with a generic target volume expansion, not considering the individual patient breathing characteristics and the mobility of the individual tumor. However, it has been widely recognized that the motion pattern of lung tumors and the breathing cycles vary greatly among patients. This empiric approach includes all surrounding healthy tissues that pass the planned target volume at any time of the breathing cycle to create a safety margin. Within this margin even the additional normal tissues will be irradiated unnecessarily, causing tissue damage or limiting the dose delivered to the target. Therefore it is attractive to define an individual treatment plan by limiting the irradiated volume to certain positions of the tumor on its path during respiration (gated technique) or to follow its respiratory movement (tracking techniques) (Li et al. 2008). Hence, the ultimate objective for radiotherapy of moving targets is to localize precisely the target in space and time in order to achieve a higher dose to be applied to the target while the maximum dose to the normal tissue is reduced, particularly for critical adjacent organs at risk. The better the delineation between target and normal tissue the lower the probability of complications and the higher the chance for tumor control eventually enhanced by the possibility to even increase tumor control by delivering an additional radiation dose solely to the target. For dedicated treatment planning, respiratory-gated four-dimensional (4D) MRI could be used to exactly define tumor size and its three-dimensional displacement during respiration in a single examination. The fourth dimension beyond the 3D space is time, in which patient motion and the change of the position of the tumor will be recorded. Ideally, 4D MRI would not only encode tumor and organ motion information, but also provide time resolved 3D data sets with reduced motion artifacts.

Numerous MR-based investigations of lung and tumor motion in the literature have been limited to examining the motion in a single plane or in a small number of orthogonal planes through the tumor. Two non-coplanar image views provided critical motion characterization, while the most significant displacement was in the cranial-caudal direction (SHIMIZU et al. 2000). For this purpose, the MR sequences derived from cardiac imaging have been adapted for respiratory motion analysis. These sequences were compared, demonstrating that fast imaging with a free precession steady-state gradient-echo provided significantly higher SNR than any fast low angle shot technique, while the latter had an advantage in higher temporal resolution.

The correlation between external fiducial markers (coils) and the internal organ motion was also studied using single-slice 4D MRI (PLATHOW et al. 2005). The correlation coefficients in the three orthogonal directions for different breathing types (thoracic or abdominal) were about 0.8, similar in magnitude to 4D CT. This quantitative information indicates that external fiducial markers might be satisfactory for predicting organ motion.

Volumetric 4D MR imaging was not possible before the recent introduction of multi-channel parallel detection systems. Parallel acquisition improves the performance of MR imaging by over an order of magnitude compared to single-channel MR systems. The signal to noise ratio (SNR) is usually degraded when using multi-element coils for multichannel imaging. Consequently, some of the gain in acceleration is sacrificed in order to maintain image quality. Compared with single-slice imaging, which requires multiple slice directions to view the critical motions of the moving organ, the volumetric 4D technique catches the entire volume in a single acquisition. However, single-slice 4D MR imaging has a higher speed and can be used to study fast heart beating and forced breathing maneuvers. Further improvement of 4D MR imaging may employ the view-sharing technique using a variable sampling rate in k-space and shares elements between image sets, reducing the acquisition time by an appropriate approximation. This technique, combined with parallel imaging, allows for volumetric 4D MR imaging in respiratory motion studies. Then the acquisition time could be below 0.7 s for a 3D torso image using a 1.5-T MRI scanner.

Concluding, significant improvement in 4D MRI has been made in the last years. Nevertheless 4D radiation therapy is still in its early stages of development. Promising advances are expected. At this point in time 4D MRI of lung tumor motion will play a larger role.

11.4.2 MR Assessment of N Classification

The descriptor *N classification* refers to the presence or absence of regional lymph node metastases (SOBIN and WITTEKIND 2002). The definitions are given in Table 11.4. In the absence of distant metastasis, locoregional lymph node spread will determine therapy and prognosis. For patients without positive lymph nodes (N0 disease) or with only intrapulmonary or hilar lymph nodes (N1 disease), direct resection remains standard therapy. In case of positive ipsilateral mediastinal lymph nodes (N2 disease), chemotherapy combined preoperatively with surgery or with concurrent or sequential radical radiotherapy is a legitimate choice (MARTINI et al. 1997; VANSTEENKISTE et al. 1998). If patients have contralateral mediastinal lymph node metastases (N3 disease), however, they are generally rejected for surgery but will receive non-surgical combination treatment.

CT has been the standard noninvasive modality for staging of lung cancer. Enlarged lymph nodes (i.e. with a short axis of more than 10 mm or a long axis of more than 15 mm) are considered to be metastatic. Although an increase in the size of mediastinal lymph nodes correlates with malignant involvement in patients with lung cancer, the sensitivity and specificity of this finding are not very high because lymph nodes can be enlarged due to infection or inflammation. In addition, small nodes can sometimes contain metastatic deposits. The RDOG reported that the sensitivity and specificity of CT for *N classification* were only 52% and 69%, respectively (WEBB et al. 1991), while the corresponding values from the Leuven Lung Cancer Group (LLCG) were 69% and 71% (DILLEMANS et al. 1994). Due to the substantial limitation of CT for depicting mediastinal lymph node metastases, additional mediastinoscopy with biopsy is necessary for adequate assessment of hilar and mediastinal nodes (GLAZER et al. 1984, 1985; MUSSET et al. 1986; POON et al. 19987; LAURENT et al. 1988; WEBB et al. 1991, 1993; McLOUD et al. 1992).

Since the 1990s, FDG-PET has been used for differentiation between metastatic and non-metastatic lymph nodes based on the biochemical mechanism of increased glucose metabolism or tumor cell duplication (WAHL et al. 1994; PATZ et al. 1995; BOISELLE et al. 1998; HIGASHI et al. 1998; GUPTA et al. 2000). However, elevated glucose metabolism may occur secondary to tumor, infection or inflammation (DEWAN et al. 1993; PATZ et al. 1993), and spatial resolution in PET is inferior to that of CT and MR, so that the diagnostic capability of the FDG-PET imaging is limited (GUPTA et al.

2000). A large number of prospective studies have compared the diagnostic capability of N stage assessment using CT and FDG-PET. A meta-analysis demonstrated that FDG-PET was significantly more accurate than CT for identifying lymph node involvement (GOULD et al. 2003). In addition, the respective median sensitivity and specificity of CT were 61% (interquartile range, 50%–71%) and 79% (interquartile range, 66%–89%), but those of FDG-PET were 85% (interquartile range, 67%–91%) and 90% (interquartile range, 82%–96%) (GOULD et al. 2003). Moreover, it has been suggested that FDG-PET is more sensitive but less specific when CT showed enlarged lymph nodes [median sensitivity, 100% (interquartile range, 90%–100%); median specificity, 78% (interquartile range, 68%–100%)] than when CT showed no lymph node enlargement [median sensitivity, 82% (interquartile range, 65%–100%); median specificity, 93% (interquartile range, 92%–100%); $P=0.002$] (GOULD et al. 2003).

Since the introduction of MR imaging for assessment of lung cancer, the criteria for tumor involvement within lymph nodes depend solely on lymph node size, and were very similar to CT criteria. In some cases, however, histological examination has shown that a normal-sized regional lymph node may have metastases, and that nodal enlargement can be due to reactive hyperplasia or other non-malignant conditions. The detectability of calcifications, which are indicative for a benign lesion, is also limited for MRI when compared with CT. The direct multiplanar capability of MR imaging, however, is an advantage for the detection of lymph nodes in areas that are sub-optimally imaged in the axial plane, such as in the aorto-pulmonary (AP) window and subcarinal regions (WEBB et al. 1991; BOISELLE et al. 1998).

Recently, cardiac- and/or respiratory-triggered conventional or black-blood STIR turbo SE imaging has been recommended for detection of metastatic tumors and metastatic lymph nodes (FUJIMOTO et al. 1995; EUSTACE et al. 1998; TAKENAKA et al. 2002; OHNO et al. 2004d, 2007c; KAWAI et al. 2006). These novel sequences may make to quantitatively assess the signal intensity of lymph nodes by means of comparison with a 0.9% normal saline phantom (TAKENAKA et al. 2002; OHNO et al. 2004d, 2007c). The STIR turbo SE sequence is a simple sequence, which can be easily included in clinical protocols to yield net of T1- and T2-relaxation times. On STIR turbo SE images, metastatic lymph nodes exhibit high signal intensity and non-metastatic lymph nodes low signal intensity (Figs. 11.15 and 11.16). Several studies have reported that sensitivity, specificity and accuracy of quantitatively and qualitatively assessed

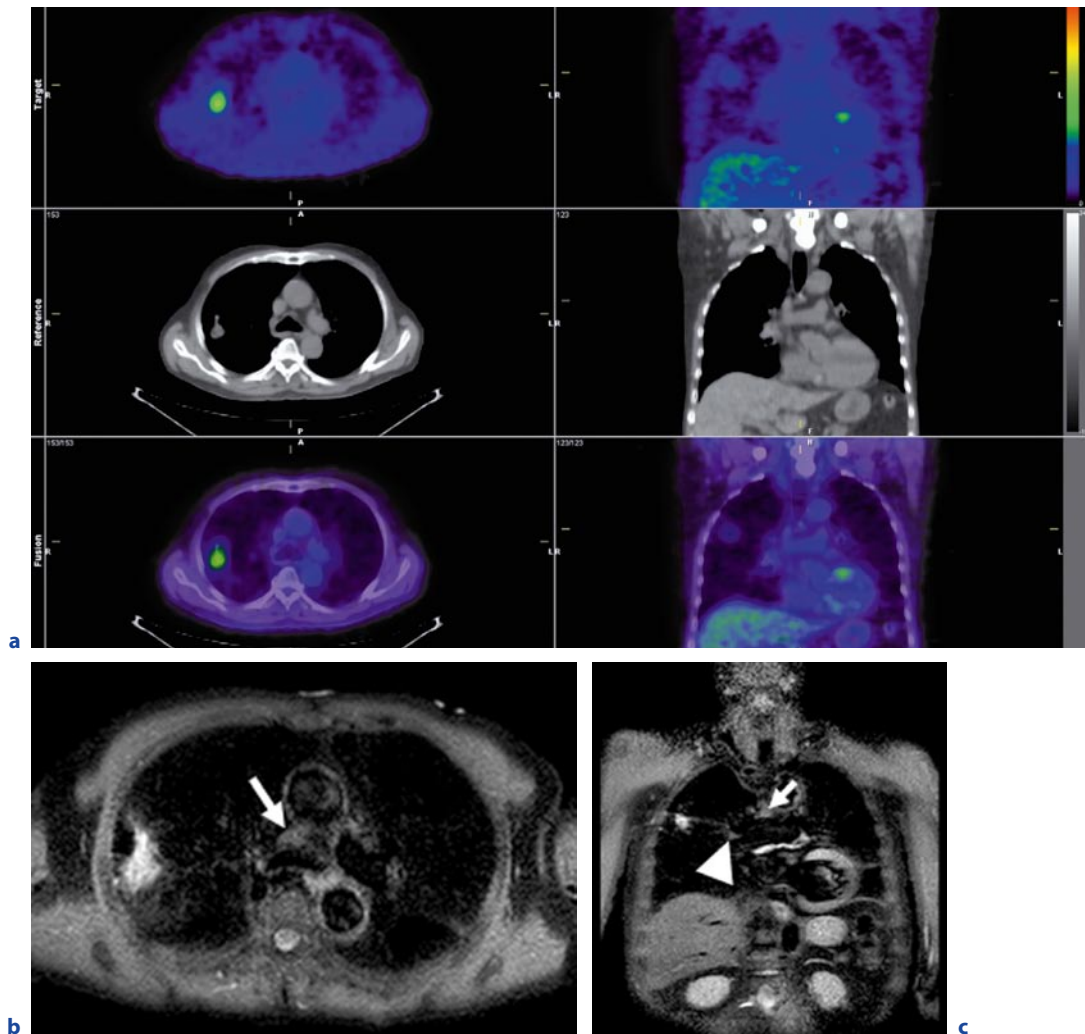


Fig. 11.15a–c. A 77-year-old male with adenocarcinoma (N0). Integrated FDG-PET/CT (**a**) demonstrates high uptake of FDG in primary tumor, but no uptake in mediastinal and hilar lymph nodes, suggesting N0. Black-blood STIR turbo SE imaging on axial (**b**) and coronal (**c**) planes show the primary tumor as high intensity, but mediastinal (*arrow*) and hilar (*arrow head*) lymph nodes as low signal intensity, suggesting N0

STIR turbo SE imaging ranged between 83.7% and 100.0%, between 75.0% and 93.1%, or between 86.0% and 92.2% on a per-patient basis (FUJIMOTO et al. 1995; TAKENAKA et al. 2002; OHNO et al. 2004d, 2007c). Direct and prospective comparisons with CT on a per-patient basis demonstrated that sensitivity and accuracy of quantitatively and qualitatively assessed STIR turbo SE imaging are significantly higher (OHNO et al. 2004d). In addition, direct and prospective comparisons with co-registered FDG-PET/CT showed that quantitative sensitivity and accuracy of STIR turbo SE imaging were

significantly higher (OHNO et al. 2007c). STIR turbo SE imaging thus should be considered as capable of enhancing the diagnostic capability of *N classification* not only due to its multiplanar capability but also its sensitive and accurate assessment of relaxation time differences between metastatic and non-metastatic lymph nodes. It should therefore be considered at least as valuable as FDG-PET/CT. In fact, MR imaging with STIR turbo SE imaging may be discussed as a substitute for FDG-PET or PET/CT.

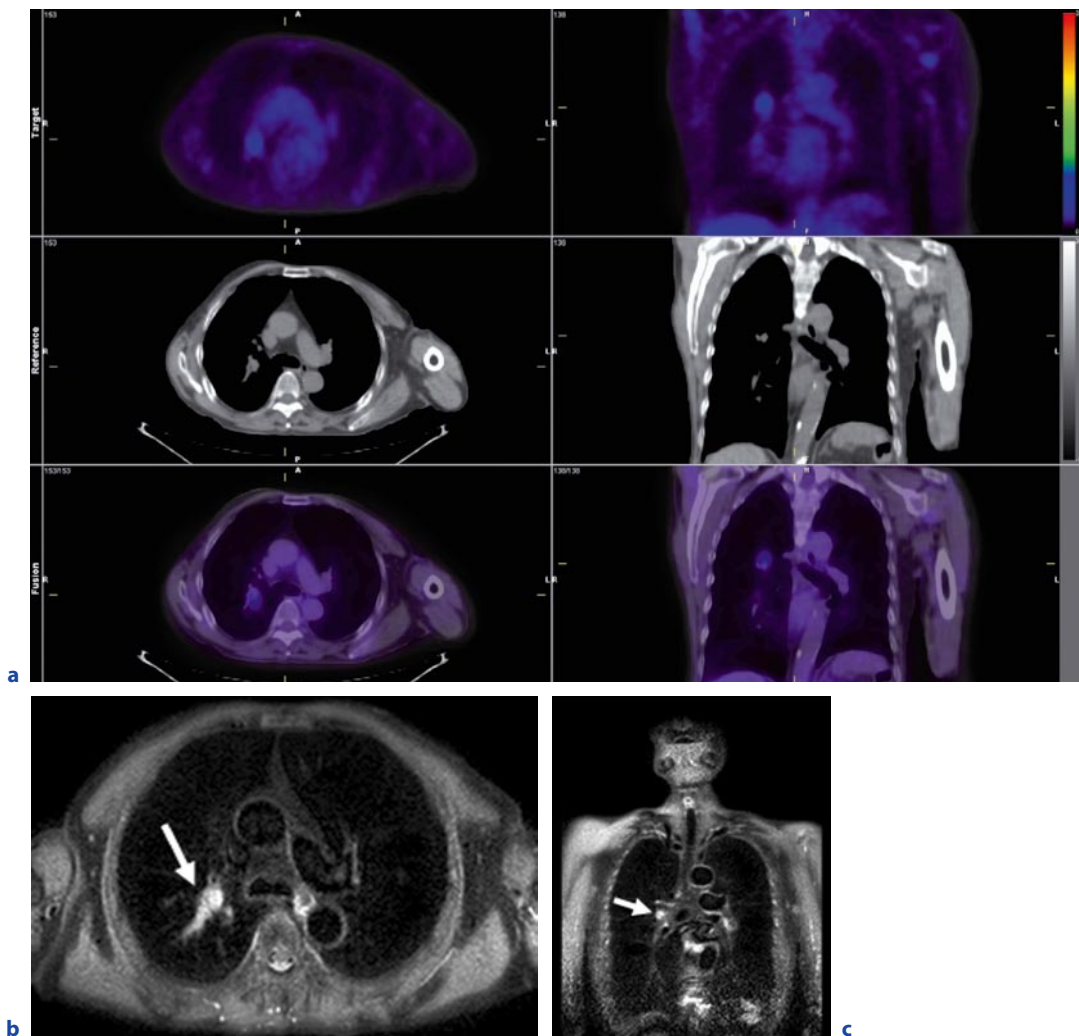


Fig. 11.16a–c. A 74-year-old male with adenocarcinoma (N1). Integrated FDG-PET/CT (**a**) demonstrates no uptake of FDG in the mediastinal and faint uptake in the hilar lymph nodes, suggesting N0, which was false-negative. Black-blood STIR turbo SE imaging on axial (**b**) and coronal (**c**) planes shows the hilar lymph node (*arrow*) as high signal intensity, suggesting N1 which was true-positive

11.4.3 MR Assessment of M Classification

The descriptor *M* relates to the presence of distant metastasis (M1) or its absence (M0) (SOBIN and WITTEKIND 2002). The definitions are given in Table 11.5. Lung cancer can metastasize widely and involve many organs, including the brain, bone, liver, and adrenal glands. The presence of metastasis beyond the intrathoracic lymph nodes is considered an indication of metastatic disease

(M1) and implies surgical non-resectability. Patients with distant metastases carry a very poor prognosis and are generally treated with chemotherapy, radiotherapy, or both or with optimal supportive care. In most cases, extrathoracic imaging is indicated for patients with lung cancer and symptoms localized to a specific organ. At present, however, there is no consensus regarding the efficacy of extrathoracic imaging for presumably resectable lung cancer without signs or symptoms localized to a specific organ (WONG et al. 1999).

The observation of metastases in patients with NSCLC has major implications for management and prognosis. Extrathoracic metastases are present in approximately 40% of patients with newly diagnosed lung cancer at presentation, most commonly in the adrenal glands, bones, liver, or brain (PANTEL et al. 1996; QUINT et al. 1996). After radical treatment for apparently localized disease, 20% of the patients developed an early distant relapse, probably due to systemic micrometastases that were present but not detected or visualized at the point of initial staging (PANTEL et al. 1996). SILVESTRI et al. (1995) updated a meta-analysis for the systemic evaluation of extrathoracic metastases in potentially resectable NSCLC patients. This study calculated that the negative predictive value was equal to or more than 90% for the clinical evaluation of patients asymptomatic for brain, abdominal, or bone metastases (SILVESTRI et al. 1995). These findings are consistent with the findings of a retrospective analysis of 755 patients with clinical stage T1-2 N0 disease, which found only five sites with silent metastasis after extensive imaging for extrathoracic disease (TANAKA et al. 1999). The current recommendation from the American College of Chest Physicians (ACCP) therefore suggests that further diagnostic testing is necessary to confirm the presence of disease only in patients with abnormal findings on clinical evaluation, although the positive predictive values among the studies included in their meta-analysis were highly variable (TOLOZA et al. 2003; SILVESTRI et al. 2007). For purposes of TNM classification, however, it would be necessary to perform in-depth surveillance of potential sites of extra-thoracic metastases for all lung cancer patients. In addition, accurate diagnosis of extra-thoracic metastases may be helpful for clinicians to provide the most appropriate treatment and/or management for lung cancer patients.

11.4.3.1 Adrenal Gland Metastasis

Enlarged adrenal glands can be visualized on CT at initial presentation in nearly 10% of NSCLC patients, and approximately two-third of these adrenal lesions are benign or asymptomatic (OLIVER et al. 1984; ETTINGHAUSEN and BURT 1991). Therefore, without pathologic proof of metastatic disease, the presence of an isolated adrenal mass in a patient with otherwise operable NSCLC should not preclude radical treatment. If the CT scan is performed without intravenous contrast media and an adrenal lesion is identified, measurement of the CT scan attenuation value can be helpful for distin-

guishing metastasis from adenoma (BOLAND et al. 1998; SZOLAR and KAMMERHUBER 1998). PET can also be a useful adjunct in this setting because the sensitivity and specificity of PET have been reported as ranging from 80% to 100% in the past literatures. This high sensitivity and specificity may result in a reduction of the number of unnecessary biopsies, which are not without risk and not always diagnostic (ERASMUS et al. 1997; MAROM et al. 1999). However, careful interpretation of PET is required for small lesions less than 10 mm in diameter, since experience with these is still limited (SCHREVEVS et al. 2004). In addition, false-positive findings on PET have also been reported, and the incidence of false-positive findings is increasing. Currently, MR imaging is also considered helpful for distinguishing metastasis from adenoma when an adrenal lesion is detected by CT. Visual assessment of adrenal lesions using chemical shift MR imaging may characterize a lesion as an adenoma on the basis of reduced signal intensity of the lesion on opposed-phase images as compared with that on in-phase images (KOROBKIN et al. 1995; SCHWARTZ et al. 1998; HUSSAIN and KOROBKIN 2004). KOROBKIN et al. (1995) applied this technique to 51 adrenal lesions and reported a sensitivity of 100% and specificity of 81% for the characterization of adenomas.

11.4.3.2 Bone Metastasis

Bone involvement is usually assessed by ^{99m}Tc -methylene diphosphate (^{99m}Tc -MDP) or hydroxymethylene diphosphate (^{99m}Tc -HMDP) bone scintigraphy. Although sensitivity of bone scintigraphy has been reported as high as 90%, its specificity was only about 60% due to false-positive findings caused by the non-selective uptake of the radionuclide tracer in any area of increased bone turnover (SCHREVEVS et al. 2004). Consequently, additional imaging by X-ray, bone CT, and/or MR imaging is often required. PET is reported to have similar sensitivity, but higher specificity and accuracy (equal to or more than 90%, equal to or more than 98% and equal to or more than 96%, respectively) (BURY et al. 1998; MAROM et al. 1999). PET is therefore considered superior to bone scintigraphy for the detection of bone metastases. Currently, MR imaging with the use of various sequences such as T1-weighted SE or turbo SE imaging, T2-weighted turbo SE imaging, STIR turbo SE imaging, contrast-enhanced T1-weighted SE or turbo SE imaging, or diffusion-weighted MR imaging is deemed useful for assessment of muscle-skeletal tumors and metastasis from various malignancies

(WEINBERGER et al. 1995; VANEL et al. 1998; MENTZEL et al. 2004; PARK et al. 2004; TOKUDA et al. 2004; GOO et al. 2005). However, only one study has directly compared the diagnostic capability of MR imaging and bone scintigraphy and found that sensitivity, specificity and accuracy of MR imaging were 80%, 96% and 93%, respectively, being superior to bone scintigraphy (40%, 92%, and 83%), although the difference was not significant (EARNEST et al. 1999).

11.4.3.3 Brain Metastasis

Some investigators have reported that brain MR imaging is useful for evaluation of asymptomatic brain metastases in patients with operable lung cancer (HILLERS et al. 1994; EARNEST et al. 1999; YOKOI et al. 1999). FDG-PET is not suitable for the detection of brain metastases since the sensitivity of PET is low due to the high glucose uptake of normal surrounding brain tissue. CT and/or MR imaging remain the method of choice for screening brain metastases. YOKOI et al. (1999) compared the efficacy of MR imaging and CT scans of brain in 332 patients with potentially operable asymptomatic NSCLC. Within 12 months of diagnosis, brain metastases were detected in 7% of the patients in this series. Preoperatively, brain metastases were detected in 3.4% of the patients by MR imaging and in 0.6% of the patients by CT scans. Other investigators have reported on the utility of contrast-enhanced brain MR imaging and found a high prevalence of asymptomatic brain metastasis in 28% of patients identified with contrast-enhanced brain MR imaging (EARNEST et al. 1999). These findings suggest that preoperative brain MR imaging may be effective for patients with lung cancer.

11.4.3.4 Whole-body MR Imaging for Assessment of M Classification in Lung Cancer Patients

Findings of a recent randomized trial suggest that the addition of whole-body FDG-PET scanning to a conventional workup can identify more patients with extra-thoracic metastases among those with suspected NSCLC (VAN TINTEREN et al. 2002). However, recent advances in MR techniques such as fast imaging and moving table techniques make it possible to perform total body MR imaging. Its usefulness has been investigated in the staging of breast cancer and the

search for primary lesions in patients with metastatic carcinoma from an unknown primary lesion (EUSTACE et al. 1998; WALKER et al. 2000; ANTOCH et al. 2003; LAUENSTEIN et al. 2004; TAKAHARA et al. 2004; GOEHDE et al. 2005; SCHMIDT et al. 2006). It was concluded that total body MR imaging may constitute a single, cost-effective imaging test for patients with metastatic carcinoma from an unknown primary (EUSTACE et al. 1998; WALKER et al. 2000; ANTOCH et al. 2003; LAUENSTEIN et al. 2004; TAKAHARA et al. 2004; GOEHDE et al. 2005; SCHMIDT et al. 2006). However, the potential of total body MR imaging for lung cancer staging has not yet been satisfactorily delineated. OHNO et al. (2007d) performed a direct comparison of the diagnostic capability of whole-body MR imaging and FDG-PET for the *M classification* (Fig. 11.17 and 11.18). They reported that the interobserver agreement for whole-body MR imaging was substantially, but not significantly better than for whole-body FDG-PET on a per-site basis and a per-patient basis (OHNO et al. 2007d). For assessment of head and neck metastases, sensitivity (84.6%) and accuracy (95.0%) of whole-body MR imaging were significantly higher than those of FDG-PET (15.4% and 89.1%, respectively) on a per-site basis (OHNO et al. 2007d). In addition, the specificity (96.1%) and accuracy (94.8%) of whole-body MR imaging for bone metastasis were significantly higher than those of FDG-PET (88.3% and 88.2%, respectively) on a per-site basis (OHNO et al. 2007d). However, when brain metastases were excluded from head and neck metastases, sensitivity, specificity and accuracy of whole-body MR imaging were not significantly different from those of FDG-PET, nor were they for diagnosis of thoracic, abdominal and pelvic metastases (OHNO et al. 2007d). In addition, when evaluation on a per-patient basis of *M classification* included brain metastases as head and neck metastases, accuracy (80.0%) of whole-body MR imaging was significantly better than that of FDG-PET (73.3%), while exclusion of brain metastases from head and neck metastases, resulted in no significant differences in sensitivity, specificity and accuracy between whole-body MR imaging and FDG-PET (OHNO et al. 2007d). Whole-body MR imaging is therefore an accurate diagnostic technique, and should be considered at least as effective as FDG-PET for *M classification* of lung cancer patients (Figs. 11.17 and 11.18). However, further investigations will be needed to determine the actual significance of whole-body MR imaging as a potential substitute for FDG-PET or PET/CT.

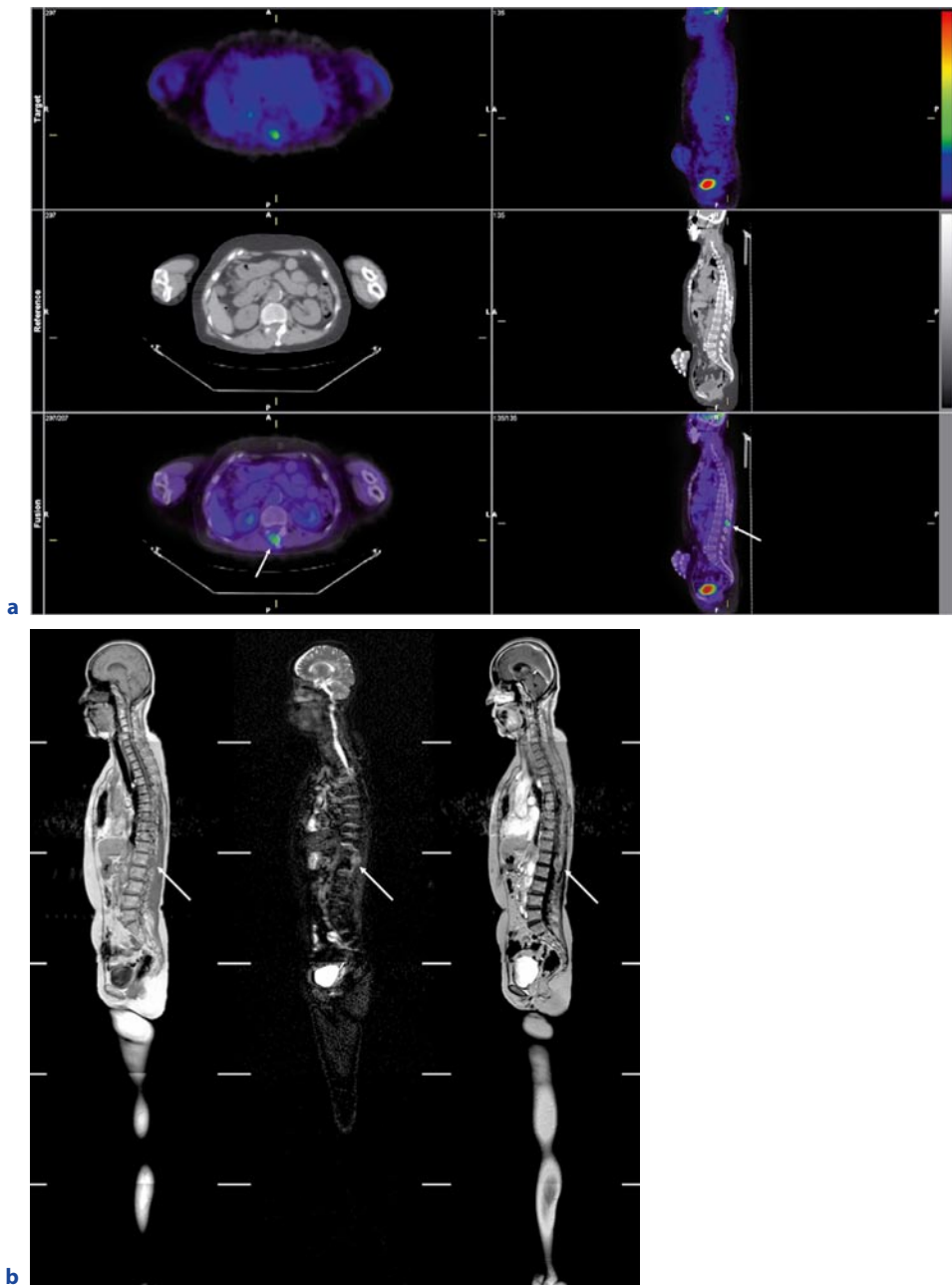


Fig. 11.17a,b. A 68-year-old female with adenocarcinoma and lumbar vertebra (L1) metastasis. Integrated FDG-PET/CT (**a**) shows high uptake of FDG at the vertebral arch (*arrow*), suggesting bone metastasis, which was true-positive. On sagittal whole-body MR images (**b**): L to R, non-contrast enhanced T1-weighted GRE image; STIR turbo SE image; and contrast enhanced T1-weighted GRE image, bone metastasis (*arrow*) is obvious, which was true-positive

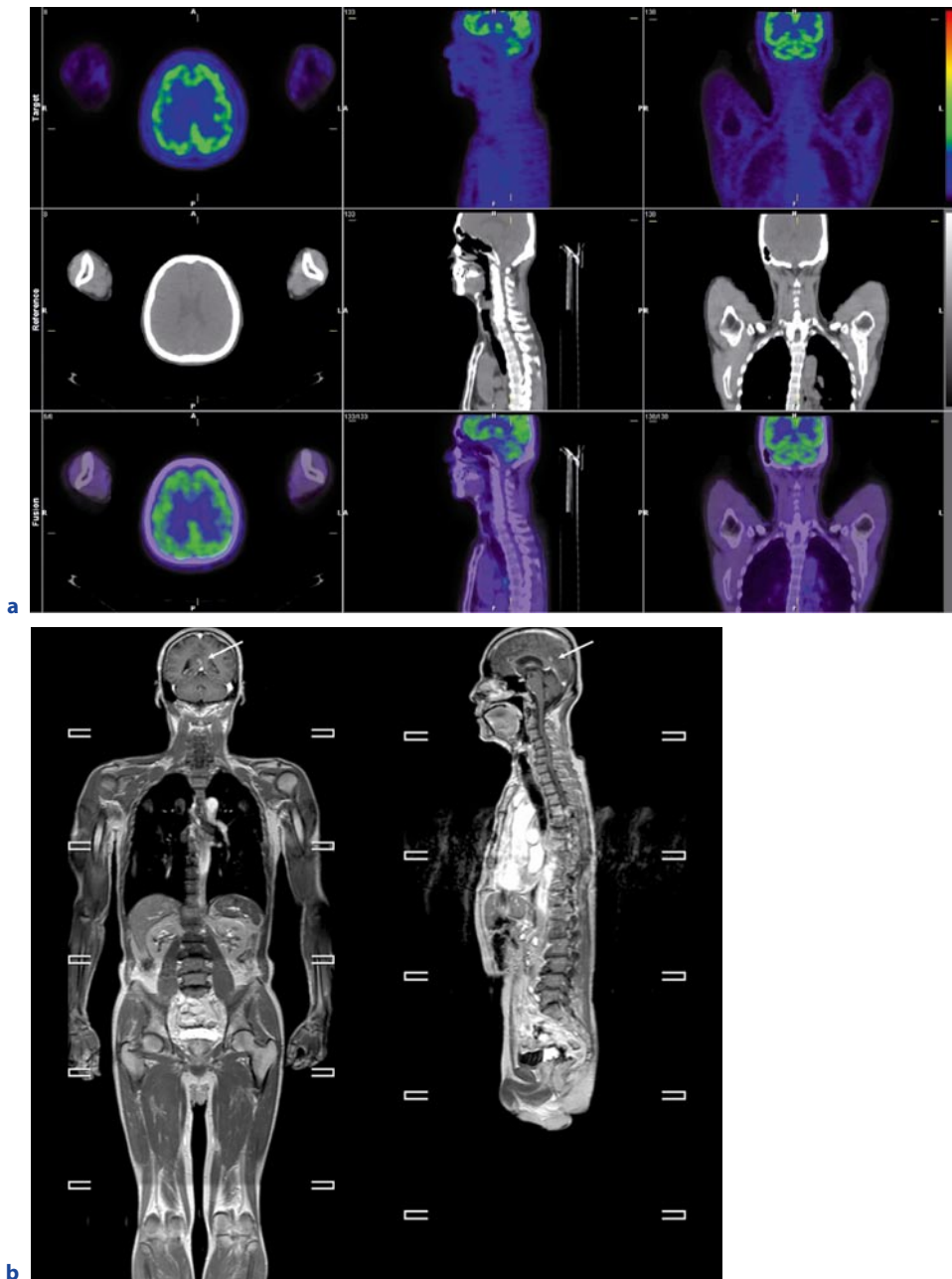


Fig. 11.18a,b. A 67-year-old male with adenocarcinoma and brain metastasis. Integrated FDG-PET/CT (**a**) does not show any abnormal uptake, and suggesting M0, which was false-negative. Contrast enhanced whole-body T1-weighted GRE (**b**): L to R, coronal and sagittal planes clearly shows brain metastasis, suggesting M1, which was true-positive

References

- Amundsen T, Kvaerness J, Jones RA, Waage A, Bjermer L, Nilsen G, Haraldseth O (1997) Pulmonary embolism: detection with MR perfusion imaging of lung—a feasibility study. *Radiology* 203:181–185
- Amundsen T, Torheim G, Waage A, Bjermer L, Steen PA, Haraldseth O (2000) Perfusion magnetic resonance imaging of the lung: characterization of pneumonia and chronic obstructive pulmonary disease. A feasibility study. *J Magn Reson Imaging* 12:224–231
- Antoch G, Vogt FM, Freudenberg LS, Nazaradeh F, Goehde SC, Barkhausen J, Dahmen G, Bockisch A, Debatin JF, Ruehm SG (2003) Whole-body dual-modality PET/CT and whole-body MRI for tumor staging in oncology. *JAMA* 290:3199–3206
- Aquino SL, Kee ST, Warnock ML, Gamsu G (1994) Pulmonary aspergillosis: imaging findings with pathologic correlation. *AJR Am J Roentgenol* 163:811–815
- Armstrong P (2000) Neoplasms of the lung, airways and pleura. In: Armstrong P, Wilson AG, Dee P, Hansell DM (eds) *Imaging of diseases of the chest*, 3rd edn. Mosby, London, pp 305–401
- Bach PB, Silvestri GA, Hanger M, Jett JR (2007) Screening for lung cancer: ACCP evidence-based clinical practice guidelines (2nd edition). American College of Chest Physicians. *Chest* 132:–69S–77S
- Bailey PV, Tracy T Jr, Connors RH, deMello D, Lewis JE, Weber TR (1990) Congenital bronchopulmonary malformations. Diagnostic and therapeutic considerations. *J Thorac Cardiovasc Surg* 99:597–602
- Baron RL, Levitt RG, Sagel SS, White MJ, Roper CL, Margbarger JP (1982) Computed tomography in the preoperative evaluation of bronchogenic carcinoma. *Radiology* 145:727–732
- Bateson EM (1973) So-called hamartoma of the lung – a true neoplasm of fibrous connective tissue of the bronchi. *Cancer* 31:1458–1467
- Blum U, Windfuhr M, Buitrago-Tellez C, Sigmund G, Herbst EW, Langer M (1994) Invasive pulmonary aspergillosis. MRI, CT, and plain radiographic findings and their contribution for early diagnosis *Chest* 106:1156–1161
- Boiselle PM, Patz EF Jr, Vining DJ, Weissleder R, Shepard JA, McLoud TC (1998) Imaging of mediastinal lymph nodes: CT, MR, and FDG PET. *Radiographics* 18:1061–1069
- Boland GW, Lee MJ, Gazelle GS, Halpern EF, McNicholas MM, Mueller PR (1998) Characterization of adrenal masses using unenhanced CT: an analysis of the CT literature. *AJR Am J Roentgenol* 171:201–204
- Bonomo L, Ciccotosto C, Guidotti A, Storto ML (1996) Lung cancer staging: the role of computed tomography and magnetic resonance imaging. *Eur J Radiol* 23:35–45
- Bourgoin PM, McLoud TC, Fitzgibbon JF, Mark EJ, Shepard JA, Moore EM, Rummeny E, Brady TJ (1991) Differentiation of bronchogenic carcinoma from postobstructive pneumonitis by magnetic resonance imaging: histopathologic correlation. *J Thorac Imaging* 6:22–27
- Bruegel M, Gaa J, Woertler K, Ganter C, Waldt S, Hillerer C, Rummeny EJ (2007) MRI of the lung: value of different turbo spin-echo, single-shot turbo spin-echo, and 3D gradient-echo pulse sequences for the detection of pulmonary metastases. *J Magn Reson Imaging* 25:73–81
- Bryant AS, Cerfolio RJ (2006) The maximum standardized uptake values on integrated FDG-PET/CT is useful in differentiating benign from malignant pulmonary nodules. *Ann Thorac Surg* 82:1016–1020
- Bury T, Dowlati A, Paulus P, Corhay JL, Benoit T, Kayembe JM, Limet R, Rigo P, Radermecker M (1996) Evaluation of the solitary pulmonary nodule by positron emission tomography imaging. *Eur Respir J* 9:410–414
- Bury T, Barreto A, Daenen F, Barthelemy N, Ghaye B, Rigo P (1998) Fluorine-18 deoxyglucose positron emission tomography for the detection of bone metastases in patients with non-small cell lung cancer. *Eur J Nucl Med* 25:1244–1247
- Caskey CI, Templeton PA, Zerhouni EA (1990) Current evaluation of the solitary pulmonary nodule. *Radiol Clin North Am* 28:511–520
- Chang JM, Lee HJ, Goo JM, Lee HY, Lee JJ, Chung JK, Im JG (2006) False positive and false negative FDG-PET scans in various thoracic diseases. *Korean J Radiol* 7:57–69
- Christensen JA, Nathan MA, Mullan BP, Hartman TE, Swensen SJ, Lowe VJ (2006) Characterization of the solitary pulmonary nodule: 18F-FDG PET versus nodule-enhancement CT. *AJR Am J Roentgenol* 187:1361–1367
- Chung MH, Lee HG, Kwon SS, Park SH (2000) MR imaging of solitary pulmonary lesion: emphasis on tuberculomas and comparison with tumors. *J Magn Reson Imaging* 11:629–637
- Costello P (1994) Spiral CT of the thorax. *Semin Ultrasound CT MR* 15:90–106
- Davis SD (1991) CT evaluation for pulmonary metastases in patients with extrathoracic malignancy. *Radiology* 180:1–12
- Dewan NA, Gupta NC, Redepenning LS, Phalen JJ, Frick MP (1993) Diagnostic efficiency of PET-FDG imaging in solitary pulmonary nodules. *Chest* 104:997–1002
- Dillemans B, Deneffe G, Verschakelen J, Decramer M (1994) Value of computed tomography and mediastinoscopy in preoperative evaluation of mediastinal nodes in non-small cell lung cancer. A study of 569 patients. *Eur J Cardiothorac Surg* 8:37–42
- Donmez FY, Yekeler E, Saeidi V, Tunaci A, Tunaci M, Acunas G (2007) Dynamic contrast enhancement patterns of solitary pulmonary nodules on 3D gradient-recalled echo MRI. *AJR Am J Roentgenol* 189:1380–1386
- Earnest F IV, Ryu JH, Miller GM, Luetmer PH, Forstrom LA, Burnett OL, Rowland CM, Swensen SJ, Midthun DE (1999) Suspected non-small cell lung cancer: incidence of occult brain and skeletal metastases and effectiveness of imaging for detection – pilot study. *Radiology* 211:137–145

- Erasmus JJ, Patz EF Jr, McAdams HP, Murray JG, Herndon J, Coleman RE, Goodman PC (1997) Evaluation of adrenal masses in patients with bronchogenic carcinoma using 18F-fluorodeoxyglucose positron emission tomography. *AJR Am J Roentgenol* 168:1357–1360
- Ettinghausen SE, Burt ME (1991) Prospective evaluation of unilateral adrenal masses in patients with operable non-small-cell lung cancer. *J Clin Oncol* 9:1462–1466
- Eustace S, Tello R, DeCarvalho V, Carey J, Melhem E, Yucel EK (1998) Whole body turbo STIR MRI in unknown primary tumor detection. *J Magn Reson Imaging* 8:751–753
- Felson B, Wiot JF (1977) Some less familiar roentgen manifestations of carcinoma of the lung. *Semin Roentgenol* 2:187–206
- Feuerstein IM, Jicha DL, Pass HI, Chow CK, Chang R, Ling A, Hill SC, Dwyer AJ, Travis WD, Horowitz ME, Steinberg SM, Frank JA, Doppman JL (1992) Pulmonary metastases: MR imaging with surgical correlation – a prospective study. *Radiology* 182:123–129
- Finck S, Milne EN (1988) A case report of segmental bronchial atresia: radiologic evaluation including computed tomography and magnetic resonance imaging. *J Thorac Imaging* 3:53–57
- Fink C, Puderbach M, Bock M, Lodemann KP, Zuna I, Schmähl A, Delorme S, Kauczor HU (2004) Regional lung perfusion: assessment with partially parallel three-dimensional MR imaging. *Radiology* 231:175–184
- Freundlich IM, Chasen MH, Varma DG (1996) Magnetic resonance imaging of pulmonary apical tumors. *J Thorac Imaging* 11:210–222
- Fujimoto K, Meno S, Nishimura H, Hayabuchi N, Hayashi A (1994) Aspergilloma within cavitary lung cancer: MR imaging findings. *AJR Am J Roentgenol* 163:565–567
- Fujimoto K, Edamitsu O, Meno S, Abe T, Honda N, Ogoh Y, Ohzono H, Nakaoda K, Kojima K, Nishimura H (1995) MR diagnosis for metastasis or non-metastasis of mediastinal and hilar lymph nodes in cases of primary lung cancer: detectability, signal intensity, and MR-pathologic correlation. *Nippon Acta Radiol* 55:162–171
- Fujimoto K, Abe T, Müller NL, Terasaki H, Kato S, Sadohara J, Kono R, Edamitsu O, Ishitake T, Hayashi A, Rikimaru T, Hayabuchi N (2003) Small peripheral pulmonary carcinomas evaluated with dynamic MR imaging: correlation with tumor vascularity and prognosis. *Radiology* 227:786–793
- Gaeta M, Blandino A, Scribano E, Vinci S, Minutoli F, Pergolizzi S, Pandolfo I (2000) Magnetic resonance imaging of bronchioloalveolar carcinoma. *J Thorac Imaging* 15:41–47
- Gaeta M, Minutoli F, Ascenti G, Vinci S, Mazziotti S, Pandolfo I, Blandino A (2001) MR white lung sign: incidence and significance in pulmonary consolidations. *J Comput Assist Tomogr* 25:890–896
- Gaeta M, Vinci S, Minutoli F, Mazziotti S, Ascenti G, Salamone I, Lamberto S, Blandino A (2002) CT and MRI findings of mucin-containing tumors and pseudotumors of the thorax: pictorial review. *Eur Radiol* 12:181–189
- Gdeedo A, Van Schil P, Corthouts B, Van Mieghem F, Van Meerbeeck J, Van Marck E (1997) Comparison of imaging TNM [(i)TNM] and pathological TNM [pTNM] in staging of bronchogenic carcinoma. *Eur J Cardiothorac Surg* 12:224–227
- Geffer WB (1992) The spectrum of pulmonary aspergillosis. *J Thorac Imaging* 7:56–74
- Glazer GM, Orringer MB, Gross BH, Quint LE (1984) The mediastinum in non-small cell lung cancer: CT-surgical correlation. *AJR Am J Roentgenol* 142:1101–1105
- Glazer GM, Gross BH, Aisen AM, Quint LE, Francis IR, Orringer MB (1985) Imaging of the pulmonary hilum: a prospective comparative study in patients with lung cancer. *AJR Am J Roentgenol* 145:245–248
- Glazer HS, Kaiser LR, Anderson DJ, Molina PL, Emami B, Roper CL, Sagel SS (1989) Indeterminate mediastinal invasion in bronchogenic carcinoma: CT evaluation. *Radiology* 173:37–42
- Goehde SC, Hunold P, Vogt FM, Ajaj W, Goyen M, Herborn CU, Forsting M, Debatin JF, Ruehm SG (2005) Full-body cardiovascular and tumor MRI for early detection of disease: feasibility and initial experience in 298 subjects. *AJR Am J Roentgenol* 184:598–611
- Goo HW, Choi SH, Ghim T, Moon HN, Seo JJ (2005) Whole-body MRI of paediatric malignant tumours: comparison with conventional oncological imaging methods. *Pediatr Radiol* 35:766–773
- Gould MK, Kuschner WG, Rydzak CE, Maclean CC, Demas AN, Shigemitsu H, Chan JK, Owens DK (2003) Test performance of positron emission tomography and computed tomography for mediastinal staging in patients with non-small-cell lung cancer: a meta-analysis. *Ann Intern Med* 139:879–892
- Gükel C, Schnabel K, Deimling M, Steinbrich W (1996) Solitary pulmonary nodules: MR evaluation of enhancement patterns with contrast – enhanced dynamic snapshot gradient – echo imaging. *Radiology* 200:681–686
- Gupta NC, Graeber GM, Bishop HA (2000) Comparative efficacy of positron emission tomography with fluorodeoxyglucose in evaluation of small (<1 cm), intermediate (1 to 3 cm), and large (>3 cm) lymph node lesions. *Chest* 117:773–778
- Hatabu H, Gaa J, Kim D, Li W, Prasad PV, Edelman RR (1996) Pulmonary perfusion: qualitative assessment with dynamic contrast-enhanced MRI using ultra-short TE and inversion recovery turbo FLASH. *Magn Reson Med* 36:503–508
- Hatabu H, Tadamura E, Levin DL, Chen Q, Li W, Kim D, Prasad PV, Edelman RR (1999) Quantitative assessment of pulmonary perfusion with dynamic contrast-enhanced MRI. *Magn Reson Med* 42:1033–1038
- Heelan RT, Demas BE, Caravelli JF, Martini N, Bains MS, McCormack PM, Burt M, Panicek DM, Mitzner A (1989) Superior sulcus tumors: CT and MR imaging. *Radiology* 170:637–641

- Henschke CI, McCauley DI, Yankelevitz DF, Naidich DP, McGuinness G, Miettinen OS, Libby D, Pasmantier M, Koizumi J, Altorki N, Smith JP (2001) Early lung cancer action project: a summary of the findings on baseline screening. *Oncologist* 6:147–152
- Herder GJ, Golding RP, Hoekstra OS, Comans EF, Teule GJ, Postmus PE, Smit EF (2004) The performance of (18) F-fluorodeoxyglucose positron emission tomography in small solitary pulmonary nodules. *Eur J Nucl Med Mol Imaging* 31:1231–1236
- Herman SJ, Winton TL, Weisbrod GL, Towers MJ, Mentzer SJ (1994) Mediastinal invasion by bronchogenic carcinoma: CT signs. *Radiology* 190:841–846
- Herold CJ, Kramer J, Sertl K, Kalhs P, Mallek R, Imhof H, Tscholakoff D (1989) Invasive pulmonary aspergillosis: evaluation with MR imaging. *Radiology* 173:717–721
- Higashi K, Nishikawa T, Seki H, Oguchi M, Nambu Y, Ueda Y, Yuasa K, Tonami H, Okimura T, Yamamoto I (1998) Comparison of fluorine-18-FDG PET and thallium-201 SPECT in evaluation of lung cancer. *J Nucl Med* 39:9–15
- Higashino T, Ohno Y, Takenaka D, Watanabe H, Nogami M, Ohbayashi C, Yoshimura M, Satouchi M, Nishimura Y, Fujii M, Sugimura K (2005) Thin-section multiplanar reformats from multidetector-row CT data: utility for assessment of regional tumor extent in non-small cell lung cancer. *Eur J Radiol* 56:48–55
- Hillers TK, Sauve MD, Guyatt GH (1994) Analysis of published studies on the detection of extrathoracic metastases in patients presumed to have operable non-small cell lung cancer. *Thorax* 49:14–19
- Hittmair K, Eckersberger F, Klepetko W, Helbich T, Herold CJ (1995) Evaluation of solitary pulmonary nodules with dynamic contrast-enhanced MR imaging – a promising technique. *Magn Reson Imaging* 13:923–933
- Hussain HK, Korobkin M (2004) MR imaging of the adrenal glands. *Magn Reson Imaging Clin N Am* 12:515–544
- Jederlinic PJ, Sicilian LS, Baigelman W, Gaensler EA (1987) Congenital bronchial atresia. A report of 4 cases and a review of the literature. *Medicine* 66:73–83
- Jeong YJ, Lee KS, Jeong SY, Chung MJ, Shim SS, Kim H, Kwon OJ, Kim S (2005) Solitary pulmonary nodule: characterization with combined wash-in and washout features at dynamic multi-detector row CT. *Radiology* 237:675–683
- Joshi U, Raijmakers PG, van Lingen A, Comans EF, Pijpers R, Teule GJ, Hoekstra OS (2005) Evaluation of pulmonary nodules: comparison of a prototype dual crystal (LSO/NAI) dual head coincidence camera and full ring positron emission tomography (PET). *Eur J Radiol* 55:250–254
- Kawai Y, Sumi M, Nakamura T (2006) Turbo short tau inversion recovery imaging for metastatic node screening in patients with head and neck cancer. *AJNR Am J Neuroradiol* 27:1283–1287
- Kersjes W, Mayer E, Buchenroth M, Schunk K, Fouda N, Cagil H (1997) Diagnosis of pulmonary metastases with turbo-SE MR imaging. *Eur Radiol* 7:1190–1194
- Kim SK, Allen-Auerbach M, Goldin J, Fueger BJ, Dahlbom M, Brown M, Czernin J, Schiepers C (2007) Accuracy of PET/CT in characterization of solitary pulmonary lesions. *J Nucl Med* 48:214–220
- Ko SF, Lee TY, Kao CL, Ng SH, Wan YL, Lin JW, Chen WJ (1998) Bronchial atresia associated with epibronchial right pulmonary artery and aberrant right middle lobe artery. *Br J Radiol* 71:217–220
- Kono M, Adachi S, Kusumoto M, Sakai E (1993) Clinical utility of Gd – DTPA - enhanced magnetic resonance imaging in lung cancer. *J Thorac Imaging* 8:18–26
- Kono R, Fujimoto K, Terasaki H, Müller NL, Kato S, Sadohara J, Hayabuchi N, Takamori S (2007) Dynamic MRI of solitary pulmonary nodules: comparison of enhancement patterns of malignant and benign small peripheral lung lesions. *AJR Am J Roentgenol* 188:26–36
- Korobkin M, Lombardi TJ, Aisen AM, Francis IR, Quint LE, Dunnick NR, Londy F, Shapiro B, Gross MD, Thompson NW (1995) Characterization of adrenal masses with chemical shift and gadolinium-enhanced MR imaging. *Radiology* 197:411–418
- Kusumoto M, Kono M, Adachi S, Yamasaki K, Itouji E, Sakai E, Endo M, Nakamura T, Kimura K (1994) Gadopentetate dimeglumine – enhanced magnetic resonance imaging for lung nodules: differentiation of lung cancer and tuberculoma. *Invest Radiol* 29:S255–S256
- Lauenstein TC, Goehde SC, Herborn CU, Goyen M, Oberhoff C, Debatin JF, Ruehm SG, Barkhausen J (2004) Whole-body MR imaging: evaluation of patients for metastases. *Radiology* 233:139–148
- Laurent F, Drouillard J, Dorcier F, Velly JF, Barat JL, Grelet P, Martigne C, Tavernier J, Couraud L (1988) Bronchogenic carcinoma staging: CT versus MR imaging. Assessment with surgery. *Eur J Cardiothorac Surg* 2:31–36
- Lee KS, Yi CA, Jeong SY, Jeong YJ, Kim S, Chung MJ, Kim HY, Kim YK, Lee KH (2007) Solid or partly solid solitary pulmonary nodules: their characterization using contrast wash-in and morphologic features at helical CT. *Chest* 131:1516–1525
- Levin DL, Chen Q, Zhang M, Edelman RR, Hatabu H (2001) Evaluation of regional pulmonary perfusion using ultrafast magnetic resonance imaging. *Magn Reson Med* 46:166–171
- Lewis JW Jr, Pearlberg JL, Beute GH, Alpern M, Kvale PA, Gross BH, Magilligan DJ Jr (1990) Can computed tomography of the chest stage lung cancer? Yes and no. *Ann Thorac Surg* 49:591–595
- Li G, Citrin D, Camphausen K et al. (2008) Advances in 4D medical imaging and 4D radiation therapy. *Technol Cancer Res Treat* 7:67–81
- Luboldt W, Wetter A, Eichler K, Vogl TJ, Wagner TO, Seemann MD (2006) Determination of the optimal MRI sequence for the detection of malignant lung nodules. *Eur J Med Res* 11:336–342
- Ma H, Kubicek CP, Röhr M (1985) Metabolic effects of manganese deficiency in *Aspergillus niger*: evidence for increased protein degradation. *Arch Microbiol* 141:266–268

- Magdeleinat P, Alifano M, Benbrahem C, Spaggiari L, Porrello C, Puyo P, Levasseur P, Regnard JF (2001) Surgical treatment of lung cancer invading the chest wall: results and prognostic factors. *Ann Thorac Surg* 71:1094–1099
- Marom EM, McAdams HP, Erasmus JJ, Goodman PC, Culhane DK, Coleman RE, Herndon JE, Patz EF Jr (1999) Staging non-small cell lung cancer with whole-body PET. *Radiology* 212:803–809
- Martini N, Heelan R, Westcott J, Bains MS, McCormack P, Caravelli J, Watson R, Zaman M (1985) Comparative merits of conventional, computed tomographic, and magnetic resonance imaging in assessing mediastinal involvement in surgically confirmed lung carcinoma. *J Thorac Cardiovasc Surg* 90:639–648
- Martini N, Kris MG, Ginsberg RJ (1997) The role of multimodality therapy in locoregional non-small cell lung cancer. *Surg Oncol Clin N Am* 6:769–791
- Matsuoka S, Uchiyama K, Shima H, Terakoshi H, Nojiri Y, Oishi S, Ogata H (2001) Detectability of pulmonary perfusion defect and influence of breath holding on contrast-enhanced thick-slice 2D and on 3D MR pulmonary perfusion images. *J Magn Reson Imaging* 14:580–585
- Matsushima H, Takayanagi N, Satoh M, Kurashima K, Kanauchi T, Hoshi T, Kanazawa M (2002) Congenital bronchial atresia: radiologic findings in nine patients. *J Comput Assist Tomogr* 26:860–864
- Mayr B, Heywang SH, Ingrisich H, Huber RM, Haussinger K, Lissner J (1987) Comparison of CT with MR imaging of endobronchial tumors. *J Comput Assist Tomogr* 11:43–48
- McLoud TC, Swenson SJ (1999) Lung carcinoma. *Clin Chest Med* 20:97–713, vii
- McLoud TC, Bourgooin PM, Greenberg RW, Kosiuk JP, Templeton PA, Shepard JA, Moore EH, Wain JC, Mathisen DJ, Grillo HC (1992) Bronchogenic carcinoma: analysis of staging in the mediastinum with CT by correlative lymph node mapping and sampling. *Radiology* 182:319–323
- Meng RL, Jensik RJ, Faber LP, Matthew GR, Kittle CF (1978) Bronchial atresia. *Ann Thorac Surg* 25:184–192
- Mentzel HJ, Kentouche K, Sauner D, Fleischmann C, Vogt S, Gottschild D, Zintl F, Kaiser WA (2004) Comparison of whole-body STIR-MRI and ^{99m}Tc-methylene-diphosphonate scintigraphy in children with suspected multifocal bone lesions. *Eur Radiol* 14:2297–2302
- Mori K, Niki N, Kondo T, Kamiyama Y, Kodama T, Kawada Y, Moriyama N (2005) Development of a novel computer-aided diagnosis system for automatic discrimination of malignant from benign solitary pulmonary nodules on thin-section dynamic computed tomography. *J Comput Assist Tomogr* 29:215–222
- Murata K, Takahashi M, Mori M, Shimoyama K, Mishina A, Fujino S, Itoh H, Morita R (1994) Chest wall and mediastinal invasion by lung cancer: evaluation with multisection expiratory dynamic CT. *Radiology* 191:251–255
- Musset D, Grenier P, Carette MF, Frija G, Hauuy MP, Desbleds MT, Girard P, Bigot JM, Lallemand D (1986) Primary lung cancer staging: prospective comparative study of MR imaging with CT. *Radiology* 160:607–611
- Naidich DP, Rumancik WM, Ettenger NA, Feiner HD, Harnanz-Schulman M, Spatz EM, Toder ST, Genieser NB (1988) Congenital anomalies of the lungs in adults: MR diagnosis. *AJR Am J Roentgenol* 151:13–19
- Ohno Y, Adachi S, Kono M, Kusumoto M, Motoyama A, Sugimura K (2000) Predicting the prognosis of non-small cell lung cancer patient treated with conservative therapy using contrast-enhanced MR imaging. *Eur Radiol* 10:1770–1781
- Ohno Y, Adachi S, Motoyama A, Kusumoto M, Hatabu H, Sugimura K, Kono M (2001) Multiphase ECG-triggered 3D contrast-enhanced MR angiography: utility for evaluation of hilar and mediastinal invasion of bronchogenic carcinoma. *J Magn Reson Imaging* 13:215–224
- Ohno Y, Hatabu H, Takenaka D, Adachi S, Kono M, Sugimura K (2002) Solitary pulmonary nodules: potential role of dynamic MR imaging in management initial experience. *Radiology* 224:503–511
- Ohno Y, Hatabu H, Takenaka D, Uematsu H, Ohbayashi C, Higashino T, Nogami M, Yoshimura M, Fujii M, Sugimura K (2004a) Dynamic MR imaging: value of differentiating subtypes of peripheral small adenocarcinoma of the lung. *Eur J Radiol* 52:144–150
- Ohno Y, Hatabu H, Higashino T, Takenaka D, Watanabe H, Nishimura Y, Yoshimura M, Sugimura K (2004b) Dynamic perfusion MRI versus perfusion scintigraphy: prediction of postoperative lung function in patients with lung cancer. *AJR Am J Roentgenol* 182:73–78
- Ohno Y, Hatabu H, Murase K, Higashino T, Kawamitsu H, Watanabe H, Takenaka D, Fujii M, Sugimura K (2004c) Quantitative assessment of regional pulmonary perfusion in the entire lung using three-dimensional ultrafast dynamic contrast-enhanced magnetic resonance imaging: preliminary experience in 40 subjects. *J Magn Reson Imaging* 20:353–365
- Ohno Y, Hatabu H, Takenaka D, Higashino T, Watanabe H, Ohbayashi C, Yoshimura M, Satouchi M, Nishimura Y, Sugimura K (2004d) Metastases in mediastinal and hilar lymph nodes in patients with non-small cell lung cancer: quantitative and qualitative assessment with STIR turbo spin-echo MR imaging. *Radiology* 231:872–879
- Ohno Y, Nogami M, Higashino T, Takenaka D, Matsumoto S, Hatabu H, Sugimura K (2005) Prognostic value of dynamic MR imaging for non-small-cell lung cancer patients after chemoradiotherapy. *J Magn Reson Imaging* 21:775–783
- Ohno Y, Hatabu H, Murase K, Higashino T, Nogami M, Yoshikawa T, Sugimura K (2007a) Primary pulmonary hypertension: 3D dynamic perfusion MRI for quantitative analysis of regional pulmonary perfusion. *AJR Am J Roentgenol* 188:48–56
- Ohno Y, Koyama H, Nogami M, Takenaka D, Matsumoto S, Yoshimura M, Kotani Y, Sugimura K (2007b) Postoperative lung function in lung cancer patients: comparative analysis of predictive capability of MRI, CT, and SPECT. *AJR Am J Roentgenol* 189:400–408

- Ohno Y, Koyama H, Nogami M, Takenaka D, Yoshikawa T, Yoshimura M, Ohbayashi C, Sugimura K (2007c) STIR turbo SE MR imaging vs. coregistered FDG-PET/CT: quantitative and qualitative assessment of N-stage in non-small-cell lung cancer patients. *J Magn Reson Imaging* 26:1071–1080
- Ohno Y, Koyama H, Nogami M, Takenaka D, Yoshikawa T, Yoshimura M, Kotani Y, Nishimura Y, Higashino T, Sugimura K (2007d) Whole-body MR imaging vs FDG-PET: comparison of accuracy of M-stage diagnosis for lung cancer patients. *J Magn Reson Imaging* 26:498–509
- Oliver TW Jr, Bernardino ME, Miller JI, Mansour K, Greene D, Davis WA (1984) Isolated adrenal masses in non-small-cell bronchogenic carcinoma. *Radiology* 153:217–218
- Padovani B, Mouroux J, Seksik L, Chanalet S, Sedat J, Rotomondo C, Richelme H, Serres JJ (1993) Chest wall invasion by bronchogenic carcinoma: evaluation with MR imaging. *Radiology* 187:33–38
- Pantel K, Izbicki J, Passlick B, Angstwurm M, Häussinger K, Thetter O, Riethmüller G (1996) Frequency and prognostic significance of isolated tumour cells in bone marrow of patients with non-small-cell lung cancer without overt metastases. *Lancet* 347:649–653
- Park SW, Lee JH, Ehara S, Park YB, Sung SO, Choi JA, Joo YE (2004) Single shot fast spin echo diffusion-weighted MR imaging of the spine; Is it useful in differentiating malignant metastatic tumor infiltration from benign fracture edema? *Clin Imaging* 28:102–108
- Park Y, Kim TS, Yi CA, Cho EY, Kim H, Choi YS (2007) Pulmonary cavitory mass containing a mural nodule: differential diagnosis between intracavitary aspergilloma and cavitating lung cancer on contrast-enhanced computed tomography. *Clin Radiol* 62:227–232
- Parmar H, Shah J, Patkar D, Varma R (2000) Intramedullary tuberculomas. MR findings in seven patients. *Acta Radiol* 41:572–577
- Patz EF Jr, Lowe VJ, Hoffman JM, Paine SS, Burrowes P, Coleman RE, Goodman PC (1993) Focal pulmonary abnormalities: evaluation with F-18 fluorodeoxyglucose PET scanning. *Radiology* 188:487–490
- Patz EF Jr, Lowe VJ, Goodman PC, Herndon J (1995) Thoracic nodal staging with PET imaging with 18FDG in patients with bronchogenic carcinoma. *Chest* 108:1617–1621
- Plathow C, Zimmermann H, Fink C et al. (2005) Influence of different breathing maneuvers on internal and external organ motion: use of fiducial markers in dynamic MRI. *Int J Rad Oncol Biol Phys* 62:238–245
- Poon PY, Bronskill MJ, Henkelman RM, Rideout DF, Shulman HS, Weisbrod GL, Steinhardt MI, Dunlap HJ, Ginsberg RJ, Feld R (1987) Mediastinal lymph node metastases from bronchogenic carcinoma: detection with MR imaging and CT. *Radiology* 162:651–656
- Puderbach M, Risse F, Biederer J et al. (2008) In vivo Gd-DTPA concentration for MR lung perfusion measurements: assessment with computed tomography in a porcine model. *Eur Radiol* (in press)
- Quint LE, Francis IR (1999) Radiologic staging of lung cancer. *J Thorac Imaging* 14:235–246
- Quint LE, Glazer GM, Orringer MB (1987) Central lung masses: prediction with CT of need for pneumonectomy versus lobectomy. *Radiology* 165:735–738
- Quint LE, Francis IR, Wahl RL, Gross BH, Glazer GM (1995) Preoperative staging of non-small-cell carcinoma of the lung: imaging methods. *AJR Am J Roentgenol* 164:1349–1359
- Quint LE, Tummala S, Brisson LJ, Francis IR, Krupnick AS, Kazerooni EA, Iannettoni MD, Whyte RI, Orringer MB (1996) Distribution of distant metastases from newly diagnosed non-small cell lung cancer. *Ann Thorac Surg* 62:246–250
- Rapoport S, Blair DN, McCarthy SM, Desser TS, Hammers LW, Sostman HD (1988) Brachial plexus: correlation of MR imaging with CT and pathologic findings. *Radiology* 167:161–165
- Regier M, Kandel S, Kaul MG, Hoffmann B, Ittrich H, Bannmann PM, Kemper J, Nolte-Ernsting C, Heller M, Adam G, Biederer J (2007) Detection of small pulmonary nodules in high-field MR at 3 T: evaluation of different pulse sequences using porcine lung explants. *Eur Radiol* 17:1341–1351
- Rendina EA, Bognolo DA, Mineo TC, Gualdi GF, Caterino M, Di Biasi C, Facciolo F, Ricci C (1987) Computed tomography for the evaluation of intrathoracic invasion by lung cancer. *J Thorac Cardiovasc Surg* 94:57–63
- Sakai F, Sone S, Maruyama A, Kawai T, Imai S, Aoki J, Morimoto M, Haniuda M, Ueda H, Honda T (1992) Thin-rim enhancement in Gd-DTPA-enhanced magnetic resonance images of tuberculoma: a new finding of potential differential diagnostic importance. *J Thorac Imaging* 7:64–69
- Sakai F, Sone S, Kiyono K, Maruyama A, Kawai T, Aoki J, Ueda H, Ishii K, Honda T, Morimoto M (1994) MR of pulmonary hamartoma: pathologic correlation. *J Thorac Imaging* 9:51–55
- Sakai S, Murayama S, Murakami J, Hashiguchi N, Masuda K (1997) Bronchogenic carcinoma invasion of the chest wall: evaluation with dynamic cine MRI during breathing. *J Comput Assist Tomogr* 21:595–600
- Schaefer JE, Vollmar J, Schick F, Vonthein R, Seemann MD, Aebert H, Dierkesmann R, Friedel G, Claussen CD (2004) Solitary pulmonary nodules: dynamic contrast-enhanced MR imaging – perfusion differences in malignant and benign lesions. *Radiology* 232:544–553
- Schaefer JE, Schneider V, Vollmar J, Wehrmann M, Aebert H, Friedel G, Vonthein R, Schick F, Claussen CD (2006) Solitary pulmonary nodules: association between signal characteristics in dynamic contrast enhanced MRI and tumor angiogenesis. *Lung Cancer* 53:39–49
- Schaefer-Prokop C, Prokop M (2002) New imaging techniques in the treatment guidelines for lung cancer. *Eur Respir J Suppl* 35:71s–83s
- Schmidt GP, Haug AR, Schoenberg SO, Reiser MF (2006) Whole-body MRI and PET-CT in the management of cancer patients. *Eur Radiol* 16:1216–1225

- Schrevers L, Lorent N, Doooms C, Vansteenkiste J (2004) The role of PET scan in diagnosis, staging, and management of non-small cell lung cancer. *Oncologist* 9:633–643
- Schroeder T, Ruehm SG, Debatin JF, Ladd ME, Barkhausen J, Goehde SC (2005) Detection of pulmonary nodules using a 2D HASTE MR sequence: comparison with MDCT. *AJR Am J Roentgenol* 185:979–984
- Schwartz LH, Ginsberg MS, Burt ME, Brown KT, Getrajdman GI, Panicek DM (1998) MRI as an alternative to CT-guided biopsy of adrenal masses in patients with lung cancer. *Ann Thorac Surg* 65:193–197
- Seo JS, Kim YJ, Choi BW, Choe KO (2005) Usefulness of magnetic resonance imaging for evaluation of cardiovascular invasion: evaluation of sliding motion between thoracic mass and adjacent structures on cine MR images. *J Magn Reson Imaging* 22:234–241
- Shimizu S, Shirato H, Aoyama H et al. (2000) High-speed magnetic resonance imaging for four-dimensional treatment planning of conformal radiation therapy of moving body tumors. *Int J Rad Oncol Biol Phys* 48:471–474
- Siegelman SS, Khouri NF, Scott WW Jr, Leo FP, Hamper UM, Fishman EK, Zerhouni EA (1986) Pulmonary hamartoma: CT findings. *Radiology* 160:313–317
- Silvestri GA, Littenberg B, Colice GL (1995) The clinical evaluation for detecting metastatic lung cancer. A meta-analysis. *Am J Respir Crit Care Med* 152:225–230
- Silvestri GA, Gould MK, Margolis ML, Tanoue LT, McCrory D, Toloza E, Detterbeck F, (2007) Noninvasive staging of non-small cell lung cancer: ACCP evidenced-based clinical practice guidelines, 2nd edn. American College of Chest Physicians. *Chest* 132:178S–201S
- Sobin L, Wittekind Ch (2002) Lung cancer. In: Sobin L, Wittekind Ch (eds) *TNM classification of malignant tumors*, 6th edn. Wiley-Liss, New York, pp 99–103
- Sochocky S (1958) Tuberculoma of the lung. *Am Rev Tuberc* 78:403–410
- Suzuki N, Saitoh T, Kitamura S (1993) Tumor invasion of the chest wall in lung cancer: diagnosis with US. *Radiology* 187:39–42
- Swensen SJ, Morin RL, Schueler BA, Brown LR, Cortese DA, Pairolero PC, Brutinel WM (1992) Solitary pulmonary nodule: CT evaluation of enhancement with iodinated contrast media – a preliminary report. *Radiology* 182:343–347
- Swensen SJ, Brown LR, Colby TV, Weaver AL, Midthun DE (1996) Lung nodule enhancement at CT: prospective findings. *Radiology* 201:447–455
- Swensen SJ, Viggiano RW, Midthun DE, Müller NL, Sherrick A, Yamashita K, Naidich DP, Patz EF, Hartman TE, Muhm JR, Weaver AL (2000) Lung nodule enhancement at CT: multicenter study. *Radiology* 214:73–80
- Swensen SJ, Jett JR, Hartman TE, Midthun DE, Mandrekar SJ, Hillman SL, Sykes AM, Aughenbaugh GL, Bungum AO, Allen KL (2005) CT screening for lung cancer: five-year prospective experience. *Radiology* 235:259–265
- Szolar DH, Kammerhuber FH (1998) Adrenal adenomas and nonadenomas: assessment of washout at delayed contrast-enhanced CT. *Radiology* 207:369–375
- Takahara T, Imai Y, Yamashita T, Yasuda S, Nasu S, Van Cauwen M (2004) Diffusion weighted whole body imaging with background body signal suppression (DWIBS): technical improvement using free breathing, STIR and high resolution 3D display. *Radiat Med* 22:275–282
- Takahashi K, Furuse M, Hanaoka H, Yamada T, Mineta M, Ono H, Nagasawa K, Aburano T (2000) Pulmonary vein and left atrial invasion by lung cancer: assessment by breath-hold gadolinium-enhanced three-dimensional MR angiography. *J Comput Assist Tomog* 24:557–561
- Takahashi M, Shimoyama K, Murata K, Mori M, Nitta N, Mishina A, Matsuo H, Morita R, Fujino S, Inoue S, Kato H (1997) Hilar and mediastinal invasion of bronchogenic carcinoma: evaluation by thin-section electron-beam computed tomography. *J Thorac Imaging* 12:195–199
- Takenaka D, Ohno Y, Hatabu H, Ohbayashi C, Yoshimura M, Ohkita Y, Sugimura K (2002) Differentiation of metastatic versus non-metastatic mediastinal lymph nodes in patients with non-small cell lung cancer using respiratory-triggered short inversion time inversion recovery (STIR) turbo spin-echo MR imaging. *Eur J Radiol* 44:216–224
- Tanaka K, Kubota K, Kodama T, Nagai K, Nishiwaki Y (1999) Extrathoracic staging is not necessary for non-small-cell lung cancer with clinical stage T1-2 N0. *Ann Thorac Surg* 68:1039–1042
- Therasse P, Arbuck SG, Eisenhauer EA, Wanders J, Kaplan RS, Rubinstein L, Verweij J, Van Glabbeke M, van Oosterom AT, Christian MC, Gwyther SG (2000) New guidelines to evaluate the response to treatment in solid tumors. *J Natl Cancer Inst* 92:205–216
- Tokuda O, Hayashi N, Matsunaga N (2004) MRI of bone tumors: Fast STIR imaging as a substitute for T1-weighted contrast-enhanced fat-suppressed spin-echo imaging. *J Magn Reson Imaging* 19:475–481
- Toloza EM, Harpole L, McCrory DC (2003) Noninvasive staging of non-small cell lung cancer: a review of the current evidence. *Chest* 123:137S–146S
- Tuddenham WJ (1984) Glossary of terms for thoracic radiology: recommendations of the Nomenclature Committee of the Fleischner Society. *AJR Am J Roentgenol* 143:509–517
- van der Heide S, Kauffman HF, de Vries K (1985) Cultivation of fungi in synthetic and semi-synthetic liquid medium. II. Immunochemical properties of the antigenic and allergenic extracts. *Allergy* 40:592–598
- van Tinteren H, Hoekstra OS, Smit EF, van den Bergh JH, Schreurs AJ, Stallaert RA, van Velthoven PC, Comans EF, Diepenhorst FW, Verboom P, van Mourik JC, Postmus PE, Boers M, Teule GJ (2002) Effectiveness of positron emission tomography in the preoperative assessment of patients with suspected non-small-cell lung cancer: the PLUS multicentre randomised trial. *Lancet* 359:1388–1393
- Vanel D, Bittoun J, Tardivon A (1998) MRI of bone metastases. *Eur Radiol* 8:1345–1351

- Vansteenkiste J, De Leyn P, Deneffe G, Menten J, Lerut T, Demedts M (1998) Present status of induction treatment in stage IIIA-N2 non-small cell lung cancer: a review. The Leuven Lung Cancer Group. *Eur J Cardiothorac Surg* 13:1–12
- Vogt FM, Herborn CU, Hunold P, Lauenstein TC, Schröder T, Debatin JF, Barkhausen J (2004) HASTE MRI versus chest radiography in the detection of pulmonary nodules: comparison with MDCT. *AJR Am J Roentgenol* 183:71–78
- Wahl RL, Quint LE, Greenough RL, Meyer CR, White RI, Orringer MB (1994) Staging of mediastinal non-small cell lung cancer with FDG PET, CT, and fusion images: preliminary prospective evaluation. *Radiology* 191:371–377
- Walker R, Kessar P, Blanchard R, Dimasi M, Harper K, De-Carvalho V, Yucel EK, Patriquin L, Eustace S (2000) Turbo STIR magnetic resonance imaging as a whole-body screening tool for metastases in patients with breast carcinoma: preliminary clinical experience. *J Magn Reson Imaging* 11:343–350
- Watanabe A, Shimokata K, Saka H, Nomura F, Sakai S (1991) Chest CT combined with artificial pneumothorax: value in determining origin and extent of tumor. *AJR Am J Roentgenol* 156:707–710
- Webb WR, Gatsonis C, Zerhouni EA, Heelan RT, Glazer GM, Francis IR, McNeil BJ (1991) CT and MR imaging in staging non-small cell bronchogenic carcinoma: report of the Radiologic Diagnostic Oncology Group. *Radiology* 178:705–713
- Webb WR, Sarin M, Zerhouni EA, Heelan RT, Glazer GM, Gatsonis C (1993) Interobserver variability in CT and MR staging of lung cancer. *J Comput Assist Tomogr* 17:841–846
- Weinberger E, Shaw DW, White KS, Winters WD, Stark JE, Nazar-Stewart V, Hinks RS (1995) Nontraumatic pediatric musculoskeletal MR imaging: comparison of conventional and fast-spin-echo short inversion time inversion-recovery technique. *Radiology* 194:721–726
- White CS (1996) MR evaluation of the pericardium and cardiac malignancies. *Magn Reson Imaging Clin N Am* 4:237–251
- White PG, Adams H, Crane MD, Butchart EG (1994) Preoperative staging of carcinoma of the bronchus: can computed tomographic scanning reliably identify stage III tumours? *Thorax* 49:951–957
- Wong J, Haramati LB, Rozenshtein A, Yanez M, Austin JH (1999) Non-small-cell lung cancer: practice patterns of extrathoracic imaging. *Acad Radiol* 6:211–215
- World Health Organization (1979) WHO handbook for reporting the results of cancer treatment. World Health Organization, Geneva, Switzerland
- Yamashita K, Matsunobe S, Tsuda T, Nemoto T, Matsumoto K, Miki H, Konishi J (1995) Solitary pulmonary nodules: preliminary study of evaluation with incremental dynamic CT. *Radiology* 194:399–405
- Yi CA, Lee KS, Kim EA, Han J, Kim H, Kwon OJ, Jeong YJ, Kim S (2004) Solitary pulmonary nodules: dynamic enhanced multi-detector row CT study and comparison with vascular endothelial growth factor and microvessel density. *Radiology* 233:191–199
- Yi CA, Lee KS, Kim BT, Choi JY, Kwon OJ, Kim H, Shim YM, Chung MJ (2006) Tissue characterization of solitary pulmonary nodule: comparative study between helical dynamic CT and integrated PET/CT. *J Nucl Med* 47:443–450
- Yi CA, Jeon TY, Lee KS, Lee JH, Seo JB, Kim YK, Chung MJ (2007) 3-T MRI: usefulness for evaluating primary lung cancer and small nodules in lobes not containing primary tumors. *AJR Am J Roentgenol* 189:386–392
- Yilmaz S, Ekici A, Erdogan S, Ekici M (2004) Endobronchial lipomatous hamartoma: CT and MR imaging features. *Eur Radiol* 14:1521–1524
- Yokoi K, Mori K, Miyazawa N, Saito Y, Okuyama A, Sasagawa M (1991) Tumor invasion of the chest wall and mediastinum in lung cancer: evaluation with pneumothorax CT. *Radiology* 181:147–152
- Yokoi K, Kamiya N, Matsuguma H, Machida S, Hirose T, Mori K, Tominaga K (1999) Detection of brain metastasis in potentially operable non-small cell lung cancer: a comparison of CT and MRI. *Chest* 115:714–719
- Zhang M, Kono M (1997) Solitary pulmonary nodules: evaluation of blood flow patterns with dynamic CT. *Radiology* 205:471–478
- Zinreich SJ, Kennedy DW, Malat J, Curtin HD, Epstein JI, Huff LC, Kumar AJ, Johns ME, Rosenbaum AE (1988) Fungal sinusitis: diagnosis with CT and MR imaging. *Radiology* 169:439–444

KOJI TAKAHASHI

CONTENTS

| | | |
|--------|---|-----|
| 12.1 | Introduction | 217 |
| 12.2 | Mediastinal Cystic Masses | 218 |
| 12.2.1 | Bronchogenic Cysts | 218 |
| 12.2.2 | Esophageal Duplication Cysts | 220 |
| 12.2.3 | Neurenteric Cysts | 220 |
| 12.2.4 | Pericardial Cysts | 220 |
| 12.2.5 | Thymic Cysts | 221 |
| 12.2.6 | Other Cystic and Cyst-Like Lesions | 222 |
| 12.3 | Thymus and Thymic Tumors | 224 |
| 12.3.1 | Normal Thymus | 224 |
| 12.3.2 | Thymic Hyperplasia and Thymic Rebound | 226 |
| 12.3.3 | Thymoma | 228 |
| 12.3.4 | Thymic Carcinoma | 232 |
| 12.3.5 | Thymolipoma | 233 |
| 12.3.6 | Thymic Neuroendocrine Neoplasm | 233 |
| 12.4 | Mediastinal Germ Cell Tumors | 235 |
| 12.4.1 | Teratoma | 235 |
| 12.4.2 | Seminoma | 237 |
| 12.4.3 | Nonseminomatous Malignant Germ Cell Tumor | 238 |
| 12.5 | Mediastinal Malignant Lymphoma | 239 |
| 12.5.1 | Hodgkin's Disease | 239 |
| 12.5.2 | Lymphoblastic Lymphoma | 240 |
| 12.5.3 | Primary Mediastinal Diffuse Large B-Cell Lymphoma | 241 |
| 12.5.4 | MRI of Lymphoma | 242 |
| 12.6 | Neurogenic Tumor | 244 |
| 12.6.1 | Peripheral Nerve Sheath Tumors | 244 |
| 12.6.2 | Sympathetic Ganglia Tumors | 246 |
| 12.6.3 | Paraganglioma | 246 |
| 12.7 | Other Mediastinal Diseases | 249 |
| 12.7.1 | Mediastinal Goiters | 249 |
| 12.7.2 | Ectopic Parathyroid Gland | 249 |
| 12.7.3 | Fibrosing Mediastinitis | 249 |
| 12.7.4 | Extramedullary Hematopoiesis | 250 |
| | References | 250 |

KEY POINTS

Cystic masses are generally congenital and arise anywhere in the mediastinum, and MRI is useful to confirm their cystic nature, especially in the cysts with soft tissue attenuation at CT. In the thymus, chemical-shift MRI can characterize the normal thymus and thymic hyperplasia by detecting tiny amounts of fat tissue within the thymus and differentiate such benign processes from thymic tumors. Malignant lymphoma is a relatively common disease in the mediastinum, and MRI provides important information, especially in the assessment of viability of residual masses in treated lymphoma. In the diagnosis of neurogenic tumors, MRI can precisely evaluate shape, location, intraspinal extension, and internal components of the tumors.

12.1

Introduction

In assessment of mediastinal disease, CT is generally the first-choice modality of diagnostic imaging. But not uncommonly, MRI provides important findings that are diagnostic of a disease and facilitates precise assessment of location, pattern of extensions, and anatomical relationship with adjacent structures of the disease. In addition to conventional T1- and T2-weighted spin echo sequences, chemical shift images, dynamic studies with first gradient-echo 2- or 3- dimensional sequences, and diffusion-weighted images are available to obtain specific findings of the mediastinal diseases.

K. TAKAHASHI, MD, PhD
 Department of Radiology, Asahikawa Medical College, 2-1-1-1, Midorigaoka-higashi, Asahikawa, Japan

We describe the role of MRI in the assessment of various mediastinal diseases, including congenital and acquired cystic masses, thymus and thymic tumors, germ cell tumors, Hodgkin's and non-Hodgkin's lymphoma, and neurogenic tumors with emphasis of their characteristic and specific findings on MRI.

12.2

Mediastinal Cystic Masses

Cystic masses of the mediastinum are encapsulated lesions that contain fluid and are lined with epithelium. Most cystic lesions are congenital in origin and include foregut duplication cysts (i.e., bronchogenic cysts, esophageal duplication cysts, and neurenteric cysts), pericardial cysts, pleural cysts, and parathyroid cysts. Thymic cysts and thoracic duct cysts are either congenital or acquired in origin. Meningocele, pancreatic pseudocysts, hydatid disease, abscess, hematoma, and various solid lesions associated with cystic degeneration (i.e., schwannoma, germ cell tumor, thymoma, and parathyroid adenoma) also appear as cystic mediastinal masses.

In a study of 105 cases with mediastinal cysts, cystic disease comprises 13.0% of mediastinal masses and is more prevalent in adult populations (14.1%) than in children (7.7%) ($p < 0.05$). Overall, 36.2% of the patients were symptomatic, and common symptoms were retrosternal chest pain (14.3%), which was followed by dyspnea (7.6%), cough (6.7%), fever (5.7%), and hoarseness (4.8%). The incidence of each cystic masses is 45% in bronchogenic, 28% in thymic, 11% in pericardial, 7% in pleural cysts, and 4% in esophageal duplication cysts (TAKEDA et al. 2003).

On radiographs, mediastinal cystic masses usually appear as focal deformity or obscuration of mediastinal contours and lines and may be associated with displacement of normal mediastinal structures. Generally, CT is the diagnostic modality of first choice for mediastinal cystic masses and the following typical features are diagnostic: (1) an encapsulated smooth round or oval mass, (2) homogeneous attenuation in the range of water attenuation (0–20 HU), (3) no enhancement of cyst contents, and (4) no infiltration of adjacent mediastinal structures (KUHLMAN et al. 1988; FEUNG et al. 2002).

On MR images, mediastinal cysts that usually contain serous fluid typically show homogeneous low signal intensity on T1-weighted images and high signal intensity on T2-weighted images, due to their long T1 and T2 relaxation time. In some mediastinal cysts, CT may reveal high attenuation similar to solid lesions due

to a high level of protein and calcium oxalate in the cystic contents (YERNAULT et al. 1986). In such situations, MRI can be useful in the differentiation of cystic masses from solid lesions. High signal intensity corresponding to cerebrospinal fluid on T2-weighted images, a fluid–fluid level, and lack of contrast enhancement are highly suggestive of the cystic nature of the lesions. It should be noted that signal intensity on MR images of mediastinal masses also varies depending on its content including, calcium, protein, and blood products, especially on T1-weighted images (MURAYAMA et al. 1995). The lesions that contain proteinaceous or hemorrhagic contents show high signal on T1-weighted images. One of disadvantages of MRI is inability of visualization of calcification, which may occur occasionally in the wall or within the lesion.

12.2.1 Bronchogenic Cysts

Bronchogenic cysts are the most common foregut cysts and result from defective development (abnormal budding of the ventral foregut) during the fetal period (RIBET et al. 1995). The cyst wall is lined by respiratory epithelium (pseudostratified ciliated columnar epithelium) and contains cartilage, smooth muscle, and mucous glands. Cyst fluid is usually serous, but can contain various amounts of protein and calcium and can be hemorrhagic or highly viscous.

Bronchogenic cysts most commonly present in the first few decades of life, and the majority is incidentally detected on chest radiograph or on chest CT. However, they may occasionally be symptomatic due to compression of adjacent structures. In a series of surgically diagnosed cases, 70–80% of patients had symptoms including chest pain, cough, dyspnea, fever, and purulent sputum (ST-GEORGES et al. 1991; RIBET et al. 1996). In infants and young children, they are usually symptomatic and sometimes life threatening.

The bronchogenic cysts most commonly are located in the near carina (52%) and in the paratracheal region (19%); less often adjacent to the esophagus or retrocardiac region; and rarely in the anterior mediastinum, within the lung, in the pleura, and in the diaphragm (REED et al. 1974; MCADAMS et al. 2000). As a rare case, solitary pedunculated bronchogenic cyst that appeared as a pleural nodule located apart from the mediastinum has been reported (YOSHIOKA et al. 2000).

Bronchogenic cysts typically appear as a well-defined round or elliptical mass with a uniformly thin wall. On CT, 50% of bronchogenic cysts reveal typical water attenuation, whereas in the other half, the cysts

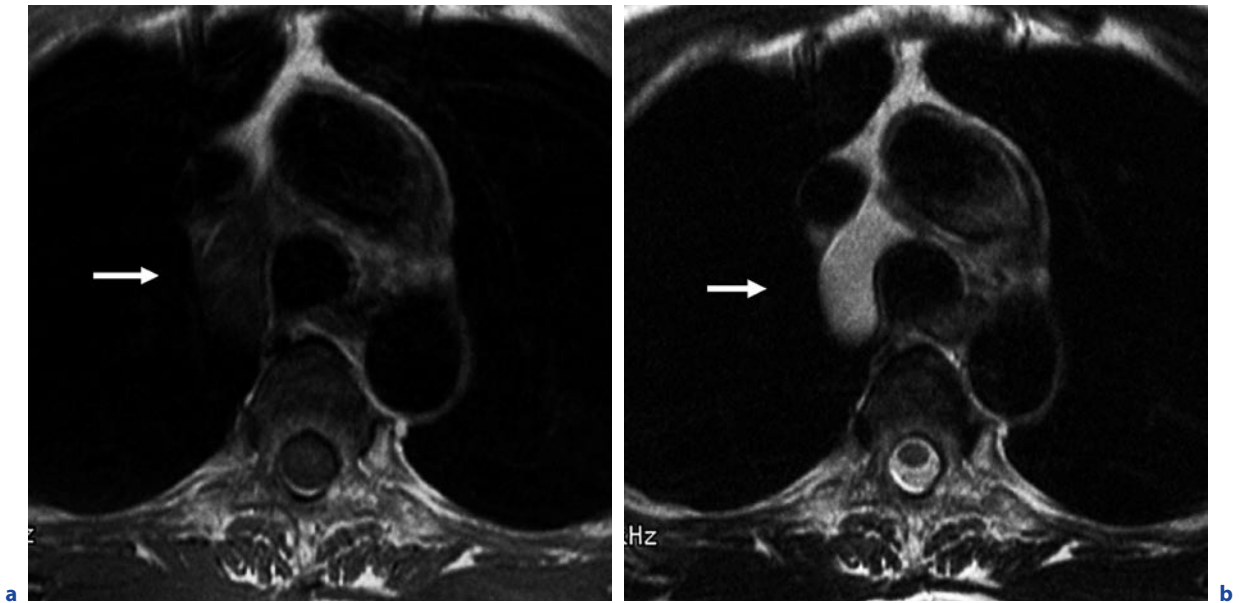


Fig. 12.1a,b. Bronchogenic cyst. (a) T1-weighted and (b) T2-weighted MR images showing a well-demarcated mass lesion right of the trachea (arrows). The lesion shows low signal

intensity on T1-weighted images (a) and homogeneous high signal intensity on T2-weighted images (b). The signal pattern suggests cystic nature of the lesion

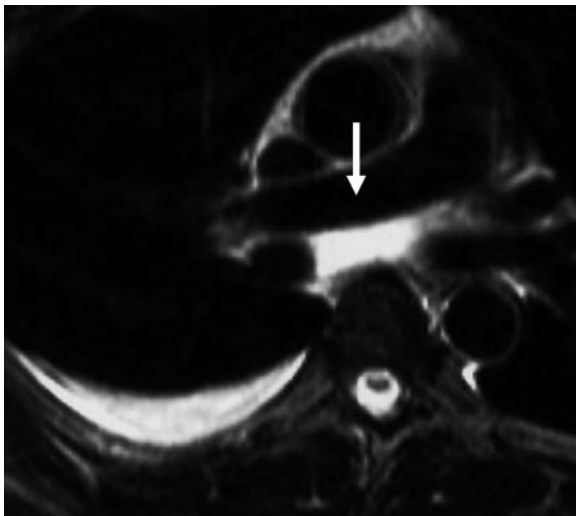


Fig. 12.2. Ruptured bronchogenic cyst. The bronchogenic cyst ruptured after abrupt increase in size. T2-weighted MR image reveals a bronchogenic cyst at the carina (arrow) and right-sided pleural effusion

have variously higher attenuation and may be indistinguishable from soft tissue lesions (YERNAULT et al. 1986). On T2-weighted MRI, bronchogenic cysts constantly have high signal intensity, but variable patterns of signal intensity are seen on T1-weighted MRI, depending on cystic contents including, protein, hemorrhage, mucoid material, and calcium (FEUNG et al. 2002) (Fig. 12.1). McADAMS et al. (2000) have reported that on T1-weighted MR images ($n = 23$), 18 cysts were hyperintense, and 5 were isointense to cerebrospinal fluid, and on T2-weighted MR images ($n = 18$), 17 cysts were

isointense or hyperintense, and 1 was hypointense to cerebrospinal fluid. Invariable high signal intensity on T2-weighted MR images is diagnostic of cystic nature of the lesion. Bronchogenic cysts may reveal fluid–fluid level on MR images (MURAYAMA et al. 1995). Rarely, bronchogenic cysts contain air that suggests secondary infection or communication with the tracheobronchial tree. Bronchogenic cysts are typically stable in size or may enlarge over years. Abrupt increase in size indicates hemorrhage or infection (FEUNG et al. 2002) and may result in rupture of the cyst (Fig. 12.2).

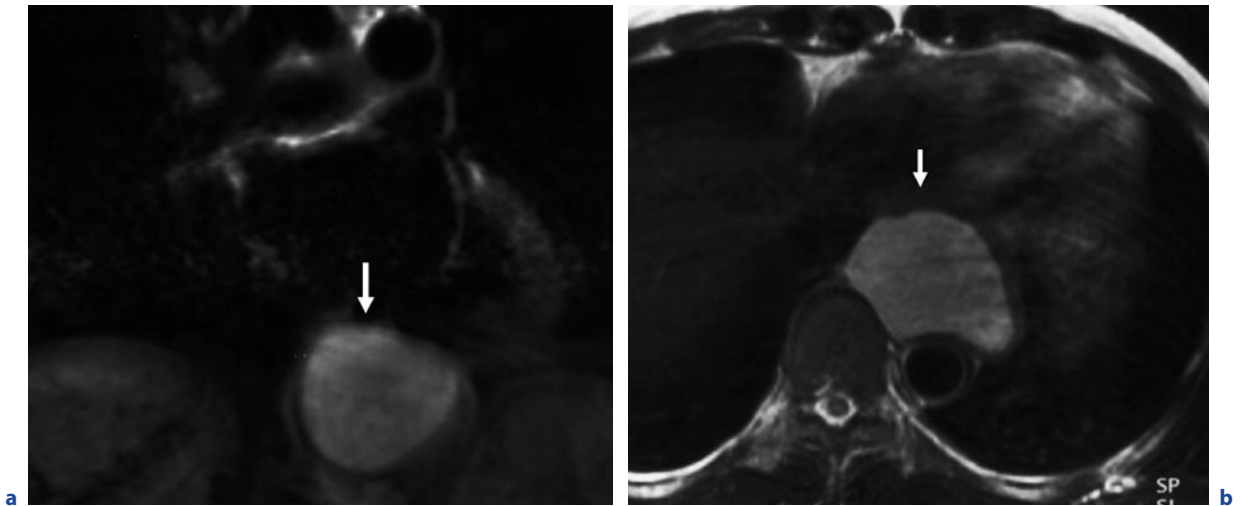


Fig. 12.3a,b. Esophageal cyst. (a) T1-weighted coronal and (b) T2-weighted axial MR images showing a well-defined mass lesion adjacent to the lower esophagus (*arrow*). The cyst shows high signal intensity on T1- and T2-weighted images (*arrow*)

12.2.2 Esophageal Duplication Cysts

Esophageal duplication cysts may result from either abnormal budding of the foregut or a failure of complete vacuolation of the originally solid esophagus (SALO and ALA-KULJU 1987). The cysts are lined by gastrointestinal tract mucosa and have a double layer of smooth muscle. The cysts are commonly located in the lower mediastinum, adjacent to the esophagus (Fig. 12.3). Imaging features of esophageal duplication cysts are similar to those of other mediastinal congenital cysts. However, the cyst walls may be thicker and the lesions may be more tubular in shape and be in more intimate contact with the esophagus.

12.2.3 Neurenteric Cysts

Neurenteric cysts result from incomplete separation of endoderm from notochord and usually have either a fibrous connection to the spine or an intraspinal component. The cysts occasionally are associated with various vertebral anomalies, such as hemivertebra, butterfly vertebra, or spina bifida. Findings of neurenteric cysts at CT and MRI are similar to those of other foregut cysts. MRI is indicated to exclude intraspinal extension of the cysts (STROLLO et al. 1997).

12.2.4 Pericardial Cysts

Pericardial cysts are outpouchings of the parietal pericardium, which have no communication with the pericardial space and result from a defect in the embryogenesis of the celomic cavity. These cysts are commonly round or spherical in shape, thin walled, unilocular, and contain clear or straw-colored fluid. Cyst walls consist of connective tissue and a single layer of mesothelial cells.

The majority of pericardial cysts are located in the cardiophrenic angles, and they are more frequent on the right side. In one large series of 72 cases with pericardial cysts, 54 are located in the cardiophrenic angle, of which two thirds are on the right side, and the remaining 18 are found in the higher mediastinum up to the level of pericardial reflection (WYCHULIS et al. 1971). Patients are almost invariably asymptomatic, and cysts are detected incidentally on a screening chest radiograph.

On CT, the cysts characteristically show water attenuation, but occasionally its content is of soft tissue attenuation. At MRI, they typically have low or intermediate signal intensity on T1-weighted images and homogeneous high intensity on T2-weighted images (Fig. 12.4). The cysts with proteinaceous fluid show high signal intensity on T1-weighted images. The cysts do not enhance with the administration of gadolinium chelates (WANG et al. 2003). Pericardial cysts in unusual locations, including upper mediastinum and anterior mediastinum, may be indistinguishable from bronchogenic or thymic cysts (Fig. 12.5).

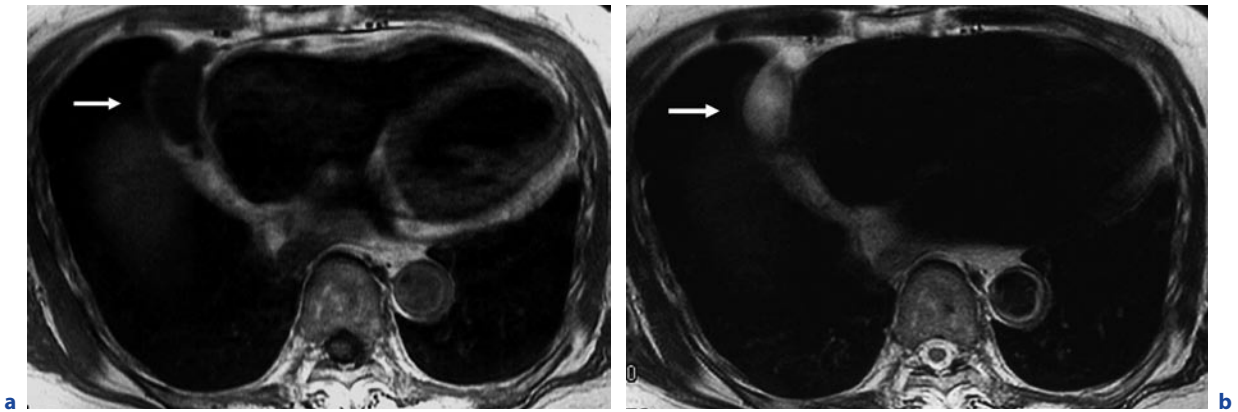


Fig. 12.4a,b. Pericardial cyst. The right cardiophrenic angle is the most common site of pericardial cyst (*arrow*). The cyst typically shows low signal intensity on T1-weighted image (**a**) and high signal intensity on T2-weighted MR image (**b**)

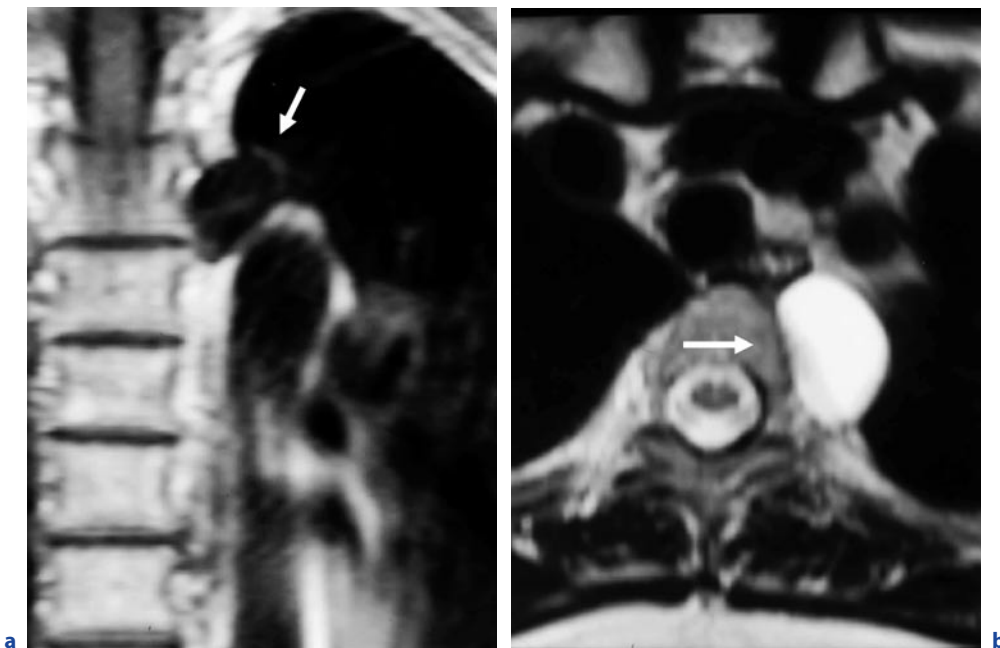


Fig. 12.5a,b. Pericardial cyst at the upper mediastinum. T1-weighted coronal (**a**) and T2-weighted axial (**b**) MR images show a well-defined cyst adjacent to the aortic arch (*arrow*)

12.2.5 Thymic Cysts

Congenital thymic cysts are derived from a remnant of the thymopharyngeal duct, and they are usually unilocular and generally small. Most patients with congenital thymic cyst are asymptomatic; however, patients can present with cough or dyspnea or with pain if intracystic bleeding occurs. Acquired thymic cysts, occasion-

ally referred to multilocular thymic cysts, are probably pathologically unrelated to congenital cysts, and may be associated with various inflammatory process or certain thymic neoplasms, including Hodgkin's disease, seminoma, thymoma, and thymic carcinoma (SUSTER and ROSAI 1991). Although some cysts develop after irradiation of the mediastinum or after chemotherapy (BARON et al. 1981), thymic cysts can coexist with Hodgkin's disease, unrelated to therapy.

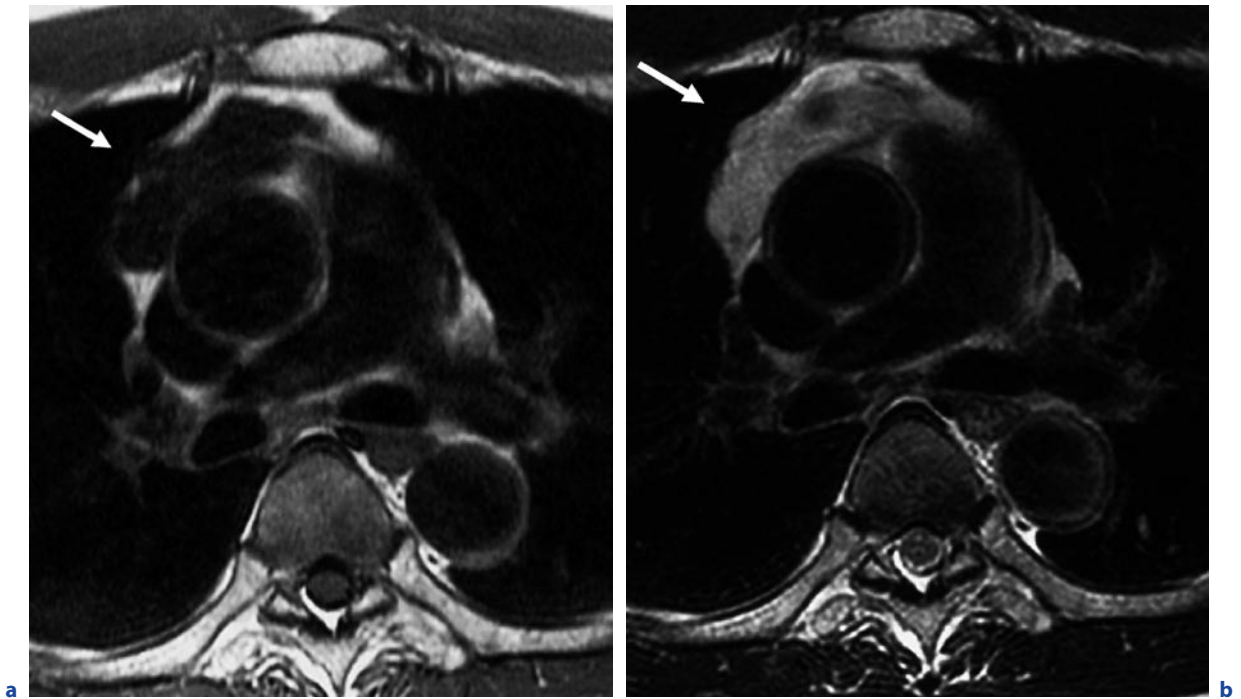


Fig. 12.6a,b. Thymic cyst. T1-weighted (**a**) and T2-weighted (**b**) MR images show a well-defined lesion within the anterior mediastinal fat (*arrow*). The thymic cyst reveals low and high signal intensity on T1-weighted (**a**) and T2-weighted (**b**) MR images, respectively

Thymic cysts show low signal intensity on T1-weighted MR images and high signal intensity on T2-weighted MR images (Fig. 12.6). Hemorrhage into the cysts results in increased signal on T1-weighted images (Fig. 12.7). If the cyst is multilocular, thick walled, or associated with a soft tissue, then biopsy or surgical resection may be indicated to exclude malignancy.

12.2.6 Other Cystic and Cyst-Like Lesions

Thoracic duct cyst is an extremely rare cystic lesion in the mediastinum. The cysts occur anywhere along the course of the thoracic duct and occasionally communicate with the duct. In a review of 29 patients with thoracic duct cysts, the cyst was found in the mediastinum in 19, in the cervical region in 9, and in the abdomen in 1 (MATTILA et al. 1999). The cysts may be associated

with various conditions, including portal hypertension, liver cirrhosis, thoracic duct obstruction, and lymphangiomyomatosis.

Mediastinal pancreatic pseudocysts are rare complications of acute or chronic pancreatitis and result from the extension of pancreatic juice through the diaphragm. Most mediastinal pseudocysts are retrocardiac, since inflammatory process extends through the esophageal or the aortic hiatus (TAN et al. 2002). Multiplanar capability of MRI is beneficial in the pretreatment assessment of the precise location and range of extension of the pseudocysts (TANAKA et al. 2000).

Lateral thoracic meningocele is a rare disorder that occurs frequently in association with neurofibromatosis type I. MRI permits a diagnostic, noninvasive assessment of its cystic nature, communication with the spinal meninges, and associated spinal abnormalities (NAKASU et al. 1991).

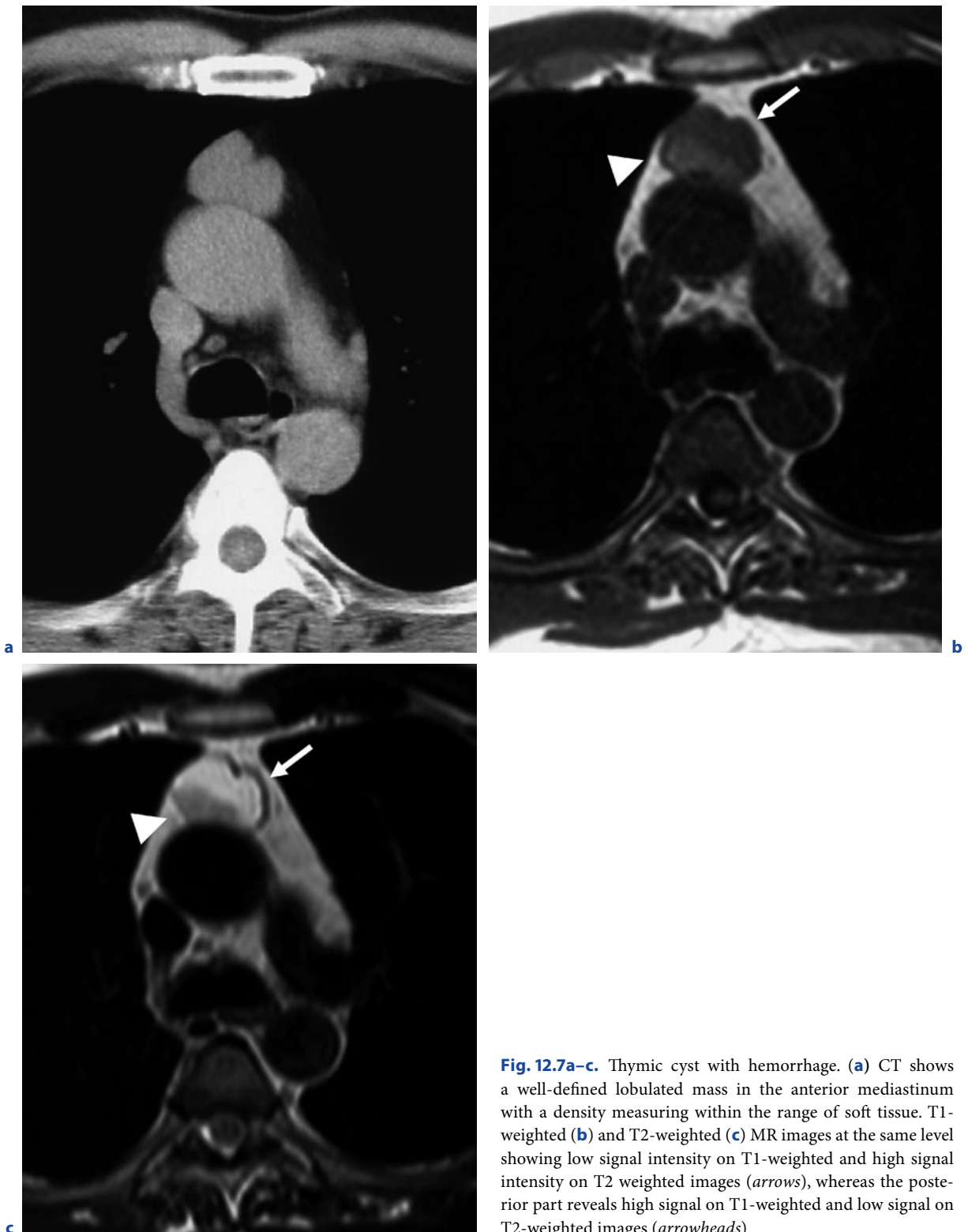


Fig. 12.7a-c. Thymic cyst with hemorrhage. (a) CT shows a well-defined lobulated mass in the anterior mediastinum with a density measuring within the range of soft tissue. T1-weighted (b) and T2-weighted (c) MR images at the same level showing low signal intensity on T1-weighted and high signal intensity on T2 weighted images (*arrows*), whereas the posterior part reveals high signal on T1-weighted and low signal on T2-weighted images (*arrowheads*)

12.3

Thymus and Thymic Tumors

12.3.1

Normal Thymus

The thymus is a bilobed, triangular-shaped organ that occupies retrosternal space and extends over the great vessel and the heart. The normal thymus varies widely in size and shape depending on age (FRANCIS et al. 1985). In infants and younger children, the thymus appears quadrilateral in shape rather than triangular in the axial plane. Its margins are convex in infants and usually become straight in older children (BARON et al. 1982). The thymus reaches a maximum weight at puberty, and then its weight and size decrease with age as the gland undergoes involution with fatty infiltration. From puberty to young adult around 25 years, the thymus appears as bilobed triangular structure and its margins are flat or concave laterally.

The widely accepted CT measurement of the thymus is the thickness of the lobes measured perpendicular to their long axis. On CT, the normal maximal thickness of the thymus is 18 mm before the age 20 years and 13 mm in older patients (BARON et al. 1982). On MRI, the thymus may appear to have a slightly greater thickness than measured on CT, when MR images are obtained under breathing. On CT, the thymus shows soft tissue attenuation similar to muscle in infants and young children. Its attenuation decreases with age after puberty due to fatty infiltration. On MRI, the normal thymus characteristically shows homogeneous and intermediate signal intensity on T1-weighted images, which is less intense than mediastinal fat but greater than muscle. In older patients, after puberty, the T1-weighted signal intensity of the thymus increases with age, since the thymus begins to involute and is replaced by fat. On T2-weighted images, the thymus shows high signal intensity similar to fat at all ages (DE GEER et al. 1986; BOOTHROYD et al. 1992). Besides the measurement of the size, CT attenuation, and MR signal intensity, the

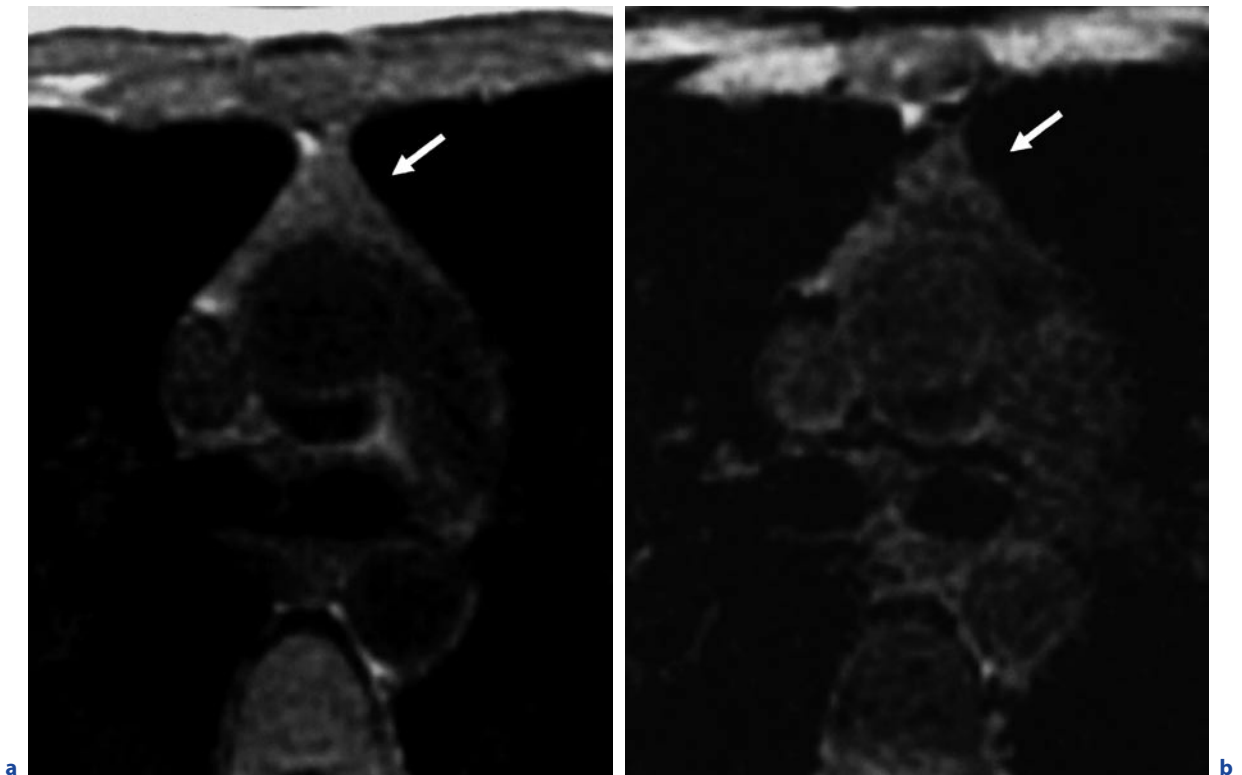


Fig. 12.8a,b. Normal thymus in an 18-year-old girl. In-phase (a) and opposed-phase (b) gradient echo T1-weighted MR images. The thymus shows a homogeneous decrease in signal intensity at opposed-phase image (b) in contrast to in-phase image (a) (arrow)

shape of the thymus is also an important indicator for its abnormality. Focal contour abnormality of the thymus—especially that associated with displacement of the adjacent structures—is suggestive of underlying mass (DE GEER et al. 1986).

Chemical-shift MRI can depict intravoxel fat and water within the tissue and has been used clinically to diagnose adrenal adenoma and assess fatty liver. It has been recently reported that chemical-shift MRI is useful for characterizing the normal thymus by detecting the intravoxel fat tissue within the thymus. Chemical-shift MRI can depict physiological fatty replacement of the normal thymus in nearly 50% of subjects aged 11–15 years, and in nearly 100% of those over 15 years (INAOKA et al. 2005) (Fig. 12.8).

Ectopic thymus results from defective pathways of the embryologic descent of the thymus and can occur anywhere along the path of the thymopharyngeal duct. Ectopic cervical thymus usually presents as an asymptomatic neck mass in infancy, childhood, and early adulthood and is often located in the subman-

dibular region, adjacent to the thyroid gland, and near the carotid bifurcation (HE et al. 2008; LIU et al. 2006; KHARIWALA et al. 2004). CT reveals a homogeneous soft tissue mass with little or no contrast enhancement (LIU et al. 2006; KHARIWALA et al. 2004). MRI demonstrates signal intensity equal to that of muscle on T1-weighted images and greater than that of muscle on T2-weighted images, identical to the mediastinal thymus. In the diagnosis of ectopic thymus, it should be noted that the normal thymus occasionally extends to the upper mediastinum or lower neck (Fig. 12.9).

Although a previous report has suggested that an apparent diffusion coefficient (ADC) lower than $1.22 \times 10^{-3} \text{ mm}^2/\text{s}$ for pediatric neck lesions indicates malignancy, there is a case report of ectopic cervical thymus which has a low ADC value of $0.35 \sim 0.40 \times 10^{-3} \text{ mm}^2/\text{s}$ (LIU et al. 2006). The authors said that the histological characteristics of normal thymic tissue, which consists of many lymphocytes with tight diffusion space of water protons in the extracellular dimension, might result in a low ADC (LIU et al. 2006).

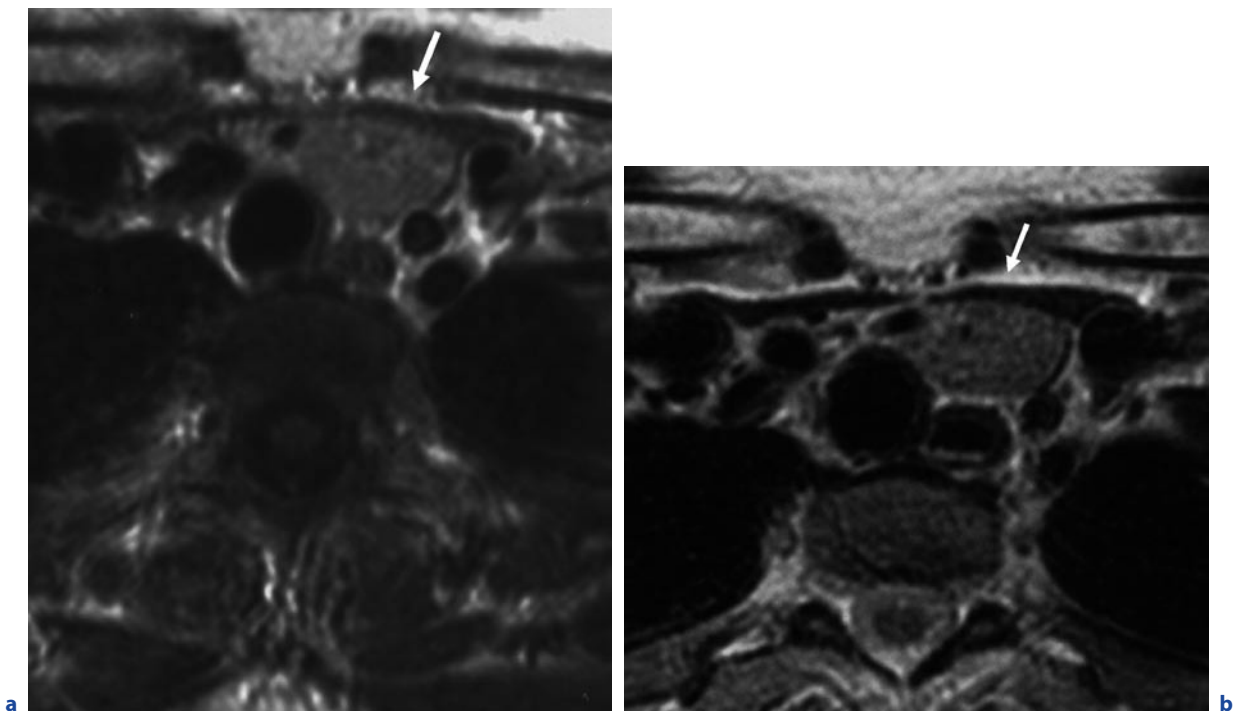


Fig. 12.9a,b. Normal thymus in the upper mediastinum. T1-weighted (a) and T2-weighted (b) MR images at the upper mediastinum. A part of the normal thymus extends to the upper mediastinum and appears as a mass lesion (arrow)

12.3.2 Thymic Hyperplasia and Thymic Rebound

Lymphoid follicular hyperplasia is pathologically diagnosed by the presence of hyperplastic lymphoid germinal centers in the medulla of the thymus in association with a lymphocytic and plasma cell infiltrate (GOLDSTEIN et al. 1969). Lymphoid follicular thymic hyperplasia is seen in more than 50% of patients with myasthenia gravis and is associated with various conditions: thyrotoxicosis, systemic lupus erythematosus, Hashimoto's thyroiditis, and polyarteritis nodosa (LEVINE et al. 1978).

In CT findings of the thymus in a series of 22 patients with myasthenia gravis and lymphoid follicular hyperplasia, 10 had a normal appearance, 7 had an enlarged thymus, and 5 had a focal thymic mass (NICOLAOU et al. 1996). The usefulness of CT to establish the diagnosis of lymphoid follicular hyperplasia is limited. Also on MRI, thymic hyperplasia appears as diffuse enlargement of the thymus with MR signals similar to those of normal thymus (MOLIN et al. 1990).

True thymic hyperplasia is defined as an increase in size of the thymus with normal gross and histologic appearance, and commonly occurs as a rebound phenomenon secondary to atrophy caused by chemotherapy for malignancy, corticosteroid therapy, and radiotherapy (LINEGAR et al. 1993). In patients younger than 35 years

and especially in children, the thymus may exhibit rebound to a size significantly larger than its original size (CHOYKE et al. 1987). When rebound thymic hyperplasia occurs in patients who previously underwent chemotherapy for malignancy, distinction of thymic rebound from recurrent neoplasm may be difficult. Clinically, thymic rebound is most problematic when it is seen in patients with malignant lymphoma who had undergone chemotherapy.

On CT and MRI, rebound thymic hyperplasia appears as an enlargement of the thymus and its attenuation at CT and signal at MRI are similar to those of normal thymus (SIEGEL et al. 1989). In patients with enlarged thymus older than 15 years of age, chemical-shift MRI can diagnose thymic hyperplasia by detecting fatty infiltration within the thymus and is useful in its differentiation from neoplastic process (TAKAHASHI et al. 2002; INAOKA et al. 2007). In a series of 41 patients of whom 23 had thymic hyperplasia and 18 thymic neoplasm, chemical-shift MRI could differentiate thymic hyperplasia from thymic neoplasms in all patients. All patients with hyperplastic thymus showed an apparent decrease in the signal intensity of the thymus at opposed-phase images in contrast to in-phase images, while none of the patients with thymic tumors showed a decrease in signal intensity at opposed-phase images (INAOKA et al. 2007) (Figs. 12.10, 12.11).

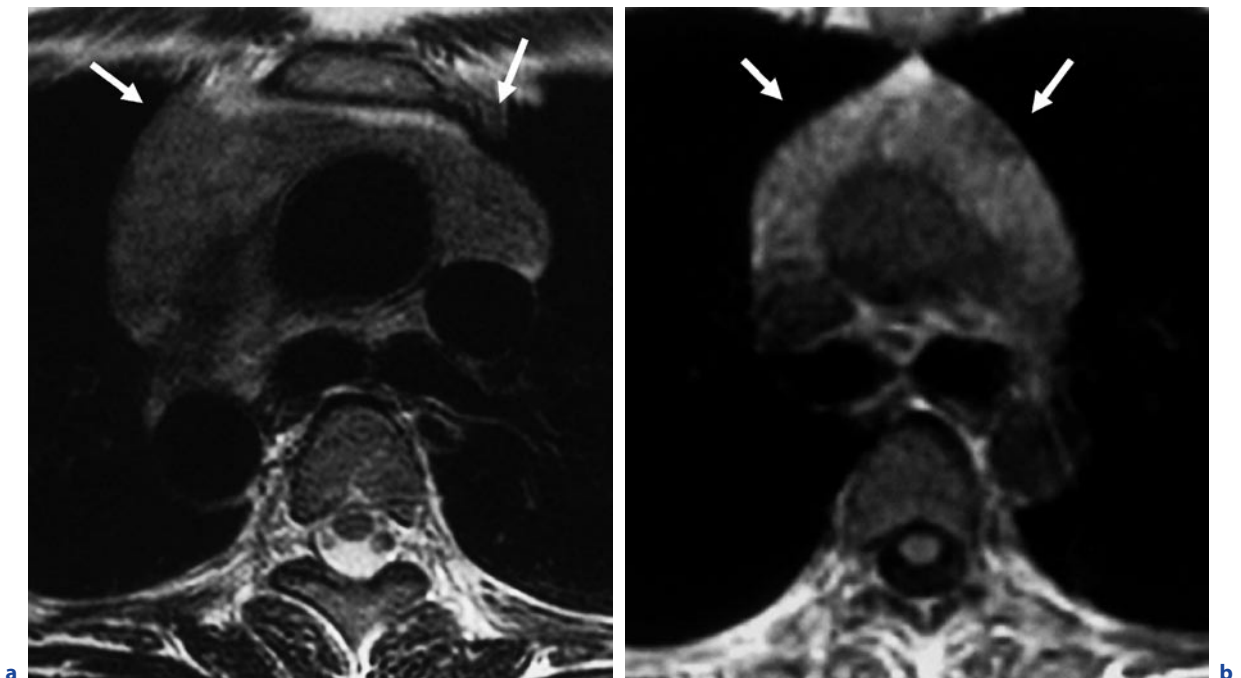


Fig. 12.10a–c. Thymic hyperplasia in hyperthyroidism at 25-year-old woman. T2-weighted (a) and in-phase (b) and opposed-phase (c) gradient-echo T1-weighted MR images. The

thymus is diffusely enlarged but shows decrease in signal at opposed-phase image (c) in contrast to in-phase image (b), due to physiologic fatty infiltration within the thymus (arrows)



Fig. 12.10a–c. (continued) Thymic hyperplasia in hyperthyroidism at 25-year-old woman. T2-weighted (a) and in-phase (b) and opposed-phase (c) gradient-echo T1-weighted MR images. The thymus is diffusely enlarged but shows decrease in signal at opposed-phase image (c) in contrast to in-phase image (b), due to physiologic fatty infiltration within the thymus (arrows)

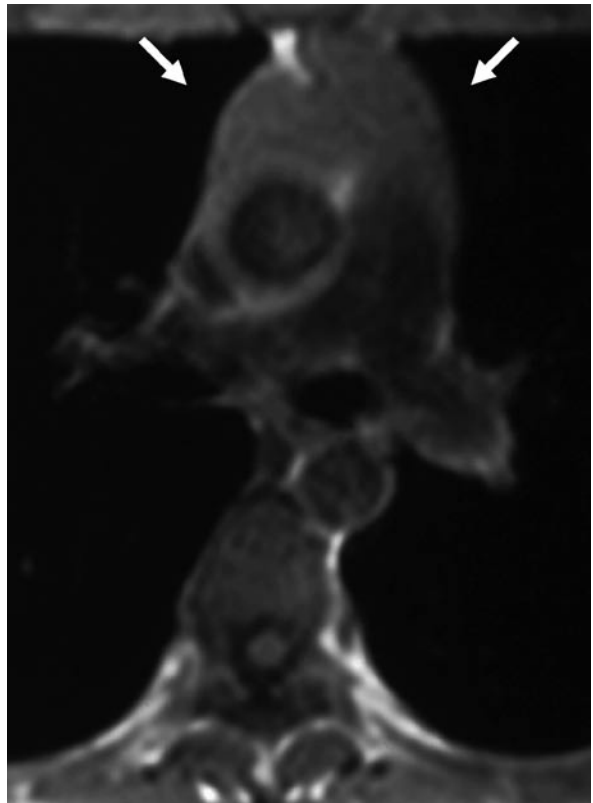
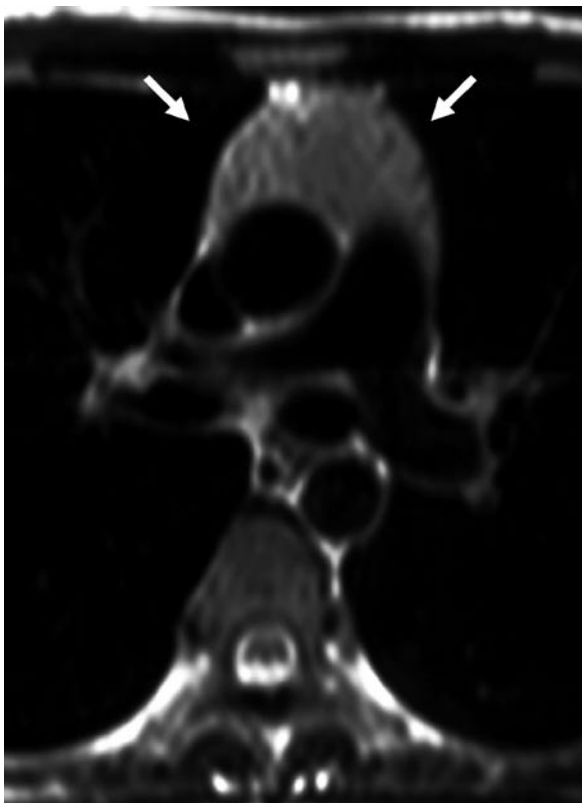


Fig. 12.11a–c. Noninvasive thymoma. T2-weighted (a), in-phase (b) and opposed-phase (c) gradient-echo T1-weighted MR images. A lobulated mass lesion is depicted in the anterior

mediastinum. In contrast to in-phase image (b), the thymoma does not show a significant decrease in signal on the opposed-phase image (c) (arrow)

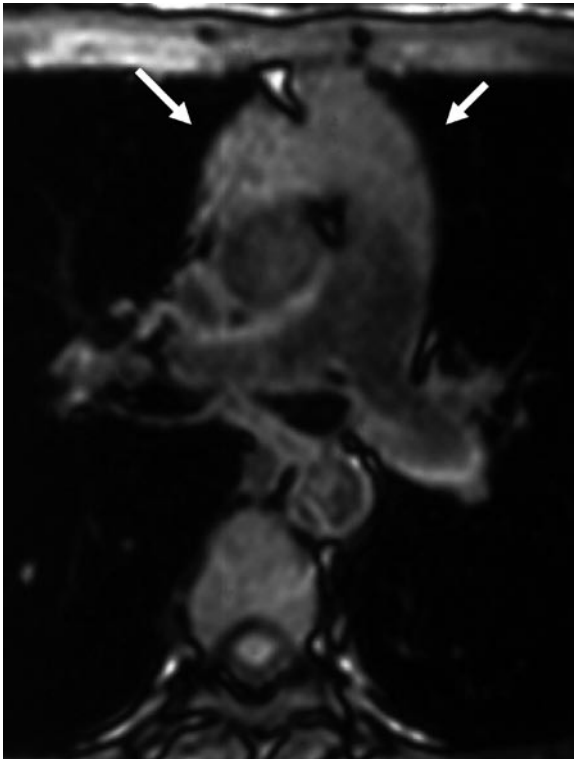


Fig. 12.11. (continued) Noninvasive thymoma. T2-weighted (a), in-phase (b) and opposed-phase (c) gradient-echo T1-weighted MR images. A lobulated mass lesion is depicted in the anterior mediastinum. In contrast to in-phase image (b), the thymoma does not show a significant decrease in signal on the opposed-phase image (c) (arrow)

12.3.3 Thymoma

Thymoma is the most common primary tumor in the entire mediastinum, and it comprises approximately 20% of all mediastinal tumors (HOFFMAN et al. 1993). Thymoma is a benign or low-grade malignant tumor of the thymic epithelium, frequently associated with a variable population of immature but non-neoplastic T-cell lymphocytes. It is divided into an encapsulated noninvasive type and an invasive type that has spread beyond the capsule. Fifteen to 40% of thymomas show invasion beyond the capsule and turn out to be of the invasive type. Invasive thymoma initially invades the adjacent mediastinal fat and eventually spreads to the pleura, pericardium, lung, or mediastinal vessels.

Thymomas most commonly arise in the upper part of the anterior mediastinum: anterior to the ascending

aorta, the right ventricular outflow tract, and the main pulmonary artery. Uncommon location of thymoma includes inferior mediastinum as low as the cardiophrenic angle, middle or posterior mediastinum, lower and upper neck as high as the submandibular region, or lung parenchyma (NAGASAWA et al. 2004; YAMAZAKI et al. 2007; HUANG et al. 2007).

Thymomas usually occur in middle-aged adults, and the average age at diagnosis is approximately 50 years (LEWIS et al. 1987). Thymomas are unusual below the age of 20 and extremely rare under the age of 15 years. Patients with encapsulated thymoma are usually asymptomatic but may have symptoms such as chest pain, cough, dyspnea, dysphagia, or hoarseness due to compression to the adjacent structures. Most patients with invasive thymoma have clinical symptoms due to its invasion. Thymomas are occasionally associated with paraneoplastic syndrome, and myasthenia gravis is the most common disease. Approximately 10–23% of patients with myasthenia gravis have thymoma, and 35–40% of patients with thymoma have myasthenia. Other paraneoplastic syndromes associated with thymoma include pure red cell aplasia, acquired hypogammaglobulinemia, and non-thymic cancers.

Most thymomas show a lobulated external contour and are either completely or partially encapsulated by fibrous capsule. The capsule connects with fibrous band within the tumor that divides it into multiple lobules. Cystic change, hemorrhage, and necrosis are relatively common, and sometimes the tumor may be entirely cystic.

The World Health Organization (WHO) proposed a consensus classification of thymic epithelial tumors which is based on the morphology of epithelial cells and on the lymphocyte-to-epithelial cell ratio in 1999 (ROSAI and SOBIN 1999). In 2004, WHO updated the classification (TRAVIS et al. 2004). In the latest classification (Table 12.1), the thymic epithelial tumors are classified into two major categories, five types of thymomas (types A, AB, B1, B2, and B3) and thymic carcinomas (various histologic types of carcinomas including neuroendocrine carcinoma). Thymomas were divided into two groups, depending on whether the neoplastic epithelial cells and their nuclei have a spindle and/or oval shape (type A) or whether these cells have a dendritic or plump (epithelioid) appearance (type B). Tumors that combine these two morphologies are designated type AB. Type B tumors were subdivided further into three subtypes, designated B1, B2, and B3, respectively, on the basis of the proportional increase of the epithelial component and the emergence of atypia of the neoplastic cells.

Table 12.1. Definitions of World Health Organization classification of thymic epithelial tumors (according to TRAVIS et al. 2004)

| Thymoma type | Definition |
|------------------|--|
| A | An organotypical thymic epithelial neoplasm composed of bland spindle/oval epithelial tumor cells with few or no lymphocytes |
| AB | An organotypical thymic epithelial neoplasm composed of a mixture of a lymphocyte-poor type A thymoma component and a more lymphocyte-rich type B-like component. Both components are present in most sections |
| B1 | A tumor of thymic epithelial cells with a histological appearance, practically indistinguishable from the normal thymus composed predominantly of areas resembling cortex with epithelial cells scattered in a prominent population of immature lymphocytes, and areas of medullary differentiation, with or without Hassall's corpuscles, similar to normal thymic medulla |
| B2 | An organotypical thymic epithelial neoplasm composed of large, polygonal tumor cells that are arranged in a loose network and exhibit large vascular nuclei with prominent large nucleoli, closely resembling the predominant epithelial cells of the normal thymic cortex. A background population of immature T cells is always present and usually outnumbers the neoplastic epithelial cells |
| B3 | An organotypical thymic epithelial neoplasm predominantly composed of medium-sized round or polygonal cells with slight atypia. The epithelial cells are mixed with a minor component of intraepithelial lymphocytes, resulting in a sheet-like growth of epithelial cell |
| Thymic carcinoma | All non-organotypical malignant epithelial neoplasms other than germ cell tumors are designated thymic carcinomas. Thymic carcinomas are termed according to their differentiation (squamous cell, mucoepidermoid, etc.). The term <i>type C thymoma</i> in the previous classification was eliminated. Thymic carcinomas lack immature T-lymphocytes |

It has been suggested that the WHO classification reflects both the clinical and the functional features of thymic epithelial tumors and significantly correlates with the invasiveness and the prognosis of thymic epithelial tumors (CHEN et al. 2002; OKUMURA et al. 2002; KONDO et al. 2003). A review of 273 patients with thymoma on the prognostic significance of the WHO classification system reported that in patients with type A, AB, B1, B2, and B3 tumors, the respective proportions of invasive tumor were 11.1, 41.6, 47.3, 69.1, and 84.6%; the respective proportions of tumors with involvement of the great vessels were 0, 3.9, 7.3, 17.5, and 19.2%; and the respective 20-year survival rates were 100, 87, 91, 59, and 36% (OKUMURA et al. 2002). In a review of 200 patients with thymic epithelial tumors, 5-year survival rates of each subtype of WHO classification were 100% in type A thymoma, 100% in type AB, 94.1% in type B1, 75.0% in type B2, and 70.0% in type B3, and 48.0% in thymic carcinoma (CHEN et al. 2002). Based on a significant correlation of the WHO histological classification and prognosis, the thymic epithelial tumors can

be divided into three main groups: low-risk thymomas (types A, AB, B1), high-risk thymomas (types B2 and B3), and thymic carcinomas (JEONG et al. 2004).

For the clinical staging of thymic epithelial tumors, criteria (MASAOKA et al. 1981) (Table 12.2), which were based on the presence of invasion of the surrounding organs, have widely been accepted and modifications were suggested by SHIMOSATO and MUKAI (1997). The staging significantly correlates with the prognosis and the 20-year survival rates were 89, 91, 49, 0, and 0% in patients with stage I, II, III, IVa, and IVb disease, respectively (OKUMURA et al. 2002). By multivariate analysis, WHO histologic classification and Masaoka's clinical staging were independent prognostic factors (CHEN et al. 2002; OKUMURA et al. 2002; KONDO et al. 2003).

On CT, thymomas usually present as sharply demarcated round or oval soft tissue masses in the region of the thymus. Tumors commonly reveal soft tissue attenuation and mild to moderate contrast enhancement. Occasionally, focal low attenuation areas are identified within tumors, reflecting hemorrhage, necrosis, or cyst

Table 12.2. Clinical staging of thymic epithelial tumors (according to MASAOKA et al. 1981)

| Stage | Description |
|-------|---|
| I | Macroscopically completely encapsulated and microscopically no capsular invasion |
| II:1 | Macroscopic invasion into surrounding fatty tissue or mediastinal pleura |
| II:2 | Microscopic invasion into capsule |
| III | Macroscopic invasion into neighboring organs, i.e., pericardium, great vessels, or lung |
| IVa | Pleural or pericardial dissemination |
| IVb | Lymphogenous or hematogenous metastasis |

formation. Rarely, a tumor appears entirely cystic. Linear or ring-like calcifications are occasionally seen in both encapsulated and invasive thymoma.

On MR images, thymomas typically appear as round, oval, or lobulated masses with a low signal intensity on T1-weighted images similar to that of muscle and relatively high signal intensity on T2-weighted images. T2-weighted images occasionally show scattered high-intensity regions and/or lobulated internal architecture within the tumors, which corresponded to cystic regions and fibrous septa, respectively, on pathologic specimens (Fig. 12.12). On T1-weighted images, the signal intensity of cystic regions was variable, depending on the protein content of the cyst fluid or the presence of hemorrhage (SAKAI et al. 1992).

Invasive thymomas invade the mediastinum beyond the capsule and occasionally spread to the pleura and pericardium. Although CT and MRI cannot detect minimal mediastinal invasion, it sometime allows distinction between invasive and noninvasive thymoma. Complete obliteration of the adjacent fat planes highly suggests mediastinal invasion (Fig. 12.13), while partial obliteration is indeterminate. Complete preservation of adjacent fat planes usually excludes extensive invasive disease but not minimal capsular invasion (CHEN et al. 1988). Transpleural spread either as a sheet of tumor or drop metastasis is a diagnostic finding of invasive thymoma (Fig. 12.14). Previous studies suggested MRI to be superior to CT in patients with invasive thymoma for defining invasion of contiguous structures: pleura, lung, and pericardium (FUJIMOTO et al. 1992; GUALDI et al. 1994; PIRRONTI et al. 2002). MRI may be more efficient than CT in detecting tumor recurrence during postoperative follow-up in patients with invasive thymoma (PIRRONTI et al. 2002).

On the assessment of anterior mediastinal tumors, dynamic contrast-enhanced MRI has been suggested to be useful in the differentiation between thymomas and non-thymomas including, thymic carcinoma, malignant lymphoma, and malignant germ cell tumor. On dynamic MRI, thymoma tended to reach a peak in the time intensity curve relatively early and other mediastinal tumors relatively late. A cut-off point in the time intensity curve of 2–2.5 min could be used to differentiate thymomas and non-thymomas (SAKAI et al. 2002).

Myasthenia gravis (MG) is commonly associated with thymic pathologies, including lymphoid follicular hyperplasia in 65–77%, and thymoma in 15–30% (PIRRONTI et al. 2002). It is generally agreed that thymectomy is indicated in patients affected by generalized MG between the age of puberty and 50–60 years. Thymectomy is most likely to be effective in young female patients with a disease of short duration, and its effectiveness is still under discussion in seronegative MG, ocular MG, and elderly patients with MG, whereas thymectomy is indicated in all patients who have thymoma. Therefore, the role of radiologic assessment in MG patients is detection of thymomas and their differentiation from thymic hyperplasia.

In a study of 104 patients with MG who underwent thymectomy, CT showed thymoma in 46 of 52 patients (sensitivity of 88.5% and specificity of 95%) and thymic hyperplasia in 16 of 44 (sensitivity of 36% and specificity of 95%) (PIRRONTI et al. 2002). In a study of 16 patients with MG, MRI provided little information as compared with CT (BATRA et al. 1987). A recent report suggested chemical-shift MRI to be beneficial in differentiation of thymomas from thymic hyperplasia in non-MG patients (INAOKA et al. 2007). Although no report has been published, MRI may provide similar information also in MG patients.

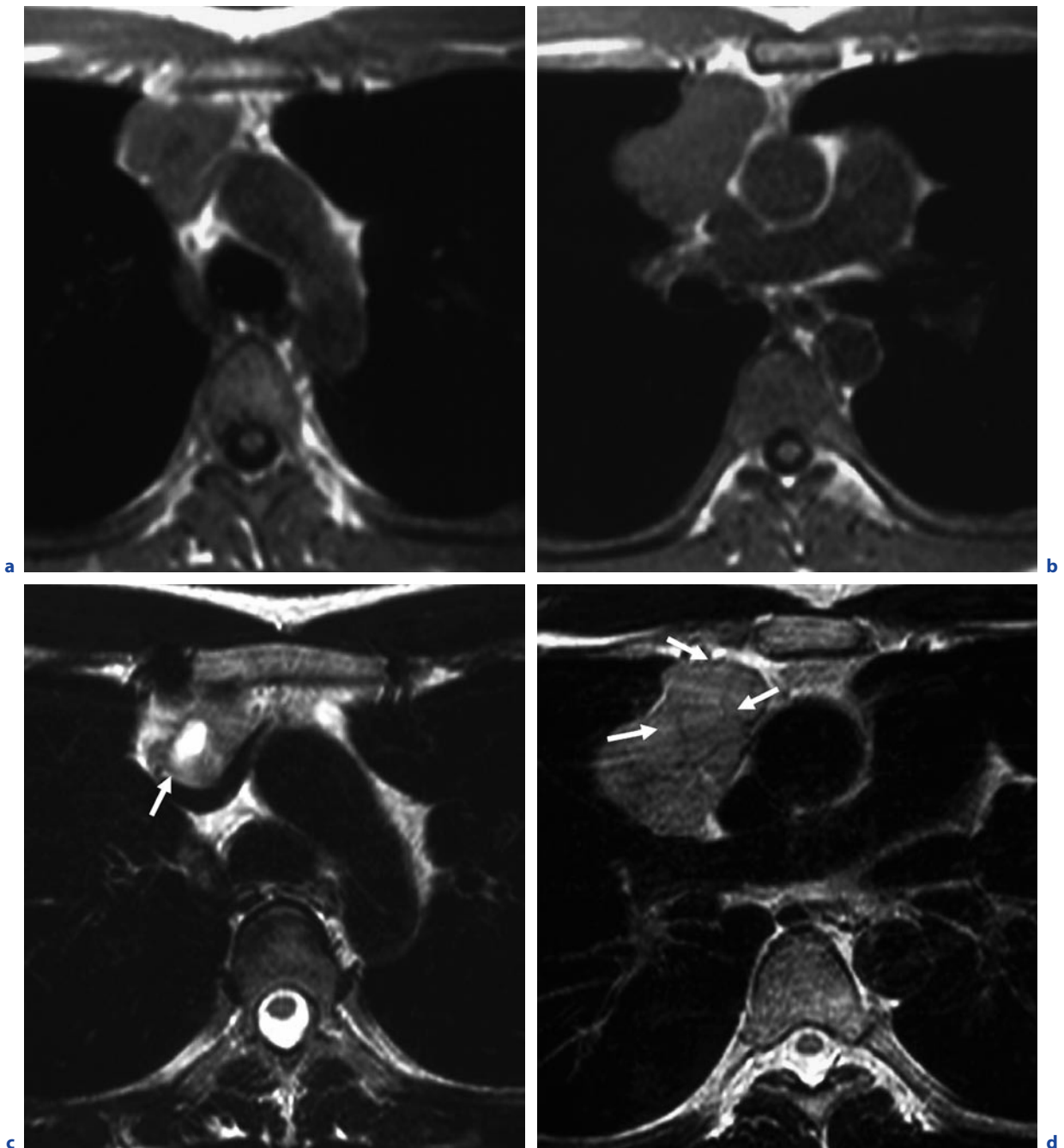


Fig. 12.12a–d. Noninvasive thymoma. T1-weighted (**a,b**) and T2-weighted (**c,d**) MR images show a lobulated mass lesion in the anterior mediastinum, which reveals low signal intensity similar to that of muscle on T1-weighted images (**a,b**) and

relatively high signal intensity on T2-weighted images (**c,d**). A high-signal region (**c** arrow) and internal, linear low-signal intensity (**d** arrow) within the lesion on T2-weighted images represent cystic changes and fibrous septa, respectively

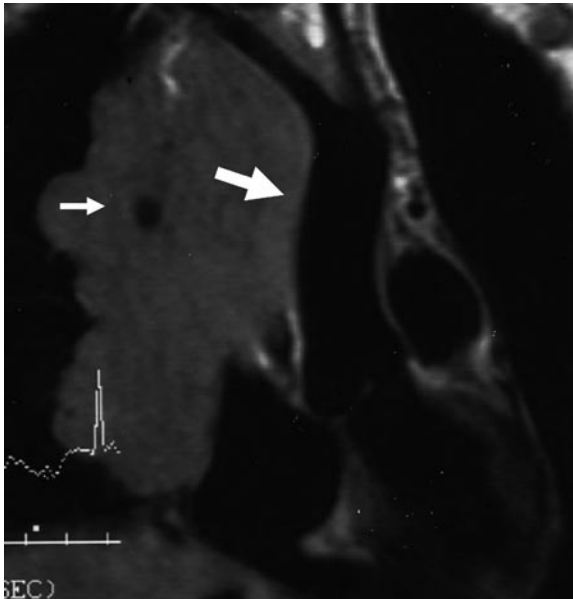


Fig. 12.13. Invasive thymoma. T1-weighted coronal MR image shows the tumor extending along and invading the mediastinal vessels, including superior vena cava (*small arrow*) and aorta (*medium arrow*)

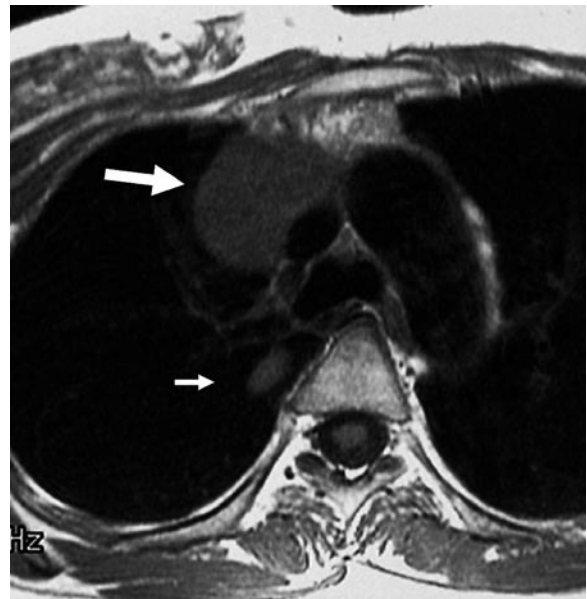


Fig. 12.14. Invasive thymoma. T1-weighted axial MR image shows a mass in the anterior mediastinum (*large arrow*) and drop metastasis at the right major fissure (*small arrow*)

12.3.4 Thymic Carcinoma

Thymic carcinoma is a thymic epithelial tumor with a high degree of histologic anaplasia, obvious cell atypia, and increased proliferative activity and is unassociated with immature T cells (SHIMOSATO and MUKAI 1997). The most common histologic variety is epidermoid or squamous cell carcinoma: following lymphoepithelioma-like carcinoma, and anaplastic or undifferentiated carcinomas.

Thymic carcinomas predominantly occur in adults and are associated with poor prognosis, even when treated with surgery and radiotherapy. At the time of diagnosis, most patients suffer from chest pain, dyspnea, cough, fever, weight loss, and superior vena cava syndrome (HARTMANN et al. 1990). A paraneoplastic syndrome is uncommon in thymic carcinomas. Thymic carcinomas occasionally infiltrate adjacent tissue and mediastinal vascular structures, or extend into the pleura, lungs, and the pericardium.

Although thymic carcinoma shows similar imaging findings to thymoma, thymic carcinomas were more commonly associated with mediastinal lymph nodes and extrathoracic metastases, but less commonly associated with pleural implants than invasive thymoma

(Do et al. 1995). JEONG et al. (2004) correlated CT findings of thymic epithelial tumors with WHO histopathologic subtypes. A lobulated contour was more often seen in high-risk thymomas (types B2 and B3) and thymic carcinomas than in low-risk thymomas (types A, AB, and B1). Mediastinal fat invasion was more often seen in thymic carcinomas than in low-risk thymomas.

In the review of MRI of 64 patients with thymic epithelial tumors, foci of low signal intensity in the mass on T2-weighted images and mediastinal lymphadenopathy were highly suggestive of thymic carcinomas (Fig. 12.15). Most of foci of low signal intensity within the tumor on T2-weighted images were collagenous tissue on pathological examinations (INOUE et al. 2006).

SADOHARA et al. (2006) assessed correlation of MR findings with three main groups of WHO histologic classification: low-risk thymomas (types A, AB, B1), high-risk thymomas (types B2 and B3), and thymic carcinomas. Thymic carcinomas were more likely to have irregular contours (75%) than were low-risk thymomas (3%) and high-risk thymomas (22%). Complete or almost complete capsule was seen in low-risk thymomas (27%) and high-risk thymomas (17%) but not in thymic carcinomas (0%). A septum was more frequently seen in low-risk (57%) and high-risk thymomas (44%) than in thymic carcinomas (8%). A necrotic or cystic com-

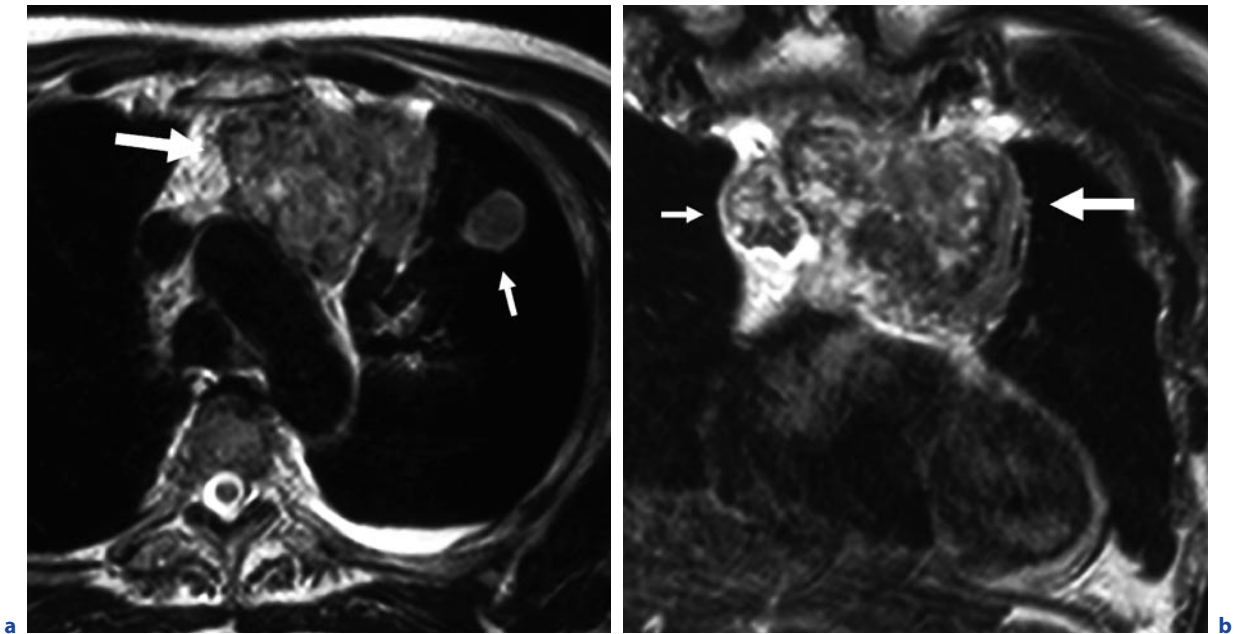


Fig. 12.15a,b. Thymic carcinoma. T2-weighted axial (**a**) and coronal (**b**) MR images show an irregular-shaped mass in the anterior mediastinum. The tumor shows heterogeneous signal intensity with foci of low signal intensity on T2-weighted im-

age. Left-sided pleural effusion with drop metastasis (**a** arrow) and mediastinal lymphadenopathy (**b** arrow) are also demonstrated

ponent was more frequently seen in thymic carcinomas (67%) than in low-risk thymomas (20%) and high-risk thymomas (28%). Thymic carcinomas had a higher prevalence of heterogeneous signal intensity (100%) than had low-risk thymomas (33%) and high-risk thymomas (56%).

12.3.5 Thymolipoma

Thymolipoma is a rare benign tumor composed of mature fat tissue and normal or involuted thymic tissue. The tumors commonly occur low in the anterior mediastinum and often in the cardiophrenic angle. The average age of the patients is 22–26 years, and most patients are asymptomatic (ROSADO-DE-CHRISTENSON et al. 1994).

On CT, thymolipomas appear as well-circumscribed masses that contain fat tissue intermingled with linear bands of soft tissue. The soft tissue histopathologically represents thymic tissue or fibrous septa. The amount of fat relative to the thymic tissue is variable.

On MRI, the fat tissue within the tumors appears as an area of high signal intensity, and the soft tissue component appears lower signal intensity bands that course

through the mass (ROSADO-DE-CHRISTENSON et al. 1994; SHIRKHODA et al. 1987).

12.3.6 Thymic Neuroendocrine Neoplasm

Primary neuroendocrine tumors of the thymus, previously known as carcinoid tumors of the thymus, are rare and account for less than 5% of all anterior mediastinal tumors. Unlike carcinoids arising from the lungs, these tumors in the thymus are highly aggressive, and nearly 80% of cases have been found to be malignant (CHAER et al. 2002). Based on histopathological findings, such as mitotic count, amount of necrosis, preservation of neuroendocrine architecture, and degree of cytologic atypia, KLEMM and MORAN (1999) have proposed a classification into well-differentiated, moderately differentiated, and poorly differentiated neuroendocrine neoplasms (TIFFET et al. 2003).

The mean age of the previously reported cases is 54 years. Nearly a third of patients are asymptomatic, and the remaining patients have symptoms resulting from a rapidly expanding mediastinal tumor. At least 20% of patients have distant metastases at presentation most commonly to the liver, lung, bone, pleura, and pancreas

(CHAER et al. 2002). Approximately 40% of patients have Cushing syndrome as a result of tumor secretion of adrenocorticotrophic hormone (DOPPMAN et al. 1989), and up to 20% have multiple endocrine neoplasia (MEN) syndromes I and II (FEROLLA et al. 2005). In the literature, the overall survival rate at 5 years ranged from 31 to 82% (TIFFET et al. 2003). As prognostic factors, unresectability and advanced clinical stage have been reported to be associated with poor survival (GAL et al. 2001).

Thymic neuroendocrine tumors do not differ significantly from thymoma in radiologic findings on CT and MRI. Neuroendocrine tumors are more aggressive than is thymoma and often presenting in advanced stage, and superior vena cava obstruction is much more common with this tumor than is with thymoma. On CT or MRI, the tumors appear as a lobulated thymic mass with heterogeneous enhancement and central areas of low attenuation secondary to necrosis or hemorrhage and may show local invasion (CHAER et al. 2002) (Fig.12. 16). Bone metastases are typically osteoblastic.

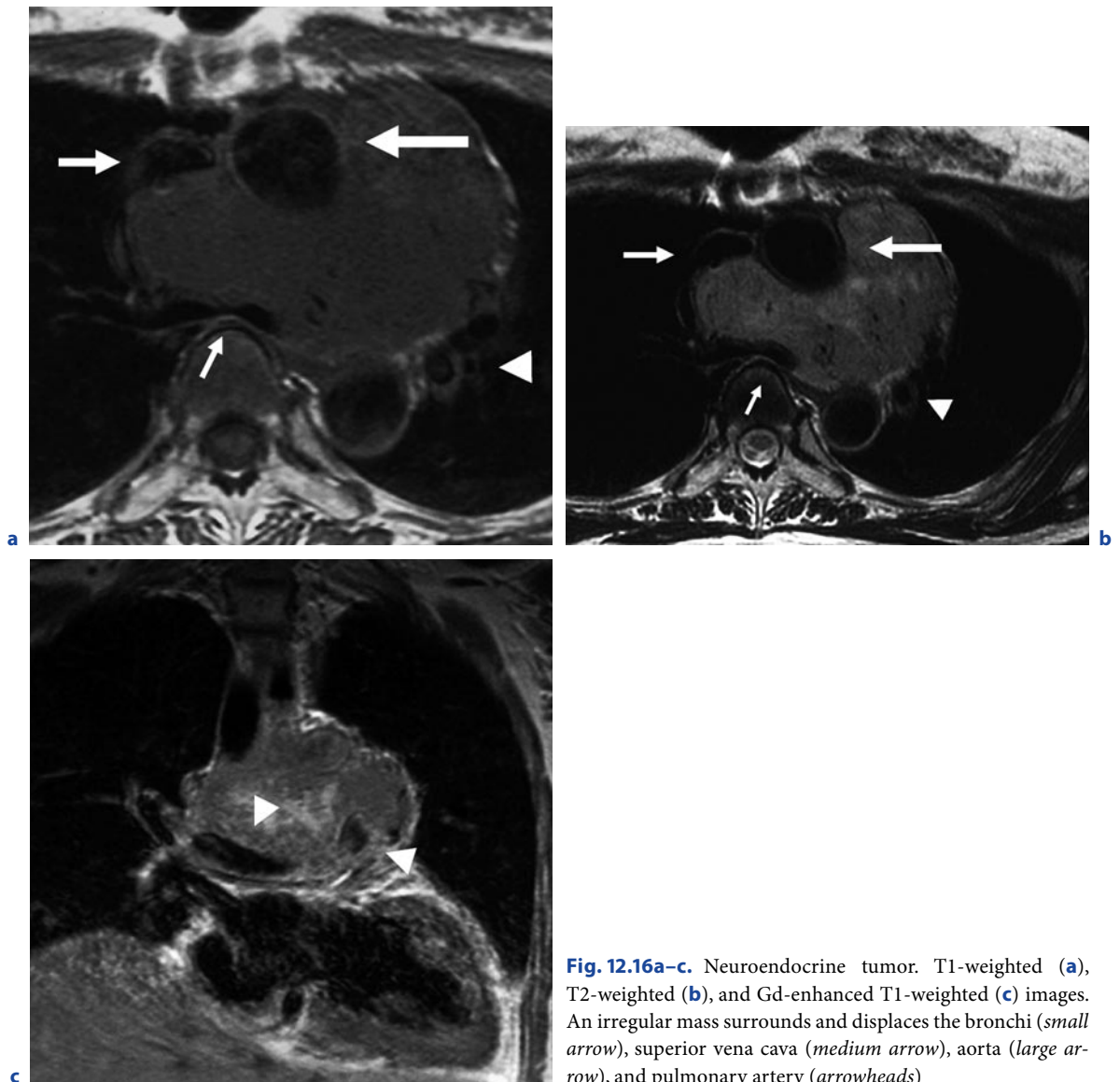


Fig. 12.16a–c. Neuroendocrine tumor. T1-weighted (a), T2-weighted (b), and Gd-enhanced T1-weighted (c) images. An irregular mass surrounds and displaces the bronchi (small arrow), superior vena cava (medium arrow), aorta (large arrow), and pulmonary artery (arrowheads)

12.4

Mediastinal Germ Cell Tumors

Germ cell tumors are believed to develop from a germ cell during the process of maturation of a primordial germ cell into a gamete. The tumors arise not only mainly in the gonads, but also in the midline of the body, including pineal region, anterior mediastinum, retroperitoneum, and sacrococcygeal region (SHIMOSATO and MUKAI 1997). The mediastinum is the most common site of extragonadal germ cell tumors. The vast majority of mediastinal germ cell tumors arises within the anterior mediastinum, within or in the proximity of the thymus, and only 3% of them arise within the posterior mediastinum (DEHNER 1983). Germ cell tumors include teratoma (mature, immature, and with malignant transformation), seminoma, embryonal carcinoma, endodermal sinus tumor, choriocarcinoma, and mixed germ cell tumor. Mature teratoma is the most common histologic type of mediastinal germ cell tumors and accounts for 75% of them. Seminoma is the most common malignant subtype. In this text, we divide mediastinal germ cell tumors into three subgroups: teratoma, seminoma, and nonseminomatous malignant germ cell tumor.

Germ cell tumors usually occur in young adults (mean age 27 years) (ERASMUS et al. 2000). Malignant germ cell tumors are more common in men. To make a diagnosis of primary mediastinal germ cell tumors, the possibility of gonadal germ cell tumors should be clinically excluded. The important differential point is that gonadal germ cell tumors involving the mediastinum almost always have concomitant retroperitoneal lymph node metastases.

12.4.1

Teratoma

Teratomas contain elements of all three germ cell layers: ectoderm, endoderm, and mesoderm and are frequently referred to “dermoid cyst,” due to the frequent expression of the ectodermal component of the teratoma. Ectodermal elements may be represented by skin, teeth, and hair; mesodermal elements by bone, cartilage, and muscle; and endodermal elements by bronchial, gastrointestinal or pancreatic tissue. Histologically, teratoma can be divided into mature teratoma, immature teratoma, and teratoma with malignant transformation.

Mature teratomas are usually unilocular or multilocular cystic lesions and consist predominantly of ectoderm elements including skin and its appendages,

which are followed in order of frequency by bronchial tissue, gastrointestinal mucosa, smooth muscle, fat, bone, cartilage, and pancreatic tissue (SHIMOSATO and MUKAI 1997). The presence of pancreatic tissue is unique in teratomas in the mediastinum, while it is not seen in those of the gonads. Although mature teratoma is usually silent, symptoms are due to local compression, rupture, or infection and include chest pain, cough, dyspnea, and fever.

A mature teratoma is a well-demarcated, occasionally lobulated anterior mediastinal mass on radiographs. On CT, mature teratoma most commonly appears as a well-defined cystic lesion containing fluid, soft tissue, and fat attenuation. Calcifications of various morphological configurations also may be present within the lesion, and a tooth or a part of bone is rarely seen. Common combinations of internal components of mature teratomas include soft tissue, fluid, fat, and calcium in 39%; soft tissue, fluid, and fat in 24%; and soft tissue and fluid in 15% of cases (MOELLER et al. 1997). In 15% of cases, mature teratomas appear as nonspecific cystic lesions without fat or calcium. However, a capsule of teratoma is characteristically thickened, whereas that of other cystic lesions in the mediastinum is usually thin (TAKAHASHI et al. 1998).

MRI typically demonstrates heterogeneous signal intensity, representing various internal elements, and this finding can be useful in differentiating teratomas from thymomas and lymphomas (ERASMUS et al. 2000; DREVELEGAS et al. 2001). The soft tissue elements reveal isointensity with muscle, cystic components show low intensity on T1-weighted images and high intensity on T2-weighted images, and fat elements appear as a high intensity area on T1-weighted images (Figs. 12.17, 12.18). The finding of a fat-fluid level within the lesion on MRI is diagnostic of a teratoma.

Mediastinal mature teratomas may be associated with complications such as atelectasis or obstructive pneumonitis due to airway compression, pneumonitis due to rupture into the lung, and effusion due to rupture into the pleural space or pericardium. Nearly 30% of mature teratomas have been reported to rupture into lung, pleural space, and pericardium and fat within these adjacent structures suggests this complication (SASAKA et al. 1998). Proteolytic or digestive enzymes derived from the tumor have been considered the cause of tumor rupture (DREVELEGAS et al. 2001).

Immature teratomas show various adult tissues derived from three germinal layers, but in addition, contain immature tissue, most commonly, primitive neuroepithelial tissue. Teratomas with malignant transformation contain foci of frankly malignant neoplasms such as angiosarcoma, rhabdomyosarcoma, adenocarcinoma,

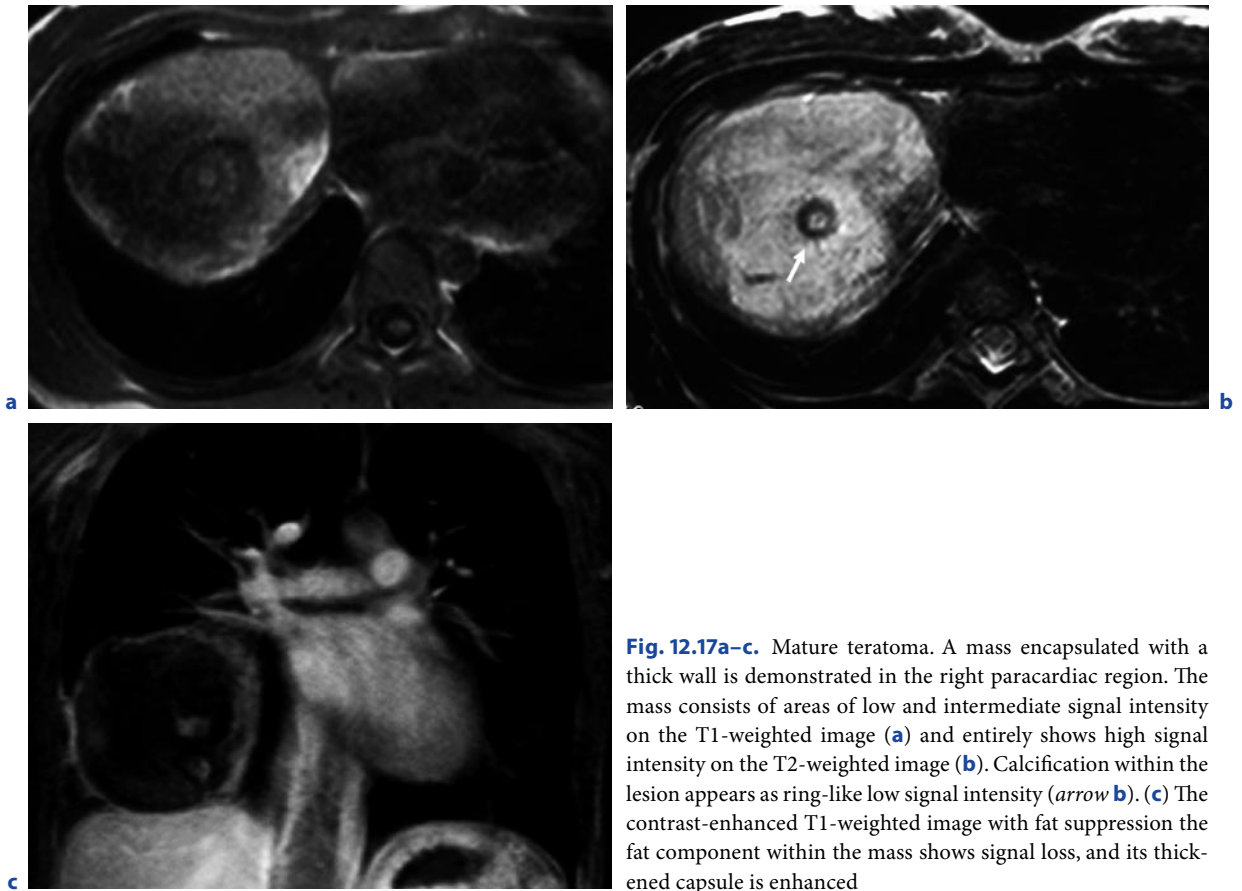


Fig. 12.17a-c. Mature teratoma. A mass encapsulated with a thick wall is demonstrated in the right paracardiac region. The mass consists of areas of low and intermediate signal intensity on the T1-weighted image (a) and entirely shows high signal intensity on the T2-weighted image (b). Calcification within the lesion appears as ring-like low signal intensity (arrow b). (c) The contrast-enhanced T1-weighted image with fat suppression the fat component within the mass shows signal loss, and its thickened capsule is enhanced

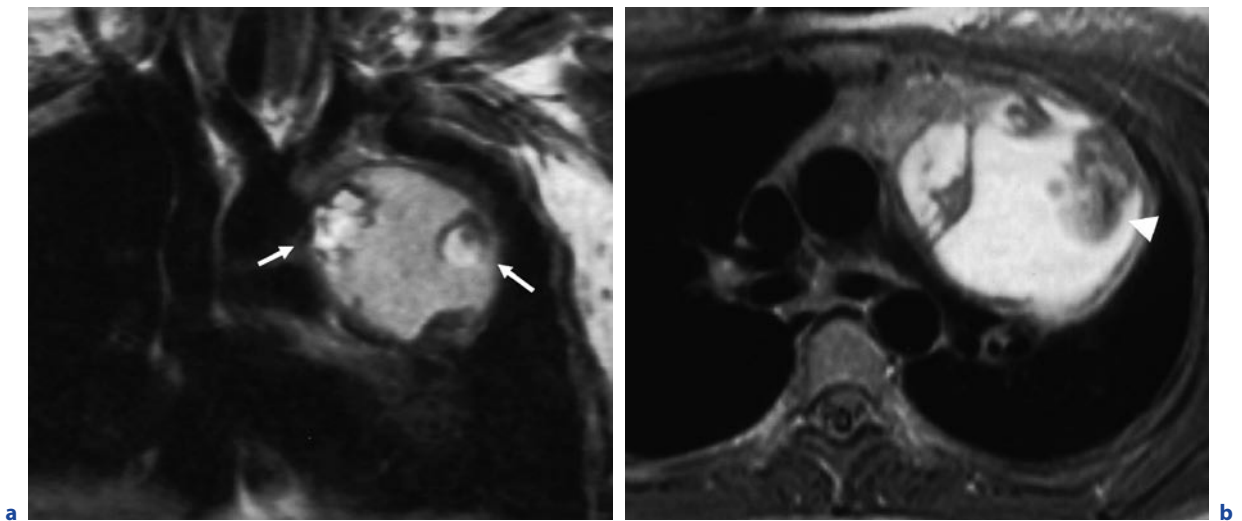


Fig. 12.18a,b. Mature teratoma. (a) T1-weighted image shows a mass lesion with a thick wall in the anterior mediastinum. Fat elements appear as a high-intensity area (arrow). Cystic components within the mass show high signal intensity on

the T2-weighted image (b). Soft tissue element shows relatively low intensity similar to muscle on both T1-weighted and T2-weighted images (short arrows a,b)

and squamous cell carcinoma. Most patients with immature teratoma and other malignant germ cell tumors are symptomatic, presenting with fatigue, weight loss, chest pain, cough, or dyspnea. Compared with benign teratomas, malignant teratomas are more likely to appear solid and poorly defined, compress adjacent structures, and less often contain fat (HOFFMAN et al. 1993; STROLLO and ROSADO-DE-CHRISTENSON 2002).

Mediastinal growing teratoma syndrome is an unusual phenomenon associated with the treatment of malignant teratoma or seminoma. When the lesions consist of teratoma and other germ cell tumors and are mixed with malignant and benign components, benign part of the tumors can enlarge after chemotherapy despite sterilization of malignant components with normalization of tumor markers (AFIFI et al. 1997; IYODA et al. 2000).

12.4.2 Seminoma

Seminoma (mediastinal germinoma) occurs almost exclusively in males during the period from the second to the fourth decade. Macroscopically, the tumor is well demarcated, large, and soft. The cut surface of the tumor is usually homogeneous but may show small foci of hemorrhage and necrosis (SHIMOSATO and MUKAI 1997). Symptoms are usually derived from presence of invasion to the adjacent mediastinal structures (airways and vessels) and include chest pain, shortness of breath, and superior vena cava syndrome.

The tumor appears as a large anterior mediastinal mass, which protrudes in one or both sides of the mediastinum. On CT and MRI, the tumor most typically appears as a well-demarcated anterior mediastinal mass lesion with homogeneous intermediate signal intensity that shows only slight enhancement after administration of contrast material (Fig. 12.19). Areas

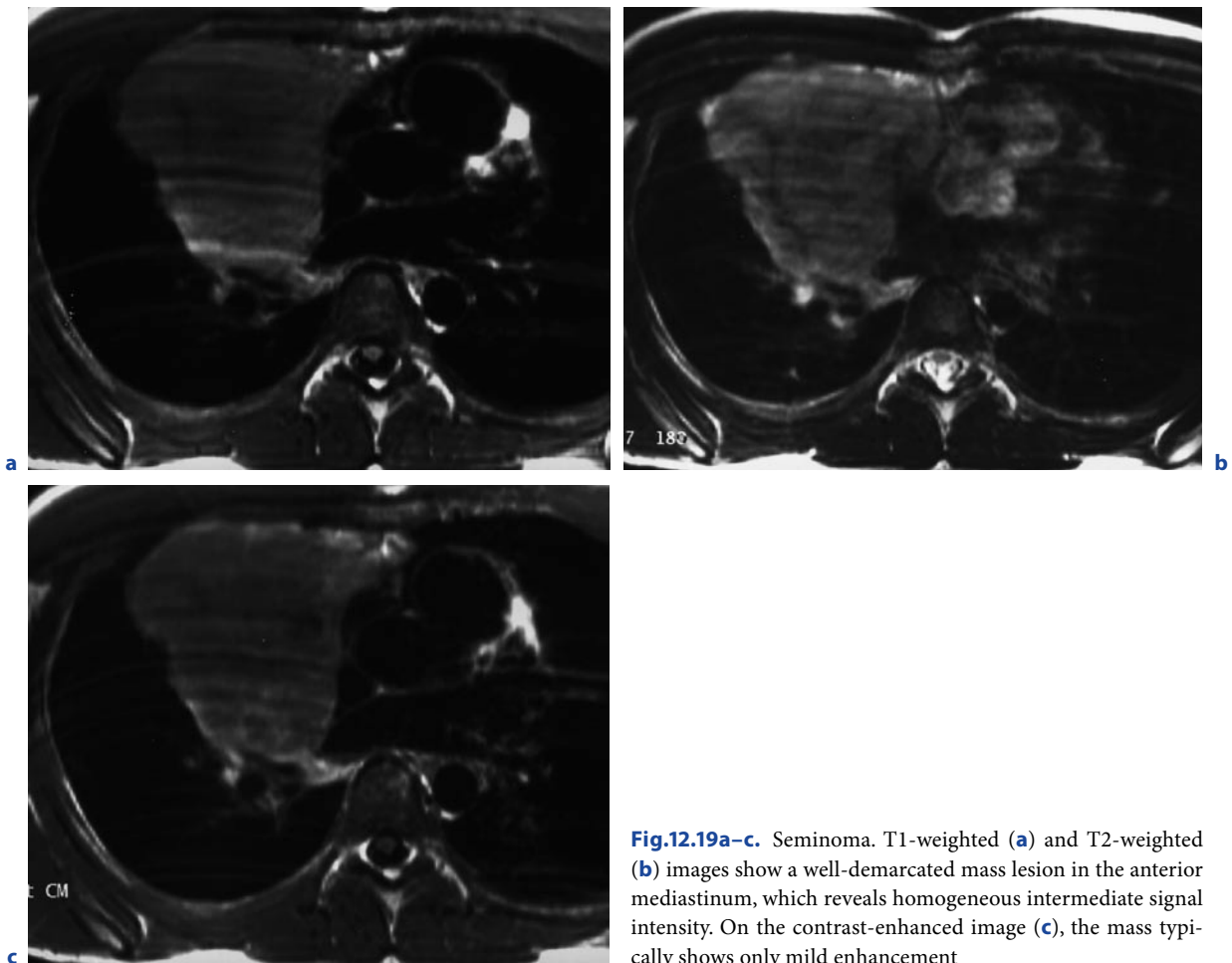


Fig.12.19a–c. Seminoma. T1-weighted (a) and T2-weighted (b) images show a well-demarcated mass lesion in the anterior mediastinum, which reveals homogeneous intermediate signal intensity. On the contrast-enhanced image (c), the mass typically shows only mild enhancement

of degeneration due to hemorrhage and coagulation necrosis may present but are usually limited (DREVELEGAS et al. 2001; LEE et al. 1989). Calcification and invasion of adjacent structures are uncommon (DREVELEGAS et al. 2001). Extension into the middle and posterior mediastinum and obliteration of the adjacent fat planes can be better evaluated by MRI (DREVELEGAS et al. 2001). Seminoma most commonly metastasizes to bone, lungs, liver, and thoracic lymph nodes.

12.4.3 Nonseminomatous Malignant Germ Cell Tumor

Nonseminomatous malignant germ cell tumors, including embryonal carcinoma, endodermal sinus (yolk sac) tumor, choriocarcinoma, and mixed types, are rare, highly malignant tumors that usually occur in young adults and are much more common in men than in women. Tumors are usually associated with symptoms

including chest pain, cough, fever, and dyspnea, and occasional elevation of tumor markers—alpha-fetoprotein (AFP) from endodermal sinus tumor, and embryonal carcinoma components and human chorionic gonadotropin (HCG) from choriocarcinoma component.

Tumors usually appear as a large anterior mediastinal mass on radiographs. On CT, the tumors consist of irregular soft tissue and multiple areas of low attenuation due to cystic necrosis and hemorrhage (DREVELEGAS et al. 2001; LEE et al. 1989). Obliteration of the adjacent fat planes and invasion of the adjacent structures may occasionally be seen. Metastases to the regional lymph nodes and distant sites are also common (SHIMOSATO and MUKAI 1997). On MRI, the tumors typically show internal heterogeneous intensities with areas of high signal intensity interspersed with areas of low signal intensity (SHIMOSATO and MUKAI 1997) (Fig. 12.20). Patients with Klinefelter's syndrome are predisposed to develop germ cell tumors of extragonadal origin.

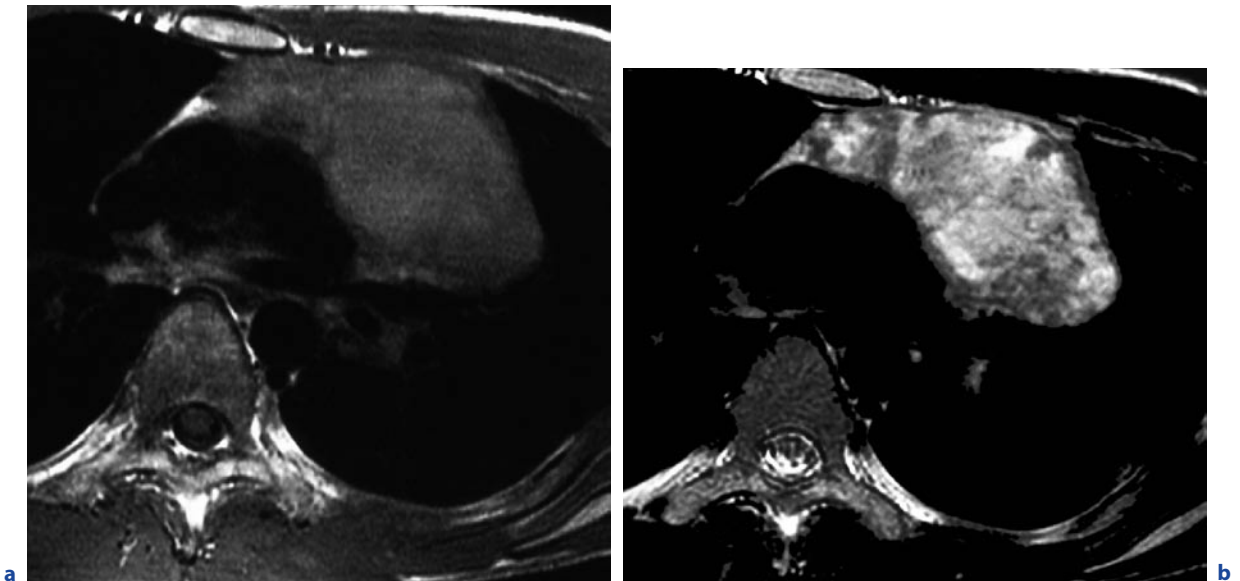


Fig. 12.20a–c. Nonseminomatous malignant germ cell tumor. (a) T1-weighted image shows a mass of intermediate signal intensity. (b) T2-weighted image typically shows heterogeneous signal intensity with areas of low, intermediate, and high signal

intensity. (c) Contrast-enhanced T1-weighted image shows little enhancement within the lesion, probably due to prominent degeneration by hemorrhage and cystic necrosis



Fig. 12.20a–c. (continued) Nonseminomatous malignant germ cell tumor. (c) Contrast-enhanced T1-weighted image shows little enhancement within the lesion, probably due to prominent degeneration by hemorrhage and cystic necrosis

12.5

Mediastinal Malignant Lymphoma

Malignant lymphoma accounts for nearly 20% of all mediastinum neoplasms in adults and 50% in children. Most often lymphoma involves the mediastinum secondary to generalized disease, while a mediastinal disease can also be a primary lesion. Hodgkin's disease is the most common primary mediastinal lymphoma. In non-Hodgkin's lymphoma, the two most common forms of primary mediastinal lymphoma are lymphoblastic lymphoma and diffuse large B-cell lymphoma, while virtually any histologic type of lymphoma may be identified. In addition to intrathoracic nodal disease, thymic involvement is also common in primary mediastinal lymphoma. Clinically, most malignant lymphomas of the mediastinum affect individuals younger than those with thymoma. Hodgkin's disease is staged using the Ann Arbor classification, which assesses the extent of nodal disease, the presence of extranodal disease, and clinical symptoms (CARBONE et al. 1971). In non-Hodgkin's lymphoma, the clinical course depends more on histologic grade and parameters, including bulk and specific organ involvement than on stage of disease.

12.5.1

Hodgkin's Disease

Hodgkin's disease is the most common lymphoma to manifest in the mediastinum and present with mediastinum adenopathy. Commonly involved lymph nodes are prevascular and paratracheal lymph nodes, followed by hilar nodes, subcarinal nodes, paracardiac nodes, internal mammary nodes, and posterior mediastinum nodes. In association with mediastinal lymphadenopathy, Hodgkin's disease also has a predilection to thymic involvement. Most patients are young female adults.

In the histologic subtypes, nodular sclerosis is by far the most common subtype and is characterized by orderly bands of interconnecting collagenous connective tissue that partially or entirely subdivides abnormal lymphoid tissue into isolated cellular nodules. The cellular proliferation within the nodules is polymorphic, with small and large lymphocytes, plasma cells, eosinophils, and histiocytes. The distinctive feature is the presence of Reed-Sternberg cells (SHIMOSATO and MUKAI 1997).

On CT, involved nodes are commonly well defined and of homogeneous soft tissue attenuation, while cystic and necrotic changes are identified within the nodes

in 10–21% of cases (POMBO et al. 1994). Thymic involvement is another common manifestation of Hodgkin's disease and thymic enlargement is seen in 40% of adult patients. Typically, thymic lesions manifest as an anterior mediastinal mass of homogeneous soft tissue attenuation, which shows gradually increasing mild to moderate contrast enhancement on CT. Direct extension of mediastinal lesion to the adjacent lung or chest wall is not uncommon in extensive mediastinal disease. Spread of lymph node disease is commonly contiguous to the adjacent lymph node groups, while skipping lymph node groups is unusual.

On T2-weighted MR images, involved nodes usually demonstrate homogeneous high signal intensity greater than that of muscle and similar to that of fat (RAHMOUNI et al. 2001). The lesions of Hodgkin's disease may reveal heterogeneous pattern with mixed areas of high and low signal intensity on T2-weighted images, which is typical of nodular sclerosing Hodgkin's disease with its histological feature comprising fibrotic areas

interspersed with more cellular areas. A thymic cyst may be present in association with Hodgkin's disease (Fig. 12.21).

12.5.2 Lymphoblastic Lymphoma

Lymphoblastic lymphoma mainly occurs in children and adolescents. Most tumors have features of thymic T cells on immunologic studies. Although lymphoblastic lymphoma and acute lymphoblastic leukemia show overlapping clinical, pathologic, cytogenetic, and molecular features, lymphoblastic lymphoma has no or minimal peripheral blood or bone marrow involvement, and lymphoblastic leukemia has predominant features of bone marrow and hematologic involvement (SHIMOSATO and MUKAI 1997). Typically, patients present with respiratory distress and superior vena cava

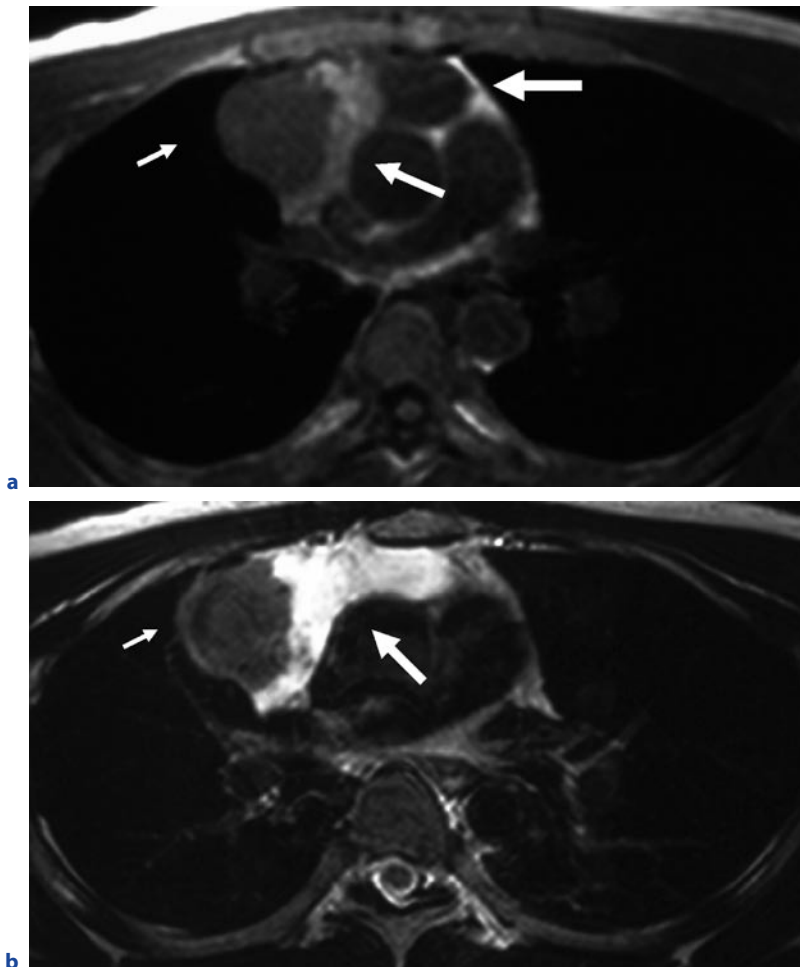


Fig. 12.21a–d. Hodgkin's disease associated with a thymic cyst. A solid lesion of Hodgkin's disease (*small arrows*) and a thymic cyst are seen. On the T1-weighted image (**a**), the lesion of Hodgkin's disease shows intermediate signal intensity similar to muscle, and the thymic cyst consists of a lateral portion of high signal (*medium arrow*) and medial portion of low signal intensity (*large arrow*). On the T2-weighted image (**b**), Hodgkin's disease shows intermediate signal intensity (*small arrow*), whereas the thymic cyst shows high signal intensity (*large arrow*)

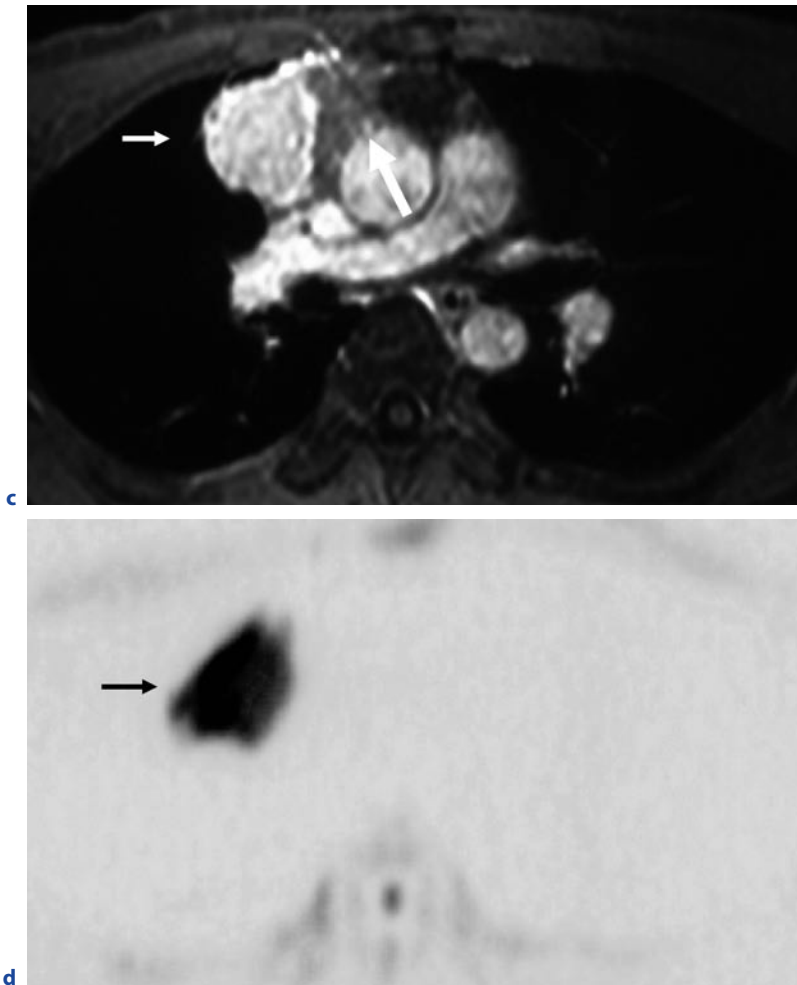


Fig. 12.21a-d. (continued) (c) On the contrast-enhanced image, the lesion of Hodgkin's disease (*small arrow*) shows enhancement, whereas the thymic cyst does not. (d) On the diffusion-weighted image ($b = 1,000$), prominent increase in signal is seen in Hodgkin's disease (*small arrow*)

syndrome due to a large mediastinal mass (PICOZZI and COLEMAN 1990).

The most common CT appearance is a large mediastinal mass, representing thymic and lymph node enlargement, which compresses the airway and cardiovascular structures. Low-attenuation areas reflecting necrosis are commonly seen after contrast enhancement. Pleural and pericardial effusions are also frequent. Pleural effusions may allow diagnosis with thoracentesis (LINK 1985). Lymphoblastic non-Hodgkin's lymphoma has a predilection toward rapid dissemination, and the tumor spreads to extrathoracic lymph nodes, bone marrow, central nervous system, and gonads in extensive disease (HAMRICK-TURNER et al. 1994). Since recurrence occurring 2–4 years after therapy is not unusual

in lymphoblastic lymphoma, meticulous follow-up is necessary (HAMRICK-TURNER et al. 1994).

12.5.3 Primary Mediastinal Diffuse Large B-Cell Lymphoma

Primary mediastinal diffuse large B-cell lymphoma has recently been described as a distinct subtype of non-Hodgkin's lymphoma (TATEISHI et al. 2004). Immunopathologic examination shows most tumors to be of B-cell origin. The majority of tumors tend to occur in young to middle-aged adults, with a mean age of 30 years (SHAFFER et al. 1996). Common symptoms in-

clude dyspnea, cough, chest pain, malaise, and fever, and superior vena cava syndrome occurs in nearly 40% of patients.

The tumors appear as a large, smooth or lobulated, anterior mediastinal mass in nearly all patients. Average diameters were 10 cm or bigger (SHAFFER et al. 1996). On CT, the tumors show low-attenuation areas, representing hemorrhage, necrosis, or cystic degeneration in 50% of cases and heterogeneous enhancement in about 40% of cases (TATEISHI et al. 2004; SHAFFER et al. 1996). The tumors are large and commonly invade the adjacent mediastinal structures, chest wall, and lung. Pleural and pericardial effusions are seen in about a third.

In one study of 21 patients, mediastinal lymph node enlargement is seen in 67% of patients, but extrathoracic lymph node enlargement is unusual (TATEISHI et al. 2004). The most commonly involved lymph nodes in the mediastinum are anterior mediastinum and paratracheal nodes, which are followed by the subcarinal, hilar, internal mammary, pericardial, and posterior me-

diastinal nodes in order of decreasing frequency (CASTELLINO et al. 1996) (Fig. 12.22).

12.5.4 MRI of Lymphoma

Generally, lymphomas are relatively homogeneous on MRI, and are hypointense to fat and slightly hyperintense to muscle in T1-weighted images but isointense to fat and hyperintense to muscle in T2-weighted images (NEGENDANK et al. 1990). A unique finding with greater brightness in T2-weighted images was seen in lymphomas with dense fibrosis, which contributes to the greater brightness of Hodgkin's disease than that of non-Hodgkin's lymphomas. The increased brightness of lymphomas is considered not caused by the fibrosis itself but by some other tissue element that has a very long T2 value, including edema, a greater proportion of vascular space, and inflammation (NEGENDANK

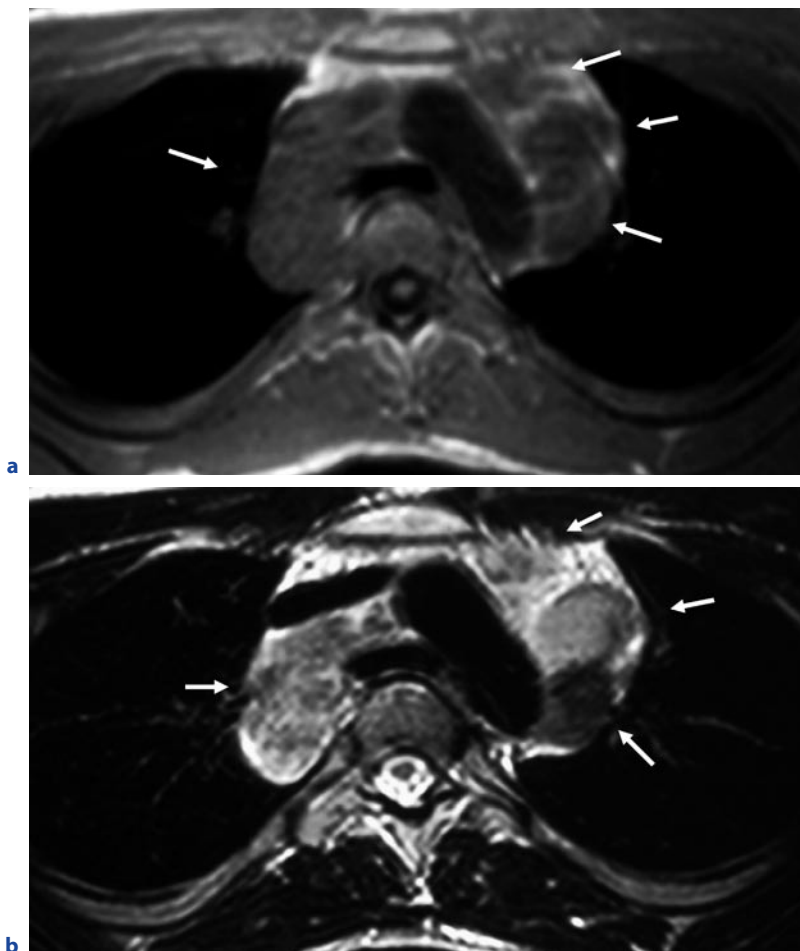


Fig. 12.22a,b. Anaplastic diffuse large B-cell lymphoma. T1-weighted (**a**) and T2-weighted (**b**) images show multiple enlarged lymph nodes in the anterior mediastinal, paratracheal, and posterior mediastinal regions.

et al. 1990). If the initial mass shows high signal on T2-weighted images, the likelihood of recurrence might be higher (NYMAN et al. 1989).

In mediastinal lymphomas, a residual mass is common after treatment, especially in cases with a bulky initial mass, and MRI provides important information in distinguishing viable tumors from residual benign masses. Residual tumors can reveal various signal patterns on T1- and T2-weighted MR images. Heterogeneous signal intensity on T2-weighted images is seen in both residual and sterilized tumors. High signal intensity on T2-weighted images and low signal intensity on T1-weighted images may represent residual active lym-

phoma, areas of necrosis, and inflammation. In the mass lesions of sterilized tumors, heterogeneous signal pattern on T2- and T1-weighted images represents mixed fat and fibrous tissue. Inactive residual fibrotic masses characteristically show homogeneous hypointensity (RAHMOUNI et al. 1990, 1993). The use of Gd-enhanced MRI is also useful. In a study of 31 patients with bulky mediastinal lymphoma (17 with Hodgkin's disease and 24 with non-Hodgkin's lymphoma), enhancement of mediastinal masses in lymphoma decreases markedly after treatment in patients in complete remission but not in patients with relapse (RAHMOUNI et al. 2001) (Fig. 12.23).

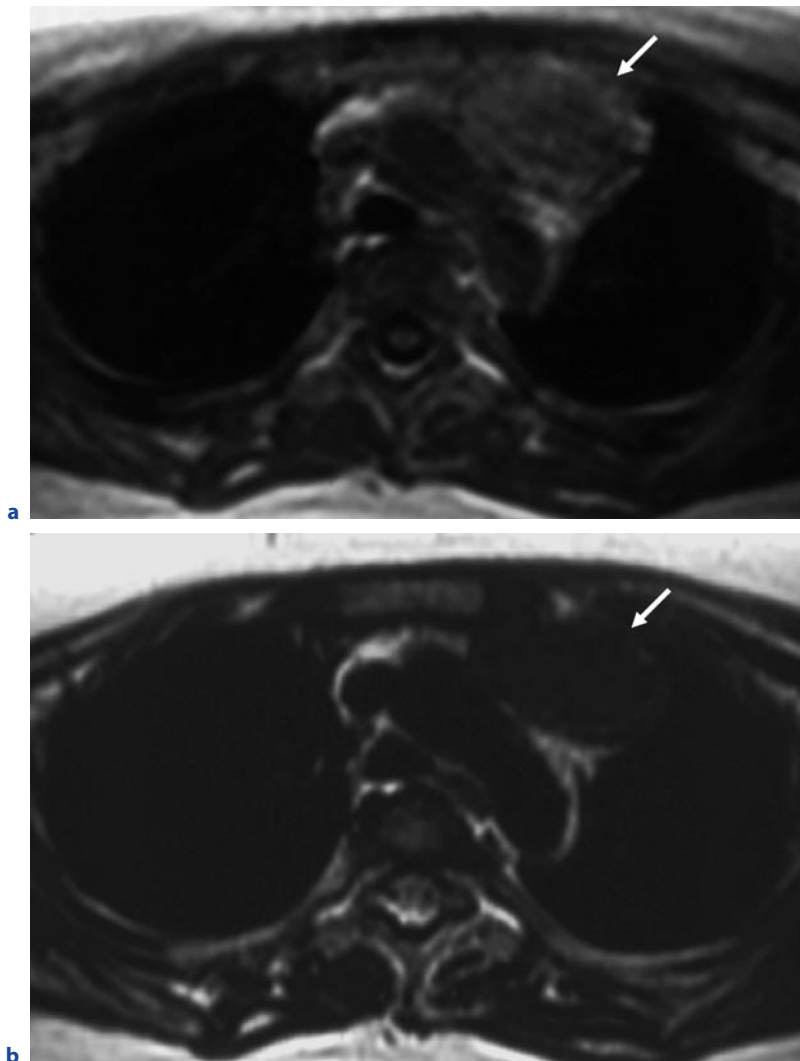


Fig. 12.23a–d. A residual mass of non-Hodgkin's lymphoma after chemotherapy. T1-weighted (**a**) and T2-weighted (**b**) images show a well-demarcated mass of low signal intensity in the anterior mediastinum (*arrow*). (**c**) The diffusion-weighted image ($b = 1,000$) does not show a significant increase in signal intensity (*arrow*). Contrast-enhanced T1-weighted image (**d**) shows little enhancement (*arrow*). Overall, the findings suggest the nonviable nature of the residual mass

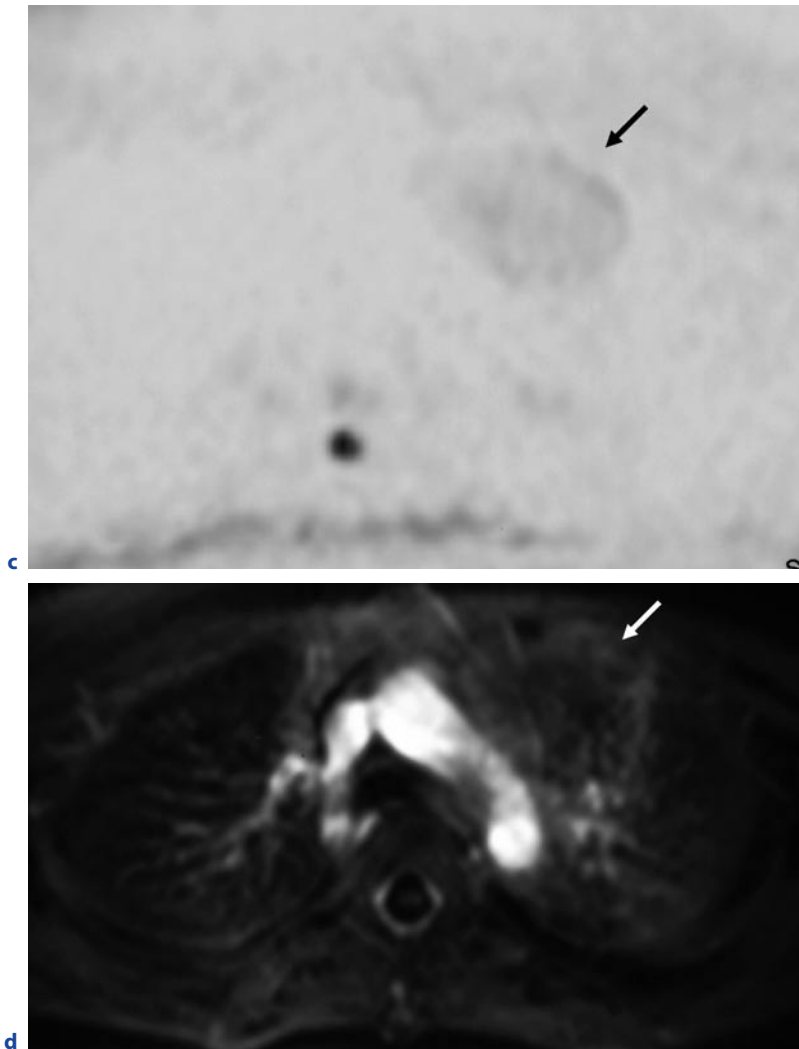


Fig.12.23a–d. (continued) A residual mass of non-Hodgkin's lymphoma after chemotherapy. (c) The diffusion-weighted image ($b = 1,000$) does not show a significant increase in signal intensity (arrow). Contrast-enhanced T1-weighted image (d) shows little enhancement (arrow). Overall, the findings suggest the nonviable nature of the residual mass

12.6

Neurogenic Tumor

Neurogenic tumors account for approximately 9–20% of primary mediastinal neoplasms in adults and 29–35% in children (STROLLO et al. 1997; RIBET and CARDOT 1994). Nearly 90% of neurogenic tumors occur in the posterior mediastinum. Tumors arise from peripheral nerves and nerve sheaths (schwannoma, neurofibroma, malignant peripheral nerve sheath tumor), sympathetic ganglia (neuroblastoma, ganglioneuroblastoma, ganglioneuroma), and rarely parasympathetic ganglia (paraganglioma). Nerve sheath tumors are more common in adults, whereas sympathetic ganglia tumors are more common in children. The mean age at diagnosis was

5.8 years for neuroblastoma, 8.4 years for ganglioneuroblastoma, 19.6 years for ganglioneuroma, 29.7 years for neurofibroma, and 38 years for schwannoma.

12.6.1

Peripheral Nerve Sheath Tumors

Peripheral nerve sheath tumors of the mediastinum usually arise from intercostal nerves and rarely from the vagus, phrenic, or recurrent nerve. *Schwannomas* are encapsulated and arise from the nerve sheath. *Neurofibromas* are non-encapsulated and result from a disorganized proliferation of all nerve elements. *Malignant peripheral nerve sheath tumors* represent the malignant counterparts of schwannomas and neurofibromas and

nearly 50% of them occur in patients with neurofibromatosis.

Schwannoma and neurofibroma typically appear as smooth, well-defined, rounded, or elliptical masses in the paravertebral region or along the course of other nerves (Fig. 12.24). Paravertebral tumors may extend into the spinal canal. On MRI, peripheral nerve sheath tumors typically show slightly higher signal intensity than shows muscle on T1-weighted images, and markedly increased intensity on T2-weighted images (BURK et al. 1987; SAKAI et al. 1992). On T2-weighted images, schwannomas occasionally reveal central high intensity due to cystic degeneration, whereas neurofibromas show central low intensity and peripheral high intensity

(“target sign”), representing central tumor tissue and peripheral myxoid degeneration (SAKAI et al. 1992). Neurofibromas may be associated with von Recklinghausen’s disease. Plexiform neurofibroma is pathognomonic of von Recklinghausen’s disease and appears as an extensive fusiform or infiltrating mass (Fig. 12.25).

Malignant peripheral nerve sheath tumors appear as a rounded well-defined mass in the posterior mediastinum, but may locally invade mediastinal structures and adjacent chest wall (STROLLO et al. 1997). Hematogenous metastases occur most commonly to the lung. Cystic degeneration due to hemorrhage and necrosis may be seen within the lesions.

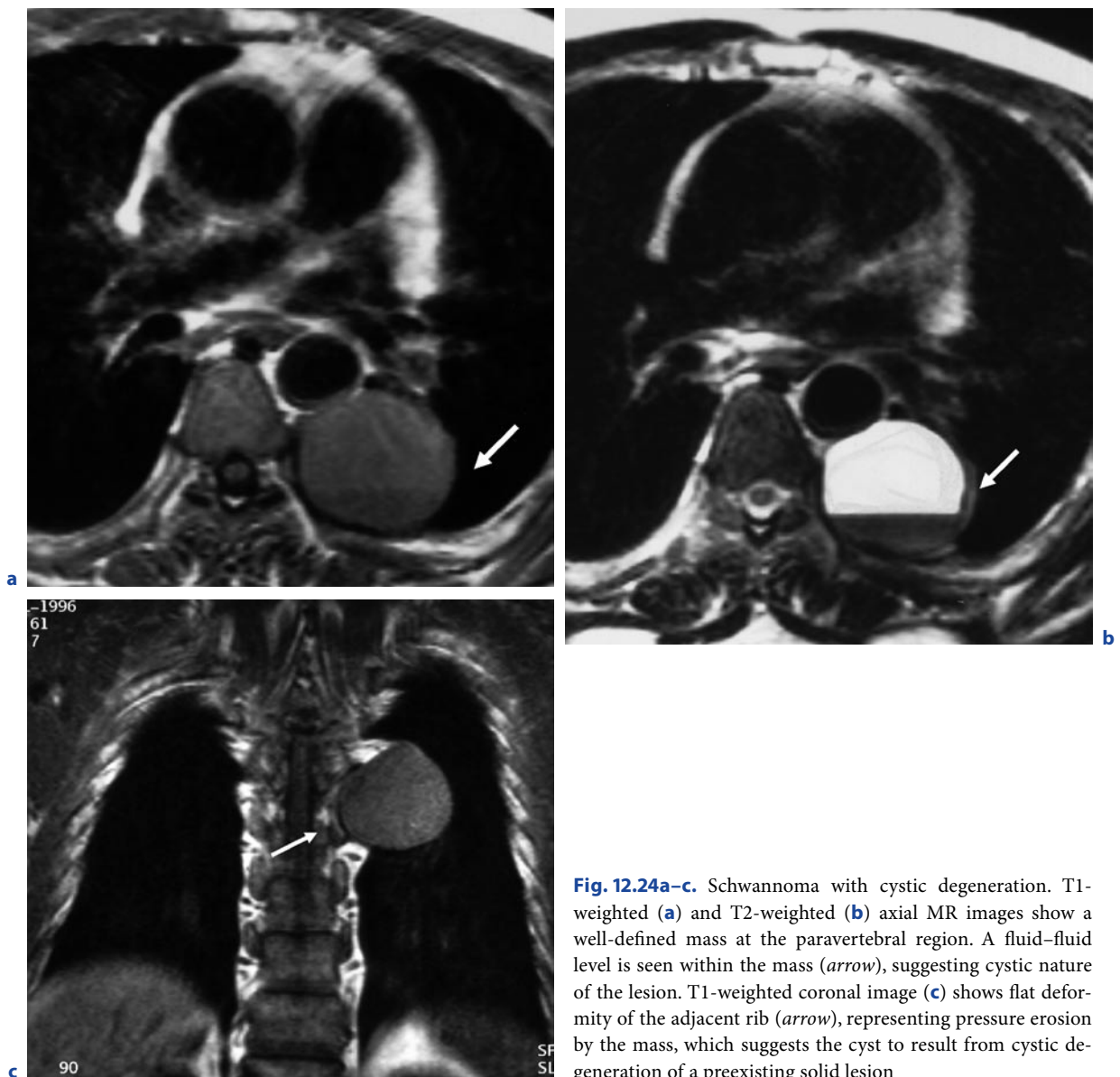


Fig. 12.24a–c. Schwannoma with cystic degeneration. T1-weighted (a) and T2-weighted (b) axial MR images show a well-defined mass at the paravertebral region. A fluid–fluid level is seen within the mass (arrow), suggesting cystic nature of the lesion. T1-weighted coronal image (c) shows flat deformity of the adjacent rib (arrow), representing pressure erosion by the mass, which suggests the cyst to result from cystic degeneration of a preexisting solid lesion



Fig. 12.25. Plexiform neurofibroma in neurofibromatosis type 1 (von Recklinghausen's disease). T2-weighted coronal image shows an extensive fusiform mass around the trachea (arrows)

12.6.2 Sympathetic Ganglia Tumors

Neuroblastoma, *ganglioneuroblastoma*, and *ganglioneuroma* are tumors of the sympathetic nervous system and they originate from the primordial neural crest cells that form the sympathetic nervous system. Ganglioneuroma and ganglioneuroblastoma arise most commonly from the sympathetic ganglia in the posterior mediastinum. Fifty percent of neuroblastomas arise from the adrenal gland, and nearly 30% arise in the mediastinum (STROLLO et al. 1997). Ganglioneuroma is the most benign tumor, which is composed of gangliocytes and mature stroma; ganglioneuroblastoma is of intermediate malignant potential and has both mature gangliocytes and immature neuroblasts; and neuroblastoma is the most malignant tumor of the three and composed primarily of neuroblasts. Ganglion cell tumors typically appear as a paravertebral mass elongated along the mediastinum.

On MRI, ganglioneuroma commonly shows low signal intensity on T1-weighted images and heterogeneous high signal intensity on T2-weighted images. The heterogeneous high signal intensity on T2-weighted images of ganglioneuroma has been considered to result from a combination of myxoid material and relatively low amounts of ganglion cells (ICHIKAWA et al. 1996; SERRA et al. 1992; SAKAI et al. 1992) (Fig. 12.26). Ganglioneuroma does not typically show early enhancement at dynamic MR study but does accumulate contrast material over time (LONERGAN et al. 2002; ICHIKAWA et al. 1996; SAKAI et al. 1992) (Fig. 12.27). A ganglioneuroma containing a fat component has rarely been reported and is considered to result from spontaneous regression of the tumor with subsequent infiltration of fat tissue from the mediastinum (HARA et al. 1999) (Fig. 12.26).

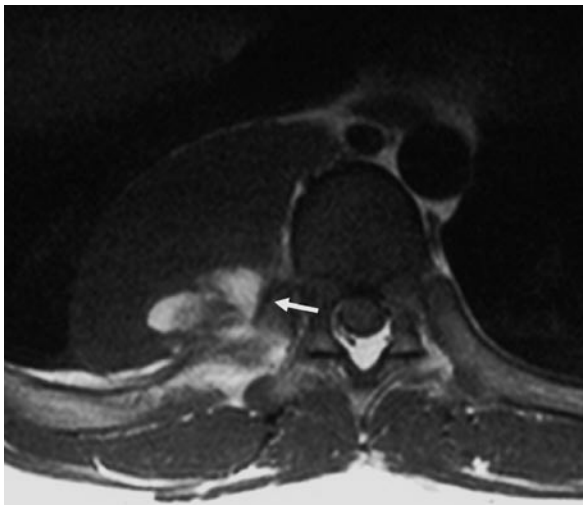
Neuroblastoma and ganglioneuroblastoma are of relatively low signal intensity on T1-weighted images and high signal intensity on T2-weighted images (Figs. 12.28, 12.29). And, they typically show heterogeneous signal pattern due to hemorrhage and cystic change within the lesions, which manifest as areas of high signal intensity on T1- and T2-weighted images, respectively (LONERGAN et al. 2002).

MRI has a few advantages over CT: in the evaluation of intraspinal extension of primary tumor, in detection of marrow disease, and detection of diffuse hepatic metastases (ABRAMSON 1997; COUANET et al. 1988; KING et al. 1975; SIEGEL et al. 1986). MR well demonstrates the range of extension of epidural tumor and its anatomical relation to the spinal cord and nerve roots. MR can depict marrow disease, which shows low signal on T1-weighted images and high signal on T2-weighted images.

12.6.3 Paraganglioma

Paraganglioma is a rare tumor originating from paraganglionic cells and accounts for 4% of thoracic neurogenic tumors (REED et al. 1978). The mediastinal paragangliomas predominantly arise in two locations, around the aortic arch (aortic body tumors) and in the paravertebral region. Aortic body tumors may occur in the following four locations: lateral to the brachiocephalic artery, anterolateral to the aortic arch, at the angle of the ductus arteriosus, or above and to the right of the right pulmonary artery (OLSON and SALYER 1978).

The appearance of thoracic paragangliomas is similar to that of paragangliomas seen in other locations, and the tumors are of intermediate signal intensity on T1-weighted images and high signal intensity on T2-

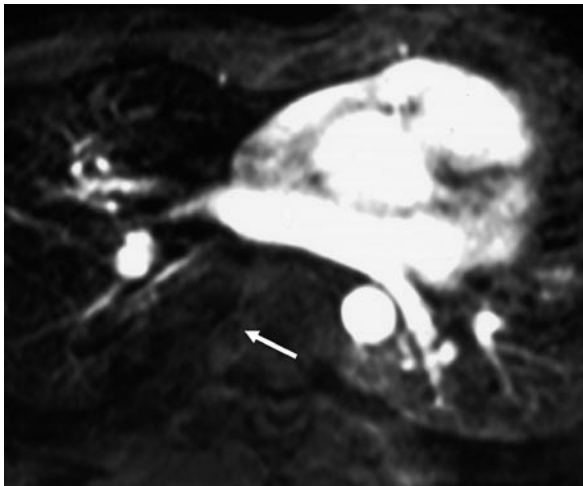


a

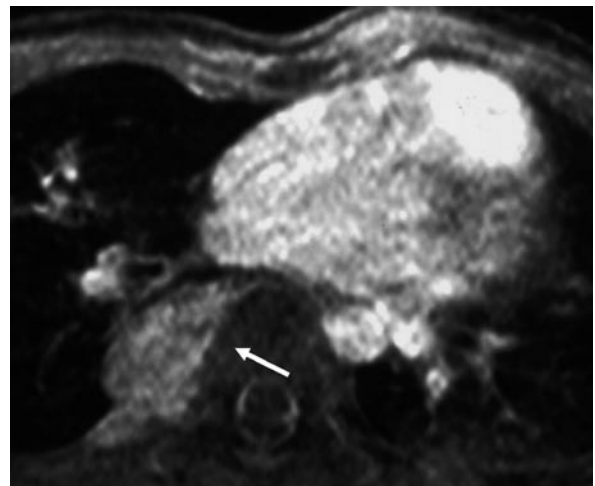


b

Fig. 12.26a,b. Ganglioneuroma. T1-weighted image (a) shows a paravertebral mass of low signal intensity similar to muscle, which contains areas of high signal, representing mediastinal fat within the mass. On T2-weighted coronal image (b), the mass shows heterogeneous high signal intensity, which may result from prominent myxoid material and low amounts of ganglion cells



a



b

Fig.12.27a,b. Ganglioneuroma. Early phase (a) and equilibrium phase (b) of contrast-enhanced dynamic study. The mass shows no apparent enhancement in the early phase (arrow a) but homogeneous enhancement on the equilibrium phase (arrow b)

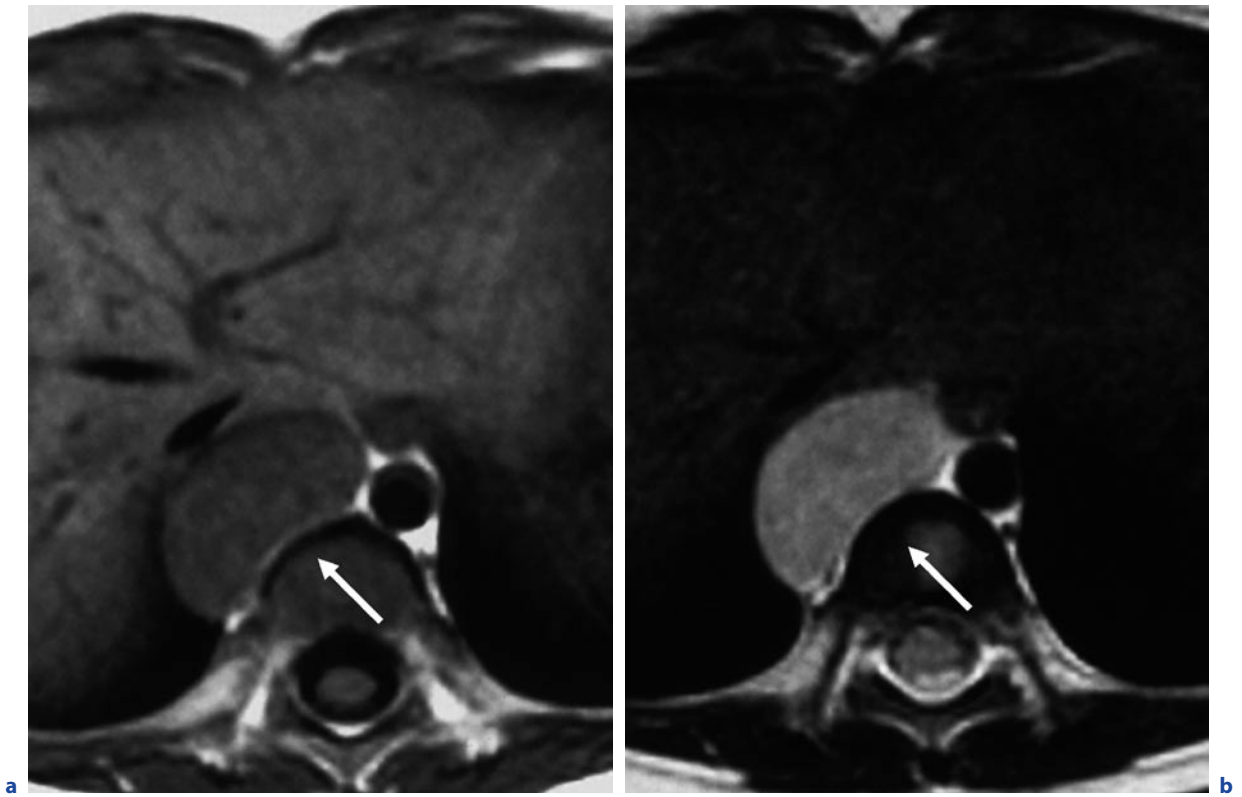


Fig. 12.28a,b. Ganglioneuroblastoma. A right paravertebral mass shows low signal intensity on T1-weighted image (a) and high signal intensity on T2-weighted image (b) (arrow). Ganglion cell tumor typically arises anteriorly alongside the vertebral body

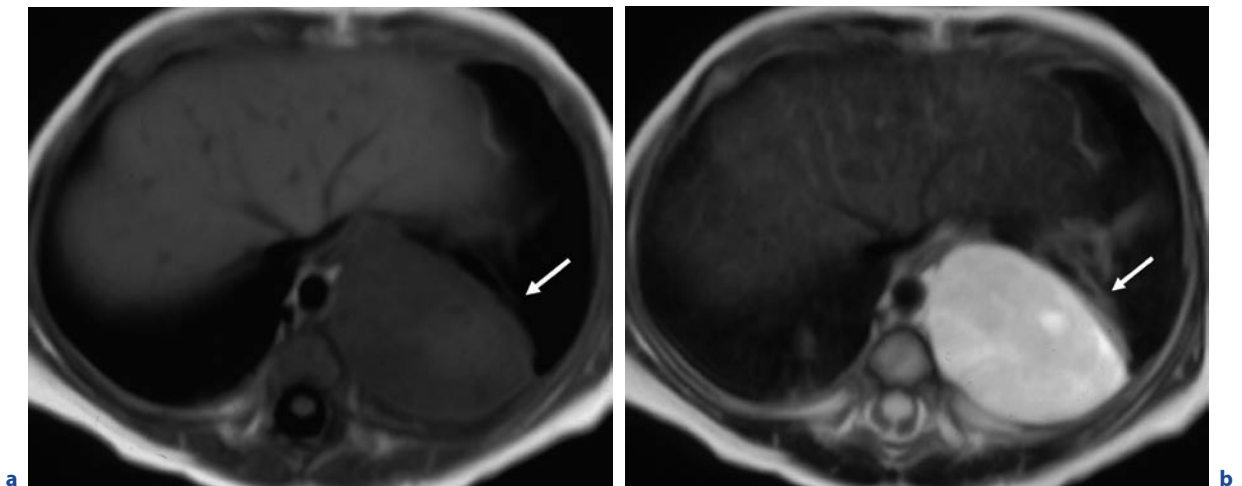


Fig. 12.29a,b. Neuroblastoma. T1-weighted (a) and T2-weighted (b) images show a huge left paravertebral mass. The mass is low in signal intensity on T1-weighted image and high on T2-weighted image

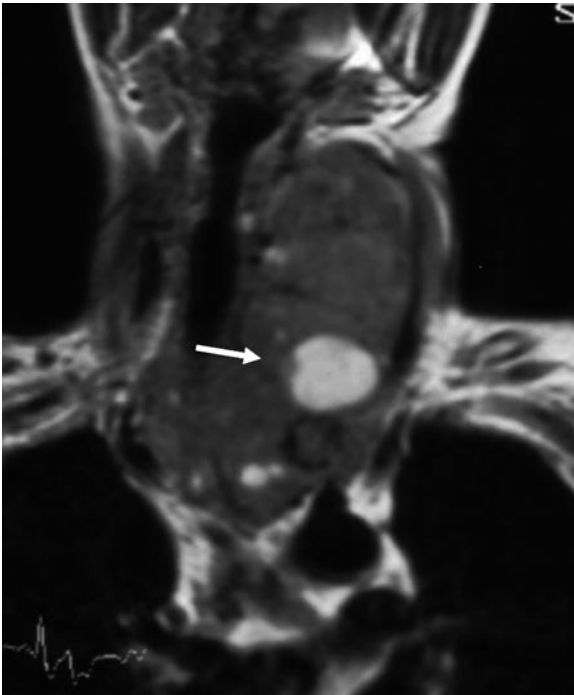


Fig. 12.30. Mediastinal goiter. A thyroid mass extends into the anterior mediastinum. The mass shows intermediate signal intensity with foci of high intensity (*arrow*), representing hemorrhage or cystic necrosis

weighted images (BALCOMBE et al. 2007; OLSEN et al. 1987). Smaller masses tend to have uniform intensity, whereas larger tumors more likely reveal heterogeneous appearance due to necrosis. Since paragangliomas are typically hypervascular, tumors generally reveal intense enhancement on CT or MRI after administration of intravenous contrast (BALCOMBE et al. 2007; SPIZARNY et al. 1987). Numerous serpiginous vascular channels may be seen within the large tumors.

12.7

Other Mediastinal Diseases

12.7.1

Mediastinal Goiters

Intrathoracic goiters usually result from direct contiguous extension into the mediastinum from thyroid lesions, which are most commonly benign multinodular goiter. Thyroid carcinoma and thyroid enlargement due to thyroiditis may also extend into the mediastinum. Intrathoracic extension of thyroid masses is commonly

into the anterior mediastinum (in 80%) and anterior to the recurrent laryngeal nerve and the brachiocephalic vessels. Posterior mediastinal extension of goiters is nearly 10–25% (KATLIC et al. 1985; SHAHIAN and ROSSI 1988).

On T1-weighted MR images, the masses usually show intermediate signal intensity similar to muscle and occasionally can show high signal regions, representing hemorrhage or colloid cyst formation (HIGGINS et al. 1986; GEFTER et al. 1987). On T2-weighted images, the masses usually show heterogeneous intensity. Continuity of the mediastinal mass with the thyroid gland in the neck is an important diagnostic clue and MRI is generally useful in its evaluation (Fig. 12.30).

12.7.2

Ectopic Parathyroid Gland

Parathyroid glands are located near the thyroid gland in 90% of cases and are ectopic in nearly 10% of cases. In a review of ectopic parathyroid glands, 81% are located in the anterior mediastinum and 19% are in the posterior mediastinum (CLARK 1988).

Generally, parathyroid adenomas are of intermediate signal intensity on T1-weighted images, and prominent high signal intensity on T2-weighted images (SPRITZER et al. 1987). Due to fibrosis and hemorrhage, nearly 10% of abnormal glands do not show high signal intensity on T2-weighted images (SPRITZER et al. 1987).

12.7.3

Fibrosing Mediastinitis

Fibrosing mediastinitis is a rare disease, manifested by chronic inflammation and fibrosis that focally or diffusely involves the mediastinum. The most common causes of fibrosing mediastinitis are histoplasmosis and tuberculosis, but it can also be related to autoimmune disease, or radiation therapy, retroperitoneal fibrosis, methysergide therapy, or may be idiopathic (MOLE et al. 1995). Histoplasmosis infection typically results in focal disease, whereas the idiopathic type is usually diffuse. Complications result from obstruction of various mediastinal structures, most commonly the superior vena cava (39%), which is followed by the bronchi (33%), pulmonary artery (18%), and esophagus (9%) (SHERRCK et al. 1994). The most common clinical symptoms are related to the superior vena cava syndrome: headache, cyanosis, and puffiness of the face, neck, and arms (SCHOWENGERDT et al. 1969).

CT shows the enlarged calcified nodes most commonly in the right paratracheal region, whereas other regions such as the left paratracheal, subcarinal, or posterior mediastinal may also be involved (SHERRCK et al. 1994). Calcification is rare in the diffuse form, which typically shows a diffuse increase in attenuation of the mediastinal fat tissue. CT is useful for assessing the involvement of mediastinal structures: narrowing and compression of superior vena cava, airway, pulmonary arteries, and veins. Although MRI and CT are equivalent in assessing the extent of adenopathy or fibrosis, MR allows for assessment of vascular involvement without contrast material. On MRI, fibrosing mediastinitis commonly shows heterogeneous signal intensity on T1- and T2-weighted images (ROSSI et al. 2001). Markedly decreased signal intensity on T2-weighted images is occasionally seen due to fibrosis and calcification within the lesions (RHOLL et al. 1985). The major disadvantage of MR is that it cannot confidently identify calcification.

12.7.4

Extramedullary Hematopoiesis

Extramedullary hematopoiesis is typically seen in patients with severe hemolytic anemia and intrathoracic manifestations appear as multiple lobulated paravertebral masses. On CT, they appear as well-defined multiple masses of homogeneous soft tissue attenuation and may show areas of fat attenuation (GLAZER et al. 1992). On T1-weighted MR images, the masses show heterogeneous signal intensity with increased signal intensity due to the contained fat tissue.

References

- Abramson SJ (1997) Adrenal neoplasms in children. *Radiol Clin North Am* 35:1415–1453
- Affi HY, Bosl GI, Burt ME (1997) Mediastinal growing teratoma syndrome. *Ann Thorac Surg* 64:359–362
- Balcombe J, Torigian DA, Kim W, Miller WT Jr (2007) Cross-sectional imaging of paragangliomas of the aortic body and other thoracic branchiomic paraganglia. *Am J Roentgenol* 188:1054–1058
- Baron RL, Sagel SS, Baglan RJ (1981) Thymic cysts following radiation therapy for Hodgkin disease. *Radiology* 141:593–597.
- Baron RL, Lee JK, Sagel SS, Peterson RR (1982) Computed tomography of the normal thymus. *Radiology* 142:121–125
- Boothroyd AE, Hall-Graggs MA, Dicks-Mireaux C, Shaw DG (1992) The magnetic resonance appearances of the normal thymus in children. *Clin Radiol* 45:378–381
- Burk DL Jr, Brunberg JA, Kanal E, Brunberg JA, Latchaw RE, Wolf GL (1987) Spinal and paraspinous neurofibromatosis: surface coil MR imaging at 1.5 T. *Radiology* 162:797–801
- Carbone PP, Kaplan HS, Musshoff K, Smithers DW, Tubiana M (1971) Report of the committee on Hodgkin's disease staging classification. *Cancer Res* 31:1860–1861
- Castellino RA, Hilton S, O'Brien JP, Portlock CS (1996) Non-Hodgkin's lymphoma: contribution of chest CT in the initial staging evaluation. *Radiology* 199:129–132
- Chaer R, Massad MG, Evans A, Snow NJ, Geha AS (2002) Primary neuroendocrine tumors of the thymus. *Ann Thorac Surg* 74:1733–1740
- Chen J, Weisbrod GL, Herman SJ (1988) Computed tomography and pathologic correlations of thymic lesions. *J Thorac Imaging* 3:61–65
- Choyke PL, Zeman RK, Gootenberg JE, Greenberg JN, Hoffer F, Frank JA (1987) Thymic atrophy and regrowth in response to chemotherapy: CT evaluation. *Am J Roentgenol* 149:269–272
- Clark OH (1988) Mediastinal parathyroid tumors. *Arch Surg* 123:1096–1100
- Couanet D, Geoffroy A, Hartmann O, Leclere JG, Lumbroso JD (1988) Bone marrow metastases in children's neuroblastoma studied by magnetic resonance imaging. *Prog Clin Bio Res* 271:547–555
- De Geer G, Webb WR, Gamsu G (1986) Normal thymus: associated with MR and CT. *Radiology* 158:313–317
- Dehner LP (1983) Gonadal and extragonadal germ cell neoplasia of childhood. *Hum Pathol* 14:493–511
- Do YS, Im J-G, Lee BH, Kim KH, Oh YW, Chin SY, Zo JI, Jang JJ (1995) CT findings in malignant tumors of thymic epithelium. *J Comput Assist Tomogr* 19:192–197
- Doppman JL, Nieman L, Miller DL, Pass HI, Chang R, Cutler GB, Schaaf M, Chrousos G, Norton JA, Ziessman HA, Oldfield EH, Loriaux DL (1989) Ectopic adrenocorticotropic hormone syndrome: localization studies in 28 patients. *Radiology* 172:115–124
- Drevelgas A, Palladas P, Scordalaki A (2001) Mediastinal germ cell tumors: a radiologic-pathologic review. *Eur Radiol* 11:1925–1932
- Erasmus JJ, McAdams HP, Donnelly LF, Spritzer CE (2000) MR imaging of mediastinal masses. *MRI Clin North Am* 8:59–89
- Ferolla P, Falchetti A, Filosso P, Tomassetti P, Tamburrano G, Avenia N, Daddi G, Puma F, Ribacchi R, Santeusano F, Angeletti G, Brandi ML (2005) Thymic neuroendocrine carcinoma (carcinoid) in MEN 1 syndrome: the Italian series. *J Clin Endocrinol Metab* 90:2603–2609
- Feung MY, Gasser B, Gangi A, Bogorin A, Charneau D, Wihlm FM, Dietemann FL, Catherine R (2002) Imaging of cystic masses of the mediastinum. *RadioGraphics* 22:S79S–93
- Francis IR, Glazer GM, Bookstein FL, Gross BH (1985) The thymus: reexamination of age-related changes in size and shape. *Am J Roentgenol* 145:249–254

- Fujimoto K, Nishihara H, Abe T, Edamitsu O, Uchida M, Kumabe T, Ueda H, Sakoda J, Kojima K, Uozumi J, Oshibuchi M, Hayabuchi N (1992) MR imaging of thymoma—comparison with CT, operative, and pathological findings. *Nippon Igaku Hoshasen Gakkai Zasshi* 25:1128–1138
- Gal AA, Kornstein MJ, Cohen C, Duarte IG, Miller JI, Mansour KA (2001) Neuroendocrine tumors of the thymus: a clinicopathological and prognostic study. *Ann Thorac Surg* 72:1179–1182
- Geffer WB, Spritzer CE, Eisenberg B, LiVolsi VA, Axel L, Velchik M, Alavi A, Schenck J, Kressel HY (1987) Thyroid imaging with high-field strength surface-coil MR. *Radiology* 164:483–490
- Glazer HS, Wick MR, Anderson DJ, Semenkovich JW, Molina PL, Siegel MJ, Sagel SS (1992) CT of fatty thoracic masses. *Am J Roentgenol* 159:1181–1187
- Goldstein G, Mackey IR (1969) The human thymus. Green, St Louis
- Gualdi GF, Volpe A, Poletini E, D'Agostino A, Ceroni AM, Piroli FM (1994) Role of magnetic resonance in the evaluation of space-occupying mediastinal pathology. *Clin Ter* 145:141–147
- Hamrick-Turner JE, Saif MF, Powers CI, Blumenthal BI, Royal SA, Iyer RV (1994) Imaging of childhood non-Hodgkin lymphoma: assessment by histologic subtype. *Radiographics* 14:11–28
- Hara M, Ohba S, Andoh K, Kitase M, Sasaki S, Nakayama J, Fukai I, Goodman PC (1999) A case of ganglioneuroma with fatty replacement: CT and MRI findings. *Radiat Med* 17:172–178
- Hartmann CA, Roth Chr, Minck C, Niedobitek G (1990) Thymic carcinoma. *J Cancer Res Clin Oncol* 116:69–82
- He Y, Zhang Z-Y, Zhu H-G, Guo W, Wang L-Z (2008) Infant ectopic cervical thymus in submandibular region. *Int J Oral Maxillofac Surg* 37:186–189
- Hoffman OA, Gillespie DJ, Aughenbaugh GL, Brown LR (1993) Primary mediastinal neoplasms (other than thymoma). *Mayo Clin Proc* 68:880–891
- Huang TW, Cheng YL, Tzao C, Chang H, Tsai WC, Lee SC (2007) Middle mediastinal thymoma. *Respirology* 12:934–936
- Higgins CB, McNamara MT, Fisher MR, Clark OH (1986) MR imaging of the thyroid. *Am J Roentgenol* 147:1255–1261
- Ichikawa T, Ohtomo K, Araki T, Fujimoto H, Nemoto K, Nanbu A, Onoue M, Aoki K (1996) Ganglioneuroma: computed tomography and magnetic resonance features. *Br J Radiol* 69:114–121
- Inaoka T, Takahashi K, Iwata K, Fajardo L, van Beek E, Sato Y, Yamada T, Nagasawa K, Shuke N, Aburano T (2005) *J Magn Reson Imaging* 22:341–346
- Inaoka T, Takahashi K, Mineta M, Yamada T, Shuke N, Okizaki A, Nagasawa K, Sugimori H, Aburano T (2007) Thymic hyperplasia and thymus gland tumors: Differentiation with chemical shift MR imaging. *Radiology* 243:869–876
- Inoue A, Tomiyama N, Fujimoto K, Sadohara J, Nakamichi I, Tomita Y, Aozasa K, Tsubamoto M, Murai S, Natsag J, Sumikawa H, Mihara N, Honda O, Hamada S, Johkoh T, Nakamura H (2006) MR imaging of thymic epithelial tumors: correlation with world health organization classification. *Radiat Med* 24:171–181
- Iyoda A, Hiroshima K, Yusa T, Toyozaki T, Fujisawa T, Ohwada H (2000) The primary mediastinal growing teratoma syndrome. *Anticancer Res* 20:3723–3728
- Jeong YJ, Lee KS, Kim J, Shim YM, Han J, Kwon OJ (2004) Does CT of thymic epithelial tumors enable us to differentiate histologic subtypes and predict prognosis. *Am J Roentgenol* 183:283–289
- Katlic MR, Wang C, Grillo HC (1985) Substernal goiter. *Ann Thorac Surg* 39:391–399
- Khariwala SS, Nicollas R, Triglia JM, Garabedian EN, Marianowski R, Van Den Abbeele T, April M, Ward R, Koltai PJ (2004) Cervical presentations of thymic anomalies in children. *Int J Pediatr Otorhinolaryngol* 68:909–914
- King D, Goodman J, Hawk T, Boles ET, Sayers MP (1975) Dumbbell neuroblastomas in children. *Arch Surg* 110:888–891
- Klemm KM, Moran CA (1999) Primary neuroendocrine carcinomas of the thymus. *Semin Diagn Pathol* 16:32–41
- Kuhlman JE, Fishman EK, Wang KP, Zerhouni EA, Siegelman SS, (1988) Mediastinal cysts; diagnosis by CT and needle aspiration. *Am J Roentgenol* 150:75–78
- Lee KS, Gilm J, Han CH, et al (1989) Malignant primary germ cell tumors of the mediastinum: CT features. *Am J Roentgenol* 153:947–951
- Levine GD, Rosai J (1978) Thymic hyperplasia and neoplasia: a review of current concepts. *Hum Pathol* 9:495–515
- Lewis JE, Wick MR, Scheithauer BW, Bernatz PE, Taylor WF (1987) Thymoma: a clinicopathological review. *Cancer* 60:2727–2743
- Linegar AG, Odell JA, Fennell WM, Close PM, De Groot MK, Casserly DR, Perold JI (1993) Massive thymic hyperplasia. *Ann Thorac Surg* 55:1197–1201
- Link MP (1985) Non-Hodgkin lymphoma in children. *Pediatr Clin North Am* 32:699–719
- Liu D, Kitajima M, Awai K, Nakayama Y, Tamura Y, Suda H, Asonuma K, Inomata Y, Yamashita Y (2006) Ectopic cervical thymus in an infant. *Radiat Med* 24:452–455
- Masaoka A, Monden Y, Nakahara K, Tanioka T (1981) Follow-up study of thymomas with special reference to their clinical stages. *Cancer* 48:2485–2492
- Mattila PS, Tarkkanen J, Mattila S (1999) Thoracic duct cyst: a case report and review of 29 cases. *Ann Otol Rhinol Laryngol* 108:505–508
- McAdams HP, Kirejczyk WM, Posado-de-Christenson ML, Matsumoto S (2000) Bronchogenic cyst: imaging features with clinical and histopathologic correlation. *Radiology* 217:441–446
- Mole TM, Glover J, Sheppard MN, (1995) Sclerosing mediastinitis: a report on 18 cases *Thorax* 50:280–283
- Molina PL, Siegel MJ, Glazer HS (1990) Thymic masses on MR imaging. *Am J Roentgenol* 155:495–500

- Murayama S, Murakami J, Watanabe H, Sakai S, Hinaga S, Soeda H, Nakata H, Masuda K (1995) Signal intensity characteristics of mediastinal cystic masses on T1-weighted MRI. *J Comput Assist Tomogr* 19:188–191
- Nagasawa K, Takahashi K, Hayashi T, Aburano T (2004) Ectopic cervical thymus. *Am J Roentgenol* 182:262–263
- Nakasu Y, Minouchi K, Hatsuda N, Nakasu S, Handa J (1991) Thoracic meningocele in neurofibromatosis: CT and MR findings. *J Comput Assist Tomogr* 15: 1062–1064
- Negendank WG, Al-Katib AM, Karanes C, Smith MR (1990) Lymphomas: MR imaging contrast characteristics with clinical-pathologic correlations. *Radiology* 177:209–216
- Nicolaou S, Muller NL, Li DKB, Oger JFF (1996) Thymus in myasthenia gravis: comparison of CT and pathologic findings and clinical outcome after thymectomy. *Radiology* 200:471–474
- Nyman RS, Rehn SM, Glimelius BLG, Hagberg HE, Hemmingsson AL, Sundstrom CJ (1989) Residual mediastinal masses in Hodgkin disease: prediction of size with MR imaging. *Radiology* 170:435–440
- Olsen WL, Dillon WP, Kelly WM, Norman D, Brant-Zawadzki M, Newton TH (1987) MR imaging of paragangliomas. *Am J Roentgenol* 148:201–204
- Olson JL, Salyer WR (1978) Mediastinal paragangliomas (aortic body tumor): a report of four cases and a review of the literature. *Cancer* 41:2405–2412
- Picozzi VJ, Coleman CN (1990) Lymphoblastic lymphoma. *Semin Oncol* 17:96–103
- Pirronti T, Rinaldi P, Batocchi AP, Evoli A, Di Schino C, Marano P (2002) Thymic lesions and myasthenia gravis. Diagnosis based on mediastinal imaging and pathological findings. *Acta Radiol* 43:380–384
- Pombo F, Rodriguez E, Caruncho MV (1994) CT attenuation values and enhancing characteristics of thoracoabdominal lymphomatous adenopathy. *J Comput Assist Tomogr* 18:59–64
- Rahmouni AD, Zerhouni EA (eds) (1990) Role of MRI in the management of thoracic lymphoma. Churchill-Livingstone, New York
- Rahmouni A, Tempany C, Jones R, Mann R, Yang A, Zerhouni E (1993) Lymphoma: monitoring tumor size and signal intensity with MR imaging. *Radiology* 188:445–451
- Rahmouni A, Divine M, Lepage E, Jazaerli N, Belhadj K, Gaulard P, Golli M, Reyes F, Vasile N (2001) Mediastinal lymphoma: quantitative changes in gadolinium enhancement at MR imaging after treatment. *Radiology* 219:621–628
- Rholl KS, Levitt RG, Glazer HS (1985) Magnetic resonance imaging of fibrosing mediastinitis. *Am J Roentgenol* 145:255–259
- Rosado-de-Christenson ML, Pugatch RD, Moran CA, Galobardes J (1994) Thymolipoma: analysis of 27 cases. *Radiology* 193:121–126
- Rosai J, Sobin LH (1999) Histological typing of tumors of the thymus, In: International histological classification of tumors 2nd edn. Springer, Berlin Heidelberg New York, pp 5–14
- Rossi SE, McAdams HP, Rosado-de-Christenson ML, Franks TF, Galvin FR (2001) Fibrosing mediastinitis. *Radiographics* 21:737–757
- Reed JC, Sobonya RE (1974) Morphologic analysis of foregut cysts in the thorax. *Am J Roentgenol* 120:851–860
- Reed JC, Hallett KK, Feigin DS, (1978) Neural tumors of the thorax: subject review from the AFIP. *Radiology* 126:9–17
- Ribet ME, Cardot GR (1994) Neurogenic tumors of the thorax. *Ann Thorac Surg* 58:1091–1095
- Ribet ME, Copin MC, Gosselin BH (1995) Bronchogenic cysts of the mediastinum. *J Thorac Cardiovasc Surg* 109:1003–1010
- Ribet ME, Copin MC, Gosselin BH (1996) Bronchogenic cysts of the lung. *Ann Thorac Surg* 61:1636–1640
- Sadohara J, Fujimoto K, Muller NL, Kato S, Takamori S, Ohkuma K, Terasaki H, Hayabuchi N (2006) Thymic epithelial tumors: comparison of CT and MR imaging findings of low-risk thymomass, high-risk thymomas, and thymic carcinomas. *Eur J Radiol* 60:70–79
- Sakai F, Sone S, Kiyono K, Kawai T, Maruyama A, Ueda H, Aoki J, Honda T, Morimoto M, Ishii K, Ikeda S (1991) MR imaging of thymoma: Radiologic-pathologic correlation. *Am J Roentgenol* 158:751–756
- Sakai F, Sone S, Kiyono K, Maruyama A, Ueda H, Aoki J, Kawai T, Ishii K, Morimoto M, Haniuda M, Koizumi T (1992) Intrathoracic neurogenic tumors: MR-pathologic correlation. *Am J Roentgenol* 159:279–283
- Sakai S, Murayama H, Soeda H, Matsuo Y, Ono M, Masuda K (2002) Differential diagnosis between thymoma and non-thymoma by dynamic MR imaging. *Acta Radiol* 43:262–268
- Salo JA, Ala-Kulju K (1987) Congenital esophageal cysts in adults. *Ann Thorac Surg* 44:135–138
- Sasaka K, Kurihara Y, Nakajima Y, Seto Y, Endo I, Ishikawa T, Takagi M (1998) Spontaneous rupture: a complication of benign mature teratomas of the mediastinum. *Am J Roentgenol* 170:323–328
- Schowengerdt CG, Suyemoto R, Main FB, (1969) Granulomatous and fibrous mediastinitis—a review and analysis of 180 cases. *J Thorac Cardiovasc Surg* 57:365–379
- Serra AD, Rafal RB, Markisz JA (1992) MRI characteristics of two cases of adrenal ganglioneuromas. *Clin Imaging* 16:37–39
- Shaffer K, Smith D, Kirn D, Kaplan W, Canellos G, Mauch P, Shulman LN (1996) Primary mediastinal large-B-cell lymphoma: radiologic findings at presentation. *Am J Roentgenol* 167:425–430
- Shahian DM, Rossai R (1988) Posterior mediastinal goiter. *Chest* 94:599–602
- Sherrick AD, Brown LR, Harms GF, Myers JL (1994) Radiologic findings of fibrosing mediastinitis. *Chest* 106:484–489
- Shimosato Y, Mukai K (1997) Epithelial tumors. In: Rosai J (ed) Tumors of the mediastinum, 3rd edn. Armed Forces Institute of Pathology, Washington, D.C., pp 40–157
- Shimosato Y, Mukai K (1997) Germ cell tumors. In: Rosai J (ed) Tumors of the mediastinum, 3rd edn. Armed Forces Institute of Pathology, Washington, D.C., 183–206

- Shimosato Y, Mukai K (1997) Malignant lymphoma. In: Rosai J (ed) *Tumors of the mediastinum*, 3rd edn. Armed Forces Institute of Pathology, Washington, D.C., 207–226
- Shirkhoda A, Chasen MH, Eftekhari F, Goldman AM, Decaro LF (1987) MR imaging of mediastinal thymolipoma. *J Comput Assist Tomogr* 11:364–365
- Siegel MJ, Jamroz GA, Glazer HS, Abramson CL (1986) MR imaging of intraspinal extension of neuroblastoma. *J Comput Assist Tomogr* 10:593–595
- Siegel MJ, Glazer HS, Wiener JI, Molina PL (1989) Normal and abnormal thymus in childhood: MR imaging. *Radiology* 172:367–371
- Spizarny DL, Rebner M, Gross BH, (1987) CT evaluation of enhancing mediastinal masses. *J Comput Assist Tomogr* 11:990–993
- Spritzer CE, Geffer WB, Hamilton R, Greenberg BM, Axel L, Kressel H (1987) Abnormal parathyroid glands: high-resolution MR imaging. *Radiology* 162:487–491
- St-Georges R, Deslauriers J, Duranceau A, Vaillancourt R, Deschamps C, Beauchamp G, Page A, Brisson J (1991) Clinical spectrum of bronchogenic cysts of the mediastinum and lung in the adult. *Ann Thorac Surg* 52:6–13.
- Strollo DC, Rosado-de-Christenson ML, Jett JR (1997) Primary mediastinal tumors: Part II. Tumors of the middle and posterior mediastinum. *Chest* 112:1344–1357
- Strollo DC, Rosado-de-Christenson ML, Jett JR (2002) Primary mediastinal malignant germ cell neoplasms: imaging features. *Chest Surg Clin North Am* 12:645–658
- Suster S, Rosai J (1991) Multilocular thymic cyst: an acquired reactive process. *Am J Surg Pathol* 15:388–398
- Takahashi K, Inaoka T, Kamishima T (1998) Mature teratoma of the mediastinum: relationship of inflammatory process around the tumor with clinical, radiologic, and pathologic findings. *Jpn J Clin Radiol* 43:163–170
- Takahashi K, Inaoka T, Murakami N, Hirota H, Iwata K, Nagasawa K, Yamada T, Mineta M, Aburano T (2003) Characterization of the normal and hyperplastic thymus on chemical-shift MR imaging. *Am J Roentgenol* 180:1265–1269
- Takeda S, Miyoshi S, Minami M, Ohta M, Masaoka A, Matsuda H (2003) Clinical spectrum of mediastinal cysts. *Chest* 124:125–132
- Tan MH, Kirk G, Archibold P, Kennedy P, Regan MC (2002) Cardiac compromise due to a pancreatic mediastinal pseudocyst. *Eur J Gastroenterol Hepatol* 14:1279–1282
- Tanaka A, Takeda R, Utsunomiya H, kataoka M, Mukaihara S, Hayakawa K (2000) Severe complications of mediastinal pancreatic pseudocyst: report of esophagobronchial fistula and hemothorax. *J Hepatobiliary Pancreat Surg* 7:86–91
- Tateishi U, Muller NL, Johkoh T, Onishi Y, Arai Y, Satake M, Matuno Y, Tobinai K (2004) Primary mediastinal lymphoma: characteristic features of the various histological subtypes on CT. *J Comput Assist Tomogr* 28:782–789
- Tiffet O, Nicholson AG, Ladas G, Sheppard MN, Goldstraw P (2003) A clinicopathologic study of 12 neuroendocrine tumors arising in the thymus. *Chest* 124:141–146
- Travis WD, Brambilla E, Muller-Hermelink HK, Harris CC (2004) *WHO classification of tumors. Pathology and genetics of tumors of the lung, pleura, thymus and heart*. IARC Press, Lyon, France
- Yamazaki K, Yoshino I, Oba T, Yohena T, Kameyama T, Tagawa T, Kawano D, Koso H, Maehara Y (2006) Ectopic pleural thymoma presenting as a giant mass in the thoracic cavity. *Ann Thorac Surg* 83:315–317
- Yernault JC, Kuhn G, Dumortier P, Rocmans P, Ketelbant P, De Buyst P (1986) “Solid” mediastinal bronchogenic cyst: mineralogic analysis. *Am J Roentgenol* 146:73–74
- Yoshioka N, Minami M, Inoue Y, Kawauchi N, Nakajima J, Oka T, Yoshioka K, Ohtomo K (2000) Pedunculated Bronchogenic cyst mimicking pleural lesion. *J Comput Assist Tomogr* 24:581–583
- Wang ZF, Reddy GP, Gotway MB, Yeh BM, Hettis SW, Higgins CB (2003) CT and MR imaging of pericardial disease. *RadioGraphics* 23:s167-s180
- Wychulis AR, Payne WS, Clagett OT, Woolner LB (1971) Surgical treatment of mediastinal tumors; A 40-year experience. *J Thorac Cardiovasc Surg* 62:379–392

ROGER EIBEL

CONTENTS

- 13.1 **Definition** 255
- 13.2 **Pathogenesis** 256
- 13.3 **Classification** 256
 - 13.3.1 Community Acquired Acute Pneumonia (CAP) 256
 - 13.3.2 Community-acquired Atypical Pneumonias 257
 - 13.3.3 Nosocomial Pneumonia 257
 - 13.3.4 Chronic Pneumonia 257
 - 13.3.5 Pneumonia in the Immunocompromised Host 258
- 13.4 **MRI – Historical Overview and Imaging Concepts** 261
- 13.5 **MRI – Comparison with CT** 267
- 13.6 **Morphology of Different Types of Pneumonia in MR Imaging** 269
- 13.7 **Protocol** 271
- References** 274

KEY POINTS

The different appearances of pneumonia such as ill-defined nodules, ground-glass opacities, and consolidations can be easily detected and differentiated with MRI. Since very small nodules and calcifications are extremely challenging due to rather thick slices and loss of signal, MRI is highly recommended as a follow-up tool, to avoid repetitive investigations using ionizing radiation. With the sensitivity of T2-weighted sequences and the potential of contrast-enhanced T1-weighted sequences important differential diagnostic considerations can be provided. Additionally, developing complications, such as pericardial or pleural effusions, empyema or lung abscess, are easily recognized. Current and future studies are to demonstrate that MRI is well suited as a monitoring and follow-up tool during and after therapy and compares favorably with CT or other imaging methods regarding sensitivity and specificity.

13.1

Definition

Pneumonia is an infection of the gas-exchanging units of the lung, caused most commonly by bacteria but occasionally by viruses, fungi, parasites, and other infectious agents.

Pneumonia is the sixth leading cause of death in the United States, and the leading cause of death from infectious disease (NIEDERMAN et al. 2001). In hospitalized patients, particularly those who are mechanically ventilated, pneumonia is the leading cause of death from nosocomial infection (CAMPBELL et al. 1996).

R. EIBEL, MD

Chief of the Department of Radiology and Neuroradiology, HELIOS Clinics Schwerin, Teaching Hospital of the University of Rostock, Wismarsche Str. 393, 19049 Schwerin, Germany

13.2

Pathogenesis

Pneumonia can result whenever the pulmonary defense mechanisms are impaired or whenever the resistance of the host in general is lowered. Factors that affect resistance in general include:

- Chronic diseases
- Immunologic deficiency
- Treatment with immunosuppressive agents
- Leukopenia
- Unusually virulent infections

The clearing mechanisms can be interfered with by many factors, such as the following:

- Loss or suppression of the cough reflex (coma, drugs)
- Injury to the mucociliary apparatus (cigarette smoke, gas inhalation, viral diseases)
- Interference with the phagocytic or bactericidal action of alveolar macrophages (alcohol, smoke)
- Pulmonary congestion and edema
- Accumulation of secretions (cystic fibrosis, bronchial obstruction)

Some other points need to be emphasized, before listened up the different classification schemes. (1) One type of pneumonia sometimes predisposes to another, especially in debilitated patients. (2) Although the portal of entry for most pneumonias is the respiratory tract, hematogenous spread from one organ to other organs can occur. (3) Many patients with chronic disease acquire terminal pneumonias while hospitalized.

13.3

Classification

Pneumonias are classified by the specific etiologic agent, who determines the treatment, or, if no pathogen can be isolated, by the clinical setting in which the infection occurs. Below the different entities of the pneumonia syndromes are briefly discussed to clarify the terms and the characteristics and the peculiarities.

13.3.1

Community Acquired Acute Pneumonia (CAP)

CAP may be bacterial or viral. Often, the bacterial infection follows an upper respiratory tract viral infection.

Bacterial invasion of the lung parenchyma causes the alveoli to be filled with an inflammatory exudate, thus causing consolidation of the pulmonary tissue (HUSAIN and KUMAR 2005). Predisposing conditions include extremes of:

- Age
- Chronic diseases (congestive heart failure, COPD, and diabetes)
- Congenital or acquired immune deficiencies
- Decreased or absent splenic function (post splenectomy, sickle cell disease)

It is beyond the scope of this book chapter, to describe the different pneumonias caused by various organisms, but with regard to magnetic resonance imaging it is necessary to mention the different morphologic features common to most pneumonias.

According to the anatomic distribution in the lung, the two major categories are lobar versus bronchopneumonia. *Lobar pneumonia* is a classic manifestation of pneumococcal pneumonia in which an entire lobe is affected by the inflammatory infiltrate, with extension up to the pleura or a major fissure. In patients with this type, the stages of pneumonia progress from:

- Edema to
- Red hepatization (alveolar fibrin, neutrophils, lymphocytes, and pneumocyte hyperplasia)
- Gray hepatization (predominantly neutrophilic infiltrates with lysis of erythrocytes and inflammatory cells)
- Resolution (organizing pneumonia, macrophages, proliferation of loose connective tissue in distal air-spaces)

The basic *radiographic pattern* of this type of pneumonia is a homogeneous consolidation with or without air bronchogram. The consolidation is bounded by fissure and in contrast to an atelectasis no shrinkage or volume loss can be delineated in the acute phase.

Bronchopneumonia is also known as lobular or focal pneumonia. It is characterized by centrilobular inflammation that is concentrated around respiratory bronchioles, with spread to the surrounding alveolar ducts and alveolar spaces. When lobular pneumonia becomes confluent, it may be difficult to separate from lobar pneumonia. From a clinical standpoint it is sometimes difficult to apply these classic categories. More important for imaging is the determination of the extent of disease and the delineation of complications such as abscess formation, empyema, organization, and dissemination.

Common *radiographic findings* are nodular and patchy patterns due to involvement and sparing of acini. Sometimes volume loss can be found.

13.3.2 Community-acquired Atypical Pneumonias

The term “*atypical*” refers to the following findings:

- Moderate amount of sputum
- No physical findings of consolidation
- Only moderate evaluation of white cell count
- Lack of alveolar exudate

Most commonly this type of pneumonia is caused by *Mycoplasma pneumoniae*, viruses, and *Chlamydia pneumoniae*. These agents produce primarily an interstitial inflammation within the walls of the alveoli, resulting in thickening of the alveolar septa, later fluid accumulation and cellular exudate into the alveolar spaces. Superimposed bacterial infection modifies the histologic and the subsequent radiologic picture (HUSAIN and KUMAR 2005).

Interpreting chest films and especially CT, *radiographic patterns* which can be found in this category are peribronchial thickening, reticular and reticulonodular pattern, with filling of the acini ground-glass and sometime a crazy-paving pattern. A subsegmental collapse additional can be delineated.

13.3.3 Nosocomial Pneumonia

In 1995, the American Thoracic Society published a consensus statement defining nosocomial or hospital-acquired pneumonia (HAP) as a pneumonia that is:

- Not incubating at the time of hospital admission and
- Begins more than 48 h after admission (CAMPBELL et al. 1996)

There are 300,000 cases of HAP annually in the United States and it carries an associated mortality of 30%–70% (MCEACHERN and CAMPBELL 1998). It is common in patients with severe underlying disease, prolonged antibiotics, intravascular devices, and mechanical ventilation. The last one is also termed ventilator-associated pneumonia (VAP). In a prospective study of 1014 mechanically ventilated patients, VAP developed in 177 patients. The mean time to onset was 9 days, with a median time to onset of 7 days after ICU admission. However, when the daily hazard rate of infection was calculated, it was estimated to be 3.3% at day 5, 2.3% at day 10, and 1.3% at day 15 (COOK et al. 1998). This documents a significant decline in pneumonia risk with time. Because the risk for pneumonia is so high early

after intubation, pneumonias beginning within the first 5 days (*early-onset infection*) account for 50% of all episodes of VAP, and the natural history and pathogens of this infection differ from those associated with VAP of *late onset* (PROD’HOM et al. 1994). Common isolates are Gram-negative bacteria and *Staphylococcus aureus*. Typical radiologic patterns cannot be described. This is due to the different circumstances and risk factors, which contribute to the development of HAP. The other explanations are the different organisms responsible for the pneumonia. Within the first days the more common organisms are *Streptococcus pneumoniae*, *Moraxella catarrhalis*, *Staphylococcus aureus*, and *Hemophilus influenzae* (CRAVEN and STEGER 1995). Later on, Gram-negative rods predominate. The risk factors for mortality from VAP are summarized in Table 13.1.

Microaspiration of contaminated oropharyngeal secretions seems to be the most cause of HAP (MCEACHERN and CAMPBELL 1998). After macroaspiration another subtype of pneumonia can occur, termed *aspiration pneumonia*. This resultant pneumonia is partly chemical, owing to the extremely irritating effects of the gastric acid appearing like pulmonary edema, and partly bacterial (from the oral flora). This type of pneumonia is often necrotizing, with abscess formation is a common complication (HUSAIN and KUMAR 2005). As *radiographic patterns* in this particular type of pneumonia, patchy consolidations in the dependent portions of the lungs with a usually multilobar and bilateral distribution is common.

Diagnosing HAP is difficult because there is no method for obtaining a diagnosis that is reliable in all cases. The diagnosis is initially made on clinical grounds by the finding of a new infiltrate on chest radiograph, fever, purulent sputum, or other signs of clinical deterioration. Unfortunately, this clinical method was shown to be specific for HAP in only 27 of 84 patients in a series reported by FAGON et al. (1993) because many other conditions such as congestive heart failure, pulmonary embolism, atelectasis, ARDS, pulmonary hemorrhage, or drug reactions may mimic pneumonia, particularly in critically ill patients. While there are many different testing modalities that may be employed to this end, all have their limitations and none is sufficiently sensitive and specific to be considered a “gold standard” test (RELLO et al. 2001).

13.3.4 Chronic Pneumonia

Chronic pneumonia results from granulomatous inflammation, due to bacteria (e.g. *Mycobacterium tuber-*

Table 13.1. Risk factors for an adverse outcome (mortality) from ventilator-associated pneumonia (adapted from NIEDERMAN 2004)

| Patient risk factors | |
|---|--|
| Historical data | |
| | Prolonged mechanical ventilation before pneumonia |
| Medical (vs surgical) diagnosis | |
| | Age >60 years |
| Physiologic factors | |
| | Underlying fatal or serious illness |
| | Severe pneumonia (with sepsis or ARDS) |
| | Coma on admission |
| | Multiple system organ failure |
| Laboratory data | |
| | Bilateral lung infiltrates |
| Bacteriologic risk factors | |
| High-risk pathogen | |
| | <i>Pseudomonas aeruginosa</i> |
| | Acinetobacter species |
| | <i>Stenotrophomonas maltophilia</i> |
| | Methicillin-resistant <i>Staphylococcus aureus</i> |
| Antibiotic resistant pathogen, especially if acquired during therapy | |
| Superinfection after a first course of therapy | |
| Therapy-related risk factors | |
| Prior antibiotic therapy | |
| Inadequate initial therapy (organisms not sensitive to therapeutic agent) | |
| Inadequate dose or dose regimen | |

culosis) or fungi (e.g. *Histoplasma capsulatum*, *Blastomyces dermatidis*, *Coccidioides immitis*). It is most often a localized lesion in the immunocompetent patient. Unlike tuberculosis, the above mentioned fungal species are geographic in that it causes disease in particular localization in the United States and in Mexico.

In the lungs these infections produce epithelioid cell granulomas, which usually undergo coagulative necro-

sis and coalesce to produce larger areas of consolidation. Also they can liquefy to form cavities. Spontaneously or during therapy these lesions can undergo fibrosis and concentric calcification. As a consequence the typical *radiographic appearance* of this type of pneumonia is the single or multiple lung nodules with or without calcification.

13.3.5 Pneumonia in the Immunocompromised Host

The appearance of a pulmonary infiltrates and signs of infection (e.g., fever) is one of the most common and serious complications in patients whose immune and defense systems are suppressed by disease, immunosuppression for organ transplantation and tumors, or irradiation (ROSENOW 1990).

The host defense system includes physical and chemical barriers to infection, the inflammatory response, and the immune response. Physical barriers, such as the skin and mucous membranes, prevent invasion by most organisms. Chemical barriers include lysozymes and hydrochloric acid. Lysozymes destroy bacteria by removing cell walls. Hydrochloric acid breaks down food and mucus that contains pathogens. The inflammatory response involves polymorphonuclear leukocytes, basophils, mast cells, platelets and, to some extent, monocytes and macrophages. The immune response primarily involves the interaction of lymphocytes (T and B), macrophages, and macrophage-like cells and their products. These cells may be circulating or may be localized in the immune system's tissues and organs (SPRINGHOUSE 2007). Primary immune deficiency diseases are disorders in which part of the body's immune system is missing or does not function properly. In contrast to secondary immune deficiency disease in which the immune system is compromised by factors outside the immune system, such as viruses or chemotherapy, the primary immune deficiency diseases are caused by intrinsic or genetic defects in the immune system.

Primary immunodeficiencies are complex diseases. Since each one can be traced to the failure of one or more parts of the immune system, one of the more convenient ways to group them is according to the part of the immune system that is faulty:

- B cell (antibody) deficiencies
- Combined T cell and B cell (antibody) deficiencies
- T cell deficiencies
- Defective phagocytes
- Complement deficiencies
- Deficiencies/cause unknown

Antibody deficiencies can hinder or prevent the immune system from recognizing and marking for destruction bacteria, viruses and other foreign invaders. X-linked agammaglobulinemia, an inherited deficiency that appears in the first 3 years of life, leaves infants and young children with recurrent infections of the ears, lungs, sinuses and bones, and increased susceptibility to such viruses as hepatitis and polio.

Combined immunodeficiencies occur in people who lack the T lymphocytes that develop into killer cells that destroy infected cells or become helper cells that communicate with other immune cells. X-linked severe combined immunodeficiency, most often diagnosed during the first year of life, allows organisms that do not affect people with healthy immune systems to cause frequent and life-threatening infections.

Complement deficiencies usually involve an absence of one or several of the proteins that contribute to the complement system's ability to attach to antibody-coated foreign invaders. In childhood or early adulthood, a complement deficiency can result in severe infections such as meningitis, or it can contribute to an autoimmune disease such as lupus erythematosus.

Phagocytic cell deficiencies result in the inability of cells that engulf and kill antibody-coated invaders to act efficiently to remove pathogens or infected cells from the body. Chronic granulomatous disease, the most severe form of phagocytic deficiency, usually appears in early childhood. It causes frequent and severe infections of the skin, lungs and bones, leaving swollen collections of inflamed tissue called granulomas.

In comparison to the secondary, the primary immunodeficiencies syndromes are rare.

Common conditions associated with *secondary immune deficiency* are adapted from Bonilla FA, Secondary immune deficiency due to immunosuppressive drugs and infections other than HIV (personal communication 2008):

- Immunosuppressive therapy
 - Cytotoxic chemotherapy for malignancy
 - Treatment of autoimmune disease
 - Bone marrow ablation prior to transplantation
 - Treatment or prophylaxis of graft vs host disease following bone marrow transplantation
 - Treatment of rejection following solid organ transplantation
- Microbial infection
 - Viral infection
 - HIV, AIDS
 - Measles
 - Herpes viruses
 - Bacterial infection (superantigens)

- Mycobacterial infection
- Parasitic infestation
- Malignancy
 - Hodgkin's disease
 - Chronic lymphocytic leukemia
 - Multiple myeloma
 - Solid tumors
- Disorders of biochemical homeostasis
 - Diabetes mellitus
 - Renal insufficiency/dialysis
 - Hepatic insufficiency/cirrhosis
 - Malnutrition
- Autoimmune disease
 - Systemic lupus erythematosus
 - Rheumatoid arthritis
- Trauma
 - Burns
- Environmental exposure
 - Radiation
 - Ionizing
 - Ultraviolet
 - Toxic chemicals
- Other
 - Pregnancy
 - Stress
 - Asplenia/hyposplenism
 - Allogeneic blood transfusion
 - Aging

A wide variety of so-called opportunistic infectious agents, many of which rarely cause infection in normal hosts, can cause these pneumonias, and often, more than one agent is involved. The mortality from these opportunistic infections is high. On the other hand, the list of differential diagnoses of such infiltrates is long and includes drug reactions, cardiac failure, and involvement of the lung by tumor or other underlying conditions. Table 13.2 lists some of the opportunistic agents according to their prevalence and whether they cause local or diffuse pulmonary infiltrates. The large group of immunocompromised patients sometimes is divided into AIDS and non-AIDS causes of immunosuppression. The types of infection to which HIV-positive patients become susceptible vary as cell-mediated immunity becomes less effective at eradicating viruses, fungi, protozoa, and facultative intracellular bacteria, such as *Mycobacterium tuberculosis*. Knowledge of the CD4 lymphocyte count can thus be helpful for interpretation of radiologic images in AIDS patients (MARQUARDT and JABLONOWSKI 2003). Table 13.3 gives a short overview of the CD4 counts and corresponding infections.

As mentioned previously the radiographic patterns in most of the cases are not pathognomonic and the pat-

Table 13.2. Causes of pulmonary infiltrates in immunocompromised hosts (from HUSAIN and KUMAR 2005)

| Causes of pulmonary infiltrates in immunocompromised hosts | |
|--|-------------------------------|
| Diffuse infiltrates | Focal infiltrates |
| Common | Common |
| Cytomegalovirus | Gram-negative rods |
| <i>Pneumocystis jiroveci</i> | <i>Staphylococcus aureus</i> |
| Drug reaction | Aspergillus |
| | Candida |
| | Malignancy |
| Uncommon | Uncommon |
| Bacteria | Cryptococcus |
| Aspergillus | Mucor |
| Cryptococcus | <i>Pneumocystis jiroveci</i> |
| Malignancy | <i>Legionella pneumophila</i> |

Table 13.3. Overview of the CD4 counts and corresponding infections

| HIV – Complications at CD4 >500/mm ³ | HIV – Complications at CD4 200–500/mm ³ |
|---|--|
| Infectious | Infectious |
| Acute retroviral syndrome | Pneumococcal pneumonia |
| Candida vaginitis | Tuberculosis |
| | Herpes zoster |
| | Kaposi sarcoma |
| | Oral hairy leukoplakia (OHL) |
| | Oropharyngeal candidiasis (thrush) |
| Other | Non-Infectious |
| Generalized lymphadenopathy | Cervical carcinoma |
| Guillain-Barre (very rare) | Lymphomas |
| Vague constitutional symptoms | Immune thrombocytopenic purpura (ITP) |

tern approach is limited by underlying and concomitant diseases, the severity and time factor of manifestation, and treatment. It is frequently impossible for the clinician to identify the causative organism of a pneumonic infiltrate. Narrowing of the etiologic differential diagnosis may be possible using *radiologic pattern* recognition and the integration with clinical and laboratory information. Although with pattern recognition, specific etiologic diagnoses can hardly ever be established, patterns help to classify groups of potentially underlying organisms.

As a general rule of thumb, localized segmental or lobar aveolar densities can be attributed to typical or atypical bacterial infections. Diffuse bilateral interstitial and/or interstitial alveolar infiltrates most commonly are caused by viruses, atypical bacteria, and protozoa. Micro-nodular disease is most often caused by miliary tuberculosis (miliary pattern), candidiasis, and histoplasmosis (small nodules), or viruses such as herpes or varicella zoster virus (diffuse nodules with hazy borders). Large, nodular lesions may represent bacterial abscesses, and in immuno-compromised patients, may be caused by invasive aspergillosis and nocardia.

In conclusion, the important tasks of imaging the lung with respect to pneumonia are:

- Detection of pulmonary abnormalities
- Support in narrowing the etiology or differential diagnosis
- Recognition of developing complications
- Demonstration of a therapeutic effect (however, radiographic patterns may change, even deteriorate with the immunologic status of the patient)

Looking at MRI for detection of pneumonia, the next part of this chapter is divided into a historical overview mentioning older and recent MR imaging concepts and a comparison of MRI with CT in the detection of pulmonary abnormalities suspicious for pulmonary infection.

13.4

MRI – Historical Overview and Imaging Concepts

In the beginning, MRI was an extension of traditional NMR spectroscopy in which the quantitative chemical analysis of a homogeneous sample is determined by the application of magnetic fields. Even in the 1970s and 1980s the use of MRI to diagnose the presence and extent of cancer was an active area of research. Another area of clinical interest was the use of proton MRI in the diagnosis of diseases, related to water content and

movement, such as edema, heart diseases, and circulation problems. Effective MRI section thicknesses at that time were approximately 1 cm (PARTAIN et al. 1980).

JAMES et al. (1982) concluded in a review that, because of its limited signal-to-noise ratio and inherent low sensitivity, MRI, in many respects, is not comparable to CT. But recognition that the information provided is fundamentally different from the attenuation of energy as in CT is conceptually important.

One of the first preliminary studies about MRI of the thorax was published by GAMSU et al. (1983). The study population consisted of 10 normal volunteers and 12 adult patients; 9 of these had advanced lung cancer, and 3 had nonmalignant lesions of the thorax. They were imaged with a 0.35-T superconducting magnet using spin-echo sequences, the individual sections were 7 mm thick and adjacent sections were separated by 5 mm. Ten patients underwent CT, and all underwent chest radiography. In conclusion of the results the authors found that hilar masses and lymphadenopathy were easily distinguished from blood vessels and hilar fat because of differences in T1 time. But the spin-echo images and the relaxation times did not show differences between tumor and consolidated lung tissue (GAMSU et al. 1983).

In 1984, 33 patients with a variety of chest abnormalities were examined at 0.6-T; 28 of the patients had proved malignant disease. In this study population ROSS et al. (1984) found that MRI was considered to be as diagnostic as CT in determining abnormalities in 15. MR was superior to CT in one patient who had a right suprahilar carcinoma. CT proved superior to MRI in two patients. One patient had tracheal stenosis and one patient had an esophageal carcinoma. Another important result in this publication was the detection of disadvantages of MRI in chest imaging:

- Prolonged data acquisition time (the total time for an MR study of the chest averaged 1–1.5 h, vs 30 min for a CT examination)
- Relatively thick imaging section with associated partial volume averaging
- Failure to visualize calcium
- Pleural effusions were not easily characterized (ROSS et al. 1984).

A more detailed comparison of MRI and CT for the staging of bronchogenic carcinoma was performed by WEBB et al. (1985). They investigated 33 patients with histologically proved bronchogenic carcinoma at 0.35-T MR using multi-section spin-echo technique. Scanning was performed without electrocardiogram (ECG) gating. In comparison with CT, MRI provided comparable information regarding the presence and size of medi-

Table 13.4. Comparison of MRI and CT in 25 patients with chronic infiltrative lung disease (from MÜLLER et al. 1992)

| Findings | No. of Patients by Imaging Study | | | |
|---|----------------------------------|----|----|----|
| | CT | T1 | PD | T2 |
| <i>Vessels</i> | | | | |
| Central | 25 | 25 | 24 | 24 |
| Peripheral | 25 | 25 | 18 | 3 |
| <i>Airways</i> | | | | |
| Lobar | 25 | 25 | 25 | 25 |
| Segmental | 25 | 21 | 20 | 8 |
| Subsegmental | 25 | 8 | 5 | 4 |
| <i>Secondary pulmonary lobule</i> | | | | |
| Interlobular septum or vein | 25 | 19 | 15 | 7 |
| Centrilobular arteriole | 25 | 11 | 5 | 1 |
| <i>Interstitial abnormality</i> | | | | |
| Reticulation | 15 | 13 | 12 | 4 |
| Honeycombing | 10 | 9 | 6 | 0 |
| Septal thickening | 16 | 12 | 11 | 4 |
| Nodules | 6 | 5 | 6 | 5 |
| <i>Distribution of interstitial abnormalities</i> | | | | |
| Peribronchovascular | 4 | 4 | 4 | 4 |
| Peripheral | 11 | 10 | 10 | 9 |
| Diffuse | 7 | 7 | 7 | 7 |
| Patchy | 4 | 5 | 5 | 4 |
| <i>Air-space abnormality</i> | | | | |
| Ground-glass opacity | 18 | 19 | 18 | 17 |
| Consolidation | 5 | 5 | 5 | 5 |

astinal lymph nodes. Bronchial abnormalities were better seen on CT, primarily because of its better spatial resolution. Direct invasion of the mediastinum adjacent to a hilar mass was usually better demonstrated on MRI because of the ease with which tumor and mediastinal vessels could be distinguished. In three of four patients who had a surgically proved hilar mass with a peripheral obstructive pneumonia, the central tumor could be

distinguished from collapsed peripheral lung on MR images performed with a repetition time (TR) of 2.0 s. The peripheral lung appeared more intense than tumor (WEBB et al. 1985).

To find if it is possible to differentiate further various causes of pulmonary consolidation with MRI, MOORE et al. (1986) analyzed patients with pulmonary edema, postobstructive pneumonitis, alveolar proteinosis,

Pneumocystis pneumonia, lobar nonobstructive pneumonia, pulmonary hemorrhage, and acute radiation pneumonitis. The study was performed with a 0.35-T MR scanner, using spin-echo pulse sequences with repetition times of 500 and 2000 ms and echo times (TE) of 28 and 56 ms. In summarizing the results, the authors could demonstrate that measuring T1 and T2 values the different entities showed considerable overlap. The two patients with pulmonary alveolar proteinosis showed much lower values of T1, which probably reflects the relative absence of water within the airspaces and the presence of lipoprotein. In general, T1 and T2 values increase in proportion to the water content of fluids or tissue, but they are also influenced by the presence of lipids and by interaction between water and both large and small molecules with which they come in contact (MOORE et al. 1986).

High-resolution computed tomography (HRCT) had become the gold standard in the evaluation of chronic infiltrative lung diseases and it was shown that it accurately reflects the pathologic abnormalities. The aim of a study from MÜLLER et al. (1992) was to compare MRI with HRCT in the assessment of these entities. All MR studies were performed on a 1.5-T MR imager. Cardiac-gated proton density-weighted and relatively T2-weighted images were obtained at two or three RR intervals. The slice thickness was 10 mm, with a 1- or 2-mm interslice gap. In comparison to this the CT scans were obtained by using 1.5-mm collimation scans, and 10-mm intervals. Table 13.4 summarizes the results.

As a result, MRI was consistently inferior in the anatomic assessment of lung parenchyma and in showing interstitial abnormalities, particularly fibrosis. Furthermore, areas of mild interstitial abnormalities seen on CT were often not apparent on MRI. But, on the other hand, MRI was comparable to CT in the assessment of air-space abnormalities. In all patients, areas with ground-glass opacities or air-space consolidation on CT corresponded to areas of increased signal intensity on MRI (MÜLLER et al. 1992).

Primack et al. noticed that the use of MRI in the assessment of infiltrative lung disease has been limited by the low proton density of lung parenchyma and by loss of signal due to motion and the difference in diamagnetic susceptibility of air and soft tissue. On the other hand, the presence of pulmonary infiltrates leads to a marked increase in signal intensity. This is due to both the increase in proton density and a decrease in magnetic susceptibility effects. They included 22 consecutive patients with idiopathic pulmonary fibrosis, sarcoidosis, extrinsic allergic alveolitis, Churg-Strauss syndrome, Wegener granulomatosis, necrotizing sarcoid granu-

lomatosi, hypersensitivity drug reaction, desquamative interstitial pneumonia-like drug reaction, silicosis, lymphangitic carcinomatosis, talcosis, and bronchiolitis obliterans organizing pneumonia (BOOP). All patients had MRI and open lung biopsy. Ten of the 12 patients with parenchymal opacification as the predominant abnormality on MRI had cellular infiltrates pathologically, while fibrosis was present in the other 2. This study demonstrated that the MRI findings correlate with the pathologic findings and that parenchymal opacification on MRI usually indicates an inflammatory process, and therefore potentially treatable disease. Localized areas of fibrosis were easier to identify on CT than on MRI. Again, as mentioned in previous studies, these authors found out that a major limitation of MRI in the assessment of infiltrative lung disease was the low spatial resolution compared with HRCT (PRIMACK et al. 1994).

One of the earlier studies that focused on contrast-enhanced pulmonary MRI was published by HARALDSETH et al. (1999). They reviewed different forms of contrast agent enhancement: MR perfusion imaging, contrast enhanced MR angiography, and MR ventilation imaging. In the clinical context of pneumonia they included 13 patients. The MR perfusion was obtained with a standard low flip-angle gradient-echo sequence with an inversion prepulse. The time-intensity curves after intravenous application of a gadolinium-based non-specific contrast agent showed that in pneumonic tissue there was a steep increase without first passage peak; the dynamics of the contrast agent passage was different from normal lung tissue (Fig. 13.1). The authors did not suggest replacement of chest X-rays for routine pneumonia diagnosis, but in cases where the differential diagnosis between pulmonary embolism and pneumonia were two main options, patients might benefit from an MR perfusion examination (HARALDSETH et al. 1999).

A more detailed description of MRI of the pulmonary parenchyma was published by KAUCZOR and KREITNER (1999). As a brief summary of the technical considerations the authors noticed the following three factors hampering the application of MRI to the lung and suggested the following strategies to resolve the problems:

1. *Low proton density*: This is valid for the normal lung parenchyma and especially for lung diseases with loss of tissue such as emphysema. In all other lung diseases, the amount of tissue, fluid, and/or cells is increased. The recommended investigation techniques are:
 - a) T1-weighted spin-echo sequences with short echo times (<7 ms)

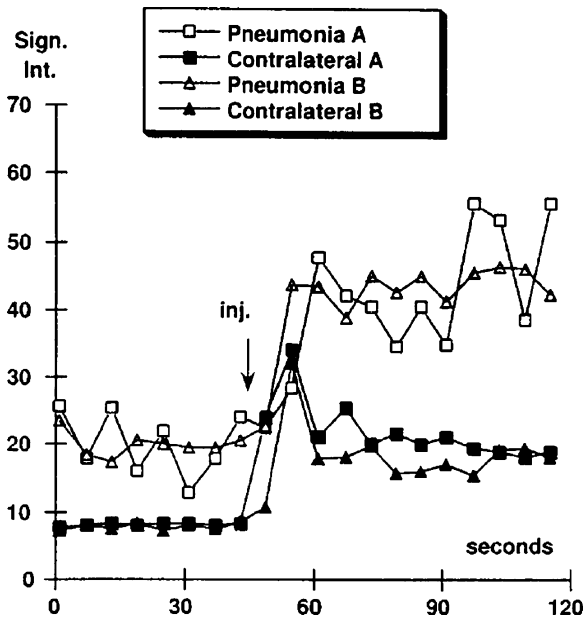


Fig. 13.1. Time-intensity curves depicting the first passage in two patients with pneumonia; in the inflammatory tissue and in the contralateral lung (from HARALDSETH et al. 1999)

- b) T1-weighted gradient-echo sequences, such as fast low-angle shot (FLASH), with short echo times (3 ms)
 - c) Higher number of acquisitions
 - d) Administration of contrast agents
2. *Signal loss due to physiological motion:*
 - a) Breath-hold imaging with fast sequences like FLASH or half-Fourier acquired single-shot turbo spin echo (HASTE)
 - b) Respiratory gating with navigating techniques, gating in expiration using a belt, and respiratory compensation using reordering of phase encoding
 - c) ECG triggering
 3. *Susceptibility artefacts because of the multiple air-tissue interfaces:* As mentioned previously these artefacts degrade imaging of normal lung tissue. After loss of air and concomitant increase of tissue, cells, or fluid significantly reduces the number of air-tissue interfaces and the degree of susceptibility artefacts:
 - a) Use of short echo times for T1-weighted spin-echo or gradient-echo sequences
 - b) Use of T2-weighted turbo-spin-echo (TSE) sequences or T2-weighted ultrafast TSE-sequences with high turbo factors

With regard to infiltrations, the authors concluded that MRI can be used for the detection and characterization of inflammatory pulmonary round infiltrates in immunocompromised patients. Post-contrast T1-weighted FLASH showed a strongly enhancing, ill-defined round infiltration (Fig. 13.2), and with HASTE sequence moderate signal intensity was found in a patient with bronchopneumonia (Fig. 13.3a-e) (KAUCZOR and KREITNER 1999).

GAETA et al. (2000) revisited the value of gadolinium-enhanced MRI in the evaluation of chronic infiltrative lung disease. They found out that the presence of enhancing lesions on gadolinium-enhanced T1-weighted MRI studies may be a reliable indicator of inflammation and, consequently, indicates potentially treatable disease. Their study was performed on a 1.5-T scanner obtaining a spoiled gradient-echo T1-weighted sequence during full inspiration (TR 168 ms, TE 4.8 ms, FA 75°, slice thickness 5 mm) (GAETA et al. 2000).

Another topic in literature is the differentiation between benign and malignant nodular lesions of the lung. Growth factors and calcification pattern are only two of a noninvasive diagnostic armamentarium to separate benign from suspicious lesions, to avoid unnecessary invasive tests. To overcome the limitation of morphological features LI et al. (2000) included 62 patients to evaluate suspicious lung nodules with CT and dynamic Gd-DTPA enhanced MRI. Axial T1-weighted images (TR 500 ms, TE 10 ms) with a slice thickness of



Fig. 13.2. A 45-year-old male patient with invasive aspergilloma. Post-contrast T1-weighted FLASH (TR >200 ms, TE = 4 ms, FA = 80°) shows a strongly enhancing, ill-defined round infiltration (arrow) (from KAUCZOR and KREITNER 1999)

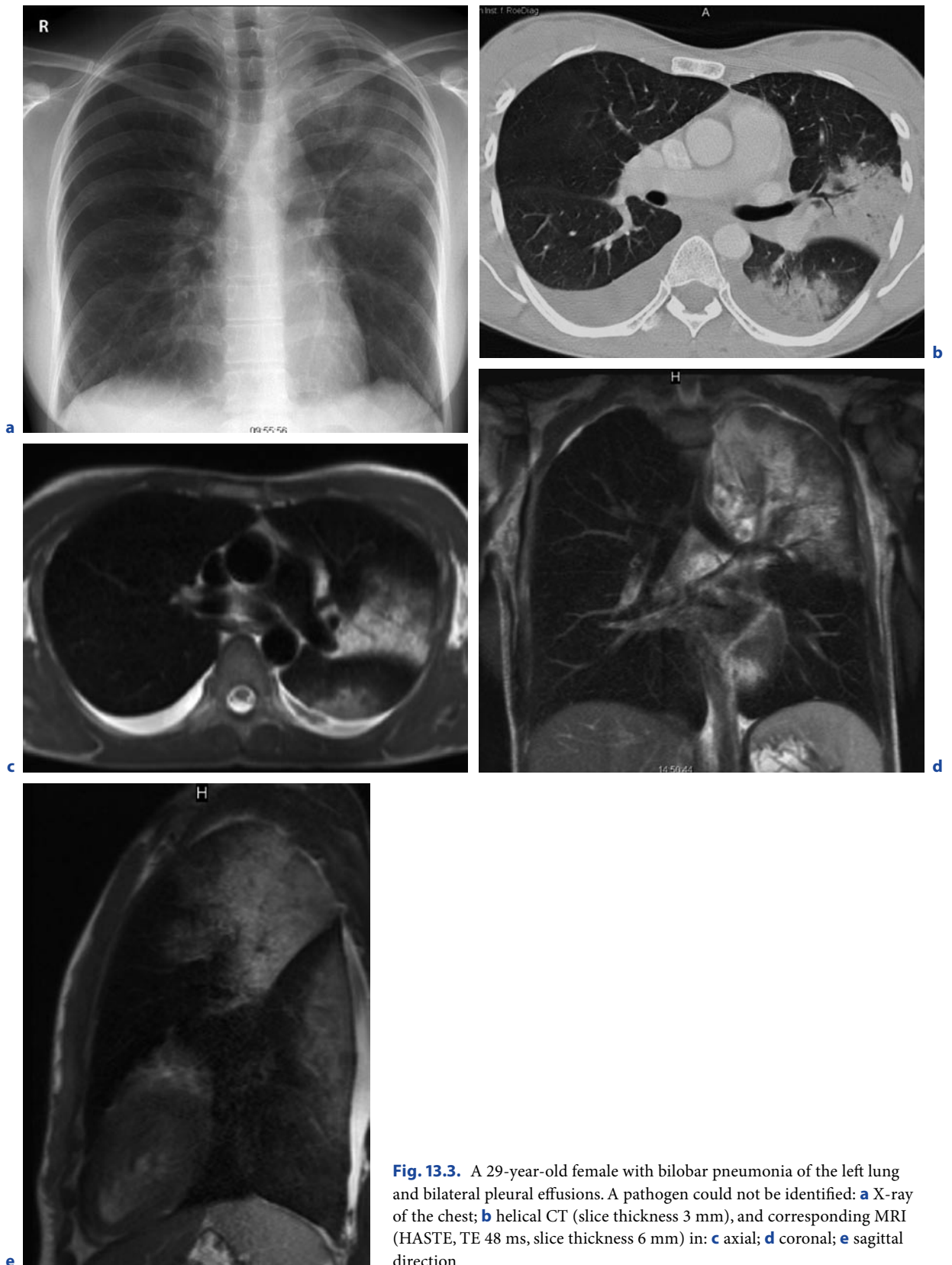


Fig. 13.3. A 29-year-old female with bilobar pneumonia of the left lung and bilateral pleural effusions. A pathogen could not be identified: **a** X-ray of the chest; **b** helical CT (slice thickness 3 mm), and corresponding MRI (HASTE, TE 48 ms, slice thickness 6 mm) in: **c** axial; **d** coronal; **e** sagittal direction

5 mm at 0, 15, 45, 75, 110, and 140 s, and 3, 5, 8, and 10 min were obtained. Additional T2-weighted images (TR 3000 ms, TE 80 ms) were obtained before contrast application. After correlation with pathological findings they found out that nodular fibrosis, inflammatory granulomas, cryptococcoma and inflammatory pseudotumor had a more or less low rate of contrast uptake. On the other hand, focal organizing pneumonia and sclerosing hemangioma had a significant and early enhancement. Taking into account that malignant nodules are characterized by a fast increase in signal intensity during the first pass of the contrast agent (GÜCKEL et al. 1996), at least some nodular lesions could be excluded to be malignant with dynamic MR (LI et al. 2000).

That further developments in sequence design will have potential in imaging the lung parenchyma was investigated by BADER et al. (2002) and RUPPRECHT et al. (2002). BADER et al. (2002) included 20 patients with pulmonary diseases comprising non-small-cell, and bronchioalveolar carcinomas, endobronchial mucoepidermoid carcinoma, metastases, pneumonia, Wegener's granulomatosis, chronic obstructive pulmonary disease, arterio-venous malformation, and bronchogenic cyst. MRI studies were performed at 1.5 T before and after administration of gadolinium using a modified volumetric interpolated breath-hold examination (VIBE) (TR 4.6 ms, TE 1.8 ms, FA 15°, effective slice thickness 4 mm). Their results demonstrated that reproducible high image quality with effective suppression of artefacts, high resolution, and visualization of gadolinium enhancement could be obtained. RUPPRECHT et al. (2002) performed a study without contrast agent and investigated a steady-state free precession sequence (true FISP) as a potential alternative to the conventional X-ray in pediatric patients with suspected pneumonia. A true FISP sequence was chosen because of its high spatial resolution and signal-to-noise ratio (S/N) in fluid- and thus T2-dominated infectious pulmonary disease. To overcome breathing artefacts in this particular patient group and to increase the S/N ratio they obtained slice thicknesses of 30–55 mm at a 0.2-T low-field MR system. The true FISP sequence had the following parameters: TR 6 ms, TE 3 ms, FA 90°. The acquisition time for a triple slice scan was 4.8 s, and the door-to-door time was between 10 and 15 min. All pathological findings in the conventional chest X-ray could be identified in the corresponding MR investigation and the MRI was superior in demonstrating pleural and pericardial effusions. Two small retrocardial pneumonic infiltrates were noted in the MRI only. The authors concluded that this technique could represent an alternative to the conventional chest X-ray (RUPPRECHT et al. 2002). Such an alternative might be of special interest in children with Nijmegen-

Breakage-Syndrome. This entity is an autosomal recessive chromosomal instability syndrome, characterized by microcephaly, growth retardation, skin abnormalities, immunodeficiency, radiation sensitivity, and a strong predisposition to lymphoid malignancy. Because of their sensitivity to ionizing radiation X-ray and CT examination should be avoided (ALIBEK et al. 2007).

Whether it is possible not only to detect but also to quantify pulmonary lesions due to pneumococcal pneumonia was investigated in a murine model by MARZOLA et al. (2005). Infection was induced in a group of mice (N = 5) by intranasal administration of a suspension containing *Streptococcus pneumoniae*, and a group of noninfected animals (N = 5) was used as a control group. Axial, ECG-gated, spoiled GRE images with 1.2 mm slice thickness were acquired with a 4.7-T scanner. After sacrifice and histological evaluation a good concordance with regard to the anatomical localization and a good correlation between the volume of the pneumoniae by histology and MRI was found (MARZOLA et al. 2005).

Another interesting experimental study was published by TOURNEBIZE et al. (2006). The aim of this work was to prove if MRI is able to provide spatio-temporal visualization of edema and inflammation caused by *Klebsiella pneumoniae* induced pneumonia in mice. The study was performed with a 7-T scanner. After inoculation with avirulent and virulent strains of *Klebsiella*, treatment by bactericidal doses of antibiotics was initiated. Images were acquired up to 8 days post infection. The virulent strain caused an intense inflammation within 2 days in the whole lungs, while an avirulent strain did not show significant changes. The increase in cell density accompanied with extravascular leakage results in an increase in high water content detectable by MRI. After treatment with antibiotics the inflammation disappeared after a week. The lesions observed by MRI correlated with the damage seen by histological analysis. In summary MRI allows observing the appearance and regression of inflammation (TOURNEBIZE et al. 2006).

The next important topic was the investigation of the sensitivity of MRI in detecting alveolar infiltrates. To provide reliable data, BIEDERER et al. (2002) performed an experimental study using porcine lung explants and a dedicated chest phantom to evaluate the signal intensity of artificial alveolar infiltrates with T1- and T2-weighted MRI sequences. Ten porcine lung explants were examined with MRI at 1.5 T before and after intra-tracheal instillation of either 100 or 200 ml gelatine-stabilised liquid to simulate alveolar infiltrates. Control studies were acquired with helical CT. Table 13.5 summarizes the applied MR sequences.

After administration of the gelatine-stabilised liquid, the CT images demonstrated patchy areas of ground-glass opacities in both lungs. The 2D and 3D T1-weighted sequences could not sufficiently visualize the infiltrates. In contrast the T2-weighted sequences showed clearly visible infiltrates with an increase in signal intensity of approximately 30% at 100 ml ($p < 0.01$) and 60% at 200 ml ($p < 0.01$). For practical reasons: T2-weighted sequences can be highly recommended for the delineation of infiltrates in the lung. T1-weighted sequences without intravenous application of contrast agents are not sufficient for this task. Because of the extremely different acquisition times between HASTE and the T2-TSE, the HASTE sequence has to be preferred. Table 13.6 overviews the results in detail (BIEDERER et al. 2002).

After these historical and technical developments it is necessary to evaluate the potential of MRI in detecting pneumonia in the immunocompromised patient. Especially in this particular group of patients, pneumonia is an important cause of morbidity and mortality. The imaging of infiltrates is very challenging, because the immunosuppression decreases the response of the lung to infectious agents. On the other hand, the patterns of pneumonia are highly variable and depend on multiple factors, like underlying diseases, time course, treatment, e.g. By now, a considerable proportion of pulmonary fungal infections is not diagnosed ante mortem in cancer patients. In addition, especially patients after bone marrow transplantation are often younger

and repetitive CT examinations carry an additional radiation burden.

LEUTNER et al. (2000) tried to find out how MRI compares with CT regarding the depiction of typical features of pneumonia and the detectability of lesions. MR studies was performed with a 1.5-T system and the imaging protocol consisted of a transversal T2-weighted ultrashort turbo spin-echo sequence (TR 2000–4000 ms, TE 90 ms, slice thickness 6 mm, and six numbers of excitation). In comparison to helical CT (slice thickness 8 mm) they evaluated presence, number, and location of pulmonary infiltrates (nodular, reticular, cysts, cavitation, consolidation, and ground-glass infiltration). In summary, most of the CT and MR examinations (75%) were rated as showing identical results concerning not only the number but also the morphology of different lesions that were due to opportunistic pneumonia. In addition, MRI was able to differentiate between consolidation and ground-glass infiltration (LEUTNER et al. 2000).

13.5

MRI – Comparison with CT

The advent of multislice CT and the implementation of parallel imaging in MRI pushed the limits towards new possibilities with regard to examination volume, time, and slice thickness. Multislice CT offers the opportunity

Table 13.5. Summary of the applied sequences for the investigation of the chest phantom (from BIEDERER et al. 2002)

| Sequence | 2D-GRE | 3D-GRE (VIBE) | 3D-GRE (VIBE) | HASTE | HASTE | T2-TSE |
|-----------------------|-----------|------------------------|------------------------|-----------|-----------|------------|
| Weighting | T1 | T1 | T1 | T2 | T2 | T2 |
| Slice orientation | Axial | Axial | Coronal | Axial | Coronal | Axial |
| TR/TE (ms) | 100/2.2 | 4.5/1.9 | 4.5/1.9 | 2000/43 | 2000/43 | 3000/120 |
| FA | 50 | 12 | 12 | 180 | 180 | 120 |
| FOV (mm) | 350 | 350 | 350 | 350 | 350 | 350 |
| Matrix | 222 × 256 | 502 × 512 interpolated | 502 × 512 interpolated | 224 × 256 | 224 × 256 | 270 × 512 |
| Slice thickness (mm) | 6 | 2.5 interpolated | 2.5 interpolated | 7 | 7 | 8 |
| Slice per acquisition | 19 | 32 | 32 | 7 | 7 | 12 |
| Acquisition-time | 23 s | 23 s | 23 s | 18 s | 18 s | 4 min 51 s |

Table 13.6. Measurement of signal intensities (SI), calculation of standard deviations (SD) and signal-to-noise ratios before (native) and after instillation of liquid (with infiltration) (adapted from BIEDERER et al. 2002)

| Sequence | Infiltration with 100 ml | | | | | Infiltration with 200 ml | | | | |
|-------------------|--------------------------|------|------|--------------|----------|--------------------------|------|------|--------------|----------|
| | SI | SD | S/N | Increase (%) | | SI | SD | S/N | Increase (%) | |
| 2D-GRE | | | | | | | | | | |
| Native | 31.28 | 3.2 | 1.15 | | | 30.2 | 2.3 | 1.11 | | |
| With infiltration | 31.51 | 3.3 | 1.16 | 0.74 | p = 0.32 | 31.8 | 2.6 | 1.12 | 5.6 | p < 0.01 |
| 3D-GRE | | | | | | | | | | |
| Native | 17.0 | 1.11 | 1.13 | | | 17.2 | 1.16 | 1.16 | | |
| With infiltration | 17.3 | 1.36 | 1.15 | 2.2 | p = 0.02 | 18.0 | 1.16 | 1.22 | 4.4 | p < 0.01 |
| T2-HASTE | | | | | | | | | | |
| Native | 94.9 | 18.6 | 3.62 | | | 96.2 | 17.6 | 3.74 | | |
| With infiltration | 127 | 21.2 | 5.03 | 34.4 | p < 0.01 | 153 | 20.0 | 6.0 | 60.5 | p < 0.01 |
| T2-TSE | | | | | | | | | | |
| Native | 14.13 | 2.8 | 1.39 | | | 14.3 | 3.0 | 1.34 | | |
| With infiltration | 18.41 | 3.7 | 1.85 | 30.3 | p < 0.01 | 23.4 | 3.5 | 2.23 | 63.4 | p < 0.01 |
| CT (in HU) | | | | | | | | | | |
| Native | 150 | 24.3 | 16.1 | | | 139 | 21.2 | 13.9 | | |
| With infiltration | 167 | 25.3 | 17.3 | 11.2 | p = 0.02 | 234 | 10.4 | 23.4 | 68.4 | p < 0.01 |

to investigate the entire lung with 1 mm slice thickness or less in much shorter than 1 min. Parallel imaging in MRI reduced dramatically the examination time that makes acquisition of the lungs in a few seconds possible.

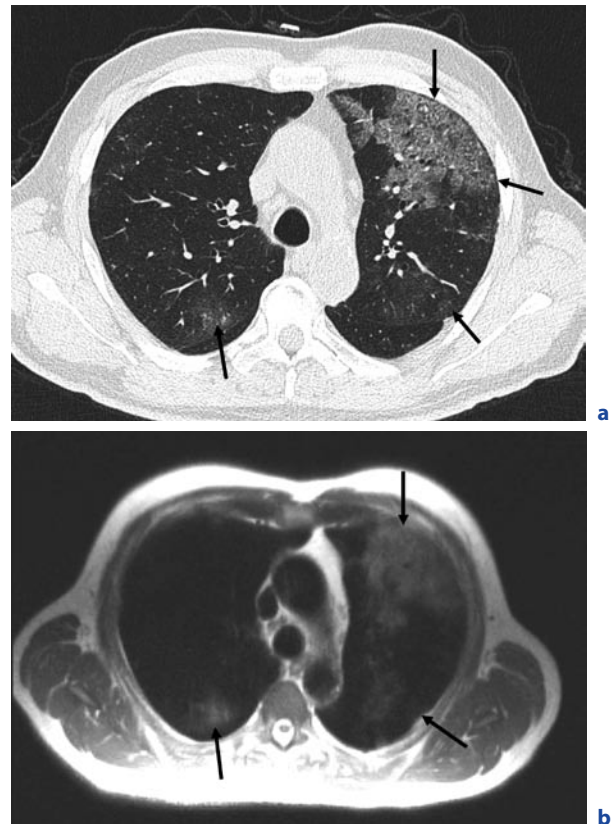
Thin-section helical CT is the gold standard for the evaluation of the lung even for very subtle lesions like small ground-glass opacities around lung nodules. That means, to classify the value of MRI of the lung, studies are necessary that compare MRI with the best CT techniques that are available nowadays.

EIBEL et al. (2006b) performed a study where they investigated pulmonary abnormalities in 30 immunocompromised patients with parallel MRI and thin-section helical CT. Table 13.7 summarizes the MR examination protocol for the applied HASTE sequence. It was not the intention of this study to investigate the lung comprehensively. In order not to exceed 1 min examination time, only the HASTE sequence was selected. The result-

ing in-room-time was not more than 10 min. The motivation was that MRI can only serve as a real alternative to CT, when the examination time is comparable.

One of the inclusion criteria for this study was an X-ray of the chest that was either normal or did not show abnormalities suggestive of pulmonary infection. Ill-defined nodules, ground-glass opacity areas, and consolidations, their location and distribution, and their lesion characteristics (e.g. margin contour, cavitation, calcification) were systematically analyzed. Twenty-two patients had pulmonary abnormalities on CT. In 21 (95%) patients, pneumonia was correctly diagnosed with MRI. One false-negative finding occurred in a patient with ill-defined nodules smaller than 1 cm at CT. One false-positive finding with MR was the result of blurring and respiratory artefacts. That results in a sensitivity of MRI in comparison to 1-mm CT slices of 95%, specificity of 88%, positive predictive value of 95%, and a negative predictive value of 88% (EIBEL et al. 2006a). In the

Fig. 13.4 A 76-year-old patient with myelodysplasia suffering from *Pneumocystis jiroveci* pneumonia (from EIBEL et al. 2006a): **a** thin-section CT above the level of the carina. Ground-glass opacity is the predominant finding in the ventral portion of the left upper lobe. Please note also the more subtle lesions in the dorsal parts of the both upper lobes; **b** axial HASTE-sequence at the same level (TE 27 ms). All lesions in the upper lobes are easily detectable



detection of ground-glass opacity areas (Fig. 13.4), consolidations (Fig. 13.5), and pleural effusion, MRI seems to be equal to thin-section CT. But the overall detection rate of nodules with MRI was only 72% (186/259). Detailed analyses found out that all nodules larger than 10 mm were reliably detected. The mean size of nodular lesions not found with MRI was 4 mm. This difference likely relates to the section thickness used with CT (1 mm) and MR imaging (6 mm). After this study the authors came to the conclusion that pulmonary imaging for the detection and quantification of infiltrates is highly reliable with modern MR scanners (EIBEL et al. 2006b).

Despite these encouraging results it is important to keep in mind is that CT has to be preferred in the detection of calcification, which can indicate some special disease entities and can be a sign of pulmonary scarring.

13.6

Morphology of Different Types of Pneumonia in MR Imaging

Before summarizing briefly the different MR features of pneumonia, already mentioned in the paragraphs before, the following statements are valid for MR imaging of pneumonia:

- Nodules larger than 1 cm in diameter, consolidations and ground-glass opacifications are detectable on MR images with a nearly identical sensitivity and accuracy with regard to lesion size and contour compared to CT. Obviously the definition of nodule, consolidation and ground-glass according to the Fleischner Society seems to be valid even for MRI (HANSELL et al. 2008).
- With MR images it might be more challenging or even impossible to delineate small nodules (<10 mm) and small areas of air or calcifications

Table 13.7. Parameters of the HASTE sequence, applied in the study of EIBEL et al. (2006b)

| | |
|---------------------------------------|---|
| Magnet | 1.5-T |
| TR | 440 ms |
| TE | 27 ms |
| Bandwidth | 488 Hz/pixel |
| Echo spacing | 3.76 ms |
| Slice thickness | 6 mm |
| Gap | 50% |
| FOV | 256 × 256 (axial) 320 × 256 (coronal and sagittal) |
| Modus | Interleaved |
| Acquisition | GRAPPA |
| iPAT-factor | 2 (24 reference lines) |
| Examination time for the entire lungs | 2–3 × 15 s (per direction) |

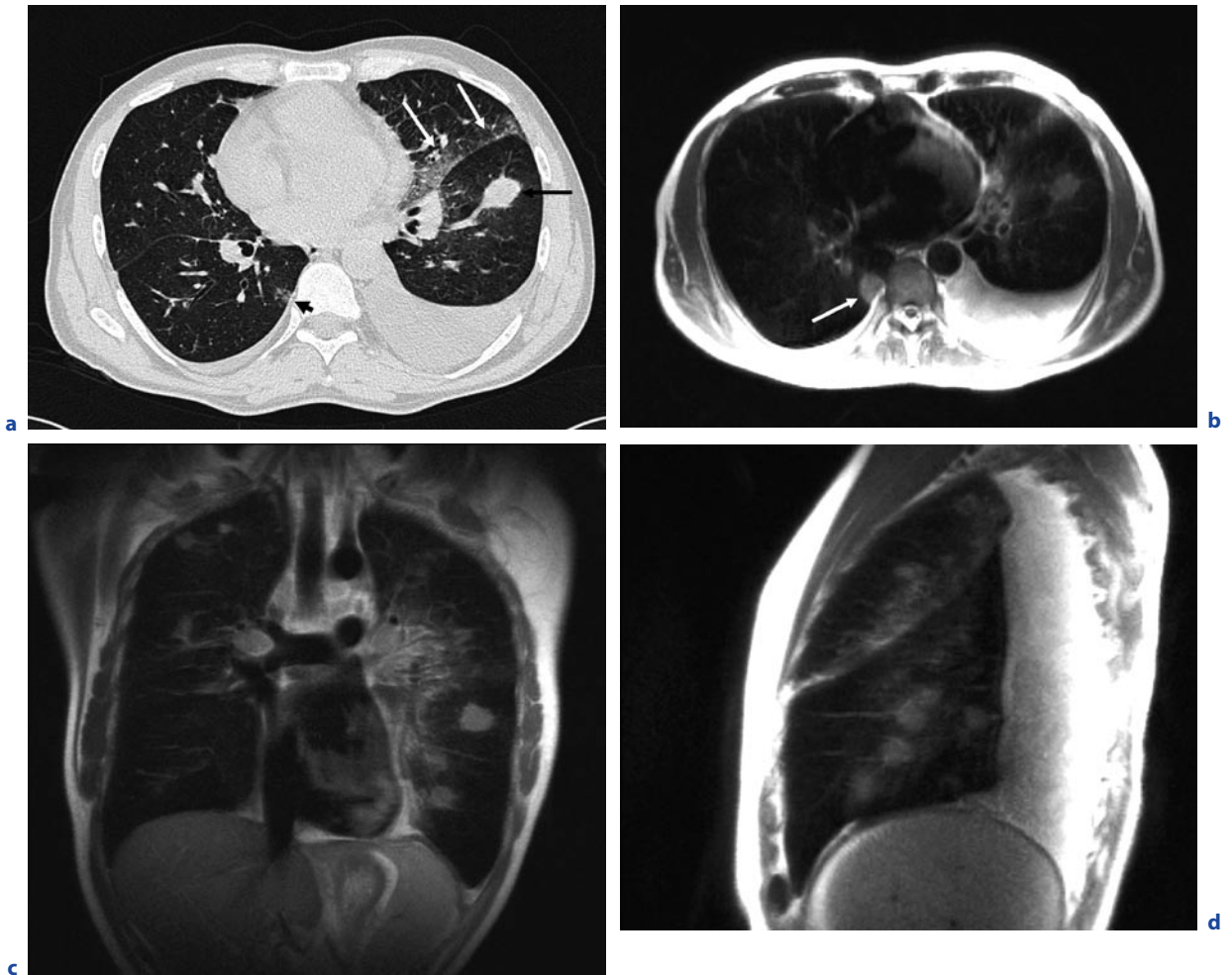


Fig. 13.5. A 45-year-old male with chronic lymphatic leukemia, suffering now from angioinvasive aspergillosis (from EIBEL et al. 2006a): **a** thin-section CT below the level of the carina shows a consolidation in the left lower lobe (*black arrow*), ground-glass opacity in the lingular lobe adjacent to the fissure (*white arrow*), and both-sided pleural effusions. Please

note also the subtle lesion in the right lower lobe adjacent to the spine (*short arrow*); **b** axial; **c** coronal; **d** sagittal HASTE. The pathologic findings are again comprehensively delineated by MRI, even the subtle lesion in the left lower lobe adjacent to the spine (*arrow*)

within lung nodules or consolidations in comparison to thin-section helical CT.

In Table 13.8 the most common and important features of pneumonia on MR images and the likely causative organisms are summarized.

Fungal pneumonia is an important topic, necessary to go a little bit more into detail, especially when dealing with MR imaging. Some organisms like *Histoplasma capsulatum* and *Coccidioides immitis* are primary pathogens, but are found only in specific geographic areas. On the other hand, organisms like *Aspergillus* and *Candida* species are opportunistic agents that affect patients which already suffer from an underlying pulmo-

nary disease or are immunocompromised. As invasive organisms the latter can cause severe tissue destruction and can influence the clinical outcome dramatically.

The pathogenesis of *Aspergillus* infection is complex, but worthy to know is the fact that this fungus causes necrosis in lung parenchyma due to extensive vascular permeation and occlusion of small to medium arteries. This permeation and especially the separation of necrotic lung from viable parenchyma in the recovery phase of the patient can cause life-threatening intra-alveolar hemorrhage.

Because of the different therapeutic approaches in patients with fungal pneumonia and because of the high morbidity and mortality in immunosuppressed patients

Table 13.8. MRI findings and corresponding likely causative organisms

| MRI finding | Likely causative organisms |
|---|---|
| Lobar consolidation = Lobar pneumonia | <i>Streptococcus pneumoniae</i> , <i>Klebsiella pneumoniae</i> , <i>Legionella pneumophila</i> , <i>Mycoplasma pneumoniae</i> |
| Patchy, sometimes bilateral interlobular consolidation = Bronchopneumonia | Streptococci, gram-negative bacilli, Legionella, anaerobes, virus |
| Ground-glass opacification and reticular pattern = Interstitial pneumonia | Virus, <i>Mycoplasma pneumoniae</i> , <i>Pneumocystis jiroveci</i> (Fig. 13.4) |
| Cavitation | <i>Staphylococcus aureus</i> , <i>Mycobacterium tuberculosis</i> , gram-negative bacilli, anaerobic bacteria |
| Round consolidation, halo, air-crescent sign, reverse target sign | <i>Aspergillus fumigatus</i> (Fig. 13.5) |

with invasive aspergillosis it is necessary to know the signs of this type of infection in imaging studies:

- Single or multiple nodular infiltrates
- Nodule with halo phenomenon
- Homogeneous consolidation in segmental or sub-segmental spread
- Cavitation (air crescent sign)
- Reverse target sign

The ground-glass attenuation surrounding some of the nodules is termed as halo. Histopathologic studies delineated that the cause for this finding is hemorrhage around the nodule. With MR the halo sign is clearly detectable and thus can help to differentiate the causative agents. Air crescent is a finding more common detectable in the recovery phase and relates to resorption of necrotic tissue in the periphery of the lesion or to retraction of the sequestrum from viable lung parenchyma (KIM et al. 2001). This crescent like air collection is associated with a higher risk of massive hemoptysis.

BLUM et al. (1994) observed another characteristic feature of necrotizing pneumonia. On T2-weighted images higher signal intensity in the center combined with comparatively lower signal intensity in the rim outlined a characteristic feature that they called “reverse target sign”. While the halo phenomenon is strongly suggestive of invasive aspergillosis in its early course, the reverse target sign is detectable in later stages. Probably because of the excellent soft-tissue contrast on MR imaging, LEUTNER et al. (2000) found that this issue is superior to contrast-enhanced CT in diagnosing necrotizing pneumonia.

Up to now, no comprehensive study compared the sensitivity and specificity of different imaging modalities for the diagnosis of invasive aspergillosis. BLUM et al. (1994) found out that MRI may be of diagnostic value in later stages of the disease and for the follow-up of nodular infiltrates on unknown etiology in immunocompromised patients. So, further studies are necessary to lower the high mortality of angioinvasive aspergillosis by making the diagnosis earlier and with a higher reliability.

13.7

Protocol

In this last paragraph a short protocol recommendation (Table 13.9) is listed, confirmed and illustrated by an upper lobe pneumonia (Fig. 13.6).

The T2-weighted HASTE sequence is the workhorse, necessary for detection and characterization of infectious lesions of the lung. Performing only the topogram and the axial HASTE in patients which are severely ill and breathless, the investigation time is below 2 min. The T1-weighted FLASH sequence with and without intravenous application of gadolinium is helpful for further characterization of infiltrates. This extends the investigation time to 15 min. The STIR and TrueFISP sequences can give additional information selected cases, but are not required in routine settings.

Table 13.9. Suggested investigation protocol at a 1.5-T MR scanner (Avanto, Siemens Medical Systems, Erlangen, Germany)

| Sequence | Type | Weighting | Slice orientation | TR (ms) | TE (ms) | Flip angle | FS | Slice thickness (mm) | Gd IV |
|-----------------------|-------|-----------|-------------------|---------|---------|------------|----|----------------------|-------|
| Topogram | | | | | | | | | |
| HASTE | SE | T2 | Axial | 1000 | 84 | 180 | | 6 | |
| | | T2 | Coronal | 1000 | 84 | 180 | | 6 | |
| | | T2 | Sagittal | 1000 | 84 | 180 | | 6 | |
| FLASH 2D | GE | T1 | Axial | 118 | 2 | 70 | | 6 | |
| | | T1 | Coronal | 78 | 2 | 70 | + | 6 | |
| STIR [*] | SE/IR | T2 | Axial | 3980 | 100 | 150 | + | 6 | |
| TrueFISP [*] | SS | T2 | Axial | 3 | 1 | 60 | | 6 | |
| | | T2 | Coronal | 3 | 1 | 60 | | 6 | |
| FLASH 2D | GE | T1 | Axial | 118 | 2 | 70 | + | 6 | + |
| | | T1 | Coronal | 78 | 2 | 70 | + | 6 | + |

Abbreviations: FLASH (Fast Low Angle Shot), Gd IV (Gadolinium intravenously), GE (Gradient Echo), FS (Fat Saturation), HASTE (Half fourier Acquisition Single shot Turbo spin Echo), IR (Inversion Recovery), SE (Spin Echo), SS (steady state), STIR

(Short TI Inversion Recovery), TE (time to echo), TR (repetition time), TrueFISP (True Fast Imaging with Steady state Precession), ^{*}(not required in routine settings)

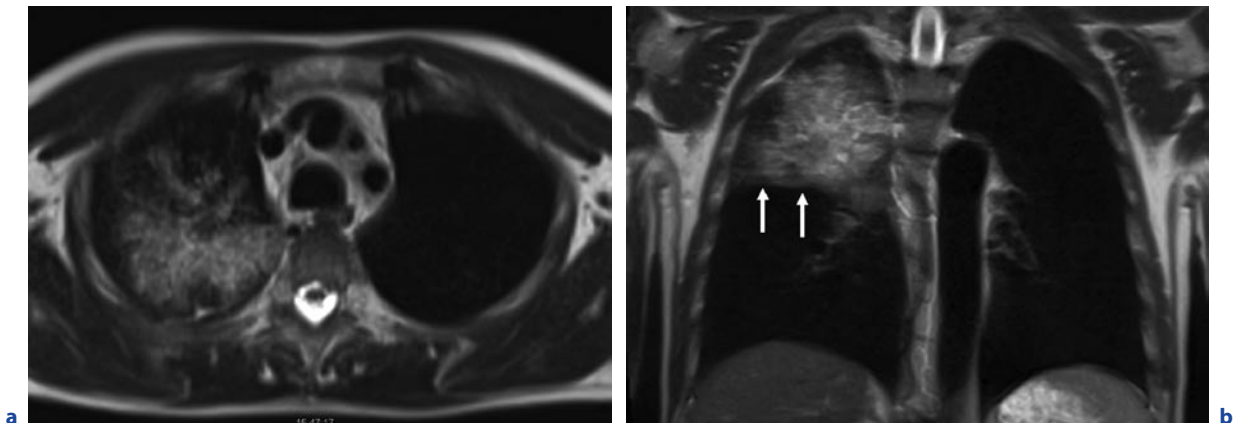


Fig. 13.6. A 51-year-old male with right upper lobe pneumonia (Streptococcus): **a** axial HASTE. Consolidation with surrounding ground-glass in the right upper lobe; **b** coronal HASTE. The horizontal fissure (*arrows*) is not exceeded by the pneumonia; **c-h** see next page

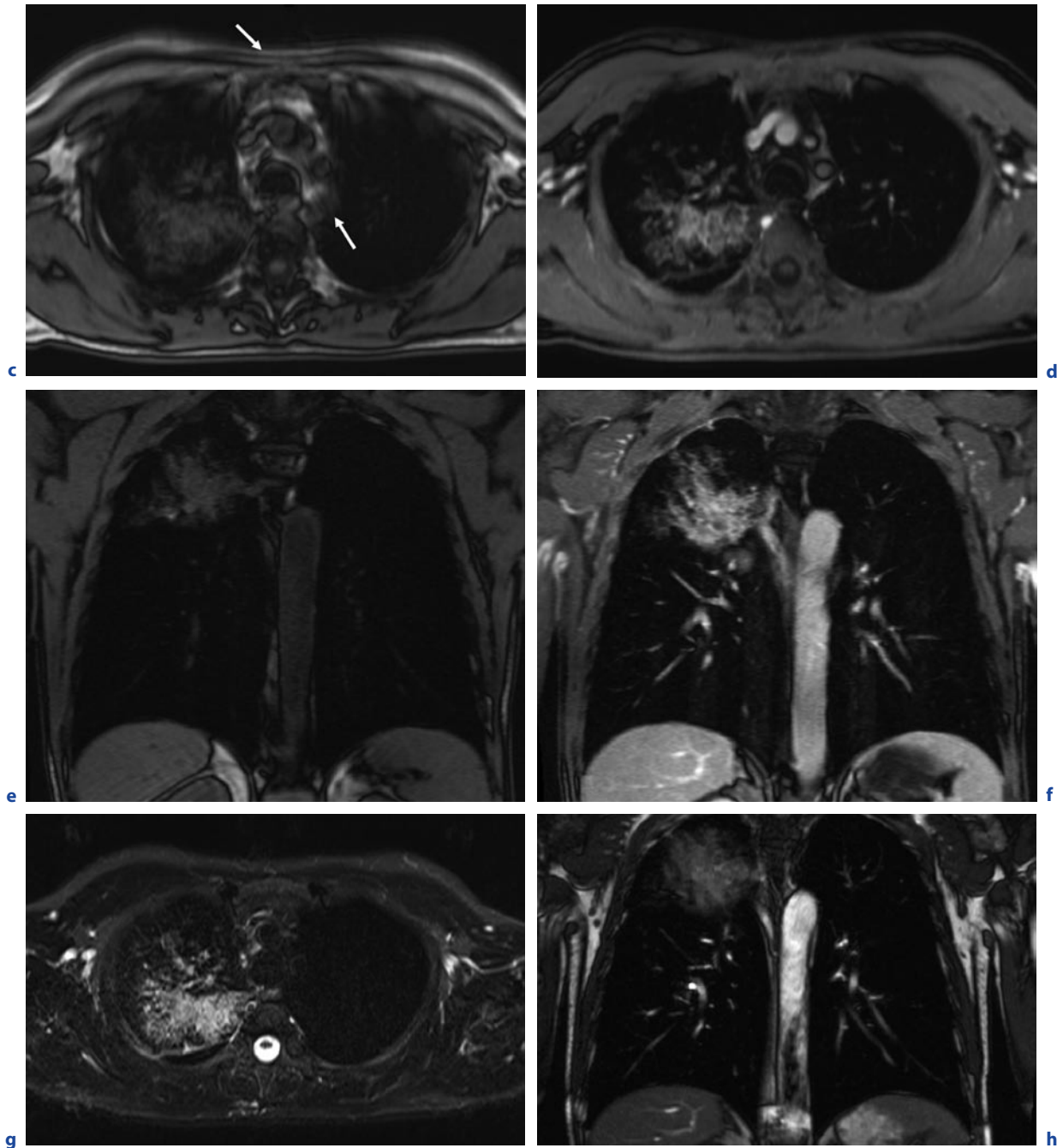


Fig. 13.6. (continued) A 51-year-old male with right upper lobe pneumonia (Streptococcus): **c** axial FLASH without fat saturation, not contrast enhanced. Without intravenous contrast application no additional information is given by this sequence in comparison to the HASTE sequence. Note the higher degree of artefacts in the mediastinum and chest wall (*arrows*); **d** axial FLASH with spectral fat saturation after delivery of 14 ml gadolinium IV. As a result of infection a significant enhancement is visualized; **e** coronal FLASH with spectral fat sat-

uration, before intravenous contrast administration; **f** coronal FLASH, after gadolinium; **g** axial STIR. The edema is clearly detectable in the right upper lobe pneumonia, but the degree of artefacts and noise is higher in comparison to the HASTE sequence; **h** coronal TrueFISP. The vessels are clearly detectable. So this sequence can be an alternative to the contrast enhanced FLASH to delineated adjacent vasculature. The pneumonia itself is not better appreciable in comparison to the HASTE and contrast enhanced FLASH

References

- Alibek S, Holter W, Staatz G (2007) The radiosensitive child: pulmonary MR tomography in EBV-induced lymphoproliferation in Nijmegen-breakage syndrome. *FortschrRöntgenstr* 179:1075–1077
- Bader TR, Semelka RC, Pedro MS, Armao DM, Brown MA, Molina PL (2002) Magnetic resonance imaging of pulmonary parenchymal disease using a modified breath-hold 3D gradient-echo technique: initial observations. *J Magn Reson Imaging* 15:31–38
- Biederer J, Busse I, Grimm J, Reuter M, Muhle C, Freitag S, Heller M (2002) Sensitivity of MRI in detecting alveolar infiltrates: experimental studies. *FortschrRöntgenstr* 174:1033–1039
- Blum U, Windfuhr M, Buitrago-Tellez C, Sigmund G, Herbst EW, Langer M (1994) Invasive pulmonary aspergillosis. MRI, CT, and plain radiographic findings and their contribution for early diagnosis. *Chest* 106:1156–1161
- Campbell GD, Niederman MS, Broughton WA et al. (1996) Hospital-acquired pneumonia in adults: diagnosis, assessment of severity, initial antimicrobial therapy, and preventative strategies: a consensus statement. *Am J Resp Crit Care Med* 153:1711–1725
- Cook DJ, Walter SD, Cook RJ et al. (1998) Incidence of and risk factors for ventilator-associated pneumonia in critically ill patients: results from a multicenter prospective study on 996 patients. *Ann Intern Med* 129:433–440
- Craven DE, Steger KA (1995) Epidemiology of nosocomial pneumonia. New perspectives on an old disease. *Chest* 108:15–16S
- Eibel R, Herzog P, Dietrich O, Rieger C, Ostermann H, Reiser M, Schoenberg S (2006a) Magnetic resonance imaging in the evaluation of pneumonia. *Radiologe* 46:267–270, 272–274
- Eibel R, Herzog P, Dietrich O, Rieger CT, Ostermann H, Reiser MF, Schoenberg SO (2006b) Pulmonary abnormalities in immunocompromised patients: comparative detection with parallel acquisition MR imaging and thin-section helical CT. *Radiology* 241:880–891
- Fagon JY, Chastre J, Hance AJ, Domart Y, Trouillet JL, Gibert C (1993) Evaluation of clinical judgment in the identification and treatment of nosocomial pneumonia in ventilated patients. *Chest* 103:547–553
- Gaeta M, Blandino A, Scribano E, Minutoli F, Barone M, Andò F, Pandolfo I (2000) Chronic infiltrative lung diseases: value of gadolinium-enhanced MRI in the evaluation of disease activity—early report. *Chest* 117:1173–1178
- Gamsu G, Webb WR, Sheldon P, Kaufman L, Crooks LE, Birnberg FA, Goodman P, Hinchcliffe WA, Hedgcock M (1983) Nuclear magnetic resonance imaging of the thorax. *Radiology* 147:473–480
- Güchel C, Schnabel K, Deimling M, Steinbrich W (1996) Solitary pulmonary nodules: MR evaluation of enhancement patterns with contrast-enhanced dynamic snapshot gradient-echo imaging. *Radiology* 200:681–686
- Hansell DM, Bankier AA, MacMahon H, McLeod TC, Müller NL, Remy J (2008) Fleischner Society: glossary of terms for thoracic imaging. *Radiology* 246:697–722
- Haraldseth O, Amundsen T, Rinck PA (1999) Contrast-enhanced pulmonary MR imaging. *MAGMA* 8:146–153
- Husain AN, Kumar V (2005) The lung. In: Klatt EC, Kumar V (eds) *Robbins and Cotran pathologic basis of disease*, 7th edn. Elsevier Saunders, pp 711–772
- James AE Jr, Partain CL, Holland GN, Gore JC, Rollo FD, Harms SE, Price RR (1982) Nuclear magnetic resonance imaging: the current state. *AJR Am J Roentgenol* 138:201–210
- Kauczor HU, Kreitner KF (1999) MRI of the pulmonary parenchyma. *Eur Radiol* 9:1755–1764
- Kim MJ, Lee KS, Kim J, Jung KJ, Lee HG, Kim TS (2001) Crescent sign in invasive pulmonary aspergillosis: frequency and related CT and clinical factors. *J Comput Assist Tomogr* 25:305–310
- Leutner CC, Gieseke J, Lutterbey G, Kuhl CK, Glasmacher A, Wardelmann E, Theisen A, Schild HH (2000) MR imaging of pneumonia in immunocompromised patients: comparison with helical CT. *AJR Am J Roentgenol* 175:391–397
- Li F, Sone S, Maruyama Y, Takashima S, Yang ZG, Hasegawa M, Honda T, Yamada T, Kubo K (2000) Correlation between high-resolution computed tomographic, magnetic resonance and pathological findings in cases with non-cancerous but suspicious lung nodules. *Eur Radiol* 10:1782–1791
- Marquardt T, Jablonowski H (2003) Opportunistic diseases. Risk can be estimated. *MMW Fortschr Med* 145:33–37
- Marzola P, Lanzoni A, Nicolato E, Di Modugno V, Cristofori P, Osculati F, Sbarbati A (2005) (1)H MRI of pneumococcal pneumonia in a murine model. *J Magn Reson Imaging* 22:170–174
- McEachern R, Campbell GD Jr (1998) Hospital-acquired pneumonia: epidemiology, etiology, and treatment. *Infect Dis Clin North Am* 12:761–779
- Moore EH, Webb WR, Muller N, Sollitto R (1986) MRI of pulmonary airspace disease: experimental model and preliminary clinical results. *AJR Am J Roentgenol* 146:1123–1128
- Müller NL, Mayo JR, Zwirwich CV (1992) Value of MR imaging in the evaluation of chronic infiltrative lung diseases: comparison with CT. *AJR Am J Roentgenol* 158:1205–1209
- Niederman MS (2004) Pneumonia, including community-acquired and nosocomial pneumonia. In: Crisp JD, Glassroth J, Karlinsky J, King TE (eds) *Baum's textbook of pulmonary diseases*, 7th edn. Lippincott Williams and Wilkins, pp 425–454
- Niederman MS, Mandell LA, Anzueto A et al. (2001) Guidelines for the management of adults with community-acquired lower respiratory tract infections: Diagnosis, assessment of severity, antimicrobial therapy and prevention. *Am J Resp Crit Care Med* 163:1730–1754
- Partain CL, James AE, Watson JT, Price RR, Coulam CM, Rollo FD (1980) Nuclear magnetic resonance and computed tomography: comparison of normal human body images. *Radiology* 136:767–770

- Primack SL, Mayo JR, Hartman TE, Miller RR, Müller NL (1994) MRI of infiltrative lung disease: comparison with pathologic findings. *J Comput Assist Tomogr* 18:233–238
- Prod'hom G, Leuenberger P, Koefer J et al. (1994) Nosocomial pneumonia in mechanically ventilated patients receiving antacid, ranitidine, or sucralfate as prophylaxis for stress ulcer: a randomized controlled trial. *Ann Intern Med* 120:653–662
- Rello J, Paiva JA, Baraibar J et al. (2001) International Conference for the Development of Consensus on the Diagnosis and Treatment of Ventilator-associated Pneumonia. *Chest* 120:955–970
- Rosenow EC III (1990) Diffuse pulmonary infiltrates in the immunocompromised host. *Clin Chest Med* 11:55–64
- Ross JS, O'Donovan PB, Novoa R, Mehta A, Buonocore E, MacIntyre WJ, Golish JA, Ahmad M (1984) Magnetic resonance of the chest: initial experience with imaging and in vivo T1 and T2 calculations. *Radiology* 152:95–101
- Rupprecht T, Böwing B, Kuth R, Deimling M, Rascher W, Wagner M (2002) Steady-state free precession projection MRI as a potential alternative to the conventional chest X-ray in pediatric patients with suspected pneumonia. *Eur Radiol* 12:2752–2756
- Springhouse (2007) Professional guide to disease. An up-to-date encyclopedia of illnesses, disorders, and injuries and their treatments. Lippincott Williams and Wilkins
- Tournebise R, Doan BT, Dillies MA, Maurin S, Beloeil JC, Sansonetti PJ (2006) Magnetic resonance imaging of *Klebsiella pneumoniae*-induced pneumonia in mice. *Cell Microbiol* 8:33–43
- Webb WR, Jensen BG, Sollitto R, de Geer G, McCowin M, Gamsu G, Moore E (1985) Bronchogenic carcinoma: staging with MR compared with staging with CT and surgery. *Radiology* 156:117–124

Interstitial Lung Disease

KATHARINA MARTEN and FRANCESCO MOLINARI

CONTENTS

- 14.1 **Introduction** 277
- 14.2 **Role of MRI for Morphologic Imaging in ILD** 278
- 14.3 **Sarcoidosis** 279
- 14.4 **Idiopathic Interstitial Pneumonias** 279
- 14.5 **Collagen-vascular Diseases** 282
 - 14.5.1 Rheumatoid Arthritis 282
 - 14.5.2 Progressive Systemic Sclerosis (Scleroderma) 283
 - 14.5.3 Systemic Lupus Erythematosus 283
- 14.6 **Miscellaneous Interstitial Lung Diseases** 283
- 14.7 **MR Strategies to Investigate Lung Function in ILD** 284
- 14.8 **Imaging of Lung Function with Hyperpolarized Gases** 286
- 14.9 **Imaging of Lung Function with Oxygen** 287
- 14.10 **MR Protocols for Imaging Lung Morphology and Function in ILD** 288
- References** 288

KEY POINTS

Imaging is important in the differential diagnosis as well as in the assessment of functional constraints and therapy response in interstitial lung disease. Imaging has to address three main topics: (1) visualization and recognition of morphological changes and their patterns; (2) assessment of pulmonary function, i.e. restrictive ventilatory impairment, reduction of perfusion and gas exchange; and (3) assessment of inflammatory activity. MRI is capable to provide image-based answers to all three topics. Typical patterns, such as reticular and reticulonodular changes, ground glass, consolidation and honey-combing are easily visualized. Functional imaging using contrast-enhanced perfusion MRI and ventilation MRI with hyperpolarized gases or oxygen are available for the assessment of restrictive constraints. Routine contrast-enhanced MRI allows estimating inflammatory activity in different types of interstitial lung disease which is a clear advantage over CT which has limitations in this regard.

14.1

Introduction

The use of MRI in the assessment of interstitial lung diseases (ILD) has been limited by the low proton density of the lungs, resulting in low signal-to-noise ratios, and signal loss due to respiratory and cardiac motion artefacts as well as susceptibility artefacts due to air-tissue interfaces (KAUCZOR and KREITNER 1999). These restrictions lead to a much lower spatial resolution compared to thin-section CT which, with its supreme ability to reflect the macroscopic pathologic abnormalities in

K. MARTEN, Priv.-Doz. Dr. med.
 Universitätsklinikum Göttingen, Abteilung Diagnostische Radiologie, Robert-Koch-Str. 40, 37075 Göttingen, Germany

F. MOLINARI, MD
 Department of Bioimaging and Radiological Sciences
 Catholic University of Rome, Policlinico A. Gemelli
 L.go F. Vito, no. 1, 00168 Rome, Italy

ILD, remains the mainstay for diagnosis and differential diagnosis of these disorders. However, evidence suggests that MRI may play a role in the assessment of disease activity in ILD, and recent technological refinements have led to a considerable improvement of MRI image quality, which may open avenues for the use of MRI in selected patients with ILD. This chapter reviews reports on the application of MRI to different ILD and considers potential future applications for morphological and functional MRI imaging in patients with ILD.

14.2

Role of MRI for Morphologic Imaging in ILD

To date, few studies have addressed the use of MRI for depiction of morphologic changes in patients with ILD. PRIMACK et al. (1994) investigated 5 patients with idiopathic pulmonary fibrosis, 3 patients with hypersensitivity pneumonitis, 4 patients with sarcoidosis, and 10 patients with miscellaneous infiltrative lung diseases and recorded the predominant patterns of abnormality seen on proton-weighted and T1-weighted MRI (parenchymal opacification with or without reticulation, a reticular pattern, nodularity, and interlobular septal thickening). The authors found that the MRI patterns correlated well with pathologic features seen on lung biopsy: the majority of patients with parenchymal opacification showed active inflammation on biopsy, whereas in a minority of patients parenchymal opacification represented fibrosis. Thus, MRI can depict treatable disease with reasonably high sensitivity (KAUCZOR and KREITNER 1999; PRIMACK et al. 1994). Architectural distortion in patients with fibrosis was depicted on MRI. All patients with reticulation showed fibrosis on biopsy, and nodularity was found in patients with sarcoidosis. Interlobular septal thickening, however, was seen in patients with lymphangitic carcinomatosis and Churg-Strauss syndrome, respectively (PRIMACK et al. 1994).

Another study compared the value of proton-weighted and T1-weighted MRI compared to that of thin-section CT in the assessment of chronic infiltrative lung diseases and found that in the majority of the patients, gross assessment of morphologic changes and distribution of disease was feasible (MÜLLER et al. 1992). In that study, nine patients with usual interstitial pneumonia, six patients with sarcoidosis, four patients with hypersensitivity pneumonitis, and six patients with miscellaneous diseases were included. The authors found that MRI was inferior to CT in demonstrating mild fibrosis, and also inferior in the anatomic assessment of the pulmonary parenchyma. However, MRI was compa-

rable to CT in the assessment of air-space opacification, and proved to be a suitable tool for longitudinal studies: In six patients, follow-up scans were obtained with both MRI and CT and revealed equal degrees of air-space opacification over time (MÜLLER et al. 1992).

A number of studies have focused on the differentiation of the active (alveolitic) and inactive (fibrotic) stages of ILD. In an early study, MCFADDEN et al. (1987) studied patients with interstitial lung disease and found that signal intensity on MRI correlated with disease severity and response to treatment, as a decrease in signal intensity could be observed on follow-up in some patients. Further evidence that MRI is a suitable tool for the assessment of disease activity comes from experimental studies. KERSJES et al. (1999) investigated rabbits with bleomycin-induced lung damage and correlated MRI findings with histopathology. They demonstrated that lesions in the alveolitic phase displayed high pre- and post-contrast signal intensity on T1-weighted and also on T2-weighted images, whereas with progressive fibrosis the signal intensity and contrast enhancement showed a marked decrease. In detail, the authors observed a marked increase in signal intensity on T1- and T2-weighted images after instillation of bleomycin, corresponding to interstitial and alveolar pulmonary edema (acute alveolitis). Fourteen days later, the progressive fibrotic transformation of the pulmonary parenchyma was paralleled by a decrease in signal intensity on both T1- and T2-weighted images (KERSJES et al. 1999). VINITSKI et al. (1986) who chose a similar experimental approach in rats, demonstrated a close correlation between signal intensities at different stages of the disease and lung water content. Other studies, however, failed to show differentiation of acute and chronic changes in ILD by calculating T1 and T2 proton relaxation times (SHIOYA et al. 1990; TAYLOR et al. 1987). In another experimental study, macromolecular contrast agents could be shown to improve further differentiation between alveolitis and pulmonary fibrosis (BERTHEZENE et al. 1992). In the early alveolitic phase after bronchial instillation of cadmium chloride, rats demonstrated a gradually increasing contrast enhancement over 45 min, indicating leakage of the contrast agent into the extravascular space. By contrast, in the fibrotic phase markedly lower enhancement was observed and attributed to a decrease in plasma volume in the fibrotic lung (BERTHEZENE et al. 1992).

The time course demonstrated in bleomycin-induced lung damage is comparable to radiation pneumonitis (KAUCZOR and KREITNER 1999). Preliminary clinical studies have addressed the value of MRI in the assessment of radiation-induced fibrosis and differentiation of fibrosis from recurrent disease. Early on,

GLAZER et al. (1984) investigated 21 patients who had undergone radiotherapy and compared the findings with 15 patients with untreated tumours. T2-weighted images proved suitable for differentiation of fibrosis and tumour, as radiation fibrosis showed low signal intensity on both T1- and T2-weighted images, whereas the signal intensity of untreated tumour was much higher. In another study, the surrounding pulmonary parenchyma in patients receiving radiotherapy for lung cancer displayed a steady increase in signal intensity on T1- and T2-weighted images over several months, followed by a decrease in signal intensity (YANKELEVITZ et al. 1994).

The following paragraphs review the MRI appearance of the most important interstitial lung diseases.

14.3

Sarcoidosis

Sarcoidosis is a systemic disorder characterized by the presence of non-caseating granulomas, which may resolve spontaneously or progress to fibrosis (COLBY and CARRINGTON 1994). As many as 90% of patients show pulmonary manifestations (WEBB 2001). Pathologically, granulomas are found in a perilymphatic or lymphatic distribution and display a centre of histiocytes, surrounded by lymphocytes and mononuclear cells (COLBY and CARRINGTON 1994). The intervening lung parenchyma is normal.

Granulomatous disease is closely mirrored by high-resolution CT (HRCT), which is the method of choice for assessment of patients with sarcoidosis (WEBB 2001). The most characteristic abnormality consists of small pulmonary nodules in a perilymphatic or peribronchovascular distribution. These nodules are usually well defined. Furthermore, nodules show a predilection for the fissures, the subpleural parenchyma, and the centre of the secondary pulmonary lobule. Their size normally does not exceed a few millimetres; however, nodules may coalesce forming larger opacities 1–4 cm in diameter or confluent masses surrounded by confluent small nodules (GRENIER et al. 1991). Upper lobe predominance is a frequent finding, but not invariably present. The characteristic location of the granulomas often causes smooth or nodular peribronchovascular interstitial thickening. Furthermore, nodules are seen along the interlobular septa, causing irregular or nodular interlobular septal thickening which is a common albeit minor feature in patients with sarcoidosis. Patchy areas of ground glass opacity result from interstitial disease rather than alveolitis (LEUNG et al. 1993). Airway involvement is common and commonly presents

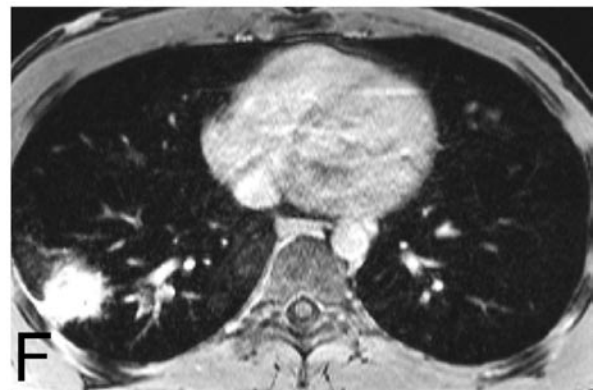
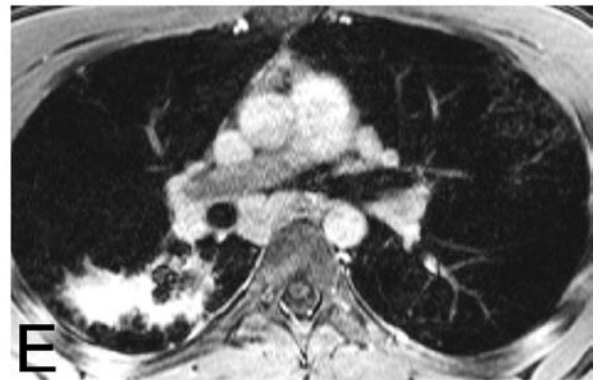
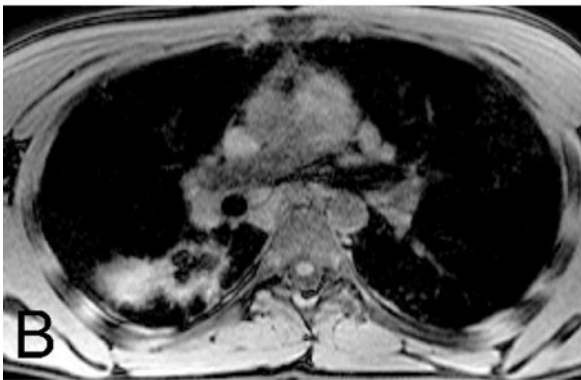
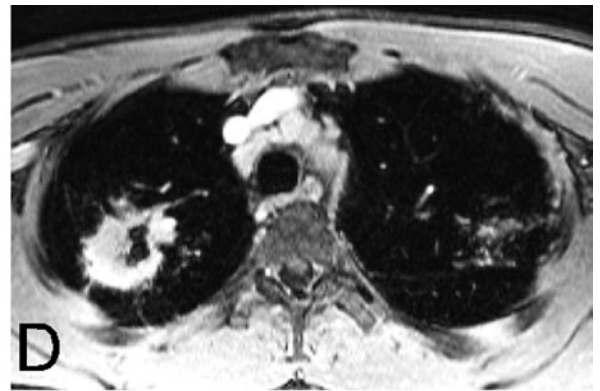
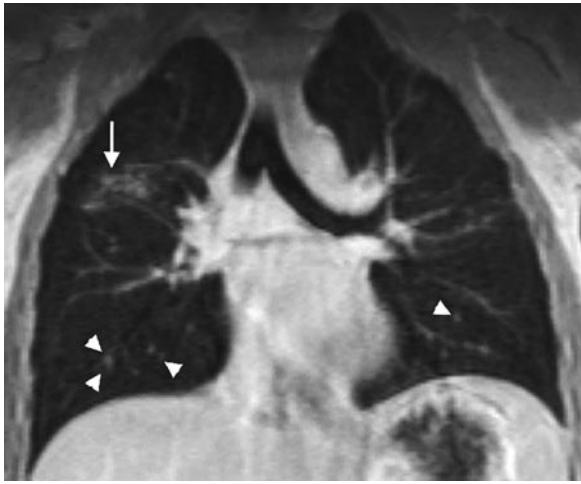
as bronchial wall thickening (often indistinguishable from peribronchovascular thickening) and bronchial luminal abnormalities (WEBB 2001; DAWSON and MÜLLER 1990; MILLER et al. 1995).

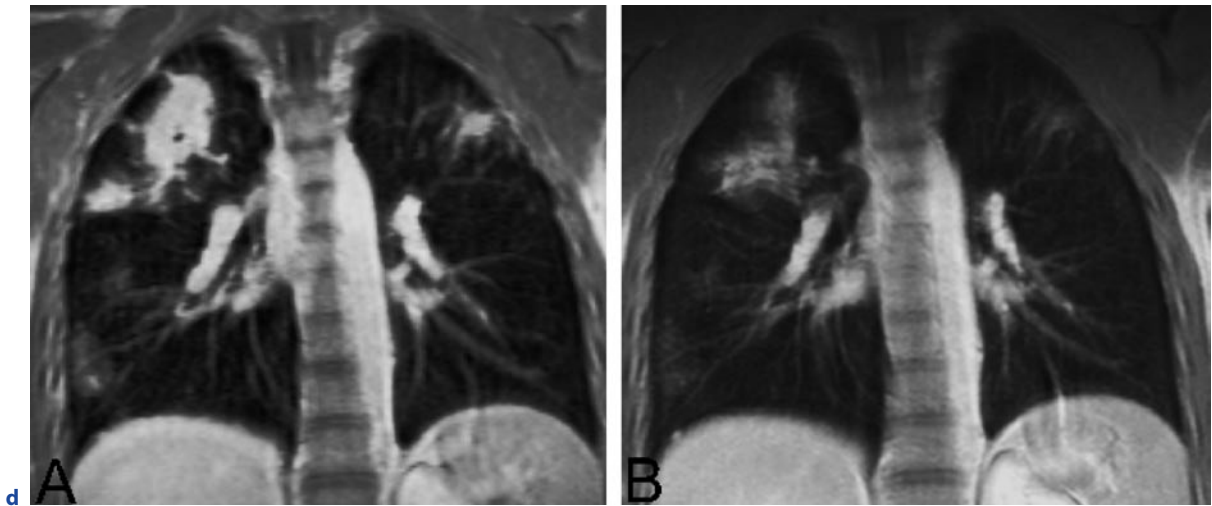
Data on the MRI appearance of sarcoidosis is scarce. As early as in 1988, however, CRAIG et al. (1998) investigated nine patients with pulmonary sarcoidosis and compared the findings with chest radiographs. In that study, MRI detected hilar and mediastinal lymphadenopathy as well as coalescent parenchymal disease but failed to show widespread interstitial disease. A more meaningful comparison of MRI and HRCT features was performed in other studies in a total of 10 patients. In the study by PRIMACK et al. (1994), MRI findings in sarcoidosis included parenchymal opacification, peribronchovascular thickening and nodularity, as well as parenchymal opacification with mild architectural distortion (Fig. 14.1). They could show that parenchymal opacification reflected the presence of non-caseating granulomas on open lung biopsy. Peribronchovascular nodularity was seen in four of five patients, MRI appearances in the remaining patient were normal. MÜLLER et al. (1992) reported ground-glass opacities in a patient with sarcoidosis which improved on follow-up, whereas another patient with sarcoidosis showed no appreciable change. Taken together, despite its lower spatial resolution compared to HRCT, MRI may depict cardinal features of pulmonary sarcoidosis such as nodularity, peribronchovascular thickening as well as confluent masses. Furthermore, lesions in sarcoidosis usually show vivid contrast enhancement in MRI (Fig. 14.1), and it is therefore conceivable that MRI may play a future role in staging disease activity in patients with sarcoidosis and in longitudinal studies of younger patients (Fig. 14.1), particularly when its lack of ionizing radiation is considered.

14.4

Idiopathic Interstitial Pneumonias

Idiopathic interstitial pneumonias form a heterogeneous group of interstitial lung diseases. Reclassification by the American Thoracic Society and European Respiratory Society has proposed five distinct histological types: usual interstitial pneumonia (UIP), desquamative interstitial pneumonia (DIP), respiratory bronchiolitis-associated interstitial lung disease (RBILD), acute interstitial pneumonia (AIP), and non-specific interstitial pneumonia (NSIP) (ATS/ERS 2000). UIP is the most common type of idiopathic interstitial pneumonia (MCADAMS et al. 1996). Histopathologically, it shows a het-





◀**Fig. 14.1a–d.** A 26-year-old male patient with sarcoidosis. **a** Post-contrast T1-weighted 3D-FLASH coronal image displays peribronchovascular thickening (*arrow*) and nodularity (*arrowheads*). Note mediastinal lymphadenopathy. **b** IR-HASTE (inversion recovery half-Fourier acquisition single-shot turbo spin-echo) coronal image shows areas of consolidation (*arrows*). **c** Pre- (A–C) and post-contrast (D–F) T1-weighted

VIBE (volumetric interpolated breath-hold examination) axial images show vivid contrast enhancement of the larger nodular lesions in the right upper lobe and the diffuse nodularity in the left upper lobe. **d** Post-contrast T1-weighted 3D-FLASH coronal images (**A**: before initiation of steroid therapy, **B**: 8 weeks later) show regression of the parenchymal manifestations of sarcoidosis

erogeneous pattern of normal and inflammatory lung, fibroblastic foci, interstitial fibrosis, and honeycombing. This “temporal heterogeneity” is a characteristic feature (KATZENSTEIN and MYERS 1998; KADOTA et al. 1995). Fibrosis and honeycombing in UIP display a striking basal and subpleural predominance. UIP is the most common histopathological pattern in patients with the clinical picture of idiopathic pulmonary fibrosis (IPF); however, it may also occur secondary to environmental or drug exposure, radiation, or in association with collagen-vascular diseases (COLBY and CARRINGTON 1994).

On HRCT, UIP/IPF is characterized by the presence of irregular reticular abnormalities reflecting fibrosis (WEBB et al. 1988). The most important HRCT features are honeycombing and intralobular septal thickening (WEBB et al. 1988). These findings indicate progressive disease and a poor prognosis (WELLS et al. 1993; TERRIFF et al. 1992). Ground glass opacities, however, are less conspicuous findings and if present, may indicate the presence of active inflammation or, alternatively, may reflect very fine fibrosis beyond the spatial resolution of HRCT (LEUNG et al. 1993). Honeycombing refers to thick-walled, wall-sharing cysts which are usually 2–20 mm in diameter, and which occur in layers in a subpleural location. Differentiation from traction bronchiolectasis is not always straightforward. Intralobular

septal thickening results in a fine reticular pattern and is often associated with traction bronchiolectasis (WEBB et al. 1988). Irregular interfaces between the pulmonary parenchyma and vasculature result from thickening of the intralobular interstitium. If fibrosis is severe, larger bronchi become dilated and distorted, a finding referred to as traction bronchiectasis.

The major HRCT features in patients with UIP/IPF are also depicted with MRI (Fig. 14.2) PRIMACK et al. (1994) investigated five patients with IPF using MRI and reported peripheral reticulation with or without areas of parenchymal opacification, dense reticulation, or architectural distortion. Peripheral reticulation was identified in all patients and reflected fibrosis on biopsy. If reticulation occurred in association with parenchymal opacification, biopsy demonstrated both fibrosis and active alveolitis (PRIMACK et al. 1994). MÜLLER et al. (1992) showed that at that time, MRI was slightly inferior to HRCT in the depiction of fibrosis and honeycombing: Of 15 patients with reticulation on CT, 13 and 12 showed abnormalities on T1-weighted and proton density-weighted MRI, respectively. Furthermore, of 10 patients with the HRCT finding of honeycombing, 9 and 6 patients displayed honeycombing on T1-weighted and proton density-weighted MRI (MÜLLER et al. 1992).

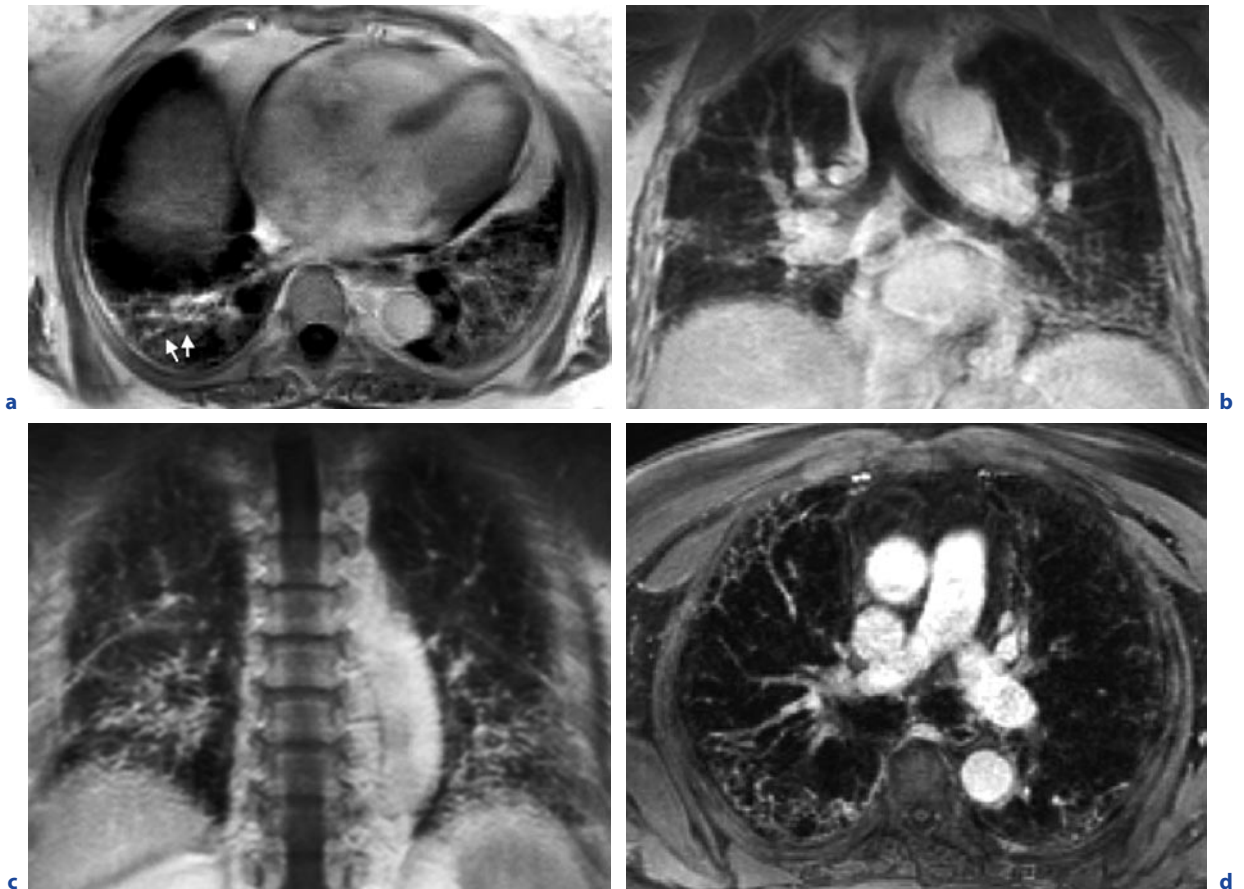


Fig. 14.2a–d. A 74-year-old female patient with usual interstitial pneumonia associated with rheumatoid arthritis. **a** Post-contrast T1-weighted 3D-FLASH axial image displays a reticular pattern with extensive traction bronchiectasis/bronchiolectasis (*arrowheads*). **b** Post-contrast T1-weighted 3D-FLASH coronal image depicts typical basal and subpleural predominance of the findings. **c** Post-contrast T1-weighted 3D-FLASH coro-

nal image shows extensive architectural distortion in the dorsal parts of the lungs. **d** Post-contrast T1-weighted 3D-FLASH axial image indicating typical fibrotic changes in a patient with IPF. Note the extensive reticulation and architectural distortion predominant in the subpleural regions of the lung

In conclusion, using MRI gross morphologic features of pulmonary fibrosis can be depicted; however, mild interstitial disease may go undetected.

14.5

Collagen-vascular Diseases

Interstitial lung disease is a common feature in patients with underlying collagen-vascular disorders (CVD). As CVD are sharing common imaging features, the MRI appearances of interstitial lung disease associated with rheumatoid arthritis, scleroderma and systemic lupus erythematosus are summarized at the end of this paragraph after a brief introduction of the different entities.

14.5.1 Rheumatoid Arthritis

Rheumatoid arthritis is a chronic inflammatory autoimmune disorder which is commonly associated with thoracic disease, e.g. interstitial fibrosis, necrobiotic nodules, pleural disease, bronchiectasis, and obliterative bronchiolitis (REMY-JARDIN et al. 1994; PEREZ et al. 1998). The prevalence of radiologically evident interstitial lung disease is around 10%, with the most common histopathologic pattern being UIP. A small percentage of patients, however, have findings of NSIP on lung biopsy (KATZENSTEIN and FIORELLI 1994). In a study by REMY-JARDIN et al. (1994), HRCT findings of fibrosis (with or without honeycombing) were seen in 10% of patients. Ground-glass opacities were found in 14%.

Bronchial abnormalities including bronchiectasis were present in 21% of patients, consolidation in 6%, lymphadenopathy in 9%, and pleural disease in 16%. Another frequent finding was predominantly subpleural nodularity (22%).

14.5.2 Progressive Systemic Sclerosis (Scleroderma)

Progressive systemic sclerosis is an autoimmune disorder characterized by excessive amounts of collagen fibres in different organs. The vast majority of patients with progressive systemic sclerosis (PSS) show some degree of interstitial fibrosis, although pulmonary function tests are frequently normal (TAORIMINA 1981; ARROLIGA et al. 1992). PSS is commonly associated with a pattern of NSIP, pulmonary vasculitis and pulmonary hypertension. HRCT findings include honeycombing, reticulation, ground-glass opacities, and subpleural predominance (WEBB et al. 1988). In a recent study, CT features of lung disease in PSS were compared with IPF and NSIP (DESAI et al. 2004). In PSS, interstitial lung disease was shown to be less extensive, less coarse, and characterized by a greater proportion of ground-glass opacification than that in patients with IPF. CT features closely resembled those in patients with idiopathic NSIP (DESAI et al. 2004). Other findings in patients with PSS include oesophageal dilatation, diffuse pleural thickening, and mediastinal lymphadenopathy.

14.5.3 Systemic Lupus Erythematosus

Systemic lupus erythematosus (SLE) is a multisystemic autoimmune disorder associated with increased serum antinuclear antibodies. It is commonly associated with pleuropulmonary abnormalities. Up to 85% of autopsy cases show pleuritis or pleural fibrosis, and pleural effusion is a common feature on chest radiographs of patients with SLE (WIEDEMANN and MATTHAY 1992). Pulmonary complications in SLE are common and include pneumonia, lupus pneumonitis, and pulmonary haemorrhage (KIM et al. 2000). Organizing pneumonia and pulmonary fibrosis may occur in patients with SLE (GAMMON et al. 1992).

HRCT shows findings of fibrosis, albeit less frequently than in patients with IPF, rheumatoid arthritis or PSS. Other abnormalities include ground-glass opacities, pulmonary nodules, bronchiectasis or bronchial wall thickening, and pleural disease (BANKIER et al. 1995). The incidence of pulmonary fibrosis is estimated

to be 30%–35% (BANKIER et al. 1995; FENLON et al. 1996; SANT et al. 1997). Frequent findings are interlobular or intralobular septal thickening (33%), and architectural distortion (88%) (BANKIER et al. 1995). Honeycombing is uncommon.

The findings of ground glass opacification and consolidation may be caused by pneumonia, lupus pneumonitis, or pulmonary haemorrhage, and may also occur in organizing pneumonia (PRIMACK et al. 1994). Airway abnormalities occur in 18%–20%, pleuroparietal disease in 15%–17% of patients (FENLON et al. 1996; SANT et al. 1997).

There are currently no data available on the use of MRI in patients with interstitial lung disease associated with collagen vascular diseases. From our experience, morphological features such as frank fibrosis with architectural distortion or honeycombing, as well as ground glass opacities, can easily be depicted with MRI (Figs. 14.3–14.5), whereas subtle fibrosis may go undiagnosed. Architectural distortion, consolidation, nodularity, and interlobular septal thickening are other abnormalities which can reliably be seen. In addition, findings pointing to the underlying disorder such as oesophageal dilatation in PSS or pleuropulmonary disease in SLE are readily depicted. Interestingly, ground glass opacities in collagen-vascular disorders may show intense contrast enhancement, and it is presumed albeit not proven that in this case an active inflammatory process, i.e. alveolitis, is the underlying pathology. In this context, it is conceivable that contrast-enhanced MRI may play a role in longitudinal studies investigating new therapeutic regimens, as differentiation between inflammation and fibrosis may be facilitated.

14.6

Miscellaneous Interstitial Lung Diseases

Progressive massive fibrosis (PMF) in coal worker's pneumoconiosis was studied in 12 patients using MRI. The majority of lesions were isointense to skeletal muscle on T1-weighted images with post-contrast enhancement. On T2-weighted images, signal intensity was low, with central high signal intensity corresponding to necrosis (MATSUMOTO et al. 1998).

In *Wegener's granulomatosis*, pulmonary nodules are depicted with MRI and may show post-contrast enhancement (KALAITZOGLOU et al. 1998). MRI in patients with *asbestosis* may show round atelectasis and interstitial fibrosis, along with pleural plaques which appear hyperintense on T1- and T2-weighted images and do not enhance (BEKKELUND et al. 1998).

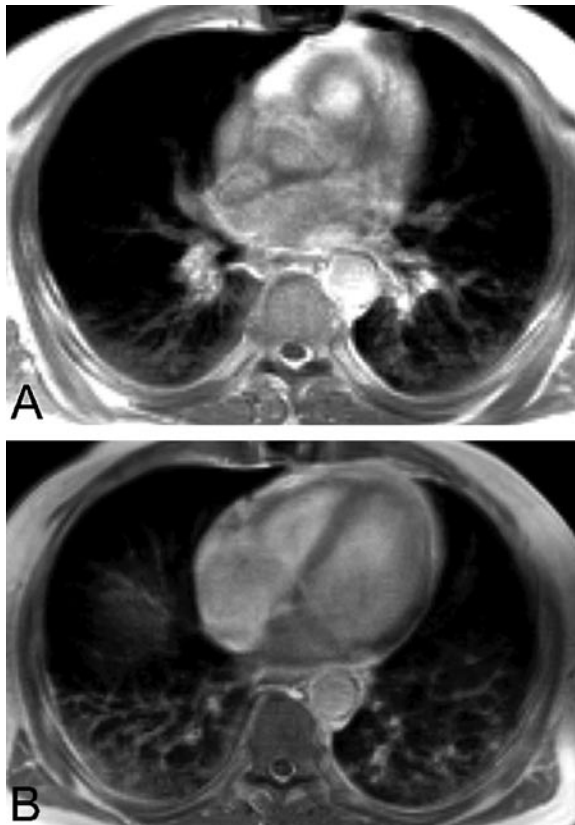


Fig. 14.3. A 61-year-old male patient with interstitial lung disease associated with rheumatoid arthritis, with MR findings suggestive of non-specific interstitial pneumonia. Post-contrast T1-weighted 3D-FLASH axial images depict subpleural ground-glass opacification with reticulation in the apical lower lobes (A) as well as extensive fibrosis with no evident honeycombing in the dorsobasal parts of the lungs (B)

14.7

MR Strategies to Investigate Lung Function in ILD

The assessment of lung function is critically important for the diagnosis and management of ILD patients. Notoriously, ILDs include a wide spectrum of pathologic entities which often manifest with overlapping clinico-radiologic patterns (ATS/ERS 2002; WELLS and HOGABOAN 2007). At the presentation of the disease, the diagnosis is difficult and usually requires careful analysis of clinical and HRCT data, and the knowledge of the type of functional impairment of the lung. Invasive procedures, such as lung biopsy with video-assisted thoracic surgery (VATS) may be also needed, primarily to exclude the unfavourable occurrence of IPF/UIP pattern

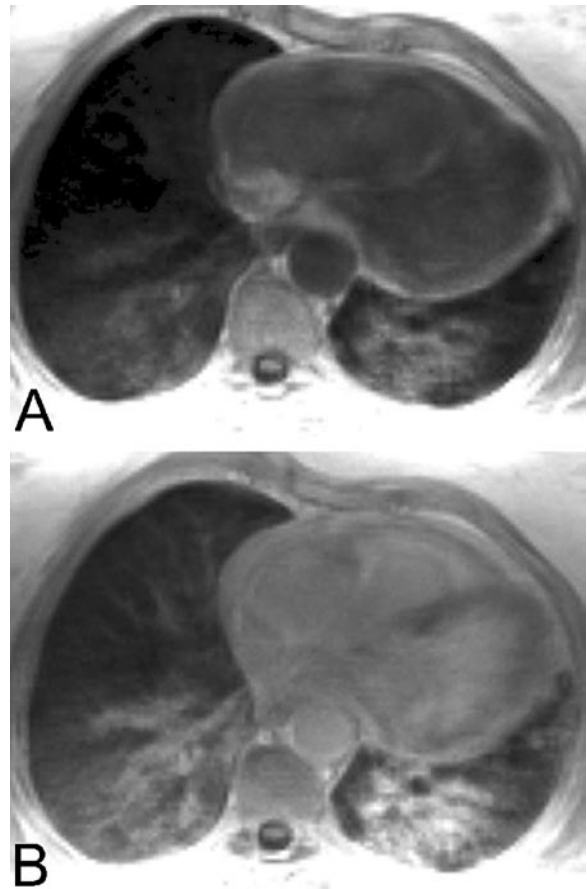


Fig. 14.4. A 70 year-old female patient with interstitial lung disease associated with systemic lupus erythematosus. Pre-contrast (A) and post-contrast (B) T1-weighted 3D-FLASH axial images display bilateral subpleural and basal dense fibrosis with substantial contrast enhancement

(HUNNINGHAKE et al. 2001). Biopsy specimens can also provide valuable information on the disease activity. However the procedure is associated with known issues. Mortality and complication rates for lung biopsy in ILD patients have been reported, with complications being more frequent in patients dependent on oxygen and having pulmonary hypertension (KREIDER et al. 2007). An experienced pathologist is required for the assessment of the biopsy specimens. Inconclusive results may also be possible when the distribution of the disease is highly heterogeneous (WELLS and HOGABOAN 2007). Therefore, the decision of performing lung biopsy for the diagnosis of ILD is largely dependent on the clinical condition of the patient. In particular, when the patient is old and has numerous comorbidities that may significantly outweigh the risk of complications against the benefit of obtaining histological samplings, the diagno-

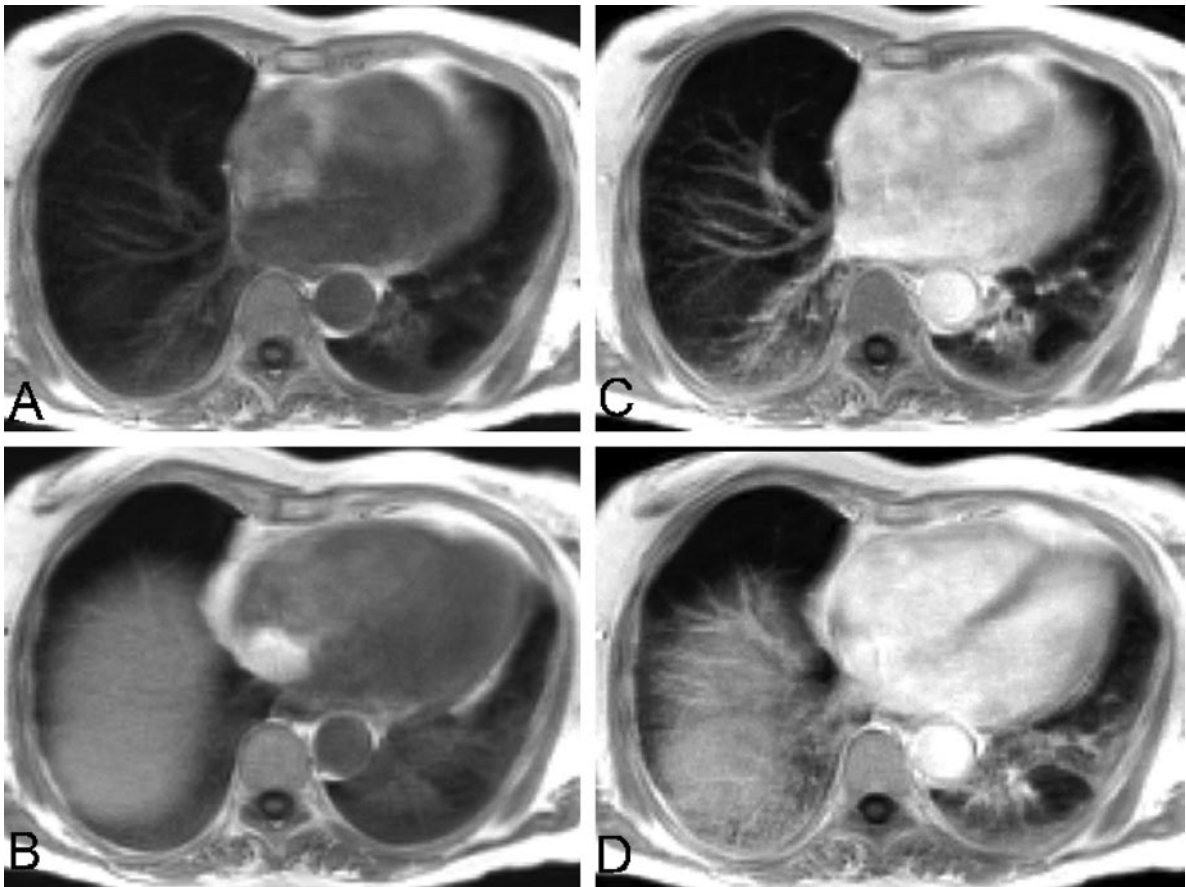


Fig. 14.5. A 68-year-old female patient with interstitial lung disease associated with progressive systemic sclerosis (scleroderma). Pre- (A,B) and post-contrast (C,D) T1-weighted 3D-

FLASH axial images show a subpleural and basal reticular pattern with architectural distortion suggestive of frank fibrosis with vivid contrast enhancement

sis and prognosis of the disease are determined clinically by serial monitoring of lung function and follow-up HRCT examinations.

Lung function is commonly evaluated with a broad range of techniques, known as pulmonary function tests (PFTs). PFTs of static lung volumes, gas diffusion, arterial blood gas analysis, and exercise capacity are typically assessed in ILD patients (CHETTA et al. 2004). Some general limitations of these tests include a degree of variability of the results and the need of patient cooperation (ULMER et al. 1993). The standardized technique and relatively inexpensive equipment required for testing ensure large clinical applicability for studying the ventilatory and gas exchange abnormalities of ILD.

The ventilatory defect in ILD is a consequence of several mechanisms, such as loss of lung volume, reduction in alveolar distensibility and/or size, and increased

surface tension caused by surfactant alterations (GIBSON and PRIDE 1977; KNUDSON and KALTENBORN 1981; THOMPSON and COLEBATCH 1989; MCCORMACK et al. 1991). These pathophysiologic changes cause a global impairment of lung mechanics that is known as restrictive ventilatory pattern. At rest, ventilation is characterized by rapid breathing frequency to compensate the small tidal volumes and the reduced alveolar distensibility. Static lung volumes are not uniformly altered. Possibly as a consequence of premature closure of small airways caused by peribronchial fibrosis or cystic modification of the lung, functional residual capacity (FRC) and residual volume (RV) are less decreased than vital capacity (VC). Total lung capacity (TLC) is therefore less reduced than VC. The RV/TLC ratio may be greater than normal. Because large airways are usually patent, dynamic lung volumes and particularly volume-corrected indices of

airflow (forced expiratory volume in 1 s to VC, FEV1/VC) are normal or greater than normal.

The impairment of gas exchange depends on both ventilation/perfusion mismatch and alveolar-capillary damage. Gas diffusion through the alveolar-capillary barrier is estimated with high sensitivity from the diffusing capacity for carbon monoxide (DLCO) (CHETTA et al. 2004; GROSS and HUNNINGHAKE 2001). The DLCO decrease reflects partly the poor distribution of inspired gas and reduced lung volumes. Using the carbon monoxide transfer coefficient (KCO is not dependent from the lung volume) the diffusing abnormality is assessed even more accurately (HUGHES 2003). Oxygen desaturation is possible at resting, but it is more evident during exercise. Because of the ventilatory and gas exchange abnormalities, and concurrent cardiac dysfunction, the overall exercise tolerance is markedly reduced.

The PFTs alterations in ILD are typical but rather unspecific. They more likely express a general dysfunctional pattern of the lung that occurs in different pathological conditions evolving towards fibrosis. In serial functional monitoring of ILD patients, the PFTs show variable accuracy as prognostic factors. The capability to predict patient survival depends on the form of ILD. In sarcoidosis, for instance, the use of pulmonary function testing to predict the course of the disease is controversial (CHETTA et al. 2004). In experimental treatment studies, the assessment of therapeutic effects on the sole basis of functional monitoring with PFTs is also difficult (WELLS and HOGABOAN 2007). Considering that conventional therapies for ILDs are associated with significant risks, the research of new diagnostic strategies to assess lung function is largely needed for both patient management and treatment control.

Despite the technical issues that in the past have limited the clinical application of lung MRI, the potential of this imaging modality in assessing pulmonary function has been widely investigated. Along with the obvious advantage of providing information on regional morphology with a radiation-free diagnostic tool, the most attractive feature of lung imaging with MR consists in its flexibility to combine different data-acquisition techniques with the use of new classes of contrast agents. Of particular interest in recent years has been the introduction of inhalatory paramagnetic contrast media, such as hyperpolarized gases and molecular oxygen to explore lung ventilation and diffusion. Concurrently, time-resolved three-dimensional visualization of lung parenchyma during intravenous administration of gadolinium-based contrast agents has been established as a clinical tool to assess pulmonary perfusion. Since technical improvements in MR systems have largely

reduced data acquisition times, imaging protocols that include morphologic and functional assessment of the lung are recently accessible for clinical application (PUDERBACH et al. 2007). To date, few studies have explored the potential of MRI to investigate lung function in ILD patients. In the following paragraphs the MR techniques that have been investigated for the assessment of lung function in ILD patients will be addressed.

14.8

Imaging of Lung Function with Hyperpolarized Gases

The use of exogenous inhalatory contrast agents in lung MRI was first demonstrated in the mid 1990s with the introduction of hyperpolarized or laser-polarized noble gasses, such as xenon-129 (Xe) and helium-3 (He) (ALBERT et al. 1994; MIDDLETON et al. 1995; MACFALL et al. 1996; BLACK et al. 1996; KAUCZOR et al. 1996). The polarization process, achieved by optical pumping, causes a non-equilibrium state in the nuclei of the gas which represents the source of the MR signal (GUENTHER et al. 2000). The gas inhalation allows for the direct assessment of the airways and pulmonary airspaces. In this setting the proton density of lung tissues (i.e. blood and interstitium) is neglected. A dedicated RF coil and an MR system adapted to the frequency of resonance of the gas is required. The sequence design is based on gradient echo techniques. For a detailed description of the principles, design and practical implementation of the laser polarization techniques, and the setup for MR imaging of the lung with hyperpolarized gasses, the reader is referred to the reviews in the literature (GOODSON 2002; MOLLER et al. 2002) and to other chapters of this book.

Although He-3 is less abundant in nature than Xe-129, its use has been preferred because of its larger gyromagnetic ratio and polarization levels (KAUCZOR et al. 2002). The images obtained from hyperpolarized He-3 MRI of the lung are generally characterized by excellent SNR and good spatial and temporal resolution. Additionally, He-3 is not absorbed by the lung and can be inhaled in relatively large quantities without substantial risks. Different strategies to explore lung function with hyperpolarized He-3 have been established (KAUCZOR et al. 2002). By simple visualization of lung areas that exhibit signal enhancement, ventilated lung tissue is demonstrated (spin or gas density imaging). Other techniques have been also developed including the calculation of ventilated lung volume, the assessment of the diffusion of gas molecules in the pulmonary

airspace (diffusion-weighted imaging), dynamic ventilation imaging and measurement of the alveolar pO₂ (KAUCZOR et al. 2002).

Because lung function imaging with hyperpolarized noble gases primarily allows for the depiction of airways and ventilated airspaces, it is not surprising that most of the studies focused on the clinical application of this diagnostic modality for COPD, asthma and chronic bronchitis. ILD patients have not been investigated systematically by MRI and hyperpolarized gases (KAUCZOR et al. 2001). All current literature available on the application of this imaging tool to the study of lung fibrosis derives from few reports and results from patients that have been treated with single lung transplantation (MARKSTALLER et al. 2002; GAST et al. 2003, 2007; ZAPOROZHAN et al. 2004, 2005; BINK et al. 2007). In these studies, the most typical alteration reported was an inhomogeneous distribution of the signal generated by the gas in ventilated regions of the lung and of the ADC values calculated from diffusion imaging. These alterations have been interpreted as focal ventilatory defects caused by fibrotic obstruction of peripheral bronchi. These areas of heterogeneous signal contain information about ventilatory state as well as other parameters (i.e. time constants, compliance, and alveolar oxygen concentration). Functional and clinical significance of these findings are still to be investigated.

14.9

Imaging of Lung Function with Oxygen

Indirect assessment of lung function using molecular oxygen as an inhaled contrast agent was first proposed by EDELMAN et al. (1996). Since then, the technical feasibility and clinical relevance of oxygen-enhanced MRI of the lung have been investigated in animals, healthy volunteers, and patients with various diseases. Because oxygen causes signal changes in the lung after diffusing through the alveolar-capillary barrier (OHNO et al. 2002; JAKOB et al. 2004), this technique is potentially suitable for the functional assessment of pulmonary diseases that lead to an altered gas diffusion. The physical characteristics of molecular O₂ and the physiological basis that explain its paramagnetic effect in the lung are described in other chapters of this book. The following paragraphs offer a survey on the research relevant for understanding the potential of oxygen-enhanced MRI in the functional evaluation of ILD.

To date, ILD patients have been investigated with oxygen ventilation imaging only in a limited number of

studies. A correlation between the results of this technique and the DLCO was firstly assessed by MULLER et al. (2002). In their study, either the SI slope calculated by imaging the lung during the wash-in phase of oxygen or the overall SI change from room air ventilation to the maximal oxygen enhancement correlated with DLCO. Similar results have been found also in another recent study conducted in patients with IPF and sarcoidosis (MOLINARI et al. 2007). From the analysis of the extent of the areas that showed oxygen enhancement in the lung, a semiquantitative parameter was correlated with the tests that characterize the gas exchange impairment of ILD. A good correlation was found with the DLCO, KCO, the arterial partial pressure and the saturation of oxygen. The higher correlation was found between the results of oxygen-enhanced MRI and KCO. This is particularly interesting considering that, as mentioned above, KCO is generally regarded as more sensitive to the alteration of the alveolar-capillary gas exchange. Both studies seem to confirm the possibility to obtain information from this imaging modality that can be used clinically to predict the loss of lung function in ILD.

A quantitative model to assess the pulmonary gas exchange was developed recently by Jakob and colleagues using multiple oxygen concentrations and a T1 mapping procedure (JAKOB et al. 2001, 2004; ARNOLD et al. 2007). Based on the linear proportionality between the longitudinal relaxivity of the lung (i.e. R1) and the local oxygen concentration, the model allows for the calculation of an "oxygen transfer function" (OTF) which represents the slope of the plot of R1 vs O₂ concentration. The OTF has been proposed as an indicator of the gas transfer ability of the lung. Although the study was conducted in a small group of patients with cystic fibrosis, the approach relies on general principles of lung physiology and it might be also considered for the evaluation of ILD. Research has to be conducted to confirm the clinical applicability of this quantitative method for oxygen-enhanced MRI of the lung. Additionally, other more general aspects of oxygen ventilation imaging that might require further investigation have been also indicated (JAKOB et al. 2004). In particular, the amount of O₂ physically dissolved in pulmonary blood is a function of the diffusing capacity of the lung, but also of the local ventilation-perfusion ratio (JAKOB et al. 2004). Hence, oxygen ventilation imaging should not be regarded as a direct surrogate test for the assessment of lung diffusion. The assessment of lung function with this technique in combination with perfusion MRI has been suggested.

14.10

MR Protocols for Imaging Lung Morphology and Function in ILD

In a recent study (PUDERBACH et al. 2007), the technical requirements and basic MR sequences for imaging the lung at 1.5 T have been reviewed. A routine MRI protocol based on short echo times (TE) to counteract the rapid signal decay of the lung and acquisitions within single or multiple consecutive breath-holds has been proposed. The basic protocol comprises a localizer, a coronal T2-weighted single-shot half-Fourier turbo spin-echo sequence, a transversal T1-weighted three-dimensional (3D) gradient-echo, a coronal steady-state free precession, and a transversal T2-weighted short- τ inversion-recovery (STIR). An extent to this protocol includes a post contrast transversal T1-weighted 3D gradient-echo sequence (not always required). With this approach the assessment of a variety of lung diseases including ILD is feasible in a reasonable time (approximately 20 min).

The infiltrative processes and fibrotic changes which represent the common manifestations of many ILDs are well depicted by the T2-weighted images, such as those obtained with partial-Fourier (HASTE) or ultra-short TE acquisition techniques. The reticular pattern caused by thickening of interstitial septa, potentially associated to ground-glass opacities, traction bronchiectases/bronchiolectases, cystic changes with honey combing and overall architectural distortion of the lung can be visualized easily by transversal or coronal images. In the coronal plane, the dorsal and basal location of the peripheral reticulations is demonstrated in full extent by few images, giving immediate perception of the distribution of the disease (Fig. 14.2). T1 contrast-enhanced images, used primarily to characterize focal masses among the interstitial changes, are similar to CT in depicting the subpleural reticulations (Fig. 14.2). The use of fat saturation increases the visualization of contrast-enhanced fibrotic changes and vascular distortion against the low-signal chest wall. The nodular pattern (for instance, in sarcoidosis) can be demonstrated using non-enhanced 3D T1-weighted gradient echo sequences (T1-GRE). On most scanners equipped with parallel imaging technique 3D-T1-GRE are capable of isotropic voxels of 2 mm³ or even lower in-plane spatial resolution (PUDERBACH et al. 2007). Large focal consolidations or fibrotic masses are usually well depicted in both T2-HASTE and non-enhanced T1-GRE images. As mentioned, contrast administration at the end of the protocol may be considered when the nature of the con-

solidation is unclear. The coronal steady-state free precession sequence visualizes with high sensitivity the restricted motion of the lung, which is typically associated with fibrosis. The transversal T2-weighted STIR images are generally used to visualize enlarged mediastinal and hilar lymph nodes.

On current systems equipped with time-resolved echo-shared fast gradient-echo techniques, images of lung perfusion can be obtained with a minimal extension to the total examination time of the basic contrast-enhanced protocol. Immediate qualitative assessment of these images in ILD may indicate lung perfusion defects in areas of advanced architectural distortion. In some cases large or multiple perfusion changes are visualized even with mild parenchymal alterations as a consequence of perivascular fibrosis. This may help understanding the functional impairment of the patient. As described in other chapters of this book, quantitative parameters of lung perfusion can be obtained in a post-processing phase.

Finally, in an advanced setup, oxygen-enhanced MRI of the lung may be added to the protocol described so far. It must be noted that oxygen ventilation imaging requires at least two acquisitions (normoxic and hyperoxic ventilation) interleaved with five minutes for the wash in and wash out of the gas. This results in a prolongation of the protocol of 15 minutes, with a comprehensive morphologic and functional assessment obtained in a total of approximately 40–50 min depending on the patient breathing rate.

References

- Albert MS, Cates GD, Driehuys B et al. (1994) Biological magnetic resonance imaging using laser-polarized ¹²⁹Xe. *Nature* 370:199–201
- Arnold JF, Kotas M, Fidler F et al. (2007) Quantitative regional oxygen transfer imaging of the human lung. *J Magn Reson Imaging* 26:637–645
- Arroliga AC, Podell DN, Matthay RA (1992) Pulmonary manifestations of scleroderma. *J Thorac Imag* 7:30–45
- ATS/ERS (2002) American Thoracic Society/European Respiratory Society International Multidisciplinary Consensus Classification of the Idiopathic Interstitial Pneumonias. *Am J Respir Crit Care Med* 165:277–304
- Bankier AA, Kiener HP, Wiesmayr MN et al. (1995) Discrete lung involvement in systemic lupus erythematosus: CT assessment. *Radiology* 196:835–840
- Bekkelund SI, Aasebo U, Pierre-Jerome C et al. (1998) Magnetic resonance imaging of the thorax in the evaluation of asbestosis. *Eur Respir J* 11:194–197

- Berthezene Y, Vexler V, Kuwatsuru R et al. (1992) Differentiation of alveolitis and pulmonary fibrosis with a macromolecular MR imaging contrast agent. *Radiology* 185:97–103
- Bink A, Hanisch G, Karg A et al. (2007) Clinical aspects of the apparent diffusion coefficient in 3He MRI: results in healthy volunteers and patients after lung transplantation. *J Magn Reson Imaging* 25:1152–1158
- Black RD, Middleton HL, Cates GD et al. (1996) In vivo He-3 MR images of guinea pig lungs. *Radiology* 199:867–870
- Chetta A, Marangio E, Olivieri D (2004) Pulmonary function testing in interstitial lung diseases. *Respiration* 71:209–213
- Colby TV, Carrington CB (1994) Infiltrative lung disease. In: Thurlbeck WM (ed) *Pathology of the lung*. Thieme Medical Publishers, New York, pp 589–737
- Craig DA, Colletti PM, Ratto D et al. (1988) MRI findings in pulmonary sarcoidosis. *Magn Reson Imaging* 6:567–573
- Dawson WB, Müller NL (1990) High-resolution computed tomography in pulmonary sarcoidosis. *Semin Ultra CT MR* 11:423–429
- Desai SR, Verrarraghavan S, Hansell DM et al. (2004) CT features of lung disease in patients with systemic sclerosis: comparison with idiopathic pulmonary fibrosis and non-specific interstitial pneumonia. *Radiology* 232:560–567
- Edelman RR, Hatabu H, Tadamura E et al. (1996) Noninvasive assessment of regional ventilation in the human lung using oxygen-enhanced magnetic resonance imaging. *Nat Med* 2:1236–1239
- Fenlon HM, Doran M, Sant SM et al. (1996) High-resolution chest CT in systemic lupus erythematosus. *AJR Am J Roentgenol* 166:301–307
- Gammon RB, Bridges TA, al-Nezir H et al. (1992) Bronchiolitis obliterans organizing pneumonia associated with systemic lupus erythematosus. *Chest* 102:1171–1174
- Gast KK, Puderbach MU, Rodriguez I et al. (2003) Distribution of ventilation in lung transplant recipients: evaluation by dynamic 3He-MRI with lung motion correction. *Invest Radiol* 38:341–348
- Gast KK, Biedermann A, Herweling A et al. (2007) Oxygen-sensitive (3)He-MRI in bronchiolitis obliterans after lung transplantation. *Eur Radiol* 18:530–537
- Gibson GJ, Pride NB (1977) Pulmonary mechanics in fibrosing alveolitis: the effects of lung shrinkage. *Am Rev Respir Dis* 116:637–647
- Glazer H, Levitt RG, Lee JK et al. (1984) Differentiation of radiation fibrosis from recurrent pulmonary neoplasm by magnetic resonance imaging. *AJR Am J Roentgenol* 143:729–730
- Goodson BM (2002) Nuclear magnetic resonance of laser-polarized noble gases in molecules, materials, and organisms. *J Magn Reson* 155:157–216
- Grenier P, Valeyre D, Cluzel P et al. (1991) Chronic diffuse interstitial lung disease: diagnostic value of chest radiography and high-resolution CT. *Radiology* 179:123–132
- Gross TJ, Hunninghake GW (2001) Idiopathic pulmonary fibrosis. *N Engl J Med* 345:517–525
- Guenther D, Hanisch G, Kauczor HU (2000) Functional MR imaging of pulmonary ventilation using hyperpolarized noble gases. *Acta Radiol* 41:519–528
- Hughes JM (2003) The single breath transfer factor (Tl, co) and the transfer coefficient (Kco): a window onto the pulmonary microcirculation. *Clin Physiol Funct Imaging* 23:63–71
- Hunninghake GW, Zimmerman MB, Schwartz DA et al. (2001) Utility of a lung biopsy for the diagnosis of idiopathic pulmonary fibrosis. *Am J Respir Crit Care Med* 164:193–196
- Jakob PM, Hillenbrand CM, Wang T et al. (2001) Rapid quantitative lung (1)H T(1) mapping. *J Magn Reson Imaging* 14:795–799
- Jakob PM, Wang T, Schultz G et al. (2004) Assessment of human pulmonary function using oxygen-enhanced T(1) imaging in patients with cystic fibrosis. *Magn Reson Med* 51:1009–1016
- Kadota J, Kusano S, Kawakami K et al. (1995) Usual interstitial pneumonia associated with primary Sjögren's syndrome. *Chest* 108:1756–1758
- Kalaiztoglou I, Drevelengas A, Palladas P et al. (1998) MRI appearance of pulmonary Wegener's granulomatosis with concomitant splenic infarction. *Eur Radiol* 8:367–370
- Katzenstein AL, Fiorelli RF (1994) Nonspecific interstitial pneumonia/fibrosis: histologic features and clinical significance. *Am J Surg Pathol* 18:136–147
- Katzenstein AL, Myers JL (1998). Idiopathic pulmonary fibrosis: clinical relevance of pathologic classification. *Am J Respir Crit Care Med* 157:1301–1315
- Kauczor U, Kreitner KF (1999) MRI of the pulmonary parenchyma. *Eur Radiol* 9:1755–1764
- Kauczor HU, Hofmann D, Kreitner KF et al. (1996) Normal and abnormal pulmonary ventilation: visualization at hyperpolarized He-3 MR imaging. *Radiology* 201:564–568
- Kauczor HU, Chen XJ, van Beek EJ et al. (2001) Pulmonary ventilation imaged by magnetic resonance: at the doorstep of clinical application. *Eur Respir J* 17:1008–1023
- Kauczor HU, Hanke A, Van Beek EJ (2002) Assessment of lung ventilation by MR imaging: current status and future perspectives. *Eur Radiol* 12:1962–1970
- Kersjes W, Hildebrandt G, Cagil H et al. (1999) Differentiation of alveolitis and pulmonary fibrosis in rabbits with magnetic resonance imaging after intrabronchial administration of bleomycin. *Invest Radiol* 34:13–21
- Kim JS, Lee KS, Koh EM et al. (2000) Thoracic involvement of systemic lupus erythematosus: clinical, pathologic, and radiologic findings. *J Comput Assist Tomogr* 24:9–18
- Knudson RJ, Kaltenborn WT (1981) Evaluation of lung elastic recoil by exponential curve analysis. *Respir Physiol* 46:29–42
- Kreider ME, Hansen-Flaschen J, Ahmad NN et al. (2007) Complications of video-assisted thoracoscopic lung biopsy in patients with interstitial lung disease. *Ann Thorac Surg* 83:1140–1144
- Leung AN, Staples CA, Müller NL (1993) Parenchymal opacification in chronic infiltrative lung diseases: CT-pathologic correlation. *Radiology* 188:209–214

- MacFall JR, Charles HC, Black RD et al. (1996) Human lung air spaces: potential for MR imaging with hyperpolarized He-3. *Radiology* 200:553–558
- Markstaller K, Kauczor HU, Puderbach M et al. (2002) 3He-MRI-based vs. conventional determination of lung volumes in patients after unilateral lung transplantation: a new approach to regional spirometry. *Acta Anaesthesiol Scand* 46:845–852
- Matsumoto S, Mori H, Miyake H et al. (1998) MRI signal characteristics of progressive massive fibrosis in silicosis. *Clin Radiol* 53:510–514
- McAdams HP, Rosado-de-Christenson ML, Wehunt WD et al. (1996) The alphabet soup revisited: the chronic interstitial pneumonias in the 1990s. *Radiographics* 16:1009–1034
- McCormack FX, King TE Jr, Voelker DR et al. (1991) Idiopathic pulmonary fibrosis. Abnormalities in the bronchoalveolar lavage content of surfactant protein A. *Am Rev Respir Dis* 144:160–166
- McFadden R, Carr TJ, Wood TE (1987) Proton magnetic resonance imaging to stage activity of interstitial lung disease. *Chest* 92:31–39
- Middleton H, Black RD, Saam B et al. (1995) MR imaging with hyperpolarized 3He gas. *Magn Reson Med* 33:271–5
- Miller BH, Rosado-de-Christenson ML, McAdams HP et al. (1995) From the archives of the AFIP. Thoracic sarcoidosis: radiologic-pathologic correlation. *Radiographics* 15:421–437
- Molinari F, Eichinger M, Risse F et al. (2007) Navigator-triggered oxygen-enhanced MRI with simultaneous cardiac and respiratory synchronization for the assessment of interstitial lung disease. *J Magn Reson Imaging* 26:1523–1529
- Moller HE, Chen XJ, Saam B et al. (2002) MRI of the lungs using hyperpolarized noble gases. *Magn Reson Med* 47:1029–1051
- Müller N, Mayo JR, Zwirerich CV (1992) Value of MR imaging in the evaluation of chronic infiltrative lung disease: comparison with CT. *AJR Am J Roentgenol* 158:1205–1209
- Muller CJ, Schwaiblmair M, Scheidler J et al. (2002) Pulmonary diffusing capacity: assessment with oxygen-enhanced lung MR imaging preliminary findings. *Radiology* 222:499–506
- Ohno Y, Hatabu H, Takenaka D et al. (2002) Dynamic oxygen-enhanced MRI reflects diffusing capacity of the lung. *Magn Reson Med* 47:1139–1144
- Perez T, Remy-Jardin M, Cortet B (1998) Airways involvement in rheumatoid arthritis: clinical, functional, and HRCT findings. *Am J Respir Crit Care Med* 157:1658–1665
- Primack S, Mayo JR, Hartman TE et al. (1994) MRI of infiltrative lung disease: comparison with pathologic findings. *J Comput Assist Tomogr* 18:233–238
- Puderbach M, Hintze C, Ley S et al. (2007) MR imaging of the chest: a practical approach at 1.5T. *Eur J Radiol* 64:345–355
- Remy-Jardin M, Remy J, Cortet B et al. (1994) Lung changes in rheumatoid arthritis: CT findings. *Radiology* 193:375–382
- Sant SM, Doran M, Fenelon HM et al. (1997) Pleuropulmonary abnormalities in patients who have systemic lupus erythematosus: assessment with high resolution computed tomography, chest radiography and pulmonary function tests. *Clin Exp Rheumatol* 15:507–513
- Shioya S, Haida M, Fukuzaki M et al. (1990) A 1-year time course study of the relaxation times and histology for irradiated rat lungs. *Magn Reson Med* 14:358–368
- Taorimina VJ (1981) Progressive systemic sclerosis subgroups: variable pulmonary features. *AJR Am J Roentgenol* 137:277–285
- Taylor CR, Sostman HD, Gore JC et al. (1987) Proton relaxation times in bleomycin-induced lung injury. *Invest Radiol* 22:621–626
- Terriff BA, Kwan SY, Chan-Yeung MM et al. (1992) Fibrosing alveolitis: chest radiography and CT as predictors of clinical and functional impairment at follow-up in 26 patients. *Radiology* 184:445–449
- Thompson MJ, Colebatch HJ (1989) Decreased pulmonary distensibility in fibrosing alveolitis and its relation to decreased lung volume. *Thorax* 44:725–731
- Ulmer WT, Gillissen A, Reichel G et al. (1993) Lung function and normal values [in German]. *Pneumologie* 47:403–408
- Vinitski S, Pearson MG, Karlik SJ et al. (1986) Differentiation of parenchymal lung disorders with in vitro proton nuclear magnetic resonance. *Magn Reson Med* 3:120–125
- Webb WR (2001) Sarcoidosis. In: Webb WR, Müller NL, Naidich DP (eds) *High-resolution CT of the lungs*. Lippincott Williams and Wilkins, Philadelphia, pp 286–303
- Webb WR, Stein MG, Finkbeiner WE et al. (1988) Normal and diseased isolated lungs: high-resolution CT. *Radiology* 166:81–87
- Wells AU, Hogaboam CM (2007) Update in diffuse parenchymal lung disease 2006. *Am J Respir Crit Care Med* 175:655–660
- Wells AU, Rubens MB, du Bois RM et al. (1993) Serial CT in fibrosing alveolitis: prognostic significance of the initial pattern. *AJR Am J Roentgenol* 161:1159–1165
- Wiedemann HP, Matthay RA (1992) Pulmonary manifestations of systemic lupus erythematosus. *J Thorac Imaging* 7:1–18
- Yankelevitz D, Henschke CI, Batata M et al. (1994) Lung cancer: evaluation with MR imaging during and after irradiation. *J Thorac Imaging* 9:41–46
- Zaporozhan J, Ley S, Gast KK et al. (2004) Functional analysis in single-lung transplant recipients: a comparative study of high-resolution CT, 3He-MRI, and pulmonary function tests. *Chest* 125:173–181
- Zaporozhan J, Ley S, Gast KK et al. (2005) [Visual assessment of functional lungs parenchyma on HRCT and (3)He-MRI in patients after single lung transplantation: comparison with quantitative volumetric results]. *Fortschr Röntgenstr* 177:516–523

CLAUS PETER HEUSSEL and CHRISTIAN PLATHOW

CONTENTS

| | | |
|--------|--|-----|
| 15.1 | Introduction and History of Asbestos and Mesothelioma | 291 |
| 15.1.1 | Asbestosis | 292 |
| 15.1.2 | Mesothelioma | 293 |
| 15.2 | Tumour Staging and Measurement | 295 |
| 15.2.1 | Staging | 295 |
| 15.2.2 | Challenges | 297 |
| 15.2.3 | Why Measure Tumour Response? | 297 |
| 15.2.4 | WHO Criteria | 297 |
| 15.2.5 | RECIST | 297 |
| 15.2.6 | Modified RECIST Criteria | 300 |
| 15.3 | MRI in Asbestosis | 300 |
| 15.4 | Imaging of Mesothelioma | 301 |
| 15.5 | MRI of Mesothelioma | 301 |
| 15.6 | MRI of Other Pleural Diseases | 302 |
| 15.6.1 | Solitary Fibrous Tumours of the Pleura | 302 |
| 15.6.2 | MRI of Other Chest Wall Diseases | 303 |
| | References | 303 |

KEY POINTS

Pleural tumours are rare in comparison with tumours of the lung such as bronchial carcinomas. Malignant pleural mesothelioma is an aggressively growing tumour and a rising incidence is expected in the next decades. CT is still the general diagnostic tool for staging and therapy planning of malignant pleural mesothelioma. However, within the last few years novel MRI techniques have been developed and introduced into clinical routine to improve tumour delineation and characterization in order to optimize individual therapy planning. Typical findings of pleural tumours, especially malignant pleural mesothelioma, using modern MRI techniques are discussed. Techniques are compared with CT and modern PET techniques especially concerning precision of tumour delineation, therapy planning and monitoring.

15.1

Introduction and History of Asbestos and Mesothelioma

People have been exposed to asbestos for thousands of years but to a much greater extent since its industrial mining in the 1970s. In 1955, Doll established the causal association between asbestosis and lung cancer. In the 1960s, a third asbestos-related disease was discovered when the possible association between the formation of malignant pleural mesothelioma (MPM) and crocidolite exposure was found.

The word asbestos itself is a misapplication of the Latin term asbestos “quicklime” from Greek (σβεστος; a, “not” and sbestos, “extinguishable”) which describes any of a group of minerals that can be fibrous, many of

C. P. HEUSSEL, PD Dr med.
Department of Radiology, Clinic for Thoracic Diseases Heidelberg, Amalienstr. 5, 69126 Heidelberg, Germany

C. PLATHOW, PD Dr med., MSc
Department of Nuclear Medicine, University of Freiburg, Hugstetterstr. 55, 79106 Freiburg, Germany

which are metamorphic, and mainly consist of hydrous magnesium silicates. According to data from the U.S. Geological Survey, 182.2 million metric tonnes (Mt) of asbestos were mined between 1900 and 2003 (TOS-SAVAINEN 2004). Global production peaked in 1975 at 5 Mt. Despite a slight downturn, output remained at over 4 Mt a year until 1991. In 2003, 2.15 Mt of chrysotile (white asbestos) were mined. Blue asbestos (crocidolite) is commonly thought of as the most dangerous type of asbestos, while white asbestos (chrysotile) is the most frequently used type accounting for about 95% of the asbestos found in buildings in the United States. While the use of asbestos has been prohibited or restricted in many Western countries, especially because of the proven association with MPM, the consumption is still growing in Asia and Latin America. Research by TOS-SAVAINEN (2004) found that “170 tonnes of produced and consumed asbestos will cause at least one death from MPM, most often as a consequence from occupational exposure”. But before an MPM develops, asbestosis shows typical changes of the pleura which have to be kept in mind for early detection, diagnosis and potential prevention of malignant transformation.

15.1.1 Asbestosis

In general, asbestos fibres cause an inflammation of the parietal pleura, leading to pleural plaques, diffuse pleural fibrosis, rounded atelectasis, pleural effusion, bronchogenic carcinoma and MPM (SCHWARTZ 1991; MOSSMANN and GEE 1989). Bilateral scattered calcified

pleural plaques are pathognomonic signs for asbestos exposure (PEACOCK et al. 2000). Pleural plaques are the most commonly observed signs after asbestos exposure, observed in 60%–70% of exposed workers (FALASCHI et al. 1995). The average latency period is about 15 years for uncalcified and at least 20 years for calcified plaques (MÜLLER NL 1993). Their detection is important because patients with plaques have an approximately threefold higher risk of developing lung cancer and MPM. The average latency period from the first asbestos exposure to detection of a malignant tumour ranges from 20 to 43 years (KISHIMOTO et al. 2003). The detection of subtle pleural lesions associated with asbestos exposure is a challenging task for the radiologist because the radiologist has to raise the suspicion of an occupational disease, which may result in a possible financial compensation of the patient. Detection of pleural plaques is important because they are a marker of a significant asbestos exposure in these patients. Although pleural plaques are not considered to be premalignant, such patients have a higher incidence of malignancy, such as MPM and lung cancer. Therefore, pleural plaques may be regarded as risk indicators of possibly asbestos-related tumours in an asbestos-exposed population. Currently, computed tomography (CT) is the gold standard tool for the detection of benign asbestos-induced changes of the pleura (LYNCH et al. 1989) (Fig. 15.1). Conventional chest radiography has a low sensitivity, varying from 13% to 53%, even in persons with prolonged exposure to asbestos. In general, magnetic resonance imaging (MRI) is rarely used for the diagnosis of pleural plaques and only as an adjunct to CT.

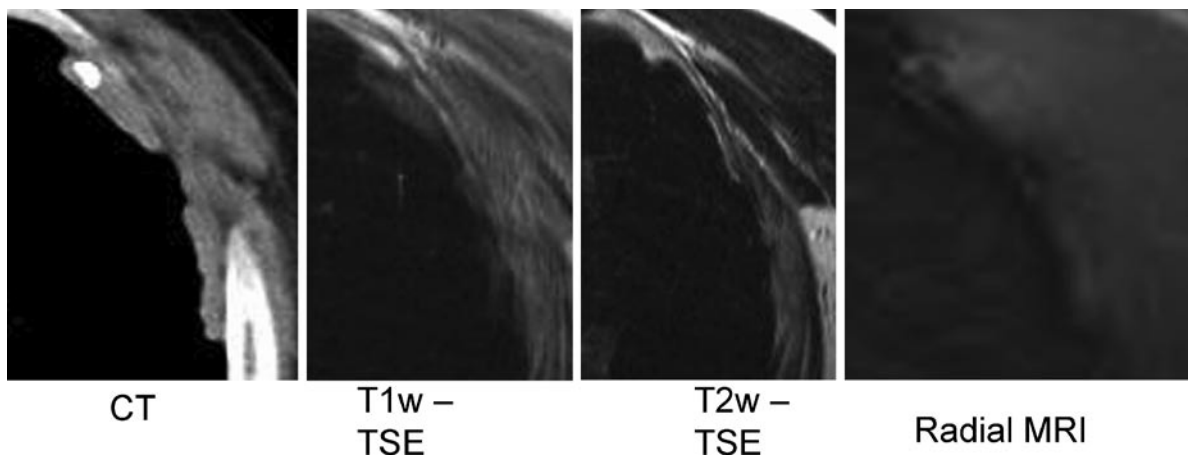


Fig. 15.1. Comparison of CT with T1w TSE, T2w TSE and radial MRI sequences in a patient with an asbestos plaque. The T1w sequence shows the plaque isointense to soft tissue, while the T2w sequence shows it with low signal intensity (hypoin-

tense). Using the radial sequence even the calcified areas can be visualized. (with permission: Weber MA, Bock M, Plathow C et al. *Invest Radiol* (2004))

15.1.2 Mesothelioma

Malignant pleural mesothelioma is the most common cancer in persons occupationally exposed to asbestos, and it develops after a long average latency period. It is 1000 times more common in a population exposed to asbestos. Its incidence is strongly correlated with the individual exposure to asbestos; a correlation to smoking history has not been found. It is an uncommon neoplasm arising from mesothelial cells of the visceral or parietal pleura, divided into three histological categories: epithelial (55%–65%), sarcomatoid (10%–15%), and mixed (20%–35%). The annual incidence in the United States is 15 cases per million inhabitants and the number of deaths is predicted to be 72,000 in the next 40 years (PRICE and WARE 2004; ROBINSON and LAKE 2005). The cancer incidence has been rising and is expected to peak between 2010 and 2030 in industrialized countries despite regulatory restrictions during the 1980s and 1990s (PETO et al. 1995). Typical radiological signs are pleural effusion, focal thickening of the pleura and infiltration of the diaphragm and chest wall (Figs. 15.2 and 15.3). MPM frequently metastasizes to the ipsilateral (60%) or contralateral lung and to hilar and mediastinal lymph nodes. Distant metastases are rare. The major differential diagnosis is metastatic adenocarcinoma. There is currently no universally accepted standard therapy for MPM even though in the

meantime there are some promising study results. Still the prognosis is poor with a median survival of 8–18 months after diagnosis (MARTINO and PASS 2004). However, important advances in the treatment of patients with MPM have occurred over the past few years, including the acceptance of a universal staging system, new active chemotherapeutic regimens, novel targeted agents, improved radiation therapy techniques for local control, as well as innovative techniques for curative surgical resection which are associated with decreased morbidity and mortality (KHALIL et al. 2003; SUGARBAKER et al. 1999; VOGELZANG et al. 2003; CACCIOTTI et al. 2002). Furthermore, multimodality regimens combining chemotherapy, radiotherapy, immunotherapy, and surgery are being used more frequently because of the failure of single-modality therapy (YOSHINO et al. 2004; ZELLOS and SUGARBAKER 2002). In cases of limited disease, there has been an increasing tendency to perform surgical resection. Extrapleural pneumonectomy (EPP), or the removal of the visceral and parietal pleura, ipsilateral lung, hemidiaphragm, and part of the pericardium (P3D) is the surgical treatment of choice in the 10%–15% of patients who present with resectable disease. These techniques seem to prolong survival (74% 2-year survival and 39% 5-year survival). The greatest survival benefit in patients with MPM after EPP is seen in those with epithelial histology, a primary tumour that is limited in extent and has no nodal metastases. In contrast, patients with sarcomatoid histology and nodal

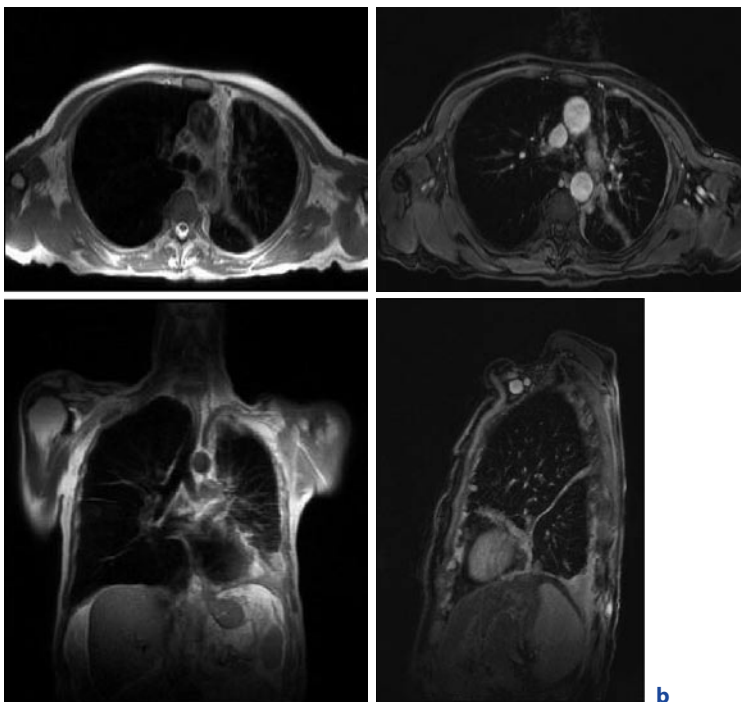


Fig. 15.2. MRI sequences to image malignant pleural mesothelioma. HASTE (a), VIBE (b); c,d see next page

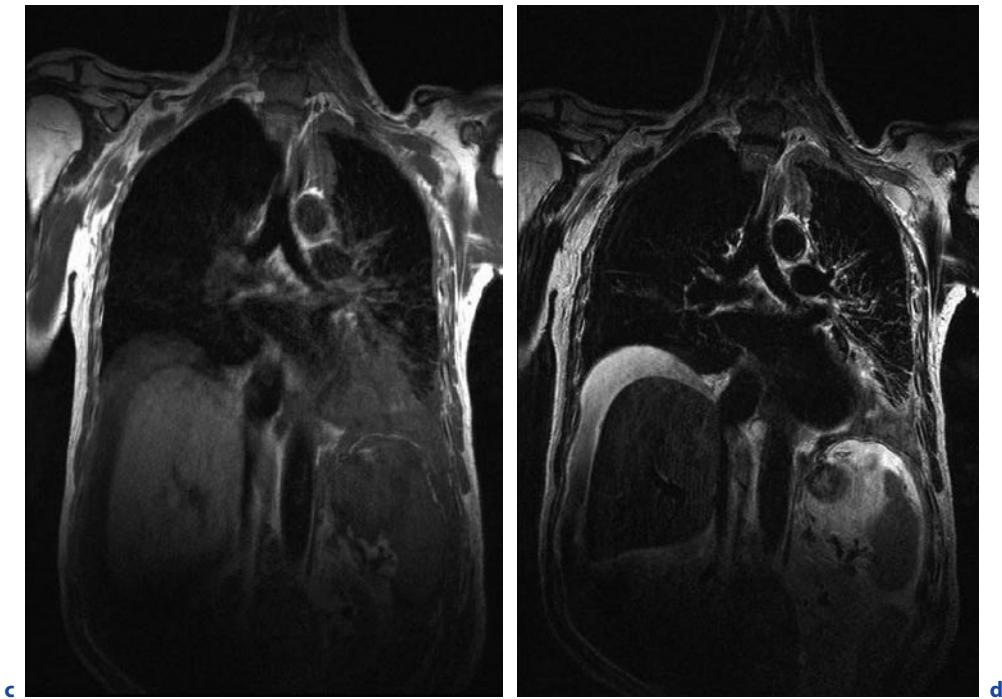


Fig. 15.2. (continued) MRI sequences to image malignant pleural mesothelioma. T1-TSE (c) and T2-TSE with respiratory gating (d) are shown in a patient with left-sided pleural mesothelioma. Note the excellent morphologic resolution concerning chest wall and mediastinal infiltration especially when using T2-TSE with respiratory gating

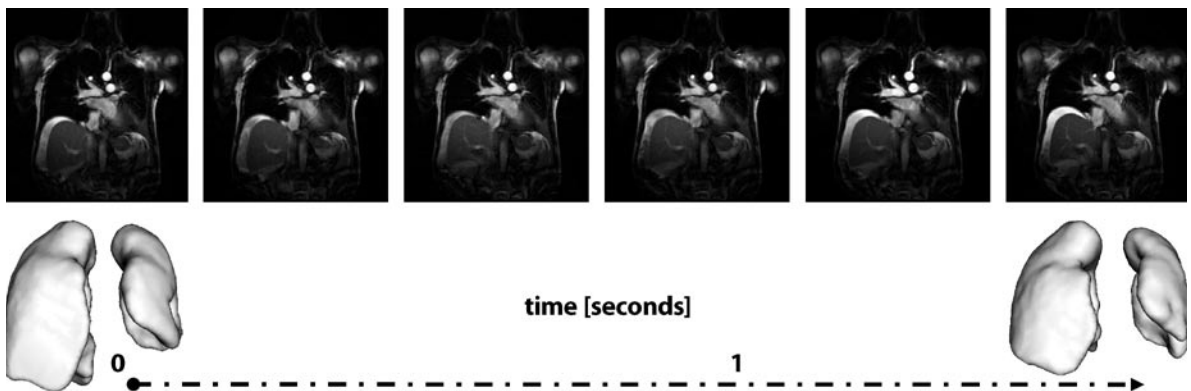


Fig. 15.3. Dynamic MRI using a trueFISP sequence in a patient with a left-sided pleural mesothelioma during maximum inspiration and expiration. There is almost no volume change of the left lung due to the pleural mesothelioma

metastases have a poor survival benefit after EPP and are typically primarily treated with palliative chemotherapy.

Recently, positive results have been reported for pemetrexed, a multitargeted antifolate, in combination with cisplatin. In a multicenter phase III study of 448 patients an objective response rate of 41% and overall survival benefit of 3 months was achieved (VOGELZANG

et al. 2003). Consequently, the combination of cisplatin and an antifolate is generally accepted as the standard therapy for MPM (BAAS 2005).

Recent publications also show that state-of-the-art radiotherapy techniques improve target volume in MPM and thus might enhance clinical outcome (STERZING et al. 2008).

15.2

Tumour Staging and Measurement

15.2.1
Staging

At least five different staging systems of MPM exist. BUTCHART et al. (1976) introduced a classification system into four stages which became widely used. These are given in Table 15.1. Most staging systems including the one from Butchart did not use the T, N and M descriptors as used in the classical TNM-classifications for tumours. However, in an attempt to distinguish patients who would benefit from surgical resection with curative intent from those needing palliative treatment, the International Mesothelioma Interest Group (IMIG) has introduced a staging system for MPM in 1995 which has gained universal acceptance. TNM-staging and stage grouping are given in Tables 15.2 and 15.3. This staging system was adopted by the American Joint Committee on Cancer (AJCC) and the Union Internationale Centre le Cancer (UICC) (BRIDDA et al. 2007). It reconciles previous staging systems and is similar to those for other solid tumours and especially non-small cell lung cancer. It also incorporates data on the natural history and influence of T and N status on overall survival.

T1 indicates that there is usually a free pleural space, and these patients often present with a large pleural effusion. However, the presence of pleural fluid has no effect on staging. By non-invasive staging it is rather difficult to make a distinction between T1a, T1b and T2 disease. Correct estimation of extent of disease is only possible during thoracotomy. In case of T1b disease, pleurectomy and decortication are usually feasible. In

case of a T2 tumour there is more extensive involvement of the visceral pleura and lung, often necessitating a pleuropneumectomy. T3 implies locally advanced but potentially resectable MPM whereas T4 characterizes a non-resectable tumour. The prognosis of a T4 tumour is similar to M1 disease, and for this reason it is included in stage IV. In the IMIG system, lymph node staging is similar to the staging of non-small cell lung cancer. N1 disease relates to the involvement of the ipsilateral bronchopulmonary and/or hilar lymph node(s). N2 disease includes invasion of the ipsilateral mediastinal, subcarinal or the ipsilateral internal mammary nodes, and N3 disease the contralateral hilar, mediastinal, internal mammary nodes and/or the ipsilateral or contralateral supraclavicular or scalene lymph nodes. As there is probably not a large survival difference between N1 and N2 involvement in MPM, all patients with nodal involvement are classified as stage III (N1, N2) or stage IV (N3 disease), in contrast to non-small cell lung cancer where N1 usually belongs to stage II, and N3 disease to stage IIIB.

Precise evaluation of the superior mediastinal lymph nodes often requires cervical mediastinoscopy. In a single study chest CT scan revealed enlarged lymph nodes in 39% of the patients (MILLER et al. 1981). Lymph node metastases were detected by mediastinoscopy in 26%. Not only for mediastinal nodal involvement, but also in the case of early mesothelioma, there is a discrepancy between non-invasive (clinical) and surgical staging. The IMIG classification presumes that early tumours are evaluated surgically to determine local extension and subsequent treatment. It should also be stated that within a specific TN subset differences in tumour biology are possible, resulting in a variable prognosis within the same group.

Table 15.1. Staging system by Butchart

| Stage | Description |
|-------|---|
| I | Tumour confined within the “capsule” of the parietal pleura, i.e., involving only ipsilateral pleura, lung, pericardium, and diaphragm |
| II | Tumour invading chest wall or involving mediastinal structures, e.g., oesophagus, heart, opposite pleura. Lymph node involvement within the chest |
| III | Tumour penetrating diaphragm to involve peritoneum; involvement of opposite pleura. Lymph node involvement outside the chest |
| IV | Distant blood borne metastases |

Table 15.2. Staging system for diffuse malignant pleural mesothelioma introduced by the International Mesothelioma Interest Group (IMIG) (INTERNATIONAL MESOTHELIOMA INTEREST GROUP 1995)

| Primary tumour (T) | |
|--------------------------|---|
| Tx | Primary tumour cannot be assessed |
| T0 | No evidence of primary tumour |
| T1 | Tumour involves ipsilateral parietal pleura, with or without focal involvement of visceral pleura T1a Tumour involves ipsilateral parietal (mediastinal, diaphragmatic) pleura. No involvement of the visceral pleura T1b Tumour involves ipsilateral parietal (mediastinal, diaphragmatic) pleura, with focal involvement of the visceral pleura |
| T2 | Tumour involves any of the ipsilateral pleural surfaces with at least one of the following confluent visceral pleural tumour (including fissure) invasion of diaphragmatic muscle invasion of lung parenchyma |
| T3 | Tumour involves any of the ipsilateral pleural surfaces, with at least one of the following: -invasion of the endothoracic fascia -invasion into mediastinal fat -solitary focus of tumour invading the soft tissue of the chest wall -non-transmural involvement of the pericardium |
| T4 | Tumour involves any of the ipsilateral pleural surfaces, with at least one of the following: -diffuse or multifocal invasion of soft tissues of the chest wall -any involvement of rib -invasion through the diaphragm to the peritoneum -invasion of any mediastinal organ(s) -direct extension to the contralateral pleura -invasion into the spine -extension to the internal surface of the pericardium -pericardial effusion with positive cytology -invasion of the myocardium -invasion of the brachial plexus |
| Regional Lymph Nodes (N) | |
| NX | Regional lymph nodes cannot be assessed |
| N0 | No regional lymph node metastases |
| N1 | Metastases in the ipsilateral bronchopulmonary and/or hilar lymph node(s) |
| N2 | Metastases in the subcarinal lymph node(s) and/or the ipsilateral internal mammary or mediastinal lymph node(s) |
| N3 | Metastases in the contralateral mediastinal, internal mammary, or hilar lymph node(s) and/or the ipsilateral or contralateral supraclavicular or scalene lymph node(s) |
| Distant Metastases (M) | |
| MX | Distant metastases cannot be assessed |
| M0 | No distant metastasis |
| M1 | Distant metastases |

Table 15.3. Stage grouping of malignant pleural mesothelioma

| | | | |
|-----------|--------|------------|----|
| Stage I | T1 | N0 | M0 |
| Stage IA | T1a | N0 | M0 |
| Stage IB | T1b | N0 | M0 |
| Stage II | T2 | N0 | M0 |
| Stage III | T1, T2 | N1 | M0 |
| | T1, T2 | N2 | M0 |
| | T3 | N0, N1, N2 | M0 |
| Stage IV | T4 | Any N | M0 |
| | Any T | N3 | M0 |
| | Any T | Any N | M1 |

15.2.2 Challenges

Besides of the most frequent pleural manifestation of mesothelioma, a peritoneal affection as well as a solely peritoneal origin (20%) of mesothelioma is possible (BRIDDA et al. 2007). The identification of an intercostal infiltration by the tumour is crucial for the surgical planning as inoculation metastasis develop, e.g. after transthoracic drainage. Furthermore, the extension of the tumour into the recessus is an underestimated problem since this is crucial for radiation planning.

Tumour measurements in MPM provide many challenges for clinical investigators. First, MPM has a unique growth pattern, growing as a “rind” around the hemithorax, and along interlobular fissures. It does not conform to the roughly spherical growth pattern of many other malignancies. Multiple thoracic levels may be involved, and while anatomical landmarks for measurement are available in the upper and mid thorax (carina, aortic arch), there are few landmarks in the lower thorax where levels of measurement can be reproducibly identified from one scan to another. There may or may not be bi-dimensionally measurable lesions, and where lesions are bi-dimensionally measurable, they may not always be the most representative and appropriate sites. Furthermore, at CT it is often difficult to distinguish tumour from pleural effusions or atelectasis without measuring Hounsfield units. In many centres, tumour measurements are performed by physicians or study nurses instead of radiologists, who may only have access to hard copies.

15.2.3 Why Measure Tumour Response?

When discussing tumour measurements, it is important to remember why we should do it. Palliative chemotherapy aims to benefit patients by decreasing symptoms and prolonging survival, rather than to decrease tumour size. A decrease in tumour size may or may not coincide with palliation in individual patients. Also stable disease and prolonged time to progression might be rated as effective. However, tumour response is an important surrogate for patient benefit in clinical trials where symptom improvement and increased survival are difficult to assess. Objective tumour size response evaluation remains nowadays the most often used primary endpoint in many clinical trials, allowing determining the efficacy of a treatment regimen. Novel alternative techniques are focused onto functional or biological surrogates, such as tumour perfusion, e.g. by MRI (Fig. 15.4), and metabolism, e.g. by PET (Fig. 15.5).

15.2.4 WHO Criteria

The previously widely-used WHO tumour response criteria were poorly suited to the growth pattern of MPM (MILLER et al. 1981). These response criteria were most useful for measuring spherical lesions bi-dimensionally, taking the sum of the products of the longest diameter of each lesion and its perpendicular diameter as the baseline tumour measurement. A partial response was defined by a 50% decrease in the sum of these products. Whilst uni-dimensional measurements were allowed, the acquired 50% decrease in the sum of uni-dimensional measurements actually equated mathematically to a 75% decrease in the sum of the products of perpendicular diameters, making it more difficult for tumours measured uni-dimensionally to meet the criteria for partial response.

15.2.5 RECIST

In contrast, RECIST criteria, which are becoming increasingly used in clinical trials, use uni-dimensional measurements only (THERASSE et al. 2000). A partial response is defined as a 30% decrease in the sum of the uni-dimensional tumour measurements (Fig. 15.6). Despite the use of these uni-dimensional measurements, application of the RECIST criteria is not straightforward in MPM. The RECIST criteria evolved from the

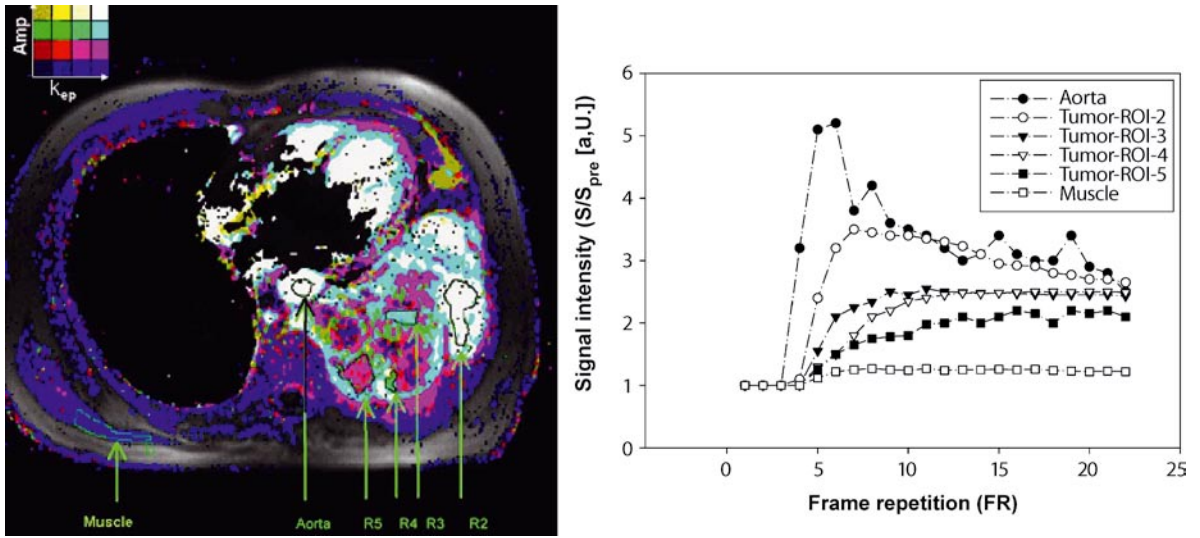


Fig. 15.4. Substantial heterogeneity of malignant pleural mesothelioma can be visualized by contrast enhanced dynamic MRI illustrating high and low perfusion areas. (with permission: Giesel F, Bischoff H, von Tengg-Kobligh H et al. Chest (2006))

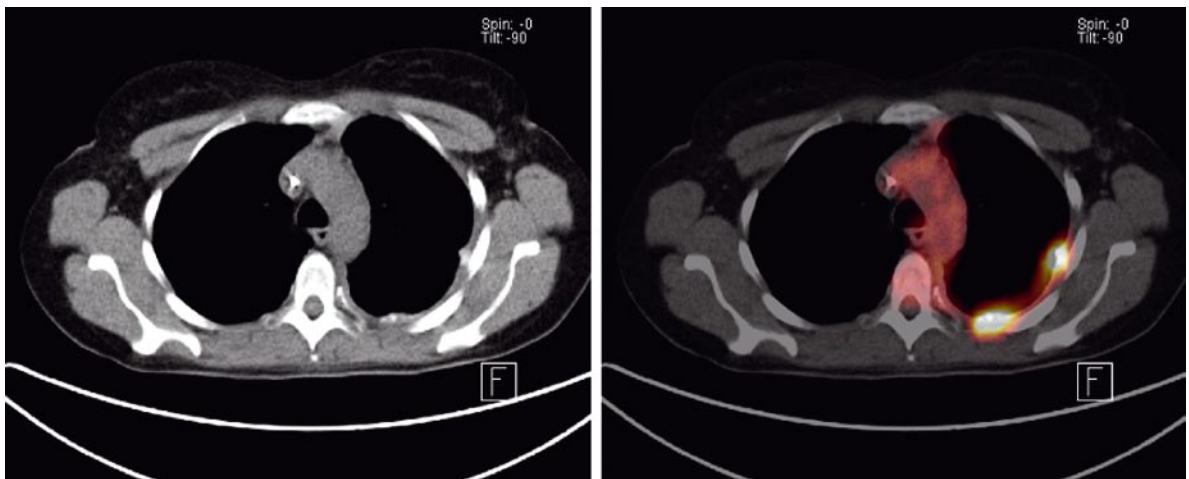


Fig. 15.5. CT and PET/CT of a patient with a small malignant pleural mesothelioma on the left developing as a transformation of asbestosis plaques

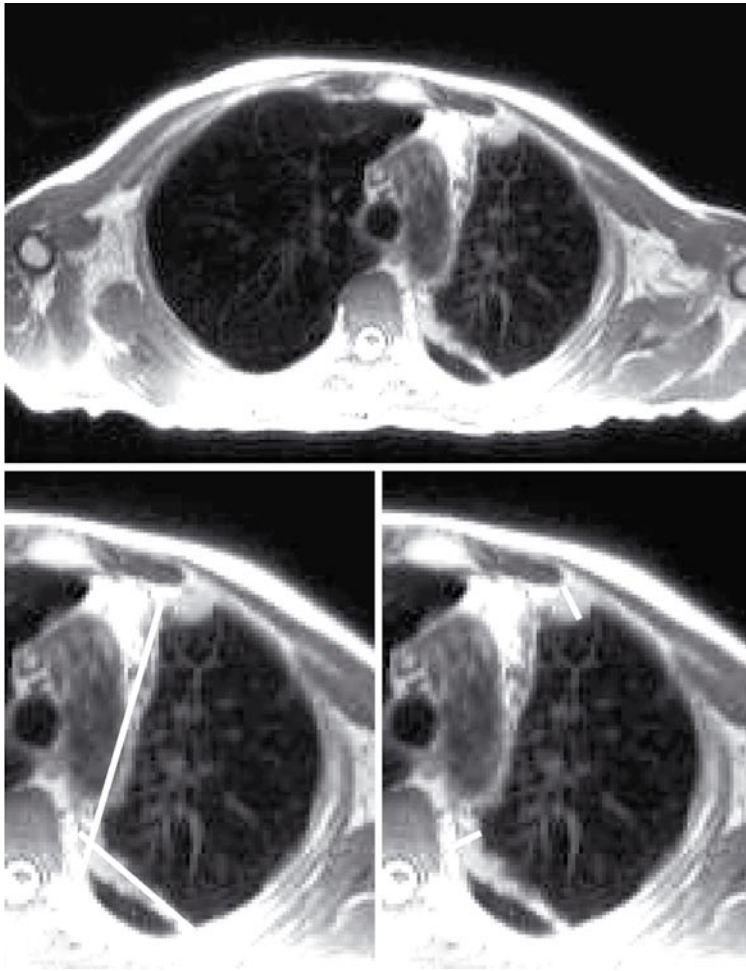


Fig. 15.6 Size measurement of malignant pleural mesothelioma on a HASTE image. **a** Lines represent possible interpretation “longest tumour diameter” according to current RECIST criteria. **b** Lines represent measurement sites perpendicular to fixed structures, chest wall, sternum and vertebral column, according to modified RECIST criteria

measurements of roughly spherical lesions common in other solid malignancies, and assume concordant changes in the three axes (length, width and height) of the tumour as for spherical lesions. The RECIST criteria suggest that “All measurable lesions up to a maximum of 5 lesions per organ and 10 lesions in total, representative of all involved organs, should be identified as target lesions and recorded and measured at baseline”. In MPM, the hemithorax is often extensively involved with tumour at multiple levels without involvement of other organs. The RECIST criteria do not guide the investigator as to which lesions should be considered as a “target lesion”. Furthermore, the requirement to identify and record all other lesions or sites of disease as “non-target lesions” is difficult in view of the rind-like growth pattern of this disease.

In MPM, there are numerous possible interpretations of the RECIST criteria, and more guidelines for applying these criteria are needed if investigators from different sites and countries are to be consistent in their definition of response. Consistency is vital for interpretation of results, particularly in phase II clinical trials. The straight “longest diameter”, which is measured in RECIST, is not applicable in mesothelioma since the relatively thin tumour mass usually follows the curvature of the chest wall. Besides this, defining the limits of such a lesion is often difficult or impossible. While tumour thickness may change in response to successful treatment, the extent of tumour along the chest wall, and thus this putative “longest diameter”, may change little. Furthermore, the longest diameter may be between two fixed structures, such as the carina and thoracic vertebra, and should not be used to as-

sess response. More guidance is needed to choose the anatomical level of tumour measurement, how many levels should be assessed, how to choose 5 lesions from the hemithorax, and what lesions should be recorded, if any, as “non-target lesions”.

VAN KLAVEREN et al. (2004) reported a series of tumour measurements comparing the use of RECIST and WHO criteria for assessment of response. They found a discrepancy in response as defined by the two sets of criteria in 9 of 34 cases (27%). Of 34 cases, 8 demonstrated progression on the WHO criteria which was missed by RECIST at some time point. These results were no better in the subset of patients with bi-dimensionally measurable lesions. However, problems with both the WHO criteria and the unmodified RECIST criteria suggest that neither should be considered a “gold standard” for tumour measurement in this disease.

15.2.6 Modified RECIST Criteria

With the widespread adoption of the RECIST criteria in other malignancies, the need to use both uni-dimensional and bi-dimensional lesions to assess response in MPM became less important. The modified RECIST criteria use uni-dimensional measurement of tumour thickness perpendicular to the chest wall or mediastinum, measured in two sites at three different levels on the CT scan (NOWAK et al. 2002; BYRNE and NOWAK 2004). Transverse cuts used for measurement must be at least 1 cm apart, and related to anatomical landmarks in the thorax, preferably above the level of division of the main bronchi. At reassessment, pleural thickness must be measured at the same position and level. Extensive documentation of non-measurable lesions is not required, however nodal, subcutaneous, and other bi-dimensionally measurable lesions are measured uni-dimensionally as per the RECIST criteria. Uni-dimensional measurements are added to produce a total tumour measurement. Definitions of complete and partial response are concordant with the RECIST criteria. As Nowak et al. could demonstrate a benefit to patients in terms of survival and lung function using the modified RECIST criteria; they are accepted as a valid clinical trial endpoint. There was a significant difference in survival between the two patient groups, with a median survival of 15.1 months for responding patients and 8.9 months for non-responding patients. Lung function as measured by forced vital capacity improved significantly over the course of treatment for responding patients as compared with non-responding, and there was a significant correlation between lung function and change in

linear tumour measurement. Recently it could be shown that modified RECIST criteria also can be applied using MRI (PLATHOW et al. 2008).

15.3 MRI in Asbestosis

There are only a few studies which have investigated the role of MRI in asbestosis. A landmark study used high-resolution respiratory-gated T2w turbo-spin-echo (TSE), breath-hold T1w TSE, and contrast-enhanced fat-suppressed breath-hold T1w TSE images with an in-plane resolution of less than 1 mm and a short T2* time (WEBER et al. 2004). Also a pulse sequence with radial k-space-sampling was used (TE = 0.5 ms) before and after administration of Gd-DTPA. Using such a protocol a differentiation between normal pleura and pleura with plaques is easily possible. In this study interobserver agreement is comparable for MRI and CT in detecting pleural plaques (median kappa = 0.72 for MRI and 0.73 for CT) and significantly higher with CT than with MRI for detection of plaque calcification. Median sensitivity of MRI was 88% for detection of plaque calcification compared with CT. For assessment of pleural thickening, pleural effusion, and extrapleural fat, interobserver agreement with MRI was significantly higher than with CT. Pleural plaques appear hypointense on T2-weighted and muscle-isointense on T1-weighted MR images. Pleural plaques appear hypointense on T2-weighted MR images due to their high content of collagen fibrils. It could be shown that on radial MR images an estimation of plaque calcification is possible. Blurring artefacts between pleura and lung tissue can be observed on radial MR images that reduce spatial resolution. Less calcified plaques appear more hyperintense than calcified plaques. On T2-weighted images, some plaques exhibit a hyperintense rim between the hypointense plaque center and the lung parenchyma. The slightly hyperintense rim of the plaques next to the lung parenchyma on the T2-weighted images possibly corresponds histologically to a loosening of the plaque collagen fibrils next to the surface. It cannot be attributed to the cells of the parietal pleura, which only form a single cell layer and are therefore too small to create a detectable signal in MRI. Also, according to our experience, pleural plaques are best diagnosed on non-enhanced T1-weighted MR images. T2-weighted sequences are most suitable for assessing and differentiating pleural effusion.

15.4

Imaging of Mesothelioma

The primary imaging modality used in the staging of MPM is computed tomography (CT) (MAROM et al. 2002; WANG et al. 2004; LAYER et al. 1999). CT is usually performed to assess the extent of chest wall, mediastinal, and diaphragmatic invasion, and the presence or absence of nodal and distant metastases (HEELAN et al. 1999). But in recent studies it could be shown that MRI is superior to CT in the evaluation of pleural effusion, chest wall and diaphragmatic invasion and pleural thickening. CT proved to be superior to MRI only in the evaluation of calcifications. Thus, especially in T2 and T3 situations (see below), MRI proved to be superior to CT in tumour delineation; and MRI should be used to complement CT in the evaluation of patients with MPM being considered for surgical resection. In the preoperative staging evaluation of patients with MPM, MRI is typically used to address equivocal findings on CT concerning the local extent of tumour. On both CT and MRI, the same findings are used to determine local invasion. They include irregularity of the surface of the diaphragm, loss of normal adjacent fat planes, and/or infiltration of the endothoracic fat. Due to the high soft tissue contrast, MRI is superior to CT in the evaluation of local invasion of the endothoracic fascia and single chest wall foci (accuracy 69% vs 46%) and the diaphragm (accuracy 82% vs 55%). The use of positron emission tomography (PET) with [18F]-fluoro-2-deoxy-D-glucose (FDG) in the evaluation of patients with MPM has been reported (NANNI et al. 2004; FLORES et al. 2003). In these studies, the poor spatial resolution of PET images often precludes assessment of the presence and extent of local tumour invasion. However, PET can be useful in the detection of unsuspected nodal metastases and occult distant metastases (HEELAN et al. 1999) or for restaging. Integrated PET/CT imaging with coregistration of anatomic and functional imaging data improves the localization of regions of increased FDG uptake and the accuracy of staging in patients with MPM (ERASMUS et al. 2005). In addition, PET may have an additional role in predicting treatment response and prognosis (STEINERT et al. 2005).

15.5

MRI of Mesothelioma

MPM appears inhomogeneously hypointense to isointense on T1-weighted and hyperintense on T2-weighted

MR images and shows contrast media enhancement (BONOMO et al. 2000). Malignant pleural disease tends to involve the entire pleural surface, whereas reactive pleurisy usually does not affect the mediastinal pleura except in cases of tuberculous empyema (HIERHOLZER et al. 2000). Mediastinal pleural involvement, circumferential pleural thickening, nodularity, irregularity of pleural contour, and infiltration of the chest wall and/or diaphragm are most suggestive of a malignant cause both on CT and MRI. Pleural calcification on CT is suggestive of a benign cause. Contrary to what has been previously reported, neither on CT nor on MRI, a pleural thickness of more than 1 cm reveals a significant difference between malignant and benign pleural disease (HIERHOLZER et al. 2000). High signal intensity in relation to the intercostal muscles on T2-weighted and contrast-enhanced T1-weighted MR images is suggestive for malignant disease with a sensitivity of 100% and a specificity of 93% for MRI in the detection of pleural malignancy (HIERHOLZER et al. 2000).

Besides these static imaging techniques (NOWAK et al. 2002; BYRNE and NOWAK 2004; HEELAN et al. 1999) there are also dynamic approaches. It has been shown that MRI is able to measure lung volumes in steady state (QUANADLI et al. 1999; LEY et al. 2004). However, MRI is a possible tool to describe local geometrical and volumetric changes corresponding to different phases of the breathing cycle (WHITELAW 1987; HAAGE et al. 2005; PLATHOW et al. 2004) as a functional parameter of therapy response (PLATHOW et al. 2006a). This might have the advantage of detecting subtle changes of lung mechanics and volumetry early. Recently it could be shown that dynamic MRI techniques are able to quantify and visualize volumetric changes of the thorax in patients with MPM during therapy (PLATHOW et al. 2006b). Using FLASH (fast low angle shot) sequences and trueFISP (true Fast Imaging with Steady-state Precession) sequences, therapeutic influence on MPM on the breathing cycle can be quantified and visualized using 3D dynamic MRI with a temporal resolution of 1 slab/s (Fig. 15.3). Dynamic contrast enhanced (DCE) MRI is a non-invasive procedure in which sequential images with high spatial and temporal resolution are obtained in order to observe the kinetics of contrast media arrival and clearance through the tumour microcirculation and adjacent tissues. The contrast agent enhancement pattern enables visualization, characterization and quantification of lesion microcirculation. GIESEL et al. (2006, 2008) could show that DCE MRI is an attractive tool to monitor tumour microvascular properties and to demonstrate tumour heterogeneity for therapy monitoring (Fig. 15.4). Thus, assessing the enhancement profiles non-invasively might allow the characterization of biological aggress-

Table 15.4. Recommended protocol for MRI of malignant pleural mesothelioma

| Sequence | Intention |
|---|--|
| HASTE (half-Fourier acquired single-shot turbo spin-echo) coronal and axial | Investigation of the lung, parenchyma and short overview of the thorax |
| VIBE (volume interpolated breath-hold examination) post contrast coronal and sagittal | Demonstration of well perfused tumour areas |
| T1-TSE (Turbo spin echo) non-breath-hold coronal | High-resolution images of the thorax and the MPM |
| T2-TSE respiratory gated coronal | Ultra high-resolution images of the thorax and the MPM. Detection of a potential infiltration of vessels, chest wall, brachial plexus etc. |
| Optional: dynamic TrueFISP (true Fast Imaging with Steady-state Precession) coronal | Investigation of mobility of lung, diaphragm and chest wall |

siveness of the tumours and help identify those that are unlikely to respond to standard regimens and who, therefore, should be directed to more aggressive therapy regimes or experimental clinical trials. Whether this multi-modal characterization may be clinically useful in selecting possible tumour subtypes and if this information might be a benefit from anti-angiogenic therapy have to be shown in further research.

On the basis of the present literature and our own experience, we recommend a basic MRI protocol to image MPM (Table 15.4).

15.6

MRI of Other Pleural Diseases

The characterization of pleural fluid collections, either transudates or exudates, can be determined by MRI to some extent. Exudative pleural effusions show a higher degree of enhancement after IV gadolinium-based contrast administration than transudative pleural effusions (FIOLA et al. 1997). Diffusion-weighted imaging with an echoplanar imaging sequence may differentiate exudates from transudates based on the apparent diffusion coefficient (ADC) value (BAYSAL et al. 2003). High signal intensity on T1-weighted images identifies a chylothorax (McLOUD and FLOWER 1991). Subacute and chronic hematoma can be recognized in the pleural space based on its signal characteristics (MITCHEL 2003). These non-invasive techniques can be used to characterize pleural fluid collection and may obviate

the need for thoracocentesis, especially in high-risk patients.

15.6.1

Solitary Fibrous Tumours of the Pleura

The vast majority of solitary fibrous tumours of the pleura are benign (Fig. 15.7), and complete surgical resection remains the mainstay of therapy for both the benign and malignant variants. These entities usually appear as well-delineated, homogeneous, and occasionally lobulated masses of soft tissue attenuation. Rarely, pleural effusion is associated with solitary fibrous tumors of the pleura (DE PERROT et al. 2002) and MRI has limited use in the assessment of such pleural diseases. However, the morphology and relationship of large lesions to adjacent mediastinal and major vascular structures may be better delineated using MRI compared with CT. MRI is helpful in differentiating tumour from other structures and in confirming intrathoracic localization if the tumour abuts the diaphragm. In general, on T2-weighted images benign lesions have low signal intensity, whereas malignant fibrosis invariably appears with high signal intensity because of increased vascularity, edema, and cellularity. Benign and malignant lesions have low signal intensity on T1-weighted images. Unfortunately, benign solitary fibrous tumours of the pleura often can also have areas of high signal intensity on T2-weighted images because of intratumoral necrosis or myxoid degeneration and thus may not be differentiable from malignant formations. They

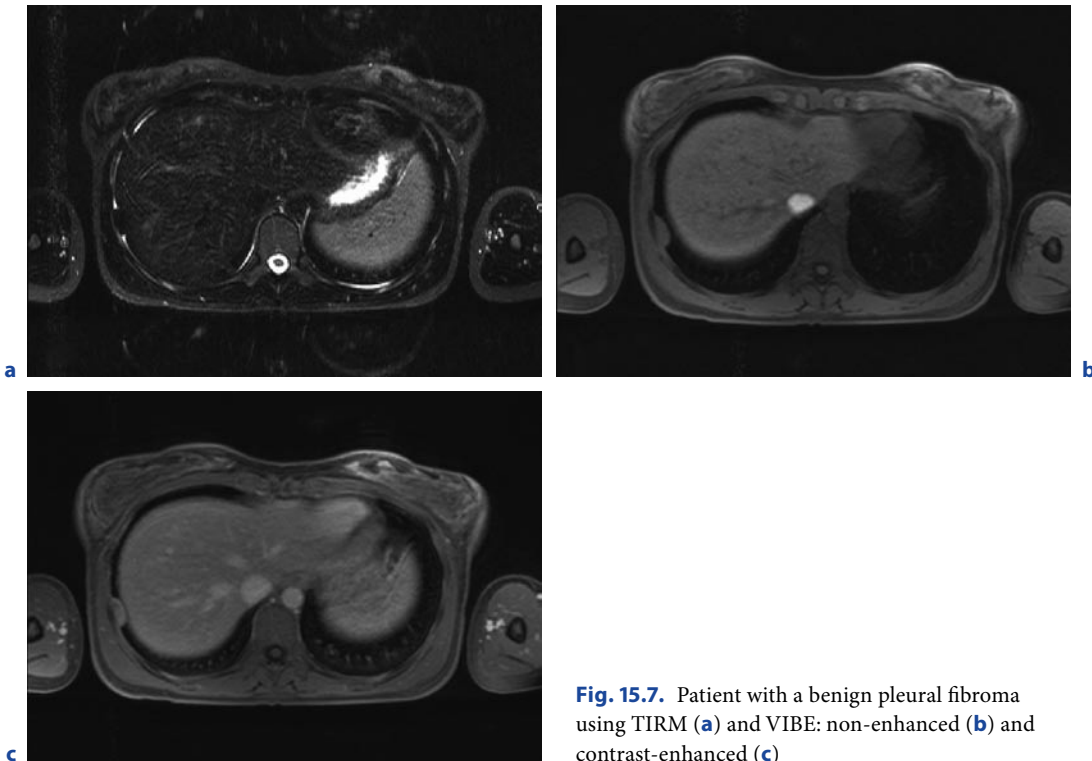


Fig. 15.7. Patient with a benign pleural fibroma using TIRM (a) and VIBE: non-enhanced (b) and contrast-enhanced (c)

might also show significant enhancement after contrast administration on T1weighted images.

15.6.2 MRI of Other Chest Wall Diseases

Besides breast, malignant and benign chest wall tumours, tumours like elastofibroma, SAPHO (LAIHO et al. 2001), and sarcomas (MÜLLER LP et al. 1999) are to be imaged and treated according to musculoskeletal procedures. In general, MRI and CT have complementary roles in the evaluation of sternal tumours. CT is useful for imaging the cortical bone and the spongy matrix while multiplanar MRI is the technique of choice for evaluating the extent of extraosseous tumour and its relationship to adjacent structures with regard to operability (ASLAM et al. 2002). Breath-hold imaging is usually necessary in supine position; however, prone position might be helpful to reduce breathing artefacts. Rib lesions need special attention in MR planning and may require individualized double angulated data acquisition.

In each of these entities, MRI helps in delineation of normal anatomical structures and is helpful in guiding surgery or biopsy. Therefore, the anatomical relation-

ship of the lesion to the surrounding structures needs to be demonstrated and available in the operating theatre.

References

- Aslam M, Rajesh A, Entwisle J et al. (2002) Pictorial review: MRI of the sternum and sternoclavicular joints. *Br J Radiol* 75:627–634
- Baas P (2005) Chemotherapy for malignant mesothelioma. *Lung Cancer* 49:S61–S64
- Baysal T, Bulut T, Gokimak M et al. (2003) Diffusion-weighted MR imaging of pleural fluid: differentiation of transudative vs exudative pleural effusions. *Eur Radiol* 14:890–896
- Bonomo L, Feragalli B, Sacco R et al. (2000) Malignant pleural disease. *Eur J Radiol* 34:98–118
- Bridda A, Padoan I, Mencarelli R, Frego M (2007) Peritoneal mesothelioma: a review. *MedGenMed* 9:32
- Butchart EG, Ashcroft T, Barnsley WC et al. (1976) Pleuro-pneumectomy in the management of diffuse malignant mesothelioma of the pleura. Experience with 29 patients. *Thorax* 31:15–24
- Byrne MJ, Nowak AK (2004) Modified RECIST criteria for assessment of response in malignant pleural mesothelioma. *Ann Oncol* 15:257–260

- Cacciotti P, Strizzi L, Vianale G et al. (2002) The presence of simian-virus 40 sequences in mesothelioma and mesothelial cells is associated with high levels of vascular endothelial growth factor. *Am J Respir Cell Mol Biol* 2:189–193
- De Perrot M, Fischer S, Brundler M-A (2002) Solitary fibrous tumors of the pleura. *Ann Thorac Surg* 74:285–293
- Erasmus JJ, Truong MT, Smythe WR et al. (2005) Integrated computed tomography-positron emission tomography in patients with potentially resectable malignant pleural mesothelioma: staging implications. *J Thorac Cardiovasc Surg* 6:1364–1370
- Falasci F, Boraschi P, Neri S et al. (1995) High-resolution computed tomography (HRCT) in the detection of "early asbestosis". *Eur Radiol* 5:291–296
- Fiola C, Cantoni S, Turtulici I et al. (1997) Transudative vs exudative pleural effusions: differentiation using Gd-DTPA-enhanced MRI. *Eur Radiol* 7:860–867
- Flores RM, Akhurst T, Gonen M et al. (2003) Positron emission tomography defines metastatic disease but not locoregional disease in patients with malignant pleural mesothelioma. *J Thorac Cardiovasc Surg* 1:11–16
- Giesel FL, Bischoff H, von Tengg-Kobligk H et al. (2006) Dynamic contrast-enhanced MRI of malignant pleural mesothelioma: a feasibility study of noninvasive assessment, therapeutic follow-up, and possible predictor of improved outcome. *Chest* 129:1570–1576
- Giesel FL, Choyke PL, Mehndiratta A, Zechmann CM, von Tengg-Kobligk H, Kayser K, Bischoff H, Hintze C, Delorme S, Weber MA, Essig M, Kauczor HU, Knopp MV (2008) Pharmacokinetic analysis of malignant pleural mesothelioma – initial results of tumor microcirculation and its correlation to micro-vessel density (CD-34). *Acad Radiol* 15(5):563–570
- Haage P, Karaagac S, Spuntrup E et al. (2005) Feasibility of pulmonary ventilation visualization with aerosolized magnet resonance contrast media. *Invest Radiol* 40:85–88
- Heelan RT, Rusch VW, Begg CB et al. (1999) Staging of malignant pleural mesothelioma: comparison of CT and MR imaging. *AJR Am J Roentgenol* 4:1039–1047
- Hierholzer J, Luo L, Bittner RC et al. (2000) MRI and CT in the differential diagnosis of pleural disease. *Chest* 118:604–609
- International Mesothelioma Interest Group (1995) A proposed new international TNM staging system for malignant pleural mesothelioma. *Chest* 108:1122–1128
- Khalil MY, Mapa M, Shin HJ et al. (2003) Advances in the management of malignant mesothelioma. *Curr Oncol Rep* 4:334–341
- Kishimoto T, Ohnishi K, Saito Y (2003) Clinical study of asbestos-related lung cancer. *Ind Health* 41:94–100
- Laiho K, Soini I, Martio J (2001) Magnetic resonance imaging findings of manubriosternal joint involvement in SAPHO syndrome. *Clin Rheumatol* 20:232–233
- Layer G, Schmitteckert H, Steudel A et al. (1999) MRT, CT and sonography in the preoperative assessment of the primary tumor spread in malignant pleural mesothelioma. *Fortschr Röntgenstr* 170:365–370 (in German)
- Ley S, Zaporozhan J, Morbach A et al. (2004) Functional evaluation of emphysema using diffusion-weighted ³Helium-magnetic resonance imaging, high-resolution computed tomography, and lung function tests. *Invest Radiol* 39:427–434
- Lynch DA, Gamsu G, Aberle DR (1989) Conventional and high resolution computed tomography in the diagnosis of asbestos-related diseases. *Radiographics* 9:523–551
- Marom EM, Erasmus JJ, Pass HI et al. (2002) The role of imaging in malignant pleural mesothelioma. *Semin Oncol* 1:26–35
- Martino D, Pass HI (2004) Integration of multimodality approaches in the management of malignant pleural mesothelioma. *Clin Lung Cancer* 5:290–298
- McLoud TC, Flower CD (1991) Imaging of the pleura: sonography, CT, and MR imaging. *AJR Am J Roentgenol* 156:1145–1152
- Miller AB, Hoogstraten B, Staquet M, Winkler A (1981) Reporting results of cancer treatment. *Cancer* 47:207–214
- Mitchell JD (2003) Solitary fibrous tumor of the pleura. *Semin Thoracic Cardiovasc Surg* 15:305–309
- Mossman BT, Gee JB (1989) Asbestos-related diseases. *N Engl J Med* 320:1721–1730
- Müller LP, Wolf HK, Heussel CP et al. (1999) Bilateral elastofibroma dorsi. *Chirurg* 70:1357–1360
- Müller NL (1993) Imaging of the pleura. *Radiology* 186:297–309
- Nanni C, Castellucci P, Farsad M et al. (2004) Role of ¹⁸F-FDG PET for evaluating malignant pleural mesothelioma. *Cancer Biother Radiopharm* 2:149–154
- Nowak AK, Byrne MJ, Williamson R et al. (2002) A multicentre phase II study of cisplatin and gemcitabine for malignant mesothelioma. *Br J Cancer* 87:491–496
- Peacock C, Copley SJ, Hansell DM (2000) Asbestos-related benign pleural disease. *Clin Radiol* 55:422–432
- Peto J, Hodgson JT, Matthews FE et al. (1995) Continuing increase in mesothelioma mortality in Britain. *Lancet* 345:535–539
- Plathow C, Ley S, Fink C et al. (2004) Evaluation of chest motion and volumetry during the breathing cycle by dynamic MRI in healthy subjects – comparison with pulmonary function tests. *Invest Radiol* 39:202–209
- Plathow C, Hof H, Kuhn S et al. (2006a) Therapy monitoring using dynamic MRI: analysis of lung motion and intrathoracic tumor mobility before and after radiotherapy. *Eur Radiol* 16:1942–1950
- Plathow C, Klopp M, Schoebinger M et al. (2006b) Monitoring of lung motion in patients with malignant pleural mesothelioma using two-dimensional and three-dimensional dynamic magnetic resonance imaging: comparison with spirometry. *Invest Radiol* 41:443–448
- Plathow C, Klopp M, Zuna I, Schmähl M, Kauczor HU (2008) Therapy response in malignant pleural mesothelioma – role of MRI using RECIST, modified RECIST and volumetric approaches in comparison with CT. *Eur Radiol* 2008 Mar 28 [Epub ahead of print]

- Price B, Ware A (2004) Mesothelioma trends in the United States: an update based on Surveillance, Epidemiology, and End Results Program data for 1973 through 2003. *Am J Epidemiol* 2:107–112
- Quanadli SD, Orvoen-Frija E, LaCombe P et al. (1999) Estimation of gas and tissue volumes by MRI: functional approach of lung imaging. *J Comput Assist Tomogr* 23:743–748
- Robinson BW, Lake RA (2005) Advances in malignant mesothelioma. *N Engl J Med* 353:1591–1603
- Schwartz DA (1991) New developments in asbestos-induced pleural disease. *Chest* 99:191–198
- Steinert HC, Santos Dellea MM, Burger C et al. (2005) Therapy response evaluation in malignant pleural mesothelioma with integrated PET-CT imaging. *Lung Cancer* 49:S33–S35
- Sterzing F, Sroka-Perez G, Schubert K et al. (2008) Evaluating target coverage and normal tissue sparing in the adjuvant radiotherapy of malignant pleural mesothelioma: Helical tomotherapy compared with step-and-shoot IMRT. *Radiother Oncol* 86:251–257
- Sugarbaker DJ, Flores RM, Jaklitsch MT et al. (1999) Resection margins, extrapleural nodal status, and cell type determine postoperative long-term survival in trimodality therapy of malignant pleural mesothelioma: results in 183 patients. *J Thorac Cardiovasc Surg*. 117:54–63
- Therasse P, Arbuuck SG, Eisenhauer EA et al. (2000) New guidelines to evaluate the response to treatment in solid tumors. *J Natl Cancer Inst* 92:205–216
- Tossavainen A (2004) Global use of asbestos and the incidence of mesothelioma. *Int J Occ Env Health* 19:22–25
- Van Klaveren RJ, Aerts JGJV, de Bruin HG et al. (2004) Inadequacy of the RECIST criteria for the evaluation of response in patients with malignant pleural mesothelioma. *Lung Cancer* 43:63–69.
- Vogelzang NJ, Rusthoven JJ, Symanowski J et al. (2003) Phase III study of pemetrexed in combination with cisplatin versus cisplatin alone in patients with malignant pleural mesothelioma. *J Clin Oncol* 14:2636–2644
- Wang ZJ, Reddy GP, Gotway MB et al. (2004) Malignant pleural mesothelioma: evaluation with CT, MR imaging, and PET. *Radiographics* 24:105–119
- Weber MA, Bock M, Plathow C et al. (2004) Asbestos-related pleural disease: value of dedicated magnetic resonance imaging techniques. *Invest Radiol* 39:554–564
- Whitelaw WA (1987) Shape and size of the human diaphragm in vivo. *J Appl Physiol* 62:180–186
- Yoshino I, Yamaguchi M, Okamoto T et al. (2004) Multimodal treatment for resectable epithelial type malignant pleural mesothelioma. *World J Surg Oncol* 2:11
- Zellos LS, Sugarbaker DJ (2002) Multimodality treatment of diffuse malignant pleural mesothelioma. *Semin Oncol* 29:41–50

Subject Index

A

abdominal pressure gradient 97
abscess 10
adenomatous hyperplasia 181
adrenals 206
AIDS 259
air crescent sign 189, 190, 271
air trapping 5, 140, 143, 146, 147, 150, 156, 161, 172, 173
alveolar proteinosis 263
alveolitis 278, 279, 281, 283
aneurysm 134
angiogenesis 185, 193
apparent diffusion coefficient (ADC) 47, 48, 49, 60, 72, 73
arterial input function (AIF) 31, 32, 33
arterial switch operation 123, 130
arteriopathy 110
artery-to-bronchus ratio 114
asbestos 291, 292, 293, 300
asbestosis 283
aspergillosis 185, 189, 261, 271
aspiration 257
asthma 48, 113, 126
atelectasis 142, 180, 195, 199, 235, 256
– round atelectasis 283, 292
atrial fibrillation 133

B

Behçet's disease 134
belt 4, 6, 82, 203, 264
Bhalla score 170, 174
Blalock-Taussig procedure 128
bleomycin 278
Boltzmann polarisation 36
bolus 11, 12, 18, 29, 33
– bolus arrival time 29
– bolus profile 18
– bolus timing 18, 133
– care bolus 12
– dual bolus 33
– test bolus 11, 12
bone 206
brain 207
bronchial arteries 110, 113, 114, 173, 174, 187, 192
bronchial hyperresponsiveness 140, 147
bronchioalveolar carcinoma (BAC) 185, 188

bronchocele 185, 186
bronchopneumonia 256, 264
Brownian diffusion 38, 41, 46, 47, 49, 150

C

cancer 4, 80, 179, 180, 184, 188–216
cavity 189, 190, 191, 267
chemical shift 61
chest wall 10, 13, 180, 184, 195, 200
choriocarcinoma 238
Chrispin-Norman Score 170
chronic bronchitis 155
Churg-Strauss syndrome 263, 278
collagen-vascular disease 281, 282
collateral ventilation 49
conduit 122, 126, 127
convolution 31
COPD 108, 109, 140, 155–168
cor pulmonale 111, 165
crazy paving pattern 257
cryptococcosis 183, 266
Cushing syndrome 234
cyanosis 128
cyst
– bronchogenic cyst 189, 218
– dermoid 235
– esophageal duplication cyst 220
– neurenteric cyst 220
– pericardial cyst 220
– thoracic duct cyst 218, 222
– thymic cyst 221, 240
cystic fibrosis 3, 4, 25, 80, 92, 113, 169–177

D

diffusion. *see* Brownian diffusion
distensibility 114
drug exposure 281
ductus arteriosus Botalli 128, 129

E

ECG 4, 6, 26, 28, 82, 181, 196, 197, 203, 261, 264
echocardiography 122, 124, 130, 132, 166

edema 87, 156, 261, 262, 278
Eisenmenger syndrome 113
ejection fraction 116, 130, 166
elastofibroma 303
embolism 4, 5, 8, 12, 17, 21, 80, 108, 110, 111, 134, 164, 263
emphysema 5, 29, 48, 49, 63, 80, 100, 140, 155–166
empyema 301
endarterectomy 111, 112, 113, 116
endodermal sinus tumor 238
Evian classification 108
exercise-induced bronchoconstriction 147

F

FEV1 maneuver 9, 45, 98, 99, 143, 158, 202
fibrosis 185, 242, 250, 258, 263, 266, 278, 281, 282, 283, 285, 286, 288
– progressive massive fibrosis 283
Fontan-like operation 129

G

gamma variate 31
ganglioneuroblastoma 244, 246, 248
ganglioneuroma 244, 246, 247
germinoma 237
Glenn procedure 129, 130
gradient 142
grid-tagging 85, 101
ground glass opacity 257, 263, 267, 268, 269, 279, 281, 282, 288

H

haemorrhage 263, 270, 283
halo 271
hamartoma 185, 188
Helbich-Score 170
hematoma 302
hemoptysis 171
hexafluoroethane (C₂F₆) 69, 70, 71, 72, 73
histoplasmosis 249
HIV 259
honeycombing 281, 282
Hughes-Stovin syndrome 134
hyperinflation 156, 158
hypoxic vasoconstriction 151, 156, 163, 173

I

indicator dilution theory 31, 163
IPF 109, 263, 278, 281, 284, 287

K

Klebsiella pneumoniae 266
Klinefelter's syndrome 238
k-space 5, 6, 12, 18, 28, 41, 47, 82, 202, 300
– central 12, 18, 28
– oversampled 5
– radial 5, 40, 41, 43, 44, 300
– segmented 5
– spiral 18, 41, 43, 44

L

Larmor frequency 69, 76, 142
liquid ventilation 86
lung volume reduction surgery (LVRS) 100, 158
lymphangitic carcinomatosis 263, 278
lymph node 8, 10, 13, 134, 195, 203, 205, 232, 235, 238, 239, 241, 250, 279, 288, 293, 295
lymphoblastic leukemia 240

M

major aortopulmonary collateral arteries (MAPCA) 123, 128
malignant peripheral nerve sheath tumor 244, 245
mean transit time 31, 110, 163, 164
mediastinoscopy 295
mediastinum 6, 12, 13, 180, 184, 195, 196, 201, 217–253
meningocele 218, 222
mesothelioma 4, 10, 291, 295, 297, 301
metastasis 10, 181, 184, 203, 205, 206, 207, 230, 232, 233, 235
methacholine 142, 143, 147, 148
MR-guided intervention 124
mucocele 185, 186
mucus 141, 149, 199
multiple endocrine neoplasia (MEN) 234
myasthenia gravis 228, 230
mycetoma 191

N

navigator 4, 19, 82, 264
necrosis 185, 192, 229, 232, 233, 234, 237, 238, 239, 242, 243, 245, 249, 258
neuroblastoma 244, 246, 248
neurofibroma 244, 245
– plexiform 245
neurofibromatosis 222
Nijmegen-Breakage syndrome 266
nitric oxide 165
nodular sclerosis 239

nodule 6, 14, 180, 181, 184, 185, 192, 261, 269, 283
 – calcified nodules 6, 185, 258
 – infectious nodules 192, 193
 – inflammatory nodules 185
 – necrobiotic nodules 282
 non-target lesion 299

O

obstructive bronchiolitis 155
 octafluorobutane (C₄F₄) 69, 70, 71
 optical pumping 36, 37, 58
 Osler-Weber-Rendu syndrome 133
 oximetry 4, 132
 oxygen 75–90, 160, 173
 – oxygen activated pixel 79, 80
 – oxygen enhancement 75, 77, 78, 79, 80, 86, 87, 88, 89, 141, 160, 287, 288
 – oxygen partial pressure 40, 46, 72
 – oxygen transfer function 79, 80, 287
 – oxygen uptake 45

P

Pancoast tumor 13, 180, 200
 pancreatic pseudocyst 218, 222
 parallel imaging 5, 6, 18, 21, 28, 40, 82, 83, 150, 163, 202, 268
 peak 29, 164, 230, 293
 pericardium 6, 195, 196, 230
 phase contrast 45
 pleura 184, 195, 201, 230
 pleural effusion 241, 242, 283, 302
 pleural plaque 292, 300
 pneumatocele 189
 pneumoconiosis 283
 pneumonia 3, 4, 6, 255–275
 – atypical 257, 261
 – bacterial 256
 – fungal 270
 – hospital acquired 257
 – lobar 256
 – necrotizing 271
 – obstructive 195, 199, 262
 – opportunistic 259
 – organizing 185, 266, 283
 – pneumococcal 266
 – typical 261
 – ventilator associated 257
 – viral 256
 pneumonitis 199
 – cholesterol 199
 – hypersensitivity 278
 – lupus 259, 283
 – obstructive 235

– radiation 263, 278
 pneumothorax 5
 – artificial pneumothorax 200
 polarizer 37, 38, 58, 59, 66
 postoperative lung function 193, 195
 pulmonary hypertension 4, 19, 25, 107–119, 127, 128, 134, 156, 164, 165, 166, 174, 283, 284

R

radiotherapy 100, 202, 203, 249, 279
 RECIST 199
 regurgitation 126
 respiratory pump 94, 97, 100
 reverse target sign 271
 round infiltrate 264

S

SAPHO 303
 sarcoidosis 189, 263, 278, 279, 286, 287, 288
 scarring 185
 schwannoma 244, 245
 Scimitar syndrome 131
 scleroderma 108
 scoliosis 91, 100
 sequestration 189
 shunt 122, 163, 174
 spirometry 5, 48, 60, 92, 94, 98, 99, 140, 142, 146, 156, 174, 175, 285
 – online 5
 sulphur hexafluoride (SF₆) 69, 70, 71, 72, 73

T

target lesion 299
 tetrafluoromethane (CF₄) 69, 70, 71, 72
 thrombolysis 110, 111
 thymus 224
 – carcinoma 228, 232
 – ectopic thymus 225
 – hyperplasia 226
 – rebound 226
 – tumor 228
 thyroid gland 249
 thyroiditis 249
 time-to-peak 29
 total cavopulmonary connection (TCPC) 129, 130
 tracheal instability 158
 transplantation 112, 134, 161
 – bone marrow 259
 – heart-lung 112
 – lung 112, 134, 161
 tree in bud 171

tuberculoma 185, 187
tuberculosis 189, 249, 261

V

vascular pruning 109, 157
vasomotor tone 110
Venice classification 108
ventilation-perfusion ratio 72, 151
view-sharing 18, 28, 202
volume defects per slice (VDS) 43, 144, 146

W

wash-out 192
web 111, 112
Wegener's granulomatosis 263, 283
white lung sign 188

Y

yolk sac tumor 238

Z

Zeeman system 36, 38

List of Contributors

TALISSA A. ALTES, MD
Department of Radiology
University of Virginia Medical Center
Charlottesville, VA 22908
USA

and
Department of Radiology
Children's Hospital of Philadelphia
34th St. and Civic Bank Blvd.
Philadelphia, PA 19104
USA

Email: altes@email.chop.edu

JUERGEN BIEDERER, MD
Professor, Department of Diagnostic Radiology
University Hospital Schleswig-Holstein
Campus Kiel
Arnold-Heller-Strasse 9
24105 Kiel
Germany

Email: juergen.biederer@rad.uni-kiel.de

JAMES P. BUTLER, MD
Department Environmental Health
Harvard School of Public Health and
Department of Medicine
Harvard Medical School
Boston, MA 02115
USA

Email: jbutler@hsph.harvard.edu

OLAF DIETRICH, PhD
Josef Lissner Laboratory for Biomedical Imaging
Department of Clinical Radiology
University Hospitals – Grosshadern
Ludwig Maximilian University of Munich
Marchioninistrasse 15
81377 Munich
Germany

Email: olaf.dietrich@med.uni-muenchen.de

JULIEN DINKEL, MD, MSc
Department of Radiology
German Cancer Research Center (DKFZ)
Im Neuenheimer Feld 280
69120 Heidelberg
Germany

Email: j.dinkel@dkfz.de

ROGER EIBEL, MD
Chief of Department of Radiology and Neuroradiology
HELIOS Clinics Schwerin
Teaching Hospital of the University of Rostock
Wismarsche Strasse 393
19049 Schwerin
Germany

Email: Roger.Eibel@helios-kliniken.de

MONIKA EICHINGER, MD
Department of Radiology
German Cancer Research Center (DKFZ)
Im Neuenheimer Feld 280
69120 Heidelberg
Germany

Email: m.eichinger@dkfz.de

SEAN B. FAIN, PhD
Associate Professor
Departments of Medical Physics and Radiology
University Wisconsin Medical School
J5/M158 Clinical Science Center
600 Highland Avenue
Madison, WI 53792
USA

Email: sfain@wisc.edu

CHRISTIAN FINK, MD
Associate Chair of Clinical Operations
Assistant Professor of Radiology
Section Chief Cardiothoracic Imaging
Department of Clinical Radiology
University Hospital Mannheim
Theodor-Kutzer-Ufer 1-3
68167 Mannheim
Germany
Email: christian.fink@rad.ma.uni-heidelberg.de

AHMED F. HALAWEISH
Department of Biomedical Engineering/Radiology
University of Iowa Hospitals and Clinics
200 Hawkins Drive
Iowa City, IA 52242-1077
USA
Email: ahmed-halaweish@uiowa.edu

HIROTO HATABU, MD
Department of Radiology
Harvard Medical School
Center of Pulmonary Functional Imaging
Brigham and Women's Hospital
221 Longwood Avenue
Boston, MA 02115
USA
Email: hhababu@partners.org

CLAUS PETER HEUSSEL, MD
Assistant Professor, Department of Radiology
Clinic for Thoracic Diseases Heidelberg
Amalienstrasse 5
69126 Heidelberg
Germany
Email: heussel@uni-heidelberg.de

F. WILLIAM HERSMAN, PhD
Department of Physics
University of New Hampshire
and Xemed LLC
Durham, NH 03824
USA
Email: hersman@unh.edu

CHRISTIAN HINTZE, MD
Department of Radiology
German Cancer Research Center (DKFZ)
Im Neuenheimer Feld 280
69120 Heidelberg
Germany
Email: christian.hintze@dkfz.de

JAMES H. HOLMES, PhD
Research Associate
Department of Medical Physics
J5/M158 Clinical Science Center
600 Highland Avenue
Madison, WI 53792
USA
Email: jhholmes@wisc.edu

MIRKO I. HROVAT, PhD
Mirtech, Inc.
Brockton, MA 02301
USA

HANS-ULRICH KAUCZOR, MD
Chairman, Medical Director
Diagnostic and Interventional Radiology
University Clinic Heidelberg
Im Neuenheimer Feld 110
69120 Heidelberg
Germany
Email: hu.kauczor@med.uni-heidelberg.de

HISANOBU KOYAMA, MD, PhD
Department of Radiology
Kobe University Graduate School of Medicine
7-5-2 Kusunoki-cho, Chuo-ku
Kobe, 650-0017
Japan

KARL-FRIEDRICH KREITNER, MD
Department of Diagnostic and Interventional Radiology
Johannes Gutenberg University Mainz
Langenbeckstrasse 1
55131 Mainz
Germany
Email: kreitner@radiologie.klinik.uni-mainz.de

SEBASTIAN LEY, MD
Department of Pediatric Radiology
University Hospital Heidelberg
Im Neuenheimer Feld 430
69120 Heidelberg
Germany

Email: ley@gmx.de

JULIA LEY-ZAPOROZHAN, MD
Department of Pediatric Radiology
University Hospital Heidelberg
Im Neuenheimer Feld 430
69120 Heidelberg
Germany

Email: julia.leyzaporozhan@gmail.com

KATHARINA MARTEN, MD
Universitätsklinikum Göttingen
Abteilung Diagnostische Radiologie
Robert-Koch-Str. 40
37075 Göttingen
Germany

Email: kmarten@med.uni-goettingen.de

FRANCESCO MOLINARI, MD
Department of Bioimaging and Radiological Sciences
Catholic University of Rome
Policlinico A. Gemelli
L.go F. Vito, no. 1
00168 Rome
Italy

Email: francmol@gmail.com

IGA MURADIAN, PhD
Department of Radiology
Harvard Medical School
Center of Pulmonary Functional Imaging
Brigham and Women's Hospital
221 Longwood Avenue
Boston, MA 02115
USA

YOSHIHARU OHNO MD, PhD
Director of Diagnostic and Functional Imaging Research
Director of Thoracic Radiology
Associate Professor of Radiology
Department of Radiology
Kobe University Graduate School of Medicine
7-5-2 Kusunoki-cho, Chuo-ku
Kobe, 650-0017
Japan

Email: yosirad@kobe-u.ac.jp

SAMUEL PATZ, PhD
Associate Professor of Radiology
Harvard Medical School
Scientific Director, Center of Pulmonary Functional
Imaging
Brigham and Women's Hospital
221 Longwood Avenue
Boston, MA 02115
USA

Email: patz@bwh.harvard.edu

CHRISTIAN PLATHOW, MD, MSc
Assistant Professor of Radiology
Department of Nuclear Medicine
University of Freiburg
Hugstetterstrasse 55
79106 Freiburg
Germany

Email: christian.plathow@uniklinik-freiburg.de

MICHAEL PUDERBACH, MD
Department of Radiology
German Cancer Research Center (DKFZ)
Im Neuenheimer Feld 280
69120 Heidelberg
Germany

Email: m.puderbach@dkfz.de

FRANK RISSE, PhD
Department of Medical Physics in Radiology
German Cancer Research Center (DKFZ)
Im Neuenheimer Feld 280
69120 Heidelberg
Germany

Email: f.risse@dkfz.de

WOLFGANG G. SCHREIBER, PhD
Section of Medical Physics
Department of Radiology
Mainz University Hospital
Langenbeckstrasse 1
55131 Mainz
Germany

Email: wschreib@uni-mainz.de

RONALD L. SORKNESS, PhD
Professor, School of Pharmacy and
Morris Institute for Respiratory Research
600 Highland Avenue
Madison, WI 53792
USA

KOJI TAKAHASHI, MD, PhD
Associate Professor
Department of Radiology
Asahikawa Medical College
2-1-1-1 Midorigaoka-higashi
Asahikawa, 078-8510
Japan

Email: taka1019@asahikawa-med.ac.jp

RALF TETZLAFF, MD
Department of Radiology
German Cancer Research Center (DKFZ)
Im Neuenheimer Feld 280
69120 Heidelberg
Germany

Email: r.tetzlaff@dkfz.de

EDWIN J. R. VAN BEEK, MD, PhD
Professor of Radiology, Medicine and Biomedical
Engineering
Roy J and Lucille A Carver College of Medicine
University of Iowa Hospitals and Clinics
Department of Radiology
C-751 GH
200 Hawkins Drive
Iowa City, IA 52242-1077
USA

Email: edwin-vanbeek@uiowa.edu

JIM M. WILD, PhD, MINSTP
Unit of Academic Radiology
University of Sheffield
Floor C
Royal Hallamshire Hospital
Glossop Road
Sheffield S10 2JF
UK

Email: j.m.wild@sheffield.ac.uk

DIAGNOSTIC IMAGING

Innovations in Diagnostic Imaging

Edited by J.H. Anderson

Radiology of the Upper Urinary Tract

Edited by E.K. Lang

The Thymus - Diagnostic Imaging, Functions, and Pathologic Anatomy

Edited by E. Walter, E. Willich, and W.R. Webb

Interventional Neuroradiology

Edited by A. Valavanis

Radiology of the Pancreas

Edited by A.L. Baert, co-edited by G. Delorme

Radiology of the Lower Urinary Tract

Edited by E.K. Lang

Magnetic Resonance Angiography

Edited by I.P. Arlart, G.M. Bongartz, and G. Marchal

Contrast-Enhanced MRI of the Breast

S. Heywang-Köbrunner and R. Beck

Spiral CT of the Chest

Edited by M. Rémy-Jardin and J. Rémy

Radiological Diagnosis of Breast Diseases

Edited by M. Friedrich and E.A. Sickles

Radiology of the Trauma

Edited by M. Heller and A. Fink

Biliary Tract Radiology

Edited by P. Rossi

Radiological Imaging of Sports Injuries

Edited by C. Masciocchi

Modern Imaging of the Alimentary Tube

Edited by A.R. Margulis

Diagnosis and Therapy of Spinal Tumors

Edited by P.R. Algra, J. Valk, and J.J. Heimans

Interventional Magnetic Resonance Imaging

Edited by J.F. Debatin and G. Adam

Abdominal and Pelvic MRI

Edited by A. Heuck and M. Reiser

Orthopedic Imaging. Techniques and Applications

Edited by A.M. Davies and H. Pettersson

Radiology of the Female Pelvic Organs

Edited by E.K. Lang

Clinical Applications of Magnetic Resonance in Cardiovascular Disease

Edited by J. Bogaert, A.J. Duerinckx, and F.E. Rademakers

Modern Head and Neck Imaging

Edited by S. Mukherji and J.A. Castellijn

Radiological Imaging of Endocrine Diseases

Edited by J.N. Bruneton - in collaboration with B. Padovani and M.-Y. Mourou

Trends in Contrast Media

Edited by H.S. Thomsen, R.N. Muller, and R.F. Mattrey

Functional MRI

Edited by C.T.W. Moonen and P.A. Bandettini

Radiology of the Pancreas 2nd revised edition

Edited by A.L. Baert,

Co-edited by G. Delorme and L. Van Hoe

Emergency Pediatric Radiology

Edited by H. Carty

Spiral CT of the Abdomen

Edited by F. Terrier, M. Grossholz, and C. Becker

Radiology of Peripheral Vascular Diseases

Edited by E. Zeidler

Liver Malignancies

Diagnostic and Interventional Radiology

Edited by C. Bartolozzi and R. Lencioni

Medical Imaging of the Spleen

Edited by A.M. De Schepper and F. Vanhoenacker

Diagnostic Nuclear Medicine

Edited by C. Schiepers

Radiology of Blunt Trauma of the Chest

(Authors) P. Schnyder and M. Wintermark

Portal Hypertension

Edited by P. Rossi, P. Ricci, and L. Broglio

Recent Advances in Diagnostic Neuroradiology

Edited by Ph. Demaerel

Virtual Endoscopy and Related 3D Techniques

Edited by P. Rogalla, J. Terwisscha van Scheltinga, and B. Hamm

Transfontanellar Doppler Imaging in Neonates

(Authors) A. Couture and C. Veyrac

Multislice CT

Edited by M.F. Reiser, M. Takahashi, M. Modic, and R. Bruening

Diagnostic and Interventional Radiology in Liver Transplantation

Edited by E. Bücheler, V. Nicolas, C.E. Broelsch, and X. Rogiers

Pediatric Uroradiology

Edited by R. Fötter

Radiology of AIDS.

A Practical Approach

Edited by J.W.A.J. Reenders and P.C. Goodman

Pediatric Chest Imaging

Chest Imaging in Infants and Children

Edited by J. Lucaya and J.L. Strife

Radiological Imaging of the Small Intestine

Edited by N. Gourtsoyiannis

Magnetic Resonance Angiography. 2nd Revised Edition

Edited by I.P. Arlart, G.M. Bongartz, and G. Marchal

CT of the Peritoneum

(Authors) A. Rossi and G. Rossi

Pediatric ENT Radiology

Edited by S.J. King and A.E. Boothroyd

Applications of Sonography in Head and Neck Pathology

Edited by J.N. Bruneton. In Collaboration with C. Raffaelli and O. Dassonville

Radiological Imaging of the Ureter

Edited by F. Joffre and Ph. Otal

Imaging of the Knee.

Techniques and Applications

Edited by A.M. Davies and V.N. Cassar-Pullicino

Radiology of Osteoporosis

Edited by S. Grampp

Gastrointestinal Tract Sonography in Fetuses and Children

Edited by A. Couture

Imaging of Orbital and Visual Pathway Pathology

Edited by W.S. Müller-Forell

Imaging of the Larynx

Edited by R. Hermans

3D Image Processing.

Techniques and Clinical Applications

Edited by D. Caramella and C. Bartolozzi

Imaging and Intervention in Abdominal Trauma

Edited by R.F. Dondelinger

Perinatal Imaging. From Ultrasound to MR Imaging

Edited by F. Avni

Interventional Radiology in Cancer

Edited by A. Adam, R.F. Dondelinger, and P.R. Mueller

Radiological Imaging of the Neonatal Chest

Edited by V. Donoghue

Imaging of the Foot & Ankle.

Techniques and Applications

Edited by A.M. Davies, R.W. Whitehouse, and J.P.R. Jenkins

Pelvic Floor Disorders

Edited by C.I. Bartram and J.O.L. DeLancey
Associate Editors: S. Halligan, F.M. Kelvin, J. Stoker

Imaging of the Pancreas.

Cystic and Rare Tumors

Edited by C. Procacci and A. J. Megibow

High-Resolution Sonography of the Peripheral Nervous System

Edited by S. Peer and G. Bodner

Radiology of the Petrous Bone

Edited by M. Lemmerling, K. Marsot-Dupuch, and S.S. Kollias

Imaging of the Shoulder.

Techniques and Applications

Edited by A.M. Davis and J. Hodler

Duplex and Color Doppler Imaging of the Venous System

Edited by G.H. Mostbeck

Multidetector-Row CT of the Thorax

Edited by U.J. Schoepf

Functional Imaging of the Chest

Edited by H.-U. Kauczor

Radiological Imaging in Hematological Malignancies

Edited by A. Guermazi

Radiology of the Pharynx and the Esophagus

Edited by O. Ekberg

Ultrasound of the Musculoskeletal System

S. Bianchi and C. Martinoli

Coronary Radiology

Edited by M. Oudkerk

Radiology and Imaging of the Colon

Edited by A.H. Chapman

Multislice CT

2nd Revised Edition

Edited by M.F. Reiser, M. Takahashi, M. Modic, and C.R. Becker

Dynamic Contrast-Enhanced Magnetic Resonance Imaging in Oncology

Edited by A. Jackson, D. Buckley, and G.J.M. Parker

Imaging in Treatment Planning for Sinonasal Diseases

Edited by R. Maroldi and P. Nicolai

MR Imaging in White Matter Diseases of the Brain and Spinal Cord

Edited by M. Filippi, N. De Stefano, V. Dousset, and J.C. McGowan

Diagnostic Nuclear Medicine

2nd Revised Edition

Edited by C. Schiepers

Handbook of Clinical Cardiac MRI

With Interactive CD-ROM

Edited by J. Bogaert, S. Dymarkowski, and A.M. Taylor

Focal Liver Lesions

Detection, Characterization, Ablation

Edited by R. Lencioni, D. Cioni, and C. Bartolozzi

Multidetector-Row CT Angiography

Edited by C. Catalano

Radiology of the Stomach and Duodenum

Edited by A.H. Freeman and E. Sala

Paediatric Musculoskeletal Disease

Edited by D.J. Wilson

Magnetic Resonance Imaging in Ischemic Stroke

Edited by R. von Kummer and T. Back

Contrast Media in Ultrasonography

Basic Principles and Clinical Applications

Edited by E. Quaia

Imaging of the Hip & Bony Pelvis

Techniques and Applications

Edited by A.M. Davies, K.J. Johnson, and R.W. Whitehouse

Vascular Embolotherapy

Volume 1: A Comprehensive Approach

Edited by J. Golzarian, S. Sun, and M. Sharafuddin

Vascular Embolotherapy

Volume 2: A Comprehensive Approach

Edited by J. Golzarian, S. Sun, and M. Sharafuddin

Imaging of Kidney Cancer

Edited by A. Guermazi

Imaging of Occupational and Environmental Disorders of the Chest

Edited by P.A. Gevenois and P. De Vuyst

Contrast Media

Safety Issues and ESUR Guidelines

Edited by H.S. Thomsen

Virtual Colonoscopy

A Practical Guide

Edited by P. Lefere and S. Gryspeerdt

Spinal Imaging

Diagnostic Imaging of the Spine and Spinal Cord

Edited by J.W.M. Van Goethem, L. Van den Hauwe, and P.M. Parizel

Head and Neck Cancer Imaging

Edited by R. Hermans

Vascular Interventional Radiology

Angioplasty, Stenting, Thrombolysis and Thrombectomy

Edited by M. Cowling

Radiology of Osteoporosis

2nd Revised Edition

Edited by S. Grampp

Radiological Imaging of the Digestive Tract in Infants and Children

Edited by A.S. Devos and J.G. Blickman

MRI and CT of the Female Pelvis

Edited by B. Hamm and R. Forstner

Percutaneous Tumor Ablation in Medical Radiology

Edited by T.J. Vogl, T. Helmberger, M.G. Mack, and M.F. Reiser

Ultrasound of the Gastrointestinal Tract

Edited by G. Maconi and G. Bianchi Porro

Radiation Dose from Pediatric and Adult Multidetector Computed Tomography

Edited by D. Tack and P.A. Gevenois

Parallel Imaging in Clinical MR Applications

Edited by S.O. Schoenberg, O. Dietrich, and M.F. Reiser

Imaging of Orthopedic Sports Injuries

Edited by F.M. Vanhoenacker, M. Maas, J.L.M.A. Gielen

Clinical Functional MRI

Presurgical Functional Neuroimaging

Edited by C. Stippich

Screening and Preventive Diagnosis with Radiological Imaging

Edited by M.F. Reiser, G. van Kaick, C. Fink, and S.O. Schoenberg

Computed Tomography of the Lung

A Pattern Approach

J.A. Verschakelen and W. De Wever

Imaging in Transplantation

Edited by A. Bankier

Imaging in Percutaneous Musculoskeletal Interventions

Edited by A. Gangi, S. Guth, and A. Guermazi

Imaging of the Pancreas Acute and Chronic Pancreatitis

Edited by E.J. Balthazar, A.J. Megibow, and R. Pozzi Mucelli

Image Processing in Radiology

Current Applications

Edited by E. Neri, D. Caramella, and C. Bartolozzi

Measurements in Musculoskeletal Radiology

Edited by V.N. Cassar-Pullicino and A.M. Davies

Pediatric Chest Imaging

2nd Revised Edition

Chest Imaging in Infants and Children

Edited by J. Lucaya and J.L. Strife

Radiological Imaging of the Neonatal Chest

2nd Revised Edition

Edited by V. Donoghue

Imaging in Pediatric Skeletal Trauma

Techniques and Applications

Edited by K.J. Johnson and E. Bache

Pediatric Uroradiology

2nd Revised Edition

Edited by R. Fötter

Color Doppler US of the Penis

Edited by M. Bertolotto

Liver Radioembolization

with Y90 Microspheres

Edited by J.I. Bilbao and M.F. Reiser

High Resolution Sonography

of the Peripheral Nervous System

2nd Revised Edition

Edited by S. Peer and G. Bodner

Imaging Pelvic Floor Disorders

2nd Revised Edition

Edited by J. Stoker, S. Taylor, J. O. L. DeLancey

Intracranial Vascular Malformations and Aneurysms

From Diagnostic Work-Up to Endovascular Therapy

2nd Revised Edition

Edited by M. Forsting and I. Wanke

Coronary Radiology

2nd Revised Edition

Edited by Matthijs Oudkerk and Maximilian F. Reiser

Cardiothoracic Imaging with MDCT

Edited by M. Rémy-Jardin and J. Rémy

Multislice CT

3rd Revised Edition

Edited by M.F. Reiser, C.R. Becker, K. Nikolaou, and G. Glazer

MRI of the Lung

Edited by H.-U. Kauczor

Imaging in Percutaneous Musculoskeletal Interventions

Edited by A. Gangi, S. Gutly and A. Guermazi

RADIATION ONCOLOGY

Lung Cancer

Edited by C.W. Scarantino

Innovations in Radiation Oncology

Edited by H.R. Withers and L.J. Peters

Radiation Therapy of Head and Neck Cancer

Edited by G.E. Laramore

Gastrointestinal Cancer - Radiation Therapy

Edited by R.R. Dobelbower, Jr.

Radiation Exposure and Occupational Risks

Edited by E. Scherer, C. Streffer, and K.-R. Trott

Radiation Therapy of Benign Diseases - A Clinical Guide

S.E. Order and S.S. Donaldson

Interventional Radiation Therapy Techniques - Brachytherapy

Edited by R. Sauer

Radiopathology of Organs and Tissues

Edited by E. Scherer, C. Streffer, and K.-R. Trott

Concomitant Continuous Infusion Chemotherapy and Radiation

Edited by M. Rotman and C.J. Rosenthal

Intraoperative Radiotherapy - Clinical Experiences and Results

Edited by F.A. Calvo, M. Santos, and L.W. Brady

Radiotherapy of Intraocular and Orbital Tumors

Edited by W.E. Alberti and R.H. Sagerman

Interstitial and Intracavitary Thermo-radiotherapy

Edited by M.H. Seegenschmiedt and R. Sauer

Non-Disseminated Breast Cancer Controversial Issues in Management

Edited by G.H. Fletcher and S.H. Levitt

Current Topics in Clinical Radiobiology of Tumors

Edited by H.-P. Beck-Bornholdt

Practical Approaches to Cancer Invasion and Metastases

A Compendium of Radiation Oncologists' Responses to 40 Histories

Edited by A.R. Kagan with the Assistance of R.J. Steckel

Radiation Therapy in Pediatric Oncology

Edited by J.R. Cassady

Radiation Therapy Physics

Edited by A.R. Smith

Late Sequelae in Oncology

Edited by J. Dunst and R. Sauer

Mediastinal Tumors. Update 1995

Edited by D.E. Wood and C.R. Thomas, Jr.

Thermoradiotherapy and Thermochemotherapy

Volume 1: Biology, Physiology, and Physics
Volume 2: Clinical Applications

Edited by M.H. Seegenschmiedt, P. Fessenden, and C.C. Vernon

Carcinoma of the Prostate Innovations in Management

Edited by Z. Petrovich, L. Baert, and L.W. Brady

Radiation Oncology of Gynecological Cancers

Edited by H.W. Vahrson

Carcinoma of the Bladder Innovations in Management

Edited by Z. Petrovich, L. Baert, and L.W. Brady

Blood Perfusion and Microenvironment of Human Tumors

Implications for Clinical Radiooncology

Edited by M. Molls and P. Vaupel

Radiation Therapy of Benign Diseases. A Clinical Guide

2nd revised edition
(Authors) S.E. Order and S.S. Donaldson

Progress and Perspectives in the Treatment of Lung Cancer

Edited by P. Van Houtte, J. Klasterksy, and P. Rocmans

Combined Modality Therapy of Central Nervous System Tumors

Edited by Z. Petrovich, L.W. Brady, M.L. Apuzzo, and M. Bamberg

Age-Related Macular Degeneration. Current Treatment Concepts

Edited by W.E. Alberti, G. Richard, and R.H. Sagerman

Radiotherapy of Intraocular and Orbital Tumors

2nd revised edition
Edited by W.E. Alberti and R.H. Sagerman

Clinical Target Volumes in Conformal and Intensity Modulated Radiation Therapy

A Clinical Guide to Cancer Treatment
Edited by V. Grégoire, P. Scalliet, and K.K. Ang

Palliative Radiation Oncology

(Authors) R.G. Parker, N.A. Janjan, and M.T. Selch

Modification of Radiation Response

Edited by C. Nieder, L. Milas, and K.K. Ang

Advances in Radiation Oncology in Lung Cancer

Edited by B. Jeremic

Technical Basis of Radiation Therapy Practical Clinical Applications

4th Revised Edition

Edited by S.H. Levitt, J.A. Purdy, C.A. Perez, and S. Vijayakumar

New Technologies in Radiation Oncology

Edited by W. Schlegel, T. Bortfeld, and A.-L. Grosu

Medical Radiology volume on Multimodal Concepts for Integration of Cytotoxic Drugs and Radiation Therapy

Edited by J.M. Brown, M.P. Mehta, and C. Nieder

Clinical Practice

of Radiation Therapy for Benign Diseases Contemporary Concepts and Clinical Results

Edited by M. H. Seegenschmiedt, H.-B. Makoski, K.-R. Trott, and L.W. Brady

CURED I – LENT - Late Effects of Cancer Treatment on Normal Tissues

Edited by P. Rubin, L.S. Constine, L.B. Marks, and P. Okunieff

CURED II LENT - Cancer Survivorship Research and Education

Late Effects of Cancer Treatment on Normal Tissues

Edited by P. Rubin, L.S. Constine, L.B. Marks, and P. Okunieff

Radiation Oncology

An Evidence-Based Approach

Edited by J.J. Lu and L.W. Brady

Primary Optic Nerve Sheath Meningioma

Edited by B. Jeremić and S. Pitz